INTERDISCIPLINARY APPLIED MATHEMATICS

MATHEMATICAL BIOLOGY

Keizer's

Computational Cell Biology

An introduction to mathematical modeling
in molecular cell biology

Contents

CHAPTER 1

Dynamic Phenomena in Cells

07-28

Over the past several decades, progress in the measurement of rates of molecular and cellular processes combined with rapid advances in computer technology has initiated a revolution in our understanding of dynamic phenomena in cells. Generally speaking, the phrase *dynamic phenomenon* refers to any process or observable that changes over time. Dynamic phenomena include changes that occur in single cells, such as spikes or bursts of plasma membrane electrical activity, intracellular signaling via receptors and second messengers, or more complex processes that involve small clusters of cells, organelles, or groups of neurons. These clusters may work as signal transduction elements, like pancreatic islets that respond to an elevation of blood glucose levels by secreting insulin, or in a network like neuronal cells that either produce or process electrical and neurochemical signals. Some of the diverse dynamic phenomena that can be treated by the computational and analytical methods outlined in this book are described in this chapter.

1.1 Scope of Cellular Dynamics

Living cells are inherently dynamic. Indeed, to sustain the characteristic features of life such as growth, cell division, intercellular communication, movement, and responsiveness to their environment, cells must continually extract energy from their surroundings. This requires that cells function thermodynamically as open systems that are far from thermal equilibrium. Much energy is utilized by cells in the maintenance of gradients of ions and metabolites necessary for proper function. These processes are inherently

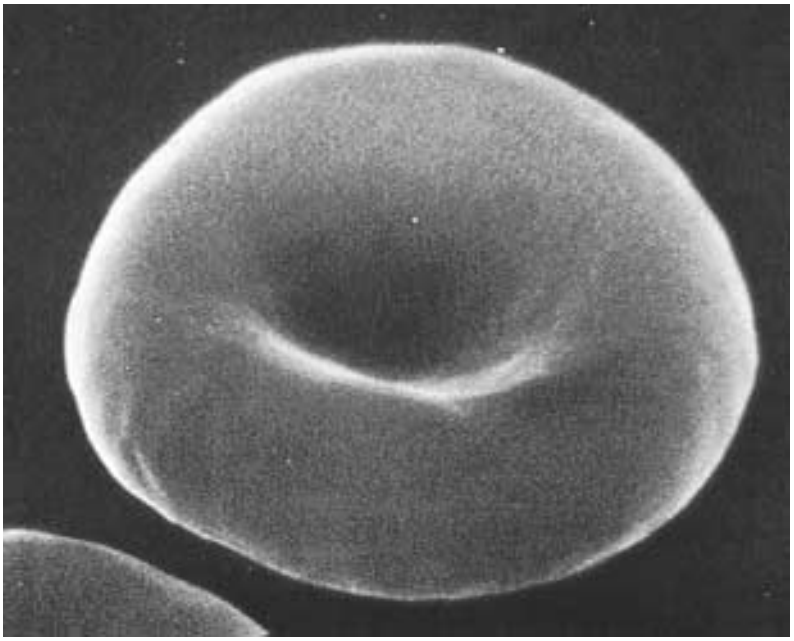

Figure 1.1 A normal red blood cell with its characteristic discoid shape. The cell is approximately 5 μm in diameter. Adapted from A. J. Grimes, *Human Red Cell Metabolism*, Blackwell Sci. Pub., 1980, pg. 58.

dynamic due to the continuous movement of ionic and molecular species across the cell membrane.

A red blood cell, for example, takes up glucose from the blood plasma and uses glycolytic enzymes to convert energy from carbon and oxygen bonds to phosphorylate adenosine diphosphate (ADP) and produce the triphosphate ATP. The ATP, in turn, is utilized to pump Ca^{2+} and Na^{+} ions from the cell and K^{+} ions back into the cell, in order to maintain the osmotic balance that helps give red cells the characteristic shape shown in Fig. (1.1). ATP is also used to maintain the concentration of 2,3-diphosphoglycerate, an intermediary metabolite that regulates the oxygen binding conformation of hemoglobin. The final products of glucose metabolism in red cells are pyruvate and lactate, which move passively out of the cell down a concentration gradient through specific transporters in the plasma membrane. Since red cells possess neither a nucleus nor mitochondria, they are not capable of cell division nor more energetically demanding processes. Nonetheless, the continual energy flow maintains the capacity of red cells to shuttle oxygen and carbon dioxide between the lungs and the capillaries. Remarkably, this is carried out in a cell that is only 5 μm across, with a volume of less than 10^{-14} L. In later chapters we will discuss models for the transport of glucose and ions through channels.

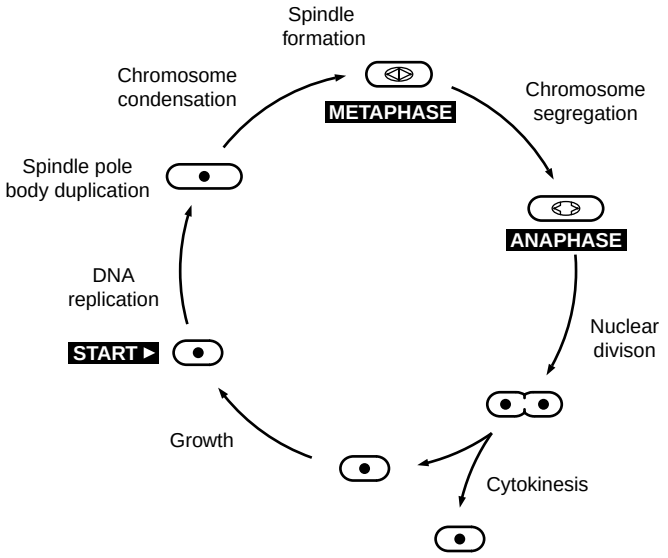

Figure 1.2 The cell division cycle in fission yeast. Spindle formation initiates metaphase, where condensed chromosomes pair up for segregation into daughter cells. The cycle is completed when cytokinesis cleaves the dividing cell.

The **cell division cycle** is an ubiquitous dynamical feature of *eukaryotic* cells, or cells with nuclei. Fig. (1.2) shows the cycle of events that occur each time a eukaryotic cell divides via mitosis. The cell cycle is comprised of a regular sequence of events as shown in the figure: chromosome replication during a restricted period of the cycle (S phase), chromosome segregation during metaphase and anaphase (M phase), and finally *cytokinesis*, in which two daughter cells separate. This cycle involves a cascade of molecular events that center around the proteins *cdc2* and *cyclin*, which make up a complex known as *M phase promoting factor*, or *MPF*. This complex has been shown to oscillate in synchrony with cell division and to be regulated by a series of phosphorylation and dephosphorylation reactions. Related dynamical changes occur during *meiosis*, in which germ line cells produce eggs and sperm. We will discuss models of the cell cycle oscillator in detail in a Chapter (**??**). After DNA replication is complete, each chromosome consists of two "sister chromatids" which must be separated during mitosis so that each daugher nucleus gets one and only one copy of each chromosome. Segregation of sister chromatids during mitosis is another complex dynamical process that involves self-organizing structures in the cell that work to pull sister chromatids apart. This process is guided by microtubules that form a bipolar spindle, with one chromatid attached by microtubules to one pole and the other sister chromatid attached to the other pole. This wonderfully coordinated dynamical behavior is just one of many examples of motile cellular processes. Other important examples include muscle contraction, cell movement, and projections of cell membrane called *pseudopodia*.

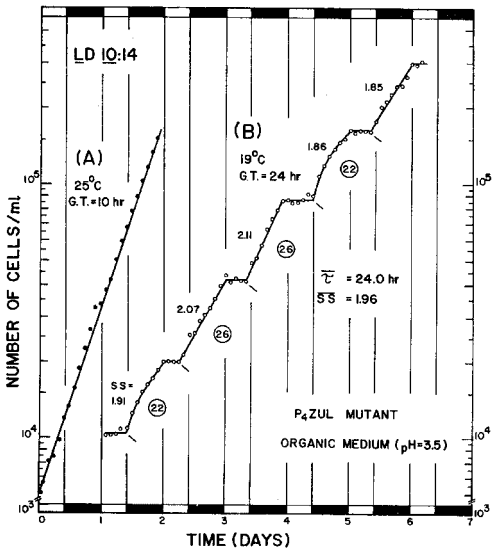

Figure 1.3 Population growth of a mutant *Euglena* strain shows log growth at 25°C independent of the light/dark cycle, indicated by the alternating light/dark bands on the time axis. At 19°C a circadian (approximatly 24 hour) growth rhythm develops that entrains with the light/dark cycle. Adapted from L. N. Edwards, Jr., *Cellular and Molecular Bases of Biological Clocks*, Springer, 1988, pg. 161.

These processes will discussed at length in Chapter (**??**).

Circadian rhythms are regular changes in cellular processes that have a period of about 24 hours (from the Latin *circa*, about + *dies*, day)and represent another dynamical phenomenon that is widely observed in cells. A great deal about the mechanisms of circadian rythms has been uncovered in recent years, and circadian biology offers a rich source of unsolved modeling problems. Internal clocks provide the ability to *predict changes in an organism's environment*, and are manifest in diverse examples ranging from the eclosion of populations of insects to hormonal regulation in mammals. Data on the growth cycle in a population of *Euglena* cells is plotted in Fig. 1.4, with the logarithm of the number of cells on the ordinate and the time in days on the abscissa. The dark/light bands correspond to periods of absence and presence of light that simulate the normal dark/light cycle during a day. As shown in Fig. (1.3), the growth rate of *Euglena* is temperature dependent and cell division only sychronizes to a 24 hour dark/light cycle when the temperature is in the range found in its natural environment. At this temperature the population doubling time is close to 24 hours. Recent experiments with the fruit fly *Drosophila* and other organisms suggest that circadian rhythms like this are controlled by oscillations in gene transcription. Further consideration of Circadean Rythms will be given in Chapter (**??**).

Electrical activity of excitable cells is a widely studied example of cellular dynamics. Experimental measurements of the membrane potential of insulin secreting cells in the pancreas have revealed regular bursts of electrical activity stimulated by increases in blood glucose levels. These oscillations occur at physiological levels of glucose, as shown in the microelectrode recordings from a pancreatic beta cell in an anesthetized rat in Fig. (1.4). Recent work *in vitro* has shown that the rapid spikes of

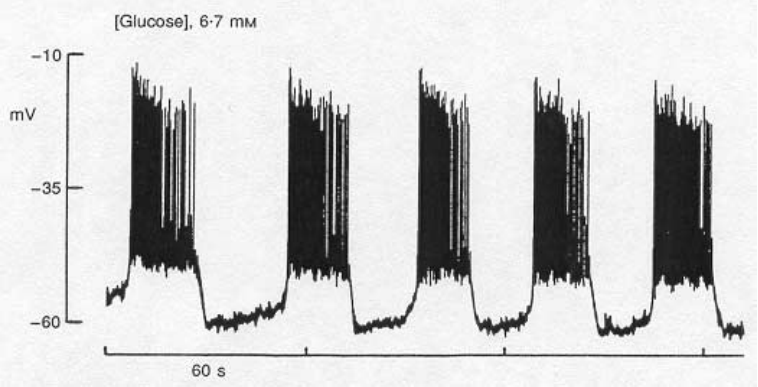

Figure 1.4 Periodic bursts of electrical activity recorded *in vivo* from a pancreatic beta cell from the intact pancreas of an anesthetized rat. Adapted from J. V. Sanchez-Andres, A. Gomis, and M. Valdeolmillos, The electrical activity of mouse pancreatic beta-cells recorded in vivo show glucose-dependent oscillations. J. Physiol. (London) 486:223-228 (1995.)

electical activity, known as *action potentials*, are caused by rapid influx of Ca^{2+} from the exterior of the beta cell followed by a slower efflux of K^+. The periods of rapid spiking are referred to as *active phases* of the burst, which are separated by intervals referred to as *silent phases*. A variety of mechanisms have been proposed to explain bursting behavior, and computer models of bursting were the first to predict that oscillations of Ca^{2+} within the cytoplasm should occur in phase with the electrical activity. Oscillations in Ca^{2+} were recorded for the first time *in vitro* eight years after they were predicted by Chay and Keizer. These oscillations are important physiologically, since cytoplasmic Ca^{2+} plays a major role in triggering insulin secretion. This topic will be revisited in Chapter 5.

Complex electrical activity is a hallmark of electrical signals in neuronal cells as well. The classical behavior of an action potential in the squid giant axon is shown in Fig. (1.5). This single spike of electrical activity, initiated by a small positive current applied by an external electode, propagates as a traveling pulse along the axonal membrane. Hodgkin and Huxley were the first to propose a satisfactory explanation for action potentials that incorporated experimental measurements of the response of the squid axon to steady depolarizations (positive deviations) of the membrane potential. The Hodgkin-Huxley model involves Na^+ and K^+ currents that are regulated by membrane potential and we will describe related models in Chapter (2).

The control of cellular processes by interlocking molecular mechanisms can also produce oscillatory Ca^{2+} signals that are independent of electrical activity. Fig. (1.6) shows the spiral pattern of cytoplasmic Ca^{2+} oscillations that occurs when an immature *Xenopus leavis* egg (an *oocyte*) is stimulated by a microinjection of inositol 1,4,5-trisphosphate (IP_3). IP_3 is a phospholipid membrane metabolite that is widely involved in signalling by receptors in the plasma membrane and that triggers release of

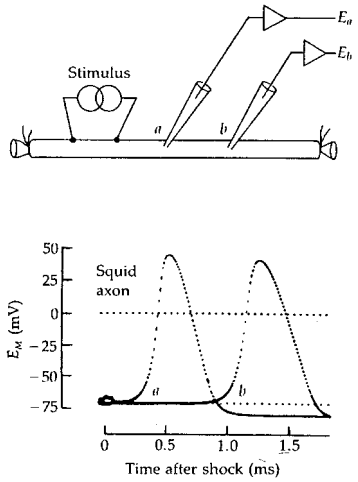

Figure 1.5 Upper Panel: Schematic diagram of the recording electrodes (a and b) used to detect action potentials following a stimulus shock in an isolated giant axon from squid. Lower Panel: The membrane potential recorded at electrodes a and b in the upper panel following a depolarizing shock. Adapted from B. Hille, *Ionic Channels of Excitable Membranes*, 2nd ed, Sinauer, 1992, pg. 25.

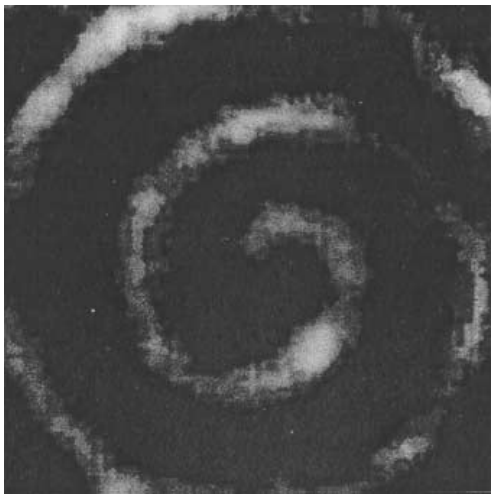

Figure 1.6 A spiral wave of Ca^{2+} ions detected as the bright fluorescence from an indicator dye after microinjection of IP_3 into an immature frog egg. Adapted from J. D. Lechleiter and D. E. Clapham, Molecular mechanisms of intracellular calcium excitability in *X. laevis* oocytes. Cell 69:283-294 (1992).

Ca^{2+} from the *endoplasmic reticulum* (ER). The ER is an intracellular compartment that functions as a storage region for Ca^{2+}, maintaining a total internal concentration that is comparable to the external medium (*ca.* 5mM). The spiral waves of Ca^{2+} in *Xenopus* oocytes can be explained quantitatively by kinetic models of the feedback mechanisms responsible for uptake and release of Ca^{2+} from the ER. Simple models of regenerative Ca^{2+} release that are solved on a spatial domain provide insight to the processes of *self organization* that result in spiral waves.

Theses examples of cellular systems provide only a glimpse of the complex dynamical behavior that has been observed in living cells. In the next section we turn

our attention to computer models and how they can be used to help explain dynamic phenomena in cells.

1.2 Role of Theory and Computation

Even the simplest of the dynamic phenomena described in the previous section are exceedingly complex, and computer models have proven to be an important tool in helping to dissect the molecular processes that control their time evolution. In the physical sciences, theoretical methods in combination with experimental measurements have provided rich insights into phenomena for many years. The abundance of quantitative experimental data that are now available at the cellular level have opened the door to a similar collaboration in neurobiology and cell physiology. The challenge in biology, however, is usually much greater than in the physical sciences because the number of molecular mechanisms and component molecular species uncovered in cells has become staggering.

Nonetheless, the interplay of experiment, theory, and computation follows a conceptual framework similar to that which has proven successful in the physical sciences:

1. Taking clues from experiment, the first step is to sort through possible molecular mechanisms and focus on the most plausible ones. Ideally, this step involves close consultation with experimentalists working on the problem.
2. The selection of mechanisms defines the basis for a schematic representation, or *cartoon*, that depicts the overall model. To be useful the cartoon should be explicit enough that it can, in turn, be translated into a series of elementary steps representing the individual mechanisms.
3. Because of their origin in molecular processes, the basic laws of physics and chemistry can be used to translate the individual mechanisms depicted in the cartoon into mathematical expressions.
4. The individual mechanisms are then combined into time dependent differential equations that quantify the changes described by the whole model.
5. Finally, a careful study of the differential equations must reveal useful information about the system.

The challenge of the theorist in biology then becomes similar to that in astrophysics or quantum mechanics: to analyze the equations, simplify them if possible, solve them, and, most importantly, make predictions that can be tested with further experiment. Further experiments may uncover inconsistencies in a model that will require changes. The process that we have outlined above and will revisit in later chapters is interative cycle of ever-improving approximation where the mathematical or computer model plays the role of a quantitative hypothesis.

The field of computational cell physiology would not be possible without the use of computers. Advances in both computer hardware and numerical analysis have made

the solution of complicated systems of ordinary differential equations fast, accurate and relatively easy. Indeed, the role of computation is critical since the differential equations describing biological processes nearly always involve control mechanisms that have nonlinear components. Simple linear differential equations often can be solved analytically, which means that we can obtain an exact solution using traditional mathematical methods. Nonlinearities often make it difficult or impossible to obtain an exact solution; however, we can obtain quite good estimates using numerical methods implemented on computers. Spatial variation is often an important feature in cellular mechanisms, so one is confronted with analyzing and solving spatially explicit *partial differential equations*, which are still more complicated and less analytically tractable than ODEs.

Computer models permit one to test conditions that may at present be difficult to attain in the laboratory or that simply have not yet been examined by experimentalists. Each numerical solution of the differential equations, therefore, can provide a *simulation* of a potential laboratory experiment. These simulations can be used to help assess parameters, such as diffusion constants or kinetic constants, that may be difficult to measure experimentally. Numerical simulations can test how intervention by pharmacological agents might affect a processes. With simulations one can test specific hypotheses about the role of individual mechanistic components or make predictions about variables that can be tested in the laboratory. Often the most important result of a simulation is negative: a well crafted model can rule out a particular mechanism as a possible explanation for experimental observations.

The scope of mathematical techniques employed to investigate problems in mathematical biology spans almost all of applied mathematics. The problems that are covered in this book involve properties of cells that change in a prescribed way over time. We use the language of *differential equations* to describe the behavior of dynamical systems with time. Mathematicians have developed techniques for the analysis of systems of differential equations that describe complex interrelated processes.

While the modeling of processes is discussed in detail, only the basics of the mathematics and the elementary tools for the analysis of these models are introduced. Rigorous analysis of complicated differential equations requires specialized training, since there are many subtleties that are appreciated only with experience. While the creation and manipulation of simple models is within the reach of all cell biologists, the careful scientist will seek collaborations with experienced mathematicians, particularly for the valid simplification of complicated models into more tractable ones. In the middle ground between established disciplines such as biology and mathematics, fruitful scientific work can be done, and all parties gain valuable insight from the interdisciplinary experience.

1.3 Cartoons, Mechanisms and Models

In this section we illustrate with a simple model of ion channel gating the kinds of phenomenon that are investigated in detail in subsequent chapters. We introduce some

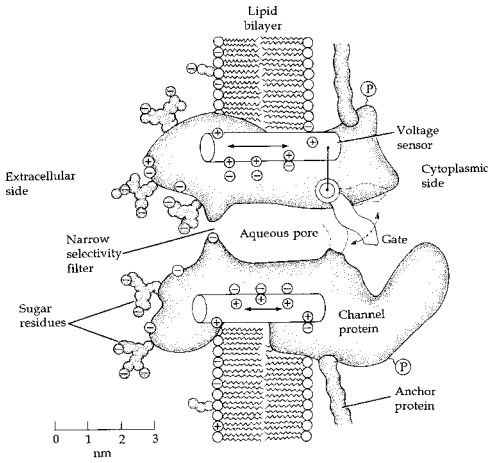

Figure 1.7 Mechanistic cartoon of a gated ionic channel showing an aqueous pore that is selective to particular types of ions. The portion of the transmembrane protein that forms the "gate" is sensitive to membrane potential, allowing the pore to be in an open or closed state. Taken from B. Hille, *Ionic Channels of Excitable Membranes*, 2nd ed, Sinauer, 1992, pg. 66.

of the methods underlying the analysis of these models and also try to demonstrate the basic conceptual modeling framework utilized throughout the book.

We begin with a simple channel because it is an intuitively clear example of transition between different molecular states corresponding to different conformations of a macromolecule. For simplicity, we are going to ignore the ion current flowing through such a channel as well as the concept of voltage dependence until Chapter (2). The simplest cartoon of gating is a channel with two states, one with the pore open and the other with it closed, corresponding to the mechanism shown in Fig. (1.7). This kinetic "cartoon" is easily translated into a conventional kinetic model of the sort often employed in biochemistry.

Here the model takes the form of the diagram in Fig. (**??**). Diagrams like this, which will be used extensively in this book, represent molecular states or entities by symbols and transitions between states by solid lines. The letters in Fig. (**??**) correspond to the open and closed states of the channel and the lines represent elementary molecular processes. The transitions between O and C are *unimolecular* process since they involve only the channel molecule (*bimolecular* processes will be introduced in Chapter (3)). An important aspect of transitions between molecular states is that they are reversible, which is a consequence of microscopic reversibility of molecular processes.

These states represent a complex set of underlying molecular states in which the pore is either permeable or impermeable to ionic charge.

$$C \leftrightarrow O, \tag{1.1}$$

Using the patch clamp, transitions between closed and open states can be measured for single ion channels. However, here the focus is on the average change for a collection of ion channels. Since it is not unusual to have several thousand ion channels of a given type in the plasma membrane of a cell, the average behavior of the entire ensemble of

channels is often what determines the cellular dynamics. This concept will be discussed in detail in Chapter (12).

The rates of the elementary processes denoted in the kinetic diagram are determined by the so-called *law of mass action*. (Despite the name, mass action is not technically a physical law, but rather is a constitutive relation which holds as a very good approximation for any well mixed system.) This "law", which dates back to the early studies of chemical kinetics, states that the rate of a processes is proportional to the product of the concentrations of the molecular species involved in the process. Thus the rate of the transition from state C to state O is given by $J_+ = k^+[C]$, where the square brackets denote concentration, with $[C]$ representing the concentration of channel molecules in state C. The factor k^+ is the rate constant, in this case unimolecular, with practical units of s^{-1}. Similarly the rate of the reverse reaction, $O \leftarrow C$, is given by $J_- = k^-[O]$ with k^- a unimolecular rate constant (with units s^{-1}).

The law of mass action is a specific example of a more general relationship that underlies the dynamics of all physicochemical processes. In its most general form these rate expressions are interpreted as probability transition rates. As described in Chapter (12), rate expressions give information about the probability of transitions between the molecular states of an individual channel. However, they also provide information about the average number of transitions per unit time for an ensemble of channels, and that is how we will use the rate expressions here.

To translate the mechanism in Fig. (**??**) into an equation, the law of mass action is applied to the concentration of channels in states C and O. For cellular transport mechanisms, a variety of measures of "concentration" can be used. For example, if the channels are in intact cells, concentration is often expressed in terms of total cell volume. Another measure in common use involves total weight of protein in a sample. The total number of transporters, N, is useful for single cells. Here we choose the latter to define concentration so that $[O] = n_O = N_O/N$, where the lowercase n will refer to the fraction of closed channels and N is the total number or channels. Since the kinetic model involves only interconversion of channel states, the total number of channels should be preserved. This introduces the idea of a conservation law, $N_C + N_O = N$, that channels are neither created nor destroyed. This implies that one of the dependent variables can be eliminated using the conservation law, say, $N_C = N - N_O$. The differential equation for N_C therefore becomes redundant and the number of differential equations to be solved is reduced to only one along with the algebraic equation for N_C. The fraction of channels in the closed state is, therefore, $1 - n_O$.

Having established the correspondence of the diagram with rate expressions, it is easy to write down the differential equations that the diagram represents. To do so one must keep track of the change that each elementary process in the diagram makes for each state, which we refer to as a it flux. Thus the process connecting states O and C causes a loss of state O in the reverse direction and a gain in the forward direction. These small, whole numbers that correspond to losses or gains of a state (*e.g.*, -1 for state C in the process $C \rightarrow O$) are called the *stoichiometric coefficients* for the mechanism. Using the coeficients in conjunction with the kinetic diagram, the ordinary differential

equations follow for the rate of change in the states:

$$flux\ O \rightarrow C = j_- = k^- n_O$$

$$flux\ C \rightarrow O = j_+ = k^+(1 - n_O)$$

$$change\ in\ n_O = j_+ - j_-$$

$$\begin{aligned} \frac{dn_O}{dt} &= j_+ - j_- \\ &= -k^- n_O + k^+(1 - n_O) \\ &= -(k^- + k^+)(n_O - \frac{k^+}{(k^- + k^+)}) \end{aligned} \tag{1.2}$$

or, defining $\tau = \frac{1}{(k^- + k^+)}$ and $n_\infty = \frac{k^+}{(k^- + k^+)}$,

$$\frac{dn_O}{dt} = \frac{-(n_O - n_\infty)}{\tau}. \tag{1.3}$$

Channels may be comprised of multiple subunits that behave similarly. This fraction can be derived from a model like that in Fig. (**??**) if it is assumed that the protein consists of independent, identical subunits, each of which has to be in the state O for the channel to be open. Thus the underlying dynamics for the state of each subunit still satisfies Eqn. (1.3), but now n_O gives only the fraction of the *subunits* in state O. To get the the fraction of open *channels*, we use the assumption that the subunits are identical and independent. Thus the open fraction of channels is the product of the fractional occupancies of all subunits. For a 4 subunit (tetrameric) channel, the fraction of open channels would be ${n_O}^4$. This topic will be covered in detail in Chapter (2).

The example we have presented here shows the basic framework under which all of the models in this book are developed and understood. With the formulation of the model equations, the first steps in the modeling process are completed. What remains is the analysis of the equations. A detailed discussion of some of the basic terminology and techniques involved in the solution of these and more complicated equations that frequently arise in the modeling process are developed and discussed in Appendix (A).

1.4 Solving and Analyzing Differential Equations

Many students have worked with differential equations quite often without being aware of it in their study of physical sciences or elementary mathematics and they may have been introduced to solution techniques explicitly in an advanced calculus course. In general, the differential equations that arise for the rate of change in cellular properties will be complicated and difficult or impossible to solve exactly using analytical

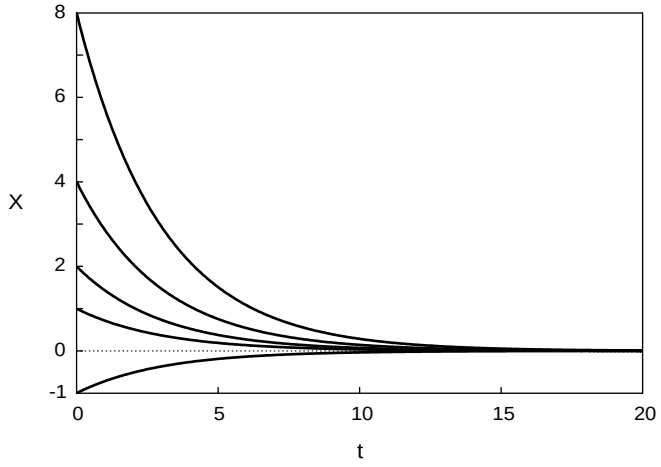

Figure 1.8 A selection from the family of solutions to equation (1.3) for $\tau = 2$.

techniques. Consider the simple linear equation:

$$\frac{dX(t)}{dt} = \frac{-X(t)}{\tau} \tag{1.4}$$

Eqn. (1.4) says that we are seeking a function $X(t)$ whose derivative is proportional to itself with proportionality constant $1/\tau$. Remembering that the derivative of the exponential function is still an exponential function, a good guess is that the exact solution to Eqn. (1.4) is

$$X(t) = X_o e^{-t/\tau} \tag{1.5}$$

It can be verified that Eqn. (1.5) is indeed a solution of Eqn. (1.4) by differentiating the solution with respect to t, thereby recovering our original equation:

$$\frac{dX(t)}{dt} = \frac{d}{dt}(X_o e^{-t/\tau}) = -\frac{1}{\tau}(X_o e^{-t/\tau}) = \frac{-X(t)}{\tau} \tag{1.6}$$

Because the same differential equation describes how a variable changes no matter where it begins initially, the solution for a differential equation has to prescribe both how a variable evolves and at what value it begins. Thus there are a family of solutions to a differential equation and the correct one is chosen by specifying an it initial condition such as X_o in Eqn. (1.6). This is an important concept that is particularly relevant to the numerical solution of differential equations. Representatives from the family of exact solutions for different values of X_o are shown in figure Fig. (1.8) for $\tau = 2$. *talk about tau and t1/2*

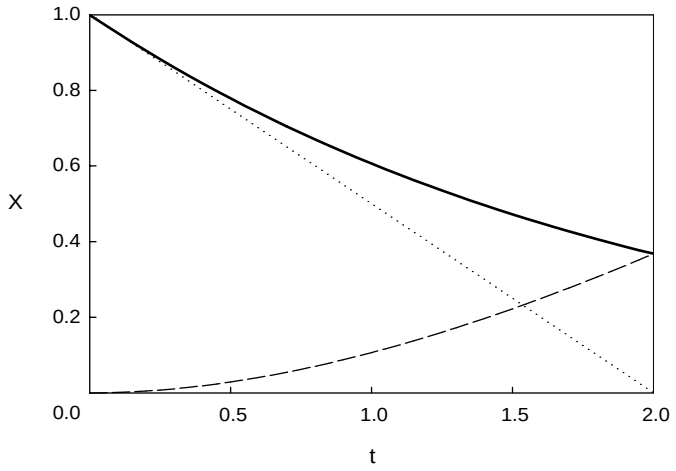

Figure 1.9 The Euler method of numerical integration relies upon a series of short linear approximations using the derivative at the old time point. The solution to equation (1.3) with $\tau = 2$ is shown in solid, the linear approximation using the derivative at $t = 0$ (-0.5)is shown in dots, and the difference between these two curves is shown in dashes. Note that, by $t = 2$, the error between the actual and approximate functions is equal to the value of the actual funtion.

1.4.1 Numerical Integration of Differential Equations

Even if Eqn. (1.4) were more complicated and could not be solved exactly, a numerical approximation can still be calculated. The simplest and perhaps the oldest method of numerical solution goes back to the mathematician Euler and is easy to understand. The method is called the *forward Euler* method and it is the prototype for all other methods of solving ODEs numerically. Consider the differential equation 1.20, but approximate the derivative by

$$\frac{dX}{dt} \approx \frac{\Delta X}{\Delta t} = \frac{X(t + \Delta t) - X(t)}{\Delta t} \tag{1.7}$$

where ΔX and Δt are small, but not infinitessimal like the differentials dX and dt. If this approximation to the derivative is substituted into the differential equation, the resulting equation can bew solved for $X(t + \Delta t)$ giving,

$$X(t + \Delta t) = X(t) - X(t)\Delta t/\tau. \tag{1.8}$$

The smaller Δt is, the better the Euler approximation of the derivative is. Also, because the Euler approximation gives a piecewise linear estimate of the solution, the farther from linear the problem is, the smaller Δt must become to give an acurate solution. The essence of numerical integration is that we start at some value and crawl along the solution in increments of Δt by estimating the change over that interval. If Δt is very small, our estimate of the rate of change is good and our solution is accurate but it may take a very long time to compute the solution. This is termed *computationally*

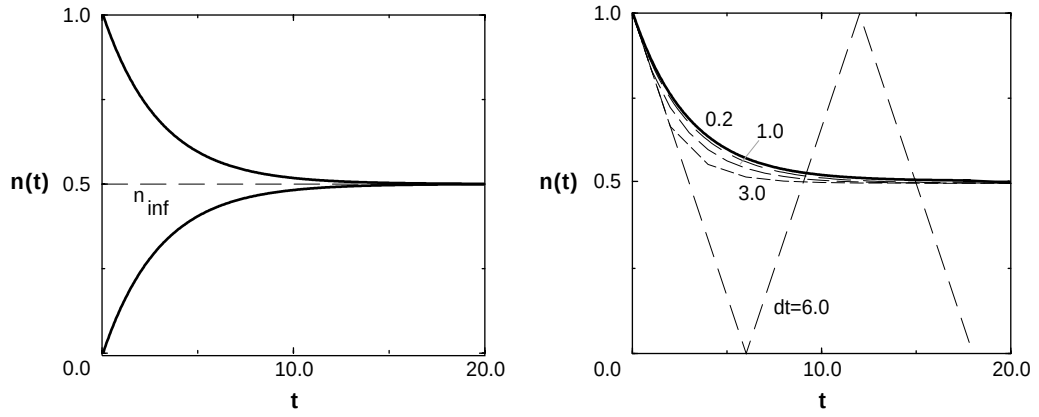

Figure 1.10 Panel A: The exponential decay of the open fraction of channels. Initial conditions at either 1 or 0 both decay to the steady state value of 0.5. Panel B: The effect of the step size in the Euler method for the simulation in Panel A starting with the initial condition $n(0) = 1$. The exact solution, $n(t) = 0.5(1 + \exp(-t/3))$, is given by the full line. Made with *linear1.ode*

expensive, since it either requires a faster (more expensive) computer or a longer time to run.

There are many other methods of numerical integration which give better approximations to the derivative. These methods are generally more complicated, but have fewer restrictions on Δt. These more complicated methods also address some other important problems that are frequently problem dependent. *XppAut* incorporates several of the most versitile of these methods. There are many fine texts on numerical analysis that discuss these issues and explain the various advantages and disadvantages of each method. As we mentioned before, however, the best way to ensure an optimal and valid means of solution is to collaborate with a mathematician who has experience in scientific computation or numerical analysis.

1.4.2 Solving ODEs with *XppAut*

An equation related to the simple exponential decay equation discussed above ($dX/dt = -X/\tau$) is the exponential approach to a steady state other than zero. For example, Eqn. (1.3), which resulted from the single channel model above, describes exponential decay (or growth) to a steady state number of open channels, n_∞. The analytic solution to Eqn. (1.3) for a given initial condition $n(0)$ is given by Eqn. (1.9). We want to introduce a practical tool for solving such equations numerically.

$$\frac{dn_O}{dt} = \frac{-(n_O - n_\infty)}{\tau}$$

$$n_O(t) = n_\infty + (n_O(0) - n_\infty)e^{(-t/\tau)} \tag{1.9}$$

1.4.3 Introduction to *XppAut*

While it is important to understand the limitations of whichever numerical algorithm is used for the solution of a problem, fortunately it is not necessary to face the task of implementing these algorithms on a computer from scratch. Several excellent software programs have been developed that not only solve ODEs, but represent solutions graphically and allow their dynamical properties to be analyzed. Among the best is a public domain package, *XppAut*, that has been developed by Bard Ermentrout at the University of Pittsburgh. The name of the program evolved from a DOS version that was called *PhasePlane*, refering to the program's ability to carry out phase plane analysis. A version that ran in X-windows under unix or linux was then developed that was called X-PhasePlane (or *Xpp* for short). Finally, when the automatic bifurcation tool *Auto*, developed by E. Doedel, was added it became X-PhasePlane-Auto or *XppAut*. *XppAut* is an excellent tool for solving and analyzing ordinary differential equations, and we adopt it as the basic software program for use with this text. Directions for downloading *XppAut*and hints for using the package are given in the appendix to this chapter.

All that is needed to start using *XppAut* is a properly formated input file that defines the functions and ODEs for the equations of interest. This is saved as "filename.ode", which is the file format recognized by *XppAut*. An *XppAut* file for Eqn. (1.9) is:

```
#linear1.ode: an XppAut file to solve single channel model
#the initial condition on the open fraction
no(0)=1
#the parameters
param ninf=0.5,tau=3
#the equation
dno/dt=-(no-ninf)/tau
#an auxiliary function
aux rate=-(no-ninf)/tau
#end of file
```

Note that the dependent variable can be given any name; here we choose n_O as in the original equation. The independent variable is always t, suggestive of "time"– although that interpretation is not always necessary. To help illustrate the meaning of the file, *comments* have been included. These are the lines that begin with `#` and that are ignored by *XppAut*. The *auxilliary function*, `rate`, keeps track of the instantaneous rate of change of n_O. Including it on the line beginning with `aux` allows it to be plotted in *XppAut*. The lines declaring *parameters* must begin with `param`. In the case of this particular equation, the exact solution to the differential equation is known Eqn. (1.9), and so it is included as a second auxiliary function for comparison:

Panel A of Fig. (1.10) illustrates two solutions to Eqn. (1.9) obtained by integrating the *linear1.ode* file using the Euler method in *XppAut*. The time step was chosen to be $dt = 0.03$ and two different initial conditions were used, `no(0)=1` and `no(0)=0`.

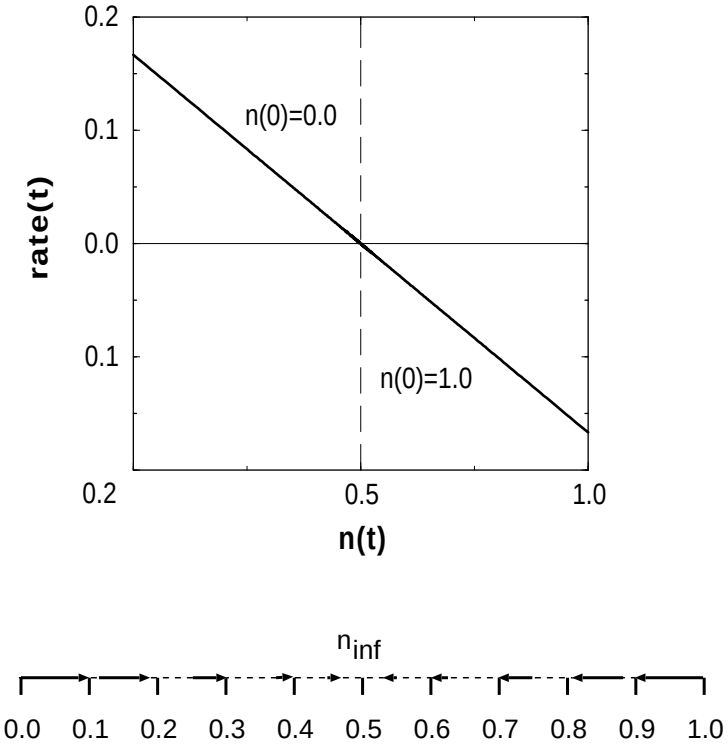

Figure 1.11 Panel A is a plot of the rate of change of n in Fig. 13A as a function of n. The lower panel is a phase portrait with the arrows representing the direction and relative magnitude of the rate for each value of n_O. All the arrows point towards the steady state, $n_{inf} = 0.5$.

Independent of the initial condition, $n_O(t)$ relaxes to its *steady state* value, `finf=0.5`. This steady state is sometimes called an *equilibrium* or a *singular point*. It corresponds to the point where the rate vanishes, as can be seen graphically in Fig. (1.10A), or by noting the form of the expression for rate in the *linear1.ode* file. The rate at which the steady state is approached depends on the value of `tau`, which is 3 in these simulations.

Panel B of Fig. (1.10) illustrates how the solution to the equation in the Euler method depends on step size. Only step sizes that are more than an order of magnitude smaller than the value of `tau` do a good job of approximating the exact exponential solution, which for the parameter values used is $fo(t) = 0.5(1 + \exp(-t/3))$. Unrealistically large step sizes like $dt = 6$ give approximations that are not even close to the exact solution. In fact, the numerical method has become *unstable*, and the computed solution oscillates around the true solution.

FOLLOWING SECTION MAY NEED REVISION - TYSON

There is a different way to plot the results of solving the differential equation that frequently gives insight into the properties of the solution. This is demonstrated in Fig. (1.11), where the function `rate = -(fo-ninf)/tau` is plotted versus the value of `fo`

for the two initial conditions in Fig. (1.10A). As f is restricted on physical grounds to be between 0 and 1, the plot shows that `finf=0.5` is the unique steady state and makes it clear that when $n_O > 0.5$, $n(t)$ decreases with time (since $df/dt < 0$) and that $n_O(t)$ increases with time when $n_O < 0.5$. To further emphasize this arrows show the direction that n_O is changing. This type of plot is called a *phase portrait*, in the case one dimensional. Phase portraits are particularly useful for analyzing ODEs with two variables, where they are typically called *phase plane* diagrams. A full discussion of phase plane diagrams appears in Appendix (A). Since phase portrait diagrams will be used extensively in the remainder of the text, it would be a useful digression to review that material now.

1.5 Exercises

1. Verify by differentiation (or by integration) that Equation (1.9) is the solution to Equation (1.8).
2. Read the sections of the *XppAut* Tutorial entitled *Introduction* and *Creating and running an ODE file*. Create and run the input file for the passive membrane model described there. Use that file to follow along with the Tutorial.
3. Do *Homework 1.2* in the section *Creating and running an ODE file* in the *XppAut* Tutorial.
4. Create an input file for *XppAut* or *Winpp* that is suitable for solving the ODE in Eqn. (1.4) and use *XppAut* to explore what happens to the solution when the intial condition and characteristic time, τ, are changed. Compare to the analytical solution in the previous exercise.

```
#decay.ode
#the initial condition is 1
X(0)=1
#the parameters
param tau=2
#the equation
dX/dt=-X/tau
#an auxiliary function
aux rate=-X/tau
#an auxiliary function for the exact solution
aux exact=1*exp(-t/tau)
end
#end of file
```

5. Using the input file *linear1.ode*, verify that the solutions graphed in Fig. 1.13 are also obtained using the Runge-Kutta or Adams numerical method.

```
#linear1.ode: an XppAut file to solve Eq. (1.29)
```

```
#the initial condition on the open fraction
n(0)=0.75
#the parameters
param ninf=0.5,tau=3
#the equation
dn/dt=-(n-ninf)/tau
#an auxiliary function
aux rate=-(n-ninf)/tau
#end of file
```

1.6 Appendix: Hints for Using *XppAut*

The mechanics of running a file in *XppAut* depend on whether you have the unix/linux version (*XppAut*) or the version of the program that runs under Windows-95/NT (*Winpp*). Either version can be downloaded over the Web from Ermentrout's site http://www.pitt.edu/~phase/. Once a file is loaded into *XppAut*, the program brings up a variety of windows that allows one easily to change the initial conditions, parameter values, and look at a tabular display of the solution. The main window contains a graph, in which the solution of the ODE can be plotted along with mouse-activated menus for plotting, graphical, and numerical options.

The hints listed here are directed at the unix/linux version of *XppAut*. Nonetheless, almost all of the menus and submenus in *XppAut* have identical (or comparable) names in *Winpp*. Two notable exceptions are that submenus in the **nUmerics** menu of *XppAut* are all contained in the **Int. Pars.** (integration parameters) submenu in *Winpp* and that the **Phaseplane** menu in *Winpp* contains the menus for setting the grid parameters. More complete information about running *XppAut* is contained in the *Xpptutorial*, which can be obtained as an *html* file at http://www.pitt.edu/~phase/, Ermentrout's internet Web site.

1. The first (and best) hint is to open up the *XPPtutorial* html file using a Web browser such as *Netscape*. Put this in a different window (or in linux in a different desktop) than the one you use for *XppAut* and use the Table of Contents and References as on-line help. A complete list of formating commands can be found under *Format of ODE files and examples*, which is linked to the *References* in the section *XPP Tutorial: Basic Idea and Introduction*.
2. Create or edit an *XppAut* file using your favorite editor. Files must be saved in ascii (text) format and end in ".ode", *i.e.* "filename.ode". If the file is not written with correct syntax, then *XppAut* will not load the file. Pay attention to the reasons that *XppAut* gives for rejecting the file, since they point you to where revisions are required. Remember that fixed quantities are evaluated in the order in which they appear. *XppAut* will not warn you about this type of error!

3. Load the file into *XppAut*, which will bring up all the windows for *XppAut* for the file named "filename.ode". You should minimize all the windows except the main window to get them out of your way until you need them; in the linux version they will be solid blue. You will probably want to maximize the *parameter* and the *initial condition* windows (or any other **XPP** window that you will use regularly).
4. Always be sure to click on the menu item **nUmerics** and set the **Method** and **Total** (duration of integration) before you begin. For almost all equations Adams or Runga-Kutta work fine with an appropriate time step (**Dt** in the **nUmerics** menu). It also helps to set the **Ncline ctrl** mesh to 100 and the **sIng pt ctrl** mesh to 150. Set **Bounds** to a number larger than the expected maximum of all of your variables; otherwise you will get an "out of bounds" message when integrating. It is not necessary to save every time point in the integration; to save fewer points, set **nOutput** to a number greater than one. Then return to the main menu.
5. Use the **InitialConds** menu to initiate integration of the equations. The **Go** option will begin the integration with the parameters and initial conditions set in the other windows. **Range** allows you to choose a range of intitial conditions or parameters. You can set the variable to plot and its range using either the **Viewaxes** or **Xi vs t** options.
6. In case you want to void a menu choice or to stop an integration prematurely, use the **Esc** key.
7. To print a graph, first save the graph to a postscript file using the menu **Graphics stuff** and then choosing **Postscript**. This prompts you with a default name ("filename.ode.ps"), which you can edit, but keep the ".ps" since it will remind you that this is a postscript file. The file prints on any postscript printer.
8. You can open up multiple graph windows using the menu item **HalfWindow**. The white square in the upper left corner of the graph tells you which window is active. All the window specific menu items (eg., **Viewaxes** and **Graphics stuff**) apply only to the active graph window. To activate a graph window, simply click the mouse anywhere in the graph, itself, and the white square will appear.
9. To exit *XppAut* use the menu item **File**, choose **Quit** and then agree.

CHAPTER 2

Voltage Gated Ionic Currents

Chris Fall and Joel Keizer

07-28

Electrophysiology is the study of ionic currents and electrical activity in cells and tissues. Because this field has its roots in classical physics, traditionally it has been the most quantitative field in cell physiology. The work of the physiologists Hodgkin and Huxley and others in elucidating the mechanism of action potentials in the squid giant axon before and after the Second World War was the first major breakthrough of dynamical modeling in physiology. In the latter half of the 20th century, the introduction of the patch-clamp technique established firmly that ionic currents are carried by proteins that act as gated ionic pores. More recently genetic engineering techniques have been employed to clone, modify, and characterize the gating mechanisms of many types of channels. In this chapter we focus on voltage gated ionic currents. We begin by reviewing the basic concepts of electrical behavior in cells. Next, we describe classical activation and inactivation gates and how the voltage clamp technique can be used to study these currents. We touch briefly on the Hodgkin-Huxley model of the squid giant axon before moving on to models more suitable for phase-plane analysis. We then study the Morris-Lecar model for action potentials in the giant barnacle muscle, which is nonlinear but involves only two variables. With only two variables, we can analyze the dynamics of the Morris-Lecar model using phase plane techniques.

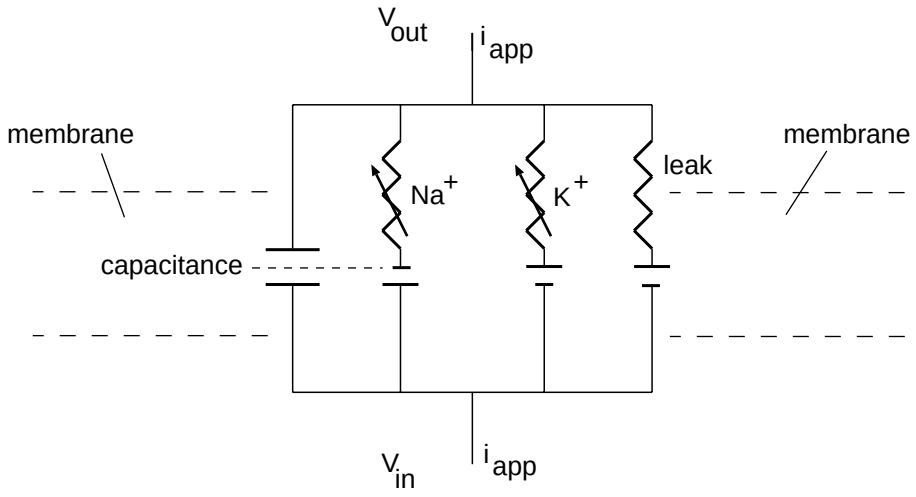

Figure 2.1 The equivalent electrical circuit for the Hodgkin-Huxley model of squid giant axon. The capacitance is due to the phospholipid bilayer separating the ions on the inside and the outside of the cell. The three ionic currents, one for Na^+, one for K^+, and one for a non-specific leak, are indicated by resistances. The conductances of the Na^+ and K^+ currents are voltage dependent, as indicated by the variable resistances. The driving force for the ions is indicated by the symbol for the electromotive force, which is given in the model by the difference between the membrane potential, $V = V_{in} - V_{out}$ and the reversal potential.

2.1 The Membrane Model

The conceptual idea behind current electrophysiological models originates in the work of K. C. Cole, who pioneered the notion that cell membranes could be likened to an electronic circuit. Cole's basic circuit elements are 1) the phospholipid bilayer, which is analogous to a capacitor in that it accumulates ionic charge as the electrical potential across the membrane changes; 2) the ionic permeabilities of the membrane, which are analogous to resistors in an electronic circuit; and 3) the electrochemical driving forces, which are analogous to batteries driving the ionic currents. These ionic currents are arranged in a parallel circuit, as shown in Fig. (2.1). This analogy to electrical circuits is now widely relied upon for developing models of electrical activity in membranes.

As with electronic circuits, the electrical behavior of cells is based upon the transfer and storage of charge. We are used to thinking about electricity as the movement of electrons, but current can be carried by any charged species - including ions such as K^+, Na^+, and Ca^{2+} in solution. Recall several important definitions from elementary Physics listed in Table (2.1). The transfer of 1 mole of K^+ions in a period of one second would carry one ampere of current. An ion's *valence* is the number of charges, plus or minus, that it carries. An equivalent number of the *divalent* ion Ca^{2+} would carry twice

Table 2.1 Important Definitions in Electrophysiology

Definition	Abbreviation	Value

Notes:

the amount of charge as the *univalent* ion K^+. Potential difference is measured in *volts*. By definition, the work required to move 1 C of charge across a 1 V gradient is 1 joule.

2.2 Basis of the Ionic Battery

Cells contain ion pumps which use energy in the form of ATP to transport ions against a concentration gradient. Consider an ion-impermeable membrane such as the phospholipid bilayer of the cellular plasma membrane with a concentration gradient of K^+ ions established by ion pumps. Based on the relationships discussed above, we could calculate the voltage across the membrane using Faraday's constant and the difference in concentration across the membrane Exercise (**??**). If a nonselective pore or a pore selective for K^+ only were inserted into the membrane, the concentration would equilibrate and the voltage gradient across the membrane would dissipate to zero.

As we have seen, biological fluids such as cytoplasm and extracellular fluid contain numerous ions. Consider the case where two ions, K^+ and any monovalent anion A^- are in solution such that the concentration is different across the membrane but the two ions are equal in concetration on the same side of the membrane. Before we make any changes, there is no potential difference across the membrane because the charge between the K^+ ions and the A^- ions is balanced on each side due to the equivalent concentrations. If we insert a nonselective pore into the membrane, concentration and charge equilibrate such that there are an equal number of each ion on both sides of the membrane and the voltage across the membrane is again zero.

It is when we insert a channel into the membrane that allows only the passage of K^+ that an interesting and useful phenomenon occurs. Because $[K^+]$ is greater on one side of the membrane, K^+ ions diffuse through the K^+ pore in order to equilibrate the concentration difference. Because the membrane is not permeable to the anion A^-, each K^+ ion that passes down the concentration gradient carries a positive charge that is not balanced by an accompanying A^-. Since the transfer of these charges establishes an electrical potential gradient, K^+ ions continue to move from high concentration to low concentration until the growing electrical potential difference is balanced by the *chemical potential* contained in the residual concentration difference.

The *equilibrium potential*, where the electrical potential is equilvalent to the chemical potential due to the concentration difference, is given by the *Nernst Equation* derived

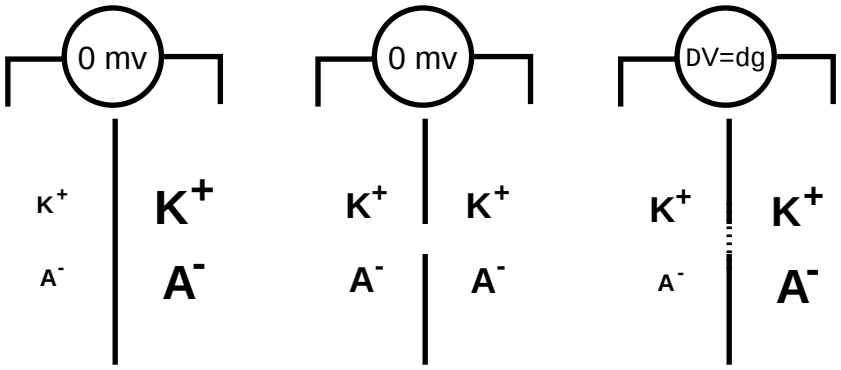

Figure 2.2

from statistical physics:

$$\begin{aligned}\Delta E = E_{in} - E_{out} &= \frac{RT}{zF} \ln \frac{[ion_{in}]}{[ion_{out}]} \\ &= 2.303 \frac{RT}{zF} \log_{10} \frac{[ion_{in}]}{[ion_{out}]} \\ &= \frac{61.5}{z} \log_{10} \frac{[ion_{in}]}{[ion_{out}]} \text{ (at } 37^o\text{C)}\end{aligned} \tag{2.1}$$

where R, and F are defined above, T is temperature (in Kelvin) and z is the valence of the ion as previously defined. At body temperature, RT/F is approximately 60. Therefore a 10 fold difference in the concentration of a monovalent ion like K^+would result in approximately 120 mV of potential difference across a membrane. Because the equilibrium potential represents the steady state of the thermodynamic system, the potential difference evolves to that given by the Nernst equation regardless of the initial starting potential. This tendency for the system to move towards the equilibrium potential is the basis of the *ionic battery* used in the modeling of electrophysiological phenomena. In electrophysiology, the equilibrium potential is called the *reversal potential*, since departure from that point of zero current flux results in the positive or negative flow of ions.

2.3 Differential Equations for Membrane Electrical Behavior

We can approximate the current flow through a K^+ channel using Ohm's law and an assumption that the reversal potential stays constant:

$$I_k = g_k(V - V_k) \tag{2.2}$$

Here g_k is the conductance of the K^+ channel. V_k is the K^+ reversal potential determined by the Nernst equation and $V - V_i$ represents the driving force across the membrane provided by the ionic battery. We assume that the reversal potential for a given ion remains constant, which is equivalent to assuming that restorative mechanisms such as ionic pumps can keep pace with electrical activity on a time scale that prevents the "ionic battery" from running down. This is a reasonable assumption for a large cell, which would have a small surface area to volume ratio. Charge is stored due to the capacitance of the plasma membrane. In a small cell, with a large surface to volume ratio, the ion transfer necessary to change the membrane potential might have a large effect on the intracellular ionic concentration and thus the strength of the "ionic battery." Exercise (**??**)

To translate the electric circuit diagram into ODEs, we use the traditional interpretation of each circuit element along with Kirchoff's law. Assuming that the membrane acts as a capacitor, the capacitive current across the membrane can be written

$$I_{cap} = C\frac{dV}{dt}, \tag{2.3}$$

where C is the capacitance of the membrane and V is the membrane potential, defined as the electrical potential difference between the inside and outside of the cell. To establish the differential equation satisfied by the voltage, V, Kirchoff's law of charge conservation is applied to the circuit in Fig. (2.1). Kirchoff's law dictates that capacitative current must balance with the ionic current and any currents that might be applied, say, through experimental manipulation. This implies that

$$I_{cap} = \sum_i I_i + I_{app} \tag{2.4}$$

where the sum is over all the ionic currents. Using the expressions in Eqn. (2.3) and Eqn. (**??**) this can be rewritten:

$$CdV/dt = -\sum_i g_i(V - V_i) + I_{app}. \tag{2.5}$$

If the form of the gated conductances, g_i, are known, this provides a differential equation for the voltage. In general, the g_i will not be linear functions of V, and therefore the problem is to find the time and possible voltage dependence of the various conductances.

2.4 Activation and Inactivation Gates

In order to control the permeability to ions, channels have *gates*, as illustrated schematically in Fig. (**??**), that regulate the permeability of the pore. These gates can be controlled by membrane potential–producing *voltage gated* channels–or by ligands–producing *ligand gated* channels. Hodkgin and Huxley and others established experimentally that sodium (Na^+) and potassium (K^+) ions were responsible for carrying the majority of current across the membrane of the squid giant axon. By using

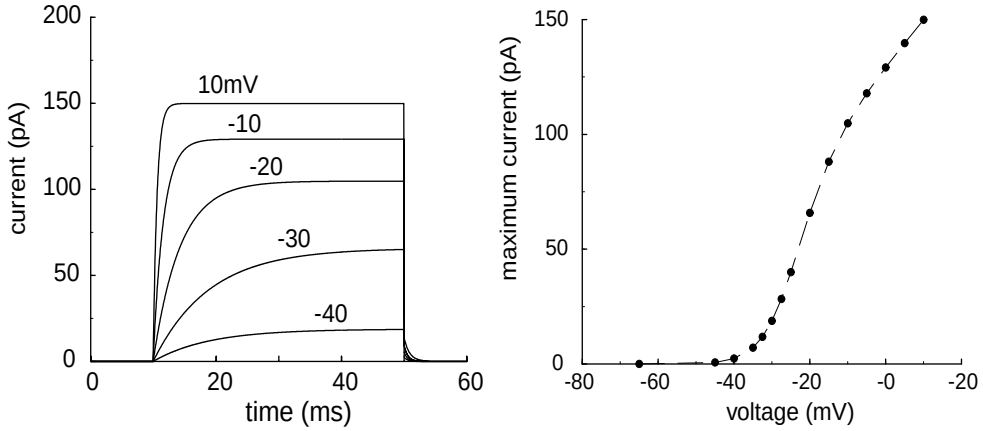

Figure 2.3 Simulation of voltage clamp experiment using Eqs. () and (). Panel A: Current records resulting from 40ms depolarizations from the holding potential of -60mV to the indicated test potentials. Panel B: the maximum (steady state) current as a function of test potential taken from records like those in Panel A.

a technique called the *voltage clamp*, Hodgkin and Huxley were able to characterize the variation in resistance of the membranes to Na^+ and K^+ currents as the membrane potential changed. This is indicated by the variable resistors for the Na^+ and K^+ conductances in the schematic membrane model shown in Fig. (2.1).

2.4.1 The Voltage Clamp

In order to measure the activation and inactivation properties of channels, whole cell currents are often used. These are recorded either in the whole cell patch clamp configuration or with microelectrodes that are used to impale cells. In order to measure the voltage dependence of a gate, a *voltage clamp* is used. This is an electronic feedback device that adjusts the applied current, I_{app}, so that it matches the membrane currents. To see what this accomplishes, consider a membrane with a single gated ionic current. If

$$I_{app}(t) = g f_O(t)(V - V_{rev}). \tag{2.6}$$

and the membrane potential satisfies the differential equation:

$$C\frac{dV}{dt} = -n_O g(V - V_{rev}) + I_{app}(t), \tag{2.7}$$

then the right hand side of Eqn. (2.7) is zero and the voltage must be unchanging, or constant. Because V is constant,the time dependence of the applied current comes only from the dependence of n_O on t as determined by the gating equation:

$$\frac{df_n}{dt} = \frac{-(n_O - n_\infty(V))}{\tau(V)}. \tag{2.8}$$

Thus the time dependence of the applied current provides a direct measurement of the gated current at a fixed voltage.

To carry out a voltage clamp measurement like this it is necessary to block all but a single type of current. While this is not always possible, specific toxins and pharmacoligical agents have proven useful. For example, tetrodotoxin (TTX) from the puffer fish selectively blocks the voltage gated Na^+ in the squid giant axon whereas charybdotoxin (CTX) and apamin selectively block different Ca^{2+} activated K^+ channels.

It is not difficult to simulate a voltage clamp measurement using Eqn. (2.6) and Eqn. (2.8). However, to carry out either an experimental measurement or a simulation, a consistent set of electrical units must be used. As we have seen, the standard unit for membrane potential is millivolts (mV) and because the characteristic times for voltage dependent gates, $\tau(V)$ is milliseconds (ms)(see Exercise (**??**)), this is taken as the standard unit of time. For typical cells a whole cell current is picoamperes (1 pA $= 10^{-12}$ A), which we use as the standard unit for current. According to the left-hand-side of Eqn. (2.7), if current is measured in pA, then the capacitance must be in picofarads (1 pF $= 10^{-12}$ F) (since the units of dV/dt are volts/second). Recalling the expression for the gated current on the right-hand-side of Eqn. (2.7), it follows that the conductance, g, must be in nanosiemens (1 nS $= 10^{-9}$ S $= 10^9$ Ohm), since the units of $V - V_{rev}$ are millivolts. This standard set of units is summarized in Table (**??**). An alternative consistent set of units uses current in femtoamperes (1 fA $= 10^{-15}$ A), conductance in pS, and capacitance in fF (see Exercise (**??**)).

To simulate a voltage clamp experiment, we have used the *XppAut* file in Exercise (**??**) to solve Eqn. (2.8) and plot the resulting current in Eqn. (2.6). Fig. (2.3A) simulates a typical set of experiments in which the membrane potential is clamped at a holding potential (-60mV in Fig. (2.3)), is then changed to various test potentials for a fixed interval (40ms), and then returned to the holding potential. The value of the holding potential generally is chosen so that there is little or no current throught the channel. This greatly simplifies the interpretation of the current at the test voltages (see Exercise (**??**)). Fig. (**??**A) shows the current that develops during this protocol for 5 test voltages, V_{test}. The increase in current when the potential is clamped at the test values is governed by the exponential increase of n_O with characteristic time $\tau(V_{test})$. When the potential is clamped again at the holding potential, the resulting current is called the *tail current*. Its

Table 2.2 Consistent Electrical Units

Name (Symbol)	Units	Abbreviation
voltage (V)	10^{-3} volt	mV
time (t)	10^{-3} second	ms
conductance (g)	10^{-9} siemens	nS
capacitance (C)	10^{-12} farad	pF
current (I)	10^{-12} ampere	pA

decline is also exponential, but since $V = -60$mV during this period, the characteristic time is now $\tau(-60mV)$.

Fig. (2.3A) gives a plot of the steady state current as a function of the test voltage. According to Eqn. (2.6) it can be expressed as $I(V) = gf_\infty(V)(V - V_{rev})$. Thus for an activating current like that in the simulations, when V is large enough $f_\infty(V) \approx 1$ and the current is a linear function of V. The curvature in Fig. (**??**) at lower voltages is caused by the shape of the activation function, $f_\infty(V)$. In the jargon of circuit theory, currents like this are said to *rectify*. The delay in the onset of the maximum current, which is determined by the value of $\tau(V)$, has lead to channels like the one simulated in Fig. (2.3B) being referred to as *delayed rectifiers*.

2.4.2 The Hodgkin Huxley model

We did not discuss the form or source of the voltage and time dependence for the computational voltage clamp "experiment" in the previous section. The squid giant axon model developed by Hodgkin and Huxley is empirical. That is, many voltage clamp experiments were performed by Hodgkin and Huxley, and their data was fit to expressions that they incorporated into the model without consideration of an underlying model of the channel gates. From their voltage clamp and other measurements, Hodgkin and Huxley deduced that the sodium conductance involved two voltage-dependent gates, an *activation* gate and an *inactivation* gate and that the potassium conductance had a single activation gate. To account for these facts they represented the ionic conductances in the following form:

$$g_{Na} = \bar{g}_{Na} m^3 h \tag{2.9}$$

$$g_K = \bar{g}_K n^4, \tag{2.10}$$

where the terms $\bar{g}$ represent maximal conductances and m and n are the activation gating variables and h the inactivation. These gating variables were postulated to satisfy linear differential equations where the variables "relax" to voltage dependent values, *e.g.* $m_\infty(V)$, that varied between zero and one with voltage-dependent time constants, *e.g.* $\tau_m(V)$.

Putting the ODEs for the gating variables together with Eqn. (2.5) gives the equations for the Hodgkin-Huxley model:

$$\begin{aligned} CdV/dt = &-\bar{g}_{Na} m^3 h(V - V_{Na}) - \bar{g}_K n^4 (V - V_K) + I_{app} \\ &- \bar{g}_{leak}(V - V_{leak}) + I_{app} \end{aligned} \tag{2.11}$$

$$dm/dt = -(m - m_\infty(V))/\tau_m(V) \tag{2.12}$$

$$dh/dt = -(h - h_\infty(V))/\tau_h(V) \tag{2.13}$$

$$dn/dt = -(n - n_\infty(V))/\tau_n(V). \tag{2.14}$$

Hodgkin and Huxley added the third conductance, $\bar{g}_{leak}$, to their voltage equation to account for a small, voltage-independent conductance that they attributed to a "leak" in the membrane, possibly through their microelectrode. The nonlinear terms in Eqn.

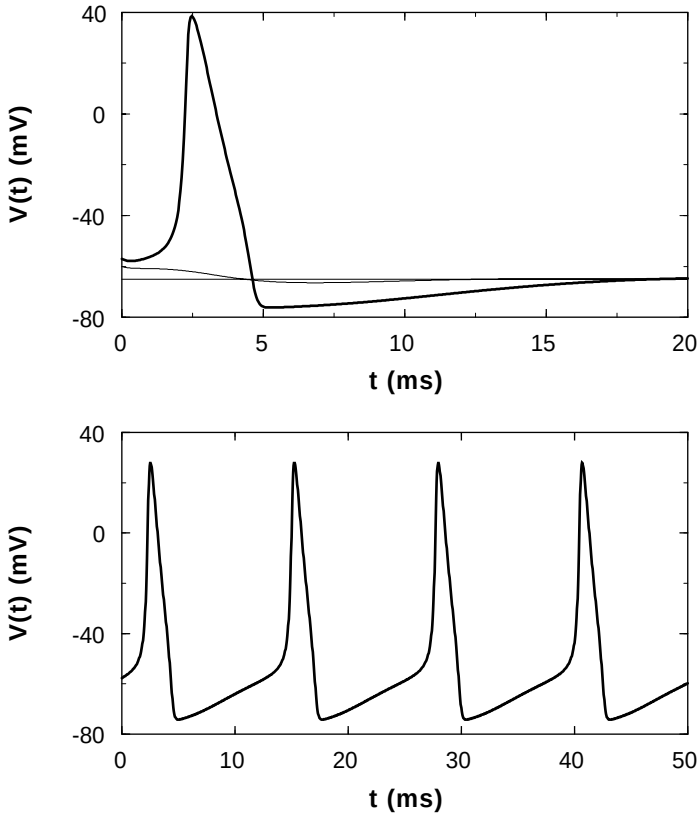

Figure 2.4 Panel A: The solution of the Hodgkin-Huxley equations for three different initial values of the membrane potential and no applied current. When the initial value exceeds *ca.* -59mV, an action potential is produced. Panel B: Continuous spiking occurs under the same conditions with an applied current $I_{app} = 15$. Made with *hh.ode*

(2.11) are obvious in the activation and inactivation gates. Not so obvious are the nonlinearities in Eqn. (2.12) -Eqn. (2.14); however all the voltage-dependent terms in those equations are nonlinear functions of V as well.

2.4.3 Solving the Hodgkin-Huxley Equations

It is not difficult to solve the Hodgkin-Huxley equations with *XppAut*. In this case the input file has more lines and one must be careful to choose a suitable numerical method of solution, but otherwise the proceedure is the same. Using parameters and functional forms for the Hodgkin-Huxley equations taken from the *XppAut* tutorial, it is not difficult to construct the appropriate input file, which is called *hh.ode*.

```
#hh.ode: an XppAut file for the Hodgkin-Huxley equations
#time in msec and voltage in mV
```

```
#the initial conditions
init V=-65,m=0.052,h=0.596,n=0.317
#the parameters
param VNa=50,VK=-77,VL=-54.4,gNa=120
param gK=36,gL=0.3,C=1,Iapp=0
#time constants and steady state functions for gating variables
taum(V)=1/(0.1*(V+40)/(1-exp(-(V+40)/10))+4*exp(-(V+65)/18))
minf(V)=(0.1*(V+40)/(1-exp(-(V+40)/10)))*taum(V)
tauh(V)=1/(0.07*exp(-(V+65)/20)+(1/(1+exp(-(V+35)/10))))
hinf(V)=0.07*exp(-(V+65)/20)*tauh(V)
taun(V)=1/(0.01*(V+55)/(1-exp(-(V+55)/10))+0.125*exp(-(V+65)/80))
ninf(V)=(0.01*(V+55)/(1-exp(-(V+55)/10)))*taun(V)
#the equations
dV/dt=(-gNa*m^3*h*(V-VNa)-gK*(V-VK)*n^4-gL*(V-VL)+Iapp)/C
dm/dt=-(m-minf(V))/taum(V)
dh/dt=-(h-hinf(V))/tauh(V)
dn/dt=-(n-ninf(V))/taun(V)
done
```

Notice that an alternative way of indicating the intial conditions has been used in the line that begins with `init`. Also in this model functions of the voltage have been defined for use in the gating equations. As described in the *XppAut* tutorial, *fixed quantities* could have been used in these formulae instead. For example, it could be written:

```
dm/dt=-(m-minf)/taum
taum=1/(0.1*(V+40)/(1-exp(-(V+40)/10))+4*exp(-(V+65)/18))
minf=(0.1*(V+40)/(1-exp(-(V+40)/10)))*taum}
```

where `minf` and `taum` are fixed quantities that are evaluated once during each time step before the right hand sides of the equations. It is important not to define `minf` *before* `taum`, however, since fixed quantities are evaluated in the order in which they appear. Reversing the order would mean that in evaluating `minf` the value of `taum` from the previous time step would be used.

To solve the Hodgkin-Huxley equations with *hh.ode* and *XppAut*, the *Runge-Kutta* method has been used with a time step of 0.05. These are the defaults in *XppAut*, and it is easily checked that reducing the time step to 0.01 gives no noticeable change in the results. Fig. (2.4) shows several simulations that can be made with these equations. The top panel shows calculations with $I_{app} = 0$, but with $V(0) = -65$, -60, and -57mV. The steady state for the voltage with these parameters is clearly -65mV; however, if the initial value of V exceeds about -59mV, then the equations produce an *action potential spike*. This is an all-or-none response that requires an initial deviation of the voltage exceeding a threshold. Action potentials are an important feature of nerve conduction and we will explore the mechanistic features that underlie them in Chapter 3.

The Hodgkin-Huxley equations can also produce repetitive firing of action potentials. This is illustrated in the lower panel of Fig. (2.4). The parameters in that simulation are identical to those in the upper panel, except that $I_{app} = 15$. The transition from an excitable membrane that can produce isolated action potentials to one that can support repetitive firing is an example of a *bifurcation*.

One of the remarkable aspects of Hodgkin and Huxley's work is that their model was developed without a molecular understanding of the mechanism. That is, they had no mechanistic cartoon to guide their modeling. In fact, it required almost thirty years of intensive research to formulate a realistic cartoon of the mechanisms underlying the ionic currents in cells. Although Hodgkin and Huxley justified these expressions on empirical grounds, it is possible to derive the gating expression used in the Hodgkin-Huxley model using mechanistic models of the channels similar to those in Chapter (1). While it remains a seminal accomplishment in the history of physiology, the HH model is complicated and not amenable to the phase plane methods of analysis that we will use here to understand dynamical electrical behavior in cells. As we shall see, it is possible to combine gated channels to derive much simpler models of neuronal firing that provide a more intuitive understanding of the mathematical structure of the underlying mechanisms.

2.4.4 The Patch Clamp

The time course of voltage changes in a whole cell is the result of the average behavior of many individual channels. Our understanding of individual channel gating comes

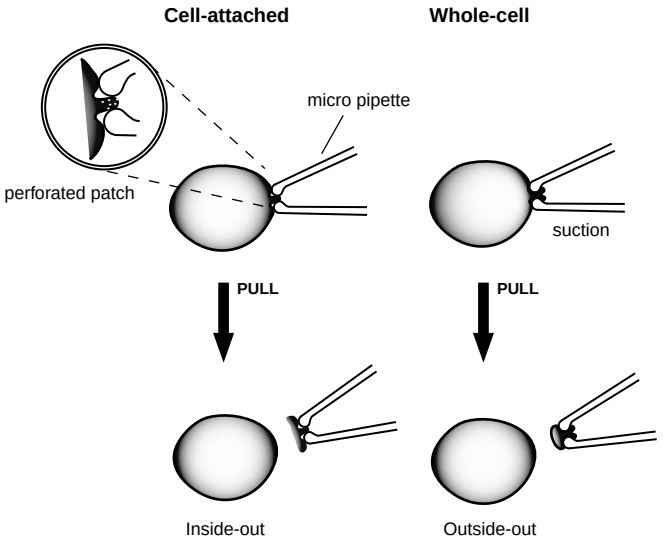

Figure 2.5 Four methods of measuring electrical responses in cells with the patch clamp technique. Taken from B. Hille, *Ionic Channels of Excitable Membranes*, 2nd Ed., Sinauer, 1992, pg. 89.

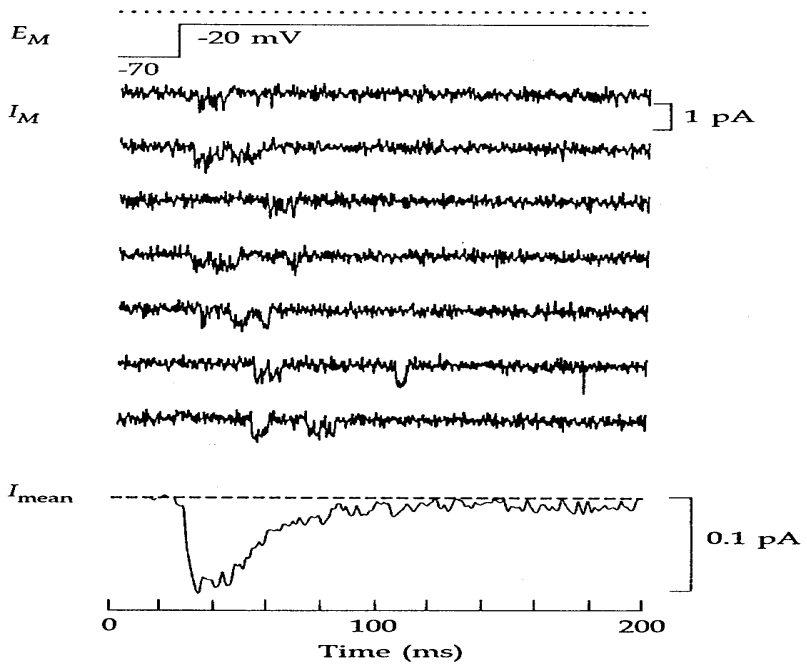

Figure 2.6 On cell patch clamp measurements of currents in T-type calcium channels. The upper panels are currents measured in a single channel at -20mV. The lower panel is the average of several hundred such records, which shows rapid activation followed by slow inactivation of the average current. Taken from B. Hille, *Ionic Channels of Excitable Membranes*, 2nd Ed., Sinauer, 1992, pg. 103.

from experiments using the patch clamp technique, which is illustrated in Fig. (2.5). In the patch technique, a pipette with an opening of *ca.* 1 μm containing an internal solution and a wire for electrical measurements is used to make a high resistance seal ("gigaOhm" = 10^8 Ohm) onto a cellular membrane. In the on-cell patch configuration all the current into the pipette flows directly through the patch, which can contain as few as one or two ion channels. In the whole cell configuration, sucking on the pipette breaks the patch and allows the current through the tip now comes from the entire cell. In a perforated patch configuation, an ionophore such as nystatin is introduced into the pipette in order to allow whole cell-like access while minimizing exchange of the cell contents with the contents of the pipette. Alternatively, patches of membrane can be torn off, leading to inside-out and outside-out patches that can be studied in isolation. Fig. (**??**) shows typical measurements from an on-cell patch of predominately T-type calcium currents in guinea pig cardiac ventricular cells. These currents were evoked when the membrane potential, which was previously clamped at -70 mV, was rapidly changed to -20 mV. The small current deviations in the negative direction indicate the opening of individual T-type channels. Statistically, two types of states of

the channel are observed: a closed state with no current flowing and an open state, in which the unitary current is *ca.* 10^{-12} amperes (1 picoampere or 1 pA). As we discuss in Chapter 10, transitions between these states are random in time. However, as illustrated in the bottom panel of Fig. (**??**), the average of several hundred records produces a behavior that shows a rapidly activating current, followed by slower inactivation.

Analysis of the these currents leads to a model of the T-type calcium current that has two kinds of voltage-dependent gates: an *activation gate*, in which the open state is favored by more positive potentials (termed *depolarization*) and an *inactivation gate*, in which the open state is favored at more negative potentials (*hyperpolarization*). This type of model simulates the average behavior of a collection of ionic channels. It provides a good representation for the behavior of a whole cell with numerous channels in the plasma membrane.

2.4.5 Models of voltage dependent Gating

The mathematical description of both activation and inactivation gates is based on the mechanism

$$C \leftrightarrow O, \tag{2.15}$$

which was presented in Chapter (1). What distinguishes a voltage dependent gating mechanism from a passive mechanism is the voltage dependence of the rate constants. Recall that the fraction of open channels, n_O, satisfies the differential equation:

$$\begin{aligned}\frac{dn_O}{dt} &= -(k^- + k^+)(n_O - \frac{k^+}{(k^- + k^+)}) \\ &= \frac{-(n_O - n_\infty)}{\tau}.\end{aligned} \tag{2.16}$$

Because ionic channels are composed of proteins with charged amino acid side chains, the potential difference across the membrane can influence the rate at which the transitions from the open to closed state occur. According to the Arrhenius expression for the rate constants, the membrane potential, V, contributes to the energy barrier for these transitions and the rate constants will have the form:

$$k^+(V) = \exp(-aV)k_o^+ \text{ and } k^-(V) = \exp(-bV)k_o^-, \tag{2.17}$$

where k_o^+ and k_o^- are independent of V. Substituting Eqn. (2.17) into the expressions for n_∞ and τ (*cf.* Eqn. (2.16))and rearranging, we obtain

$$n_\infty(V) = \frac{1}{\exp(-(V - V_o)/S_o) + 1} \tag{2.18}$$

$$\tau(V) = \frac{\exp(aV)}{k_o^+} \cdot \frac{\exp(-(V - V_o)/S_o)}{\exp(-(V - V_o)/S_o) + 1}, \tag{2.19}$$

where V_o and S_o are constants that can be expressed in terms of a, b, k_o^+, and k_o^- (see Exercise (**??**)). Both of these expressions can be rewritten in terms of hyperbolic

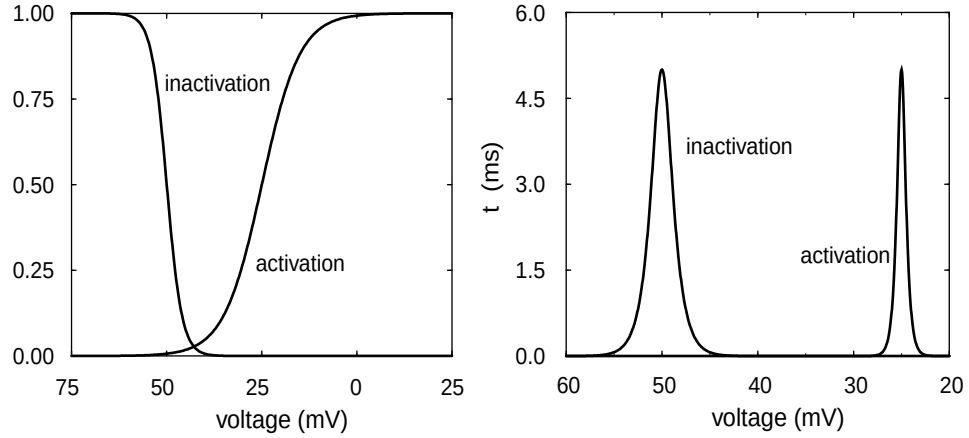

Figure 2.7 Panel A: Equilibrium open fractions (n^∞) for an inactivation gate ($V_o = -50$mV and $S_o = -2$mV) and activation gate ($V_o = -25$mV and $S_o = 5$mV) as a function of voltage. Panel B: The characteristic relaxation times, τ, for the activation and inactivation gates in Panel A as a function of voltage, which are peaked around the values of V_o and have a width determined by S_o.

functions, which

$$n_\infty(V) = 0.5(1 + \tanh((V - V_o)/2S_o)) \tag{2.20}$$

$$\tau(V) = \frac{\exp(V(a+b)/2)}{\sqrt{k_o^+ k_o^-}\cosh((V - V_o)/2S_o)} \tag{2.21}$$

Recall that $n_\infty(V)$ gives the fraction of channels open at equilibrium at the membrane potential, V. Thus for a fixed value of V it gives the open fraction after transient changes in n_O have damped out with a characteristic time $\tau(V)$.

An activation gate tends to open, whereas an inactivation gate tends to close, when the membrane is depolarized . Whether a gate activates or inactivates with depolarization is determined by the sign of S_o: a positive sign implies activation and a negative sign inactivation. This is illustrated in Fig. (2.7A), where the dependence of f_∞ on V has been plotted for an activation gate with $V_o = -25$mV and $S_o = 5$mV and an inactivation gate with $V_o = -50$mV and $S_o = -2$mV, *i.e.*,

$$f_\infty(V) = \frac{1}{\exp(-(V+25)/5) + 1} \text{ and } f_\infty(V) = \frac{1}{\exp((V+50)/2) + 1}. \tag{2.22}$$

Notice that the magnitude of S_o determines the steepness of the dependence of f_∞ on V, whereas the value of V_o determines the voltage at which half of the channels are open. Panel B in Fig. (2.7) illustrates the dependence of τ on V for these activation and inactivation gates assuming that $a = -b$ and $\sqrt{k_o^+ k_o^-} = 0.2$ ms^{-1}. The data for plotting all four of these functions was obtained using the file "plotting.ode" in *XppAut* described in ???.

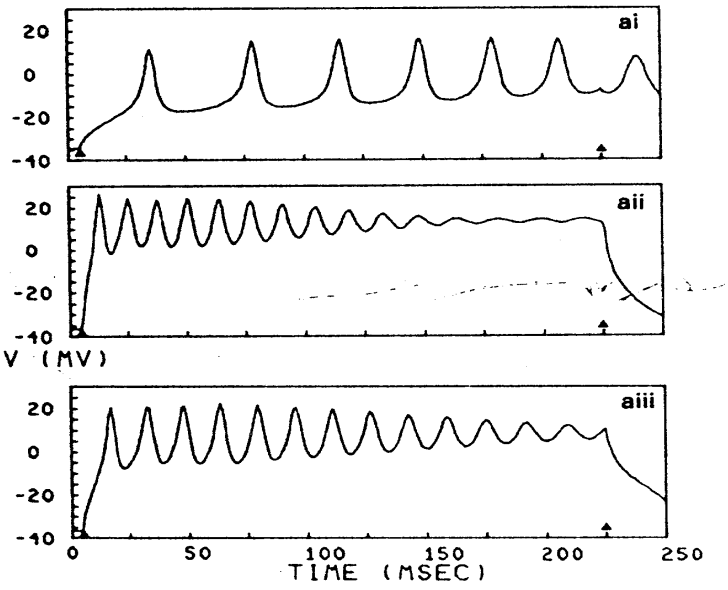

Figure 2.8 Depolarization-induced electrical activity in giant barnacle muscle fibers as measured by C. Morris and H. Lecar (*Biophys. J.* 35:193 (1981), Fig. 4A). The arrows indicated the start and end of the depolarizating currents.

2.5 Giant Barnacle Muscle: The Morris-Lecar Model

Application of a depolarizing current to barnacle muscle fibers produces a broad range of electrical activity. Fig. (2.8) illustrates the sort of oscillations that are induced by current injections of 180, 540, and 900 μAcm^{-2} into these fibers. Careful experimental work by a number of research groups has indicated that the giant barnacle muscle fiber contains primarily voltage gated K^+ and Ca^{2+} currents along with a K^+ current that is activated by intracellular Ca^{2+}, a so-called K_{Ca} current. Neither of the voltage gated currents shows significant inactivation in voltage clamp experiments. Thus the trains of depolarization-induced spikes in Fig. (**??**) must occur via a mechanism different from that proposed by Hodgkin and Huxley for the squid giant axon.

```
>From Artie:
Morris-Lecar tauw is defined as:
phi/cosh()
In the Rinzel-Ermentrout chapter in Koch and Segev, it is
1/(phi*cosh())
That is, phi is a rate ("temperature fudge factor") not a time. We need to
be consistent because several chapters are using ML in various forms
```

chris changed eqns to match rinzel and Ermentrout. Need to verify later dependencies

Morris and Lecar proposed a simple model to explain the observed electrical behavior of the barnacle muscle fiber. Their model involves only a fast activating Ca^{2+} current, a delayed rectifier K^+ current, and a passive leak. They tested the model against a number of experimental conditions in which the interior of the fiber was purfused with the Ca^{2+} *chelator* EGTA in order to reduce activation of the K_{Ca} current. Their simulations provide a good explanation of the their experimental measurements. The model translates into two equations:

$$C\frac{dV}{dt} = -g_{Ca}m_\infty(V)(V - V_{Ca}) - g_K n(V - V_K) - g_L(V - V_L) + I_{app} \tag{2.23}$$

$$\frac{dn}{dt} = \frac{\phi(n_\infty(V) - n)}{\tau(V)} \tag{2.24}$$

Here n is the fraction of open channels for the delayed rectifier K^+ channels and the conductances g_L, g_{Ca}, and g_K are for the leak, Ca^{2+} and K^+ currents, respectively. The functions

$$m_\infty(V) = 0.5[1 + \tanh((V - V_1)/V_2)] \tag{2.25}$$

$$n_\infty(V) = 0.5[1 + \tanh((V - V_3)/V_4)] \tag{2.26}$$

$$\tau(V) = 1/\cosh((V - V_3)/V_4). \tag{2.27}$$

are the equilibrium open fraction for the Ca^{2+} current, the K^+ current, and the activation time for the delayed rectifier. Representative parameters are given in Table (**??**). Also note that here m is not assumed to be a dynamic variable. The reason for this is that we have assumed that the dynamics for m are "fast enough" that they can be assumed to always be in steady state. The idea of fast and slow processes is arguably one of the most important concepts in modeling. Although we make the assumption without argument here, its implications in modeling are addressed fully in Chapter (**??**), and in a more mathematical context in Chapter (**??**).

The Morris-Lecar equations can readily be solved with *XppAut*. Using the parameters and initial conditions given in Exercise (**??**) we have solved the equations for four values of the applied current, I_{app}, and plotted the time series for $V(t)$ in Fig. (2.9A). In the absence of applied current the equations have a stable steady state near -60mV. Although increasing I_{app} to 60pA produces a brief transient action potential, the effect of the depolarization simply produces a steady state near -35mV. Depolarization with a current of 150pA, on the other hand, produces a steady train of action potentials reminiscent of those observed experimentally in Fig. (**??**). In the presence of depolarizating currents much greater than this, the simulated barnacle cell can no longer sustain continuous spiking as shown at $I_{app} = 300$pA.

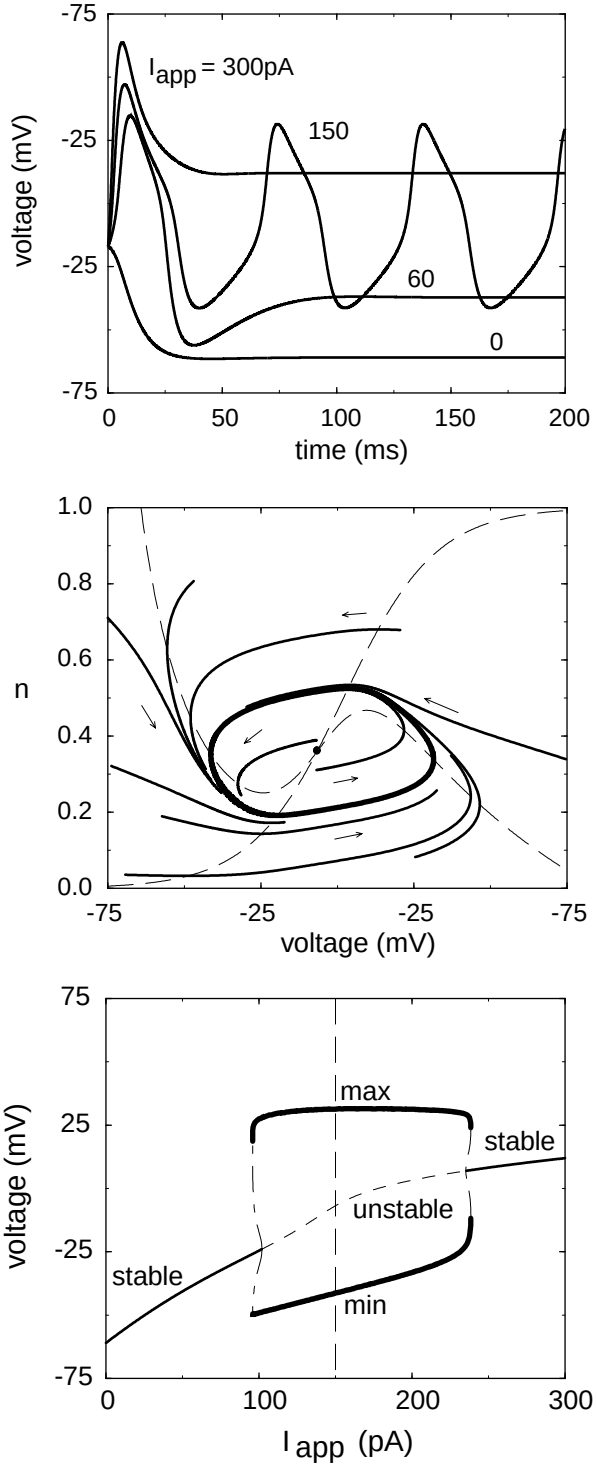

Figure 2.9 Panel A: Voltage records for the Morris-Lecar equations using the parameters in Exercise (**??**) and the indicated applied currents. Oscillations occur at $I_{app} = 150$pA. Panel B: The phase plane for the Morris-Lecar model for $I_{app} = 150$pA. The V-nullcline is the long-dashed line and the n-nullcline is the dot-dashed line. The heavy line is the limit cycle corresponding to the oscillation in Panel A, and the lighter lines are short trajectories that circulate in the counterclockwise direction toward the stable limit cycle. Panel C:A bifurcation diagram that catalogues the dynamical states of the Morris-Lecar model as a function of I_{app} with the other parameters fixed. The maximum and minimum of V on the limit cycle are represented by the heavy lines Compare the values for $I_{app} = 150$pA (long-dashed line) with the voltage record in Panel A.

2.5.1 Phase Plane Analysis

The mechanistic features underlying continuous spiking and action potentials can be understood more easily by plotting the solutions in the V-n phase plane. This is shown in Fig. (**??**) for $I_{app} = 150$pA, which leads to the pattern of repetitive spiking. Both the V-nullcline, which has the inverted "N" shape, and the n-nullcline, which is given by $n_\infty(V)$, are shown along with a number of representative trajectories. The trajectories circulate around the steady state in a counterclockwise direction as indicated by the velocity vectors. The intersection of the nullclines indicated by the filled circle is an unstable steady state with eigenvalues $\lambda_\pm = 0.265$ and 0.0221 (as determined using the *Sing pt* option in *XppAut*). This is evident from the two trajectories that start nearest to the steady state, both of which diverge from it. Indeed all of the trajectories converge towards a unique, closed trajectory indicated by the heavy line. This trajectory is called a *limit cycle* since it is the cyclic curve to which all the neighboring trajectories converge. A limit cycle cannot occur if the differential equations are linear, in which case the nullclines are straight lines. *A formal discussion of these issues are covered in Appendix (A) and should be referenced as necessary here.* The only cycles that are possible for linear equations occur around neutrally stable steady states (*cf.* Fig. (2.9)), and even then the cycles are not unique (Exercise (**??**)).

The simulations in Fig. (2.9) show that limit cycles occur only for certain parameter values and that the oscillations surround an unstable steady state. If only a single parameter, such as I_{app}, is changed, then by making small changes and testing the stability of the steady state it is possible to locate specific values at which the stability of the steady state changes. Such points where the character of the solution changes with a change in a parameter are called *bifurcation* points. Numerical algorithms have been developed that allow investigation of bifurcations to be done automatically. As we mentioned briefly in Chapter (1) *Auto*, which is one of the more useful of these algorithms, has been incorporated into *XppAut*.

Although we defer full discussion of bifurcations and bifurcation diagrams to Chapter (**??**), we have used the *Auto* option in *XppAut* to produce a bifurcation diagram for the Morris-Lecar model in Fig. (2.9C). In Fig. (2.9C), the characteristic values of the membrane potential are plotted on the ordinate as a function of I_{app}. The thin full and dashed lines are the steady state values of V for each value of I_{app}, with the full lines representing stable steady states and the dashed lines unstable states. Thus $I_{app} \approx 98$pA and 238pA are bifurcation points where the stability of the steady state changes. Near these points two new dynamical features appear: a stable limit cycle and an unstable limit cycle. The bifurcation diagram summarizes this by recording the maximum and minimum values of V on the limit cycles (heavy full line for stable and broken dashed line for unstable). For example, at $I_{app} = 150$pA the points on the heavy line correspond to the maximum and minimum of the spikes in Fig. (2.9A). This type of bifurcation is called a *subcritical Hopf bifurcation*. The mathematical properties of Hopf bifurcations are treated in more detail in Chapter (**??**). The existence of an unstable limit cycle should be no more surprising than the existence of unstable steady states.

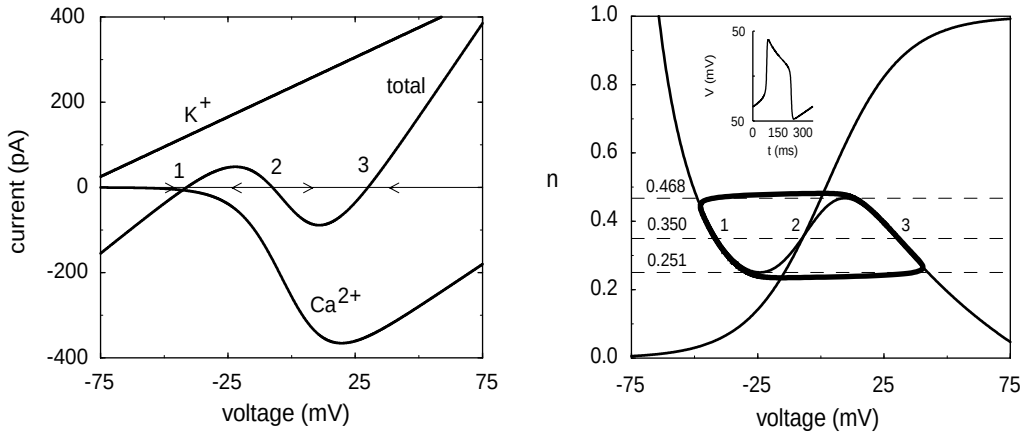

Figure 2.10 Panel A: The K^+, Ca^{2+}, and total current ($I_{Ca} + I_K + I_{leak} - I_{app}$) when $n = 0.35$. The states 1 and 3 are stable steady states and state 2 is unstable as indicated by the velocity vectors. Panel B: The phase plane for the Morris-Lecar model for $I_{app} = 150$pA, *cf.* Fig. 3.6B, except $\tau(V)$ has been increased by a factor of ten. The values $n = 0.468$ and 0.251 correspond to the maximum and minimum of the V-nullcline. The points 1, 2, and 3 at $n = 0.350$ are the steady states in Panel A. Inset shows the voltage record for a single spike.

It corresponds to a closed trajectory away from which all neighboring trajectories diverge. Exercise (**??**) illustrates a simple way to locate the unstable limit cycles for the Morris-Lecar model.

2.5.2 Why Do Oscillations Occur?

If the following three conditions on the Morris-Lecar equations hold, then oscillations will occur: 1) the V nullcline has the inverted N shape like that in Fig. (2.9B); 2) a single intersection of the V- and n-nullclines occurs between the maximum and minimum of the N and 3) the rate of change of V is much faster than n. All three conditions are met for the parameter values giving rise to oscillations in Fig. (2.9). The importance of the slow change in n, *i.e.*, the "delay" of the delayed rectifier, can be seen by examining the trajectories in Fig. (2.9B). If the rate of change of n were fast with respect to V, then the trajectories would not depolarize and hyperpolarize rapidly as they do in Fig. (**??**), but rather would bend towards the steady state, which would be stable. This is tested using *XppAut* by decreasing the value of the characteristic time for relaxation of n by decreasing the value of the parameter ϕ (see Exercise (**??**)).

It is easy to see why oscillations occur when the rate of change of V is very much faster than n and the nullcline have the shape in Fig. (2.9). In this case, we can treat changes in V under the assumption that n is constant. This describes changes on the "fast" time scale. Changes on the "slow" time scale of the delayed rectifier are then determined by changes in n. On the fast time scale we need only to consider the voltage

equation with n fixed:

$$C\frac{dV}{dt} = -g_L(V - V_L) - g_{Ca}m_\infty(V)(V - V_{Ca}) - g_K n(V - V_K) + I_{app}. \tag{2.28}$$

Since only the voltage is changing on this time scale, we can examine its dynamical behavior using the one dimensional phase portrait, rather than a phase plane. This is shown in Fig. (2.10A), where the total current, which is proportional to the the rate of change of V, is plotted along with the Ca^{2+} and K^+ currents for $n = 0.35$ and $I_{app} = 150$pA. The total current vanishes at three points, which are the steady states for the voltage when n is fixed. States 1 and 3 are stable and state 2 is unstable, as indicated by the velocity vectors in the figure. Note that at state 1 the membrane is polarized and the outward K^+ current dominates the Ca^{2+} inward current, whereas the opposite holds true at state 3. As we shall see, the oscillations can be thought of as transitions back and forth between the polarized and depolarized states, driven by slow changes in activation of the delayed rectifier current.

Fig. (2.10A) also explains why the V-nullcline in the Morris-Lecar model has the inverted N shape: The K^+ and leak current exceed the inward Ca^{2+} current at polarized voltages between states 1 and 2, whereas the Ca^{2+} current exceeds the other currents between states 2 and 3. This voltage-dependent competition between inward and outward currents leads to a maximum and minimum in total current and, therefore, the inverted N shape for the nullcline.

The three steady states of the voltage also can be found graphically in the phase plane by locating the intersection of the line $n = 0.35$ with the V-nullcline. This is shown in Fig. (2.10B). It is clear from the figure that if n exceeds 0.468 (the maximum on the right branch of the V-nullcline), then the voltage has only a single polarized steady state on the left branch of the V-nullcline. Similarly if n is smaller than 0.251 (the minimum on the left branch), then on the fast time scale the voltage has only a single depolarized steady state on the right branch. For $0.251 \leq n \leq 0.468$ two stable steady states and one unstable state occur and the voltage is said to be *bistable*.

To understand how bistability on the fast time scale leads to oscillations, we need to understand how n changes on the longer time scale. Assume that initially the membrane is polarized at state 1 in Fig. (2.10B) with $n = 0.35$. Because this point is above the n-nullcline, n will decrease. As n decreases, V will stay close to the V-nullcline because it relaxes rapidly to the closest steady state value. Thus the trajectory follows the polarized branch, as indicated by the heavy line, until the minimum at $n = 0.251$ is reached. Beyond the minimum, however, stable polarized states no longer exist and V rapidly relaxes to the only remaining steady state, which is on the depolarized branch of the V-nullcline. During the depolarization, however, the n-nullcline is crossed. Thus on the depolarized branch, n increases–tracking the V-nullcline upward until the maximum at $n = 0.468$ is reached and the membrane rapidly repolarizes.

The abrupt transitions from the polarized to depolarized branch and back again have lead to the name *relaxation oscillator* for systems of equations that have well-separated time scales. For the parameters in Fig. (**??**). the Morris-Lecar model is not

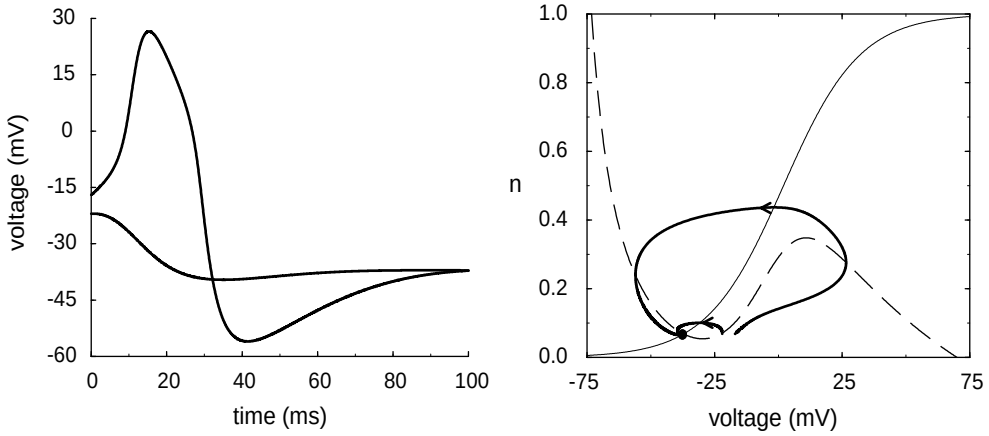

Figure 2.11 Excitability in the Morris-Lecar model for $I_{app} = 60$pA. Panel A: An initial deviation of the voltage to -22mV relaxes rapidly to the steady state voltage, whereas a deviation to -17mV produces an action potential. Panel B: The trajectories in Panel A represented in the phase plane. When V changes much faster than n, the location of the V-nullcline (long-dashed line) sets the threshold for action potential spikes.

a relaxation oscillator. However, when the characteristic time for n is increased by a factor of 10, the limit cycle (heavy line in Fig. (2.10B)) closely approximates that for a relaxtion oscillator. If the characteristic time were increased sufficiently–or the characteristic time for V were decreased sufficiently–then the trajectory would coincide with the bistable portions of the V-nullclines and the rapid excursions of the voltage would occur precisely at $n = 0.251$ and 0.468. The inset in Fig. (**??**B) shows a single voltage spike that illustrates the rapid upstroke and downstroke for the limit cycle in the figure. The inset also illustrates that the shape of the depolarized and polarized portions of the spike reflects the shape of the two branches of the V-nullcline.

2.5.3 Excitability and Action Potentials

Another dynamical feature of the Morris-Lecar model is *excitability*. The term "excitable" has generally been a bit fuzzy in its definition and has varied from publication to publication. Excitability can be precisely characterized in a spatial context, although in non-spatial settings, the definition is not as clear - hopefully this will be clear from the following explanation. An "excitable system" is one which has a single globally stable attracting rest state, but in which there exists a threshold perturbation strength for which the system supports an undiminishing propogating signal through the medium. In models which do not incorporate space, the concept is less clear since the propogation largely depends on the spatial coupling in addition to the dynamics at each spatial location. A useful working definition is that a steady state is excitable when small perturbations return to the steady state, but larger (i.e. above a threshold) perturbations

cause large transient deviations from away from the steady state. An example of this is shown in Fig. (2.11A), where the time course of the voltage with an applied current of 60pA and initial conditions of $n(0) = n^{ss} = 0.0685$ and either $V(0) = -22$ or -17mV are used. For $V(0)$ less than about -18.1mV the voltage increases only slightly before it decreases monotonically to its steady state value of *ca.* -37mV. For larger initial deviations, like that for $V(0) = -17$mV, the voltage increases dramatically producing an action potential spike before returning to steady state.

The explanation for excitability can be understood most easily in the phase plane. In Fig. (2.11B) we have plotted the trajectories for the two initial conditions in Fig. (2.11A) along with the two nullclines. The trajectories for initial conditions $V(0) \leq -22$mV start at points in phase space *above* the V-nullcline and below the n nullcline. This implies that the initial velocity vector, and therefore, the initial trajectory, points in the direction of smaller potentials and larger values of the activation of the delayed rectifier K^+ current. Thus the voltage begins to decrease and continues to do so since the K^+ current activates as n increases. This contrasts with the trajectory that starts at $V(0) = -17$mV, for which the initial velocity vector points in the direction of increasing voltage. Even though n is increasing in this region, which is also below the n-nullcline, the rate of increase of voltage exceeds that of n and the trajectory moves to higher voltages until it crosses the V-nullcline and begins to decrease.

The threshold value of $V(0)$ above which action potentials occur depends on the shape of the nullclines and the rate of activation of n. However, it is close to the point where a line drawn parallel to the V axis at n^{ss} crosses the V-nullcline. It is not hard to check that it will be exactly at that point if n changes much more slowly than the voltage (*cf.* Exercise (**??**)).

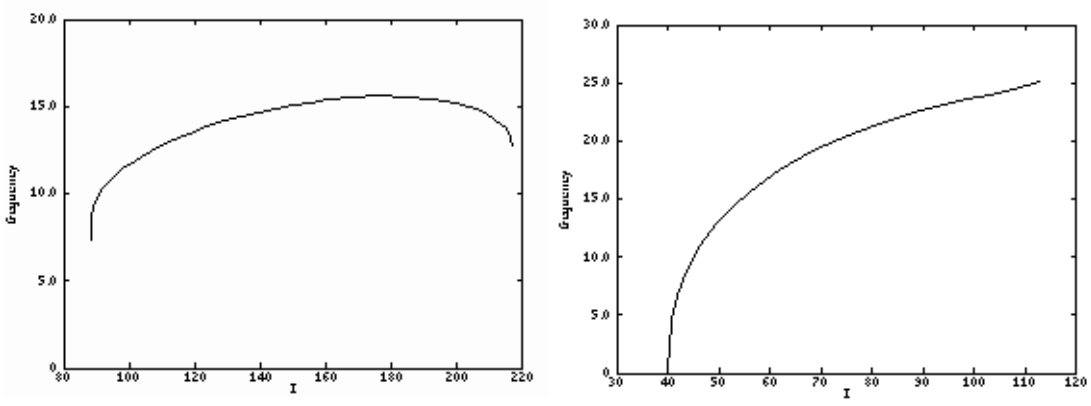

Figure 2.12 Examples of Voltage-Freqency plots for the Morris-Lecar model with parameters that result in Type I dynamics (Panel A) and Type II dynamics (Panel B). Taken from Rinzel and Ermentrout. NEED TO REMAKE FIGS IN POSTSCRIPT

2.5.4 Type I vs Type II spiking

Many investigators are now interested in applying biophysical models of neurons and other spike generating mechanisms to the study of information transfer using information theoretic measures. It is particularly important, therefore, that the dynamical behavior of a model be characterized over the space of parameters and that the characteristics of the spike generating model match the intended use. Both the Hodgkin Huxley and Morris Lecar models produce trains of action potentials when sufficiently depolarized. Muscle fiber and axons innervating muscle fiber *other examples?* are examples of situations where a strong, consistent signal is required. By varying the depolarizing current, we can see that depolarization beyond threshold results in rapid oscillations whose frequency does not vary significantly as the depolarizing stimulus is increased. (show figure). This is an example of a type II oscillator. Many neurons, including the ubiquitous cortical pyramidal cell, exhibit firing properties that are fundamentally different from the Type II oscillator. Frequency (but not amplitude) of spiking in these cells is more dependent on the input current, and, most importantly, models of these cells can produce arbitrarily low frequencies of oscillations. These models are classified as type I oscillators. The Morris-Lecar model is particularly interesting because it can exhibit Type I or Type II behavior, depending on the parameters that are chosen. Examples of Voltage-Frequency plots for the Morris-Lecar model in these two regimes are shown in Fig. (2.12). The Morris-Lecar Type II oscillator or the Hodgkin Huxley axon model would not be appropriate for the study of subtle aspects of information transfer. We have seen that Type II spiking results from a Hopf bifurcation as input current is increased. Type I spiking results from a saddle-node bifurcation. The difference between these two bifurcations is discussed in Appendix (**??**), and we explore saddle node bifurcations in the Morris-Lecar model in Exercise (**??**). We also note that there are other levels of complexity for spikeing models. Models of bursting neurons, which fire trains of action potentials separated by periods of quiescence, require additional slow variables. We do not discuss these models here.

2.5.5 Phase and Phase Response Curves

Maybe add section on this as appropriate.

2.6 Summary

The dynamical features of "fast" and "slow" variables with either N-shaped or inverted N-shaped nullclines are common to many biological mechanisms at the cellular level. In addition to producing oscillations in the barnacle muscle and the retinal ganglion cell, the same dynamical structures appear in mechanistic models of insulin secretion (Chapter (**??**)) and Ca^{2+} oscillations (Chapter (**??**)). In each of these models the nature of the fast and slow variables are determined by processes that are peculiar to

each mechanism. This dynamical paradigm appeared first in cellular neuroscience in simplications of the Hodgkin-Huxley equations by FitzHugh and later Nagumo. The simplest version of this type of system involves a linear nullcline for the slow variable and a cubic nullcline, which has the inverted N shape, for the fast variable. Equations of this type (see Exercise (**??**)) are often given the generic name *FitzHugh-Nagumo* (or FH-N) models.

Suggestions for further reading

- Ionic Channels of Excitable Membranes. Bertil Hille.
- Analysis of Neural Excitability and Oscillations. Rinzel and Ermentrout.
- ...

2.7 Appendix: Plotting Functions with *XppAut*

It is possible to evaluate and plot functions using *XppAut*, thus extending the functionality of the program. The .ode files that do this rely on solving the equation $dx/dt = 1$, *i.e.*, $x(t) = x(0) + t$. Thus any function, $f(x)$, that is declared as an auxiliary function can be plotted at the sequence of points $x(0), x(0) + t_1, \ldots, x(0) + t_n$ where $0, t_1, \ldots, t_n$ are the times at which the solution to $dx/dt = 1$ are recorded in the *DataViewer*. Choosing any of the methods for solving the ODE in the *nUmerics* menu that use a fixed time step gives $t_1 = dt, t_2 = 2dt, \ldots, t_n = ndt$. Thus by choosing the time step (*Dt*) and the length of time to integrate (*Total*) under the *nUmerics* menu, it is possible to plot representative values of $f(x)$ in a *Graph* window in *XppAut*. The file below illustrates the basic form of the plotting file ("plotting.ode") that was used to obtain the data for Fig. (**??**).

```
#plotting.ode
#.ode file for plotting the functions in Figure () where
#x is the dummy variable for plotting the auxiliary functions.
#initial value of x
x(0)=-80
#the equation
dx/dt=1
#the equilibrium activation and inactivation
#functions to plot
aux ninfact=1/(exp(-(x+25)/5)+1)
aux ninfinact=1/(exp((x+50)/2)+1)
#the characteristic times to plot
aux tauact=5/cosh((x+25)/2*5)
aux tauinact=5/cosh(-(x+50)/2*2)
done
```

The plots for Fig. (**??**) were made using this file with the Euler method, a time step of 0.25, and a total time of 140. This produced values for the function at 561 values of x ranging from -80 to +60.

2.8 Exercises

1. Show that the constants S_o and V_o in Eqs. (2.18) and (2.19) can be written as:

$$S_o = \frac{1}{a-b} \text{ and } V_o = \frac{\ln(k_o^+/k_o^-)}{a-b}. \tag{2.29}$$

2. Use the results in Exercise 2.1 to verify that the expressions in Eqs. (2.20)-(**??**) are correct. Note that a special case of Eqn. (2.21) when $a = -b$ is

$$\tau(V) = \frac{1}{\sqrt{k_o^+ k_o^-}\cosh((V-V_o)/2S_o)} \tag{2.30}$$

   [*Hint*: recall that $\tanh(x) = (e^x - e^{-x})/(e^x + e^{-x})$ and $\cosh(x) = e^x + e^{-x}$.]
3. Using Eqn. (2.7) show that mV, ms, pS, fF, and fA form a consistent set of electrical units.
4. It is possible to estimate a characteristic time for the relaxation of the membrane potential using Eqn. (2.7). When the channel is completely open, show that the equation can be written:

$$dV/dt = -(V - V_{rev})/\hat{\tau} + I_{app}/C \tag{2.31}$$

   where $\hat{\tau} = g/C$. Show that $\hat{\tau}$ is the characteristic time for relaxation of the voltage to a steady state value $V^{ss} = V_{rev} + I_{app}/g$.
5. For biological membranes a typical capacitance per unit area is 1 μFcm^{-2} whereas conductances per unit area are in the range $10^{-4} - 10^{-3}$ Scm^{-2}. Using these facts and Exercise (**??**), show that typical relaxation times for the membrane potential are in the range of 1-10 ms.
6. Use the *XppAut* file below to reproduce the voltage clamp simulations given in Fig. (**??**) for the voltage activated channel described by Eqn. (2.8) and Eqn. (2.6).

```
#voltclamp.ode
param V=-60,Vo=-25,So=5,A=10,g=2,Vrev=-65
#initial condition
nO(0)=0.0
#activation functions
ninf=1/(exp(-(V-Vo)/So)+1)
tau=A/cosh((V-Vo)/(2*So))
#equation for activation
dnO/dt=-(nO-ninf)/tau
#auxiliary variables
#current
```

```
aux i=g*n0*(V-Vrev)
#maximum current
aux imax=g*ninf*(V-Vrev)
#logarithm of relative current
aux lndi=ln((g*ninf*(V-Vrev)-g*n0*(V-Vrev))/(g*(V-Vrev)))
done
```

7. Use the analytical solution to Eqn. (2.8) to show that the time course of the rising current when the voltage is clamped from the holding potential, $V_{holding}$, to the test potential, V_{test}, in Fig. (**??**A) has the form:

$$I(t) = g \cdot (V_{test} - V_{rev}) \cdot [\exp(-t/\tau(V_{test}))(n_\infty(V_{hold}) - n_\infty(V_{test})) + n_\infty(V_{test})]. \quad (2.32)$$

Since V_{hold} is chosen so that $n_\infty(V_{hold}) \approx 0$, it follows that the rising current is given by

$$I(t) = g \cdot (V_{test} - V_{rev}) \cdot n_\infty(V_{test})(1 - \exp(-t/\tau(V_{test}))). \quad (2.33)$$

Similarly show that the tail current can be approximated by

$$I(t) = g \cdot (V_{hold} - V_{rev}) \cdot n_\infty(V_{test}) \exp(-t/\tau(V_{hold})). \quad (2.34)$$

8. Write an *XppAut* file suitable for solving the Morris-Lecar equations, (2.23)-(2.27), for the parameter values $V_K = -84$, $V_L = -60$, $V_{Ca} = 120$, $I_{app} = 0$, $g_K = 8$, $g_L = 2$, $g_{Ca} = 4$, $C = 20$, $V_1 = -1.2$, $V_2 = 18$, $V_3 = 2$, $V_4 = 30$, $\phi = 25$ and the initial conditions $V(0) = -60$ and $n(0) = 0.01$ (in the standard set of units in Table 2.1). Check your file against the one in the *XppAut* tutorial.
9. Use the *XppAut* file in Exercise (**??**) to solve the Morris-Lecar model for the four values of I_{app} given in Fig. 2.6A. Create a phase plane window in *XppAut* and use the *Nullcline* option to draw the nullclines. Using the *Initialconds/(M)ouse* option verify that there is a unique stable limit cycle. Compare your results with Fig. (**??**). Use the *Sing pts* option to locate the steady state and to obtain its eigenvalues.
10. Use the *XppAut* file in Exercise (**??**) to convince yourself that an infinite number of closed trajectories surround a neutrally stable steady state for a 2×2 system of linear equations. [Hint: Use the *Initialconds/(M)ouse* option to click on different initial conditions in the phase plane.]
11. Using the *XppAut* file in Exercise (**??**), show that the time constant of the delayed rectifier in the Morris-Lecar model determines whether or not the steady state at $I_{app} = 150$pA is stable or unstable and also determines the maximum and minimum values of the voltage on the limit cycle. For $I_{app} = 60$pA check that the value of $V(0)$ above which action potentials occur is close to the point where a line drawn parallel to the V axis at n^{ss} crosses the V-nullcline. Also verify that it will be exactly at that point in the limit that n changes much more slowly than the voltage. [Hint: Increasing the parameter ϕ increases the time constant for n.]
12. Explain how you could locate the unstable limit cycles near the bifurcation point in the Morris-Lecar model in Fig. (**??**) by integrating the equations *backwards* in

time. Use the *XppAut* file in Exercise (**??**) to do this by changing the signs of the parameters ϕ and c for $I_{app} = 99$pA. (Why does this work?) Verify that the steady state is now unstable and that trajectories that converged to the stable limit cycle in Fig. (**??**) now diverge from it.

13. The .ode file for the two variable retinal ganglion cell model discussed in Section (**??**) is

```
#rgc2.ode
#two variable model of the retinal ganglion cell
#leak current
param gL=8,VL=-70
IL=gL*(v-VL)
#sodium current
param gNa=150,VNa=75
tauh=0.3+3.5*exp((-(V+50)^2)/500)
hinf=1/(1+exp((V+50)/6.5))
minf=1/(1+exp(-(V+20)/6.5))
INa=gNa*minf*h*(V-VNa)
#applied current
param mag=70,dur=200,lag=100
Iapp(t)= mag*heav(t-lag)*(1-heav(t-(lag+dur)))
#equations
param c=10
v(0)=-50
dv/dt= (-IL-INa+Iapp(t))/c
dh/dt=(hinf-h)/tauh
#auxiliary function
aux n=1-h
done
```

The file simulates a time-dependent applied current, $I_{app}(t)$, that is zero for $0 \leq t \leq lag$ and $t \leq lag + dur$ and has a magnitude of mag during the interval $lag \leq t \leq lag+dur$. This is accomplished using the Heaviside "step" function (written heav(x) in *XppAut*), which is zero for $x \leq 0$ and one for $0 \leq x$. Use this file to simulate depolarizing currents of different durations and magnitudes and determine their effect on the voltage.

14. Modify the .ode file for the RGC in Exercise 2.13 so that the applied current no longer depends on time but is a parameter. Use this new .ode file to explore the properties of the model in the phase plane for different values of the depolarizing current.
15. Modify the .ode file in Exercise 2.14 so that $n = 1 - h$, instead of h, is the slow variable. Plot the nullclines in an *XppAut* window and show that they have the same form as in the Morris-Lecar model.

16. The FitzHugh-Nagumo model is

$$dv/dt = v(a - v)(v - 1) - w + i \tag{2.35}$$

$$dw/dt = bv - cw \tag{2.36}$$

where $0 < a < 1$, b, c, and i are parameters. Find analytic experssions for the v- and w-nullclines and sketch the phase plane for $i = 0$. Create an *XppAut* file for the FitzHugh Nagumo equations and explore their properties in the phase plane.

CHAPTER 3

Transporters and Pumps

Eric Marland and Joel Keizer

07-28

Ionic channels are not the only mechanism that cells use to transport impermeant species across membranes. Cells have developed a great variety of transport proteins for moving both ions and molecules from one cellular compartment to another. For example, to maintain the concentration imbalance of Na^+, K^+, and Ca^{2+} across the plasma membrane it is necessary to pump ions against significant concentration gradients. In the case of Ca^{2+} ions the ratio of concentrations outside to inside is greater than 4 orders of magnitude (*ca.* 2mM outside and 0.1μM inside). In addition to pumps, there are numerous specific cotransporters and exchangers that allow ions and small molecules to be transported selectively into internal compartments or out of the cell. Unlike ionic channels, for which the driving force is a passive combination of electrical potential and ionic concentration differences, most transporters and pumps expend considerable energy. In red cells, for example, it has been estimated that nearly 15% of the ATP that is produced through the metabolism of glucose is devoted to maintaining low cytoplasmic Na^+ and high cytoplasmic K^+ concentrations via Na^+/K^+ pumps.

In this chapter we provide an overview of some of the mechanisms, other than ionic channels, that cells use to pump and transport small molecules and ions. We first introduce the ideas behind passive transport, using a passive glucose transporter (GLUT) as an example. We then introduce analytic, diagrammatic, and numerical methods for calculating rates of transport and apply them to a simplfied model of GLUT transporter. Using the cotransport of glucose and Na^+ as an example, we then discuss

how to create models of transporters and how this transporter functions physiologically in intestinal epithelial cells. A great deal is known about the kinetic steps involved in the pumping of Ca^{2+} by Ca^{2+} pumps in internal stores, and we use this mechanism to illustrate how phosphorylation by ATP drives the pumping mechanism. In the final section of the chapter we focus on the cyclic nature of these mechanisms and describe additional transporters that operate via comparable kinetic cycles.

3.1 Passive Transport

We must be a little careful about what we call passive transport, since there is no free lunch. The following example is not without its energy costs, but it uses background thermal energy rather than the explicit energy in a particular molecule such as ATP.

Glucose is a six carbon sugar that is a major fuel for intermediary metabolism in animals. It is derived from carbohydrates in the gut and is transported through epithelial cells in the intestines into the blood stream and thence to the brain, pancreas, liver, muscle and other organs. There glucose is taken up and metabolized via glycolytic enzymes. Although uptake from the gut involves active co-transport of glucose with sodium ions, peripheral tissues such as fat, muscle, and liver transport glucose via a class of passive membrane transporters referred to as GLUT transporters. Since glucose is a major energy source for cells–indeed, it is the only energy source for the brain–understanding the rate of glucose transport into cells via GLUT is important physiologically.

Four isotypes of GLUT transporters have been isolated, GLUT1-GLUT4, each of which is prevalent in one or more types of tissue. GLUT2, for example, is found in pancreatic beta cells–the glucose-sensing cells that secrete insulin from pancreatic tissue–as well as liver cells. Extensive kinetic experiments have lead to a cartoon description of the steps involved in the tranport processes. The transitions of the transporter itself, facing the inside of the cell to facing the outside of the cell, is driven by heat or thermal fluctuation. Thus the heat of the system and the concentration gradient of glucose and the only driving forces in the system. Because no other energy is needed, it is called passive transport. It is similar in this sense to diffusion, which we discuss in Chapter 6.

Panel A of Fig. (3.1) shows four different states of the transporter. State S_1 has an empty binding site for glucose exposed to the exterior of the cell. When glucose binds to this state, the transporter makes a transition to state S_2, with glucose bound and facing the exterior. In S_2, a glucose molecule is bound to the transporter, which is still facing the exterior. State S_3 is the state with the transporter then facing the interior. When glucose dissociates from GLUT and ends up inside the cell, the transporter is left in state S_4. Finally, the cycle can repeat if S_4 makes the conformational transition to S_1. All of these processes are reversible.

This kinetic "cartoon" is easily translated into a conventional kinetic model of the sort often employed in biochemistry. Here the model takes the form of the diagram in Panel B of Fig. (3.1). Diagrams like this, which will be used extensively in the re-

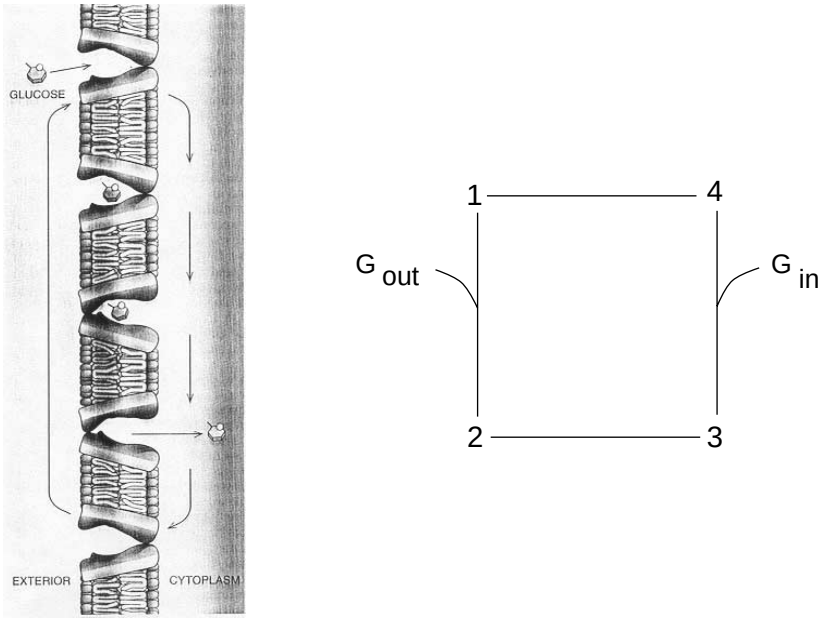

Figure 3.1 Upper Panel: Cartoon of four states of a GLUT transporter, showing the empty pore facing the exterior of the cell, glucose bound facing the exterior, glucose bound facing the interior, and the open pore facing the interior of the cell. Adapted from G. E. Leinhard, J. W. Slot, D. E. James, and M. M. Mueckler, How cells absorb glucose. *Scientific American*, January, 1992, pg. 89. Lower Panel: Four state kinetic diagram of a GLUT transporter based on the cartoon in the upper panel.

mainder of this book, represent molecular states or entities by symbols and transitions between states by solid lines. The labelled corners in Panel B correspond to the states S_1-S_4 of a GLUT transporter described in the previous paragraph and the lines represent elementary molecular processes. The transition from S_1 to S_2 is a *bimolecular* process since it requires the interaction of a glucose molecule (indicated as G_{out} in the diagram) and the GLUT molecule in S_1. The transition from S_2 to S_1, on the other hand, involves only the GLUT molecule and is, therefore, unimolecular: thus only S_2 appears at the end of the line connecting S_2 to S_1. This illustrates an important aspect of transitions between molecular states: they are reversable, corresponding to the property of microscopic reversibility of molecular processes.

The rates of the elementary processes denoted in the kinetic diagram are determined again by the law of *mass action* as we discussed in Chapter 1. Thus the rate of the transition from S_1 to S_2 is given by $J_{12} = k_{12}[G_{out}]x_1$, where the square brackets denote concentration, and x_1 represents the fraction of the GLUT molecules in S1, $x_1 = N_1/N$ where N is the total number of transporters. The factor k_{12} is the rate constant, in this case bimolecular, with practical units of $\mathrm{s}^{-1}\mathrm{mM}^{-1}$. Similarly the rate of the reverse reaction, $2 \to 1$, is given by $J_{21} = k_{21}x_2$ with k_{21} a unimolecular rate constant (with

Table 3.1 Rate Expressions for Glut Transporter

Forward Process	Rate	Reverse Process	Rate
$S_1 \rightarrow S_2$	$k_{12}[G_{out}]x_1$	$S_2 \rightarrow S_1$	$k_{21}x_2$
$S_2 \rightarrow S_3$	$k_{23}x_2$	$S_3 \rightarrow S_2$	$k_{32}x_3$
$S_3 \rightarrow S_4$	$k_{34}x_3$	$S_4 \rightarrow S_3$	$k_{43}[G_{in}]x_4$
$S_4 \rightarrow S_1$	$k_{41}x_4$	$S_1 \rightarrow S_4$	$k_{14}x_1$

units s^{-1}). Table 3.1 lists the forward and reverse rate expressions for all of the processes in the kinetic diagram.

Having established the correspondence of the diagram with rate expressions, we can write down the differential equations that the diagram represents. To do so we must keep track of the change that each elementary process in the diagram makes for each state. Thus the fraction of transporters in S_1, x_1, decreases with the transition to S_2 or S_4, and increases with transitions from S_1 or S_4. Using this idea, in conjunction with the kinetic diagram and Table 3.1, the ordinary differential equations follow for the rate of change in the number of states:

$$\begin{aligned} dx_1/dt &= -k_{12}[G_{out}]x_1 + k_{21}x_2 + k_{41}x_4 - k_{14}x_1 \\ dx_2/dt &= k_{12}[G_{out}]x_1 - k_{21}x_2 - k_{23}x_2 + k_{32}x_3 \\ dx_3/dt &= k_{23}x_2 - k_{32}x_3 - k_{34}x_3 + k_{43}[G_{in}]x_4 \\ dx_4/dt &= k_34x_3 - k_{43}[G_{in}]x_4 - k_{41}x_4 + k_{14}x_1 \end{aligned} \tag{3.1}$$

Since the kinetic model involves only interconversion of GLUT states, the total number of transporters should be preserved. This introduces the idea of a conservation law, $N_1+N_2+N_3+N_4 = N$ or $x_1+x_2+x_3+x_4 = 1$, that transporters are neither created nor destroyed. In this case, these equations preserve the total number of transporter already. This can be checked by adding together the expressions on the right hand side of Eqn. (3.1). It is easily verified that all of the terms cancel, leading to the result that $d(x_1+x_2+x_3+x_4)/dt = 0$, which shows that the sum of the fractions of transporters in different states does not change. That is, $x_1 + x_2 + x_3 + x_4$ has a constant value, which in this case is 1.

This implies that one of the dependent variables can be eliminated using the conservation law, say, $x_4 = 1 - x_1 - x_2 - x_3$. In this way, the differential equation for x_4 becomes redundant and the number of differential equations to be solved is reduced to only three along with the algebraic equation for x_4. If this is done, the equations can be written in the reduced form:

$$\begin{aligned} dx_1/dt &= m_{11}x_1 + m_{12}x_2 + m_{13}x_3 - k_{41} \\ dx_2/dt &= m_{21}x_1 + m_{22}x_2 + m_{32}x_3 \\ dx_3/dt &= m_{31}x_1 + m_{32}x_2 + m_{33}x_3 + k_{43}[G_{in}] \\ x_4 &= 1 - x_1 - x_2 - x_3 \end{aligned} \tag{3.2}$$

where the 3×3 array, m_{ij}, is a matrix whose elements can be found by substituting $x_4 = 1 - x_1 - x_2 - x_3$ into the first three equations of Eqn. (3.1). We leave it to the reader to verify, for example, that $m_{11} = -(k_{12}[G_{out}] + k_{14})$ and $m_{33} = -(k_{32} + k_{34} + k_{43}[G_{in}])$.

With the formulation of the model equations, the first steps in the modeling process are completed. What remains is the analysis of the equations. We will leave the analysis of this model for an excercise, while we will use a reduced model to demonstrate several ways to analyze the transport rates for transporters. An additional discussion of some of the basic terminology and techniques involved in the solution of these and more complicated equations that frequently arise in the modeling process are developed and discussed in the Appendix.

3.2 Transporter Rates

In the previous section we described a four-state model of a GLUT-type glucose transporter. Like all models of transporters the "states" are distinct molecular arrangements of the transporter protein and the small molecules (*ligands*) that interact with it. These states are the basic kinetic ingredients of the kinetic mechanism, and we identify the states by numbering them $S_1, S_2 \ldots M$, where M is the total number. As for the GLUT transporter, we summarize the mechanism by a kinetic diagram with lines between the states representing possible transitions. Each line stands for a forward and reverse step that can be either unimolecular or bimolecular. Which states are connected together and the nature of the transitions connecting the states must be determined experimentally, and the resulting diagrams summarize succinctly a great deal of kinetic information. As we saw, the diagram can be easily translated into differential equations that describe how the number of transporters in each state changes with time.

What is important physiologically is not the rate at which states of a transporter change with time but rather the rate at which the ions or molecules that are transported get across the membrane. This can be determined from the kinetic mechanism but requires additional analysis since the transport rate is a property of the entire mechanism rather than an individual step. To make this distinction clear, consider the simplified three-state version of the mechanism for a GLUT transporter in Fig. (3.2).

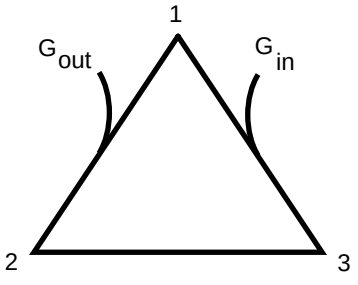

Figure 3.2 A three state diagram for the GLUT transporter.

In this simplification S_1 and S_4 in the four-state diagram in Fig. (3.1) have been treated as a single state. This type of simplification of a mechanism is described more fully in Chapter 4. The three transitions represented are the binding of glucose to the transporter from the exterior (S_1–S_2) and interior (S_1–S_3) of the cell and the conformation change in which the glucose moves from the exterior to the interior (S_2–S_3). Using x_i to represent the fraction of the total number of transporters in state $S_i = S_1, S_2, S_3$, the kinetic equations for this diagram are (*cf.* Eqn. (3.1)):

$$\begin{aligned} dx_1/dt &= -J_{12} + J_{31} \\ dx_2/dt &= J_{12} - J_{23} \\ dx_3/dt &= J_{23} - J_{31}. \end{aligned} \tag{3.3}$$

Here the J_{ij} are the *net rates* for the indicated transition with the $i \to j$ direction taken as positive. Thus,

$$J_{12} = k^*_{12}[G_{out}]x_1 - k_{21}x_2 \tag{3.4}$$

$$J_{23} = k_{23}x_2 - k_{32}x_3 \tag{3.5}$$

$$J_{31} = k_{31}x_3 - k^*_{13}[G_{in}]x_1. \tag{3.6}$$

In these equations we use a superscript $*$ to indicate a bimolecular rate constant. Net rates often appear in analyzing transport rates, and we will refer to the J_{ij} as *fluxes*. We can see by adding equations (3.3) together that the total number of tranporters is conserved. This means that the conservation equation, $x_1 + x_2 + x_3 = 1$, is already satisfied.

Experimentally, the rate at which glucose is transported into the cell is determined by the rate at which the concentration of glucose accumulate inside the cell in the absence of metabolism. Since $[G_{in}]$ is measured in millimolar, its rate of change of can be determined from the diagram and the rate equations Eqn. (3.3) to be:

$$\begin{aligned} d[G_{in}]/dt &= \frac{\text{number of millimoles of transporter}}{\text{cellular volume}} \cdot J_{31} \\ &= (10^3 N/V_{in}.500\mathsf{A}) \cdot J_{31} = R_{in}, \end{aligned} \tag{3.7}$$

where A is Avagadro's number, V_{in} is the cellular volume in liters, and the factor $10^3 N/\mathsf{A}$ converts the total number of transporters, N, to millimoles. A related measure of the transport rate is the rate of change of $[G_{out}]$, which give a measure of the transport rate, R_{out}, based on the loss of glucose from outside the cell. In analogy to Eqn. (3.7) R_{out} is easily seen to be given by

$$-d[G_{out}]/dt = (10^3 N/V_{out}\mathsf{A}) \cdot J_{12} = R_{out}. \tag{3.8}$$

In order to simplify the interpretation of experiments, V_{out} is usually chosen to be much greater than V_{in}, and so to a good approximation $[G_{out}]$ can be taken as a constant.

These two measures of the rate of transport of glucose are generally not proportional to one another since $J_{12} \neq J_{31}$. Inspection of Eqn. (3.3) shows, however, that the two

fluxes are equal at steady state, in which case

$$J_{12}^{ss} = J_{23}^{ss} = J_{31}^{ss} = J^{ss}. \tag{3.9}$$

This state condition can be inferred directly from the diagram in Fig. (3.2) by noting that the total flux into and out of each state must vanish for the number of transporters in each state to be steady. Thus at steady state J^{ss} provides a unique measure of the transport rate, which can be written:

$$R^{ss} = (10^3 N/V_{in}\mathsf{A}) \cdot J^{ss}. \tag{3.10}$$

This rate is achieved, however, only after a transient period during with the states of the transporter come to steady state.

To calculate the transport rate using Eqn. (3.10) it is necessary to calculate the value of J^{ss}, and this, in turn, requires the steady state values of the x_i. There are three ways that this can be done: numerically by solving the differential equations; with linear algebra, which gives an analytical expression for the x_i; or using diagrammatic methods. The first method is explored in the exercises using *XppAut*.

3.2.1 Algebraic Method

We can obtain the steady state value of the transport rate by solving the linear equations for the x_i. Substituting the expressions for the fluxes given in Eqn. (3.4)-Eqn. (3.6) into Eqn. (3.3) and eliminating x_3 using the conservation condition, $x_3 = 1 - x_1 - x_2$, gives the 2×2 linear equations

$$d\mathbf{x}/dt = \hat{A}\mathbf{x} + \mathbf{y} \tag{3.11}$$

with

$$\hat{A} = \begin{pmatrix} -(k_{12} + k_{13} + k_{31}) & k_{21} - k_{31} \\ k_{12} - k_{32} & -(k_{21} + k_{23} + k_{32}) \end{pmatrix} \text{ and } \mathbf{y} = \begin{pmatrix} k_{31} \\ k_{32} \end{pmatrix}. \tag{3.12}$$

To simplify notation we have introduced the *pseudounimolecular* rate constants

$$k_{12} = k_{12}^*[G_{out}] \text{ and } k_{13} = k_{13}^*[G_{in}]. \tag{3.13}$$

The steady state of Eqn. (3.11) is determined by the algebraic equation

$$\hat{A}\mathbf{x}^{ss} = -\mathbf{y}. \tag{3.14}$$

According to Eqn. (**??**) in Section (**??**), this equation has the solution

$$\mathbf{x}^{ss} = -\hat{A}^{-1}\mathbf{y}. \tag{3.15}$$

with $\hat{A}^{-1}$ the inverse matrix of $\hat{A}$. Using the explicit expression for the $\hat{A}^{-1}$ given in Appendix 2.5, Eqn. (3.15) gives

$$\begin{aligned} x_1^{ss} &= (a_{22}y_1 - a_{12}y_2)/det\hat{A} \\ x_2^{ss} &= (-a_{21}y_1 + a_{11}y_2)/det\hat{A} \\ x_3^{ss} &= 1 - x_1^{ss} - x_2^{ss}. \end{aligned} \tag{3.16}$$

To evaluate the transport rate using the algebraic method we need to substitute the expressions in Eqn. (3.16) into one of the expressions in Eqn. (3.9) for J^{ss}. For example, using the first expression gives

$$J_{12}^{ss} = \frac{1}{det\hat{A}}(k_{12}(a_{22}y_1 - a_{12}y_2) - k_{21}(-a_{21}y_1 + a_{11}y_2)). \tag{3.17}$$

To get an explicit expression in terms of the rate constants, k_{ij}, using Eqn. (3.17) we need to substitute the expressions for the matrix elements, a_{ij}, given in Eqn. (3.12) and then calculate the determinant of $\hat{a}$. The resulting expression is messy and offers numerous opportunities for making algebraic mistakes. An alternative is to use the diagrammatic method, which circumvents all of these algebraic difficulties.

3.2.2 Diagrammatic Method

Diagrams that represent mathematical expressions are in common use in both quantum electrodynamics ("Feynman diagrams") and statistical mechanics but are significantly less familiar in biology. Although the diagrammatic method for obtaining J^{ss} involves a few new ideas, it leads to vastly simpler, more transparent expressions for the fluxes than the algebraic method. To help motivate the use of diagrams, consider the following infinite sum:

$$\frac{1}{2} + \frac{1}{4} + \ldots + \frac{1}{2^n} + \ldots = \sum_{n=1}^{\infty} \frac{1}{2^n} \tag{3.18}$$

Even if the reader has previously encountered this geometric series, few probably remember that the sum converges exactly to the value one. On the other hand, a simple glance at the diagram in Fig. (3.3) makes the answer clear immediately.

Diagrams of the sort that are used in solving for the fluxes for the three-state GLUT

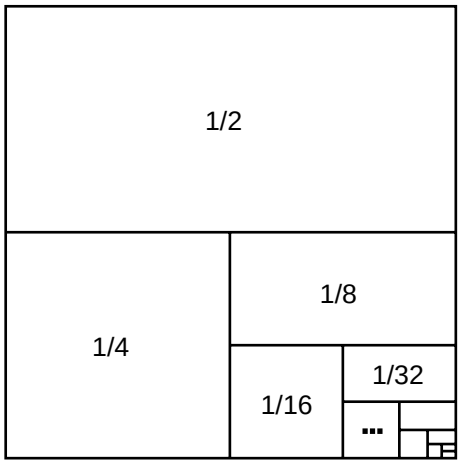

Figure 3.3 A diagram representing the geometric series in Eq.()

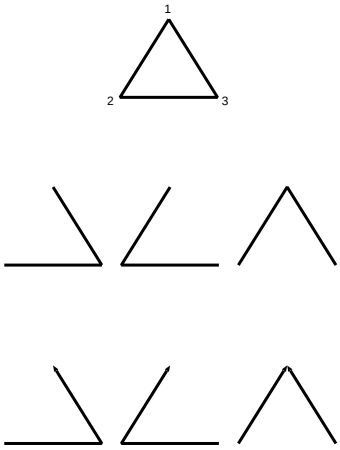

Figure 3.4 The complete diagram at the top, partial diagrams in the middle, and directed diagrams for state S_1 at the bottom for the 3-state GLUT transporter model.

transporter are shown in Fig. (3.4). In general a diagram is a set of vertices (representing the states) and lines representing unimolecular (or pseudounimolecular) transitions between states. A *complete diagram* for the GLUT transporter, which includes all of the lines and all of the vertices in the model is shown in the top panel of Fig. (3.4). Note that it differs from the kinetic diagram in Fig. (3.1) since the glucose concentrations have been absorbed into the pseudounimolecular rate constants as in Eqn. (3.13). The three *partial diagrams* for the model (with the vertices unlabeled) are shown in the middle panel of Fig. (3.4). Partial diagrams are obtained from the complete diagram by removing lines and have the maximum number of lines possible without forming a cycle. A third type of diagram, called the *directional diagram* can be constructed from the partial diagrams. Directional diagrams have arrowheads attached to the lines, such that all of the lines "flow" into a single vertex. The directional diagrams for state S_1 are given in the lower panel of Fig. (3.4). Note that for ease in writing the arrowhead on a line will be dropped whenever its direction is obvious, as in the first and second directional diagram in the lower panel of Fig. (3.4). Three comparable directional diagrams can be drawn for states S_2 and S_3.

These diagrams represent algebraic expressions just as the areas in the diagram for the geometric series in Fig. (3.3) represent fractions. For these diagrams each line with an arrowhead (a *directed line*) represents the unimolecular or pseudounimolecular rate constant for the indicated transition. For example, the two lines in the third diagram in the lower panel of Fig. (3.4) represent k_{21} and k_{31}. Diagrams with several directed lines represent the product of all the indicated rate constants. Thus the the directional diagrams stand for products of two rate constants, *e.g.*, the first directional diagram in Fig. (3.4)C is shorthand notation for the product $k_{23}k_{31}$, whereas the second and third diagrams represent $k_{21}k_{32}$ and $k_{21}k_{31}$, respectively.

There is a general theorem that connects the directional diagrams with the fractional occupancy of states in the kinetic diagram. In particular the fractional occupany

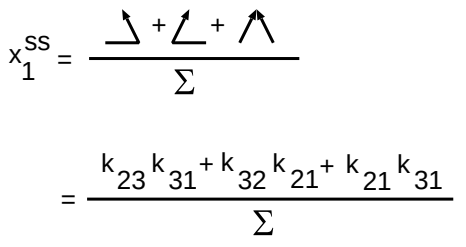

Figure 3.5 Diagrammatic expression for the fractional occupancy of GLUT transporters in state S_1 at steady state.

of state S_i is given by the expression:

$$x_i^{ss} = \frac{\text{sum of all state } S_i \text{ directional diagrams}}{\text{sum of all directional diagrams}} \tag{3.19}$$

For x_1^{ss} it yields the expressions given in Fig. (3.5), where we have adopted the symbol Σ to represent the sum of all directional diagrams. The division by Σ ensures that $\sum_i x_i^{ss} = 1$.

Although the expression for x_i^{ss} in Eqn. (3.19) can be proven for any mechanism that can be represented by a kinetic diagram, we give a proof only for the three-state GLUT model. Since the steady state solution for this model is unique, we need only show that the expression in Eqn. (3.19) leads to the equality of all the fluxes J_{ij} at steady state. Rather than write out the algebra, we use the diagrams themselves to complete the proof. This is illustrated in Fig. (3.6), where J_{12}^{ss} is calculated. The second equality uses Eqn. (3.19), and in the third we have used the directed lines corresponding to the rate constants k_{12} and k_{21} to add extra directed lines to the diagram. Two pairs of terms cancel to give the final equality in which only the difference of the two *cyclic diagrams* appear. A cyclic diagram is derived from a partial diagram with one additional flux added to produce a cycle. For more details consult the book by T. L. Hill, *Free Energy Transduction in Biology*. Similar manipulations show that the third equality

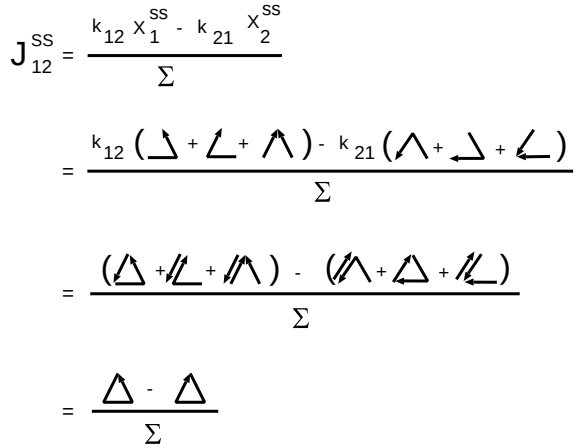

Figure 3.6 Calculation of J_{12}^{ss} using diagrams.

also holds for J_{23}^{ss} and J_{31}^{ss} (Exercise 3.5). Thus $J_{12}^{ss} = J_{23}^{ss} = J_{31}^{ss}$, which is the condition for steady state.

The final equality in Fig. (3.6) is a corollary that can be generalized for any kinetic diagram, *i.e.*:

$$J_{ij}^{ss} = \frac{\text{sum of differences of cyclic diagrams with i-j in the cycle}}{\Sigma} \tag{3.20}$$

Thus the steady state flux for the three-state model is given by the difference of the two cyclic fluxes (counterclockwise - clockwise) divided by the sum over all partial diagrams for the complete diagram.

We need one more key fact about cyclic diagrams in order to simplify the expression for the transport rate, namely, that the product of the bimolecular and unimolecular rate constants in the counterclockwise direction of a cycle equal those in the clockwise direction. This is called the *thermodynamic restriction* on the rate constants because it is a consequence of the laws of chemical thermodynamics. To see why the thermodynamic restriction is true, consider the situation in which no transport occurs, *i.e.*, $[G_{out}] = [G_{in}]$. If we revert to the notation for chemical reactions, then the three steps in the cycle for the three-state GLUT transporter can be written:

$$\begin{aligned} G_{out} + S_1 &= S_2 \text{ with equilibrium constant } K_{12} = k_{21}/k_{12}^* \\ S_2 &= S_3 \text{ with equilibrium constant } K_{32} = k_{32}/k_{23} \\ S_3 &= S_1 + G_{in} \text{ with equilibrium constant } K_{31} = k_{13}^*/k_{31} \end{aligned} \tag{3.21}$$

where S_1, S_2, and S_3 represent the three states of the transporter. It is easy to show that the equilibrium constants, K_{ij}, for the "reactions" are the ratio of the rate constants, as indicated next to each reaction in Eqn. (3.21) (see Exercise 3.6). If we add these three chemical reactions together we get the net reaction:

$$G_{out} = G_{in}. \tag{3.22}$$

A basic property of equilibrium constants (see Exercise 3.7) is that when reactions are added, the equilibrium constants are multiplied. Therefore the equilibrium constant for the net reaction Eqn. (3.22) is

$$K_{net} = K_{12}K_{23}K_{31} \tag{3.23}$$

$$= \frac{k_{21}k_{32}k_{13}^*}{k_{12}^*k_{23}k_{31}}. \tag{3.24}$$

But at chemical equilibrium the concentrations of product (G_{in}) and reactant (G_{out}) in Eqn. (3.22) are equal, so that $K_{net} = [G_{in}]^{eq}/[G_{out}]^{eq} = 1$. Using this fact in Eqn. (3.23) and Eqn. (3.24) and rearranging gives the thermodynamic restriction on the rate constants:

$$k_{13}^*k_{32}k_{21} = k_{12}^*k_{23}k_{31}. \tag{3.25}$$

When constructing models, it is essential that the thermodynamic restriction on rate constants be satisfied for all cycles. Otherwise the model will violate the second law of thermodynamics.

3.2.3 Rate of the GLUT Transporter

Using the results in the previous sections we can write an explicit expression for the rate of the three-state GLUT transporter. Combining Eqn. (3.10) with the final equation in Fig. (3.6), we obtain

$$R^{ss} = \frac{10^3 N}{V_{in}\mathsf{A}} \cdot \frac{k_{12}^*[G_{out}]k_{23}k_{31} - k_{13}^*[G_{in}]k_{32}k_{21}}{\Sigma} \tag{3.26}$$

$$= \frac{10^3 N k_{12}^* k_{23} k_{31}([G_{out}] - [G_{in}])}{V_{in}\mathsf{A}\Sigma}, \tag{3.27}$$

where in the second equality we have used Eqn. (3.25), the thermodynamic restriction on the rate coefficients. According to Eqn. (3.27), the steady state transport rate is positive when the concentration of glucose outside of the cell exceeds that inside and vanishes when the two concentrations are the same. This is a consequence of the thermodynamic restriction on the rate constants and is just what is expected for a passive transport mechanism. In the next section we consider the Na^+/glucose cotransporter, which utilizes a gradient of Na^+ to transport glucose from a low concentration to a higher concentration.

For a *symmetric* transporter there is no difference between the kinetic steps occuring inside and outside of the cell. This means that the rate constants for the transitions $2 \to 3$ and $2 \leftarrow 3$ are the same and that the association and dissociation rate constants are the same inside and outside as well. In this case there are only three different rate constants:

$$\begin{aligned} k_{12}^* &= k_{13}^* = k^+ \text{ (glucose association)} \\ k_{21} &= k_{31} = k^- \text{ (glucose dissociation)} \\ k_{23} &= k_{32} = k \text{ (transport).} \end{aligned} \tag{3.28}$$

It is not difficult to evaluate the sum of the directed diagrams, Σ, explicitly in this case (see Exercise 4.8) which is

$$\Sigma = k^+(2k + k^-)\left(K + [G_{out}] + [G_{out}]\right), \tag{3.29}$$

where we have written the dissociation constant $K = (k^-/k^+)$. Thus for the symmetic GLUT transporter model the transport rate can be written

$$R^{ss} = \frac{R_{max}([G_{out}] - [G_{in}]))}{K_d + ([G_{out}] + [G_{in}])}, \tag{3.30}$$

where the maximal rate is

$$R_{max} = \frac{10^3 N k k^-}{(2k + k^-)V_{in}\mathsf{A}}. \tag{3.31}$$

Eqn. (3.30) and Eqn. (3.31) provide explicit expressions for the transport rate for the symmetric transporter in terms of the rate constants for the model.

Experimentally glucose uptake can be measured using 3-O-methyl glucose, a non-metabolizable analogue of glucose. This further simplifies the expressions, since the concentration of the analogue is initially zero, $G_{in} = 0$, inside the cell. As a practical matter experiments involve large numbers of cells rather than a single cell. However, both N and V_{in} increase in proportion to the number of cells, so that the value of R_{max} is still characteristic of a single cell. So for this type of experiment the rate expression in Eqn. (3.30) can be written

$$R^{ss} = \frac{R_{max}[G_{out}]}{K + [G_{out}]}. \tag{3.32}$$

This has the same form hyperbolic form as the rate expression for the Michaelis-Menten model in Eqn. (**??**).

One way to analyze the experimental rate of glucose uptake is using an Eadie-Hofstee plot. The Eadie-Hofstee plot is a graph of the experimental rate of glucose uptake, R, versus $R/[G_{out}]$ for a range of values of $[G_{out}]$. According to Eqn. (3.32) this plot should give a straight line with y-intercept equal to R_{max} and slope equal to K. This can be seen using a little algebra, first rearranging Eqn. (3.32) to get

$$R/[G_{out}] = \frac{R_{max}}{K + [G_{out}]} \tag{3.33}$$

and then multiplying both sides by $K + [G_{out}]$ and then dividing by $R/[G_{out}]$ and rearranging to obtain:

$$[G_{out}] = \frac{R_{max}}{R/[G_{out}]} - K. \tag{3.34}$$

If this experssion for $[G_{out}]$ is substituted in the second factor in the following identity:

$$R = \frac{R}{[G_{out}]} \cdot [G_{out}], \tag{3.35}$$

we obtain

$$R = R_{max} - \frac{R}{[G_{out}]} \cdot K, \tag{3.36}$$

which is the Eadie-Hofstee expression for the rate. Exercise 3.9 illustrates how *XppAut* can be used to simulate transport rates for the four-state model of a GLUT transport and analyze the results using an Eadie-Hofstee plot.

3.3 How to Make a Model: The Na^+/Glucose Cotransporter

A great variety of specialized proteins have evolved to transport specific substance across membranes in cells. Whereas the mechanisms of these transporters differ in

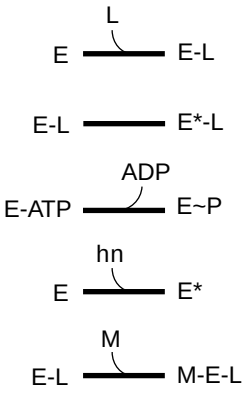

Figure 3.7 Elementary kinetic processes for transporters representing: ligand (L) binding, ligand transport, phosphorylation, light excitation, and multiple ligand binding.

detail, they also share a number of common features. For example, all of the known transporters bind the ligand or ligands that they transport and, of course, they must dissociate them as well. These steps must occur on both sides of the membrane for transport to occur, so there must be a process or processes in which the ligands are transported across the membrane. Fig. (3.7) illustrates some of the elementary kinetic processes that are found for transporters, including chemical modification of the transporter by phosphorylation, light-induced conformational changes, and multiple ligand binding.

¿From the point of view of chemical physics, the transport step can be viewed as energetic rearrangements that involve both the transporter protein and the ligand being transported. The top panel in Fig. (3.8) is a schematic representation of what the energy profile across a GLUT transporter might look like when the glucose concentration outside is high and inside is low. The energy profile is the Gibbs free energy, rather than the potential energy, since for the average kinetic events that we are considering the influence of entropy effects must be taken into account. Thus the reason that the free energy of glucose is higher outside is simply that the concentration of glucose is higher outside the cell than inside. The peaks of the free energy represent barriers to the movement of glucose across the transporter. Two possibilities for the transition from state 2 to state 3 are shown in the lower panels of Fig. (3.8). The first represents a barrier crossing in which the transition $2 \rightarrow 3$ does not influence the shape of the energy profile. In the second, on the other hand, the energy profile is different after the transition, as might be the case if the transition involved a conformational change.

Although understanding the transport step is an important feature of building a model of a transporter, it does not describe how a transporter works nor the rate of transport, which was seen in Section 3.2 to be a property of the complete model, not a single step. To illustrate how a complete model of a transporter is created, we consider the Na^+/glucose cotransporter from intestinal epithelial cells. This transporter utilizes a concentration gradient of Na^+ to transport glucose from the intestine into the epithelial cells that line the gut. This is "up hill" transport as the concentration of glucose in the

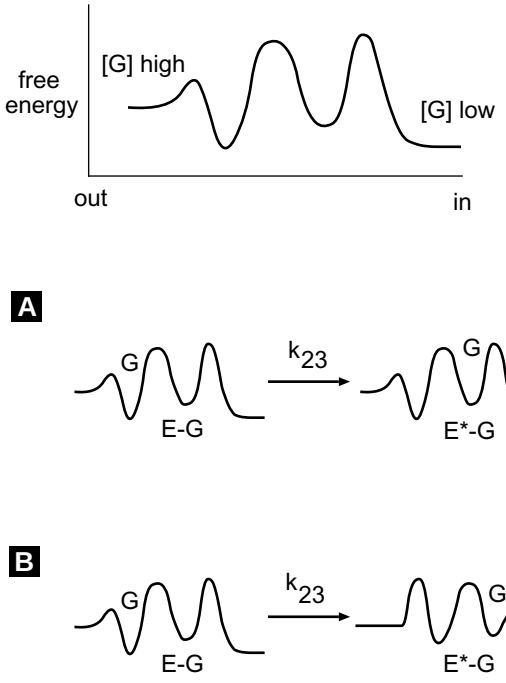

Figure 3.8 Schematic representation of the free energy profile across a membrane for a transporter protein. Two possibilities for state changes for the transport step 2 to 3 for the GLUT transporter are indicated: A, simple barrier crossing; and B, barrier crossing via a conformational transition.

epithelial cells exceeds that in the intestine. As shown schematically in Fig. (3.9), the cotransporter works in concert with a Na^+/K^+ ATPase and passive transport of glucose by GLUT transporters, both at the basolateral side of the epithelium, to move glucose from the intestine to the blood stream. The Na^+/K^+ ATPase helps eliminate the Na^+ that accompanies glucose uptake during cotransport, thereby maintaining a low concentration of Na^+ inside of the cell.

A model for any transporter must incorporate a number of basic experimental facts. One of these is *stoichiometry*, which for the cotransporter is the number of Na^+ ions transported per glucose molecule. Experimental measurements on the Na^+/glucose cotransporter from intestine yield a stochiometry is $2Na^+$ to 1 glucose. Another important fact about the cotransporter is the absolute requirement for Na^+, *i.e.*, if Na^+ is absent from the external medium, glucose is not transported. In addition, the cotransporter is *electrogenic*, *i.e.*, transport generates an electrical current due to the transport of Na^+.

These observations require 2 Na^+ and 1 glucose association steps on each side of the membrane. Thus a partial skeleton for the cotransporter might contain the kinetic steps connected together as shown in Fig. (3.10). It is also possible that the second sodium binds *after* the glucose as in the right panel of Fig. (3.10). However, this can be ruled out if the states with Na^+ and glucose bound from the outside are connected by conformational transitions to comparable states inside (as indicated by the dashed lines). In that case the six state cycle on the right in Fig. (3.10) (E to E-Na^+ to G-E-Na^+ to G-E^*-Na^+ to E^*-Na^+ to E^* to E) would transport only a single Na^+ for every glucose

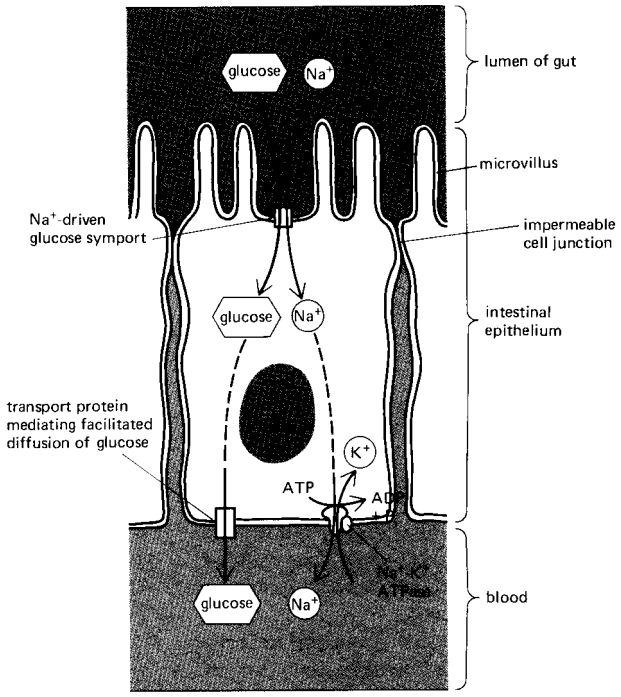

Figure 3.9 A cartoon representing the cotransport of glucose and Na^+ into intestinal epithelium, followed by the passive transport of glucose into the blood. Energy stored in the gradient of Na^+ (higher in the lumen of the gut) is utilized to transport glucose from a high concentration to a low concentration. Na^+ that accumulates in the epithelial cells is removed by active transport into the blood by the Na^+/K^+ATPase. From Alberts, et al *Molecular Biology of the Cell*, Garland Publishing, Inc., New York, 1983, pg. 297.

molecule, impying a stochiometry at steady state less than 2:1. The third possibility, not shown in Fig. (3.10), is that glucose binds first. This is ruled out, however, by the experimental observation that the cotransporter supports Na^+ currents even in the absence of glucose. Thus we are left with the ordered binding of ligands indicated on the left in Fig. (3.10).

If we number the eight states on the left in Fig. (3.10) sequentially, S_1 through S_8, starting at "E" and moving counterclockwise, there are a number of possibilities for conformational changes connecting the left and right sides of the diagram. Fig. (3.11) illustrates six alternatives. Alternative b is easily eliminated since it does not transport glucose. Although diagram C does transport glucose (S_4 to S_5), it does not includes steps that transport only Na^+, and, therefore, conflicts with the fact that the transporter produces a Na^+ current in the absense of glucose. Diagram D can be ruled out because it has the wrong stochiometry (1 Na^+:1 glucose). This leaves as possible mechanisms

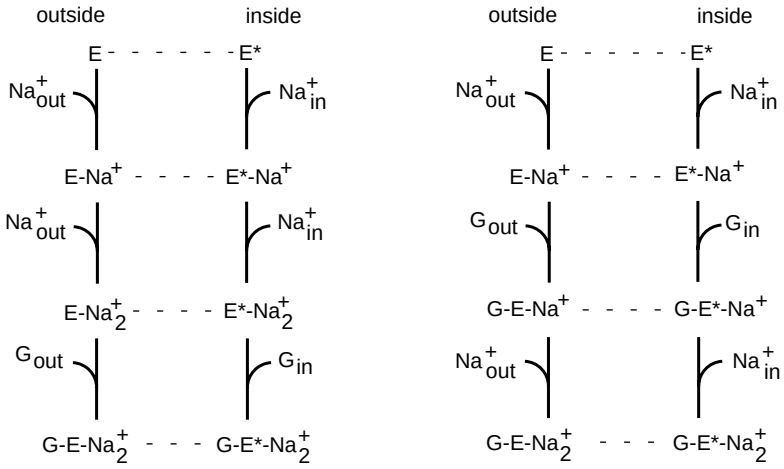

Figure 3.10 Two possible skeleton diagrams representing binding of Na^+ and glucose for the Na^+/glucose cotransporter. Only the left panel agrees with the experimental stochiometry.

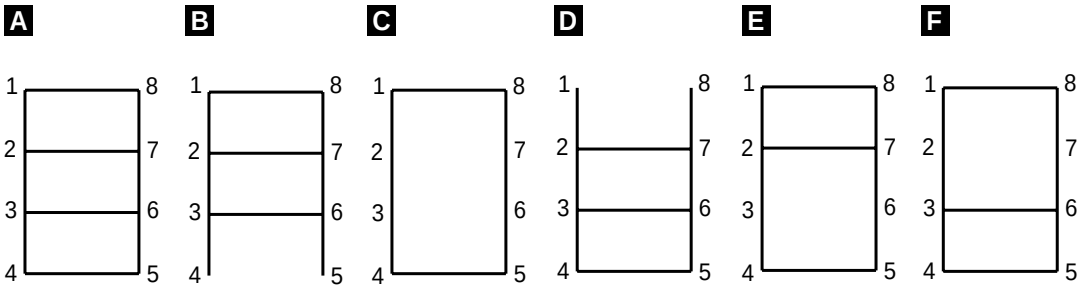

Figure 3.11 Six possible diagrams for the Na^+/glucose transporter with transport steps included. Only A, E, and F are compatible with experiment.

diagram A, the fully connected diagram, and diagrams E and F, each of which is missing Na^+ transport steps.

All three of these diagrams are compatible with the experimental evidence, and all three can be "reduced" to a diagram with the 6-state skeleton given in Fig. (3.12A). This method of reducing diagrams uses the *rapid equilibrium approximation* that applies to steps for which the forward and reverse rates are rapid with respect to other steps in the diagram. The details of how this method works are explained in Chapter 4 although the basic idea can be seen by comparing Panels A and B in Fig. (3.11). The experimental values of rate constants for the six state model have been assigned by Parent and colleagues. Step S_4 to S_5 in the six state model is the dissociation of glucose inside the cell, and this step is extremely fast. This permits the two states to be approximated as a single combined state (state $S_{4,5}$ in Panel B) and reduces the diagram to 5 states

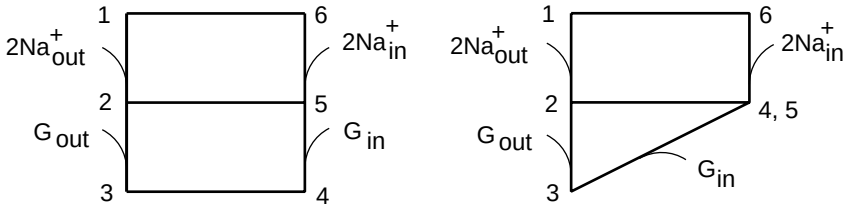

Figure 3.12 A six-state (A) and five-state (B) simplification of the eight-state diagram for the Na^+/glucose cotransporter.

Figure 3.13 Panels A and B: Two simplified models to explaining the Ca^{2+} dependence of the experimental SERCA pump rate.

as shown. We must be careful in doing so to readjust the rates to account for the reduction. The details of the process for doing this is given in Chapter 4, but it is not difficult. In short, only a portion of the combined state $S_{4,5}$ reacts to the other states. The portion to be used in each reaction is determined as a result of the reduction using simple algebra. The reduced model with experimental rates obtained by Parent, *et al* is given in the form of an *XppAut* file in Exercise 3.10.

It is possible to write diagrammatic expressions for the transport rate for either the five-state or six-state models in Fig. (3.12). However, the number of directed diagrams and cyclic diagrams increases quickly with the complexity of cycles in the complete diagram. For example, for the five-state model there are 6 pairs of cyclic diagrams and 55 directed diagrams. Nonetheless, the general expressions in Eqn. (3.19) and Eqn. (3.20) remain valid and can be used to obtain explicit expressions for the steady state fluxes. The diagrammatic method does not, however, provide information about the transient time-dependence of the fluxes. This is most conveniently obtained by numerical integration of the equations (see Exercise 3.10).

3.4 SERCA Pumps

The Ca^{2+}-ATPase that is found in the endoplasmic reticulum (ER) and sarcoplasmic reticulum (SR) of muscle is typical of transporters that utilize the chemical energy stored in ATP to pump ions against a gradient. Typical free cytosolic Ca^{2+} concentrations, $[Ca^{2+}]_i$, are of the order of 0.1 μM, whereas Ca^{2+} concentrations in the ER and

SR are in the range of 0.1-1mM. Thus these pumps, which are abbreviated SERCA for "Sarco-Endoplasmic Reticulum Ca^{2+} ATPase", have to surmount a 3-4 order of magnitude concentration difference. Topologically, the SR and ER are equivalent to the "outside" of the cell and both compartments function to store Ca^{2+} for a variety of cellular processes. In muscle Ca^{2+} release from the SR is involved in triggering muscle contraction whereas Ca^{2+} release from the ER is involved in stimulating hormone secretion and other intracellular signaling cascades. Pumping of Ca^{2+} by SERCA is the primary mechanism by which SR and ER Ca^{2+} stores are maintained. A different type of Ca^{2+} pump (PMCA), which is found in the plasma membrane, functions to pump Ca^{2+} out of the cell.

Although there a several isotypes of SERCA found in different tissues, the rate at which they pump Ca^{2+} has a simple dependence of $[Ca^{2+}]_i$. The pumping rate can be measured using vesicles prepared from either SR or ER membranes. The rate of vesicle-accumulation of $^{45}Ca^{2+}$, a radioactive isotope of Ca^{2+}, can then be used to determine the pumping rate. Experimentally, the rate has a sigmoidal dependence on $[Ca^{2+}]_i$ with a Hill coefficient close to two, *i.e.*,

$$R = \frac{R_{max}[Ca^{2+}]_i^{\,2}}{K^2 + [Ca^{2+}]_i^{\,2}}. \tag{3.37}$$

The Hill coefficient is related to the stochiometry of the SERCA pump, which is known to be $2Ca^{2+}$:1ATP. X-ray diffraction of SERCA pumps in bilayers has produced a low-resolution structure with the three segments shown in the upper panel of Fig. (3.13): a stalk region just outside the bilayer and near the binding sites for Ca^{2+}, a head region that contains the ATP binding site, and a large transmembrane region through which the Ca^{2+} is transported. Binding experiments have revealed two binding sites for Ca^{2+}.

A simple model that is consistent with the Ca^{2+} dependence of the pump rate can be constructed using only two states: an inactive state, I, and an active state, A, connected by the mechanism shown in Fig. (3.13A). This model leads to the rate expression in Eqn. (3.37) if we assume that the two states rapidly equilibrate and that only the active state transports Ca^{2+}. Rapid equilibration implies the balance of the forward and reverse rates in Fig. (3.13A). This leads to the equilibrium condition

$$k^-/k^+ = K^{eq} = \frac{[Ca^{2+}]^2[I]}{[A]}, \tag{3.38}$$

where $[I]$ and $[A]$ are the per unit area concentrations of SERCA pumps in the two states and the equilibrium constant, K^{eq}, is the ratio of the rate constants. Solving Eqn. (3.38) for $[I]$, substituting that expression into the conservation condition $[I]+[A] = N$, and then solving for $[A]$ gives the concentration of active SERCAs:

$$[A] = \frac{N[Ca^{2+}]^2}{K^2 + [Ca^{2+}]^2}. \tag{3.39}$$

Here we have defined $K = \sqrt{K^{eq}}$, which has the units of concentration. As can be seen

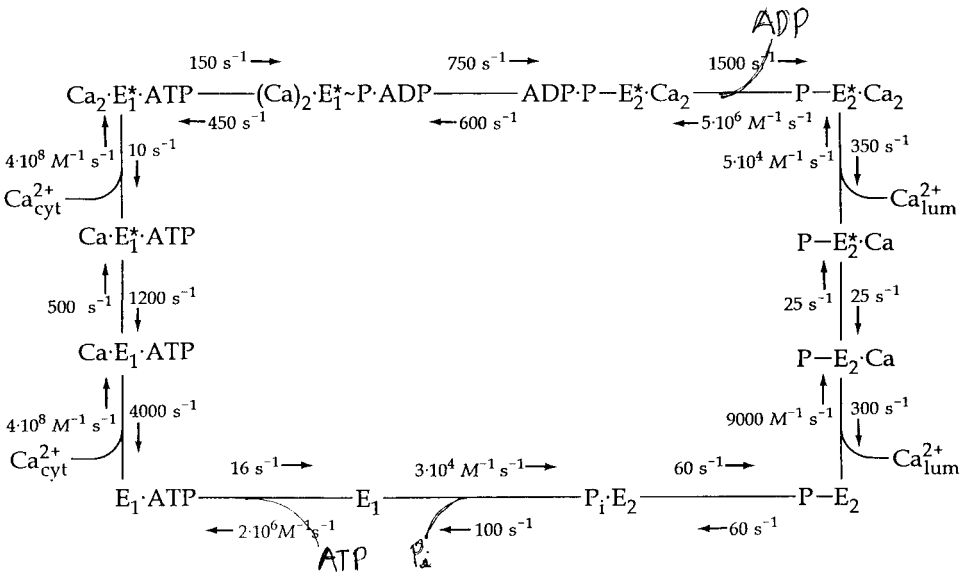

Figure 3.14 A twelve state model of the SERCA pump. Note the two sequential Ca^{2+} binding steps on the left hand side. Although the cycle is drive by the hydrolysis of ATP, all of the steps in the diagram contribute to the steady state rate. Taken from P. Läuger, *Electrogenic Ion Pumps*, Sinauer, Sunderland, MA, 1991, pg. 241.

from Eqn. (3.39), the numerical value of K equals the concentration of Ca^{2+} at which half of the SERCA are in the active state. A small value of K is said to correspond to a *high affinity* binding site and a large value to a *low affinity* site. If the rate constant for the active state to transport Ca^{2+} is k, then Eqn. (3.39) gives the transport rate

$$R = k[A] = \frac{R_{max}[\mathrm{Ca}^{2+}]_i^{\,2}}{K^2 + [\mathrm{Ca}^{2+}]_i^{\,2}} \tag{3.40}$$

with $R_{max} = kN$.

Although this mechanism agrees with the measured transport rate and provides an expression for R_{max}, there are several things wrong with it. First, it assumes the simultaneous binding of two Ca^{2+}, which is highly improbable. Second, it doesn't provide an explanation for the transport rate constant, k, and third, it doesn't explain how ATP might be involved. We can eliminate the first criticism by expanding the model to include sequential binding of two Ca^{2+}, as indicated in Fig. (3.13B). For this mechanism there are two simultaneous binding equilibria:

$$K_1 = \frac{[Ca^{2+}][I]}{[I^*]} \text{ and } K_2 = \frac{[Ca^{2+}][I^*]}{[A]}. \tag{3.41}$$

In analogy to what was done for the previous model, these equations can be combined with the conservation condition $[I] + [I^*] + [A] = N$ to obtain

$$[A] = \frac{N}{1 + (K_1 K_2/[Ca^{2+}]^2) + K_2/[Ca^{2+}]}. \tag{3.42}$$

This agrees with the rate expression in Eqn. (3.37) under the condition that $K_2 \ll [Ca^{2+}]$ *and* K_1. In this case $[A]$ is approximately given by Eqn. (3.39) with $K = \sqrt{K_1 K_2}$, the geometric mean of the two dissociation constants. Although this does not explain the pumping rate, it does suggest that the binding of Ca^{2+} might be sequential with the first site of much lower affinity than the second, *i.e.*, $K_1 \gg K_2$.

Constructing a complete kinetic model of the SERCA pump requires more experimental information than is contained in the pumping rate. In fact, a great deal is known about the other steps involve in the transport cycle. Figure 3.14 gives a 12 state model that includes rate constants for all of the steps indicated. The two conformations of the transporter, E_1 and E_2, correspond to the bound Ca^{2+} facing the cytosol and inside (*lumen*) of the ER, respectively. The cycle is initiated by ATP binding to E_1, followed by the binding of two Ca^{2+} from the cytosol. Using the fact that the Ca^{2+} binding steps are fast, the equilibrium constants can be calculated from the forward and reverse rate constants ($K = k^-/k^+$) to be $K_1 = 1 \cdot 10^{-5}$M and $K_2 = 2.5 \cdot 10^{-8}$M. So in agreement with the two state binding model, this model involves sequential binding of Ca^{2+} with the first step having much lower affinity than the second. In fact, using the expression $K = \sqrt{K_1 K_2}$ gives $K = 5 \cdot 10^{-7}$M, which is close to the experimental value obtained from rate measurements in vesicles. The cycle in Fig. (3.14) is driven by the phosphorylation of SERCA, which facilitates the conformational transition that exposes bound Ca^{2+} to the lumen.

3.5 Transport Cycles

Like enzymes, transporters are unchanged by the transport process. Indeed, transporters can be thought of as enzymes whose primary purpose is to alter the location of a molecule rather than its chemical state. If we take the more general point of view suggested by nonequilibrium thermodynamics, an enzyme and a transporter are simply different classes of the same generic type of protein that catalyze a change in free energy. As we noted in the previous section (*cf.* Fig. (3.8)), a transporter does this by altering the concentration that the molecule experiences. An enzyme, on the other hand, does this by altering the chemical bonds in the molecule.

The catalytic nature of a transporter is apparent in the cyclic structure of the transport mechanism. The GLUT transporter, the Na^+/glucose cotransporter, and the SERCA pump described in Sections 3.1-3.4 all function in cycles that leaves the transporter unchanged. Three additional examples of transport cycles that have been used to explain experimental transport rates are given in Figs. 3.15A-B and 3.16: a P-type

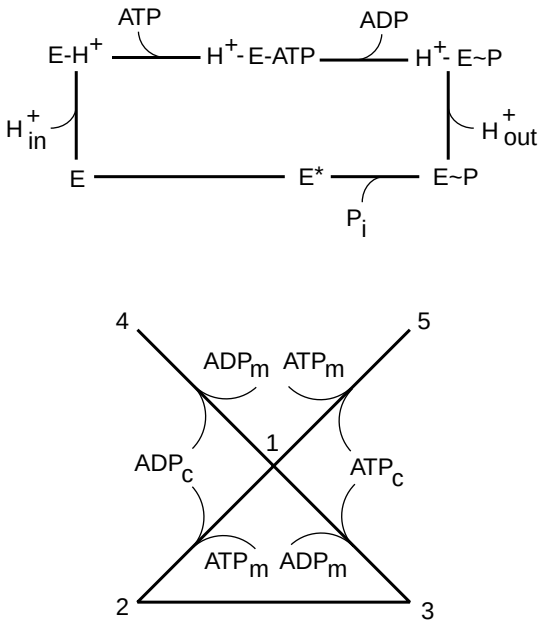

Figure 3.15 Panel A: A six state cycle for a P-type proton ATPase. The phosphorylation step preceeds and facilitates dissociation of the proton outside of the cell. Panel B: Five state cycle for the adenine nucleotide translocator from mitochondria. The cycle 1-2-3-1 exchanges an ADP^{3-} from the cytoplasm and for an ATP^{4-} from the mitochondria. Since the two ions have different charges, the translocator is electrogenic. The steps 1-4 and 1-5 slow the translocation rate by tying up the translocator in states not involved in the cycle.

proton pump, the adenine nucleotide transporter from mitochondria, and bacteriorhodopsin, a light-driven proton pump.

In a transport cycle a ligand is moved from one cellular compartment to another by some type of driving force. In passive transport, like that for the GLUT transporter, the driving force is simply the concentration difference of ligand. For transporters that involve more than one ligand, such as the Na^+/glucose cotransporter or the adenine nucleotide transporter in Fig. (3.14B), the driving force is a combination of ligand concentrations differences. For ATP-dependent pumps, on the other hand, the driving force is the chemical energy stored in the terminal phosphate bond of ATP, which is transfered in a phosphorylation step (*cf.*, Figs. 3.14 and 3.15A) to the transporter. Phosphorylation maintains the high energy state, and the high energy phosphate bond facilitates conformational transitions that lead to the transport and dissociation of the tranported ion. A third form of driving force is light, as indicated in the transport cycle for bacteriorhodopsin in Fig. (3.16). In this case energy from a photon excites a state of the transporter causing a *trans* to *cis* transformation in the structure of retinal that is otherwise inaccessible to thermal motion, thereby releasing a proton at the exterior face of the membrane.

As long as we are interested in the average properties of a transporter, it is correct to picture transport cycles as occuring in a fixed direction governed by the driving forces. Dynamic changes in an individual transporter molecule, on the other hand, are stochastic. This is a result of the microscopic reversibility of the kinetic steps in a cycle. Although it is more probable that an individual GLUT transporter will move glucose from a high concentration to a low concentration, the reverse will occur with

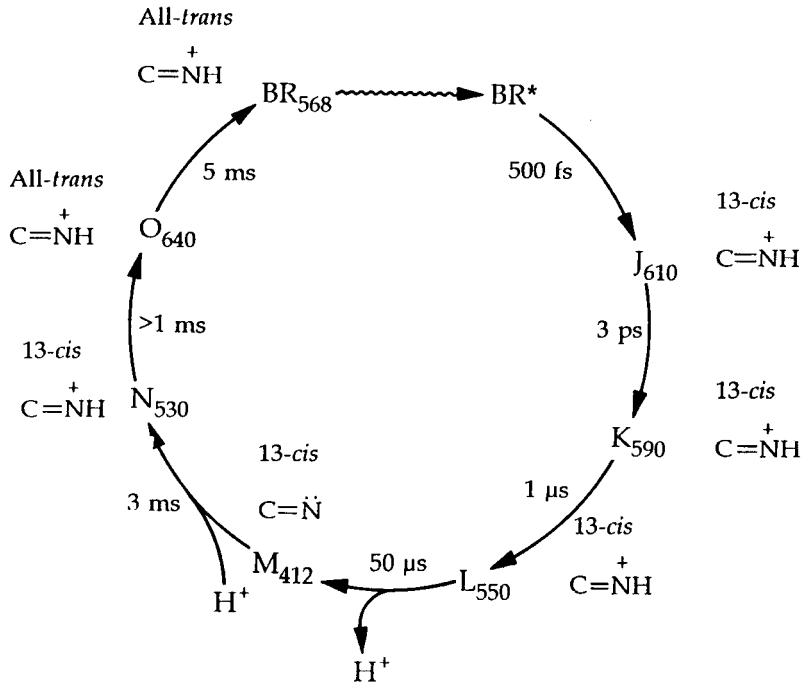

Figure 3.16 An irreversible diagram for the light driven proton pump, bacteriorhodopsin, a 27kD protein from the salt tolerent bacteria, *Halobacterium halobium*. Light absorbed in the step BR_{568}-BR^* drives the *trans* to *cis* conformational change in retinal, leading to the release of a proton. Taken from P. Läuger, *Electrogenic Ion Pumps*, Sinauer, Sunderland, MA, 1991, pg. 147.

nonvanishing probability. In fact, any step in a transport cycle can and will occur in the opposite direction to the average transport rate. This reversibility has been demonstrated experimentally for a number of transporters, one of the most convincing being the reversal of SERCA pumps to produce ATP by reversing the Ca^{2+} gradient. Thus the dynamic changes in an individual transporter molecule consist of a series of random positive and negative steps around the cycle that over time lead to an average transport rate in the direction dictated by the driving forces.

Cycles are a common feature of other cellular processes with some of the most complex cycles governing muscle contraction, the rotary motion of flagella, and other so-called molecular motors. In metabolism the operation of the F_oF_1 ATPase, which is responsible for converting proton gradients and ADP into ATP, is governed by a combined catalytic-transport cycle. The molecular kinetics underlying these cycles is still an active area of research.

Exercises

1. Verify that the fraction of transporters in the states 1 and 2 for the three-state GLUT model satisfies Eqs. (**??**) and (**??**).
2. Carry out the matrix multiplication indicated in Eq. (**??**) to verify that the expressions for the fractional occupany in Eq. (**??**) are correct.
3. Write down the directional diagrams for states 2 and 3 for the three-state GLUT transporter model (*cf.* Fig. 3.3C) and the algebraic expressions that they represent.
4. There are 9 directional diagrams for the three-state GLUT transporter model. Write down the algebraic expression for their sum, which is the denominator, Σ, in Eq. (**??**) and Fig. 3.5.
5. Show that manipulations like those in Fig. 3.5 give the same final expression for J_{23}^{ss} and J_{31}^{ss} as a difference between directed cycle diagrams.
6. The equilibrium constant for a chemical reaction is given by the ratio of the product of the concentrations of "products" divided by the ratio of the product of concentrations of "reactants". (By convention reactants are the chemical species on the left hand side of the equation and the products are on the right hand side.) Show for the three reactions in Eq. (**??**) that the equilibrium constants are the ratio of the rate constants as indicated in the equations. [Hint: Recall that "equilibrium" for a reaction occurs when the rate of the forward reaction equals the rate of the reverse reaction.]
7. Using the definition of the equilibrium constant in Exercise 3.4, show that the equilibrium constant for the sum of two chemical reactions is the product of the equilibrium constants for the individual reactions.
8. Verify that the expression for the sum of the directed diagrams, Σ, for the symmetric three-state GLUT transporter model is given by Eq. (**??**).
9. Write a .ode file for the *4-state model* of a GLUT transporter (*cf.* Fig. 1.8). Using *XppAut* and the values of the rate constants given below simulate data for an Eadie-Hofstee plot of the rate of transport of glucose when $[G_{in}] = 0$mM. Make an Eadie-Hofstee plot of the rate using a plotting program in *XppAut* (see Chapter 12 appendix) to determine R_{max} and K_d. Use the rate constants $k_{12} = k_{43} = 2.4\text{mM}^{-1}\text{min}^{-1}$, $k_{21} = k_{34} = 42\text{min}^{-1}$, $k_{14} = k_{14} = k_{41} = k_{23} = k_{32} = 1000\text{min}^{-1}$. The transport rate is given by $R = c \cdot J_{34}^{ss}$, where $c = 2$mM is the concentration of GLUT transporters per unit volume of cells. [Hints: Because of the size of the rate constant k_{14}, etc you will need to use a small step size (try 0.0001min). For the same reason you only will need to integrate for about 0.3min. Be sure to include an auxiliary expression in your .ode file for $R = c \cdot J_{34}$.]
10. The .ode file below was constructed from data gathered by Parent, *et al* on the Na^+/glucose cotransporter from rabbit intestine. It corresponds to the 5 state model in Fig. 3.11B. Steps 1 to 2 and 5 to 6 depend on the membrane potential, v, which is taken as a parameter. Use this file to calculate both the transient and the steady state flux of glucose as given by the auxiliary variable, Jglu. Explore how

the membrane potential influences the flux. For a fixed value of the flux, find the steady state transport rate as a function of [Na^+_{out}] (NaOut in the .ode file). Does your simulation give a linear Eadie-Hofstee plot? [Hint: Due to the size of the rate constants you will need to choose a small time step for the integration.]

```
#naglu5.ode (5 state Na/glucose cotransporter)
#initial values of state variables
init x1=0.15,x2=0.15,x3=0.15,x45=0.2
#parameters
parm k12=0.08,k21=500,k16=35,k61=5,k23=100,k32=20
parm k25=0.3,k52=0.3,k34=50,k43=50,k45=800,k54=40000
parm k56=10,k65=0.00005,ap=0.3,app=0,d=0.7,f=96489
parm gluIn=10,gluOut=1,NaIn=20,NaOut=100
parm n=2,z=-2,r=8314,tconst=310,v=-50
#functions and rate constants
mu(v)=f*v/(r*tconst)
k12p(v)=k12*NaOut^2*exp(-n*ap*mu(v)/2)
k21p(v)=k21*exp(n*ap*mu(v)/2)
k56p(v)=k56*exp(-n*app*mu(v)/2)
k65p(v)=k65*NaIn^2*exp(n*app*mu(v)/2)
k34p(v)=k34*exp(-(z+n)*d*mu(v)/2)
k43p(v)=k43*exp((z+n)*d*mu(v)/2)
k25p(v)=k25*exp(-(z+n)*d*mu(v)/2)
k52p(v)=k52*exp((z+n)*d*mu(v)/2)
k61p(v)=k61*exp(z*d*mu(v)/2)
k16p(v)=k16*exp(-z*d*mu(v)/2)
#the other state variables
x5=x45*k45/(k45+k54*GluIn)
x4=x45*k54*GluIn/(k45+k54*GluIn)
x6=1-x1-x2-x3-x45
#the fluxes
j12(x1,x2,v)=k21p(v)*x2-k12p(v)*x1
j16(x1,x6,v)=k61p(v)*x6-k16p(v)*x1
j23(x2,x3)=k32*x3-k23*GluOut*x2
j25(x2,x5,v)=k52p(v)*x5-k25p(v)*x2
j34(x3,x4,v)=k43p(v)*x4-k34p(v)*x3
j56(x5,x6,v)=k65p(v)*x6-k56p(v)*x5
#equations
dx1/dt=j12(x1,x2,v)+j16(x1,x6,v)
dx2/dt=-j12(x1,x2,v)+j23(x2,x3)+j25(x2,x5,v)
dx3/dt=-j23(x2,x3)+j34(x3,x4,v)
dx45/ct=-j34(x3,x4,v)+j56(x5,x6,v)-j25(x2,x5,v)
#flux of glucose
```

```
aux jGlu=j23(x2,x3)
done
```

11. Write down the 6 pairs of cyclic diagrams and the 11 directed diagrams for state 1 for the five-state diagram in Fig. 3.11. What are the directed diagrams for state 4,5?
12. The cardiac form of the Na^+/Ca^{2+} exchanger is electrogenic with a stochiometry of $3Na^+$:$1Ca^{2+}$. Assuming that the 3 Na^+ bind sequentially to sites of decreasing affinity, how do you anticipate that the transport rate will depend on $[Na^+{}_{out}]$? Prove your answer.

CHAPTER 4

Reduction of Scale

James Keener and Joel Keizer

07-28

One of the hallmarks of cellular processes is their complexity. For example, in Chapter 3 we described a detailed model for the SERCA pump that requires 11 ODEs and 22 kinetic constants for its analysis. Similarly, the Hodgkin-Huxley model, which includes only three currents in the squid giant axon, involves 4 differential equations and information about three voltage-gated currents. As complex as these processes are, they do not begin to represent the true complexity of cellular processes like muscle contraction or insulin secretion, which depend on the coupling of numerous dynamic components. In Chapter 5 we describe some simple examples of "whole-cell" modeling that attempt to deal with these larger issues. With a view toward this more complex type of modeling, here we describe several techniques that can be used to simplify the molecular mechanisms that make up these models. These techniques rely on the separation of variables into ones that are "fast" and ones that are "slow". This type of separation has already been used implicitly to simplify previous models. In the Morris-Lecar model (Section (**??**)), for example, the rate of activation of the Ca^{2+} current was assumed to be instantaneous and in Section (**??**) transient behavior was ignored in defining transport rates. In this chapter we introduce two important methods to simplify molecular models: the *rapid equilibrium approximation* and *time scale analysis*. These methods are closely related and both can be used to eliminate variables and simplify the analysis of the differential equations. First, however, we motivate the discussion with the following example.

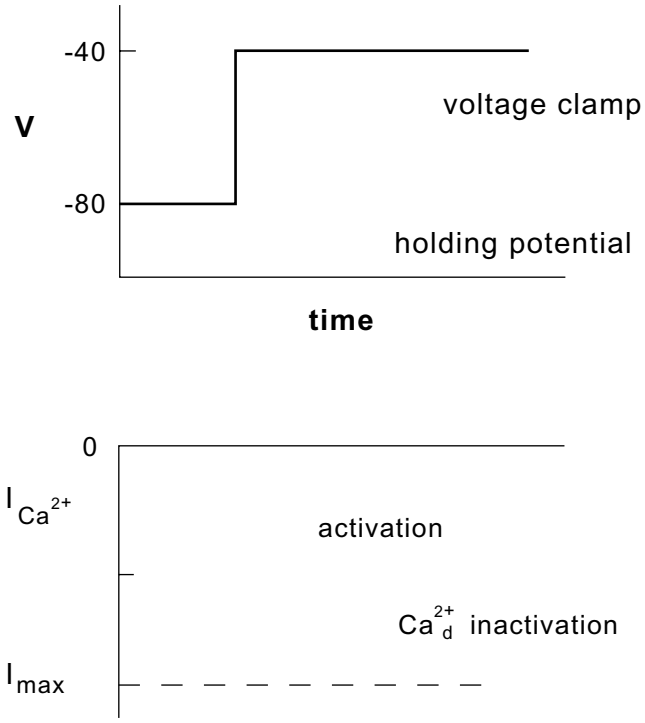

Figure 4.1 Whole-cell currents for L-type channels from a neuron in the sea hare *Aplysia*.**This figure is not yet complete**

4.1 Rapid Equilibrium Approximation

The voltage clamp measurements in Fig. (4.1) show typical whole-cell Ca^{2+} currents for L-type channels from a neuron in the sea hare *Aplysia*. The control curve in Panel A shows that these channels rapidly activate and then slowly inactivate when the cell is depolarized to 20mV. The Ca^{2+} dependence of the inactivation step is illustrated by the slowing of inactivation when the mobile Ca^{2+} chelator, EGTA, is injected into the cell. The Ca^{2+} dependence of inactivation is confirmed by the experiment in Panel B, in which Ba^{2+} replaces Ca^{2+} outside of the cell.

A cartoon for the mechanism underlying Ca^{2+} inactivation of L-type channels is given in Fig. (4.2A). The cartoon illustrates the formation of a *domain* of elevated Ca^{2+} at the cytoplasmic face of an open Ca^{2+} channel (*i.e.*, a small localized region in the vicinity of the channel in which Ca^{2+} concentration can be quite high). Domains like this have been predicted to form within a few microseconds of the opening of a channel due to the combined effects of high Ca^{2+} concentrations outside the cell (*ca.* 2mM) and low basal concentrations in the cytosol (*ca.* 0.1 μM). When this is combined with slow diffusion of Ca^{2+} within the cell[1], calculations predict Ca^{2+} domains with peak values

[1]The slow rate of diffusion of Ca^{2+} is discussed in Chapter **??**. It is caused by tight binding of Ca^{2+} to numerous sites in the cytoplasm, which greatly retards its ability to diffuse.

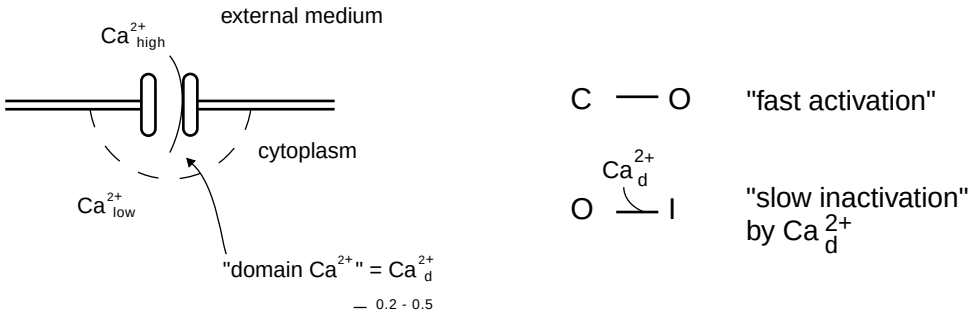

Figure 4.2 Panel A: Cartoon of domain calcium. Panel B: State diagram for Ca^{2+}channel

approaching 200-500 μM within nanometers of the channel. The high concentration of Ca^{2+} in a domain suggests that an open channel may be subject to direct block of the open state by binding of a Ca^{2+} ion at the cytoplasmic face of the channel. A simple mechanism that accounts for this is given in Fig. (4.2B).

The three states C, O, and I represent closed, open, and inactivated states of the channel. Step 1 is the activation step, whereas step 2 represents the binding of domain Ca^{2+}, written as Ca_d^{+2}. The mechanism postulates a low affinity site for Ca^{2+} binding, which means that the inactivated state can be reached only when the channel is open and the Ca^{2+} domain has formed. Since simulations show that the peak concentration in a domain falls rapidly when a Ca^{2+} channel closes, it is possible to associate a unique value of domain Ca^{2+} with the open state, whose value depends only on the current through the open channel.

This mechanism is easily translated into a mathematical model. All the steps are unimolecular, except for the binding of domain Ca^{2+}, which is bimolecular. If we represent the fractions of channels in the three states by x_C, x_O, and x_I, then the kinetic equations for the model can be written

$$dx_C/dt = -V_1, \tag{4.1}$$

$$dx_O/dt = V_1 - V_2, \tag{4.2}$$

with $x_I = 1 - x_C - x_O$ and with

$$V_1 = k_1^+ x_C - k_1^- x_O, \tag{4.3}$$

$$V_2 = k_2^+ [Ca_d^{2+}] x_O - k_2^- (1 - x_C - x_O) \tag{4.4}$$

the rates of steps 1 and 2. Since the value of Ca^{2+} in the domain, $[Ca^{2+}]_d$, depends only on the current, it is a function of the electrical driving force and the single channel conductance[2]. Specific values for the rate constants are given in Exercise **??**. Fig. (4.3) shows a simulation with the model that depicts the Ca^{2+} current for a cell that is

[2]In general, the value of $[Ca^{2+}]_d$ depends on the external Ca^{2+} concentration and the membrane potential and is proportional to the single channel conductance, *cf.*, Exercise **??**.

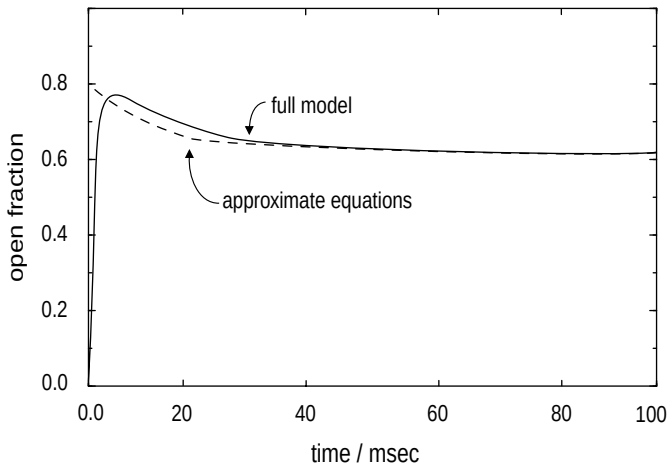

Figure 4.3 Computed solution and approximate solution for calcium current through L-type calcium channels.

depolarized at $t = 10$ms to a voltage where the channel is open. Simulations like this have been used to duplicate the time course of voltage clamp measurements for L-type Ca^{2+} currents in pancreatic beta cells. Key evidence that supports the domain model has come from recent experiments with genetically engineered L-type channels, and it now seems certain that the essential ideas of the model are correct.

In both the experiments and the simulations, activation of the channel is fast compared to inactivation. In the model this is due to the fact that both the rate constants for step 1 are much larger than those for step 2. For example, the forward rate for V_1 is about 47 times faster than that for V_2. Because of this, step 1 rapidly "equilibrates" the states C and O.

To see how this equilibration takes place, it is a good approximation to ignore V_2, at least at first. Assuming that $x_C(0) = 1$ (all channels are initially closed), it follows that $x_I = 0$ and $x_C + x_O = 1$. We use this to calculate that

$$dx_O/dt = -(x_O - \frac{1}{1+K_1})/\tau_{act} \tag{4.5}$$

with $K_1 = k_1^-/k_1^+$ and $\tau_{act} = 1/(k_1^+ + k_1^-)$. The number τ_{act} is the time constant for activation.

Because this process is fast, within a few milliseconds $V_1 \approx 0$. This condition continues to hold even as the fractional occupancies x_C, x_O, and x_I change.

The rapid equilibrium approximation is a method to exploit this observation that some kinetic steps are "fast". By "fast" we mean "faster than the times scales of phys-

iological interest", *i.e.*, faster than the slowest times scales in the process. Here the fast process is the process V_1, and for most times after the short initial phase, $V_1 \approx 0$. According to Eqn. (4.3), the condition $V_1 = 0$ implies that

$$x_C = (k_1^-/k_1^+)x_O = K_1 x_O, \tag{4.6}$$

which is the equilibrium condition for step 1 in the mechanism.

Now, it might be tempting to set $V_1 = 0$ in (4.2), but this is the wrong thing to do. Instead, we recognize that since x_C and x_O are in equilibrium, the quantity of interest is the total number of channels in the states C and O. Notice that by adding the two equations (4.1) and (4.2) together, V_1 is eliminated and we find the rate of change of the combined state $y = x_C + x_O$ to be

$$d(x_C + x_O)/dt = -V_2. \tag{4.7}$$

Using the equilibrium condition (4.6), we find that $x_O = \frac{1}{1+K_1} y, x_C = \frac{K_1}{1+K_1} y$, so that

$$dy/dt = k_2^-(1-y) - \frac{k_2^+[\mathrm{Ca}_\mathrm{d}^{2+}]}{1+K_1} y. \tag{4.8}$$

This ODE can be rearranged into the familiar form

$$dy/dt = \frac{y_\infty([\mathrm{Ca}_\mathrm{d}^{2+}]) - y}{\tau([\mathrm{Ca}_\mathrm{d}^{2+}])}, \tag{4.9}$$

where

$$\tau([\mathrm{Ca}_\mathrm{d}^{2+}]) = \frac{1+K_1}{k_2^+[\mathrm{Ca}_\mathrm{d}^{2+}] + k_2^-(K_1+1)}, \tag{4.10}$$

$$y_\infty([\mathrm{Ca}_\mathrm{d}^{2+}]) = k_2^- \tau([\mathrm{Ca}_\mathrm{d}^{2+}]). \tag{4.11}$$

Written this way, Eqn. (4.9) has the same form as Eqn. (**??**) for a voltage gated channel, except now $[\mathrm{Ca}^{2+}]_\mathrm{d}$ replaces the voltage.

The only tricky part remaining about the solution to Eqn. (4.9), which is an exponential, is finding the correct initial condition. Since we have assumed that step 1 is fast, the initial condition for (4.9) must take into account the rapid initial equilibration of C and O. As in Fig. (4.1) the initial condition typically is at a hyperpolarized potential where all the channels are closed and $x_C(0) = 1$. After the initial equilibration, some of the channels will have moved to state O, so that $y = x_C + x_O = 1$. This gives the equilibrated initial condition for Eqn. (4.9) as

$$y(0) = 1. \tag{4.12}$$

Using this initial condition, the solution to the rapid equilibrium approximation for the model is plotted as the dashed line in Fig. (4.3). Two things are notable in comparing the approximation to the complete solution. First, by neglecting the rapid activation of the channel, the approximation slightly overestimates the peak current, which is given analytically using the initial condition in Eqn. (4.12) as $I_{peak} = g(1/(1+K_1))(V - V_{Ca})$ (see Exercise **??**). Second, the exponential decline in current predicted by Eqn.

(4.9) does a good job of approximating the rate of inactivation of the current. The approximation works well because the time scale for the fast process (*ca.* 1ms) is much faster than that for inactivation (*ca.* 45 ms). As long as the time constant for the fast process is at least an order of magnitude faster than the remaining processes, the rapid equilibrium approximation provides a reasonable approximation to the complete model.

The rapid equilibrium approximation is a useful way to reduce the complexity of models. For the domain Ca^{2+} inactivation model, the simplification is not really necessary since the full model involves only two linear differential equations that can be analyzed by the matrix methods in Chapter **??**. However, the fact that the equation for the simplified model resembles that for voltage-gated channels provides a conceptual bridge to the properties of ligand-gating of channels, which are pursued in more detail in Chapter **??**.

4.2 Time Scale Analysis

Mathematicians have developed a more systematic method of dealing with fast and slow variables called *asymptotic analysis*. Although we do not work through all the intracacies of this technique here, the central idea of asymptotics is easy to understand, and it can be applied profitably to many modeling problems in cell and neurobiology. The idea is to define the fast and slow time scales in the model, and then to rescale time so that on this new scale only the slow, or alternatively only the fast, variables are changing.

To illustrate the idea we reexamine the model of Ca^{2+} currents for L-type channels introduced in the previous section. As we saw in that analysis, the two time scales are the time scale of activation $\tau_{act} = 1/(k_1^+ + k_1^-)$ and the time scale of inactivation $\tau([Ca_d^{2+}])$.

Having identified the fast and slow time scales, we proceed to *nondimensionalize* all of the variables in Eqs. (4.1)-(4.4) including time. Nondimensionalization is simply eliminating the units of a variable by dividing by a parameter in the model that has the same units as the variable. In this case the variables x_C, x_O, and x_I are percentages, and so are already nondimensional. The only variable having dimensions is t. The choice of a nondimensionalized time determines whether our analysis focuses on the fast or the slow time scale.

To nondimensionalize time using the slow time scale, we could set $\widehat{t} = \tau([Ca_d^{2+}])t$. However, it is somewhat easier and essentially equivalent to set $\widehat{t} = k_2^- t$. In terms of this new time scale, Eqs. (4.1) and (4.2) become

$$\epsilon dx_C/d\widehat{t} = -\frac{k_1^+}{k_1^-}x_C + x_O, \tag{4.13}$$

$$\epsilon dx_O/d\widehat{t} = \frac{k_1^+}{k_1^-}x_C - x_O - \epsilon\frac{k_2^+}{k_2^-}[Ca_d^{2+}]x_O + \epsilon(1 - x_C - x_O), \tag{4.14}$$

where $\epsilon = k_2^-/k_1^-$ is a small number.

The important observation is that since ϵ is small, unless the right hand side of (4.13) is small, x_C changes rapidly. However, if we add the two equations (4.13) and (4.14) together and divide by ϵ we find an equation that is independent of ϵ,

$$d(x_C + x_O)/d\widehat{t} = -\frac{k_2^+}{k_2^-}[\mathrm{Ca}_\mathrm{d}^{2+}]x_O + (1 - x_C - x_O). \tag{4.15}$$

The basic idea of asymptotic analysis is to treat ϵ not as a fixed number, but as a parameter that can be varied. In the asymptotic limit that $\epsilon \to 0$, we find that the right hand side of (4.13) is zero. This is the lowest order solution in the asymptotic analysis on the slow time scale, and is exactly the same as (4.6). This approximation is sometimes called the *quasi-steady state* approximation, where "quasi" emphasizes that $k_1^+ x_C - k_1^- x_O$ is nearly, but not exactly, zero. We complete the slow time scale analysis by using (4.13) to find x_C and x_O in terms of $y = x_C + x_O$, and then using (4.15) to find an equation describing the evolution of y. This equation turns out to be exactly (4.8).

The analysis on the fast time scale is similar. This time we choose a nondimensional time $\tilde{t} = k_1^- t$, and write the equations (4.1) and (4.15) as

$$dx_C/d\tilde{t} = -\frac{k_1^+}{k_1^-}x_C + x_O \tag{4.16}$$

$$d(x_C + x_O)/d\tilde{t} = \epsilon(-\frac{k_2^+}{k_2^-}[\mathrm{Ca}_\mathrm{d}^{2+}]x_O + (1 - x_C - x_O)). \tag{4.17}$$

This time, in the asymptotic limit that $\epsilon \to 0$, the equation (4.17) reduces to

$$d(x_C + x_O)/d\tilde{t} = 0, \tag{4.18}$$

so that $x_C + x_O = 1$, and

$$dx_C/d\tilde{t} = -\frac{k_1^+}{k_1^-}x_C + 1 - x_C, \tag{4.19}$$

at least for a short time.

This type of time scale analysis can be summarized by five steps, as follows:

- Analyze the parameters of the model to assess whether there are times scales that can be separated into "fast" and "slow".
- Define time constants for each time domain, whose ratio defines a small parameter, ϵ.
- Select appropriate parameters in the model to nondimensionalize the dependent variables.
- Nondimensionalize the differential equations in each time domain and see which terms can be neglected as $\epsilon \to 0$.
- Analyze the simplified equations, which represent the behavior of the variables on the two time scales.

In the next sections we describe how to carry out this analysis for several different arrangements of fast and slow reactions.

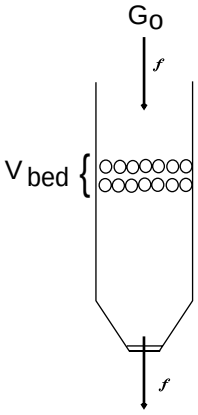

Figure 4.4 Flow system for experimental study of insulin secretion.

4.3 Glucose-Dependent Insulin Secretion

Insulin is secreted from β-cells in the pancreas in an oscillatory fashion. Glucose must be metabolized by the β-cell to stimulate insulin secretion, and the insulin, which is prepackaged in secretory vessicles, is secreted from the β-cell into the capillary system by exocytosis. However, the secreted insulin affects the transport of glucose into the cell by activating GLUT1 transporters and inactivating GLUT2 transporters. Thus, there is both positive and negative feedback, necessary ingredients for sustained oscillations.

These oscillations have been studied experimentally in a flow system depicted in Fig. (4.4). A thin layer of insulin-secreting β-cells is sandwiched between beads and exposed to a steady flow of solution. By collecting the solution exiting the bed, one can determine how the rate of insulin release from the cells in the bed depends on the composition and flow rate of the influx solution.

A mathematical model of this process must involve (at least) three variables, the extracellular glucose and insulin concentrations and the intracellular glucose concentration. We assume that the volume of islets behaves like a well stirred chemical flow reactor so that the concentration of any quantity is uniform throughout the bed (justification of this assumption uses similar time scale arguments, but is rather complicated and goes beyond the level of the discussion given here). Thus, the rate of change of a concentration is the rate of flow in minus the rate of flow out plus the rate of production in the bed. For glucose this is

$$dG/dt = -R_1 - R_2 - k_0(G - G_0) \tag{4.20}$$

and for insulin

$$dI/dt = R_s - k_0(I - I_0) \tag{4.21}$$

where G and I are the glucose and insulin concentrations of the solution, G_0 and I_0 are the respective concentrations of the inflow solution, R_1 and R_2 are the uptake rates for glucose through GLUT1 and GLUT2 receptors, respectively, R_s is the rate of insulin

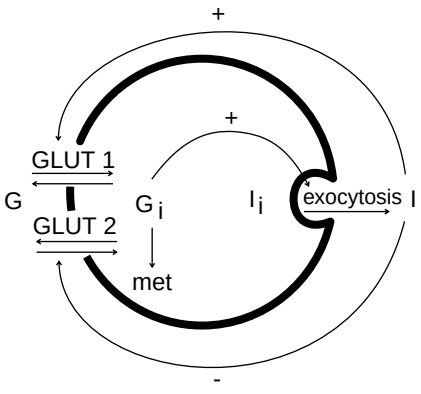

Figure 4.5 Schematic diagram of an insulin secreting cell.

secretion and $k_0 = \frac{f}{V_{bed}}$ is the inverse of the residence time for this reactor bed. (A schematic diagram of a secreting cell is shown in Fig. (4.5).

Since there is no flow associated with the intracellular space, the intracellular glucose concentration is found by keeping track of productions rates, via

$$dG_i/dt = -R_1 - R_2 + R_m \tag{4.22}$$

where R_m is the rate of glucose usage through metabolism.

Now we must specify the transfer rates. As described in Chapter 1, the GLUT transporters can be described by four states, two glucose free states and two glucose bound states. If we assume that transporter is always in quasi-equilibrium, then the flux through the transporter is given by

$$R_{GLUT} = \frac{K_G V_{max}(G - G_i)}{(K_G + G)(K_G + G_i)}. \tag{4.23}$$

The specific transporters GLUT1 and GLUT2 have fluxes of this form with the modification that GLUT1 is activated by insulin, and GLUT2 is inhibited by insulin. Thus, for the GLUT1 transporter we take

$$R_1 = \frac{K_1 V_{max1}(G - G_i)}{(K_1 + G)(K_1 + G_i)} \cdot \frac{I^n}{K_i^n + I^n} \tag{4.24}$$

and for the GLUT2 transporter

$$R_2 = \frac{K_2 V_{max2}(GJ^m - G_i)}{(K_2 + G)(K_2 + G_i)}. \tag{4.25}$$

The variable J is a (phenomenological) inhibition variable, related to I, that acts to shut down the inward flux of glucose when I is large, and satisfies the differential equation

$$dJ/dt = \frac{J^\infty(I) - J}{\tau}, \tag{4.26}$$

where $J^\infty = I/(I + K_I)$, and τ is the time constant associated with this time dependent process.

The metabolism of internal glucose is an enzymatic process, the first step of which is that glucose is phosphorylated by glucokinase, in a reaction that is Michaelis-Menten-like, and so is well described by the Michaelis-Menten rate law

$$R_m = \frac{V_m G_i}{K_m + G_i}. \tag{4.27}$$

The detailed mechanism underlying the secretion of insulin is not fully understood, so a phenomenological equation describing the rate of secretion as a function of the rate of metabolism is used,

$$R_s = \frac{V_s(R_m^4 + L^4)}{K_s^4 + R_m^4 + L^4}. \tag{4.28}$$

Notice that with $L \neq 0$, there is secretion of insulin even when $R_m = 0$. Now that the model is complete, we can begin an analysis of it. To do so we need to know something about the parameters. In Table (4.3) are listed the parameters that are fixed by the experiment, experimentally variable, and adjustable.

To reduce the complexity of the model, we would like to determine if there are any (relatively) fast or slow variables. One way to do this is to numerically simulate the full system of equations using typical parameter values and observe if there are some variables that change much faster than others. However, we suspect that there are differences in time scales here for the simple reason that the ratio of the two time constants k_0^{-1} and τ in Table 4.3 is large, being $\tau k_0 = 8 \times 10^3$. This suggests that the flow processes (involving G and I) are fast compared to inhibition through J. To be sure that this is correct, we introduce dimensionless parameters and variables $\widehat{G} = G/K_m$, $\widehat{G}_i = G_i/K_m$, $\widehat{G}_0 = G_0/K_m$, $\widehat{I} = I/K_i$, and $\widehat{t} = t/\tau$, and find the four dimensionless

Table 4.1 Standard dimensional parameters

Fixed by experiment	V_m	0.24 mM min^{-1}
	K_m	9.8 mM
	V_s	0.034 mM min^{-1}
	K_s	0.13 mM min^{-1}
	V_{max2}	32.0 mM min^{-1}
	K_2	17.0 mM
	V_{max1}	120.mM min^{-1}
	K_1	1.4 mM
	L	0.01 mM min^{-1}
Experimentally variable	k_0	400.0 min^{-1}
	I_0	0.0 mM
	G_0	8-22 mM
Adjustable in the model	K_I	1×10^{-6}mM
	K_i	4.0×10^{-5}mM
	τ	20.0 min

differential equations

$$d\widehat{G}/d\widehat{t} = -\widehat{R}_1 - \widehat{R}_2 - \widehat{k}_0(\widehat{G} - \widehat{G}_0) \tag{4.29}$$

$$d\widehat{G}_i/d\widehat{t} = -\widehat{R}_1 - \widehat{R}_2 + \widehat{R}_m \tag{4.30}$$

$$d\widehat{I}/d\widehat{t} = \widehat{R}_s - \widehat{k}_0\widehat{I} \tag{4.31}$$

$$dJ/d\widehat{t} = \widehat{J}^{\infty}(I) - J \tag{4.32}$$

where

$$\widehat{R}_1 = \frac{\widehat{K}_1\widehat{V}_{max1}(\widehat{G} - \widehat{G}_i)}{(\widehat{K}_1 + \widehat{G})(\widehat{K}_1 + \widehat{G}_i)} \cdot \frac{\widehat{I}^n}{\widehat{K}_i^n + \widehat{I}^n} \tag{4.33}$$

$$\widehat{R}_2 = \frac{\widehat{K}_2\widehat{V}_{max2}(\widehat{G}J^m - \widehat{G}_i)}{(\widehat{K}_2 + \widehat{G})(\widehat{K}_2 + \widehat{G}_i)} \tag{4.34}$$

$$\widehat{R}_m = \frac{\widehat{V}_m\widehat{G}_i}{1 + \widehat{G}_i} \tag{4.35}$$

$$\widehat{R}_s = \frac{\widehat{V}_s(\widehat{R}_m^4 + \widehat{L}^4)}{\widehat{K}_s^4 + \widehat{R}_m^4 + \widehat{L}^4} \tag{4.36}$$

$$\widehat{J}^{\infty} = \frac{1}{1 + \widehat{I}}. \tag{4.37}$$

The definitions of the dimensionless parameters and their values are given in Table 4.2.

The first noticeable feature from Table (4.2) is that there are two numbers, $\widehat{V}_s$ and $\widehat{k}_0$, that are quite large. Since these parameters both occur in Eqn. (4.31) for I, this implies that $\widehat{I}$ is a fast variable, so that $\widehat{I}$ changes rapidly in order to bring the right hand side of Eqn. (4.31) close to zero. Thus, our first quasi-steady state approximation

Table 4.2 Standard dimensionless parameters

Dimensionless parameter	Dimensional definition	Standard value
$\widehat{V}_m$	$\tau V_m/K_m$	0.50
$\widehat{V}_s$	$\tau V_s/K_i$	6.8×10^5
$\widehat{K}_s$	$\tau K_s/K_m$	0.27
$\widehat{V}_{max2}$	$\tau V_{max2}/K_m$	65.3
$\widehat{K}_2$	K_2/K_m	1.7
$\widehat{V}_{max1}$	$\tau V_{max1}/K_m$	245.0
$\widehat{K}_2$	K_1/K_m	0.14
$\widehat{L}$	$\tau L/K_m$	0.02
$\widehat{k}_0$	τk_0	8×10^3
$\widehat{G}_0$	G_0/Km	0.8-2.2
$\widehat{K}_i$	K_i/K_I	40.0

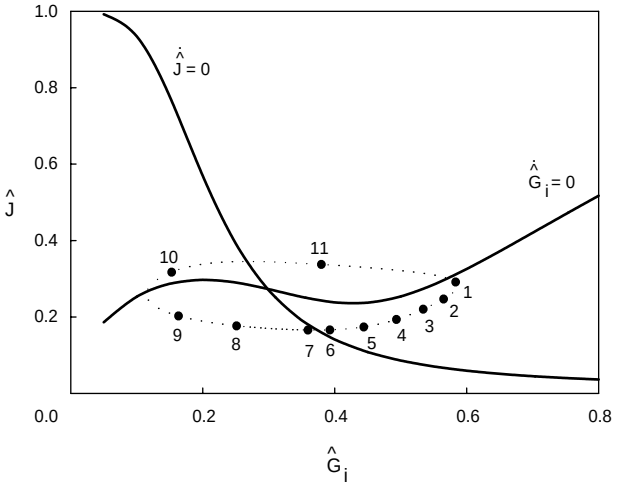

Figure 4.6 Phase portrait of glucose oscillations.

is to take

$$\widehat{I} = \frac{1}{\widehat{k}_0}\widehat{R}_s = \frac{\widehat{V}_s}{\widehat{k}_0}\left(\frac{\widehat{R}_m^4 + \widehat{L}^4)}{\widehat{K}_s^4 + \widehat{R}_m^4 + \widehat{L}^4}\right. . \tag{4.38}$$

Our second observation is that because $\widehat{k}_0$ is a large number, $\widehat{G}$, governed by Eqn. (4.29), is also a rapidly equilibrating variable, so we take the quasi-steady approximation

$$\widehat{G} = \widehat{G}_0 - \frac{1}{\widehat{k}_0}\widehat{R}_1 - \frac{1}{\widehat{k}_0}\widehat{R}_2. \tag{4.39}$$

However, since $\widehat{V}_{max1}/\widehat{k}_0 = 3.06 \times 10^{-2}$ and $\widehat{V}_{max2}/\widehat{k}_0 = 8.2 \times 10^{-3}$ are small, it is legitimate to ignore $\frac{\widehat{R}_1}{\widehat{k}_0}$ and $\frac{\widehat{R}_2}{\widehat{k}_0}$ in (4.39) and take

$$\widehat{G} = \widehat{G}_0. \tag{4.40}$$

With these simplifications we are left with a two variable model which we can readily analyze and simulate using XPPaut. We leave this simulation as an exercise, to verify that indeed there are glucose oscillations with a period of about 1 (about 20 minutes in dimensional time). So that you can check your answer, in Fig. (4.6) is shown the phase portrait for this oscillation.

4.4 Ligand Gated Channels

The Ca^{2+}-activated potassium channel provides another example in which some transitions are much faster than others and this can be used to derive simplified kinetics. This channel has two open states and two closed states. The channel has two binding sites for $Ca^{2+}$and opens when one of the sites is occupied. Thus, the closed state may

have zero or one Ca^{2+}ion bound and the open state may have one or two ions bound. The binding process is considered a fast process while the transition between open and closed states is slow.

$$C \overset{[\mathrm{Ca}^{2+}]\text{“}fast\text{”}}{\underline{\qquad}} C\cdot[\mathrm{Ca}^{2+}] \overset{\text{“}slow\text{”}}{\underline{\qquad}} O\cdot[\mathrm{Ca}^{2+}] \overset{[\mathrm{Ca}^{2+}]\text{“}fast\text{”}}{\underline{\qquad}} O\cdot([\mathrm{Ca}^{2+}])_2$$

To describe this process mathematically, we let the variables x_1, x_2, x_3, and x_4 denote the fractional occupancies of states C_1, C_2, O_1 and O_2. Then the transition rates between these states are V_A, V_B, and V_C, where

$$V_A = k_a^+[[\mathrm{Ca}^{2+}]]x_1 - k_a^- x_2, \tag{4.41}$$

$$V_B = k_b^+ x_2 - k_b^- x_3, \tag{4.42}$$

$$V_C = k_c^+[[\mathrm{Ca}^{2+}]]x_3 - k_c^- x_4. \tag{4.43}$$

Of course, $x_1 + x_2 + x_3 + x_4 = 1$.

$$\begin{array}{ccccccc} C_1 & \overset{A}{\underline{\qquad}} & C_2 & \overset{B}{\underline{\qquad}} & O_1 & \overset{C}{\underline{\qquad}} & O_2 \\ x_1 & & x_2 & & x_3 & & x_4 \end{array}$$

does this need to be set off as a figure?

Since we assume that V_A and V_C (the association/dissociation steps for binding Ca^{2+}) are fast, we use the rapid equilibrium assumption to set $V_A = V_C = 0$. This implies that

$$x_1 = \left(\frac{K_a}{[[\mathrm{Ca}^{2+}]]}\right)x_2 \tag{4.44}$$

$$x_3 = \left(\frac{K_c}{[[\mathrm{Ca}^{2+}]]}\right)x_4, \tag{4.45}$$

with dissociation constants

$$K_a = k_a^-/k_a^+, \qquad K_c = k_c^-/k_c^+. \tag{4.46}$$

Next, to find the evolution of the slow states, we combine states x_1 and x_2 into the closed state, x_C, and combine states x_3 and x_4 into the open state x_O, with

$$x_1 + x_2 = x_C, \qquad x_3 + x_4 = x_O. \tag{4.47}$$

Of course, because of our rapid equilibrium assumption,

$$x_2 = \frac{x_C}{1 + K_a/[[\mathrm{Ca}^{2+}]]}, \tag{4.48}$$

$$x_3 = \frac{x_O}{1 + K_c/[[\mathrm{Ca}^{2+}]]}. \tag{4.49}$$

The reduced equations follow from

$$dx_C/dt = -V_a + V_a - V_b = -V_b \tag{4.50}$$

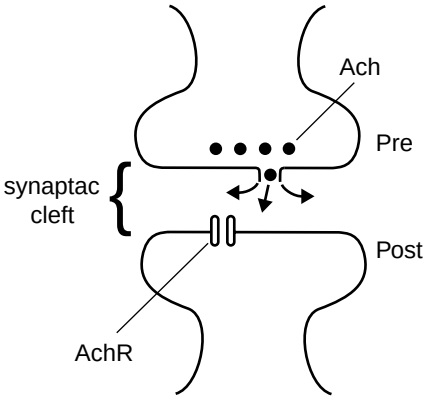

Figure 4.7 Diagram of a neuromuscular junction.

and, of course, $x_C + x_O = 1$. Therefore,

$$\begin{aligned}\frac{dx_O}{dt} &= V_b = k_b^+ x_2 - k_b^- x_3 \\ &= \frac{k^+ x_C}{1 + K_a/[[\mathrm{Ca}^{2+}]]} - \frac{k^- x_O}{1 + K_c/[[\mathrm{Ca}^{2+}]]} \\ &= k^+ x_C - k^- x_O,\end{aligned}$$

where $k^+ = \frac{k_b^+}{1+K_a/[[\mathrm{Ca}^{2+}]]}$, $k^- = \frac{k_b^-}{1+K_c/[[\mathrm{Ca}^{2+}]]}$. In other words, this process is equivalent to the two state process $C \underset{k^-}{\overset{k^+}{\rightleftharpoons}} O$.

Parameters are known from experiments to be $k_b^+ = 480s^{-1}$, $k_b^- = 280s^{-1}$, $K_a = k_a^-/k_a^+ = 180e^{-V/15.5}\mu$M, and $K_c = k_c^-/k_c^+ = 11e^{-V/13}\mu$M, where V, the voltage, is in units of mV.

4.5 Neuromuscular Junction

A similar analysis works to find a model of the acetylcholine receptor (AchR) in the postsynaptic membrane of neuromuscular junctions. Neuromuscular junctions consist of a presynaptic cell and a postsynaptic cell which are separated by a small synaptic cleft, as depicted in Fig. (4.7). When an action potential reaches the nerve terminal, several processes lead to the release of a chemical neurotransmitter, such as acetylcholine, from the presynaptic cell into the synaptic cleft. The neurotransmitter binds to receptors on the postsynaptic membrane which act as channels for some ion, such as sodium or potassium.

A model for the opening and closing of the Ach receptor (see Fig. 4.8) is based on the idea that a receptor is a four-state device, with three closed states and one open state. The three closed states have 0, 1 or 2 Ach molecules bound to it, and the open state requires that two Ach molecules be bound. We assume that the binding of Ach is a fast process and the opening and closing of the channel is slow in contrast.

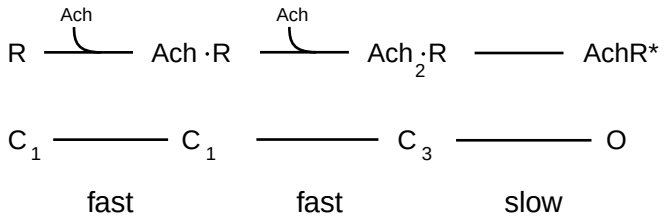

Figure 4.8 Four-state model for the Ach receptor.

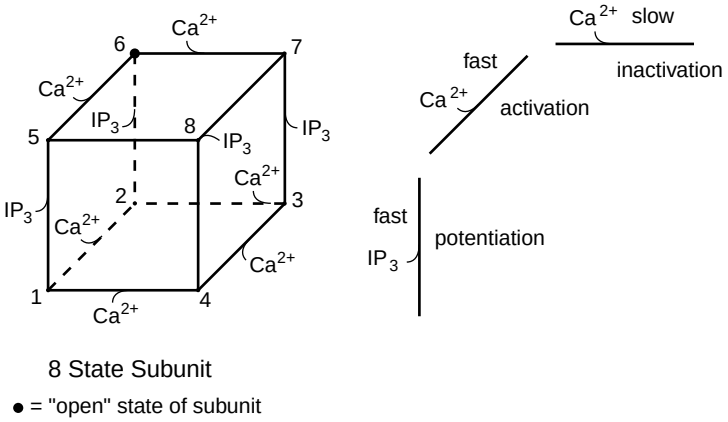

Figure 4.9 Transition diagram for the eight-state IP_3 receptor.

Using the rapid equilibrium approxmation, it is a straightforward exercise to combine the three closed states into one and to reduce this process to an equivalent two state process. In fact, it is readily found that if x_O is the proportion of receptors in the open state, then

$$dx_O/dt = k_{34}\frac{k_{23}[\text{Ach}]}{k_{32}}\frac{k_{12}[\text{Ach}]}{k_{21}+k_{12}[\text{Ach}]}(1-x_O) - k_{43}x_O. \tag{4.51}$$

4.6 The Inositol Triphosphate (IP_3) Receptor

The IP_3 receptor is a Ca^{2+}channel located in the endoplasmic reticulum that is regulated both by IP_3 and by Ca^{2+}. Each receptor consists of three independent subunits, each of which must be in the open state for the channel to be open. Each subunit has one binding site for IP_3 and two binding sites for calcium. Thus there are eight possible state for the subunit. Binding with IP_3 "potentiates" the subunit. The two calcium binding sites activate and inactivate the subunit, and a subunit is in the open

Table 4.3 Rate constants for the eight state IP_3 receptor.

$k_{15} = 400[IP_3]\mu\text{M}^{-1}\text{s}^{-1}$	$k_{51} = 52\text{s}^{-1}$
$k_{58} = 0.2[[\text{Ca}^{2+}]]\mu\text{M}^{-1}\text{s}^{-1}$	$k_{85} = 0.21\text{s}^{-1}$
$k_{48} = 400[IP_3]\mu\text{M}^{-1}\text{s}^{-1}$	$k_{84} = 377.2\text{s}^{-1}$
$k_{14} = 0.2[[\text{Ca}^{2+}]]\mu\text{M}^{-1}\text{s}^{-1}$	$k_{41} = 0.029\text{s}^{-1}$
$k_{12} = 20[[\text{Ca}^{2+}]]\mu\text{M}^{-1}\text{s}^{-1}$	$k_{21} = 1.64\text{s}^{-1}$

state when IP_3 and the activating calcium site are bound but the inactivating site is unbound.

To make a mathematical model for this receptor we must first give names to the eight different states. We denote x_i as the proportion of receptors in state i, where i is the label of the vertex on the cube in Fig. (4.9). Thus, for example, x_1 represents the state in which all binding sites are unbound, and x_6 is the open state of the subunit.

For these eight different states, there are 24 different rate constants k_{ij}. However, since each cycle must satisfy the thermodynamic constraint on kinetic constants, there are six restrictions on these 24 parameters. Notice that the rate constants that involve binding of a substrate must be proportional to the concentration of that substrate. Thus, k_{15}, k_{26}, k_{37}, and k_{48} are proportional to the concentration of IP_3, while the eight rate constants $k_{12}, k_{14}, k_{23}, k_{43}, k_{58}, k_{56}, k_{67}$ and k_{87} are all proportional to the Ca^{2+}concentration. Now we make two simplifying assumptions. First we assume that the rate constants are independent of whether activating $Ca^{2+}$is bound or not, and second we assume that the kinetics of Ca^{2+}activation is independent of IP_3 binding and Ca^{2+}inactivation. The first of these implies that $k_{14} = k_{23}, k_{15} = k_{26}, k_{58} = k_{67}$, and $k_{48} = k_{37}$, as well as for the reverse reactions. The second implies that $k_{12} = k_{56} = k_{87} = k_{43}$ and similarly for the reverse reactions. Thus we are left with *only* 10 rate constants.

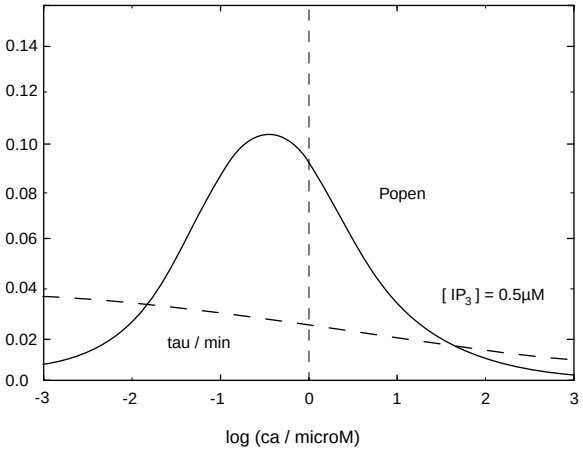

Figure 4.10 Open probability for IP_3 receptor. **need to add more curves**

The parameter values that were used by DeYoung and Keizer are displayed in Table (4.6).

An examination of the rate constants in Table 4.6 reveals that some processes are much faster than others. In fact, according to this table, the binding (and unbinding) of inactivating calcium is a slow process compared to the binding of IP_3 and activating calcium. For example, k_{15} and k_{48} are much larger than k_{58}, k_{14}, and k_{12}. Therefore we lump the eight variables into two groups with

$$y = x_1 + x_2 + x_5 + x_6 \tag{4.52}$$

$$1 - y = x_3 + x_4 + x_7 + x_8. \tag{4.53}$$

Next, we assume that all the fast processes are in quasi-equilibrium.. That is, we assume that the processes 1-5, 2-6, 3-7, 4-8 in which IP_3 is bound and the processes 5-6, 8-7, 1-2, 4-3 in which activating calcium is bound, are in quasi-equilibrium. This gives us a set of algebraic relationships which can be solved to find the variables x_i in terms of y. For example,

$$x_6 = \frac{k_{15}k_{12}}{(k_{51} + k_{15})(k_{21} + k_{12})} y. \tag{4.54}$$

We substitute these into the differential equation for y,

$$\frac{dy}{dt} = k_{41}x_4 + k_{85}x_8 + k_{76}x_7 + k_{32}x_3 - (k_{14}x_1 + k_{58}x_5 + k_{67}x_6 + k_{23}x_2) \tag{4.55}$$

and find the equation

$$\frac{dy}{dt} = (\frac{d_1 + k_{85}[IP_3]}{d_2 + [IP_3]})(1 - y) - d_4 cy. \tag{4.56}$$

Using the parameter values given in Table 4.6, we find $d_1 = 0.027\mu\text{M s}^{-1}$, $d_2 = 0.94\mu\text{M}$, $d_3 = 0.2\mu\text{M}^{-1}\text{s}^{-1}$. This equation is readily converted to an equation of the form

$$dy/dt = -\frac{(y - y^\infty([\text{Ca}^{2+}], IP_3))}{\tau([\text{Ca}^{2+}], IP_3)} \tag{4.57}$$

with an open probability

$$x_O = \left(\frac{[IP_3][[\text{Ca}^{2+}]]y}{(K_1 + [IP_3])(K_2 + [[\text{Ca}^{2+}]])}\right)^3. \tag{4.58}$$

Of course, the equilibrium open probability is

$$x_O^\infty = \left(\frac{[IP_3][[\text{Ca}^{2+}]]y^\infty}{(K_1 + [IP_3])(K_2 + [[\text{Ca}^{2+}]])}\right)^3. \tag{4.59}$$

A plot of the equilibrium open probability x_O^∞ is plotted in Fig. (4.10) for several values of $[IP_3]$. Notice that the maximum open probability increases with increasing $[IP_3]$ and the peak of the curve shifts to the right with increasing $[IP_3]$. Both of these features are observed experimentally.

Exercises

1. Create an *XppAut* file for solving the domain Ca^{2+} inactivation mechanism in Fig. (**??**). Use the parameter values $k_1^+ = 0.7\text{ms}^{-1}$, $k_1^- = 0.2\text{ms}^{-1}$, $k_2^+ = 0.05\text{mM}^{-1}\text{ms}^{-1}$, $k_2^- = 0.005\text{ms}^{-1}$, and $[Ca_d^{2+}] = 0.3\text{mM}$. Include in your model an auxiliary variable for calculating whole cell Ca^{2+} currents using $I_{Ca} = gx_O(V - V_{Ca})$, with $g = 5\text{nS}$, $V = 20\text{mV}$, and $V_{Ca} = 60\text{mV}$. Use *XppAut* to confirm the results in Fig. (4.3).
2. Use the data in Exercise 4.1 to create the simplified version of the domain Ca^{2+} inactivation model based on the rapid equilibrium approximation. Using the initial condition in Eqn. (4.12), solve the ODE using *XppAut* and compare your result for the Ca^{2+} current ($I_{Ca} = gx_O(V - V_{ca})$) to that in Fig. (4.3). Use Eqs. (4.9), (4.10) and (4.11) to calculate the numerical value of the relaxation time, τ, and the Ca^{2+} current after inactivation is complete. Verify that Eqn. (4.12) is correct and use it to show that the peak current is given by the expression $I_{peak} = g(1/(1+K_1))(V-V_{Ca})$.
3. On the fast time scale, it is a good approximation to neglect step 2 in the domain Ca^{2+} inactivation model in Fig. (**??**). Assuming that $x_C(0) = 1$, use the approximation to verify that on the fast time scale

$$dx_O/dt = -(x_O - \frac{1}{1+K_1})/\tau_{act} \tag{4.60}$$

   with $K_1 = k_1^-/k_1^+$ and $\tau_{act} = 1/(k_1^+ + k_1^-)$, the time constant for activation. Using the parameters in Exercise 1, evaluate τ_{act}.
4. A model that simulates the voltage dependence of domain Ca^{2+} activation of L-type Ca^{2+} channels in the pancreatic beta cell of mouse was developed by Sherman, Keizer, and Rinzel using the mechanism in Fig. (**??**). They fit data to experimental voltage clamp records using the voltage-dependent kinetic constants: $k_1^+(V) = 0.78/(1 + \exp[-(3 + V)/10])\text{ms}^{-1}$, $k_1^- = (0.78 - k_1^+(V))\text{ms}^{-1}$, $k_2^+[Ca_d^{2+}] = 7.56 \cdot 10^{-4}[Ca^{2+}]_{out}V/(1 - \exp(V/13.4)\text{mM}^{-1}\text{ms}^{-1}$, **there is something wrong with the units here.** $k_2^- = 0.002\text{ms}^{-1}$ with $[Ca^{2+}]_{out} = 3\text{mM}$ the external Ca^{2+} concentration and V in mV. Create an *XppAut* file for this model with the current as an auxiliary variable using the expression $I_{Ca} = gx_O[Ca^{2+}]_{out}V/(1-\exp(V/13.4)$ [3]. Use the file to simulate voltage clamp currents in which the voltage is increased from a holding potential of -100mV to depolarized test potentials with a duration of 250msec. Record the peak and final equilibrium currents and plot them as a function of the test potential. Explain the inverted bell-shaped $I - V$ curves.
5. Verify Eqn. (4.51) as a model for the Ach receptor.

[3] This is a special case of the Goldman-Hodgkin-Katz expression $[ion_{out}^z]V/(1 - \exp(zFV/RT)$ for the driving force, which is based on consideration of the rate at which an ion of charge z can diffuse through a pore with a linear gradient of electrical potential. This generalization of the Nernst expression in Eqn. (**??**) has proven particularly useful for modeling Ca^{2+} currents.

6. What are the 6 thermodynamic constraints that must hold for the kinetic parameters of the full IP_3 receptor model? Verify that these constraints hold for the parameter values in Table (4.6).
7. Use Eqn. (4.56) to calculate $y^\infty([Ca^{2+}], IP_3)$. Plot the equilibrium open probability for several values of $[IP_3]$.
8. Derive a model for ryanodine (RyR) receptors in cardiac cells. Assume that each subunit of a receptor has two binding sites for Ca^{2+}, one which activates the subunit when $Ca^{2+}$is bound and one which inactivates the subunit when $Ca^{2+}$is bound. Assume further that the binding of activating $Ca^{2+}$is independent of inactivating Ca^{2+}, and that the binding of inactivating $Ca^{2+}$is independent of activating Ca^{2+}. Show that as a result there are four independent rate constants, and that the thermodynamic constraint is automatically satisfied.
   Let x_0 be the fraction of receptors with no Ca^{2+}bound, x_1 be the fraction of receptors with only activating Ca^{2+}bound, x_3 be the fraction of receptors with only inactivating Ca^{2+}bound and x_4 be the fraction of receptors with both binding sites bound. Draw a diagram of this reaction mechanism. Which of the rate constants are proportional to the Ca^{2+}concentration?
   Using the rate constants $k_{12} = 15[[Ca^{2+}]]\mu M^{-1}s^{-1}$, $k_{13} = 0.8[[Ca^{2+}]]\mu M^{-1}s^{-1}$, $k_{21} = 7.6s^{-1}$, $k_{31} = 0.84s^{-1}$, identify which processes are fast and which are slow. Use the quasi-steady-state approximation to compress this into a two-state model. What are the effective rate constants for this compressed two state model?
9. Find the reduced slow time scale equations for a four-state transporter, such as the GLUT transporter described in Chapters 1 and 3 (exercise 9 **check this** (See Fig. (4.11).) Assume that the 1-4 and 2-3 transitions are rapid compared to other

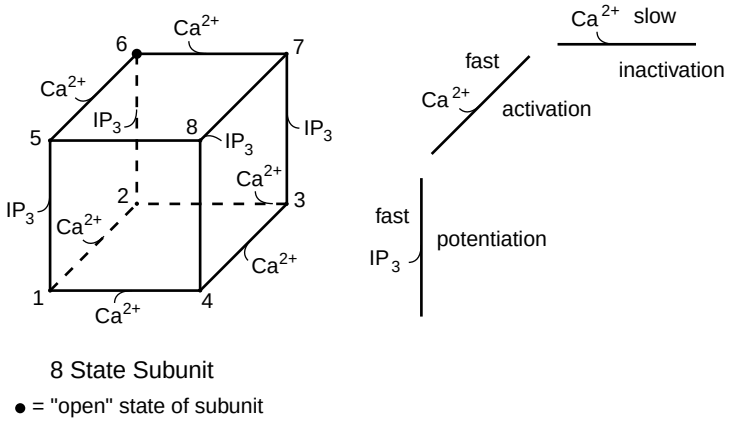

Figure 4.11 Transition diagram for sodium and GLUT four-state transporters. **These could easily be placed side-by-side**

transitions by lumping states 1 and 4 and state 2 and 3 into two variables

$$x_1 + x_4 = y_1 \qquad x_2 + x_3 = y_2. \tag{4.61}$$

where $y_1 + y_2 = 1$, and show that

$$dy_1/dt = -k_{12}x_1 + k_{21}x_2 + k_{34}x_3 - k_{43}x_4. \tag{4.62}$$

Solve the equilibrium conditions for x_1 and x_4 in terms of y_1 and for x_2 and x_3 in terms of y_2. Show that

$$dy_1/dt = -\frac{1}{\tau}(y_1 - y_1^{ss}) \tag{4.63}$$

where

$$y_1^{ss} = \frac{k_{21}^{(a)} + k_{21}^{(b)}}{k_{12}^{(a)} + k_{21}^{(a)} + k_{12}^{(b)} + k_{21}^{(b)}},$$
$$\tau = \frac{1}{k_{12}^{(a)} + k_{21}^{(a)} + k_{12}^{(b)} + k_{21}^{(b)}}.$$

$$k_{12}^{(a)} = \frac{k_{12}}{1+K'}, \qquad k_{21}^{(a)} = \frac{k_{21}}{1+K}, \qquad k_{12}^{(b)} = \frac{k_{43}K'}{1+K'}, \qquad k_{21}^{(b)} = \frac{k_{34}K}{1+K}. \tag{4.64}$$

Notice that this equation describes the transition between states 1 and 2 by two different processes, depicted in Fig. (4.12) as process "a" and "b".

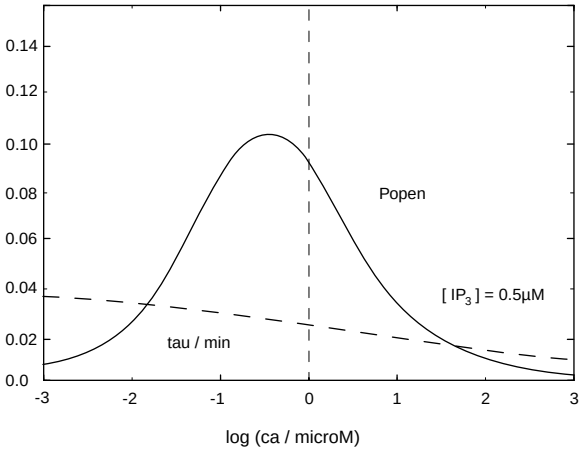

Figure 4.12 Transition diagram for reduced four-state transporter.

CHAPTER 5

Whole Cell Models

Arthur Sherman, Yue-Xian Li, and Joel Keizer

07-28

In modeling whole cells we try to understand complex properties of cells by combining together interlocking transport and regulatory mechanisms. We use a modular approach and develop models of each individual process separately using available experimental data. We then construct partial models by combining progressively more components together to understand how the components work together. In order to understand how the complete model works, we use separation of time scales or other features to develop a simplified model.

Three model systems are investigated in this chapter, the bullfrog sympathetic ganglion neuron, the pituitary gonadotroph, and the pancreatic β-cell. The order chosen is pedagogical and is in fact opposite to the historical order in which the models were developed. These models are not intended to provide a complete description of all features in cells, not even all features that have been modeled. Rather, they focus on the consequences of integrating plasma membrane and ER membrane fluxes into a coordinated system for control of membrane potential and Ca^{2+} concentrations. We will focus on the control mechanisms, but the controlled quantity, $[Ca^{2+}]_i$, is of great importance for the life and death of cells. It is a key regulator of many cell processes, such as secretion, gene transcription, and apoptosis. We further restrict our attention here to models with a small number of discrete, well-mixed compartments; diffusion in spatially extended compartments will be treated in Chapter (6). The models discussed here are far from the only ones that have been proposed for the particular systems.

refer to Keener and Sneyd chapter on calcium dynamics, Othmer review(s) for ip3 and ryr and ca oscs.

These simplified models incorporate a number of the examples of ion pumps and voltage- and ligand-gated channels discussed in the previous channels, and provide serious illustrations of the modular approach. A common dynamical theme in all three models and their variants is oscillations, some driven by the ER, some by the plasma membrane, and some by interactions between the two. As we saw previously in Chapter (2) (Chap. 2), a ubiquitous way that cells produce oscillations is through the combination of fast positive feedback with slow negative feedback.

[Add and cite in text or the exercises: Meyer-Stryer; Goldbeter-Dupont; Chay-Cuthbertson; Zweifach-Lewis; Sneyd-Atri]

5.1 General Framework for Models of ER and PM

The most striking feature of Ca^{2+} is its low concentration, approximately 0.1 μM at rest, and up to 1 μM or so at its peak. In contrast, Na^+ and K^+ are found in millimolar concentrations. Cells need to keep $[Ca^{2+}]_i$ so low because Ca^{2+} binds to many proteins and modifies their enzymatic properties. Thus, rises in Ca^{2+} must be kept brief and highly localized to avoid runaway activation of enzymatic cascades. These requirements are met by two basic mechanisms, buffering and sequestration. Buffers are specialized Ca^{2+}-binding proteins that soak up 95 – 99 % of the Ca^{2+} in the cytosol. Ca^{2+} is sequestered by Ca^{2+}-ATPases (SERCA) that pump it into internal stores, the sarcoplasmic reticulum (SR) in muscle cells and the endoplasmic reticulum (ER) in other

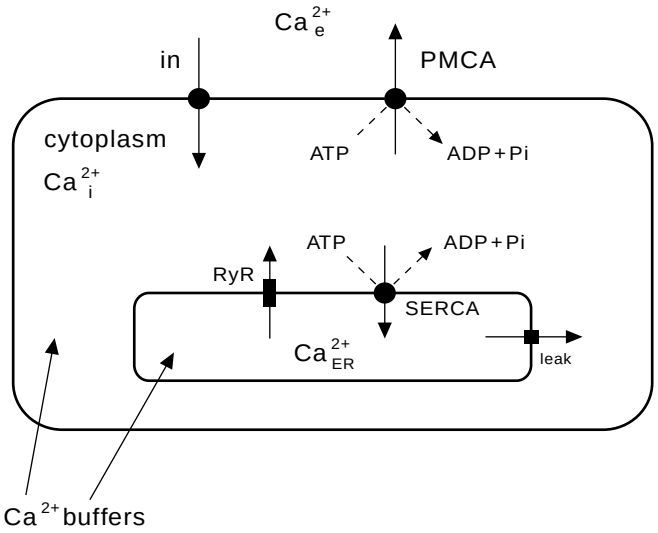

Figure 5.1 Add IP3R to this figure.

cells. Other pumps, plasma membrane Ca^{2+}-ATPases (PMCA), remove Ca^{2+} from the cell. Store membranes contain ion channels, analogous to but different from plasma membrane channels, that allow Ca^{2+} back out of the stores into the cytoplasm when needed. See Fig. (5.1). Whereas all cells have pumps for negative feedback and homeostasis, some cells have evolved ion channels such as the Ryanodine Receptor (RyR) and the IP_3-Receptor, which are both activated and inhibited by $Ca^{2+}$and provide both postive and negative feedback. The large ratios of bound to free Ca^{2+} and sequestered to cytoplasmic Ca^{2+} mean that brief channel opening can lead to large excursions of free cytoplasmic Ca^{2+} or oscillations that can be exploited for signalling.

Mitochondria and vesicles may also act as Ca^{2+} reservoirs and have their own specialized uptake and release mechanisms for Ca^{2+} and other ions. These have not been modeled as extensively, and will be treat only in passing here.

Exogenous Ca^{2+} buffers, called indicator dyes, that fluoresce differentially depending on $[Ca^{2+}]_i$ are the most common way to measure the concentration of free Ca^{2+}. As we will see below, buffers change (generally, slow down) the dynamics of Ca^{2+} in cells. Some cells possess Ca^{2+}-dependent K^+ or Cl^-channels, and these are often used as an alternative. A third approach is to exploit the luminescence of aequorin, a naturally occuring luminescent protein found in jelly fish, which can be targeted to specific organelles in cells of other organisms by genetic techniques.

5.1.1 Flux Balance Equations with Rapid Buffering

We begin with a general description applicable to any cell with a cytosolic compartment (subscripted by i) and an ER (subscripted by ER) and one species of Ca^{2+} buffer in each compartment. That gives a total of four species, bound and free Ca^{2+} in each of the two compartments.

We define N_i = total number of Ca^{2+} ions, bound and free, in the cytoplasm and N_{ER} = total number of Ca^{2+} ions in the ER. Then

$$[Ca^{2+}]_i^{tot} = \frac{N_i}{V_i},\ [Ca^{2+}]_{ER}^{tot} = \frac{N_{ER}}{V_{ER}} \tag{5.1}$$

where the V's represent the volumes of the cytosol and ER.

The fundamental physical principle used in constructing the equations is conservation of Ca^{2+} ions. The number of ions in each compartment is determined by the balance of fluxes across each of the membranes separating the compartments. The most general form is

$$\frac{dN_i}{dt} = J_{PM}^{in} - J_{PM}^{out} - J_{ER}^{in} + J_{ER}^{out} \tag{5.2}$$

$$\frac{dN_{ER}}{dt} = J_{ER}^{in} - J_{ER}^{out}. \tag{5.3}$$

The J's have units of μmoles/sec and represent fluxes through the following entities commonly found in cells: J_{PM}^{in}, flux through ion channels; $J_{PM}^{out} = J_{PMCA}$, plasma membrane Ca^{2+}-ATPase; $J_{ER}^{in} = J_{SERCA}$, ER Ca^{2+}-ATPase; and J_{ER}^{out}, one or more of J_{IP_3}

(IP_3-receptor), J_{RyR} (Ryanodine receptor), and J_{leak} (unregulated leak) (See Fig. (5.1)). In terms of concentrations we have:

$$\begin{aligned}\frac{d[\mathrm{Ca}^{2+}]_{\mathrm{i}}^{\mathrm{tot}}}{dt} &= \frac{1}{V_i}(J_{PM}^{in} - J_{PM}^{out} - J_{ER}^{in} + J_{ER}^{out}) \qquad (5.4)\\ &= j_{PM}^{in} - j_{PM}^{out} - j_{ER}^{in} + j_{ER}^{out}\\ \frac{d[\mathrm{Ca}^{2+}]_{\mathrm{ER}}^{\mathrm{tot}}}{dt} &= \frac{1}{V_{ER}}(J_{ER}^{in} - J_{ER}^{out}) \qquad (5.5)\\ &= \frac{V_i}{V_{ER}}(j_{ER}^{in} - j_{ER}^{out})\end{aligned}$$

where we have absorbed the volumes into the j's, giving them units of μM/sec.

Now we come to grips with the buffering equations. $[\mathrm{Ca}^{2+}]^{\mathrm{tot}}$ consists of free Ca^{2+} plus Ca^{2+} bound to buffer, B. In the cytosol,

$$[\mathrm{Ca}^{2+}]_{\mathrm{i}} + [\mathrm{Ca}^{2+} \cdot \mathrm{B}]_{\mathrm{i}} = [\mathrm{Ca}^{2+}]_{\mathrm{i}}^{\mathrm{tot}} \qquad (5.6)$$

$$[\mathrm{B}]_{\mathrm{i}} + [\mathrm{Ca}^{2+} \cdot \mathrm{B}]_{\mathrm{i}} = [\mathrm{B}]_{\mathrm{i}}^{\mathrm{tot}} \qquad (5.7)$$

with similar expressions for the ER. We avoid adding a differential equation to describe these reactions by assuming rapid equilibrium between Ca^{2+} and buffer:

$$[\mathrm{Ca}^{2+}]_{\mathrm{i}} = \frac{K_i[\mathrm{Ca}^{2+} \cdot \mathrm{B}]_{\mathrm{i}}}{[\mathrm{B}]_{\mathrm{i}}} \qquad (5.8)$$

Combining Eqn. (5.6) and Eqn. (5.8) gives:

$$[\mathrm{Ca}^{2+}]_{\mathrm{i}}^{\mathrm{tot}} = [\mathrm{Ca}^{2+}]_{\mathrm{i}}\left(1 + \frac{[\mathrm{B}]_{\mathrm{i}}}{K_i}\right) \qquad (5.9)$$

Combining Eqn. (5.7) and Eqn. (5.8) gives:

$$[\mathrm{B}]_{\mathrm{i}}^{\mathrm{tot}} = [\mathrm{B}]_{\mathrm{i}}\left(1 + \frac{[\mathrm{Ca}^{2+}]_{\mathrm{i}}}{K_i}\right) \qquad (5.10)$$

Finally, solving Eqn. (5.10) for $[\mathrm{B}]_{\mathrm{i}}$ and substituting into Eqn. (5.9) gives the desired algebraic relation between $[\mathrm{Ca}^{2+}]_{\mathrm{i}}^{\mathrm{tot}}$ and $[\mathrm{Ca}^{2+}]_{\mathrm{i}}$:

$$[\mathrm{Ca}^{2+}]_{\mathrm{i}}^{\mathrm{tot}} = [\mathrm{Ca}^{2+}]_{\mathrm{i}}\left(1 + \frac{[\mathrm{B}]_{\mathrm{i}}^{\mathrm{tot}}}{K_i + [\mathrm{Ca}^{2+}]_{\mathrm{i}}}\right). \qquad (5.11)$$

To get the balance equation for $[\mathrm{Ca}^{2+}]_{\mathrm{i}}$, we apply the chain rule and Eqn. (5.11) to obtain

$$\begin{aligned}\frac{d[\mathrm{Ca}^{2+}]_{\mathrm{i}}^{\mathrm{tot}}}{dt} &= \frac{d[\mathrm{Ca}^{2+}]_{\mathrm{i}}^{\mathrm{tot}}}{d[\mathrm{Ca}^{2+}]_{\mathrm{i}}}\,\frac{d[\mathrm{Ca}^{2+}]_{\mathrm{i}}}{dt}\\ &= \frac{1}{f_i([\mathrm{Ca}^{2+}]_{\mathrm{i}})}\,\frac{d[\mathrm{Ca}^{2+}]_{\mathrm{i}}}{dt}, \qquad (5.12)\end{aligned}$$

where

$$f_i([\mathrm{Ca}^{2+}]_{\mathrm{i}}) = \frac{1}{1 + \frac{K_i[\mathrm{B}]_{\mathrm{i}}^{\mathrm{tot}}}{(K_i + [\mathrm{Ca}^{2+}]_{\mathrm{i}})^2}}. \qquad (5.13)$$

This is a form of the Rapid Buffering Approximation (RBA), specialized to cells that may be considered spatially homogeneous. The extension to situations in which diffusion of $[Ca^{2+}]_i$ and buffer cannot be ignored is taken up in Chapter (6).

In general, f_i is a function of $[Ca^{2+}]_i$, but for low affinity buffers $K_i \gg [Ca^{2+}]_i$ and f_i can be taken as constant:

$$f_i \approx \frac{1}{1 + \frac{[B]_i^{tot}}{(K_i)}}. \tag{5.14}$$

In this case, f_i can be interpreted as the fraction of $[Ca^{2+}]_i^{tot}$ that is free. Typical measured values for f_i are 0.01–0.05.

Combining Eqn. (5.12) and the corresponding equation for the ER with Eqn. (5.4) and Eqn. (5.5) gives

$$\frac{d[Ca^{2+}]_i}{dt} = f_i(j_{PM}^{in} - j_{PM}^{out} - j_{ER}^{in} + j_{ER}^{out}) \tag{5.15}$$

$$\frac{d[Ca^{2+}]_{ER}}{dt} = \frac{V_i f_{ER}}{V_{ER}}(j_{ER}^{in} - j_{ER}^{out}). \tag{5.16}$$

It is sometimes convenient to replace $[Ca^{2+}]_i$ or $[Ca^{2+}]_{ER}$ by $[Ca^{2+}]_i^{tot}$. This is equivalent to using Eqs. (5.15), (5.16) because of the conservation condition $N_T = N_i + N_{ER}$, where N_T is the total number of Ca^{2+} ions in all the cell compartments. Dividing the conservation condition by the cytosolic volume gives

$$\frac{N_T}{V_i} = [Ca^{2+}]_i^{tot} + \frac{V_{ER}}{V_i}[Ca^{2+}]_{ER}^{tot}. \tag{5.17}$$

Applying the RBA and assuming that both ER and cytoplasmic buffers are low affinity (Eqs. 5.12, 5.14 and their analogs for the ER), $[Ca^{2+}]_i$ and $[Ca^{2+}]_{ER}$ are each proportional to the total Ca^{2+} in their respective compartments we have

$$[Ca^{2+}]_i = f_i[Ca^{2+}]_i^{tot},\ [Ca^{2+}]_{ER} = f_{ER}[Ca^{2+}]_{ER}. \tag{5.18}$$

Combining Eqs. (5.18) with Eqn. (5.17) yields

$$C_T = [Ca^{2+}]_i + \sigma[Ca^{2+}]_{ER} \tag{5.19}$$

where

$$C_T = \frac{f_i N_T}{V_i} \text{ and } \sigma = \frac{V_{ER} f_i}{V_i f_{ER}} \tag{5.20}$$

with C_T, σ, f_i all constants. C_T is the "total free Ca^{2+}" of the cell with the *cytosolic* volume as the reference volume. V_i/f_i and V_{ER}/f_{ER} are called the "effective volumes" of the cytosol and ER respectively, that is, the volumes taking into account the fraction of Ca^{2+} that is free in each compartment. σ is then the ratio of effective volumes.

Differentiating Eqn. (5.19) we obtain

$$\frac{dC_T}{dt} = f_i(j_{PM}^{in} - j_{PM}^{out}), \tag{5.21}$$

which is simpler than Eqn. (5.16) for $[Ca^{2+}]_{ER}$. $[Ca^{2+}]_{ER}$ can be recovered from the algebraic relation

$$[Ca^{2+}]_{ER} = (C_T - [Ca^{2+}]_i)/\sigma. \tag{5.22}$$

This formulation is particularly useful in the closed-cell models below. In those models, we assume that that there is no net flux of Ca^{2+} in or out of the cell. Then, $j_{PM}^{in} = j_{PM}^{out} = 0$, so C_T is constant. This allows us to replace Eqn. (5.16) by Eqn. (5.22), reducing the number of differential equations by one.

Go further into non-dimensional form of equations to show ratio of ER/PM surface area.

5.1.2 Expressions for the Fluxes

The final step in specifying particular models is to replace the general terms $j_{PM}^{in}, j_{PM}^{out}, j_{ER}^{in}$, and j_{ER}^{out} by appropriate biophysical expressions. Efflux from the cell is generally mediated by a pump flux, j_{PMCA}, and influx into the ER from the cytosol by j_{SERCA}. Ca^{2+} pumps were discussed in detail in Chapter (3). In the whole cell models we generally use the empirical, Hill-type formulas for pump rate of the form

$$j_{PUMP} = \frac{v[Ca^{2+}]_i^{\,2}}{K^2 + [Ca^{2+}]_i^{\,2}} \tag{5.23}$$

rather than detailed kinetic models (*cf.* Eq. 3.37). Here v is proportional to the total number of SERCA or PMCA pumps and to the rate of a single pump.

Efflux from the ER to the cytosol often includes a constant, unregulated leak conductance of the form

$$j_{leak} = v \cdot ([Ca^{2+}]_{ER} - [Ca^{2+}]_i) \tag{5.24}$$

where v is the leak permeability ($[Ca^{2+}]_{ER} - [Ca^{2+}]_i$) is the thermodynamic driving force for a symmetric channel (See Exercise (2)). *Switch v to P?*

Interesting dynamics, such as oscillations, however, generally require nonlinear feedback on the efflux rate by Ca^{2+}. This can be mediated by the RyR, for which a detailed model is presented in Section (5.2), or the IP_3R, which was discussed in Chapter (**??**) and is further developed in Section (5.3).

Ca^{2+} generally enters cells via voltage-dependent ion channels. Ionic currents are measured in pA or nA, so an additional factor is needed to convert to μmoles:

$$j_{PM}^{in} = -\alpha I_{Ca} \tag{5.25}$$

where $\alpha = 1/(2FV_i)$, $F = 96480$ C mol^{-1} is Faraday's constant ($F = eA$ = the elementary charge $\times$ Avogadro's number), and the factor 2 accounts for the two positive charges of a Ca^{2+} ion. As an example, if I_{Ca} is measured in pA, and cytosolic volume is measured in μm^3, j_{PM}^{in} will have units of M msec^{-1}. Note that by the Hodgkin-Huxley convention, an inward cation current such as I_{Ca} is negative, so the flux is positive.

5.2 Calcium Oscillations in the Bullfrog Sympathetic Ganglion Cell

5.2.1 Review of the biology

Bullfrog sympathetic ganglion neurons are excitable cells with a full complement of voltage-dependent ion channels (see W. M. Yamada, C. Koch, and P. R. Adams, Multiple Channels and Calcium Dynamics, in Methods in Neuronal Modeling, 2nd Edition, MIT Press, 1998). However, the Ca^{2+} oscillations modeled here are driven by nonlinearity in the ER, with the plasma membrane playing only a passive role. As early as 1976, Kuba and Nishi (JNP 39:547 '76) observed rhythmic hyperpolarizations of the rest potential when the neurons were exposed to caffeine.

These caffeine-induced oscillations also occur when the membrane voltage is clamped at a fixed value, suggesting that voltage-gated ion channels on the plasma membrane are not involved in producing the oscillations. Caffeine has been found to activate the RyR by shifting the Ca^{2+}-dependence of channel opening to lower and more physiological levels of $[Ca^{2+}]_i$. Ryanodine, a specific ligand to RyR, blocks the response of these neurons to caffiene. This is consistent with the fact that ryanodine blocks RyR channels by locking them into a low conductance state. These oscillations are of relaxation type with very long period (several minutes). The $[Ca^{2+}]_i$ spikes are characterized by a sharp upstroke followed by a plateau phase and a subsequent downstroke. The upstroke is associated with the dumping of Ca^{2+} by the ER store, the plateau phase is largely due to Ca^{2+}-extrusion, and the downstroke is linked to Ca^{2+}-uptake by the store. Sustained Ca^{2+} entry is indispensable during the interspike intervals, suggesting that after each spike store refilling driven by Ca^{2+} influx is necessary for the generation of the subsequent spike. Therefore, increasing the rate of Ca^{2+} entry by depolarizing the membrane leads to shortened interspike interval and increased amplitude (Friel and Tsien, '92, Friel, '95, Nohmi et al, '92). Ca^{2+}-dependent gating properties of the RyR channels were further investigated by Györke and Fill in 1993, providing data for the development of a mathematical model based on channel kinetics. Although caffeine-induced Ca^{2+} oscillations are not likely to occur in bullfrog sympathetic neurons under physiological conditions, it is good model for studying RyR-mediated Ca^{2+} oscillations in neurons.

5.2.2 Model for RyR Kinetics

We begin with equations for the RyR receptor itself as studied in conditions where Ca^{2+} is a parameter, imposed by the experimenter. For example, in the experiments of Györke and Fill (Science, 260:807–809, 1993), cardiac RyRs in lipid bilayers were exposed to controlled Ca^{2+} elevations by flash photolysis of a caged Ca^{2+} compound, DM-nitrophen. (See Exercise (7)).

Here we present a minimal model designed to capture the key features observed by those authors. Like the IP_3-receptor, the RyR exhibits fast activation and slow

inactivation in response to a rise in Ca^{2+}. In contrast, the steady-state open probability is monotonic with respect to $[Ca^{2+}]_i$. The state diagram devised by Keizer and Levine (5.2) consists of two closed states, C_1 and C_2, and two open states, O_1 and O_2. At rest (corresponding to a background Ca^{2+} level of 0.1 μM), most of the receptors are in state C_1.

Both open states have the same conductance, so the net open probability $P_O = P_{O1} + P_{O2}$. The receptors respond to a step increase in Ca^{2+} with a rapid rise in P_O as states O_1 and O_2 are populated, followed by a slow decline to a steady, plateau level as states flow into C_2 Fig. (5.3), left panel, solid curve. Fig. (5.3), right panel, shows the peak and plateau values attained after a step from $[Ca^{2+}] = 0.1$ μM to the indicated value. (Note that the jump to the peak depends on the initial conditions, which determine the number of receptors in C_1 available to be recruited by the Ca^{2+} step.) During the short time shown in Fig. (5.3), there is little back flow out of C_2, but a further increase in $[Ca^{2+}]_i$ draws more receptors out of C_1 into the open states Fig. (5.3), left panel, arrow and dashed curve.

The full 4-state model are described by 3 independent odes plus a conservation condition for the total number of channels: $P_{O1} + P_{O2} + P_{C1} + P_{C2} = 1$. We can apply the methods of Chapter (**??**) to derive a quasi-steady-state approximation (Exercise 3) assuming that P_{C2} is slow, while the other states are in rapid equilibrium:

$$P_O \approx P_O^{slow} = \frac{w \cdot (1 + ([Ca^{2+}]_i/K_b)^3)}{1 + (K_a/[Ca^{2+}]_i)^4 + ([Ca^{2+}]_i/K_b)^3} \tag{5.26}$$

where P_O^{slow} is proportional to $w = 1 - P_{C2}$, which is the fraction of non-inactivated receptors. In terms of probabilities,

$$Pr\{\text{Open}\} = Pr\{\text{Not Inactivated}\} \cdot Pr\{\text{Open}|\text{Not Inactivated}\}. \tag{5.27}$$

Given $[Ca^{2+}]_i$, w is calculated from the differential equation

$$\frac{dw}{dt} = \frac{(w_\infty([Ca^{2+}]_i) - w)}{\tau([Ca^{2+}]_i)} \tag{5.28}$$

with

$$w_\infty([Ca^{2+}]_i) = \frac{1 + (K_a/[Ca^{2+}]_i)^4 + ([Ca^{2+}]_i/K_b)^3}{1 + (1/K_c) + (K_a/[Ca^{2+}]_i)^4 + ([Ca^{2+}]_i/K_b)^3} \tag{5.29}$$

and

$$\tau([Ca^{2+}]_i) = \frac{w_\infty([Ca^{2+}]_i)}{k_c^-}. \tag{5.30}$$

As for the gating variables in Chapter (2), it is natural to write a pseudo-exponential rate equation for w because changes in w are exponential for fixed $[Ca^{2+}]_i$. Note that the rate constants of the fast processes no longer appear, just the dissociation constants, defined by $K_a^4 = k_a^-/k_a^+$, $K_b^3 = k_b^-/k_b^+$, and $K_c = k_c^-/k_c^+$. The slow time scale τ is inversely proportional to k_c^-, the rate of transition out of C_2.

Refer to other models (eg. Tang-Othmer).

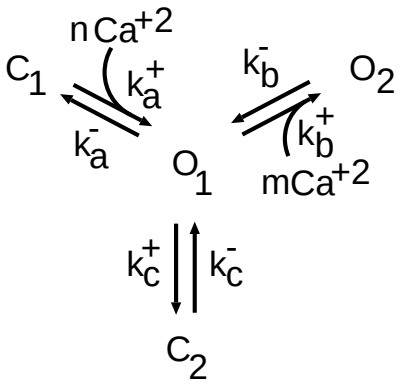

Figure 5.2 Kinetic states of the Keizer-Levine model for the RyR.

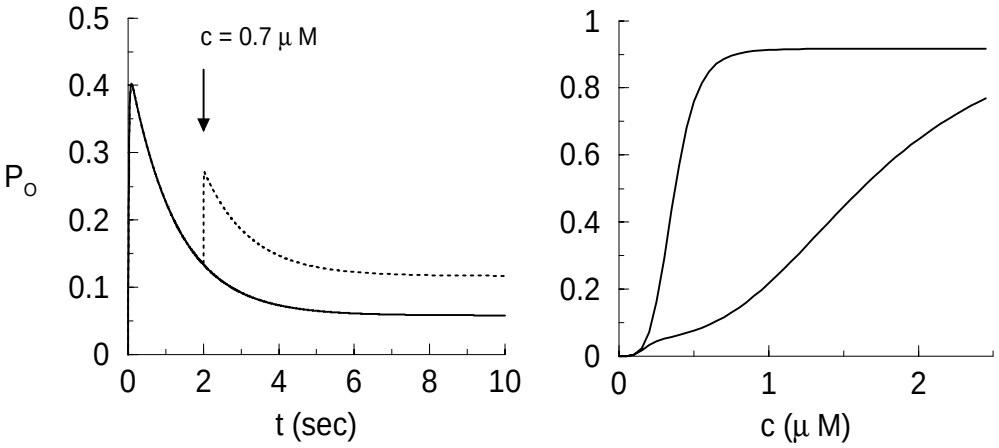

Figure 5.3 Left: Timecourse of response of P_O to a step increase in c from 0.1 to 0.35 μM (solid). Dotted curve shows "adaptation" when a second step to 0.7 μM is applied at $t = 2$ sec. Right: Peak and steady-state levels of P_O for different values of c (Equivalent to Keizer-Levine Figure 2C, D; made with *klstates.ode* and *klss.ode*). Compare to Györke and Fill, Figs. 3 and 2B. Parameters: $k_a^+ = 1500\ \mu\text{M}^{-4}\ \text{s}^{-1}$, $k_a^- = 28.8\ \text{s}^{-1}$, $k_b^+ = 1500\ \mu\text{M}^{-3}\ \text{s}^{-1}$, $k_b^- = 385.9\ \text{s}^{-1}$, $k_c^+ = 1.75\ \text{s}^{-1}$, $k_c^- = 0.1\ \text{s}^{-1}$.

5.2.3 Closed Cell Model

We proceed to write down the equations for a closed cell using Eqn. (5.15) (with $j_{PM}^{in} = j_{PM}^{out} = 0$) together with appropriate expressions for the fluxes due to the ryanodine receptors, a leak out of the ER, and a SERCA pump:

$$\frac{d[\text{Ca}^{2+}]_\text{i}}{dt} = f_i(j_{RyR} + j_{leak} - j_{SERCA}). \tag{5.31}$$

The RyR flux is

$$j_{RyR} = v_1 P_O \cdot ([\text{Ca}^{2+}]_\text{ER} - [\text{Ca}^{2+}]_\text{i}), \tag{5.32}$$

where v_1 is proportional to the number of RyR's and P_O is the probability that a receptor is open. (Note that here we are generalizing Eqn. (5.24) for a symmetric leak channel, but symmetry is only an approximation for the RyR. See Exercise (2). We use the quasi-steady-state approximation Eqn. (5.26)–Eqn. (5.30) of the previous section for P_O. Because of conservation of ions, we do not need a differential equation for $[Ca^{2+}]_{ER}$, but just the algebraic relation Eqn. (5.22).

The leak is given by

$$j_{leak} = v_2([Ca^{2+}]_{ER} - [Ca^{2+}]_i), \tag{5.33}$$

and the pump flux is

$$j_{SERCA} = v_3 \frac{[Ca^{2+}]_i^{\,2}}{[Ca^{2+}]_i^{\,2} + K_3^{\,2}}. \tag{5.34}$$

The closed cell model consists of the two differential equations for $[Ca^{2+}]_i$ (Eqn. 5.31) and w (Eqn. 5.28) plus the associated algebraic equations.

With the parameters given in Fig. (5.4) (corresponding roughly to the small store case in Keizer-Levine), the model is not able to produce oscillations, but instead is bistable; it can assume either a high-$[Ca^{2+}]_i$ steady state or a low-$[Ca^{2+}]_i$ steady state. This behavior can be understood by looking at the nullclines (This is possible because we reduced the kinetic equations for the RyR to one slow equation.) In the closed-cell model total Ca^{2+} (C_T) is constant, and this is a natural parameter to use to characterize the system. For low values of C_T, the steady-state $[Ca^{2+}]_i$ is low, and w is high (few receptors are adapted). For high values of C_T, steady-state $[Ca^{2+}]_i$ is high, and w is low (many receptors are adapted). For intermediate values of C_T, there are three steady states. Examination of the eigenvalues of the jacobian in this case reveals that the low and high steady states are stable nodes (see Appendix), while the middle steady state is a saddle. Sample nullclines are plotted in the top panel of Fig. (5.4), and the summary of how the steady states vary with C_T (*i.e.*the bifurcation diagram) is plotted in the bottom panel. This global view reveals a large region of bi-stability or hysteresis bracketed by two saddle-node bifurcations (the turning points, where the determinant changes sign) that give birth to all of the steady states in the system. Such features are worth study because they are ubiquitous in biological models. However, there are no Hopf bifurcations (points where the trace of the Jacobian changes sign) that give rise to oscillations Geometrically, this is because for no value of C_T does the w-nullcline intersect the $[Ca^{2+}]_i$-nullcline with a more negative slope.

By making a small change in the Ca^{2+}-handling parameters it is possible to obtain oscillations with the closed-cell model. See Exercise (4). Nonetheless, Keizer and Levine concluded that that this is not a good model for the oscillations observed by Friel and Tsien; they are not robust (*i.e.* the oscillations only exist for a small range of C_T, and it is difficult to get oscillations with period greater than one minute. This is because the time scale of the oscillations is determined by the reciproal of $k_c^{\,-}$, which is about 10 seconds. In order to obtain robust oscillations on the minute time scale, it is necessary to add another, slower process to the system, which we do in the next section.

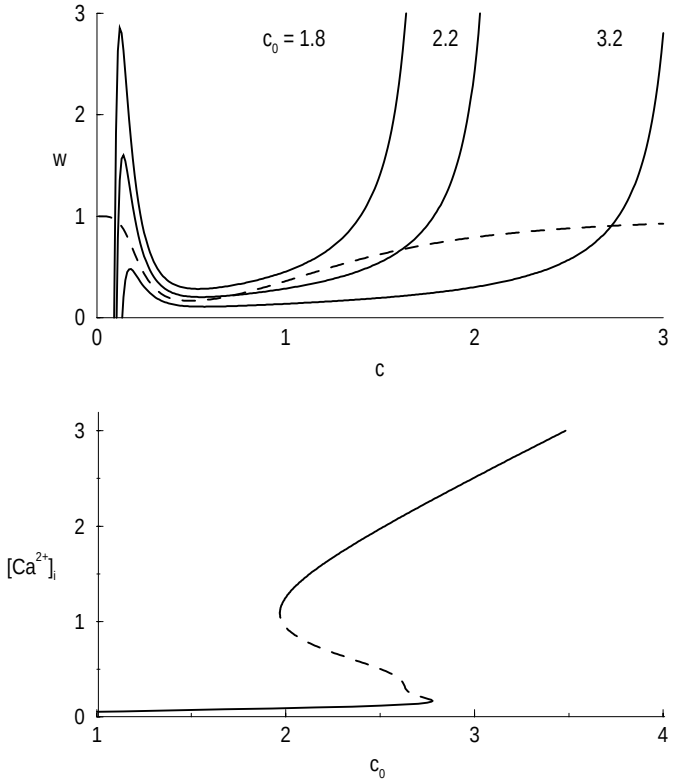

Figure 5.4 Top: Nullclines for $[Ca^{2+}]_i$ (solid), w (dashed) for closed-cell Keizer-Levine model. Bottom: Intersections of nullclines (steady states)in top panel for various values of C_T. Parameters: As in Fig. (5.2) plus: $f_i = 0.01, v_1 = 5\ s^{-1}$, $v_2 = 0.2\ s^{-1}$, $v_3 = 100\ \mu M\ s^{-1}$, $K_3 = 0.2\ \mu M$, $\sigma = 0.02$, $C_T = 1.0\ \mu M$, $K_a = 0.4\ \mu M$, $K_b = 0.6\ \mu M$, $K_c = 0.1\ \mu M$, and $k_c{}^- = 0.1\ s^{-1}$. Made with *klclose.ode*. Yue-Xian: Check for HB.

5.2.4 Open Cell Model

In the previous section we saw that adaptation of the RyR is not likely the mechanism behind slow oscillations in the BFSG cell, and that another slower process is needed. A natural extension suggested by the analysis of the closed cell is to make C_T a slow variable rather than a constant parameter. Biophysically, this allows for larger variation in the filling state of the ER. We will see that in each cycle the stores almost completely empty and refill. In other words, the net flux in and out of the cell over a cycle is 0, but there is a large efflux at some points in the cycle that is balanced by a large at other points.

The open cell expands on the closed cell model by adding an equation to describe changes in C_T due to fluxes into the cell and PMCA pumps that remove Ca^{2+},

$$\frac{dC_T}{dt} = f_i(j_{in} - j_{PMCA}). \tag{5.35}$$

The PMCA flux is given by

$$j_{PMCA} = \frac{v_{out}[Ca^{2+}]_i^{\,2}}{K_{out}^2 + [Ca^{2+}]_i^{\,2}}. \tag{5.36}$$

Since oscillations occur under voltage-clamp, we can represent influx of Ca^{2+}as a constant, j_{in} (understood as influx across the plasma membrane). The equation for $[Ca^{2+}]_i$ must also be augmented by the additional fluxes:

$$\frac{d[Ca^{2+}]_i}{dt} = f_i(j_{RyR} + j_{leak} + j_{SERCA} + j_{in} - j_{PMCA}). \tag{5.37}$$

The open cell model thus consists of three differential equations Eqn. (5.28), Eqn. (5.35), and Eqn. (5.37) and associated algebraic expressions for the fluxes. We can collapse this system back into just two equations for $[Ca^{2+}]_i$ and C_T. This is justified because variation in w is fast compared to the oscillation period. (See Exercise (6)). We eliminate the equation for w by writing $w = w_\infty([Ca^{2+}]_i)$. The RyR channel flux is then given by

$$j_{RyR} = \frac{v_1 w_\infty([Ca^{2+}]_i)(1 + [[Ca^{2+}]]/K_b)^3}{1 + (K_a/[Ca^{2+}]_i)^4 + ([Ca^{2+}]_i/K_b)^3}. \tag{5.38}$$

Solutions of the reduced open cell model (Eqn. (5.35) and Eqn. (5.37) with j_{RyR} replaced by the expression in Eqn. (5.38)) are shown in Fig. (5.5). With adequate Ca^{2+} influx, oscillations of the right shape and duration are seen. However, if Ca^{2+} influx is suppressed, say by removal of external Ca^{2+}, the oscillations cease immediately, also in agreement with experiment (ref).

The closed cell model can be viewed as the *fast subsystem* of the open cell. That is, the bifurcation diagram of the closed cell model with C_T as a parameter is a phase plane of the reduced open cell model with C_T as a slow variable (slow compared to $[Ca^{2+}]_i$). We illustrate this by projecting the trajectory of the open cell onto the diagram computed with the closed cell supplemented with the nullcline for C_T. We can predict further from this that if j_{in} is increased so that the C_T nullcline intersects the s-shaped $[Ca^{2+}]_i$ nullcline above the upper limit point or below the lower limit point, there will be no oscillations. (See Exercise (5)). This is confirmed by the bifurcation diagram of the reduced open cell with respect to j_{in} Fig. (5.7). Within the oscillatory range, variation of j_{in} produces a broad range of frequencies, but almost no change in amplitude. This follows from the relaxation oscillator character of the model (compare with discussion of the Morris-Lecar model, Chapter (2), Fig. 2.9).

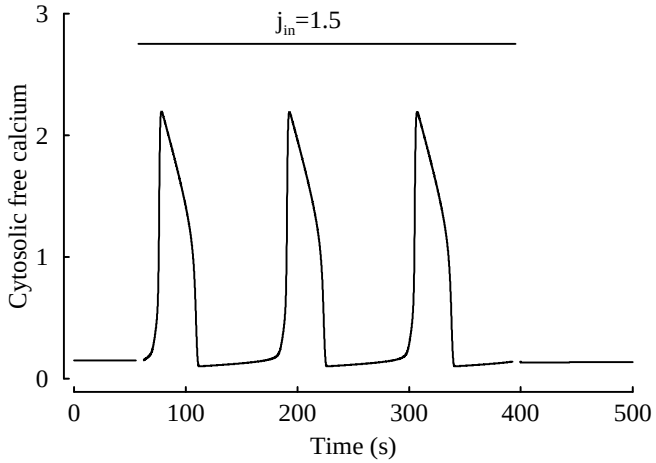

Figure 5.5 Reduced open cell Keizer-Levine model. At time = 50 seconds, oscillations are initiated by stepping j_{in} from 0 to 1.5. At time = 400 seconds, oscillations are terminated by reducing j_{in} back to 0. Parameters as in Fig. (5.4) plus: $v_{out} = 5.0$ μM s^{-1}, $K_{out} = 0.6$ μM, $j_{in} = 1.5$ μM s^{-1}. (Equivalent to KL Fig. 5. Made with *klopen_red.ode*.)

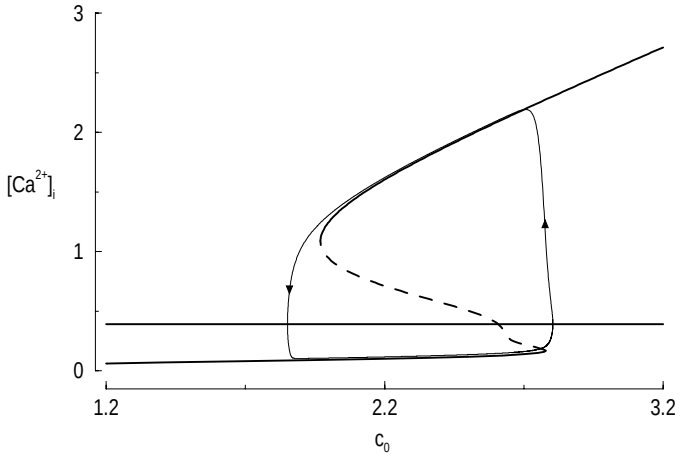

Figure 5.6 Equivalent to KL Fig. 3. Made with *klclose.ode* (S-curve) and *klopen_red.ode* (trajectory). S-curve is $[Ca^{2+}]_i$ nullcline, horizontal line is C_T nullcline. Direction of motion along trajectory indicated by arrows. Parameters as in Fig. (5.4).

5.3 The Pituitary Gonadotroph

5.3.1 Review of the biology

Our next example of a whole cell model is the coupling of electrical signaling and Ca^{2+} signaling in anterior pituitary gonadotrophs. Gonadotrophs release gonadotropins

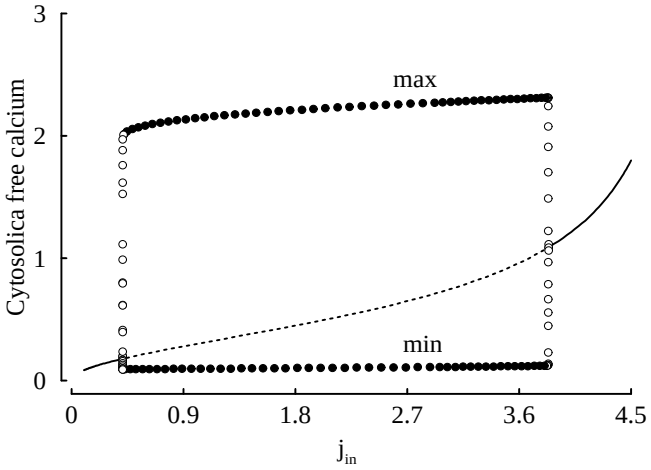

Figure 5.7 Equivalent to KL Fig. 8. Made with *klopen_red.ode*. NOTE: cytosolic misspelled

(gonad-stimulating hormones) in response to the GnRH (gonadotropin-releasing hormone) that comes from GnRH-secreting neurons in the hypothalamus. Ca^{2+} signaling is crucial for these cells to fulfill their secretory functions which are part of the complex neuro-endocrine control of reproduction in mammals. Physiological levels of GnRH have been shown to trigger large amplitude Ca^{2+} oscillations in cultured gonadotrophs. It has further been shown that these oscillatory Ca^{2+} signals are directly coupled to the exocitosis of hormone-containing vesicles in these cells (Tse et al, 1992). These Ca^{2+} signals are complicated by the ability of gonadotrophs to generate Ca^{2+} action potentials that drive Ca^{2+} from the extracellular medium into the cell in an oscillatory manner. Thus, gonadotrophs are equipped with two distinct mechanisms of generating dynamic Ca^{2+} signals, one due to voltage-gated Ca^{2+} entry (PM oscillator) and the other due to the oscillatory release of Ca^{2+} from the intracellular store (ER oscillator). This makes gonadotroph an ideal system to study complex Ca^{2+} signaling mechanisms and to apply the modular approach in developing mathematical models. Therefore, the model of Ca^{2+} signaling in gonadotrophs consists of two coupled dynamic signaling systems: ER-mediated, cytosolic Ca^{2+} oscillations and electrical activity in the plasma membrane.

5.3.2 The ER oscillator in a closed cell

As for the bullfrog, it is useful to study the gonadotroph first in the closed-cell case, when the ER oscillator is decoupled from the PM oscillator. This allows us to concentrate on the intracellular mechanisms that are independent of the influence of Ca^{2+} exchanges across the plasma membrane.

ER-mediated Ca^{2+} oscillations in gonadotrophs are linked to the activation of IP_3 receptor channels. In contrast to the caffeine-induced and Ca^{2+} oscillations in the bull-

frog sympathetic neurons, mediated by the RyR, the ER-dependent Ca^{2+} oscillations in gonadotrophs are induced by the endogenous intracellular messenger IP_3 produced when the physiological ligand GnRH binds to its receptors on the surface of the cell. Agonist-induced Ca^{2+} oscillations in a large number of cell types including gonadotrophs are generated by the dynamic interactions between IP_3 channels and SERCA pumps expressed in the membrane of the intracellular Ca^{2+} store (ER or SR). Of crucial importance is the Ca^{2+}-dependent gating properties of the IP_3 channels. As we have already discussed in previous chapters, cytosolic free Ca^{2+} can both activate and inactivate the opening of IP_3 channels. This leads to the characteristic bell-shaped Ca^{2+}-dependence of steady-state channel opening with the peak typically located at the mid submicromolar level of Ca^{2+} (see Fig. (**??**) in Chapter (**??**); ref. Iino, Bezprozvanny, Parker and Ivorra). It has also been shown that Ca^{2+}-dependent activation occurs on a faster time scale than Ca^{2+}-dependent inactivation (Finch etal, Parker and Ivorra).

The De Young-Keizer model that was discussed in Chapter (**??**) was the first model to incorporate all these experimental data. Other models based on similar data were also developed later (Atri etal, Othmer and Tang). Differences in the time scales of channel-gating are attributed to differences in the binding constants of IP_3 and Ca^{2+} to their binding sites on the IP_3 channels. This assumption, although not necessarily an accurate description of the real system, leads to a simple model that gives results that are identical to the observed ones. Whether the time scale differences are actually due to mechanisms other than the differences in the binding constants does not give a mathematically distinguishable model. Here we use a simplified version of the model due to Li and Rinzel (see Eqn. (**??**)). For a closed cell at a fixed level of IP_3, the Li-Rinzel simplification involves only two dynamic variables: C – the cytosolic Ca^{2+} and h – the fraction of channels not inactivated by Ca^{2+}. This simplified model gives as good a fit to the experimental data as the original model it was based on.

$$V_i^e \frac{dC}{dt} = \left[L + P \left(\frac{I}{I + K_i} \right)^3 \left(\frac{C}{C + K_a} \right)^3 h^3 \right] (C_{ER} - C) - \frac{V_e C^2}{C^2 + K_e^2} \tag{5.39}$$

$$\frac{dh}{dt} = A \left[K_d - (C + K_d) h \right] \tag{5.40}$$

where I is the IP_3 concentration; C_{ER} is the ER Ca^{2+} concentration; V_i^e is the effective volume of the cytosol; P is the maximum total permeability of IP_3 channels and and L is the leak permeability; V_e is the total, maximum SERCA pump rate; K_e specifies the Ca^{2+} level required for half maximal activation of the pumps; K_i, K_a, and K_d are the dissociation constants of the IP_3, Ca^{2+}-activation, and Ca^{2+}-inactivation sites respectively. As discussed earlier, it is often advantageous to replace C_{ER} by $(C_T - C)/\sigma$.

For any model, it can greatly deepen our understanding to scale the variables and parameters to achieve a dimensionless form of the equations. This process often reveals that some of the parameters do not affect the dynamical behavior independently, and they can be combined. In the present case, the number of parameters can be reduced from 10 in the original equations (including σ) to 6 in the scaled form. (Compare with

Eqns. (5.41), (5.42)). There are often multiple ways of scaling the same system. One strategy is to scale all the variables so that their magnitude is of order one, which facilitates comparison of magnitudes, and to achieve a maximum reduction in the number of independent parameters. The h variable in the equations above is already dimensionless. We can scale C by either K_a or K_d. We choose K_d since this leaves only one independent parameter in the h equation. Once we have made this choice, C_{ER}, K_a and K_e should also be scaled by K_d: $c = C/K_d$, $c_T = C_T/K_d$, $k_a = K_a/K_d$, and $k_e = K_e/K_d$. It is natural to scale the IP_3 concentration I by K_i: $i = I/K_i$. Finally, we scale time to obtain $\tau = (\frac{P}{\sigma V_i^e})t$. As a result, L, V_e, and A need to be scaled accordingly: $l = L/P$, *FIX:* $v_e = \sigma K_d P)V_e$, and $a = (\frac{\sigma V_i^e K_d}{P})A$. The final result is:

$$\frac{dc}{d\tau} = \left[l + \left(\frac{ich}{(i+1)(c+k_a)}\right)^3\right](c_T - (1+\sigma)c) - \frac{v_e c^2}{c^2 + k_e^2} \tag{5.41}$$

$$\frac{dh}{d\tau} = a[1 - (c+1)h]. \tag{5.42}$$

Agonist-induced and IP_3R-mediated Ca^{2+} oscillations in different cell types can have very different frequency, amplitude, and spiking profile. However, they all share the following features: (1) oscillations occur only at intermediate levels of IP_3 concentration; (2) the oscillation amplitude is almost constant for different levels of IP_3; (3) the oscillation frequency increases as the IP_3 level increases; (4) the oscillations can

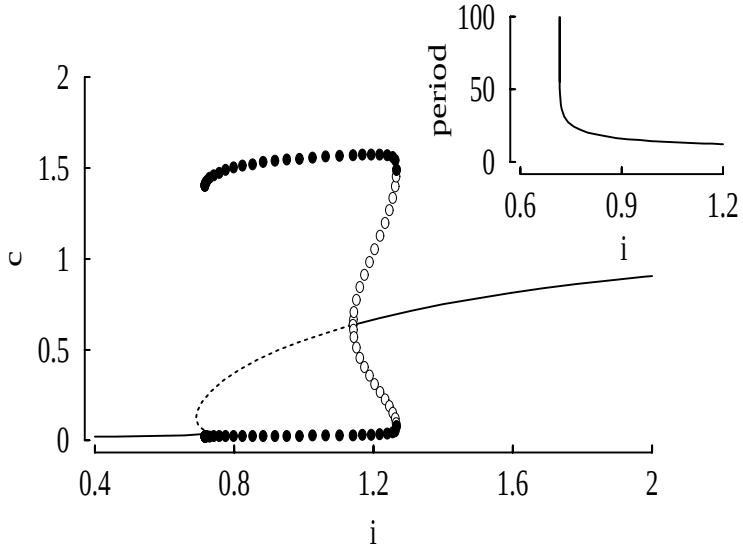

Figure 5.8 Made with *Irclose.ode*. Steady-state (curves) and periodic (circles) solutions of the closed cell model plotted against the parameter i. The amplitude remains almost unchanged within the range of i values that produce oscillations. The inset shows the oscillation period is a decreasing function of i.

occur in the absence of extracellular Ca^{2+}. Since the above model was based on key experimental data and is a general model of IP_3-triggered Ca^{2+} oscillations, it should reproduce all these common features. The feature (4) is automatically satisfied here since the model is for a closed cell that is isolated from the extracellular medium. Fig. 5.8 shows the model indeed exhibits all the other features.

This very simple model not only reproduces well established experimental observations but also predicts other possible ways Ca^{2+} oscillations can be induced. These can be easily shown by the phaseplane analysis of Eqns. (5.41-5.42). The equations for the two nullclines can be solved explicitly.

$$\text{The } c\text{-nullcline:} h = \left(1 + \frac{1}{i}\right)\left(1 + \frac{k_a}{c}\right)\left[\frac{v_e c^2}{(c^2 + k_e^2)(c_T - \sigma c)} - l\right]^{\frac{1}{3}} \tag{5.43}$$

$$\text{The } h\text{-nullcline:} h = \frac{1}{1+c} \tag{5.44}$$

The c-nullcline is "N-shaped" between the two asymptotes: one at a larger value $c = c_T/\sigma$ and another one at a smaller value $c \approx k_e\sqrt{lc_T/v_e}$ (notice that k and c_T are much larger than this value since l is very small). *Show how this gives an analytical way of determining the shape of the c-nullcline; applies to KL too.* The h-nullcline is a monotonically decreasing function of c. These two nullclines can intersect each other at either one single point or at three points depending on the choice of parameter values. Since we are interested in the conditions for the occurrence of oscillations, we only focus here on the case when the two intersect at one single point (Fig. 5.9). This point is the equilibrium or steady state solution of the system at which the rate of Ca^{2+} release from the store exactly matches the rate of Ca^{2+} uptake. Oscillations occur when this steady state becomes unstable.

Phaseplane analysis Fig. (5.9) indicates that instability of the steady state can be achieved in several possible ways. In all cases, a basal level of IP_3 is a necessary prerequisite. Notice that the h-nullcline is independent of any parameter and remains unchanged in all panels (the solid, monotonically decreasing curve). In the top panel, the c-nullcline is plotted for three different values of i. The c-nullcline moves downward as i increases (see eq.(5.43)). This is because in order to maintain balanced rates of Ca^{2+}-release and uptake more channels need to be inactivated at the same level of c at higher values of i when the channels are more permeable. Instability occurs at intermediate values of i, *i.e.* when the c-nullcline is moved downward so that it crosses the h-nullcline at locations where the slope of the latter is more negative. But the downward movement of the c-nullcline can also be achieved at fixed, basal i levels that are not themselves high enough to distablize the equilibrium. One alternative is to decrease the value of v_e (middle panel). This can be achieved experimentally by applying a drug called thapsigargin that specifically blocks the SERCA pump activity. Another alternative is to increase the leak permeability of the ER membrane (bottom panel). This can be realized by applying ionomycin, a drug that makes holes in the ER membrane. There are two other alternatives to cause instability at basal levels of i (homework problem). One is to lower the value of k_a which means increased affinity of Ca^{2+} to the activation

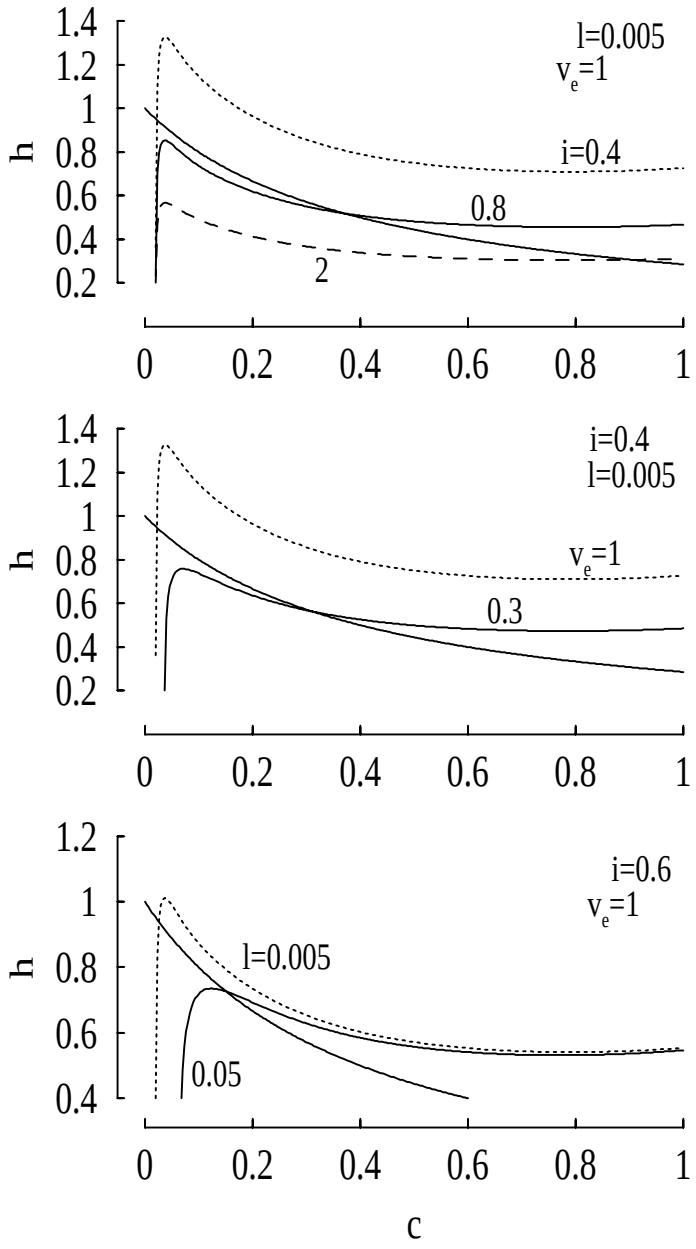

Figure 5.9 Made with *Irclose.ode*.

site. The other is to increase c_T, which is equivalent to overloading the ER store that is known experimentally to result in increased excitability of the system.

5.3.3 Open cell model with constant calcium influx

Now let us study the same model in the case when the cell is no longer closed. In an open cell, Ca^{2+} can flow into the cell from extracellular medium and vice versa. As in the bullfrog, c_T is no longer a constant – unbalanced Ca^{2+} exchange across the cell surface will change its value. Such an open cell model involves three dynamical variables: c, c_e, and h. The equations are

$$\frac{dc}{d\tau} = j_{rel}(c,h,c_T) - j_{fil}(c) + \epsilon\left[j_{in} - \frac{v_p c^2}{c^2+k_p^2}\right] \tag{5.45}$$

$$\frac{dc_e}{d\tau} = -c_1^{-1}[j_{rel}(c,h,c_T) - j_{fil}(c)] \tag{5.46}$$

$$\frac{dh}{d\tau} = a\,[1-(c+1)h] \tag{5.47}$$

where $j_{rel}(c,h,c_T) = \left[l + (\frac{ich}{(i+1)(c+k_a)})^3\right](c_T - \sigma c)$ and $j_{fil}(c) = \frac{v_e c^2}{c^2+k_e^2}$. The Ca^{2+} influx density j_{in} and maximum Ca^{2+} efflux density v_p are both multiplied by a small parameter ϵ that is proportional to the ratio of plasma membrane and ER membrane surface area (compare λ discussed in intro). *This needs to be explained more, here or earlier.* Notice that $c_T = c + c_1 c_e$. The second equation can be simplified by using the total Ca^{2+}, c_T, as the third variable.

$$\frac{dc}{d\tau} = j_{rel}(c,h,c_T) - j_{fil}(c) + \epsilon\left[j_{in} - \frac{v_p c^2}{c^2+k_p^2}\right] \tag{5.48}$$

$$\frac{dh}{d\tau} = a[1-(c+1)h] \tag{5.49}$$

$$\frac{dc_T}{d\tau} = \epsilon\left[j_{in} - \frac{v_p c^2}{c^2+k_p^2}\right] \tag{5.50}$$

The nondimensional formulation makes it clear that c_T is usually a slow variable since ϵ is usually very small.

For simplicity, we first study the case when j_{in} is a constant. This corresponds to the experimental situation in which the cells are voltage clamped (ref?). Fig. (5.10) (top two panels) shows a case in which the cell is clamped at a voltage that is not too negative, and j_{in} is large enough to sustain large amplitude Ca^{2+} oscillations and a filled store. However, when the clamping voltage is switched to a more negative value, j_{in} can become negligibly small, so that there is only Ca^{2+} extrusion but no Ca^{2+} influx at the cell surface. A similar situation can occur when the cells are placed in Ca^{2+}-defficient or zero Ca^{2+} medium. Contrary to the caffeine-induced Ca^{2+} oscillations in bullfrog sympathetic neurons (*cf.* Fig. (5.5)), the absence of Ca^{2+} influx does not kill the oscillation immediately. Instead, the amplitude gradually decreases as the store empties and stops only when the store is nearly depleted.

This phenomenon can be understood by the bifurcation analysis of the "fast subsystem" of the open cell model. Recall that c_T is a slow variable and can be treated as

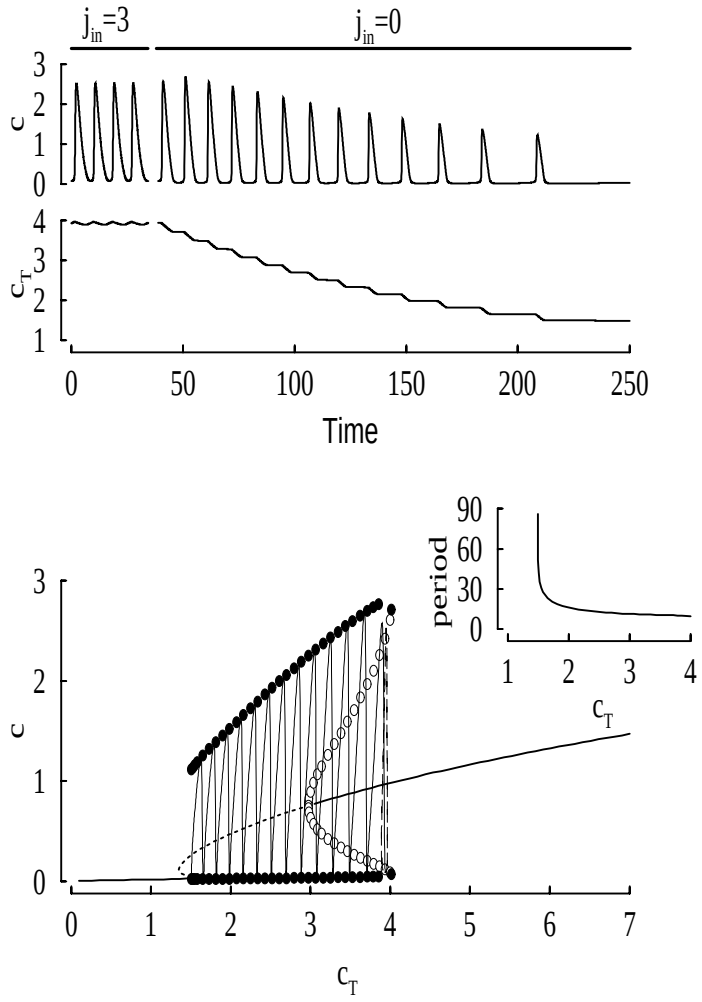

Figure 5.10 Made with *Iropen.ode*.

a parameter of the fast subsystem. Assuming that $\epsilon = 0$, this fast subsystem is identical to the closed cell model presented in the previous subsection. In Fig. 5.10 (bottom panel) is shown the bifurcation diagram of this model against c_T while holding the vlaue of i fixed. Superimposed on this bifurcation diagram is the trajectory of the full open cell model taken from the top panels.

Make this para an exercise?

Further analysis of the open cell model demonstrated (Li and Rinzel, 1994) that slow Ca^{2+} oscillations driven by Ca^{2+} influx similar to those observed in the bullfrog sympathetic neuron can also be generated by IP_3 channels. At slightly different parameter values, the fast subsystem can become bistable against c_T. In this case, oscillations

similar to those shown in Fig. 5.5 occur when j_{in} is not zero. Switching j_{in} to zero during the quiet phase will prevent the subsequent spikes from happening, thus killing the oscillation immediately. The frequency of such a slow, Ca^{2+}-influx dependent type of Ca^{2+} oscillation is closely related to the rate of Ca^{2+} influx, the larger the value of j_{in} the higher the frequency. As in the reduced open-cell version of Keizer-Levine, the time scale of Ca^{2+}-dependent channel inactivation is of no significance for such oscillations since it is much faster than that of c_T. Therefore, we can replace h by its steady state value $\frac{1}{1+c}$ in Eqn. (5.48) and eliminate the h equation:

$$\frac{dc}{d\tau} = j_{rel}(c, c_T) - j_{fil}(c) + \epsilon \left[j_{in} - \frac{v_p c^2}{c^2 + k_p^2} \right] \tag{5.51}$$

$$\frac{dc_T}{d\tau} = \epsilon \left[j_{in} - \frac{v_p c^2}{c^2 + k_p^2} \right] \tag{5.52}$$

where $j_{rel}(c, c_T) = \left[l + (\frac{ic}{(i+1)(c+k_a)(c+1)})^3 \right] (c_T - \sigma c)$.

5.3.4 The PM oscillator

The PM oscillator has been extensively studied experimentally. These studies have revealed all the major types of ion channels that are expressed in gonadotrophs as well as the detailed gating properties of these channels. The oscillations in the PM potential occur spontaneously in the absence of any hormonal signal. They are generated by several voltage-gated ion currents including L-type (noninactivating) and T-type (transient) Ca^{2+} currents, a Na^+ current which is not essential, and a delayed rectifier K^+ current. There exists another K^+ channel that is of great importance to this cell: the K(Ca) (Ca^{2+}-activated K^+) channel that is sensitive to aparmin (ref. Hille). Although the K(Ca) channels are not involved in producing the voltage spikes, they provide the key link between ER oscillator and the PM oscillator. This is because these channels are activated when cytosolic Ca^{2+} level reaches peak values, resulting in the disruption of tonic spiking in PM potential and the hyperpolarization of the cell. A realistic model of this oscillator based on experimental data can be found in Li et al, Biophys.J.,69:785-795(1995). Here, however, we use a much simpler model of the PM oscillator based on a modified Morris-Lecar model to demonstrate how the system works. All we need is a model that generates Ca^{2+} action potentials spontaneously such that each AP spike is associated with the entry of a quantum amount of Ca^{2+} into the cell. The Morris-Lecar model (see Section 2.3) is the simplest possible model of this kind, involving only an L-type Ca^{2+} current and a delayed rectifier K^+ current. The main modification involves introducing the K(Ca) current, which is absent in the original Morris-Lecar model but is crucial for gonadotrophs. The equations governing this model are

$$C_m \frac{dV}{dt} = -g_{Ca} m_\infty(V)(V - V_{Ca}) - \left[g_K n + \frac{g_{K(Ca)} C^4}{C^4 + K^4} \right] (V - V_K) \tag{5.53}$$

$$\frac{dn}{dt} = (n_\infty - n)/\tau(V) \tag{5.54}$$

where C is the Ca^{2+} level in the cytosol and is a parameter for the plasma membrane model. At low levels of Ca^{2+}, the system generates continuous spiking. When C is larger than a certain threshold value, it hyperpolarizes the membrane potential. Note that I_{app} and the leak currents are removed from the original model (Eqn. 2.17) and a K(Ca) current is introduced. Also, when the plasma membrane voltage undergoes tonic spiking, Ca^{2+} enters the cell. We take this into account in the next section.

5.3.5 Bursting driven by the ER in the full model

A full model of Ca^{2+} signaling in agonist-stimulated gonadotrophs involves both the ER oscillator and the PM oscillator. Having studied all the ingredients of this model, we now combine the modules into a complete, realistic model described by the following five differential equations:

$$C_m \frac{dV}{d\tau} = -I_{Ca} - I_K - I_{K(Ca)} \tag{5.55}$$

$$\frac{dn}{d\tau} = (n_\infty - n)/\tau(V) \tag{5.56}$$

$$\frac{dc}{d\tau} = j_{rel}(c, h, c_T) - j_{fil}(c) + \epsilon \left[-\alpha I_{Ca} - \frac{v_p c^2}{c^2 + k_p^2} \right] \tag{5.57}$$

$$\frac{dh}{d\tau} = a[1 - (c+1)h] \tag{5.58}$$

$$\frac{dc_T}{d\tau} = \epsilon \left[-\alpha I_{Ca} - \frac{v_p c^2}{c^2 + k_p^2} \right] \tag{5.59}$$

where $I_{Ca} = g_{Ca} m_\infty(V)(V - V_{Ca})$, $I_K = g_K n(V - V_K)$, $I_{K(Ca)} = g_{K(Ca)} \frac{c^4}{c^4 + k^4}(V - V_K)$, and α converts the current flux into the ion flux of Ca^{2+} (Eqn. 5.25).

The effects of the ER oscillator on the PM oscillator are determined by the $I_{K(Ca)}$ current. Whenever Ca^{2+} is high, it activates $I_{K(Ca)}$ which hyperpolarizes the PM potential and inhibits the PM oscillator. The effects of the PM oscillator on the ER oscillator are determined by the term $-\alpha I_{Ca}$ which describes the Ca^{2+} influx through voltage-gated Ca^{2+} channels. As shown in the previous section, this influx leads to fuller ER store and makes the ER more excitable. Thus, the voltage spikes activate the ER oscillator. The interaction of the two oscillators gives rise to bursting of the PM potential (Fig. 5.11). Such bursting is mainly driven by the ER oscillator that periodically hyperpolarizes the plasma membrane. However, the PM oscillations are indispensable for maintaining the bursting since the Ca^{2+} entry that accompanies each voltage spike compensates the loss of Ca^{2+} to the extracellular medium and is thus key in preventing the store from depleting (see Li etal 1997 for details of such interactions).

In the bottom panel of Fig. (5.11), the bifurcation diagram of the fast subsystem (the PM oscillator) with respect to c is plotted. Superimposed on this bifurcation di-

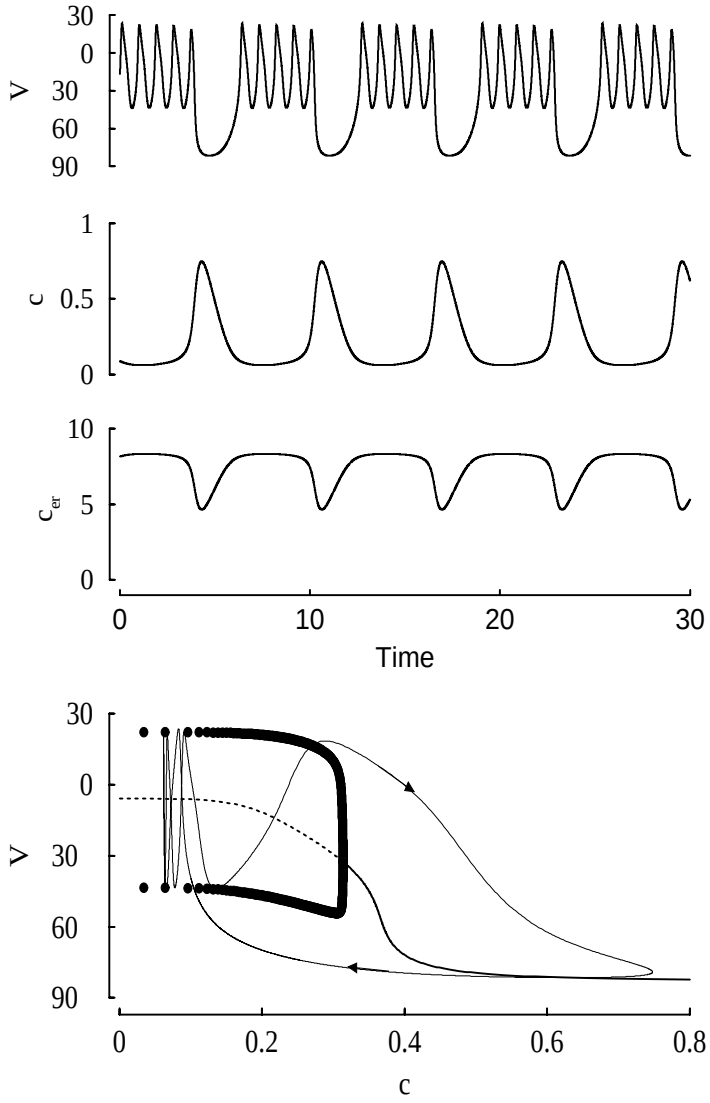

Figure 5.11 Made with *Iropen.ode*.

agram is the trajectory of the bursting shown in the top panels. Notice that the PM voltage V follows the diagram well during the spiking phase, when c changes slowly. But during the c spike, which is fast, the trajectory does not follow very closely.

5.4 The Pancreatic Beta-Cell

5.4.1 Review of the biology

The primary importance of pancreatic β-cells is that they are the cells that secrete insulin, the hormone that maintains blood plasma glucose within narrow limits in the face of variable food ingestion and metabolic activity patterns. Glucose is important as the fuel of choice for most tissues, but is subtly toxic if elevated in the blood for long periods of time. This is the hallmark of the disease diabetes, in which glucose is uncontrolled or poorly controlled, leading to blindness, kidney failure, limb amputation, cardiovascular disease and death. The causes of diabetes remain elusive, but most experts in the field agree that β-cell failure or insufficiency plays a significant role (general diabetes ref).

From a cell physiological point of view, the β-cell closely resembles the pituitary gonadotroph. Both are endocrine cells in which secretion is controlled by $[Ca^{2+}]_i$, which is in turn regulated to a large degree by bursting, and they share many mechanistic elements such as K(Ca) channels and IP_3 receptors. However, there are important and interesting differences from that point on. Bursting in β-cells is primarily driven by the plasma membrane oscillator, though the ER probably plays a significant, if still indeterminate, role in the burst mechanism. This characteristic is shared with many neurons, and β-cells provided an early paradigm for modeling of bursting. An in-depth treatment of this subject is beyond our scope, but the reader may consult (Rinzel-Ermentrout chapter in Koch and Segev; bursting chapter in Twinjim).

We will focus on membrane potential driven $[Ca^{2+}]_i$ oscillations, though β-cells have occasionally been observed to exhibit driven by the ER, similar to those in gonadotrophs. Ironically, the Keizer-DeYoung model for the IP_3 receptor was originally developed to explain this marginal phenomenon in β-cells, and was then ready to hand for application to gonadotrophs.

An important aspect of β-cell function that we will also have to neglect in this chapter is the organization of the cells into electrically coupled populations, called the islets of Langerhans. Here we take advantage of the observation that the cells in an islet are synchronized; this allows us to study a simple single-cell model, which can be taken as representative of the whole islet. More subtle effects of electrical coupling will be discussed in Chapter (8) (Chap. 8).

5.4.2 Chay-Keizer model

The model we use to illustrate β-cell bursting is based loosely on [SRK88], recast in Morris-Lecar form. Bursting occurs in response to glucose, so no applied current is needed. Morris-Lecar by itself can account for the spiking during the active phase of a burst. In order to obtain cycling between bursting and silent phases, we need to add a slow, negative feedback current. The first hypothesis, proposed by Atwater and Rojas and made into a mathematical model by Chay and Keizer (1983), was that bursting was mediated by a K(Ca) current. The idea was that $[Ca^{2+}]_i$ would build up slowly

during the spiking phase until the inhibitory effect of the increased K^+ current reached a level where spiking is terminated. The K(Ca) current is represented as

$$I_{K(Ca)} = g_{K(Ca)} \frac{[Ca^{2+}]_i}{K_d + [Ca^{2+}]_i}(V - V_K). \tag{5.60}$$

The modified Morris-Lecar equations, suplemented by a slow equation for $[Ca^{2+}]_i$, are

$$C_m \frac{dV}{dt} = -I_{Ca}(V) - I_K(V, n) - I_L(V) - I_{K(Ca)}(V, [Ca^{2+}]_i) \tag{5.61}$$

$$\frac{dn}{dt} = \frac{n_\infty(V) - n}{\tau(V)} \tag{5.62}$$

$$\frac{d[Ca^{2+}]_i}{dt} = f_i(-\alpha I_{Ca}(V) - k_c[Ca^{2+}]_i) \tag{5.63}$$

where f_i is the fraction of free $[Ca^{2+}]_i$, and $\alpha = 10^3/(2FV_i)$ converts current in fA to concentration μM/msec (*cf.* Eqn. (5.25)). $k_c[Ca^{2+}]_i$ represents a linearized form of the PMCA. Numerical results are shown in Fig. (5.12). The middle two panels demonstrate first of all that bursting can occur without participation of the ER; all that is needed is a slow negative feedback process, here supplied by $[Ca^{2+}]_i$. The sequence of panels also illustrates how β-cells sense and modify their electrical activity in response to glucose. As glucose concentration increases, the rate of the PMCA is here hypothesized to increase as well. For low glucose (low pump rate), the cell is electrically silent (top panel). For glucose above a threshold concentration, bursting appears (second panel). Further increases in glucose result in longer active spiking phases, or plateaus, and shorter silent phases (third panel). Finally, for very high glucose, the cell remains permanently in the active phase, spiking continuously. This tableau corresponds to *in vitro* experiments in which a fixed glucose can be applied. *in vivo*, the induced electrical activity and resultant Ca^{2+} influx causes insulin secretion, which in turn brings the level of plasma glucose down. This organism-level negative feedback loop has been observed in a few heroic experiments (ref).

o Explain bursting biophysically (slow negative feedback, bi-stability).

o mention Ca-Ca, J models (references)

o Explain homoclinic orbits in the phase plane.

o Explain bursting via bifurcation diagram. Paradigm for fast-slow decomposition applicable to many forms of bursting. Relate to relaxation oscillators; small τ. Mention averaging? Equivalent nullcline? (Refer to Rinzel '87 and Bertram '95 on classification of bursting.)

The ability of the first Chay-Keizer model to explain these subtle alterations in electrical activity as glucose varies was a major success, but closer observation reveals that, even though the cell is visibly more active electrically, the mean $[Ca^{2+}]_i$ does not change much. Shortly after the model came out, a new ATP-dependent K^+ channel was discovered (ref), $I_{K(ATP)}$. This current is inhibited by ATP and activated by ADP and provides a key link between glucose metabolism and membrane potential. In its

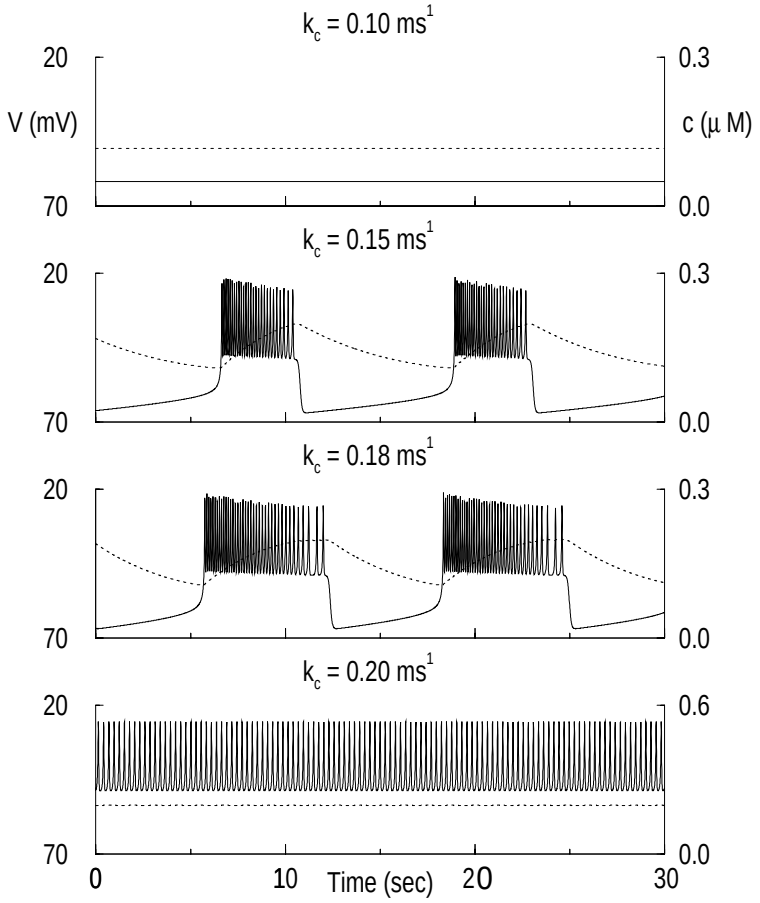

Figure 5.12 Bursting and glucose sensing of the Chay-Keizer model, Eqn. (5.61)–Eqn. (5.63). Parameters: C_m = 5300 fF, g_{Ca} = 1000 pS, V_{Ca} = 25 mV, g_K = 2700 pS, V_K = −75 mV, I_{app} = 0, V_1 = −20 mV, V_2 = 24, V_3 = −16 mV, V_4 = 11.2 mV, ϕ = 0.035 ms^{-1}, g_L = 150 pS, V_L = −75 mV, $g_{K(Ca)}$ = 2000 pS, K_d = 5 μM, f = 0.001, $\alpha = 4.5 \times 10^{-6}$ units, and k_c as indicated. Made with *mlbeta.ode*.

simplest form, $I_{K(ATP)}$ is modeled as a K^+-selective leak current,

$$I_{K(ATP)} = g_{K(ATP)}(V - V_K), \tag{5.64}$$

whose conductance decreases as glucose concentration increases. Fig. (5.14) shows the same conditions as Fig. (5.12B), but with $g_{K(ATP)}$ decreased from 150 to 135 pS, which represents a modest increase in glucose and increases plateau fraction, Further decreases in $g_{K(ATP)}$ convert the bursting to continuous spiking and sufficient increases in $g_{K(ATP)}$ suppress bursting, as in Fig. (5.12A). Thus, in all these respects $g_{K(ATP)}$ reproduces all the effects of k_c, but in addition, predicts changes in the mean $[Ca^{2+}]_i$. (exercise to explain the difference)

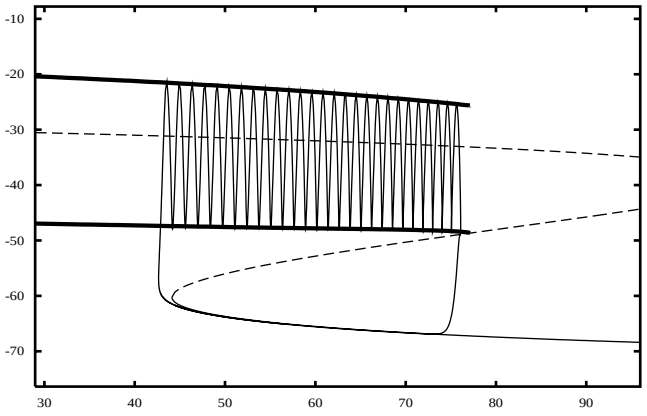

Figure 5.13 Need to add c null-cline(s). Made with *mlbeta.ode*.

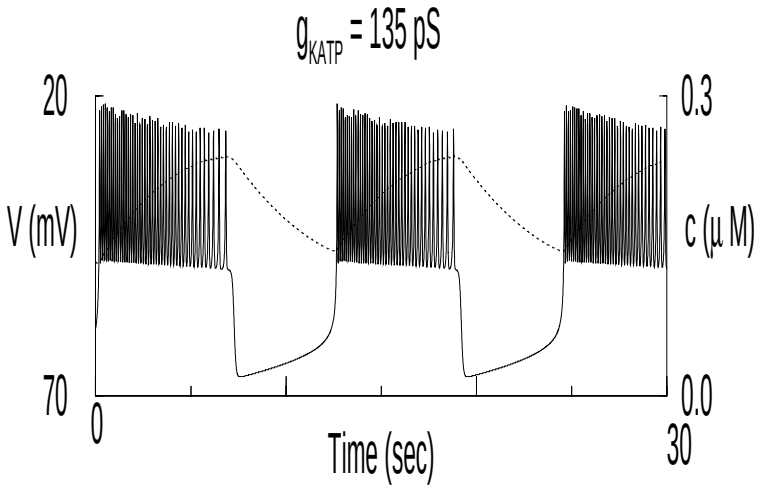

Figure 5.14 Glucose sensing of the Chay-Keizer model Eqn. (5.61)–Eqn. (5.63) modified by inclusion of $I_{K(ATP)}$ (Eqn. 5.64) in place of I_L. Parameters as in Fig. (5.12B) except: $k_c = 0.15$ ms^{-1}, $g_{K(ATP)} = 135$ pS. Made with *mlbeta.ode*.

With these distinct predictions in hand, theorists and experimentalists eagerly awaited the first recordings of $[Ca^{2+}]_i$ in bursting islets. Unexpectedly, both predictions were incorrect – $[Ca^{2+}]_i$ did not slowly rise and fall, but rather rapidly reached a plateau during the active phase (Valdeolmillos, 1989). Although $[Ca^{2+}]_i$ did fall slowly in many cases during the silent phase, this observation cast doubt on the role of $[Ca^{2+}]_i$ as a slow feedback variable and resulted in the K-Ca channel losing favor in particular. Partial resolutions of this issue are provided by the Keizer-Magnus model, and the contribution of the ER, discussed in the next two sections.

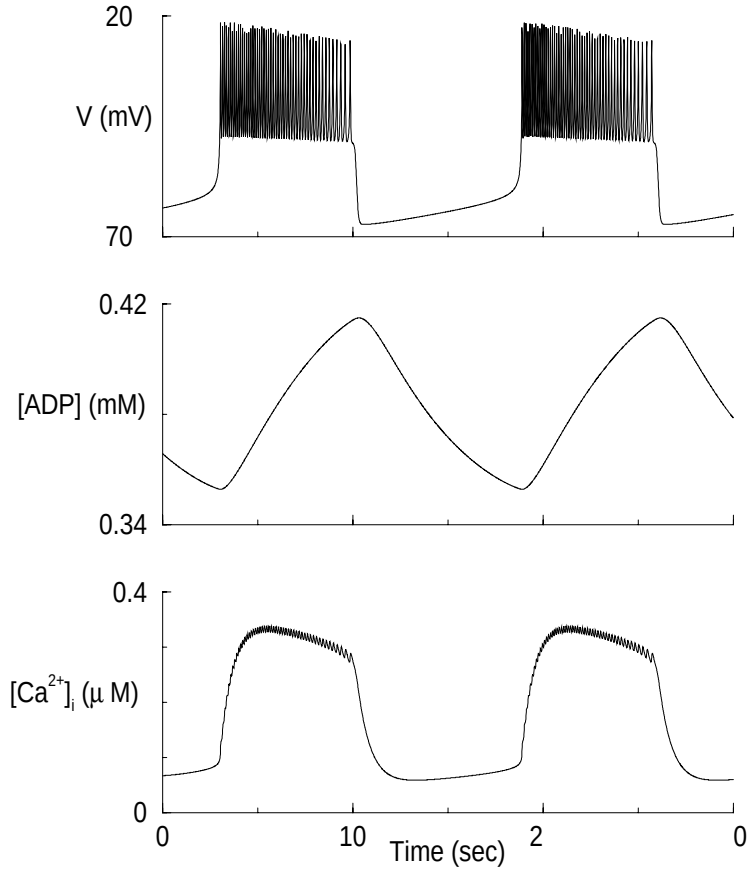

Figure 5.15 Bursting driven by oscillations of $g_{K(ATP)}$ in the Keizer-Magnus model, Eqn. (5.67)–Eqn. (5.70) together with Eqn. (5.64) – Eqn. (5.66). Parameters as in Fig. (5.12) except: $k_c = 0.15$ ms^{-1}, $g_{K(Ca)} = 0$ pS, $\bar{g}_{\mathrm{K(ATP)}} = 6000$ pS, $f_i = 0.01$, plus: $K_1 = 0.45$ mM, $K_2 = 0.012$ mM, $A_{tot} = 1.0$ mM, $R = 0.9$, $R_1 = 0.35$ mM, $k_a = 5.0 \times 10^{-5}$ ms^{-1}. Made with *km.ode*.

5.4.3 Keizer-Magnus model

Keizer and Magnus (1989) proposed that $g_{K(ATP)}$ played not simply a modulatory role in bursting, but could itself provide slow negative feedback. The central point of their hypothesis was that a rise in $[Ca^{2+}]_i$ would lead to mitochondrial uptake of Ca^{2+} and dissipate the mitochondrial membrane potential that provides the energy for ATP synthesis. (Review basic facts: electron transport chain pumps out protons; flux of protons back into the mitochondria through the ATP synthase molecule and generates ATP from ADP.) Thus, as $[Ca^{2+}]_i$ rises, ATP falls and ADP rises. The closure of the K(ATP) channel by ATP is antagonized by ADP, so the rise in $[Ca^{2+}]_i$ will result in an increase in $g_{K(ATP)}$. Keizer and Magnus derived the following expression for $g_{K(ATP)}$ based on the assumption (now thought to be incorrect, but see exercise) that ATP and

ADP compete for the same binding site:

$$g_{K(ATP)} = \bar{g}_{\mathrm{K(ATP)}} \frac{1 + [ADP]/K_1}{1 + [ADP]/K_1 + [ATP]/K_2}. \tag{5.65}$$

If one assumes further that

$$[ADP] + [ATP] = A_{tot} \tag{5.66}$$

where A_{tot} is constant, just one more expression is needed for the dependence of $[ADP]$ on $[\mathrm{Ca}^{2+}]_\mathrm{i}$ to complete the negative feedback loop. Adding a simple phenomenological equation for the mitochondrial dynamics to Chay-Keizer (modified by inclusion of $I_{K(ATP)}$) yields the following system of four differential equations:

$$C_m \frac{dV}{dt} = -I_{Ca} - I_K - I_{K(ATP)} - I_{K(Ca)} \tag{5.67}$$

$$\frac{dn}{dt} = \frac{n_\infty(V) - n}{\tau(V)} \tag{5.68}$$

$$\frac{d[\mathrm{Ca}^{2+}]_\mathrm{i}}{dt} = f_i(-\alpha I_{Ca}(V) - k_c[\mathrm{Ca}^{2+}]_\mathrm{i}) \tag{5.69}$$

$$\frac{d[ADP]}{dt} = k_{mito}\left([ATP] - [ADP]\exp\left(R\left(1 - \frac{[\mathrm{Ca}^{2+}]_\mathrm{i}}{R_1}\right)\right)\right). \tag{5.70}$$

Negative feedback proceeds from V through $[\mathrm{Ca}^{2+}]_\mathrm{i}$ and $[ADP]$ to $g_{K(ATP)}$. Thus, provided that k_{mito} is sufficiently small, $[\mathrm{Ca}^{2+}]_\mathrm{i}$ can provide indirect negative feedback onto $g_{K(ATP)}$ without itself being slow. Eqn. (5.15) shows bursting in which $[\mathrm{Ca}^{2+}]_\mathrm{i}$ rises rapidly at the beginning of the active phase of a burst, in agreement with experiment, though in this simple model, it must then also fall rapidly at the end of the active phase, which does not agree with the data. One way to achieve the required asymmetry is to bring in the ER (next section). Nonetheless, the model represents an advance in that the higher value of $f_i = 0.01$ used is more in line with experiment.

The glucose sensing is also improved in the sense that it has been moved one step closer to metabolism. A rise in the parameter R increases the rate of $[ATP]$ production, that is, mitochondrial $[ATP]$ production is more resistant to a rise in $[\mathrm{Ca}^{2+}]_\mathrm{i}$, so this corresponds to a rise in glucose concentration. See Magnus, AJP for a more detailed model of the mitochondria, including predictions for the dynamics of mitochondrial Ca^{2+}.

5.4.4 Muscarinic potentiation and other roles of the ER

Another physiological stimulus for insulin secretion is acetylcholine (ACh), secreted from vagal nerves originating in the hypothalamus and terminating in the pancreas. Although glucose alone is capable of stimulating secretion, and ACh is ineffective in the absence of glucose, it can be argued that ACh is the more relevant signal under normal conditions. The brain (and the gut, through other hormones) communicate to the islets that food is on the way and to start secreting insulin in advance without

waiting for plasma glucose to rise. If the system is functioning properly, glucose does not rise much at all.

At the cellular level, ACh works by binding to muscarinic (M3) ACh receptors, initiating production of IP_3 and dumping the stores, similar to GnRH in gonadotrophs. Thus, in order to include muscarinic effects on islets, we must include the ER. We will find that the ER can also have a profound effect on the kinetics of $[Ca^{2+}]_i$ oscillations and bursting through feedback onto $g_{K(Ca)}$. The simplest way to illustrate these points is to append an equation to the Chay-Keizer model:

$$C_m \frac{dV}{dt} = -I_{Ca} - I_K - I_{K(ATP)} - I_{K(Ca)} \tag{5.71}$$

$$\frac{dn}{dt} = \frac{n_\infty(V) - n}{\tau(V)} \tag{5.72}$$

$$\begin{aligned}\frac{d[Ca^{2+}]_i}{dt} &= f_i(-\alpha I_{Ca}(V) - k_c[Ca^{2+}]_i) \\ &\quad + \frac{f_i}{\lambda}\left(P([Ca^{2+}]_{ER} - [Ca^{2+}]_i) - k_{SERCA}\,[Ca^{2+}]_i\right)\end{aligned} \tag{5.73}$$

$$\frac{d[Ca^{2+}]_{ER}}{dt} = \frac{f_i}{\sigma\lambda}(-P([Ca^{2+}]_{ER} - [Ca^{2+}]_i) + k_{SERCA}\,[Ca^{2+}]_i) \tag{5.74}$$

This model is essentially equivalent to Theresa Chay's last β-cell model (BJ '97). For simplicity, negative Ca^{2+} feedback through the mitochondria onto $g_{K(ATP)}$ is omitted, but can be incorporated as well as or in place of $g_{K(Ca)}$ (Exercise).

Fig. (5.16) shows this model with parameters chosen to highlight the possible role of the ER in bursting. f_i is 0.01, as in the Keizer-Magnus example, which means that in the absence of the ER only very fast bursting can occur. Thus, bursting with periods of 10 – 60 seconds, as typically observed in islets, depends on slow kinetics supplied by the ER. Note that $[Ca^{2+}]_{ER}$ rises and falls slowly the way $[Ca^{2+}]_i$ does in the original Chay-Keizer model. In contrast, $[Ca^{2+}]_i$ shows two distinct time scales, fast jumps at the beginning and end of a burst, and a slow tail during the silent phase. The fast jumps reflect the intrinsic kinetics of $[Ca^{2+}]_i$, while the slow tail reflects the slow release by the ER of Ca^{2+} taken up during the active phase. The relative prominence of the fast and slow components of $[Ca^{2+}]_i$ is controlled by λ, while the burst period depends strongly on the effective ER volume, σ (Exercise 16). This result demonstrates that it is possible for negative feedback to operate through the K(Ca) channel, or some other Ca^{2+}-sensitive channel, even though $[Ca^{2+}]_i$ does not itself appear to be slow.

This section could be shortened by combining Fig. (5.16) and Fig. (5.17), adding just one panel at the end of the first showing fast v with elevated P. In words, same if $k_{SERCA} = 0$ or $\lambda_{ER} \to \infty$ (no ER).

The role of the ER in β-cell electrical activity is controversial and not yet fully understood, but the simple model of Fig. (5.16) is adequate to shed light on several key experimental observations. It is consistent with experiments showing that the slow tail is abolished by thapsigargin (Henquin). It also offers a possible explanation for some of the effects of ACh, which dramatically increases burst frequency, raises $[Ca^{2+}]_i$,

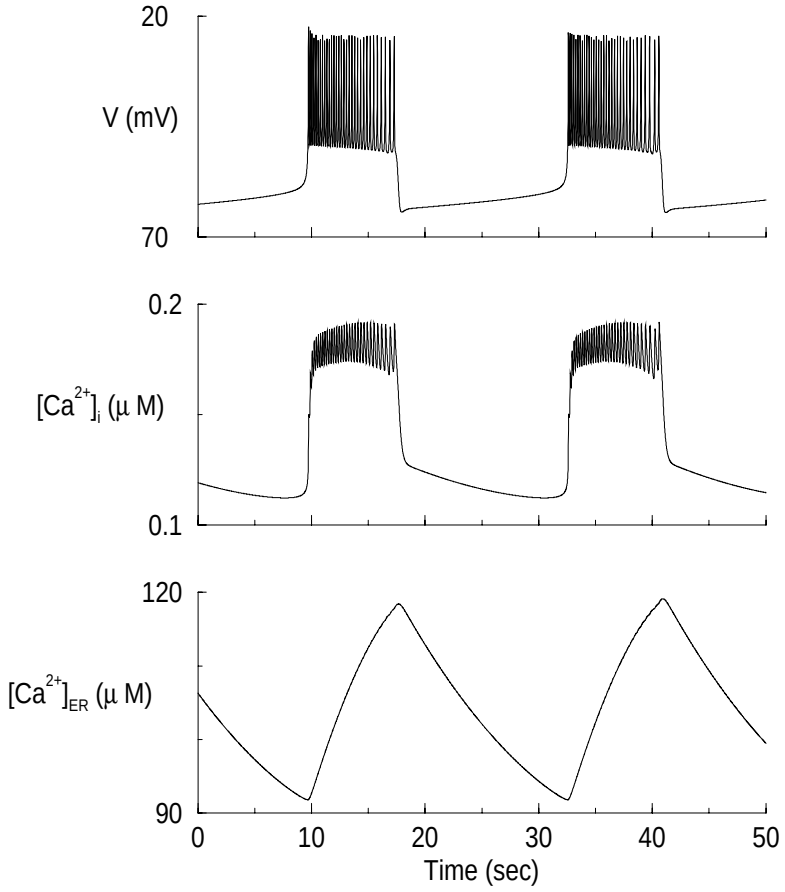

Figure 5.16 ER-dependent bursting in augmented Chay-Keizer model, Eqn. (5.71)–Eqn. (5.74). Parameters as in Fig. (5.14) except: $g_{K(ATP)} = 150$ pS, $f_i = 0.01$, plus: $P = 0.0008$ ms^{-1}, $\lambda = 2$, $\sigma = 0.032$, $k_{SERCA} = 0.6$ ms^{-1}. Made with *cker.ode*.

and enhances insulin secretion. In Fig. (5.17), top two panels, the effects of a step increase of IP_3 are modeled as a 100-fold increase in ER efflux permeability, P. After a brief transient hyperpolarization caused by a spike of released Ca^{2+}, burst frequency increases. $[Ca^{2+}]_{ER}$ (not shown) drops rapidly to near 0. However, there is no gross depolarization or rise in mean $[Ca^{2+}]_i$. The latter effects can be obtained by further assuming that ACh activates an additional inward current Fig. (5.17), bottom two panels. That current is modeled here as a store-operated current (SOC), possibly related to the calcium release activated current (I_{CRAC}) seen in non-excitable cells:

$$I_{CRAC} = g_{CRAC}(V - V_{CRAC}) \tag{5.75}$$

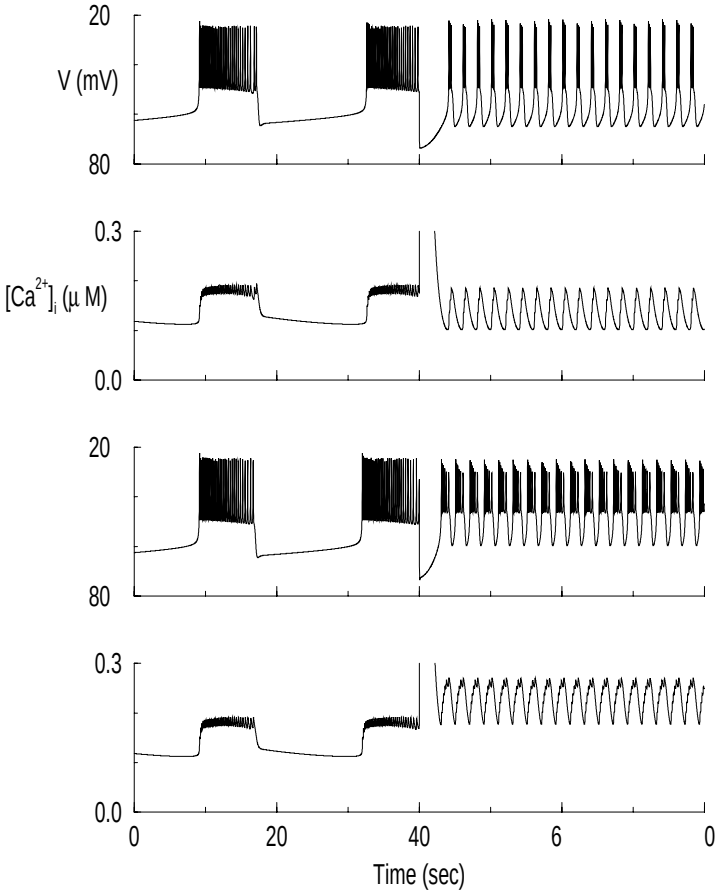

Figure 5.17 Rough model of muscarinic bursting using the Chay-Keizer model augmented with an ER, Eqn. (5.71)–Eqn. (5.74). Parameters as in Fig. (5.16), but at $t = 40$ seconds, P is stepped from 0.0008 ms^{-1} to 0.08 ms^{-1}. In the bottom two panels, in addition I_{CRAC}, with $g_{CRAC} = 20$ pS and $V_{CRAC} = -30$ mV, rapidly turns on at $t = 40$ as $[Ca^{2+}]_{ER}$ drops (not shown). $[Ca^{2+}]_i$ spike is cut-off. Made with *cker.ode*.

where g_{CRAC} increases as $[Ca^{2+}]_{ER}$ decreases. An alternative is that ACh activates an inward current directly, possibly by stimulating production diacyl glycerol (DAG), rather than indirectly, by dumping the stores.

The examples discussed here represent only the tip of the iceberg of the β-cell field. The precise contributions of the mechanisms we have treated, K(Ca) channels, $g_{K(ATP)}$ channels, and the ER, are not settled, but it seems likely that complex interactions of all three will be necessary to explain the diverse phenomena observed. The mechanisms of other important regulators of cell electrical activity and $[Ca^{2+}]_i$, such as cAMP and epinephrine remain to be elucidated. Nonetheless, the basic mechanisms and concepts presented here should fortify the reader sufficiently to profitably explore the exercises below and the literature on his or her own.

5.5 Chapter Summary

Briefly restate common themes; point to literature, further reading.

5.6 Exercises

1. Generalize Eqn. (5.13) to the case of two or arbitrarily many buffers.
2. The expression for ER leak Eqn. (5.24) can be derived from a symmetric cycle model (Fig. 5.18) representing a pore that can exist in either an unbound state (1) or a bound state (2) and bind Ca^{2+} on either the ER or the cytosolic side. A cycle from 1 to 2, binding Ca^{2+} on the ER side, and back to 1, releasing Ca^{2+} on the cytosolic side transports 1 ion from the ER to the cytosol. Assume symmetry, that is, the rates of binding $[Ca^{2+}]_i$ and $[Ca^{2+}]_{ER}$ are equal, $k_{12}^{a*} = k_{12}^{b*} = k_{12}^{*}$ and the rates of releasing $[Ca^{2+}]_i$ and $[Ca^{2+}]_{ER}$ are equal, $k_{21}^{a} = k_{21}^{b} = k_{21}$, and use the diagrammatic method of Chapter (3) to show that
$$J^{ss} = J_{21}^{ss_b} = \frac{k_{12}^{*}}{2}([Ca^{2+}]_{ER} - [Ca^{2+}]_i) \tag{5.76}$$
in an appropriate limit. ($[Ca^{2+}]_{ER} - [Ca^{2+}]_i$ is called the thermodynamic driving force.)
3. (From HW # 4, Ex. 3). (a) Write down the mass action equations corresponding to the Keizer-Levine kinetic diagram in Fig. (5.2) and calculate the steady-state fraction of open channels (those in states O_1 or O_2) as a function of Ca^{2+}. Compare to the plateau curve in Fig. (5.3). (b) Approximate the peak open fraction following a step of Ca^{2+} from rest by assuming the C_2 does not change over short times. Compare to the peak curve in Fig. (5.3). (c) Derive the quasi-steady-state approximation Eqn. (5.26)–Eqn. (5.30). Hint: Combine the result in (b) with a differential equation for $w = 1 - P_{C_2}$ assuming transitions among O_1, O_2, and C_1 are in rapid equilibrium. Simulate the two-pulse experiment of Fig. (5.3) and verify that the quasi-steady-state approximation retains the feature of adaptation. (d)

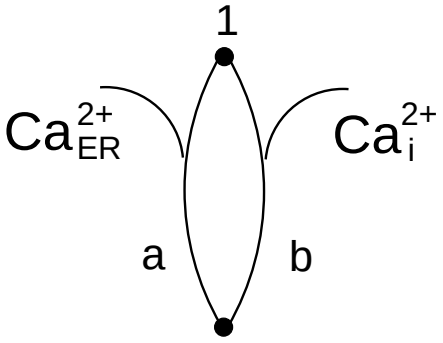

Figure 5.18 Kinetic diagram for ER leak

Draw the reduced diagram. What are the expressions for the reduced rate constants? (e) Compare the K-L model to other RyR models in the literature, such as Tang-Othmer (others?).

4. (Replaces HW # 5, Ex. 1 – K-L: closed cell.) (a) By calculating the jacobian of the closed-cell Keizer-Levine model, show that for oscillations to arise via a Hopf bifurcation, it is necessary for the w and c nullclines to intersect with negative slope and with the w nullcline steeper. (b) Using the result of (a), find parameter values for which there are oscillations. by graphing the nullclines (this can be done analytically by solving the w and $[Ca^{2+}]_i$ equations in terms of w or by using the Nullcline function within *Xpp*). (Hint: One way is to play with the affinity of the SERCA pump.) (c) Use *XppAut*to construct the bifurcation diagram for the modified system and plot the period vs. C_T. Correlate changes in the period with changes in the phase plane, particularly the invariant sets of the saddle point. (d) Find the s-curve analytically by isolating C_T.
5. Using *XppAut* plot period vs. j_{in} for the reduced open cell model. Compare the range of j_{in} for which there are oscillations predicted by the phase plane to those calculated in the bifurcation diagram. Using the phase plane in Fig. (5.6), explain the variation in period. Compare with β-cell; compare with gonadotroph (frequency-dependent specificity – get correct jargon. Refer to Tsien; Lewis Nature papers?)
6. (replaces HW # 5, Ex. 2, K-L: 3 var open cell) (a) Solve the open cell system and find values of j_{in} that support oscillations. Compare the extent of store dumping with the closed cell oscillations (Exercise 4). Plot the fluxes across the plasma membrane and ER through the cycle. (b) Investigate the effect of increasing k_c^- and explain what this implies about the reduced open cell model with $w = w_\infty([Ca^{2+}]_i)$. (c) Construct the bifurcation diagram with j_{in} as a parameter and compare to Fig. (5.7).
7. Objections were raised to the experiments of Györke and Fill (Sci. 263:986, 1994), arguing that adaptation was an artifact of a Ca^{2+} spike when Ca^{2+} is uncaged. Make a model of this situation incorporating the kinetics of Ca^{2+} binding to DM-nitrophen and form your own opinion of this controversy. To what extent does the Keizer-Levine model of BFSG oscillations depend on adaptation.
8. Compare the reduced open-cell model to the Friel-Tsien model (BJ '95) in terms of bifurcation structure and biophysical elements. Try to replace j_{RyR} in Keizer-Levine with the simple Hill function representation of Friel and Tsien.
9. Gntroph with Ca-dependent beta (fraction of free calcium) (Wagner-Keizer '94): More careful treatment of buffering only changes the picture quantitatively.
10. Show that with $h = h_\infty([Ca^{2+}]_i)$ you can get slow oscillations in the open-cell gonadotroph model paced by IICR, not IP3R inactivation; See PNAS '94 Fig.2 or Fig. 5, bottom trace. These are roughly equivalent to Keizer-Levine reduced open cell.
11. Modify bell-shaped curve as in PNAS '94 Fig. 1. Use to get PNAS '94 Fig. 2 (hard).
12. Gntroph: long-term emptying-refilling story (BJ97, TEM96 review article).

13. Play with homoclinics: Draw bifurcation diagram; grab points just before and after homoclinic; study the v-w phase planes, especially the invariant sets. Will need a separate file for the fast subsystem. Compare Utah book, Fig. 4.
14. To get bursts with a period approximating those seen experimentally, we had to set $f = 0.001$. Experimental values are in the range $0.01 - 0.05$. What is the burst period with such values? What can you change to increase the burst period (Hint: One way is to increase the range of $[Ca^{2+}]_i$ values.)
15. Set $f = 0.01$ in CK; derive Eqn. (5.65); compare to Magnus and Keizer I, AJP, and Hopkins et al, and substitute theirs. What happens in KM if gkca is not 0? (get mixed fast and slow). Study effects of R: mean $[Ca^{2+}]_i$ rises with no change in silent or active phase $[Ca^{2+}]_i$. Make a model in which a rise in $[Ca^{2+}]_i$ increases $[ATP]$ consumption, instead of hindering $[ATP]$ production (Henquin) Gall-Susa/Chay as another example of how ER can slow bursts even with larger values of f.
16. Study the effects of σ, P, λ, and k_{SERCA} in the Chay-Keizer model with ER. Explain the effects of these four parameters by examining two bifurcation diagrams, one with respect to $[Ca^{2+}]_i$ as the bifurcation parameter, with $[Ca^{2+}]_{ER}$ also a parameter, and one with respect to $[Ca^{2+}]_{ER}$ as the bifurcation parameter and treating $[Ca^{2+}]_i$ as a fast variable. Explain how $[Ca^{2+}]_{ER}$ can act as a slow variable even though it does not appear in the V equation.
17. In an alternative model for muscarinic bursting in β-cells, the ER does not actively participate in bursting but switches the cell from a slow burst mechanism to a fast one. Bertram *et al.* (1995). This scenario can be demonstrated with the Keizer-Magnus model making the following changes:
18. Something that leads on to the phantom?
19. Two-parameter study of effects of *phi*. Compare to Bertram *et al.*, 1995 (Classification).
20. β-cell-like bursting can be obtained by slow inactivation of an inward current rather than slow activation of an outward current. Add a slow inactivation factor to I_{Ca} and adjust other parameters as needed to obtain bursting. What parameter(s) can be used as glucose sensors (that is, can raise plateau fraction while preserving approximate spike amplitude invariance)?
21. An unusual burst model has spiking that stems from excitable, not oscillatory, fast dynamics [**?**]. Analyze its slow phase plane dynamics using the method of averaged nullclines [**?**, **?**].
22. Classify the burst mechanism in Sherman *et al.*, 1990 (Ca-Ca model) (Equations can also be found under "Non-Planar Fast Subsystem" on the Web page for this chapter).
23. Explore the behavior of the extended model with ER when I_{CRAC} is included, but not ikca and vice versa.
24. Find parameters to make the ER equations oscillate, and try to replicate Keizer and DeYoung's [**?**] agonist-induced bursting.

CHAPTER 6

Spatial Models

John Wagner and Joel Keizer

07-28

moving species directed movement undirected movement what is diffusion ?

6.1 Formulation

6.1.1 Conservation law in one dimension

Many equations in biology are derived using conservation laws. A conservation law is simply a mathematical statement that some quantity is balanced throughout a process.

Consider a chemical species C whose concentration $c(x,t)$ varies in both time and space, where the spatial variation is restricted to only one spatial direction x. This situation is shown in Fig. (**??**), where C is contained in an infinitely long, thin tube, and the concentration is assumed to be constant in any cross-sectional slice. Then in any arbitrary interval $x_a < x < x_b$, a conservation law can be written:

$$\begin{aligned}&\text{time rate of change of the total amount of C} = \\ &\quad \text{net rate that C flows in} + \text{rate that C is produced}\end{aligned} \tag{6.1}$$

At any time t, the total amount of C in the interval can be computed by integrating $c(x,t)$ over the interval:

$$\text{total amount of C} = \int_{x_a}^{x_b} c(x,t)\, A\, dx. \tag{6.2}$$

It is important to distinguish between the units of c (concentration, or amount/unit volume) and the units of "total amount". Thus, if c has units of micromolar (micromol/liter), then the total amount has units of micromoles.

Now suppose that C is free to randomly move about inside the tube, so that C moves in and out of the interval by passing through the slices at $x = x_a$ and $x = x_b$. If for any time t we denote by $J(x,t)$ the rate at which C moves across a slice at x from left to right, then the net movement, or flux, of C into the interval is

$$\text{net rate of entry of C} = AJ(x_a,t) - AJ(x_b,t), \tag{6.3}$$

where A is the area of the cross-sectional slice. Again, the units are important. Since the net rate of entry has units of amount/unit time, and A has units of area, the flux rate $J(x,t)$ has units of amount/unit area/unit time. It is also important to remember that $J(x,t)$ is positive when the motion is to the right, and negative when the motion is to the left. This leads to the sign convention in the flux equation: when $J(x_a,t)$ is positive, C exters the interval, and when $J(x_b,t)$ is negative, C leaves the interval.

The total amount of C in the interval can also change due to the production of C within the interval. Let $f(x,t,c)$ denote the rate of production of C at the location x and time t. Then the total amount of C produced in the interval at time t is given by

$$\text{net rate of production of C} = \int_{x_a}^{x_b} f(x,t,c(x,t))\, A\, dx \tag{6.4}$$

Note that the presence of c in the definition of f allows for the possibility that the rate of production of C depends on c itself. Since the units of the net rate of production of C are amount/unit time, the units of f must be amount/unit time/unit volume. When f is positive, it is called a source (because it leads to an increase in the total amount of C), and when f is negative, it is called a sink. Thus, f is often called a source function.

The conservation equation can now be rewritten mathematically:

$$\frac{d}{dt}\int_a^b c(x,t)\, dx = J(x_a,t) - J(x_b,t) + \int_{x_a}^{x_b} f(x,t,c(x,t))\, dx \tag{6.5}$$

where the constant A has been cancelled. The flux terms can be replaced by noting that

$$J(x_b,t) - J(x_a,t) = \int_{x_a}^{x_b} J_x(x,t)\, dx, \tag{6.6}$$

allowing all the terms in Eqn. (6.5) to be written as integrals:

$$\frac{d}{dt}\int_{x_a}^{x_b} c(x,t)\, dx = \int_{x_a}^{x_b} J(x,t)\, dx + \int_{x_a}^{x_b} f(x,t,c(x,t))\, dx. \tag{6.7}$$

If the solution is smooth enough, then the differentiation and integration can be interchanged, and Eqn. (6.5) can be rewritten as

$$\int_{x_a}^{x_b} \left[c_t(x,t)\,dx - J_x(x,t) - f(x,t,c(x,t))\right]\,dx = 0. \tag{6.8}$$

Since the interval was arbitrary, the only way this equality can hold is if the integrand is zero. Therefore, we can replace Eqn. (6.8) by the equivalent conservation law in differential form,

$$c_t + J_x = f(x,t,c). \tag{6.9}$$

Note that, in this equation there are two independent variables (x and t), and that the equation contains partial derivatives with respect to both. Such equations are called partial differential equations, and, since time is one of the independent variables, we call Eqn. (6.9) an evolution equation.

In our derivation of Eqn. (6.9), both the time t and the interval $x_a < x < x_b$ were arbitrary. As a result, Eqn. (6.9) holds for all t, and for all x in the tube. That is, the spacetime domain, or the domain of definition, on which Eqn. (6.9) is defined is R^2. However, this choice was merely a matter of convenience, as the derivation did not depend on the actual length of the tube, or the actual time; thus, it is reasonable to expect Eqn. (6.9) to hold for arbitrary domains.

6.1.2 Fick's Law of Diffusion

Eqn. (6.9) is a single equation relating two unknowns–the concentration c and the flux J–and is therefore underdetermined. In order to resolve this problem, an additional equation relating c and J is needed. Such an equation is called a constitutive relation, or an equation of state, and in contrast to conservation laws, is generally derived empirically or determined experimentally.

One such constitutive relation is Fick's law, which states that C moves from regions of high concentration to regions of low concentration, with a rate proportional to the concentration gradient. More precisely,

$$J(x,t) = -Dc_x(x,t), \tag{6.10}$$

where the proportionality constant D is called the diffusion constant, and the negative sign ensures that C moves down the concentration gradient. It is important to note that the units of D are length^2/unit time, and that these units do not change even if c is allowed to vary in more than one spatial direction. Point out that the value of D depends on the medium in which C is diffusing, as well as the size, weight, etc.

Using Fick's law, Eqn. (6.9) can be rewritten as a reaction–diffusion equation,

$$c_t - Dc_{xx} = f(x,t,c). \tag{6.11}$$

In this equation, Dc_{xx} is called the diffusion term, and f is called the reaction term. When f is zero, that is, when there are no sources or sinks, Eqn. (6.11) becomes the

diffusion equation,

$$c_t - Dc_{xx} = 0. \tag{6.12}$$

This equation is also called the heat equation because of its utility in modeling the flow of heat.

6.1.3 Advection

Now imagine that besides the random motion of C, there exists in the medium a macroscopic flow with speed v along the x-axis. Then, during a small time Δt, all of the C between $x = x_a$ and $x = x_a - v\Delta t$ would enter the interval by flowing through the slice at $x = x_a$. The total amount of C entering during this time can be found by multiplying the concentration, $c(x,t)$, by the corresponding volume, $Av\Delta t$. The corresponding flux rate is, therefore,

$$J(x,t) = vc(x,t), \tag{6.13}$$

and is often called the drift, or convective, flux. Note that whereas the diffusive flux was proportional to the concentration gradient, the convective flux is proportional to the concentration itself.

If the random and biased directional motions co-exist, the total flux is just the linear superposition of the diffusive and drift fluxes:

$$J(x,t) = vc(x,t) - Dc_x(x,t). \tag{6.14}$$

Using this constitutive relation, Eqn. (6.9) becomes a reaction–advection–diffusion equation,

$$c_t + vc_x(x,t) - Dc_{xx} = f(x,t,c). \tag{6.15}$$

6.1.4 Boundary and Initial Conditions

As we saw in Chapter (1), a differential equation typically generates a family of solutions, not just one. We must use additional constraints–initial conditions and boundary conditions–to pick out the one which solves the problem of interest. Here we discuss how these additional constraints influence the solutions of partial differential equations.

The general solution of a partial differential equation is a family of solutions depending on one or more arbitrary functions, analogous to the general solution of an ODE, which is a family of solutions depending on one or more arbitrary constants. Often, however, we are not interested in the family of solutions, but in selecting one particular solution. In the case of ODEs, this was accomplished for initial value problems by specifying one or more initial conditions, and for boundary value problems by specifying one or more boundary conditions. A similar approach can be taken with the transport equations, the only difference being that, because the equations contain both space and time, both initial and boundary conditions must be specified.

EXERCISES: finite domain, infinite domain, semi-infinite domain, what do you do about boundary conditions?

Because evolution equations define how a system evolves in time, an initial condition is needed to define the state of the system at the starting time. This requires the choice of a starting time, which, roughly speaking, is chosen to be some time that precedes the phenomenon of interest, and at which the state of the system is either known, or can be approximated. Thus, the choice of the starting time and the initial condition are intimately linked. Often, both follow directly from experiment: the start of the experiment corresponds to the starting time of the model. It is also often the case that the initial condition is specified when the system is at equilibrium. Another important aspect of the initial condition is that of equilibrium. In systems of partial differential equations, it is often necessary to ensure that all of the initial variable states are at some sort of equilibrium; this is expecially true if the biological system being modeled is assumed to be at equilibrium at the outset.

When the spatial domain is finite, boundary conditions must be specified at all boundaries. For example, if the spatial domain is $x_a < x < x_b$, we require boundary conditions at both $x = x_a$ and $x = x_b$. Boundary conditions can take one of three forms. The Neumann boundary condition constrains the solution to take on a specific functional form, that is, $c(x_a, t) = f(t)$. The Dirichlet boundary condition constrains the solution's spatial derivative to take on a specific functional form, that is, $c_x(x_a, t) = g(t)$. If g is zero, this boundary condition is often called a "no flux" boundary condition. Finally, the Robin boundary condition combines both the Neumann and the Dirichlet boundary conditions, taking the form $c(x_a, t) + \alpha(t)c_x(x_a, t) = h(t)$, where $\alpha(t)$ is a given function of t.

Boundary conditions are necessary even when the spatial domain is not finite. However, infinite domains present the minor inconvenience that there is no specific (finite) location at which to specify the boundary condition. In such cases, the solution is required to exhibit some specific behavior at large distances. For example, we may specify that the solution tend to zero as x tends to infinity. In practice, it is often convenient instead to use a large but finite domain, and to then specify Dirichlet or Neumann conditions at the boundaries. In this case, the boundaries must be far enough away that they do not affect the solution. However, this approach requires *a priori* knowledge of the exact behavior of the solution at large distances.

6.2 Diffusion in One Dimension

6.2.1 Diffusion in a Long Dendrite

As a first example, we consider the time course of calcium undergoing simple diffusion in a very long dendrite. Suppose that at some point x_0 we photorelease caged calcium in a very small region around x_0. If we denote by $c(x, t)$ the concentration of calcium

along the length of the dendrite at each time t, the the model is as follows:

$$c_t = Dc_{xx}, \tag{6.16}$$

$$c(x,0) = C_0\delta(x - x_0), \tag{6.17}$$

where C_0 is the total amount of released calcium, $\delta(x)$ is the Dirac delta function, $-\infty < x < \infty$ and $t > 0$. Note that because the dendrite is very long, the model treats it as infinite in length, and we therefore do not need to specify boundary conditions. It can be shown that the solution of this model is

$$c(x,t) = \frac{C_0}{\sqrt{4\pi Dt}} \exp\left(-\frac{(x - x_0)^2}{4Dt}\right), \tag{6.18}$$

which is illustrated in Fig. (**??**). Note that, for each fixed t, this solution is a Gaussian function, and that over time, the Gaussian becomes wider and the maximal value (at x_0) declines,

$$c(x_0,t) = \frac{C_0}{\sqrt{4\pi Dt}}. \tag{6.19}$$

It is left to the reader to show that this solution satisfies the diffusion equation.

6.2.2 Diffusion in a Short Dendrite

As a second example, we consider the case of a shorter dendrite, where the boundaries are no longer able to be neglected. Suppose that the dendrite is 40 microns in length, and that this time, caged calcium is photoreleased uniformly in the left half of the dendrite. Then an appropriate model is:

$$c_t = Dc_{xx}, \tag{6.20}$$

$$c(x,0) = C_0H(x - 20), \tag{6.21}$$

$$c_x(0,t) = 0, \tag{6.22}$$

$$c_x(40,t) = 0, \tag{6.23}$$

where now C_0 is the concentration of calcium released, $H(x)$ is the Heaviside function, $0 < x < 40$ and $t > 0$. Because the dendrite is short, we have specified (no-flux) boundary conditions at both ends. These no-flux boundary conditions might correspond to the two ends of the dendrite being sealed off, for example. The solution of this model is illustrated in Fig. (**??**).

6.2.3 Numerical solution of heat equation

THIS IS MUCH TOO COMPLICATED A TOPIC TO BE EMBEDDED INSIDE THIS ALREADY-TOO-LONG CHAPTER. THIS REQUIRES IT TO BE VERY SHORT. HOWEVER, IT MUST BE DEEP ENOUGH THAT THEY WILL BE ABLE TO USE IT AS-IS, AS WELL AS EXTEND IT

TO MORE COMPLICATED CASES The numerical solution of partial differential equations requires fairly sophisticated techniques, and we will not treat this topic here. We do, however, present one simple approach for the diffusion equation that is adequate for our purposes, and which can be implemented in *XppAut*.

Consider again the problem of photoreleasing caged calcium in the center of a dendrite 100 microns long. Again, we define the spatial domain to extend from -100 microns to 100 microns, and the starting time to be the time at which the caged calcium is photoreleased (which we take to be $t = 0$). We begin by subdividing the spatial domain into I equally-sized intervals, with $\Delta x = 200/I$ denoting the length of the intervals. If the $I + 1$ endpoints of these intervals are denoted by x_i, where $i = 0, 1, 2, \ldots, I$, then we can define an approximation to $c(x, t)$ at these points by $c(x_i, t) = c_i(t)$. In-between the discretization points, we assume $c(x, t)$ is linear.

We now introduce an approximation to the diffusive term at each discretization point. Using the definition of the derivative, we simply ignore the limit, and use the approximation

General issues. How people really solve these equations. Relationship between space and time step. Though not the best method, XPP can be used. Here's how. PDEs can be converted to odes Show XPP simulations of ODE system.

Figure: Do it an overlay with analytical solution.

6.3 Multi-dimensional Formulation

The multi-dimensional forumulation of the transport equation generalizes quite easily from that in one dimension. The primary difference is that, in multiple dimensions, the flux function is replaced by a flux vector. This flux vector now indicates not only the rate, but the direction, of net transport. While much of our presentation in this section focuses on three dimensions, the two-dimensional case is easily gleaned from the three-dimensional case.

6.3.1 Conservation Law in Multiple Dimensions

We now consider a chemical species C whose concentration $c(x, y, z, t)$ may vary in both time and in some three-dimensional volume V. The conservation law given before remains valid:

$$\begin{aligned}&\text{time rate of change of the total amount of C} = \\ &\quad \text{net rate that C flows in} + \text{rate that C is produced.}\end{aligned} \tag{6.24}$$

At any time t, the total amount of C in the volume can be computed by integrating $c(x, y, z, t)$ over the volume:

$$\text{total amount of C} = \int_V c(x, y, z, t)\, dV. \tag{6.25}$$

Now suppose that C is free to randomly move about, so that C moves in and out of the volume by passing through the volume's surface S. The flux $J(x, y, z, t)$ is now a vector, as C can move in any direction. If we denote by $n(x, y, z)$ the outward unit normal vector on S, then the net flux into V is given by

$$\text{net rate of entry of C} = -\int_S J(x, y, z, t) \cdot n(x, y, z)\, dA, \tag{6.26}$$

where dA is the surface integration element. Because n is the outward normal, $J \cdot n$ is positive when the motion is from inside to outside, which accounts for the negative sign in this equation.

The rate of production of C in the volume can now be written as $f(x, y, z, t, c)$, where as before, the rate is allowed to depend on c itself. Thus, the total rate of production of C in V is given by

$$\text{net rate of production of C} = \int_V f(x, y, z, t, c(x, y, z, t))\, dV. \tag{6.27}$$

The conservation equation can now be rewritten mathematically:

$$\frac{d}{dt}\int_V c(x, y, z, t)\, dV = -\int_S J(x, y, z, t) \cdot n(x, y, z)\, dA + \int_V f(x, y, z, t, c(x, y, z, t))\, dV. \tag{6.28}$$

The surface integral can be replaced by a volume integral using the divergence theorem, which yields the multi-dimensional integral form,

$$\frac{d}{dt}\int_V c(x, y, z, t)\, dV = \int_V \nabla \cdot J(x, y, z, t)\, dV + \int_V f(x, y, z, t, c(x, y, z, t))\, dV, \tag{6.29}$$

where ∇ is the divergence operator. As before, assuming the solution is smooth enough, and noting that the choice of the volume V was arbitrary, we can rewrite Eqn. (6.29) in differential form,

$$c_t + \nabla \cdot J(x, y, z, t) = f(x, y, z, t, c). \tag{6.30}$$

Note that there are now four independent variables (x, y, z and t), and that the equation contains partial derivatives with respect to all four.

6.3.2 Fick's Law in Multiple Dimensions

As discussed above, Fick's Law states that C moves from regions of high concentration to regions of low concentration, with a rate proportional to the concentration gradient. Thus, in multiple dimensions, Fick's Law takes the form,

$$J(x, y, z, t) = -D\nabla c(x, y, z, t), \tag{6.31}$$

where the diffusion constant D is the proportionality constant, and the negative sign ensures that C moves down the concentration gradient. Even in multiple dimensions, the units of D are still length^2/unit time.

Using Fick's law, Eqn. (6.30) can be rewritten as a reaction–diffusion equation,

$$c_t - \nabla \cdot (D\nabla c) = f(x, y, z, t, c). \tag{6.32}$$

Note that the diffusion term is now $\nabla \cdot (D\nabla c)$. When there are no sources or sinks ($f = 0$), Eqn. (6.32) becomes the multi-dimensional diffusion equation,

$$c_t - \nabla \cdot (D\nabla c) = 0. \tag{6.33}$$

6.3.3 Advection

The multi-dimensional advective flux does not change from the one-dimensional case:

$$J(x, y, z, t) = vc(x, y, z, t). \tag{6.34}$$

Note that the flux vector is in the direction of velocity vector, v.

If the random and biased directional motions co-exist, the total flux is again just the linear superposition of the diffusive and drift fluxes:

$$J(x, y, z, t) = vc(x, y, z, t) - D\nabla c(x, y, z, t). \tag{6.35}$$

Using this constitutive relation in Eqn. (6.30), the multi-dimensional reaction–advection–diffusion equation is

$$c_t + v\nabla c(x, y, z, t) - \nabla \cdot (D\nabla c) = f(x, y, z, t, c). \tag{6.36}$$

6.3.4 Boundary and Initial Conditions

As in one dimension, we must supply both initial and boundary conditions to select the solution to the problem of interest. The only difference is that the functions involved are multi-dimensional, and, when the spatial domain is complex, can be quite complicated.

6.3.5 Diffusion in Multiple Dimensions

The actual form of the "nabla" operator depends on the underlying coordinate system. In Cartesian coordinates, it takes the form

$$\nabla = \hat{i}\frac{\partial}{\partial t} + \hat{j}\frac{\partial}{\partial y} + \hat{k}\frac{\partial}{\partial z}, \tag{6.37}$$

where $\hat{i}$, $\hat{j}$ and $\hat{k}$ are the unit vectors in the x, y and z directions, respectively. Therefore, the "vectorial gradient" of c in Cartesian coordinates can be written as

$$\nabla c = \hat{i}\frac{\partial c}{\partial t} + \hat{j}\frac{\partial c}{\partial y} + \hat{k}\frac{\partial c}{\partial z}, \tag{6.38}$$

so that, for example, the gradient in the x direction is $\hat{i} \cdot \nabla\, c = \partial c/\partial x$.

If the diffusion constant D is actually constant–that is, it does not vary in time or space–then the diffusive term can be written

$$\nabla \cdot (D\nabla c) = D\nabla \cdot (\nabla c) = D\nabla^2 c. \tag{6.39}$$

In this equation, ∇^2 is called the "Laplacian operator", with the notation deriving from an anlogy with the square of a vector. When the spatial domain is more naturally fit by coordinate systems other than Cartesian, the Laplacian must also be written in terms of the new coordinates. For example, in two-dimensional polar coordinates, the Laplacian operator becomes

$$\nabla^2 c(r,\theta,t) = \frac{\partial^2 c}{\partial r^2} + \frac{1}{r}\frac{\partial c}{\partial r} + \frac{1}{r^2}\frac{\partial^2 c}{\partial \theta^2}, \tag{6.40}$$

and in three-dimensional spherical coordinates, it becomes

$$\nabla^2 c(r,\theta,\phi,t) = \frac{1}{r^2}\frac{\partial}{\partial r}\left(r^2\frac{\partial c}{\partial r}\right) + \frac{1}{r^2\sin\theta}\frac{\partial}{\partial \theta}\left(\sin\theta\frac{\partial c}{\partial \theta}\right) + \frac{1}{r^2\sin^2\theta}\frac{\partial^2 c}{\partial \phi^2}. \tag{6.41}$$

6.3.6 Using symmetry to simplify higher dimensional problems

Example: Radial diffusion equation Diffusion from a point source in 3D show 1/r solutions analytically Connect with Artie's domain stuff.

End by refering people to Carslaw and Jaeger and Crank for more complicated examples. Boundaries, etc.

6.4 Reaction-diffusion equations

6.4.1 The cable equation

Bring reaction back in now.

Refer to how this is used for spread of V in passive dendrite.

6.4.2 The radial cable equation

Diffusion and degradation. This is a model for Ca2+ domains.

Coupled local dynamics

traveling signals and waves

6.4.3 F-N equations

Analytical work.

Traveling wave solutions.

CHAPTER 7

Modeling Intracellular Calcium Waves

Gregory D. Smith, John Pearson, and Joel Keizer

07-28

7.1 Propagating Intracellular Calcium Waves

7.1.1 The fertilzation calcium wave

A good example is the fertilization Ca^{2+} wave in *Xenopus laevis* eggs. *X. laevis* eggs are large (1.2 mm diameter) so Ca^{2+} diffusion is important.

[[Description of fertilization Ca^{2+} wave]]

This egg requires IP_3R activation for the wave. It can be waveled using equations very similar to that presented in Chapter (). Without consideration of space, the whole cell equations take the form,

$$\frac{d[\mathrm{Ca}^{2+}]}{dt} = f_i \left(j_{IP_3R} + j_{\mathrm{leak}} - j_{\mathrm{SERCA}} \right) \tag{7.1}$$

$$\frac{dw}{dt} = -\left(w - w^{\infty} \right) / \tau \tag{7.2}$$

Figure 7.1 Fertilization caclium wave experimental figure.

Figure 7.2 (w,[Ca^{2+}]) phase plane for fertilization Ca^{2+} wave wavel given by Eqn(MODE:EQN:00).

where w is related to the fraction of IP_3Rs not inactivated, an

$$j_{IP_3R} = v_1 \left(\frac{w[\mathrm{Ca}^{2+}]}{[\mathrm{Ca}^{2+}] + K} \right)^3 . \tag{7.3}$$

Note also that the buffering fraction, f_i, multiplies both the reaction term and the diffusion term, giving the "effective diffusion constant" $D_{\text{eff}} = f_i D \ll D$. Thus, Ca^{2+} diffusion is slowed by binding to Ca^{2+} buffers.

The (w,[Ca^{2+}]) phase plane for this wavel is presented in Fig. (7.2). Notice that the whole cell wavel exhibits bistability, there are three equilibria or singular points given by the intersection of the Ca^{2+} and w nullclines. Equlibiria 1 and 3 are stable, while 2 is unstable.

In a closed cell wavel, we don't have to keep track of $[\mathrm{Ca}^{2+}]_{\mathrm{ER}}$, because if it isn't in the cytosol, it must be in the ER. This conservation means that

$$[\mathrm{Ca}^{2+}]_{\mathrm{T}} = f_e[\mathrm{Ca}^{2+}]_{\mathrm{ER}} + f_i[\mathrm{Ca}^{2+}]_{\mathrm{i}} \tag{7.4}$$

so that $[\mathrm{Ca}^{2+}]_{\mathrm{ER}}$ is always given by

$$[\mathrm{Ca}^{2+}]_{\mathrm{ER}} = \frac{[\mathrm{Ca}^{2+}]_{\mathrm{T}} - [\mathrm{Ca}^{2+}]_{\mathrm{i}}}{c_0} \tag{7.5}$$

where $c_0 = fs$ is the relative effective volume between the ER and cytolsol. By effective we mean that we are accounting for buffering (though in a simplistic way, see Section **??**). This value for $[\mathrm{Ca}^{2+}]_{\mathrm{ER}}$ is implicit in the terms j_{IP_3R} and j_{leak} in Eqn. (7.2).

If we are going to account for Ca^{2+} diffusion as well as release and reuptake into stores, it is easy to add a diffusion term to Eqn. (7.2). Following Chapter (), we do this, to give

$$\frac{\partial[\mathrm{Ca}^{2+}]}{\partial t} = f_i \left(D\frac{\partial^2[\mathrm{Ca}^{2+}]}{\partial x^2} + j_{IP_3R} + j_{\mathrm{leak}} - j_{\mathrm{SERCA}} \right) \tag{7.6}$$

$$\frac{\partial w}{\partial t} = -\left(w - w^{\infty}\right)/\tau \tag{7.7}$$

The first thing to note here is that a diffusion term has been added to the Ca^{2+} equation but not to the equation for w. This is because the IP_3Rs, and thus there state, represented by w, does not diffuse. Also note that in writing this equation, we have to decide if it is still appropriate to use Eqn. (7.5) for the $[\mathrm{Ca}^{2+}]_{\mathrm{ER}}$ that appears in the reactin terms of Eqn. (7.7). It turns out (see Exercise **??**) that this this assumption is valid only if the effective diffusion coefficients in the ER and cytosol are equal. If not, a third PDE must be added,

$$\frac{\partial[\mathrm{Ca}^{2+}]_{\mathrm{ER}}}{\partial t} = f_e \left(D_{er}\frac{\partial^2[\mathrm{Ca}^{2+}]_{\mathrm{ER}}}{\partial x^2} - j_{IP_3R} - j_{\mathrm{leak}} + j_{\mathrm{SERCA}} \right) \tag{7.8}$$

Note the sign difference on the reaction terms, and the diffusion constant for the ER given by D_{er}. If $D_{er} = D_i$, then Eqn. (7.7) and Eqn. (7.8) can be summed to give

$$\frac{\partial[\mathrm{Ca}^{2+}]_{\mathrm{T}}}{\partial t} = f_e \frac{\partial[\mathrm{Ca}^{2+}]_{\mathrm{ER}}}{\partial t} + f_i \frac{\partial[\mathrm{Ca}^{2+}]_{\mathrm{i}}}{\partial t} = 0 \tag{7.9}$$

So if $[\mathrm{Ca}^{2+}]_{\mathrm{T}}$ is initially uniform in space, it remains so for all time, and this concentration becomes a parameter in the wavel, rather than a variable.

7.2 Travelling fronts

In order to simplify the material covered in this section, we are going to assume that $[\mathrm{Ca}^{2+}]_{\mathrm{ER}}$ is a constant and that the dynamics of Ca^{2+} are much slower than w. In this case, $w = w^{\infty}$ and Eqn. (7.2) reduces to the following single-variable reaction-diffusion equation,

$$\frac{\partial c}{\partial t} = D_{eff} \frac{\partial^2 c}{\partial x^2} + f(c) \tag{7.10}$$

where we have written $c = [\mathrm{Ca}^{2+}]$.

Note that if the laplacian of c is zero in Eqn. (7.10), that is, the concentration profile of Ca^{2+} is homogenous, then this partial differntial equation reduces to the whole cell ODE wavel. This relationship is important, because it turns out that the types of phenomena observed in a spatial whole cell wavel that includes diffusion as well as reaction (such as signals, waves, pulses) can be understood in terms of the dynamics of the homogenous sytem. For example, the fertilization Ca^{2+} wave wavel given by Eqn. (**??**), the function $f(c)$ (using parameters given [[]]) has three zeros, and the homogenous system

$$\frac{dc}{dt} = f(c) \tag{7.11}$$

exhibits "bistability". Fig. (7.2) shows a plot of $f(c)$ (that is, $\frac{d[\mathrm{Ca}^{2+}]}{dt}$), as a function of Ca^{2+}. This phase portrait shown in the same figure shows three zeroes (1 and 3 are stable, 2 is unstable).

There is a stable resting state at low Ca^{2+} concentration with [[]], and another stable resting point at high Ca^{2+} concentration. An unstable equilibrium lies between these corresponding to a threshold. Fig. (7.2) presents a (Ca^{2+},w) phase plane that graphically summarizes the bistable dynamics of the uniform concentration case ($\frac{\partial^2[\mathrm{Ca}^{2+}]}{\partial x^2} = 0$).

[[Show how fertilization Ca^{2+} wave can be simulated using XPP.]]

Figure 7.3 The rate function $f(c)$ from Eqn. (**??**) is ploted, and the corresponding phase portrait for the reduced fertilization Ca^{2+} wave wavel indicated.

Beginning with Eqn. (7.10) we follow Chapter (**??**) and discretize space, resulting in the sytem of ODEs.

$$\frac{dc_i}{dt} = D_{eff}\frac{c_{i-1} - 2c_i + c_{i+1}}{\Delta x} + f(c_i) \tag{7.12}$$

And the no flux boundary conditions imply,

$$\begin{aligned}\frac{dc_0}{dt} &= D_{eff}\frac{c_1 - c_0}{\Delta x} + f(c_0)\\ \frac{dc_I}{dt} &= D_{eff}\frac{c_{I-1} - c_I}{\Delta x} + f(c_I)\end{aligned} \tag{7.13}$$

The XPP file would then be,

[[Include xpp file.]]

Fig. (7.4) shows a simulation of a fertilization Ca^{2+} wave calculated using this XPP file. See in the file how the initial conditions are chosen.

7.2.1 Analysis of travelling front solutions

[[I don't think nondimensionalization of time has meaning given here.]]

We can analyze the equation by 1) non-dimensionalizing x and t via the scalings $\hat{x} = x/\left(D_{eff}\tau\right)^{1/2}$ and $\hat{t} = t/\tau$, where τ is the (constant) relaxation time of w; and 2) looking for a traveling wave solution $c(x,t) = C(x - vt) = C(Z)$, as before. Substituting $c(x,t) = C(z)$ into the reaction–diffusion equation gives

$$\frac{dC}{dz} = G \tag{7.14}$$

$$\frac{dG}{dz} = -vG - g(C) \tag{7.15}$$

where $g(C) = \tau f(C)$.

When this xpp file is contructed and $\frac{d[Ca^{2+}]}{dz}$ ploted as a function of $[Ca^{2+}]$, one can find a well-behaved heteroclinic orbit (for $\tau = 20$ sec.) when $v = 5.541$, but *not* for slightly smaller or larger values of v. This heteroclinic orbit corresponds to the traveling front.

7.2.2 Travelling pulses or trigger waves

There are other examples of IP_3-dependent Ca^{2+} waves. In the immature *X. laevis* oocyte, very different types of waves are observed. Phenomena include spiral waves,

Figure 7.4 Simulation of travelling front using XPP. Show a slice as well as an array plot.

Figure 7.5 XPP plot of ODE obtained after transformation into traveling wave coordinates. A heteroclinic orbit connects the two stable equilibria (points 1 and 2).

Figure 7.6 (w,[Ca^{2+}]) phase plane similar to MODE:FIG:02 except that parameters have been changed so that ER is excitable (see text).

Figure 7.7 XPP plot of ODE obtained after transformation into traveling wave coordinates. A heteroclinic orbit connects the two stable equilibria (points 1 and 2).

travelling pulses, etc. These differences arrize because the cytosol is configured differently. There is a long process of maturation leading to the bistable cytoplasm. When still an oocyte, the cytoplasm is excitable, as opposed to bistable. A simple change in parameters converts the ODE wavel of the homogenous sytem into an excitable as opposed to bistable one. However, in order to consider this case we need to let w be time dependent again.

The XPP file used to create the phase plane diagram in Fig. (7.2) is shown in the Appendix. Use this to reproduce this figure, plot nullclines that indicate bistability. Now change the following parameters: [[]]. Replot the nullclines and you will see that the whole cell wavel is now excitable. For comparison, this phase portrait is shown in Fig. (7.6).

It is left as an exercise to construct an XPP file that adds diffusion to the wavel presented in Eqn. (7.7). Implement diffusion in the same way as the XPP file presented above. Remember that w becomes w_i (N dynamic variables for the gating of IP_3Rs at each location in space, but the w_i do not diffuse. Run a simulation using the same initial conditions as in the previous simulatino. You should be able to reproduce Fig. (7.7), which shows a travelling pulse. This traveling pulse gives a Ca^{2+} transient that is analogous to an action potential spike. Excitable dynamics produce traveling pulses like this, sometimes called "trigger waves" since a perturbation at one end of an excitiable medium triggers a signal that may propagate for a long while with undiminished amplitude. Indeed, this allows us to more clearly define what we mean by excitable, since in the 0D case some wavels, like FH, which we have called excitable, don't actually have a fixed threshold. But the spatial version of such wavels does. You can see this here by changing the amplitude of the initial condition. A value of XXX leads to abortive pulses that can't propagate across the entire length of the wavel cell.

It is interesting to graph the trajectory for one spatial position c_i on top of the nullclines. You see the trajectory going from one stable steady state to the other as the wave passes (in the bistable case) or [[]] in the excitable case. Note that this does not correspond exactly to the heteroclinic orbits shown in Fig. (7.6), since we haven't transformed into wave coordinates.

However, Fig. (7.6) and Fig. (7.7) allows us to make a correspondence between the pieces of these trajectories in the phase plane and the shape of $c_i(t)$. This correspondence is easy to make if w is slow compared to Ca^{2+}, because in that case the homogenous system is a relaxation-type excitable system. This is to some extend the case here, one can see $1 \to 2$ in the reaction phase plane is rapid, and w is nearly constant during this

phase of the wave. Then $2 \rightarrow 3$ occurs on the $[Ca^{2+}]$-nullcline, and $3 \rightarrow 4$ in the reaction phase plane is also rapid, and $4 \rightarrow 1$ occurs on the other branchof the $[Ca^{2+}]$-nullcline.

7.3 The Effect of Calcium Buffers on Calcium Waves

The important association of Ca^{2+} with intracellular Ca^{2+} buffers has been discussed in Chapter (). Remember that this was important because Ca^{2+} buffers change the time constants for ODE wavels. Now that we know how to wavel diffusion, we are able to wavel the effect that Ca^{2+} buffers have on Ca^{2+} waves. We are also able to calculate the wave of elevated Ca^{2+}-bound indicator dye that actually corresponds to an experimental measurement. This wave corresponds to the underlying Ca^{2+} wave, but to what degree. This is the sort of question that modeling can help answer.

7.3.1 Impleting Calcium Buffers in a Calcium Wave Simulation

What is the proper way to include Ca^{2+} buffers in a wavel of a Ca^{2+} wave? The association and dissociation of Ca^{2+} with buffers amounts to the presence of additional reaction terms in the wavel. Let's consider the case where there is only one Ca^{2+} buffer, either an endogenous Ca^{2+}-binding protein or the indicator dye being used to measure the Ca^{2+} signal. Following the bimolecular reaction scheme presented in Eqn. (**??**) , we write,

$$\frac{\partial [\mathrm{Ca}^{2+}]}{\partial t} = D_{Ca}\frac{\partial^2 [\mathrm{Ca}^{2+}]}{\partial x^2} + R + J_{tot}, \tag{7.16}$$

$$\frac{\partial [\mathrm{B}]}{\partial t} = D_B\frac{\partial^2 [\mathrm{B}]}{\partial x^2} + R, \tag{7.17}$$

$$\frac{\partial [CaB]}{\partial t} = D_{CaB}\frac{\partial^2 [CaB]}{\partial x^2} - R, \tag{7.18}$$

with the reaction terms given by

$$R = -k^+[\mathrm{B}][\mathrm{Ca}^{2+}] + k^-[CaB]. \tag{7.19}$$

[[or refer to equation in Artie's chapter]]. where $J_{tot} = J_{pump} + J_{[IP_3]} + J_{leak}$ is the sum of all calcium fluxes into and out of the ER. These equations (plus the equation for w in Eqn. (**??**)) make a wavel for a Ca^{2+} wave in the presence of a buffer. Note that we have included the possibility that the Ca^{2+} buffer is mobile (that is, it can diffuse when Ca^{2+} is bound or not) with the diffusion terms and coefficents D_B and D_{CaB}.

Notice that if the diffusion of buffer doesn't depend on whethor or not Ca^{2+} is bound, $D_B \approx D_{CaB}$, Eqn. (7.17) and Eqn. (7.18) can be summed to give,

$$\frac{\partial [\mathrm{B_m}]_T}{\partial t} = D_b\frac{\partial^2 [\mathrm{B_m}]_T}{\partial x^2}. \tag{7.20}$$

This means that if $[\mathrm{B}]_T$ is initially homogenous, it will remain homogeneous, and we can eliminate Eqn. (7.18) since at every spatial position, $[\mathrm{B}] = [\mathrm{B}]_T - [CaB]$. Thus, we have the reduced system,

$$\frac{\partial[\mathrm{Ca}^{2+}]}{\partial t} = D_{Ca}\frac{\partial^2[\mathrm{Ca}^{2+}]}{\partial x^2} + R + J_{tot} \tag{7.21}$$

$$\frac{\partial[CaB]}{\partial t} = D_{CaB}\frac{\partial^2[CaB]}{\partial x^2} - R, \tag{7.22}$$

with the reaction terms given by

$$R = -k^+\left([\mathrm{B}]_T - [CaB]\right)[\mathrm{Ca}^{2+}] + k^-[CaB]. \tag{7.23}$$

If we now bring back the equation for w, we can write the following XPP file to simulate a buffered Ca^{2+} wave,

[[XPP FILE]]

Fig. (**??**) shows a simulation using this XPP file. [[Description of buffer parameter changes and the effect on wave amp and speed.]]

7.3.2 The Rapid Buffer Approximation

If the buffer reactions are rapid with respect to the diffusion, it is possible to simplify our wavel further using the so-called rapid buffer approximation. If the associatoin and dissociation rate constants are large (buffers fast), then Eqn. (7.21)-Eqn. (7.22) become singularly perturbed (see Chapter (**??**)). (If, in the nondimensional version of these equations, R is large, then dividing both sides by a constant of this size results in a small parameter in front of the time derivatives). Although singular perturbations problems are beyond the scope of this text, there is a heuristic derivation of the RBA that sheds light of the effect of Ca^{2+} buffers on Ca^{2+} transport in cells.

The rapid buffer approximation begins by making the assumption that if Ca^{2+} buffers are rapid, Ca^{2+} will be in equilibrium with the buffers at each point in space. Thus, we assume,

$$[CaB] = \frac{[\mathrm{Ca}^{2+}][\mathrm{B}]_T}{[\mathrm{Ca}^{2+}] + K} \tag{7.24}$$

Let's define total cell Ca^{2+} to be

$$[\mathrm{Ca}^{2+}]_\mathrm{T} = [\mathrm{Ca}^{2+}] + [CaB_m]. \tag{7.25}$$

Now summing Eqn. (7.21) and Eqn. (7.22) results in the cancellation of the R term, leaving,

$$\frac{\partial[\mathrm{Ca}^{2+}]_\mathrm{T}}{\partial t} = \frac{\partial[\mathrm{Ca}^{2+}]}{\partial t} + \frac{\partial[CaB_m]}{\partial t} = D_c\frac{\partial^2[\mathrm{Ca}^{2+}]}{\partial x^2} + D_b\frac{\partial^2[CaB_m]}{\partial x^2} \tag{7.26}$$

These equations do not involve the rapid buffering time scales and, therefore, involve no singular perturbation. Therefore, we use our assumption of local equilibrium, which

implies Eqn. (7.24) as well as,

$$[\mathrm{Ca}^{2+}]_{\mathrm{T}} = [\mathrm{Ca}^{2+}]\left(1 + \frac{[\mathrm{B_m}]_T}{(K + [\mathrm{Ca}^{2+}])}\right). \tag{7.27}$$

and substitute these expressions for $[\mathrm{Ca}^{2+}]_{\mathrm{T}}$ and $[CaB]$ in terms of $[\mathrm{Ca}^{2+}]$ into Eqn. (7.26). This gives,

$$\frac{\partial}{\partial t}\left([\mathrm{Ca}^{2+}] + \frac{[\mathrm{Ca}^{2+}][\mathrm{B}]_T}{[\mathrm{Ca}^{2+}] + K}\right) = \frac{\partial^2}{\partial x^2}\left(D_c[\mathrm{Ca}^{2+}] + D_b\frac{[\mathrm{Ca}^{2+}][\mathrm{B}]_T}{[\mathrm{Ca}^{2+}] + K}\right) + J_{tot} \tag{7.28}$$

It is left as an exercise for the reader to confirm that taking derivatives implies,

$$\frac{\partial[\mathrm{Ca}^{2+}]}{\partial t} = \beta\left((D_c + D_m\gamma)\frac{\partial^2[\mathrm{Ca}^{2+}]}{\partial x^2} - \frac{2\gamma D_b}{K + [\mathrm{Ca}^{2+}]}\left(\frac{\partial[\mathrm{Ca}^{2+}]}{\partial t}\right)^2 + J_{tot}\right), \tag{7.29}$$

where

$$\gamma = \frac{K[\mathrm{B_m}]_T}{(K + [\mathrm{Ca}^{2+}])^2} \tag{7.30}$$

and

$$\beta = \frac{1}{1+\gamma}. \tag{7.31}$$

This equation is refered to as the rapid buffering approximation, and although complicated in form, this approximation has allowed us to elminate the equation for $[CaB]$. Fig. (**??**) uses an XPP file which implements Ca^{2+} buffers using the rapid buffer approximation. Make the association constants large while keeping the dissocation constant fixed, and compare the XPP file which uses the full equations for the buffered Ca^{2+} wave to the file which uses the rapid buffer approximation. How fast do the buffers have to be for the RBA to give a good approximation to the wave?

7.3.3 The effective diffusion coefficient

In the case of stationary buffer alone, Eq. (**??**) involves only a diffusion-like term. The introduction of mobile buffers produces a second term involving the square of the $[\mathrm{Ca}^{2+}]$ gradient. Since that (non-negative) term is subtracted from the equation, it appears as a non-diffusive term which counteracts the diffusive-like movement of unbound Ca^{2+} given by the first term. Such terms arise often in the context of density-dependent diffusion [**?**]. Although this non-diffusive term can not be eliminated, it is useful to write the equation in the form of an equivalent conservation equation [**?**]. Defining the calcium-dependent diffusion constant as

$$D(c) = \beta\left(D_c + D_b\frac{K[\mathrm{B_m}]_T}{(K+c)^2}\right). \tag{7.32}$$

and the diffusion flux as

$$j(c) = -D(c)\frac{\partial c}{\partial t}, \tag{7.33}$$

it is possible to rearrange Eq. (**??**) into the standard form of a conservation equation,

$$\frac{\partial c}{\partial t} = -\frac{\partial}{\partial t} j(c) - \frac{d\beta}{\beta dc} D(c) \left(\frac{\partial c}{\partial t}\right)^2 . \tag{7.34}$$

Using Eq. (**??**) it is easy to show that the derivative $d\beta/dc$ is non-negative. Thus the non-diffusive second term in Eq. (7.34) represents a *sink* for unbound Ca^{2+} ions. This non-diffusive sink term is a result of the uptake of Ca^{2+} by buffers that occurs when unbound Ca^{2+} ions move down their concentration gradient. Indeed, as long as $d\beta/dc > 0$, a larger fraction of the ions that move down the gradient into the lower concentration region will be taken up by the buffers there than will be released from the buffers at the high concentration end of the gradient. Only when $d\beta/dc \approx 0$, which occurs as a limiting case when $[Ca^{2+}]/K_i \ll 1$, does the non-diffusive sink term vanish. By using the explicit form for $j(c)$ in Eq. (7.33), it is possible to decompose the first term in Eq. (7.34) to obtain:

$$\frac{\partial c}{\partial t} = D(c)\frac{\partial^2 c}{\partial x^2} + \left(\frac{dD}{dc} - \frac{1}{\beta}\frac{d\beta}{dc} D(c)\right)\left(\frac{\partial c}{\partial t}\right)^2 . \tag{7.35}$$

This form of the equation makes it clear that the non-diffusive term in Eq. (**??**) has two components: one that arises from the dependence of the diffusion constant, $D(c)$, on $[Ca^{2+}]$ and the other that arises from the sink effect described in Eq. (7.34).

Exogenous buffers have been shown to alter the speed of Ca^{2+} waves in mature *Xenopus* oocytes [**?**], an effect that may in part be related to the various buffering terms in Eq. (**??**). [[Suggest some exercises using XPP. Solving simple diffusion problems with and without buffers to look at the effect of buffers on the effective diffusion coefficient. Then link to early chapters where contant fraction assumptions were made. What is that constant, exactly?]]

7.4 Interpretation of Confocal Microfluorometric Measurements

In the previous discussion of global or cell-wide Ca^{2+} excitability, oscillations, and waves, we have described mathematical models of these dynamic phenomena and theoretical studies of the effect of rapid mobile buffers on Ca^{2+} signals. However, it is important to remember that experimental observations of intracellular Ca^{2+} dynamics are made using confocal microfluorimetry, an experimental technique that involves loading Ca^{2+} indicator dyes into cells and instrumentation that optically excites these indicators and measures emmission. Ca^{2+} indicator dyes are themselves Ca^{2+} buffers (often highly mobile) that can potentially effect intracellular Ca^{2+} signalling.

Although a measured fluoresence signal is only indirectly related to the dynamics of intracellular Ca^{2+}, it is relatively straightforward to determine the free Ca^{2+} concentration during a cell-wide Ca^{2+} response using the time course of measured fluorescence.

If the Ca^{2+} and indicator dye concentrations are homogenous throughout the cell, the equilibrium relation

$$[CaB_j] = \frac{[\mathrm{Ca}^{2+}][\mathrm{B_j}]_T}{\mathrm{K_j} + [\mathrm{Ca}^{2+}]} \tag{7.36}$$

is valid as long as $[Ca^{2+}]$ changes slowly compared to the equilibration time of the buffers. Because this equilibration time is on the order of milliseconds, this condition is usually satisfied for global Ca^{2+} responses, which occur with a timescale of seconds or tens of seconds. *Perhaps link to statement of equilibration time of buffers in John's RBA section.*

If the equilibrium relation (7.36) accurately describes the relationship between bound indicator dye and free Ca^{2+}, then it is a simple matter to "backcalculate" the free Ca^{2+} concentration as a function of time. For a single excitation wavelength measurement (e.g., using a non-ratiometric dye such as fluo-3 at low concentration), we can idealize the indicator fluorescence as the sum of two components,

$$F = \eta_B[\mathrm{B_j}] + \eta_{CaB}[CaB_j] \tag{7.37}$$

where η_B and η_{CaB} are proportionality constants for free and bound dye, respectively. When $\eta_B < \eta_{CaB}$, the maximum and minimum observable fluorescence are given by $F_{min} = \lim_{[\mathrm{Ca}^{2+}]\to 0} F = \eta_B[\mathrm{B}]_T$ and $F_{max} = \lim_{[\mathrm{Ca}^{2+}]\to\infty} F = \eta_{CaB}[\mathrm{B}]_T$. Using the equilibrium relation it can be shown (see Exercise 2) that

$$[\mathrm{Ca}^{2+}] = \mathrm{K_j}\frac{[CaB_j]}{[\mathrm{B_j}]} = \mathrm{K_j}\frac{F - F_{min}}{F_{max} - F} \tag{7.38}$$

If only the Ca^{2+}-bound indicator fluoresces strongly, then $F \approx \eta_{CaB}[CaB_j]$, and a slighly simpler expression results from substituting $F_{min} = 0$ in (7.38).

It should be noted that the validity of (7.38) relies on the stability of instrument sensitivity, optical path length, and dye concentration between measurements of F, F_{min}, and F_{max}. Because determining F_{min} and F_{max} usually involves titrating the indicator released from lysed cells, this is difficult to acheive in practice [2].

In whole-cell Ca^{2+} measurements, fluoresence intensities can be measured at two excitation wavelengths (λ and λ') using indicator dyes such as fura-2. Such *ratiometric* measurements can be related to the underlying free Ca^{2+} signal by supplementing (7.37) with

$$F' = \eta'_B[\mathrm{B_j}] + \eta'_{CaB}[CaB_j] \tag{7.39}$$

where the primes indicates the second exitation wavelength [2]. Using the first equality of (7.38), the fluorescence ratio, $R = F/F'$, can be inverted to give (see Exercise 2),

$$[\mathrm{Ca}^{2+}] = \mathrm{K_j}\frac{\eta_B - \eta'_B R}{\eta'_{CaB} R - \eta_{CaB}} = \mathrm{K_j}\left(\frac{R - R_{min}}{R_{max} - R}\right)\left(\frac{\eta'_B}{\eta'_{CaB}}\right) \tag{7.40}$$

where for the second equality we use $R_{min} = \lim_{[\mathrm{Ca}^{2+}]\to 0} F/F' = \eta_B/\eta'_B$ and $R_{max} = \lim_{[\mathrm{Ca}^{2+}]\to\infty} F/F' = \eta_{CaB}/\eta'_{CaB}$. If λ' is chosen to be a wavelength at which the calibration spectra at different Ca^{2+} concentrations cross one another, then $\eta'_B \approx \eta'_{CaB}$

and the last factor in (7.40) is eliminated. An advantage of the ratiometric method is it's insensitivity to changes in dye concentration and instrument sensitivity between measurements.

7.5 Cellular heterogeneity and the continuum approximation

7.5.1 Modeling discrete Ca^{2+} release sites

Clustering of intracellular Ca^{2+} channels leads to spatially localized Ca^{2+} release events.

This is a very relevant and interesting case. Discrete release can be incorporated into multi-domain or continuum models. Example simulation showing some consequences of discreteness (or heterogeneity of Ca^{2+} release flux) on a simulated propagating Ca^{2+} wave.

Figure showing deterministic simulation where each release site is populated by large number of channels (i.e., heterogeneous Ca^{2+} flux though no discreteness in the sense of finite number of Ca^{2+} channels).

[[XPP FILE MODIFICATIONS THAT LEAD TO THIS FIGURE]]

[[Exercise looking at relationship of wave speed and D for continous and saltatory waves. A new mode of Ca^{2+} wave propagation in which wave velocity is a linear function of D and d.]]]

[[FIGURE SHOWING V as function of d and D]]]

7.5.2 The fire-diffuse-fire model of spark-mediated Ca^{2+} waves

Description of the model in which release is not instantaneous, so that model doesn't have to be redefined in the following sections.

Calculation of wave speed from the analytical model?

Figures clarifying the model.

Two nondimensional parameter, β and γ, and their significance.

7.5.3 The transition from saltatory to continuous Ca^{2+} wave propagation

Presentation of the β, γ plane. Figure showing saltatory versus continuous wave using FDF model.

The transition between saltatory and continuous waves analysis and clarification using the fire-diffuse-fire model

Validity of the continuum approximation.

7.6 Spatially localized calcium elevations

Many cellular processes (including synaptic transmission, activity-dependent synaptic plasticity, and regulation of neuronal excitability) can be initiated by changes in intracellular Ca^{2+} concentration in the absence of a global Ca^{2+} response. Such *localized* Ca^{2+} *elevations* are cellular signals of great interest, both because they can regulate cellular function in a highly specific manner, and because these localized Ca^{2+} elevations are the 'building blocks' of global Ca^{2+} release events (for review, see [4, 5]). Recent experimental observation of localized intracellular Ca^{2+} release events dubbed Ca^{2+} 'puffs' and 'sparks' has focused attention on these elementary events that are responsible for Ca^{2+} oscillations and waves [7].

The interpretation of confocal microscopic data of Ca^{2+} puffs and sparks is complicated by the fact that diffusion of Ca^{2+}, endogenous buffers, and indicator all contribute to the dynamics of Ca^{2+} transport both during and after Ca^{2+} release. While in the case of global Ca^{2+} responses, it was shown above that the equilibrium relation (7.36) will likely hold between Ca^{2+} and indicator, this is not so easily demonstrated in the case of localized Ca^{2+} elevations (though it remains true in some cases [15]). A further complicating factor in interpreting confocal microscopic measurements of puffs and sparks is the optical blurring that occurs due to the limited spatial resolution of instrumentation [16, 1].

The reaction-diffusion equations for the buffered diffusion of intracellular Ca^{2+}, (7.16)–(7.19), are the starting point of a theoretical understanding the dynamics of localized Ca^{2+} elevations. In the simplest scenario, a Ca^{2+} puff or spark is due to Ca^{2+} release through one channel or a tight cluster of channels. If Ca^{2+} is released from intracellular Ca^{2+} stores deep within a large cell (so that the plasma membrane is far away and doesn't influence the time-course of the event), and the intracellular milieu is homogenous and isotropic, then we have spherical symmetry. In this case, the evolving profiles of Ca^{2+} and buffer (though a function of time and distance from the source) will not be a function of the polar (ϕ) or azimuthal (θ) angle. In the case of such spherical or radial symmetry the Laplacian reduces to

$$\nabla^2 = \frac{1}{r^2}\frac{d}{dr}\left[r^2\frac{d}{dr}\right] = \frac{d^2}{dr^2} + \frac{2}{r}\frac{d}{dr} \tag{7.41}$$

Figure 7.8 shows a spherically symmetric calculation of a localized Ca^{2+} elevation using the full equations for the buffered diffusion of Ca^{2+}, (7.16)–(7.19), with parameters consistent with measurements of the effective diffusion coefficient in Xenopus oocyte cytoplasm [3]. Figure 7.8 is a numerically calculated snapshot of the concentration profiles for each species according to the full equations after an elapsed time of 1 ms. Ca^{2+} concentration is elevated near the source (*red line*). Because released free Ca^{2+} reacts with buffer, the concentration of bound buffer (*solid green and blue lines*) is elevated near the source. Conversely, the concentration of free buffer (*dashed lines*) decreases near the source. In this simulation, 250 μM stationary buffer was included in addition to 50 μM mobile buffer (both with K of 10 μM). A source amplitude of 5 pA

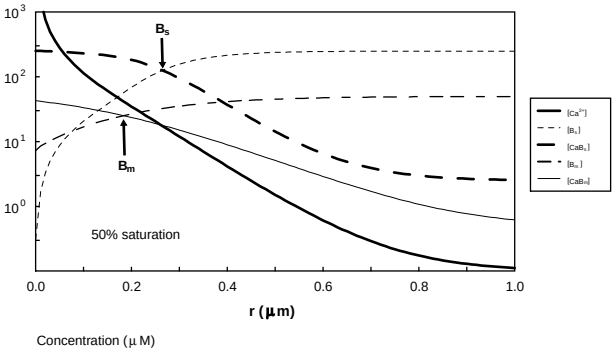

Figure 7.8 Representative full model calculation of Ca^{2+} profile near a point source for free Ca^{2+}. Source amplitude (σ) and elapsed time are 5 pA and 1 ms, respectively.

was used, corresponding to a tight cluster of IP3Rs. Interestingly, Fig. 7.8 shows that the mobile buffer is less easily saturated than stationary buffer, in spite of the fact that the stationary buffer is at five-fold higher concentration (note arrows).

Simulations such as these have played a role in understanding of the dynamics of puffs and sparks. Figure 7.9 shows a Ca^{2+} sparks simulated using parameters consistent with experimental observation in cardiac myocytes [16]. Such simulations confirm that the time-course of observed fluorescence can be explained by a 2 pA, 15 ms, Ca^{2+}-release event from a tight cluster of RyRs located on the sarcoplasmic reticulum membrane.

Parameter studies using this model indicate that Ca^{2+} spark properties (such as brightness, full width at half maximum, and decay time constant) are very dependent on indicator dye parameters (such as association rate constant, concentration, and diffusion coefficient). These relationships are not always intuitive. For example, increasing indicator dye concentration decreases the brightness of the simulated Ca^{2+} spark in Fig. 7.9. This is partly due to the fact that spark brightness is a normalized measure (peak/basal fluorescence), and partly due to the fact that high concentrations of indicator perturb the underlying free Ca^{2+} signal.

7.6.1 Steady-state equations

Numerical simulations like those in Fig. 7.8 confirm that domain Ca^{2+} concentrations acheive steady-state values very rapidly (within microseconds) near point sources. Steady-state solutions to the full equations are thus of interest because they allow estimates of "domain" Ca^{2+} concentration near open intracellular Ca^{2+} channels. These steady-state solutions lend themselves to analysis, giving insight into the limiting (long time) "shape" of localized Ca^{2+} elevations. In the case of one mobile buffer, steady-state solutions to the full equations, (7.16)–(7.19), will satisfy the following boundary-value problem [13],

$$0 = D_c \nabla^2 [\mathrm{Ca}^{2+}] - k^+ [\mathrm{B}][\mathrm{Ca}^{2+}] + k^- \left([\mathrm{B}]_T - [\mathrm{B}]\right), \tag{7.42}$$

$$0 = D_b \nabla^2 [\mathrm{B}] - k^+ [\mathrm{B}][\mathrm{Ca}^{2+}] + k^- \left([\mathrm{B}]_T - [\mathrm{B}]\right), \tag{7.43}$$

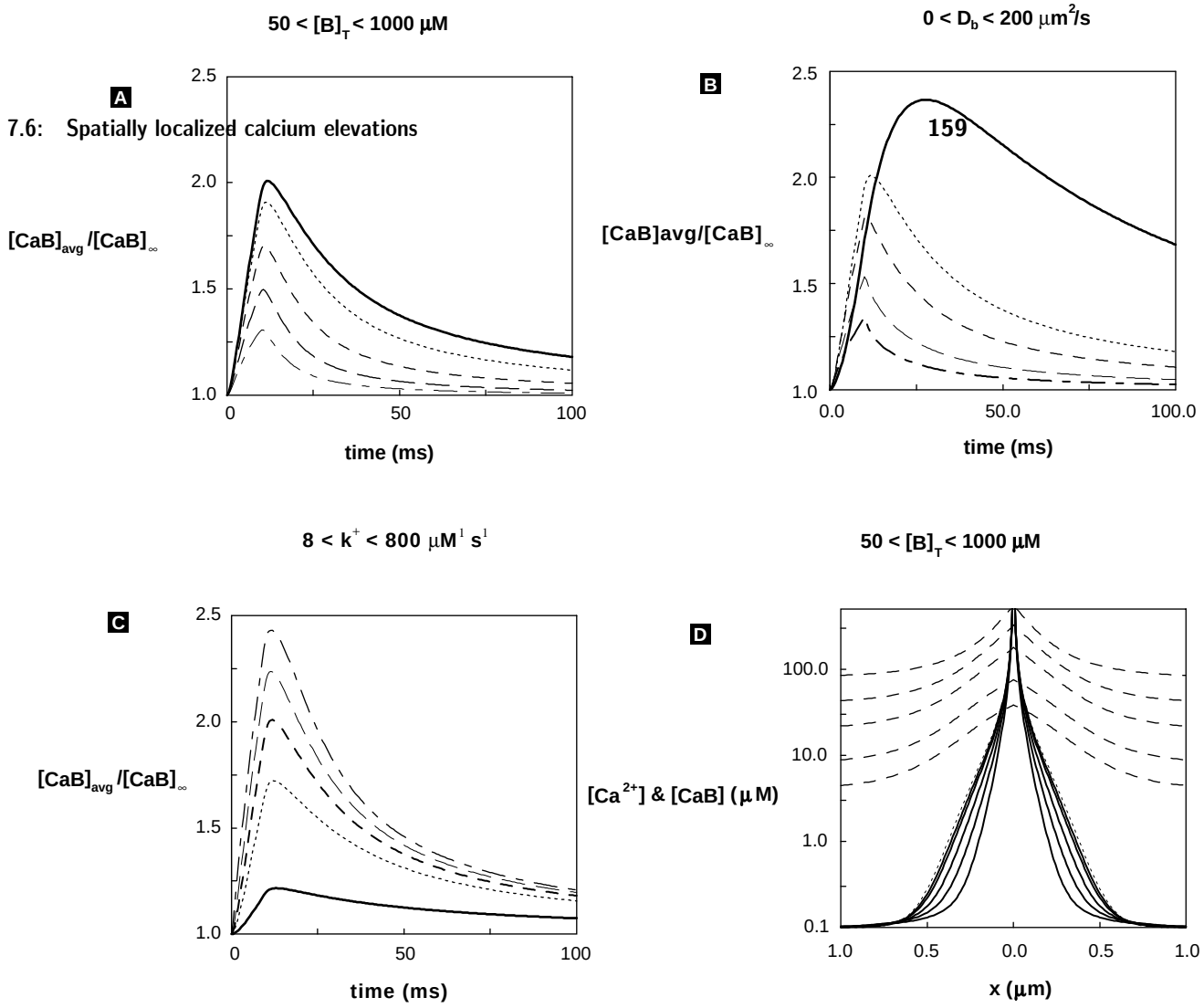

Figure 7.9 Effects of indicator dye parameters on Ca2+ spark properties. Source amplitude is 2 pA for 15 ms and simulated fluo-3 has K of 1.13 μM. (A,B,C) Time course of normalized, blurred fluorescence signal estimated according to with $\eta_B = 0$. (D) Snapshot of Ca^{2+} and CaB] profiles before termination of Ca^{2+} release. Dotted line shows the Ca^{2+} profile with no fluo-3. For details of the simulated confocal point spread function and buffer paramterssee Smith et al. 1998.

with associated boundary conditions,

$$\begin{aligned} \lim_{r\to 0}\left\{-4\pi r^2 D_c \frac{d[\mathrm{Ca}^{2+}]}{dr}\right\} &= \sigma, \qquad \lim_{r\to\infty}[\mathrm{Ca}^{2+}] = [\mathrm{Ca}^{2+}]_\infty, \\ \lim_{r\to 0}\left\{-4\pi r^2 D_b \frac{d[\mathrm{B}]}{dr}\right\} &= 0, \qquad \lim_{r\to\infty}[\mathrm{B}] = [\mathrm{B}]_\infty = \frac{K[\mathrm{B}]_T}{K + [\mathrm{Ca}^{2+}]_\infty}. \end{aligned} \tag{7.44}$$

Here we have written D_c and D_b for the diffusion coefficients of free $Ca^{2+}$and free buffer, respectively.

Note that fixed buffers, while important for the time-dependent solutions to the full equations, have no influence on steady states. This can be seen by inspecting the full

equations, (7.16)–(7.19), where $D_{CaBj} = 0$ implies $R_j = -k_j^+[\mathrm{B_j}][\mathrm{Ca}^{2+}] + k_j^-[CaB_j] = 0$ so that these terms make no contribution to the Ca^{2+} equation at steady-state.

7.6.2 Non-dimensionalization

As discussed in Chapter **??**, there are many advantages to non-dimensionalizing equations before preceeding to analyze them. A convenient nondimensionalization of (7.42)–(7.44) begins by scaling $[\mathrm{Ca}^{2+}]$ and [B] by representative concentrations, the dissociation constant of the buffer (K) and the total concentration of buffer ($[\mathrm{B}]_T$), respectively (see [17] for details). This gives two dimensionless dependent variables, c and b, given by $c = [\mathrm{Ca}^{2+}]/K$ and $b = [\mathrm{B}]/[\mathrm{B}]_T$.

If we also nondimensionalize the independent variable $\rho = r/L$, with $L = \sigma/4\pi D_c K$, it can be shown (see Exercise 3) that (7.42) and (7.43) simplify to

$$\varepsilon_c \nabla_\rho^2 c - (cb + b - 1) = 0, \tag{7.45}$$

$$\varepsilon_b \nabla_\rho^2 b - (cb + b - 1) = 0, \tag{7.46}$$

where the subscript on the Laplacian indicates the differentiation is with respect to ρ.

Note that two dimensionless diffusion coefficients (ε_c and ε_b) appear in these equations. In terms of the original dimensional parameters of the problem, they are given by $\varepsilon_c = \epsilon\alpha$ and $\varepsilon_b = \epsilon D$, where $\alpha = K/[\mathrm{B}]_T$ is a buffering factor (small when buffer is at high concentration compared to dissociation constant), $D = D_b/D_c$ is a relative diffusion coefficient between buffer and Ca^{2+}, and the common factor is given by

$$\epsilon = (4\pi)^2 D_c^3 K/\sigma^2 k^+ \tag{7.47}$$

This common factor is small for strong sources and/or fast buffers.

7.6.3 The excess buffer approximation (EBA)

The steady-state equations for the buffered diffusion of Ca^{2+} near a point source, (7.45) and (7.46), are nonlinear and no general analytical solution is known for these equations. But we can begin to understand the behavior of solutions (and the effect of Ca^{2+} buffers on Ca^{2+} domains) by considering (7.45) and (7.46) in limiting parameter regimes. The first such limit we will consider is called the "excess buffer approximation." If there is a lot of buffer (buffer is in excess), then the parameter $\alpha = K/[\mathrm{B}]_T$ will be very small, and this will cause $\varepsilon_c = \epsilon\alpha$ be small as well. Therefore, we consider in detail (7.45) and (7.46) when $\varepsilon_c \approx 0$, which in physical terms implies that the diffusion coefficient of c is small compared to the size of the reaction terms in (7.45).

The mathematically inclined reader will notice that for small ε_c, this is a singular perturbation problem. Because this technique goes beyound the scope of this book, we present only a heuristic analysis here. The interested reader is invited to consult [17] for a more rigorous treatment of this problem.

With this caveat, we formally set $\varepsilon_c = 0$ in (7.45), giving

$$cb + b - 1 = 0 \tag{7.48}$$

which implies that (7.46) simplifies to

$$\nabla^2 b = 0.$$

When combined with the boundary conditions for b (see 7.65 in Exercise 3), this equation implies

$$b = b_\infty \tag{7.49}$$

where $b_\infty = 1/(1 + c_\infty)$ (7.65). Thus, our assumption that buffer is in excess ($\varepsilon_c = 0$) implies that the buffer is not perturbed from its equilibrium value, b_∞.

Substituting (7.49) into (7.45) gives

$$\varepsilon_c \nabla^2 c - b_\infty (c - c_\infty) = 0$$

This is a linear equation is satisfied by $c = A_1/\rho + A_2$ [6, 8]. Using dimensionless boundary conditions for c that can be derived from (7.44), the constants A_1 and A_2 are found to give

$$c = \frac{1}{\rho} e^{-\rho/\Lambda} + c_\infty \tag{7.50}$$

where the dimensionless space constant $\Lambda = \sqrt{\varepsilon_c / b_\infty}$. When this result is expressed in dimensional form, we have

$$[\mathrm{Ca}^{2+}] = \frac{\sigma}{4\pi D_c r} e^{-r/\lambda} + [\mathrm{Ca}^{2+}]_\infty \tag{7.51}$$

where λ is the characteristic length constant for the mobile Ca^{2+} buffer given by $\lambda = \sqrt{D_c / k^+ [\mathrm{B}]_\infty}$. This excess buffer approximation, first derived by Neher [10], is valid when mobile buffer is in high concentration and/or when the source amplitude is small, that is, $\lim_{r \to 0} [\mathrm{B}] \approx [\mathrm{B}]_\infty$ [10, 15]. Note that λ decreases with increasing association rate constant (k^+) and free buffer concentration far from the source ($[\mathrm{B}]_\infty$), representing a restricted localized Ca^{2+} elevation.

7.6.4 The rapid buffer approximation (RBA)

The steady-state rapid buffer approximation near a point source for Ca^{2+} can be derived by noticing that rapid buffer (large k^+) leads to small values of ϵ (7.47). This results in small values for both ε_c and ε_b, which in physical terms implies that the diffusion coefficient of both c and b are small compared to the size of the reaction terms in (7.45) and (7.46).

If we formally set $\varepsilon_c = \varepsilon_b = 0$ in these equations, we find that, as before, (7.52) holds. Solving for b, we find at every spatial location b is given by

$$b = \frac{1}{1 + c} \tag{7.52}$$

or in dimensional terms,

$$[\mathrm{B}] = \frac{K [\mathrm{B}]_T}{K + [\mathrm{Ca}^{2+}]} \tag{7.53}$$

These equations are statements of *local equilibrium*, the fundamental assumption used in deriving the rapid buffer approximation in the traveling wave case (**??**).

We proceed with this derivation of the steady-state RBA by by subtracting (7.45) and (7.46) to give

$$\nabla_\rho^2 \left(\varepsilon_c c - \varepsilon_b b\right) = 0. \tag{7.54}$$

In physical terms this expression is equivalent to the statement that at steady state the flux of total Ca^{2+}, diffusing in both free and bound forms, across any spherical surface centered on the source is equal to the flux entering through the source (see Exercise 4). Integrating twice with respect to ρ, and using the boundary conditions to determine the integration constants gives

$$\varepsilon_c c - \varepsilon_b b = \frac{\varepsilon_c}{\rho} + \varepsilon_c c_\infty - \varepsilon_b b_\infty \tag{7.55}$$

Substituting (7.52) into this equation gives

$$\varepsilon_c c - \varepsilon_b \left(\frac{1}{1+c}\right) = \frac{\varepsilon_c}{\rho} + \varepsilon_c c_\infty - \varepsilon_b b_\infty. \tag{7.56}$$

which upon solving for c and converting back into dimensional form gives the steady-state RBA [14],

$$[Ca^{2+}] = \frac{1}{2D_c}\left(-D_c K + \frac{\sigma}{4\pi r} + D_c[Ca^{2+}]_\infty - D_b[B]_\infty \right. \\ \left. + \sqrt{\left(D_c K + \frac{\sigma}{4\pi r} + D_c[Ca^{2+}]_\infty - D_b[B]_\infty\right)^2 + 4D_c D_b [B]_T K}\right). \tag{7.57}$$

The rapid buffer approximation tends to be valid when ϵ is small, which may occur when buffers have a large association rate constant (k^+). Interestingly, a sufficiently large source amplitude (σ) can compensate for modest binding rates, also causing ϵ to be small and the RBA to be valid [15].

7.6.5 Complementarity of the EBA and RBA

The fundamental assumptions used in deriving the excess and rapid buffer approximations are significantly different. In the case of the RBA (7.57), we assumed that buffer and Ca^{2+} were in local equilibrium. Combined this assumption (7.53) with the fact that $[Ca^{2+}] \to \infty$ as $r \to 0$ in (7.57), implies

$$\lim_{r\to 0} [B] = 0 \quad \text{(RBA)} \tag{7.58}$$

Thus, the steady-state RBA cannot be valid unless the source is strong enough to saturate the buffer. On the other hand, in our derivation of the EBA we assumed that the buffer is not perturbed from it's equilibrium value (7.49). If this is true even near the source, then

$$\lim_{r\to 0} [B] = [B]_\infty \quad \text{(EBA)} \tag{7.59}$$

Thus, we expect the EBA and RBA approximations to be complementary, in the sense that the steady-state solution to the full equations for the buffered diffusion of Ca^{2+} near a point source (the correct answer) can not simultaneously be EBA-like (7.59) and RBA-like (7.58). In the process of extending both the EBA and RBA to higher order, this expectation that has been confirmed [17].

Exercises

1. Converting coupled PDEs to one PDE and then doing some wave analysis. [[Do we want this as an exercise?]] For simplicity, assume that $[Ca^{2+}]_{ER}$ is a constant and that the dynamics of Ca^{2+} are much slower than w. In this case, $w = w^{\infty}$ and the reaction equations reduce to those on pp. PAGE NUMBER (refers to notes page 106, see notes page 105), which is a one-variable ODE. The rate function is plotted on pp. PAGE NUMBER (refers to notes page 107, see notes page 105).
   This gives a single-variable reaction–diffusion equation:

$$\frac{\partial c}{\partial t} = D_{\text{eff}} \frac{\partial^2 c}{\partial x^2} + f(c) \tag{7.60}$$

   where $c = [Ca^{2+}]$. Note that $f(c)$ on pp. PAGE NUMBER (refers to notes page 107, see notes page 105) has three zeroes (1 and 3 are stable, 2 is unstable). So $f(c)$ exhibits "bistability".
   We can analyze the equation by 1) non-dimensionalizing x and t via the scalings $\hat{x} = x/\left(D_{\text{eff}}\tau\right)^{1/2}$ and $\hat{t} = t/\tau$, where τ is the (constant) relaxation time of w; and 2) looking for a traveling wave solution $c(x,t) = C(x - vt) = C(Z)$, as before. Substituting $c(x,t) = C(z)$ into the reaction–diffusion equation gives

$$\frac{dC}{dz} = G \tag{7.61}$$

$$\frac{dG}{dz} = -vG - g(C) \tag{7.62}$$

   where $g(C) = \tau f(C)$. The xppaut file is shown on pp. PAGE NUMBER (references notes page 109, see notes page 108).
   There is a well-behaved heteroclinic orbit (for $\tau = 20$ sec.) when $v = 5.541$ (see pp. PAGE NUMBER), but *not* for slightly smaller or larger values of v (see pp. PAGE NUMBER).
   The same dynamical model (closed cell IP_3R dynamics) but with parameters giving "excitable conditions" (see pp. PAGE NUMBER) gives a Ca^{2+} analogue of an action potential spike. Excitable dynamics produce a "trigger wave": FIGURE GOES HERE.
   The idea is if w is slow compared to Ca^{2+}, we get a relaxation-type excitable system. Thus $1 \to 2$ in the reaction phase plane is rapid. Thus we can consider $w = w_1$ to

be constant, and describe the front by

$$\frac{\partial c}{\partial t} = D_{\text{eff}} \frac{\partial^2 c}{\partial x^2} + f(w_1, c) \tag{7.63}$$

Then $2 \to 3$ occurs on the Ca^{2+}-nullcline, and $3 \to 4$ also satisfies the above reaction–diffusion equation but with $w = w_2$ (see the reaction phase plane on pp. PAGE NUMBER – see notes bottom of page 112). The value of C at 3 is determined by the condition that the wave speed of the "front" and the "tail" of the wave are the same. Finally, $4 \to 1$ occurs on the Ca^{2+}-nullcline.

2. Show that (7.36) and (7.37) imply (7.38). Also derive (7.40) from (7.37) and (7.39).

3. Confirm that nondimensionalizing (7.42)–(7.43) as described in text results in (7.45)–(7.46). Show that the boundary conditions (7.44) become

$$\lim_{\rho \to 0} \left\{ -\rho^2 \frac{dc}{d\rho} \right\} = 1, \quad \lim_{\rho \to \infty} c = c_\infty, \tag{7.64}$$

$$\lim_{\rho \to 0} \left\{ -\rho^2 \frac{db}{d\rho} \right\} = 0, \quad \lim_{\rho \to \infty} b = b_\infty = \frac{1}{1 + c_\infty}. \tag{7.65}$$

where $c_\infty = [Ca^{2+}]_\infty / K$ and and $b_\infty = [B]_\infty / [B]_T$. For help see [17].

4. Show that in physical terms, (7.54) is equivalent to the statement that at steady state the flux of total Ca^{2+}, diffusing in both free and bound forms, across any spherical surface centered on the source is equal to the flux entering through the source. First, convert (7.54) into dimensional form. Then substitute $[B] = [B]_T - [CaB]$ and $[B]_\infty = [B]_T - [CaB]_\infty$ and simplify. Finally, use this expression to calculate $J_{total} = J_{free} + J_{bound}$ where

$$J_{free} = -4\pi r^2 D_c \frac{d[Ca^{2+}]}{dr} \qquad J_{bound} = -4\pi r^2 D_b \frac{d[CaB]}{dr}$$

Confirm that $J_{total} = \sigma$ (independent of r).

5. To rigorously derive the EBA and RBA, asymptotic methods are required [17]. An alternative analysis of the steady-state equations for the buffered diffusion of Ca^{2+} involves linearizing (see Chapter *Need link to chapter where linearization is described*) the equations around the equilibrium concentrations of Ca^{2+} and buffer, c_∞ and b_∞ [9, 12, 19] (for review, see [11]). Begining with the dimensionless equations, define $\delta c = c - c_\infty$ and $\delta b = b - b_\infty$. Substitute these expressions into (7.45) and (7.46) and drop the quadratic terms $\delta c\, \delta b$ to find

$$\varepsilon_c \nabla_\rho^2 \delta c - [(1 + c_\infty)\, \delta b + b_\infty \delta c] = 0 \tag{7.66}$$

$$\varepsilon_b \nabla_\rho^2 \delta b - [(1 + c_\infty)\, \delta b + b_\infty \delta c] = 0 \tag{7.67}$$

and associated boundary conditions,

$$\lim_{\rho \to \infty} \delta c = 0, \quad \lim_{\rho \to 0} \left(-\rho^2 \frac{d\delta c}{d\rho} \right) = 1, \quad \lim_{\rho \to \infty} \delta b = 0, \quad \lim_{\rho \to 0} \left(-\rho^2 \frac{d\delta b}{d\rho} \right) = 0.$$

When this system of linear equations is solved, and the result converted back to dimensional form, the following steady-state profiles for Ca^{2+} and buffer result:

$$[Ca^{2+}] = [Ca^{2+}]_\infty + \frac{\sigma}{4\pi r\left(D_c + \gamma_\infty D_b\right)}\left[1 + \frac{\gamma_\infty D_b}{D_c} e^{-r/\lambda}\right], \tag{7.68}$$

$$[B] = [B]_\infty + \frac{\sigma\gamma_\infty}{4\pi r\left(D_c + \gamma_\infty D_b\right)}\left[e^{-r/\lambda} - 1\right] \tag{7.69}$$

where

$$\frac{1}{\lambda^2} = \frac{1}{\tau}\left(\frac{1}{D_b} + \frac{\gamma_\infty}{D_c}\right) \quad \frac{1}{\tau} = k^+[Ca^{2+}]_\infty + k^- \quad \gamma_\infty = \frac{K[B]_T}{\left(K + [Ca^{2+}]_\infty\right)^2} \tag{7.70}$$

Convert (7.68)–(7.69) into dimensionless form to find expressions for δc and δb and show that these satisfy (7.66)–(7.67).

Show that when γ_∞ is large (lots of buffer), (7.68) reduces to (7.51), the EBA solution for $[Ca^{2+}]$.

6. Substitute the spherical polar Laplacian (7.41) in (**??**), show that the steady-state RBA can be found by directly integrating. For help see [14].

References

[1] Pratusevich, V.R., and C.W. Balke, *Factors shaping the confocal image of the calcium spark in cardiac muscle cells*, Biophys. J. 71 (1996), pp. 2942–57.

[2] Grynkiewicz, G., M. Poenie, and R.Y. Tsien, *A new generation of Ca2+ indicators with greatly improved fluorescence properties*, J. Biol. Chem., 260 (1985), pp. 34400-50.

[3] Allbritton, N. L., T. Meyer, L. Stryer, *Range of messenger action of calcium ion and inositol 1,4,5-trisphosphate*, Science, 258 (1992), pp. 1812–5.

[4] Berridge, M. J., *Elementary and global aspects of calcium signalling*, J. Physiol. (Lond.), 499 (1997), pp. 291–306.

[5] Berridge, M.J., *Neuronal calcium signaling*, Neuron, 21 (1998), pp. 13–26.

[6] Carslaw, H. S. and J. C. Jaeger, *Conduction of Heat in Solids*, 2nd edition, Clarendon Press, Oxford, 1959.

[7] Cheng, H., W. J. Lederer, and M. B. Cannell, *Calcium sparks: elementary events underlying excitation-contraction coupling in heart muscle*, Science, 262 (1993), pp. 740–744.

[8] Crank, J., *The Mathematics of Diffusion*, 2nd edition, Clarendon Press, Oxford, 1975.

[9] Naraghi, M., and E. Neher, *Linearized buffered* Ca^{2+} *diffusion in microdomains and its implications for calculation of [*Ca^{2+}*] at the mouth of a calcium channel*, J. Neurosci., 17 (1997), pp. 6961–73.

[10] Neher, E., *Concentration profiles of intracellular* Ca^{2+} *in the presence of diffusible chelator*, in Calcium electrogenesis and neuronal functioning, U. Heinemann, M. Klee, E. Neher, and W. Singer, eds., Exp. Brain Res., Series 14, Springer, Berlin, 1986, pp. 80–96.

[11] Neher, E., *Usefulness and limitations of linear approximations to the understanding of* Ca^{2+} *signals*, Cell Calcium, 24 (1998), pp. 345.

[12] Pape, P. C., D. S. Jong, and W. K. Chandler, *Calcium release and its voltage dependence in frog cut muscle fibers equilibrated with 20 mM EGTA*, J. Gen. Physiol. 106 (1995), pp. 259–336.

[13] Roberts, S. M., *Localization of calcium signals by a mobile calcium buffer in frog saccular hair cells*, J. Neurosci., 14 (1944), pp. 3246–62.

[14] Smith, G. D., *Analytical steady-state solution to the rapid buffering approximation near an open* Ca^{2+} *channel*, Biophys. J., 71 (1996), pp. 3064–72.

[15] Smith, G. D., J. Wagner, and J. Keizer, *Validity of the rapid buffering approximation near a point source for* Ca^{2+} *ions*, Biophys. J., 70, (1996), pp. 2527–39.

[16] Smith, G. D., J. Keizer, M. Stern, W. J. Lederer, and H. Cheng, *A simple numerical model of* Ca^{2+} *spark formation and detection in cardiac myocytes*, Biophys. J., 75 (1998), pp. 15–32.

[17] Smith, G. D., L. Dai, R. Miura, and A. Sherman, *Asymptotic analysis of buffered Ca2+ diffusion near a point source*, SIAM J. Applied Math. (2000), Submitted.

[18] Sneyd, J., P. D. Dale, and A. Duffy, *Traveling waves in buffered systems: applications to calcium waves*, SIAM J. Applied Math., 58 (1998), pp. 1178–92.

[19] Stern, M. D., *Buffering of calcium in the vicinity of a channel pore*, Cell Calcium, 13, pp. 183–192.

[20] Wagner, J., and J. Keizer, *Effects of rapid buffers on* Ca^{2+} *diffusion and* Ca^{2+} *oscillations*, Biophys. J. 67 (1994), pp. 447–56.

CHAPTER 8

Intercellular Communication

John Rinzel and Joel Keizer

07-28

Orchestrating the activity of cell populations for physiological functioning of the brain, organs, and musculature depends on transmission of signals, learning and memory devices, and feedback control systems. By what biophysical mechanisms do cells communicate in order to coordinate their activity as local ensembles, as multimodal circuits and across system levels? Here, we only scratch the surface of this fascinating topic. We will focus on electrically active cells; for this, you can have in mind for example cardiac cells, many types of secretory cells, and neurons.

We know that ionic currents underlie cellular electrical activity. Hence, one way that cells can interact is by directly passing ionic current between each other. Perhaps the simplest mechanism for such intercourse is the analog of resistive coupling between units, i.e. with the intercellular current being proportional to the voltage difference between cells. Heart cells, and many other types of cells, communicate in this manner with the ions flowing directly between two coupled cells. In this case, referred to as electrical coupling (and sometimes, in the neural context, electrotonic coupling), the current flows through channel proteins that span the plasma membranes of both cells (Fig. (8.1)). The clusters of such channel proteins that are found at cell-to-cell contacts are called gap junctions.

While gap junctions are occasionally found in neural circuits they seem to be less uncommon during development or they may not constitute an exclusive means of interaction. Neurons have a rich repertoire of other ways for exciting or inhibiting other

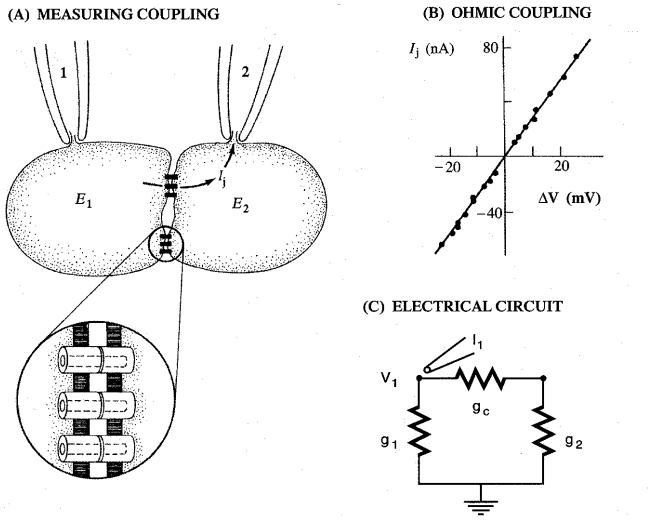

Figure 8.1 schematic or drawing of gap jn w/ ch's + electrical ckt. Probably a modified version of Fig 4.13 from Koch: Biophysics of Computation

target neurons, via the indirect means of chemical synaptic transmission (Fig. (8.4)). At a terminal of a neuron's axon the neurotransmitter of one type or another is bundled in vesicles that are released with increased probability when the terminal is active (depolarized). The transmitter, released into the extracellular space in the terminal region, diffuses and binds to receptors on the post-synaptic cell's nearby membrane. These receptors may be part of a receptor-channel complex or be linked indirectly through second messengers to a nearby channel. The activated channels then lead to the post-synaptic current and action. The variety of transmitters and receptors enable many different time scales and "sign" of the input that is being delivered to the target cell. We find synapses that are excitatory or inhibitory; they can be fast or slow; they can be shunting; their synaptic parameters can change with usage - either, depressing or facilitating ; they can be voltage-gated or not on the post-synaptic side.

Gap-junctional coupling is typically localized, certainly for cells without spatially extended processes, to nearby neighbors. Prime examples include the heart and islets of Langerhans in the pancreas. In contrast, neurons can interact across distances that are many times greater than a cell body diameter - by means of their potentially far-reaching axonal and dendritic arbors. The synaptic interactions enable them to participate in local calculations and with distant assemblies, on selective time scales, fast or slow and to various degrees. For long distance communication between cells propagated action potentials typically mediate signal transfer to the synapses via axons.

Given the variety of coupling mechanisms and connectivity patterns there are many possible behavioral modes, spontaneous and/or stimulus-driven, that such circuits may

exhibit. Obviously we cannot elaborate on many of these behaviors; we will restrict attention to a few examples and focus on pairwise interactions. Also we choose to not present here some other mechanisms for intercellular interaction such as coupling by cell-generated electrical fields, diffusion and exchange of ions (that effect Nernst equilibrium potentials) and second messengers, mechanical and hormonal effects.

8.1 Electrical Coupling and Gap Junctions

The proteins that comprise the channels at gap junctions are of the connexion family. Connexion molecules in the plasma membrane of one cell link up those in an adjacent cell to form the channels. These channels pass most ions as well as various molecules up to molecular weights of 10s of kD, including those, for example, involved in second messenger systems such as IP3, CAMP, etc. The single channel conductance can be in the range of 75-150 pS, and in most known instances they are fairly voltage-independent. The variety of connexins provide a rich repertoire for diverse modulatory effects as instigated (in some cases rapidly) by changes in intracellular pH, second messengers, neurotransmitters, or voltage. [ref'ce Carlen, TINS 2000] For example, the reduction of gap junctional coupling due to increasing levels of $[\mathrm{Ca}]_i$ is described as a protection mechanism.

Typically, for cell-level modeling, we represent the net conductance of a gap junction as a constant, the product of the mean number of open channels at the junction and the single channel conductance. Simultaneous pairwise recordings, at least for geometrically simple, neighboring cells. could be used to quantitatively estimate this conductance. For spatially extended cells, like neurons with branching dendrites, such measurements would be confounded especially if the gap junctions are at electrically remote sites. Gap junctions may also be detected by dye coupling, although this method is problematic without good controls to test how readily the dye passes.

Consider an idealized case of two cells, each isopotential. The gap junctional current that flows from cell 2 into cell 1 is written as $g_c(V_2 - V_1)$, where g_c is the net coupling conductance of all the gap junctions formed between the two cells. This current appears as a source term in the current balance equation for cell 1. Defined as such, with the current as leaving from cell 2, it appears as a sink term for cell 2 (or, equivalently $g_c(V_1 - V_2)$ is a source term into cell 2). Thus we have:

$$V_1' = (-I_{ion}(V_1, w_1) + g_c(V_2 - V_1))/C_m \tag{8.1}$$

$$V_2' = (-I_{ion}(V_2, w_2) + g_c(V_1 - V_2))/C_m \tag{8.2}$$

where w_1, w_2 correspond to the set of gating variables in each cell. Let us first predict the behavior, say in the case when the gap junction conductance is large. This means that the cells are very tightly electrically coupled. We would then expect them to have approximately the same voltage. Indeed if the cells are identical then $V_1 = V_2$ is always a solution - the coupling current would be zero in this case. Of course a perturbation

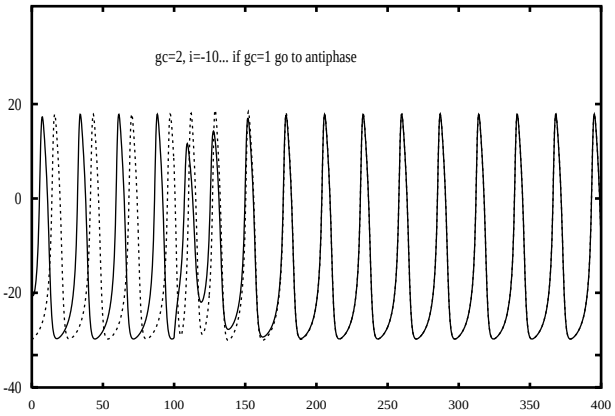

Figure 8.2 Two identical Morris-Lecar neuron models, auto-rhythmic, synchronize with electrical coupling (turned on at $t = 100$ ms). Parameter values for the model are those of Chapter XX with the following exceptions: $vc = -5, vd = 10, \phi = 0.5, g_{Ca} = 8, i = 10$. Net gap junction coupling conductance is $g_c = 2$. Initial conditions: $V_1 = -20$ mV, $w_1 = 0.2$, $V_2 = -30$ mV, $w_2 = 0$.

(eg, brief current pulse) to just one cell would make their V's differ, transiently. By subtracting the two equations and then dividing by g_c we see that after dropping the term which is of order $1/g_c$:

$$\tau_c(V_1 - V_2)' \approx -(V_1 - V_2) \tag{8.3}$$

where $\tau_c = C_m/g_c$. This shows that the cells will re-establish uniformity with an effective time constant of τ_c, that is very short when g_c is large.

This is illustrated in Fig. (8.2) for two Morris-Lecar cells that are tuned into an oscillatory regime. In this example the cells are initially out-of-phase and uncoupled. Synchronization occurs promptly after the coupling is introduced at $t = 100$ ms.

Such synchronization also occurs for spatially distributed multi-cell systems; even though electrical coupling is localized it can, when large enough, synchronize a population that might be spread over a sizable spatial region. In order to formalize this, one can introduce the concept of an electrical length scale that involves coupling conductance as well as leakage conductance. This emphasizes the relativeness of intercellular current to the current flowing across a cell's plasma membrane. By using this notion we can refer to the "electrical size" of a cellular array - it could be quite compact even though the spatial extent might not be.

In order to formalize this notion we consider the simple case of a chain of gap-junction-coupled cells which have passive membrane properties, i.e. $I_{ion} = g_m V$. Thus we have the equations for a typical cell, cell j:

$$dV_j/dt = [g_c(V_{j+1} - V_j) + g_c(V_{j-1} - V_j) - g_m V_j]/C_m. \tag{8.4}$$

Suppose that we have a very long chain of cells (and, for now, ignore end effects) and suppose we voltage clamp the cell in the middle for which $j = 0$ ($j > 0$ refers to cells to the right and $j < 0$ is for cells to the left). In this passive system the voltage distribution will go to a steady state after some transient, and the voltage will decrease

from V_0 as $|j|$ increases. This attenuation occurs as current spreads from one cell to the next away from $j = 0$ and because of current loss through the "leaky" membrane of each cell.

The steady voltage decays in an exponential fashion with distance. The decay "rate" γ can be found by considering the steady state case of eqn () (ie, setting $dV_j/dt = 0$) and seeking a solution of the form $V_j = V_0\gamma^j$. This leads to a quadratic eqn for γ:

$$\gamma^2 - (2 + g_m/g_c)\gamma + 1 = 0 \tag{8.5}$$

Hence, there are two values of γ:

$$\gamma_\pm = 1 + g_m/(2g_c) \pm \sqrt{[1 + g_m/(2g_c)]^2 - 1} \tag{8.6}$$

Note, both roots are positive with $\gamma_+ > 1$ and $\gamma_- < 1$.

For a voltage profile that decays with distance to the right of $j = 0$ we must disallow γ_- (such a term would grow with j). Thus, ignoring end effects due to termination of the chain the steady state profile for $j \geq 0$ has the form

$$V_j = V_0\gamma_-^j. \tag{8.7}$$

The solution for $j \leq 0$ is $V_j = V_0\gamma_+^j = V_0 - \gamma_-^j$, since $\gamma_+ = \gamma_-^{-1}$.

We can test our intuition by considering some limiting cases. When g_m/g_c is large the leakage conductance is dominant and the voltage should attenuate rapidly with distance from $j = 0$. Indeed, $\gamma_- \approx g_c/g_m$ so that V_j decays steeply. On the other hand, when g_m/g_c is small, then $\gamma_- \approx 1 - \sqrt{g_m/g_c}$ and the spatial decay is gradual.

Pursuing this latter case a bit more, if cell-to-cell attenuation is small and the spatial profile changes smoothly we might treat the one-dimensional cellular array approximately as a continuum with position $x \approx j\Delta x$, where Δx is a cell size parameter, considered small. The leakage conductance g_m is proportional to a cell's surface area, which is perimeter of a cross section times Δx. We will take some care with the representation of g_c. Let's think about the reciprocal, $r_c = 1/g_c$, the resistance to longitudinal current flow between cells, say from one cell center to the next. Then, r_c involves resistance due to the gap junctions as well as cytoplasmic resistance along the cells axial direction. If there are many gap junctions between adjacent cells then the major contribution to r_c will be the cytoplasmic term which is proportional to area of a cross section time Δx. Consequently, the ratio g_m/g_c $(= g_m r_c)$ is proportional to Δx^2 and may be written as $(\Delta x/\lambda)^2$. Finally, combining this with our expression for γ_- (from Eqn. (8.6) for small g_m/g_c) and noting that $log(\gamma_-) \approx -\sqrt{g_m/g_c}$ the solution form for the continuum approximation is:

$$V(x) = V_j = V_0 exp(j\ log\ \gamma_-) \approx V_o exp(-j\Delta x/\lambda) = V_0 exp(-x/\lambda) \tag{8.8}$$

Thus, λ is the electrical length constant for the continuum approximation.

This treatment relates nicely, in a converse fashion, to continuum models for current spread in individual cells that have extended processes, like neurons with their dendrites or axons. These processes behave like electrical cables, current flows along the axis and leaks through the membrane. In this case of a neuronal process, we could think of it for simulation purposes as a chain of short compartments (length Δx) each with a membrane surface area and connected by axial resistances - there are no gap junctions between the fictitious adjacent compartments. If d is the diameter of the cross section then we would have $g_m = \Delta x \pi d G_m$, where G_m is the leak conductance density (S/cm^2) and $r_c = \Delta x 4 R_i/(\pi d^2)$ where R_i the cytoplasmic specific resistivity (ohm cm). Putting this together we obtain for the electrical length constant of a passive neuronal dendrite or axon $\lambda = \sqrt{d/(4 G_m R_i)}$. As an illustration, for a cortical pyramidal cell we've seen estimates $G_m =, R_i =$ so that with $d =$ – yields $\lambda = -$. This means for a dendritic branch of physical length, the corresponding electrotonic length is about XX, so we do not expect excessive attenuation for steady or slow voltage changes. Transients decay more abruptly. Also, the attenuations are more severe from dendritic locations to the cell body to dendrites than vice versa.

We note that this discretization of neuronal cable-like processes is called the compartmental method and was first developed by Rall for treating the effect of spatio-temporally distributed synaptic inputs over a neuron's somatic-dendritic area. (cite rall chapt and K-S book)

In electrically-coupled excitable systems with weaker gap junctions synchrony is not quickly established and localized perturbations may lead to waves or other spatio-temporal patterning.

Returning back to our setup of discrete electrically active cells, we can also see the uniformizing property of gap junctional coupling even if the cells are different. The simplest case is if the ionic currents are passive. Do the averaging in the eqn to show that $V_1 - V_2$ gets small, rapidly. Show also that $V_1 = V_2 = \overline{V}$ - which satisfies the "mean" eqn. applications are to inf olive and to beta-cell islet - gives 1-2 parag's. An application is to pancreatic beta cells in an islet (this example should go below, after we discuss anti-phase). gap jns enable param averaging: [show a figure from Smolen et al; or from Manor et al??]

While electrical coupling is typically considered as a mechanism for uniformizing cells one should be aware that the outcome depends alot on coupling strength and dynamic features of the individual cells. For example, the same cells used above when coupled weakly with gap junctions do not synchronize. Instead, they establish a rhythm with the two cells in a stable anti-phase locked pattern - just the opposite of togetherness (Fig. (8.3)). Also, for this situation the period of the network oscillation depends on the value of g_c [see Skinner or Manor et al, for the olive]. This not true for the in-phase pattern. When the coupling strength is large enough, the period (for a pair of identical cells) is that of the isolated cell and is therefore independent of g_c. (ref'ce to Sherman/Rinzel; Chow/Kopell)

Discuss the application to beta-cell islets and period extension. Mention the implications for multiple cells with weak gc – clustering or splay-phase. (see Chow/Kopell

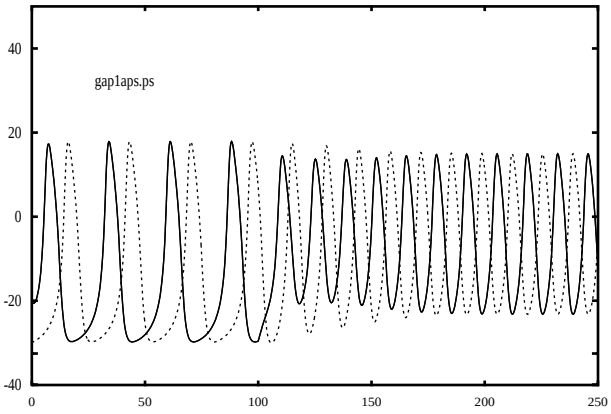

Figure 8.3 Time courses of V1, V2 showing antiphase behavior... start with cells in phase, uncoupled, then switch on the coupling at t-on and see them go into antiphase

for addtl refces) Mention possible roles in patho states, like epilepsy - Carlen review. Mention that for slower membrane dynamics, like pacemaker currents and waveforms, the gap junctions do not lead to anti-phase behaviors.

8.2 Synaptic Transmission Between Neurons

In the preceding section we saw that strong gap junctions can be used for coordinating cellular electrical activity, subserving functions in which cells might work together in near or approximate synchrony. The bi-directionality and instantaneous nature of gap junction coupling are well-suited for achieving these goals. In the nervous system there are demands for more complex patterning. Individual cells generally are likely involved in numerous different computations, with possibly different time scales, sometimes being called into action with a brief wake-up-call but in other cases only after a long barrage of inputs. In some cases the precise timing of action potentials might be important and we would expect fast coupling mechanisms. But when firing rate, rather than spike timing, is more important one might expect slower coupling mechanisms might be invoked. Of course some flexibility is attainable for multiplexing with a variety of intrinsic mechanisms - i.e., the many different ionic channels, however by using synapse specific mechanisms one enhances the computational potential - the number of ensembles that can be dynamically constructed and/or released as needed.

It is hard to imagine how instantaneous bidirectional coupling could allow in an efficient way such a rich set of alternatives. However, the one-way signaling via chemical synapses enables the system to employ a few transmitters but yet enrich the possibilities for postsynaptic response by having many choices for the post-synaptic receptors and channels. Sites for modulatory action can be implemented on either the post-synaptic or pre-synaptic side. Thus while packaged transmitter is released in punctate fashion, like the AP, the time scale and even the "sign" of the response is determined alot by the machinery on the post-synaptic cell.

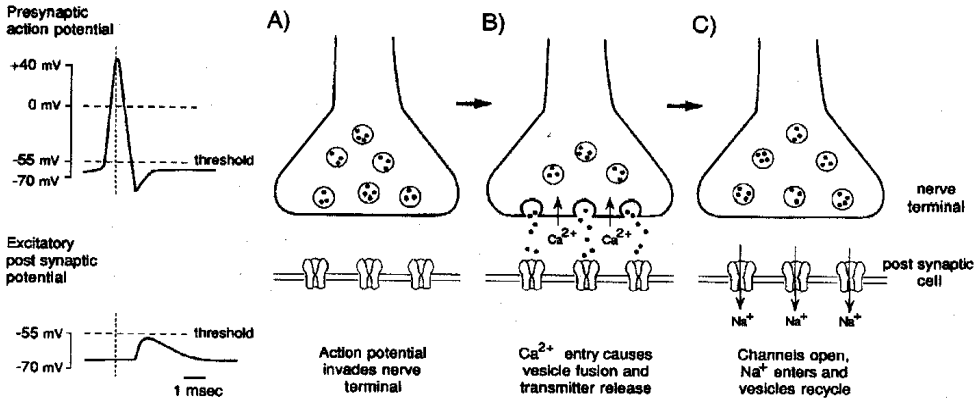

Figure 8.4 a multi-panel schematic showing pre-syn and post-syn elements. P1: AP arriving, Ca entry and vesicles in pre-syn; P2: vesicle fused, T diffusing, T binding to receptor/channels; P3: opening of post-syn channels; P4: time course of post syn condtce and PSC for AMPA and $GABA_A$; probably the schematic Fig 4.2 from Koch: Biophysics of Computation

We will formulate an idealized model for the current generated in a post-synaptic cell due to transmitter release by a pre-synaptic cell in which an action potential has occured. The sender's action potential opens voltage-gated calcium channels at the axon terminal where vesicles are poised ready to fuse with the membrane and release transmitter.

Whether or not release occurs is a probabilistic event. The failure rate can be high at some, e.g. cortical, synapses. There is also a small probability of spontaneous release. Experiments at NMJ and central synapses use the quantal release hypothesis to analyze the statistics of post-synaptic responses for spontaneous and evoked release to estimate the number of active sites, quantal content, and release probability. We will not consider these issues here, nor the details of transmitter diffusion in and removal from the synaptic cleft, the small extracellular space between the pre- and post-synaptic sites.

We suppose that transmitter is available briefly, and that during this time it can bind to receptors, actually receptor-channel complexes, on the postsynaptic membrane. For this simple model we imagine a two-state channel. Binding of transmitter to receptor favors opening of the channel and unbinding leads (statistically) to closing. A kinetic scheme for this is the following:

$$C + T \underset{\beta'}{\overset{\alpha'}{\rightleftharpoons}} O$$

If s is the fraction of complexes in the open state, O, then $1 - s$ is the fraction closed and we have, given a transmitter concentration $[T]$

$$ds/dt = \alpha'[T](1 - s) - \beta' s \tag{8.9}$$

This representation assumes unlimited transmitter and receptor availability. Also, it requires us to specify a time course for $[T]$; for example, we might assume a square pulse over some time duration (perhaps with a modest delay, on the order of a ms or less) when the presynaptic cell fires. We will adopt a simpler, and easy to implement, scheme - supposing that maximal transmitter is available when the pre-synaptic membrane potential V_{pre} is above some level, say θ_{syn}. This would mean $[T] = T_{max} s_\infty(V_{pre})$ with $s_\infty(V_{pre}) = H(V_{pre} - \theta_{syn})$, where $H(x)$ is the Heaviside step function. We will smooth this out using a sigmoidal function for s_∞. Redefining the rate constants, which we view as adjustable depending on the desired time course of postsynaptic conductance, we get

$$ds/dt = \alpha s_\infty(V_{pre})(1 - s) - \beta s \tag{8.10}$$

The current through the post-synaptic membrane is

$$I_{syn} = g_{syn} s(V - V_{syn}) \tag{8.11}$$

where the reversal potential V_{syn} depends on the concentration differences for the ion species that flow through the open receptor-channels in the post-synaptic membrane; g_{syn} is the maximal conductance at the synapse if all the available channels are open.

This type of model has been used to describe some common types of synapses, both excitatory and inhibitory, that have relatively simple kinetics. The different transmitters and different receptors and different ions that pass through the synaptic channels lead to different types of synapses. The most commonly known transmitter that is used for excitatory synapses is glutamate. It can activate AMPA receptor-channels that typically pass inward current (carried mostly by sodium ions, but also some potassium and other ions). The postsynaptic conductance is relatively fast with a rise time ($\approx \alpha^{-1}$) of order 1 ms and decay times ($\approx \beta^{-1}$) of a few to 10s of ms. The Eqn. (8.10) has been used for these synapses. The value of V_{syn} in this case is typically about 100 mV above rest. Glutamate can also evoke slower post-synaptic responses by activating NMDA receptors (fast rise, of order ms, and slow decay, of order many 10s to 100s ms) or a number of different types of metabotropic glutamate receptors with very slow rise and slow decay (order secs). The conductance associated with NMDA receptors is, curiously, also gated by the post-synaptic voltage, V_{post}. If V_{post} is too small the NMDA-associated channels are blocked by magnesium ions from the outside; sufficient depolarization relieves this block and the channels can open. The dependence of synaptic current on pre- and post-synaptic activity implicate the NMDA conductance in various models for associative learning and synaptic plasticity generally. (say Hebb? anything about LTP?) The very

slow metabotropic glutamate mediated effects are believed to be primarily modulatory, acting for example to effectively change the firing threshold of a cell. In the examples below of excitatory synaptic coupling we will be thinking primarily of AMPA-mediated excitatory synapses, for which Eqn. (8.10) is a good first approximation. (more complete descriptions, even for this simple receptor-channel complex might involve kinetic models with additional states.) (Ref'ce: Destexhe and Sejnowski)

Fast inhibitory synapses are activated by the transmitter GABA when they bind to $GABA_A$receptor-channels. The post-synaptic conductance has a fast rise time, a ms or few, and somewhat slower decay than the AMPA-excitatory conductance, on the order of 10s of ms. The current is carried largely by cloride ions. Interestingly, the value for V_{syn} can be quite variable, typically -60 mV to -80 mV but in some cases as depolarized as -35 mV; this variability likely reflects different types or activities of cloride pumps that regulate intracellular Cl^- concentration. If a cell is sitting near its resting potential of say -65 mV the synaptic current that is generated by activating these channels would be outward (hyperpolarizing) if V_{syn} is below -65 mV or inward (depolarizing) if V_{syn} is above -65 mV. It is not uncommon for $GABA_A$- mediated currents to be depolarizing in developing neural tissue. Thus it is not strictly correct, although frequently done, to refer to GABA as an inhibitory transmitter. One should take care in describing a $GABA_A$- mediated synapse as inhibitory; the current's sign depends on where V_{syn} is relative to V. Note, if V is close to V_{syn} little synaptic current will be generated, even if a large conductance $g_{syn}s$ is activated. On the other hand the membrane potential would be effectively clamped to V_{syn} until the conductance de-activates. In this case the $GABA_A$synapse acts as a strong shunt in the membrane; other modest-sized synaptic inputs would be ignored during this time. (XX see exercise XX).

The transmitter GABA acting through $GABA_B$ receptors can lead to a very slow inhibition with a conductance that rises and decays on the order of 100 or more ms. The current is carried primarily by K^+ ions and so the reversal potential may be -70 to -90 mV. The simple model in Eqn. (8.10) cannot account for this slow current. One shortcoming is that the model predicts a peak shortly after the depolarization of V_{pre} while $GABA_B$ mediated inhibition peaks only much later. A minimal model for this current would involve at least two dynamic variables.

Typical sizes of I_{syn} at a single synapse are a few picoamperes and may evoke responses (e.g. in cortical neurons) of 0.1 to 1 mV. Many inputs must be summed in order to bring the neuron to firing threshold. Generally the post-synaptic response to multiple inputs, even in the subthreshold regime, however is not a linear summation of individual inputs. This is because the synaptic current depends on V_{post}, in particular through the driving force $V_{post} - V_{syn}$. If V_{post} is far from V_{syn} then the dependence on V_{post} is very weak, as say for AMPA-mediated excitation if V_{post} is near rest. But in other cases, say for a $GABA_A$-mediated synapse we would not get linear summation: doubling say the number of inputs does not double the synaptic current. This is easy to see for a passive membrane system, as we considered above, with steady synaptic conductance input, $g_s = constant = g_{syn}s$. The steady response $\overline{V}$ would be

$$\overline{V} = V_{syn} g_s / (g_m + g_s) \tag{8.12}$$

saturating for large g_s at V_{syn}, as we expect. While increasing g_s drives V_{post} closer to V_{syn} the increment in synaptic current diminishes for large g_s: dI_{syn}/dg_s behaves like g_s^{-2} for large g_s; this is the sublinear summation effect.

In exercises we do transient input to passive cell, then to active cell. This conveys a general msg - but is it really impt for understanding syn fn? Demonstrate shunting effect: brief epsc on top of slow shunt - if shunt is large, then do not see the epsc. Do the following in the text: Also, timing of inhib'n and excitation: before or after as in dir'n selectivity (contrast with APs arriving from 2 cells w/ gap jn coupled – no difference which one is first). For a neuron in which inputs are distributed over the dendritic tree, the spatial, as well the, temporal distribution of incoming signals determines the net response. For example, suppose there is simultaneously timed excitation and inhibition delivered at different locations along one dendritic branch. An inhibitory synapse located closer to the soma will be more effective at reducing the response to the excitatory input than if it is located more distally on the branch.

8.3 When Active Cells Might or Not Synchronize

In order to illustrate some effects of mutual synaptic coupling between cells we will consider the simple case of two identical cells, each of which is autorhythmic, and examine conditions for which the cells tend to fire together or apart. We are asking about the synchronization patterns in this simple two-cell network. Classical notions are that mutual excitation tends to make cells synchronous (in-phase) while mutual inhibition pushes them apart leading to anti-phase behavior. That is, if two excitatory cells are somewhat out-of-phase the firing of the leading cell encourages the follower to fire sooner and thus bringing the cells more nearly in-phase. While for inhibitory cells that are somewhat out-of-phase the leading cell's firing will delay the follower, increasing their phase difference. Successive cycles would increase their phase difference to 180^o but not beyond, since then the follower would act as the leader pushing the phase difference back toward 180^o. These expectations and some surprises will be illustrated below when we consider the effects of synaptic time scales.

Here we will use the Morris-Lecar model in Type I mode, so that near the threshold for repetitive firing the steady firing frequency can be made arbitrarily low. We dictate here that the gating variable's kinetics are relatively slow and that the stimulating current is adjusted so that the cell model is firing slowly, about 15 Hz.

First we consider the case of mutual excitation. In Fig. (8.5) (left panels) we confirm the expectation that the cells will fire together. The cells are substantially out-of-phase before we actually implement the coupling, but then afterwards they converge to a pattern of near sychrony with one cell preceding the other by just a slight bit. When the coupling is first turned on the follower cell immediately advances and throughout

the transient phase of synchronization the cells are causing each other to fire faster. Interestingly, as synchrony is established the cells slow down to nearly their intrinsic frequencies - as if the coupling is only to synchronize them. When comparing the time courses we see that during the transient phase the leader cell's voltage is more affected than the follower's. The synaptic current from the follower at first reduces the leader's post-spike hyperpolarization. Then, as the follower catches up, this synaptic current is delivered when the leader is still strongly depolarized and it's intrinsic conductances swamp the perturbing effect of the synaptic input.

For this preceding example the synaptic conductance time course has fast rise and fast decay phases; the conductance is essentially activated only during the presynaptic depolarization. If we allow for the synaptic decay to be much slower, with all other parameters and initial conditions unchanged, we find that these two cells now fire in anti-phase (Fig. (8.5), right panels). The frequency of each cell is nearly twice that of an isolated cell. This is understandable. Since the synaptic current decays more slowly it provides a longer-lived depolarizing influence, and it is strongest during a cell's trajectory as it rises toward threshold, when it most responsive to depolarizing influences. Note, if the output of this two-cell network converges onto a common target the effective delivery rate, because of the antiphase pattern, is twice that of each - four times that of an individual cell.

For the examples in this Section, we have chosen the parameter values in order to emphasize the importance of synaptic time scales in determining firing patterns in networks. This is an active area of research. Deeper understanding will be achieved and, for now, we caution that it should not to be taken as universal that fast (slow) excitatory synaptic coupling leads to in-phase (anti-phase) firing. In fact, for the example in Fig. (8.5) (left) different initial conditions to such coupled cells can lead to anti-phase locking even for these fast synapses.

Next we consider the case of two cells (the same cells as above) coupled with inhibitory synapses. We start the cells with different initial voltages and watch them settle slowly into an antiphase rhythm (Fig. (8.6)) during the first 800 ms of the simulation. During this portion the inhibitory synapses have fast kinetics and we are confirming the classical expectation that inhibition leads to antiphase firing between a cell pair. In these voltage time courses one can clearly see the hyperpolarizing effect of the synaptic inputs. As a cell's voltage rises from its minimum the partner fires and sends a brief pulse of outward current which halts transiently the rising voltage. At $t = 800$ ms the decay rate of inhibition is slowed from $\beta = 1$ to $\beta = 0.1$. Within a few cycles the cells lock into perfect synchrony. Slowly decaying mutual inhibition can lead to in-phase locking amongst neural oscillators. This behavior has been proposed as the mechanism for gamma rhythms that are seen in various brain regions, and are believed to have a functional role in some cognitive processes [ref'ces].

As a secondary note, although we do not show it here this particular network with the fast inhibitory synapses is bistable. In addition to the anti-phase behavior (for $t < 800$ ms) it also has a stable in-phase behavior for some set of initial states.

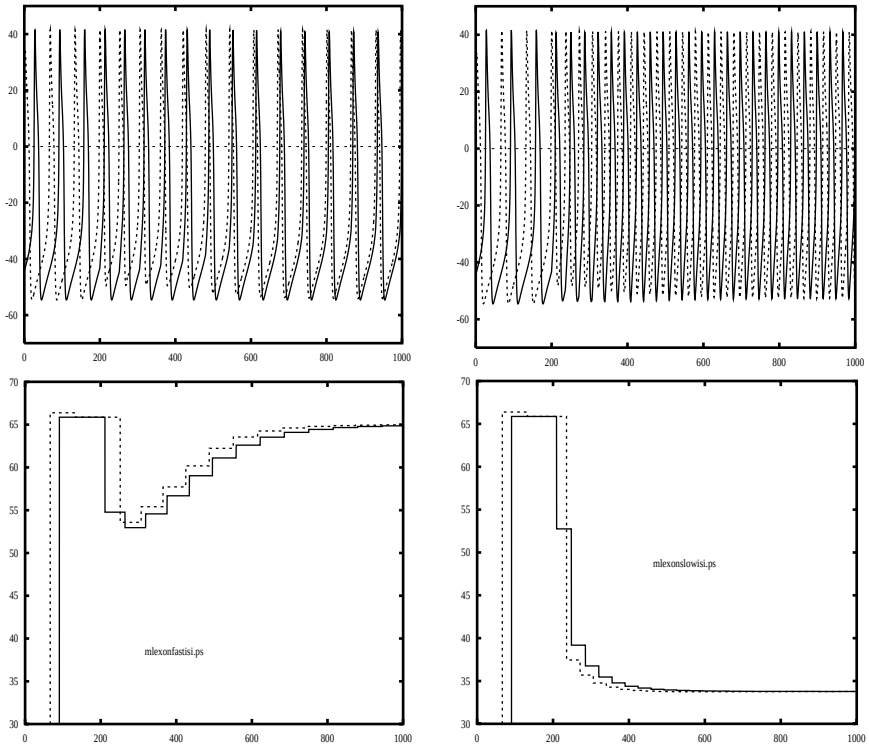

Figure 8.5 Left Panels: time courses of V1, V2 and ISIs (below)- synchrony with fast excitation. Right Panels: V1 and V2 and ISI- antiphase synchrony with slow excitation. Maybe an inset to show schematic. Cells are uncoupled until t=200 ms. Params as in Figs 2-3 except here $\phi = 0.1$ and $I_{app} = 15$; for A: $\alpha = 3, \beta = 1$; for B: $\alpha = 3, \beta = 0.1$

The examples above are very idealized, and primarily directed toward rhythmicity. The parameters have been chosen in order for us to illustrate several features about temporal patterning in mutually coupled pairs with just minimal adjustments from one case to the next. Important questions arise about how these features might carry over to larger networks. In a case of mixed fast and slow synaptic coupling are the synchronizing or de-synchronizing effects more important? Are the patterns robust to effects of noise and heterogeneity? What if there is a mixture of gap junctional and synaptic coupling, in regimes where their effects counteract?

Beyond these examples one seeks to understand how circuits that underlie cognitive function are wired up. How does a neural system use to advantage these various biophysical knobs in addition to connectivity schemes to implement various computational strategies? Give an example of a simple network that does ("computes") something.

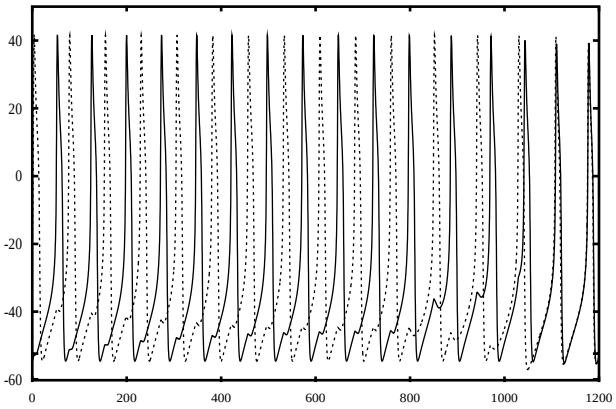

Figure 8.6 Fast inhibition to get anti-phase behavior for $t < 800$ ms; slowly decaying inhibition for $t > 800$ ms leads to in-phase.

CHAPTER 9

Biochemical Oscillations

John J. Tyson

07-28

Biochemical and biophysical rhythms are ubiquitous characteristics of living organisms, from rapid membrane oscillations in nerve cells to slow cycles of ovulation in mammals Table (**??**). In this chapter we will consider how certain fundamental molecular interactions (autocatalysis and negative feedback) combine to generate some of these rhythms. Along the way, we apply these ideas to simple models of glycolysis, cAMP signaling, periodic cell division, circadian rhythms, and calcium oscillations. Some of these phenomena are described in more detail in other chapters of this book.

One of the first biochemical oscillations to be discovered was the periodic conversion of sugar to alcohol in anaerobic yeast cultures (Chance et al., 1973). The oscillation was easily observed as periodic changes in fluorescence Fig. (9.1) from the essential intermediate, NADH, which shuttles electrons from the sugars (1/2 Hexose $\rightarrow$ 3-phosphoglyceric acid + 2 e^-) to pyruvate (pyruvic acid + 2 e^- $\rightarrow$ CO_2 + ethanol). In the laboratories of Britton Chance and Benno Hess it was demonstrated that these oscillations arise from a curious property of the enzyme, phosphofructokinase (PFK), which catalyzes the phosphorylation of fructose-6-phosphate to fructose-1, 6-bisphosphate, using ATP as the phosphate donor Fig. (9.2A). To properly regulate the production of ATP by the glycolytic pathway, PFK is inhibited by the endproduct of the pathway (ATP) and activated by ADP. Hence, the substrate of the regulatory enzyme is also an allosteric inhibitor, and the product an allosteric activator (these terms will be defined and illustrated shortly). As we shall see, "substrate inhibition" and "product activa-

Figure 9.1 Glycolytic oscillations. Sustained oscillations in NADH fluorescence in yeast cells *Saccharomyces* from Pye 1971. GOLDBETER FIG 2.2

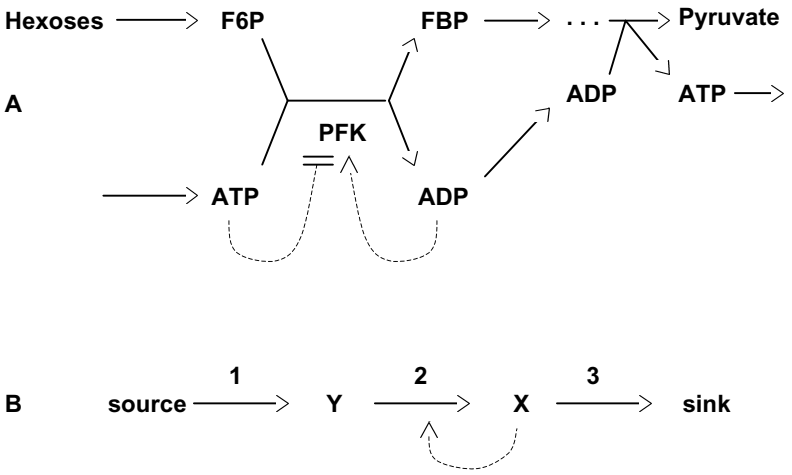

Figure 9.2 Mechanism of glycolytic oscillations. (A) The control properties of the enzyme phosphofructokinase (PFK) are thought to be responsible for the generation of oscillations in the glycolytic pathway. PFK catalyzes the conversion of fructose-6-phosphate (F6P) into fructose-1,6-bisphosphate (FBP), using ATP as phosphate-group donor. PFK activity is allosterically modulated by ATP (inhibitor) and ADP (activator). F6P is steadily supplied to PFK by a sugar source ("Hexoses") and FBP is steadily utilized in the production of metabolites ("Pyruvate"). ADP and ATP are also recycled by other metabolic processes. (B) Simplified mechanism. Reaction 1 is a steady supply of substrate Y for reaction 2, whose product X is removed by reaction 3. X activates the enzyme (PFK) catalyzing reaction 2. Roughly speaking, $Y = F6P + ATP, X = FBP + ADP$, "source" = hexoses, and "sink" = pyruvate.

tion" are regulatory signals that destabilize the steady state of a dynamical system and generate the possibility of oscillations.

Another classic example of rhythmic behavior in biology is periodic growth and division of well-nourished cells. This phenomenon will be studied thoroughly in the next chapter, but for now, to illustrate some basic ideas, we focus on the periodic accumulation and degradation of cyclins during the division cycle of yeast cells Fig. (9.3). Kim Nasmyth (1996) and others have shown that these oscillations are intimately connected to dynamical interactions between CLN-type cyclins and CLB-type cyclins Fig. (9.4). CLNs (in combination with a kinase subunit called CDC28) activate their own synthesis (product activation or "autocatalysis") and inhibit the degradation of CLBs. As CLBs accumulate, they inhibit the synthesis of CLNs, causing CLN-dependent kinase activity to drop and CLB degradation to increase. The mutual interplay of CLN and CLB generate periodic appearance of their associated kinase activities, which drive the crucial events of the budding yeast cell cycle (bud emergence, DNA synthesis, mitosis, and cell division).

Figure 9.3 Cyclin fluctuations during the cell cycle in budding yeast

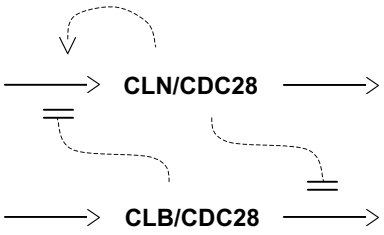

Figure 9.4 Mechanism of cyclin oscillations. Budding yeast cells contain two classes of cyclins: CLN and CLB. These cyclins combine with a kinase partner (CDC28) to make active dimers. CDC28 subunits are always in excess, so dimer activity is limited by cyclin availability (i.e., cyclin synthesis and degradation, arrows 1-4 in the diagram). CLN/CDC28 activates the transcription factor that promotes CLN synthesis and inhibits the proteolytic enzymes that degrade CLB. In return, CLB/CDC28 inhibits the transcription factor that promotes CLN synthesis.

The third example that we shall use in this chapter concerns periodic changes in physiological properties (physical activity, body temperature, reproduction, etc.) entrained to the 24 h cycle of light and darkness so prevalent to life on earth. These rhythms are not driven solely by the external timekeeper, because they persist under constant conditions of illumination and temperature Fig. (9.5). Under constant conditions, the organism exhibits its own "endogenous" rhythm, which is close to, but not exactly, 24 h (hence, "circadian" or "nearly daily"). The basic molecular mechanism of circadian rhythms has been uncovered only recently, by research in the laboratories of Michael Rosbash, Michael Young, Jay Dunlap, and others (Dunlap, 1999). Central to the mechanism is a protein called PER, which, after being synthesized in the cytoplasm, moves back into the nucleus to inhibit the transcription of its own mRNA Fig. (9.6A). The time-delayed negative-feedback loop in Fig. (9.6B), as we shall see, is another common theme in biochemical oscillators.

In this chapter, we explore in detail the connections among autocatalysis, positive feedback, and negative feedback in generating oscillatory behavior in biochemical reaction systems. The chapter is based in part on a paper written under my direction by Emery Conrad, in partial fulfillment of an M.S. degree in Mathematics at Virginia Tech.

9.1 Biochemical Kinetics and Feedback

In general, a biochemical reaction network is a schematic diagram of "boxes and arrows". Each box is a chemical species. Solid arrows coming into the box represent chemical reactions producing that species; solid arrows leaving the box represent reactions consuming that species. Dashed arrows from a box to a solid arrow represent control by one species of a chemical reaction involving other species. For instance, one of the reactive species may be a protein that catalyzes reactions elsewhere in the network, or it may be a metabolite that modifies the activity of enzymes catalyzing distant reactions in the network. Dashed arrows can have either barbed (>) or blunt (||) ends, representing activatory or inhibitory influences, respectively.

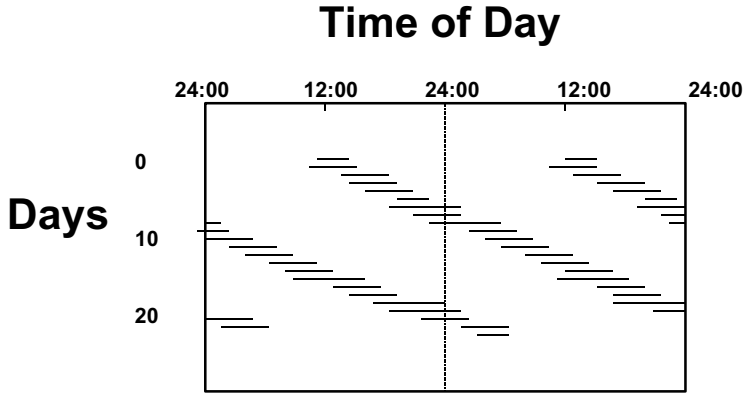

Figure 9.5 . Endogenous circadian rhythm of activity. The black bars represent the sleep episodes of a human being isolated from all external temporal cues (variable light, temperature, etc.). The sleep episodes are plotted twice on each line to emphasize that the endogenous period of sleepiness is longer than 24 h. From ???????????

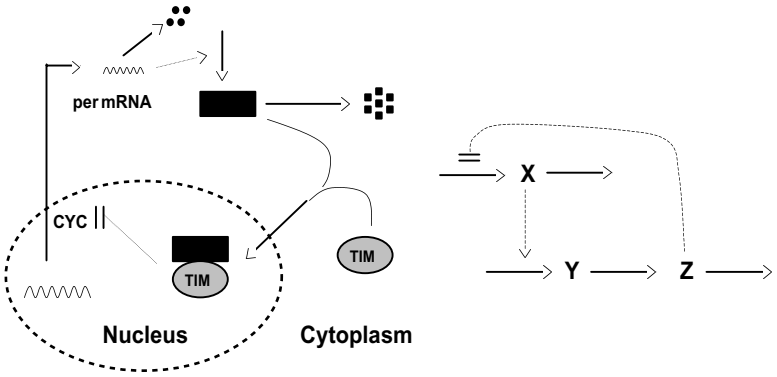

Figure 9.6 . A mechanism for circadian rhythms in animals. (A) A protein called PER is known to play a crucial role in circadian rhythms in fruit flies and mice. The per gene is transcribed in the nucleus, with the help of two transcription factors, CLK and CYC. per mRNA is then transported to the cytoplasm where it codes for PER protein. PER protein is processed in the cytoplasm by phosphorylation and by binding to other proteins, such as TIM and CRY. Properly processed PER then moves back into the nucleus, where it disrupts the binding of CLK and CYC, turning off the transcription of per. (B) A schematic representation of the negative feedback loop in panel A. This is Goodwin's (1966) classical mechanism for periodic protein expression, driven by feedback repression of transcription.

To each reaction in a biochemical network is associated a rate law (with accompanying kinetic parameters). Hence, the network implies a set of rate equations of the form

$$\frac{dx}{dt} = v_{in1} + v_{in2} + \ldots - v_{out1} - v_{out2} - \ldots = f(x;p) \tag{9.1}$$

where t = time, x = concentration of species X, and $v_{in1}, v_{out1}, \ldots$ are the rates of the various reactions that produce and consume X. We lump together all these rate laws into a nonlinear function $f(x;p)$, where p is a vector of kinetic parameters. In general, we can think of x as a vector of concentrations of all the time-varying components in the reaction network, $x_i = [X_i]$, and f as a vector-valued function. In component form,

$$\frac{dx_i}{dt} = f_i(x_1, x_2, \ldots, x_n; p_1, p_2, \ldots, p_r), i = 1, \ldots, n. \tag{9.2}$$

In the theory of biochemical oscillations, based on rate equations of this sort, a crucial role is played by elements of the Jacobian matrix, $\mathbf{J} = [a_{ij}]$, where $a_{ij} = \partial f_i / \partial x_j$. $\mathbf{J}$ is a square matrix $(n \times n)$. We remark, first of all, that the diagonal elements of the Jacobian matrix of a chemical reaction system are usually negative, $a_{ii} < 0$. This is so because v_{out} terms in Eqn. (9.1) are always proportional to the concentration of the substance being destroyed, so $\partial f_i / \partial x_i$ always has one or more negative terms. Positive contributions to a_{ii} are rare because autocatalysis (reactions that produce X_i at a rate that increases with $[X_i]$) are rare.

Common to biochemical networks are complex feedback loops, whereby the products of one reaction affect the rates of other reactions. A feedback loop can be defined as a set of non-zero elements of the Jacobian matrix that connect in a loop: $a_{ij}a_{jk}a_{kl}\ldots a_{mi} \neq 0$

Representative feedback loops are illustrated in Fig. 9.7.

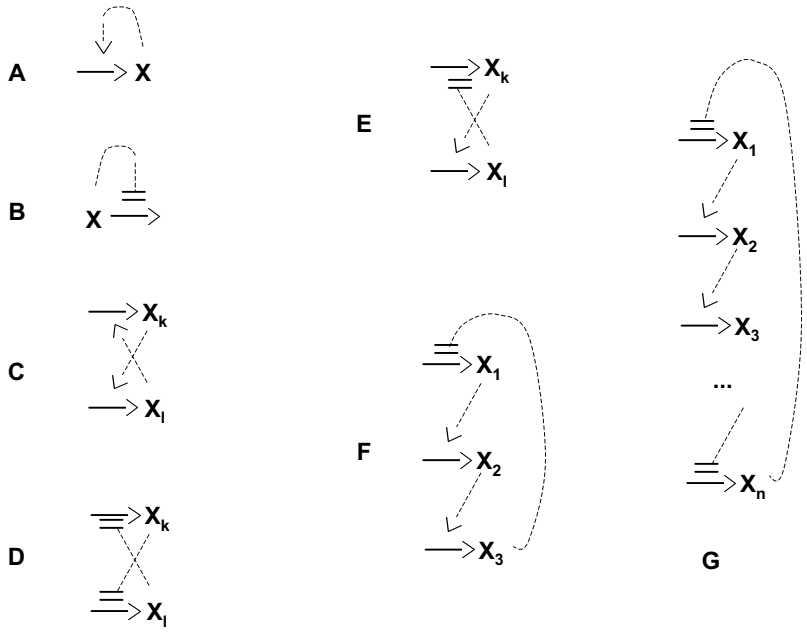

Figure 9.7 . Representative feedback loops.

(A) Autocatalysis ($a_{ii} > 0$), though rare, plays a major role in biochemical oscillations, as will become clear. We have already seen examples of autocatalysis in the mechanisms of glycolysis and yeast division Fig. (9.2) and Fig. (9.4).
(B) Autocatalysis also occurs when a chemical decelerates the rate of its own destruction.
(C) Indirect autocatalysis occurs through a positive feedback loop (a_{ij} and $a_{ji} > 0$), whereby X_i activates the production of X_j and X_j returns the favor.
(D) A two-component, positive feedback loop is also created by a pair of antagonistic species ($a_{ij} < 0$ and $a_{ji} < 0$).
(E) A two-component, negative feedback loop ($a_{ij}, a_{ji} < 0$) is created when X_i activates the production of X_j and X_j inhibits the production of X_i.
(F) Longer negative feedback loops are common.
(G) Long feedback loops are either positive or negative, depending on the sign of the product $a_{1n}a_{n,n-1}\ldots a_{43}a_{32}a_{21}$.

Before we can speak definitively about the effects of feedback in biochemical reaction networks, we need to know how to characterize the rates of enzyme-catalyzed reactions that are subject to regulation by "distant" effectors, i.e., chemical species other than the reactants and products of the enzyme.

9.2 Regulatory Enzymes

Regulatory enzymes are usually multisubunit proteins with binding sites both for reactants (on the catalytic subunits) and for activators and inhibitors (on the regulatory subunits). They are often called "allosteric" enzymes (allo = other, steric = shape) because they bind small molecules whose shapes are unrelated to the structure of the enzyme's substrates. Although there are more sophisticated and accurate ways to characterize allosteric regulatory enzymes, we shall limit ourselves to straightforward generalization of the Michaelis-Menten equation Section (**??**) (4.4?). First, we consider the effects of cooperative binding of substrate to a multisubunit enzyme.

For simplicity, consider a two-subunit enzyme (EE) that converts substrate (S) into product (P). The binding constant and turnover number of each subunit depends on whether the other (identical) subunit is bound to S or not. The mechanism can be written:

$EE + S \leftrightarrow EES$	dissociation constant $= k_{-1}/k_1$
$EES \rightarrow EE + P$	rate constant $= k_3$
$EES + S \leftrightarrow SEES$	dissociation constant $= k_{-2}/k_2$
$SEES \rightarrow EES + P$	rate constant $= k_4$

As in Section (**??**) (4.4?), we can make pseudo-steady state approximations on the enzyme-substrate complexes,

$$\frac{[EES]}{[EE_T]} = \frac{[S]/K_{m1}}{1 + ([S]/K_{m1}) + ([S]^2/K_{m1}K_{m2})}$$

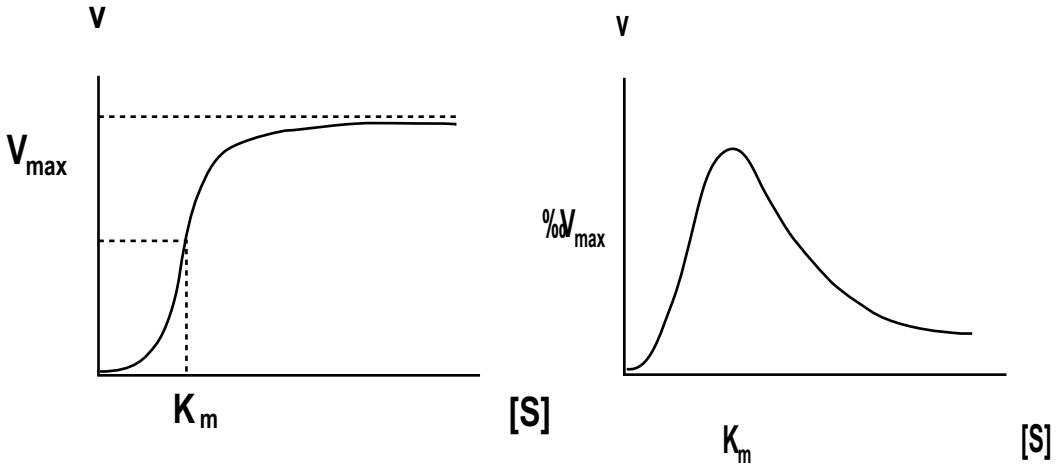

Figure 9.8 Rate laws for activation and inhibition of multisubunit enzymes by cooperative binding. See Eqn. (**??**)

$$\frac{[SEES]}{[EE_T]} = \frac{[S]^2/K_{m1}K_{m2}}{1 + ([S]/K_{m1}) + ([S]^2/K_{m1}K_{m2})}$$

where $[EE_T] = [EE]+[EES]+[SEES], K_m1 = (k_{-1}+k_3)/k_1$, and $K_{m2} = (k_{-2}+k_4)/k_2$. Now it is easy to write an equation for the rate of the reaction:

$$v = \frac{d[P]}{dt} = -\frac{d[S]}{dt} = \frac{[EE_T]\left(\frac{[S]}{K_{m1}}\right)\left(k_3 + k_4\left(\frac{[S]}{K_{m2}}\right)\right)}{1 + \left(\frac{[S]}{K_{m1}}\right) + \left(\frac{[S]^2}{K_{m1}K_{m2}}\right)} \tag{9.3}$$

We can distinguish two interesting, limiting cases of Eqn. (9.1).

Hill equation: $K_{m1} \to \infty, K_{m2} \to 0$, such that $K_{m1}K_{m2} = K_m^2 =$ constant

$$v = \frac{V_{max}([S]/K_m)^2}{1 + ([S]/K_m)^2}, V_{max} = k_4[EE_T] \tag{9.4}$$

Substrate inhibition: $k_3 \to \infty, K_{m1} \to \infty, K_{m2} \to 0$, such that $K_{m1}K_{m2} = K_m^2 =$ constant, $k_3K_{m2} \to \infty$, and $k_3[EE_T]K_m/K_{m1} = V_{max} =$ constant

$$v = \frac{V_{max}[S]/K_m}{1 + ([S]/K_m)^2} \tag{9.5}$$

Eqn. (9.4) and Eqn. (9.5) are plotted in Fig. (**??**).

It is easy to generalize these equations to the case of 3 or more subunits.

Rate laws like Eqn. (9.3) are said to express "cooperative" kinetics. The "empty" enzyme (EE) has low affinity for substrate (K_{m1} large), but as the enzyme picks up its first substrate molecule, the two subunits change their conformation to a high affinity form (K_{m2} small, such that $K_m = (K_{m1}K_{m2})^{1/2}$ is physiologically significant). In the

case of Hill's equation (9.1a), we say that the enzyme shows positive cooperativity; in the other case (9.1b), negative cooperativity.

Cooperative binding of ligands to a multisubunit enzyme is not limited to substrates. Other small molecules may bind to the enzyme and alter its catalytic properties (either its affinity for substrates or its rate of converting bound substrates into products). Such enzymes are called "allosteric" because, in addition to substrate-binding sites, they have "other sites" for binding regulatory molecules that either activate or inhibit the enzyme. Allosteric proteins play crucial roles in the regulation of metabolic pathways, membrane transport, gene expression, etc. Relatively simple algebraic expressions for allosteric effects can be derived by the reasoning above.

For instance, consider a tetrameric enzyme, with two catalytic subunits (EE) and two regulatory subunits (RR), which bind substrate (S) and ligand (L), respectively. In this case, the holoenzyme may exist in 9 different forms. If these forms are in rapid equilibrium with each other, at any given concentrations of substrate and ligand, then

$$[E_T] = [E_{00}]\left(1 + \frac{[S]}{K_{m1}} + \frac{[S]^2}{K_{m1}K_{m2}}\right)\left(1 + \frac{[L]}{K_{11}} + \frac{[L]^2}{K_{11}K_{12}}\right)$$

where $[E_T]$ = total concentration of enzyme in all 9 forms, $[E_{00}]$ = concentration of holoenzyme unbound to substrate or ligand, $[S]$ = substrate concentration, $[L]$ = ligand concentration, K_m's = Michaelis constants for substrate binding (as defined above), and K_l's = Michaelis constants for ligand binding (defined similarly). If, for example, the only form of the enzyme with significant catalytic activity is $\begin{bmatrix} SEES \\ LRRL \end{bmatrix}$, then the rate of the reaction is

$$v = V_{max}\frac{[S]^2/K_{m1}K_{m2}}{1 + \frac{[S]}{K_{m1}} + \frac{[S]^2}{K_{m1}K_{m2}}} \cdot \frac{[L]^2/K_{11}K_{12}}{1 + \frac{[L]}{K_{11}} + \frac{[L]^2}{K_{11}K_{12}}} \tag{9.6}$$

In this case, the ligand is an allosteric activator of the enzyme. For an allosteric inhibitor,

$$v = V_{max}\frac{[S]^2/K_{m1}K_{m2}}{1 + \frac{[S]}{K_{m1}} + \frac{[S]^2}{K_{m1}K_{m2}}} \cdot \frac{1}{1 + \frac{[L]}{K_{11}} + \frac{[L]^2}{K_{11}K_{12}}} \tag{9.7}$$

A comprehensive and accurate kinetic theory of allosteric enzymes is much more complicated than what has been presented (see, e.g., Rubinow, 1980; Goldbetter, 1996), but Eqn. (9.6) and Eqn. (9.7) will serve our purposes in this chapter.

Finally, suppose EE and S above are not "multisubunit enzyme" and "substrate" but "dimeric transcription factor" and "ligand". The active form of the transcription factor promotes the expression of some gene, and the presence of ligand alters the distribution of transcription factor among its various forms: EE, EES and SEES. Depending on which form of transcription factor is most active, the rate of gene expression can be activated and/or inhibited by ligand:

ligand effect	active form	relative rate of gene expression
inhibition	EE	$\frac{1}{1+([S]/K_{m1})+([S]^2/K_{m1}K_{m2})}$
activation	$SEES$	$\frac{[S]^2/K_{m1}K_{m2}}{1+([S]/K_{m1})+([S]^2/K_{m1}K_{m2})}$
mixed	EES	$\frac{[S]/K_{m1}}{1+([S]/K_{m1})+([S]^2/K_{m1}K_{m2})}$

9.3 Two-component Oscillators Based on Autocatalysis

First, we consider some minimal requirements for oscillations in chemical reaction systems. If the "network" is absurdly simple, with only one time-varying component, then oscillations are, generally speaking, impossible because, for $x(t)$ to be periodic, dx/dt must take on both positive and negative values at some values of x, which is impossible if $f(x;p)$ is a continuous, single-valued function of x. Thus, to understand biochemical oscillations, we must start with two-component networks, described by a pair of ODEs

$$\frac{dx}{dt} = f(x,y) \tag{9.8}$$

$$\frac{dy}{dt} = g(x,y) \tag{9.9}$$

where x and y are (non-negative) concentrations of the two components, and we have suppressed the dependence of f and g on parameters, for the time being.

Bendixson's negative criterion states that if $\frac{\partial f}{\partial x} + \frac{\partial g}{\partial y}$ is of constant sign in some region R of the x, y plane, then there can be no periodic solution of system Eqn. (9.9) in R. Hence, autocatalysis is a necessary requirement for sustained oscillations in a two-component chemical reaction system.

In general, we can expect system Eqn. (9.9) to have one or more steady-state solutions (x^*, y^*), satisfying $f(x^*, y^*) = 0$ and $g(x^*, y^*) = 0$. The stability of such steady states is determined by the eigenvalues of the Jacobian matrix (see Section (**??**))

$$\mathbf{J} = \begin{bmatrix} f_x(x^*,y^*) & f_y(x^*,y^*) \\ g_x(x^*,y^*) & g_y(x^*,y^*) \end{bmatrix} = \begin{bmatrix} a_{11} & a_{12} \\ a_{21} & a_{22} \end{bmatrix}$$

The eigenvalues of $\mathbf{J}$ are the roots of the characteristic equation $\lambda^2 - (a_{11} + a_{22}) + (a_{11}a_{22} - a_{12}a_{21}) = 0$, namely

$$\lambda = \frac{1}{2}\left[a_{11} + a_{22} \pm \sqrt{(a_{11} + a_{22})^2 - 4(a_{11}a_{22} - a_{12}a_{21})}\right]$$

For the steady state to be stable, $\mathrm{Re}(\lambda)$ must be < 0 for both eigenvalues. If $a_{11}a_{22} - a_{12}a_{21} = \det(\mathbf{J}) < 0$, then $\mathbf{J}$ has one positive and one negative eigenvalue, and the steady state is a saddle point. If $\det(\mathbf{J}) > 0$ and $a_{11} + a_{22} = \mathrm{tr}(\mathbf{J}) < 0$, then the steady state is stable, whereas, if $\det(\mathbf{J}) > 0$ and $\mathrm{tr}(\mathbf{J}) > 0$, then the steady state is an unstable node or focus.

In general, the trace and determinant of $\mathbf{J}$ depend continuously on the kinetic parameters in f and g. If, by varying one of these parameters (call it p_1), we can carry $\mathrm{tr}(\mathbf{J})$ from negative to positive values, with $det(\mathbf{J}) > 0$, then the steady state loses stability at $\mathrm{tr}(\mathbf{J}) = 0$ (when $p_1 = p_{crit}$, say), and small amplitude limit cycle solutions surround the steady state for values of p_1 close to p_{crit}. We say that periodic solutions arise by a Hopf bifurcation at $p_1 = p_{crit}$ (see Section (**??**)).

Biochemical oscillations usually arise by this mechanism, so we will consider first the requirements for Hopf bifurcation in a two-component network. In chemical reaction systems, the diagonal elements of the Jacobian matrix are usually negative numbers, reflecting the various steps by which species X is transformed into something else. If both a_{11} and a_{22} are always < 0, then a Hopf bifurcation cannot occur. At least one of them must be > 0 for some values of the kinetic parameters. For a diagonal element to be positive, species X must be "autocatalytic," i.e., with increasing [X], the rates of production of X increase faster than the rates of destruction. If a_{11} and a_{22} are of opposite sign, then a_{12} and a_{21} must also be of opposite sign in order for $\det(\mathbf{J})$ to be positive. Thus we have two characteristic sign patterns for Jacobian matrices that typically produce Hopf bifurcations in chemical reaction systems:

$$\mathbf{J} = \begin{bmatrix} + & + \\ - & - \end{bmatrix} \text{ and } \begin{bmatrix} + & - \\ + & - \end{bmatrix} \tag{9.10}$$

Next, we describe the sorts of biochemical networks that produce these sign patterns and generate periodic solutions via Hopf bifurcations.

9.3.1 Substrate-Depletion Oscillator

The simplest oscillatory mechanism is probably the linear pathway in Fig. (**??**). Species Y is converted into X by an enzyme that is activated by its product. Hence, the production of X is autocatalytic; the reaction speeds up as [X] increases, until the substrate, Y, is depleted so much that the reaction ceases.

Using a rate law for the allosteric enzyme like those derived in the previous section, we can write a pair of ODEsdescribing this mechanism:

$$\frac{d[X]}{dt} = v_2[Y]\frac{\epsilon^2 + ([X]/K_l)^2}{1 + ([X]/K_l))^2} - k_3[X] \tag{9.11}$$

$$\frac{d[Y]}{dt} = k_1 - v_2[Y]\frac{\epsilon^2 + ([X]/K_l)^2}{1 + ([X]/K_l))^2} \tag{9.12}$$

Clearly, the Jacobian of system Eqn. (9.12) at its steady state could potentially have the first sign pattern in Eqn. (9.10).

It is convenient to define "dimensionless" variables, $x = [X]/K_l, y = [Y]/K_l$ and $t' = k_3 t$, and a new variable, $z = x + y$, and write system (9.7) as

$$\frac{dx}{dt'} = \nu(z - x)\frac{\epsilon^2 + x^2}{1 + x^2} - x \tag{9.13}$$

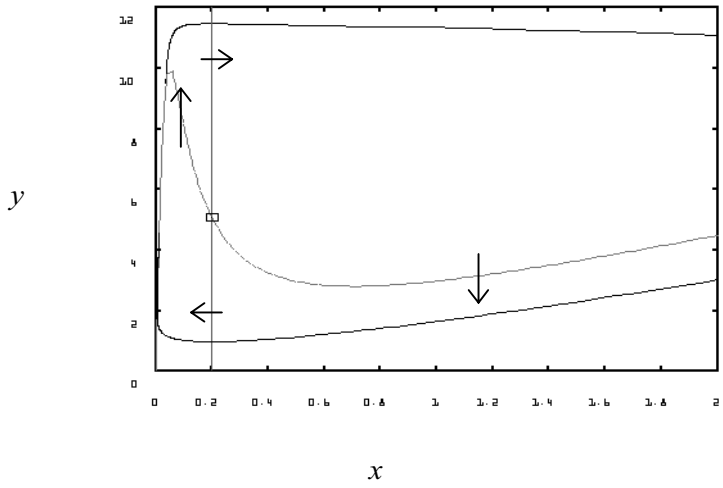

Figure 9.9 Phase plane portrait of a typical substrate-depletion oscillator, Eq. (9.8). Parameter values: v = 1, k = 0.2, e = 0.05. The solid lines are the x-nullcline (marked by short vertical arrows) and the y-nullcline (horizontal arrows). The nullclines intersect at an unstable steady state (o). The dashed line is the stable limit cycle solution (periodic orbit) of the dynamical system.

$$\frac{dz}{dt'} = \kappa - x \tag{9.14}$$

where $\nu = v_2/k_3$ and where $\kappa = \frac{k_1}{k_3 K_l}$. The steady state for this model satisfies $x = \kappa$ and $\nu(z - x) = \kappa\frac{1+\kappa^2}{\epsilon^2+\kappa^2}$. For the Jacobian matrix of system Eqn. (9.14) at the steady state, it is easy to show that $\det(\mathbf{J}) > 0$ and

$$\mathrm{tr}(\mathbf{J}) = -1 - \nu\frac{\epsilon^2+\kappa^2}{1+\kappa^2} + \frac{2\kappa^2(1-\epsilon^2)}{(\epsilon^2+\kappa^2)(1+\kappa^2)} \tag{9.15}$$

$$= -\frac{(1+\nu)\kappa^4 - (1-3\epsilon^2-2\nu\epsilon^2)\kappa^2 + \epsilon^2(1+\nu\epsilon^2)}{(\epsilon^2+\kappa^2)(1+\kappa^2)} \tag{9.16}$$

It should be obvious from Eqn. (9.16) that $\mathrm{tr}(\mathbf{J}) < 0$, if x^* is either close to 0 or very large. On the other hand, $\mathrm{tr}(\mathbf{J}) > 0$ and the steady state is unstable if x^* takes on intermediary values. For ϵ small, the steady state is unstable when

$$\epsilon < \kappa < (1-\nu)^{(} - 1/2) \tag{9.17}$$

which may, alternatively, be expressed as conditions on the input rate of Y

$$\epsilon k_3 < \frac{k_1}{k_3 K_l} < \sqrt{\frac{k_3}{k_3 + v_2}} \tag{9.18}$$

Between these limits the system executes stable limit cycle oscillations.

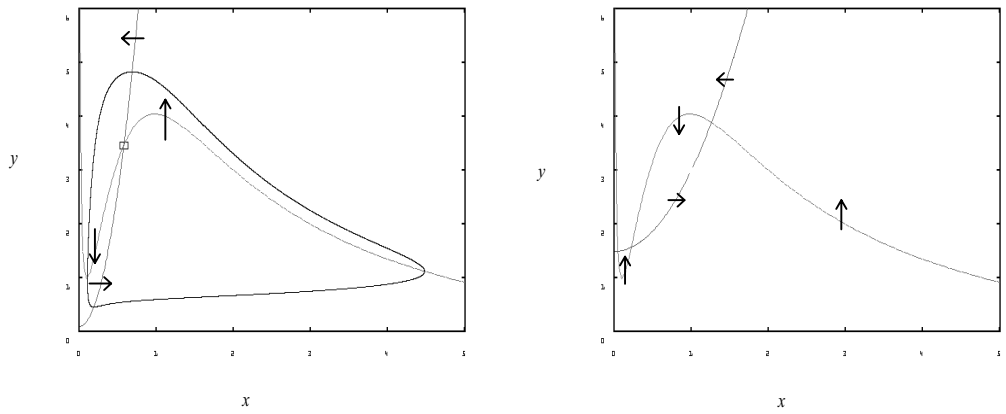

Figure 9.10 Phase plane portrait of a typical activator-inhibitor system, Eq. (9.11). The solid lines are nullclines, intersecting at stable () or unstable (o) steady states. The dashed lines are representative orbits of the dynamical system. (A) Oscillation, for a = 0.1, b = 0.1, c = 100, e = 0.1, t = 5. (B) Bistability, for a = 0.1, b = 1.5, c = 1, e = 0.1, t = 5.

As we have often seen in this book, for two-component dynamical systems, it is informative to plot nullclines in the phase plane. For System (**??**)),

$$\begin{aligned} z &= x + \frac{x(1+x^2)}{\nu(\epsilon^2+x^2)} && \text{“}x \text{ nullcline”} \\ x &= \kappa && \text{“}z \text{ nullcline”} \end{aligned}$$

These nullclines are plotted in Fig. (**??**). The x' nullcline has extrema at the roots of

$$(1+\nu)x^4 - (1 - 3\epsilon^2 - 2\nu\epsilon^2)x^2 + \epsilon^2(1+\nu\epsilon^2) = 0$$

Notice that the steady state loses stability exactly when x^* passes through the extrema of the x nullcline.

9.3.2 Activator-Inhibitor Oscillator

Looking back to Eqn. (**??**), we see that there are two sign patterns consistent with Hopf bifurcation in a two-component biochemical reaction system. The first is illustrated by the substrate-depletion oscillator in Fig. (**??**), and the second by the activator-inhibitor model in Fig. (**??**). The ODEs describing Fig. (**??**) are

$$\begin{aligned} \frac{d[X]}{dt} &= v_1 \frac{\epsilon^2 + ([X]/K_m)^2}{1 + ([X]/K_m)^2} \cdot \frac{1}{1 + ([Y]/K_l)^2} - k_2[X] \\ \frac{d[Y]}{dt} &= k_3 - \frac{k_4[Y]}{1 + ([X]/K_j)} \end{aligned}$$

In terms of dimensionless variables ($x = [X]/K_m, y = [Y]/K_l, t' = v_1 t/K_m$), these equations become

$$\frac{dx}{dt'} = \frac{\epsilon^2 + x^2}{1 + x^2} \cdot \frac{1}{1 + y^2} - ax \tag{9.19}$$

$$\tau \frac{dy}{dt'} = b - \frac{y}{1 + cx} \tag{9.20}$$

where $a = k_2 K_m / v_1, b = k_3/k_4 K_l, c = K_m/K_j, \tau = v_1/k_4 K_m$.

Rather than analyze the stability of the steady state algebraically, which is difficult, we go directly to phase plane portraits Fig. (**??**). It is easy to find parameter values that give limit cycle solutions to Eqn. (9.20).

Intuitively, the origin of the oscillations is clear. When Y is rare, X increases autocatalytically. Abundant X stimulates accumulation of Y (by inhibiting Y's degradation), which feeds back to inhibit the production of X. After X disappears, Y is also destroyed, and then X can make a comeback. Mechanisms like this one, whose Jacobian matrix has sign pattern $\begin{bmatrix} + & - \\ + & - \end{bmatrix}$, are called "activator-inhibitor" models.

Two-component mechanisms without autocatalysis easily generate oscillations and bistabilty, as we have just seen. They also exhibit a rich structure of bifurcations to more complicated behavior: see Boissonade & deKepper (1980) and Guckenheimer (1986).

9.4 Three-component Networks without Autocatalysis

In the previous section we have seen that two-component reaction systems can oscillate if they have autocatalysis (a_{11} or a_{22} positive) and negative feedback (a_{12} and a_{21} opposite sign). In this section we examine networks of three components (x, y, z) with Jacobian matrices of the form

$$\mathbf{J}_{\pm} = \begin{bmatrix} -\alpha & 0 & \pm\phi \\ c_1 & -\beta & 0 \\ 0 & c_2 & -\gamma \end{bmatrix}$$

where $\alpha, \beta, \gamma, c_1, c_2, \phi$ are all positive constants. Since the diagonal elements of the Jacobian are all negative, the system lacks autocatalysis. $\mathbf{J}_+$ describes a system with a positive feedback loop, and $\mathbf{J}_-$ one with a negative feedback loop.

9.4.1 Positive Feedback Loop and Routh-Hurwitz Theorem

First, let us see if Hopf bifurcations are possible in a system with a pure positive feedback loop, i.e., a Jacobian of the form $\mathbf{J}_+$ at the steady state. The eigenvalues of

this Jacobian matrix are roots of the characteristic equation

$$\begin{aligned} g(\lambda) &= \lambda^3 + (\alpha+\beta+\gamma)\lambda^2 + (\alpha\beta+\beta\gamma+\gamma\alpha)\lambda + \alpha\beta\gamma - c_1c_2\phi \\ &= \lambda^3 + A\lambda + B\lambda + C = 0 \end{aligned}$$

The roots of this equation can be characterized by the

Routh-Hurwitz Theorem: Let $g(\lambda_i) = 0$ for $i = 1, 2, 3$. Then $Re(\lambda_i) < 0$ for $i = 1, 2, 3$, if and only if (i) $A > 0$, (ii) $C > 0$, and (iii) $AB > C$.

Hence, in order for the steady state of the positive feedback loop to be unstable, we must insist that $C = \alpha\beta\gamma - c_1c_2\phi < 0$. In this case, $\mathbf{J}_+$ has at least one real positive root, call it $\lambda_1 > 0$. Then, $g(\lambda) = (\lambda - l_1)h(\lambda)$, where $h(\lambda) = \lambda^2 + D\lambda + E$ and $D = A + \lambda_1 > 0, E = -C/\lambda_1 > 0$. From the quadratic formula, it follows that the two roots of $h(\lambda) = 0$ must have $Re(\lambda_i) < 0$. Hence, it is impossible for a steady state with Jacobian matrix $\mathbf{J}_+$ to undergo a Hopf bifurcation.

It is possible for a positive feedback loop to have multiple steady state solutions, with two stable nodes separated by a saddle point. At the saddle point, $\lambda_1 > 0$ and $Re(\lambda_i) < 0$ for $i = 2, 3$. See Exercise (**??**) and Exercise (**??**).

9.4.2 Negative Feedback Oscillations

$\mathbf{J}_-$ determines the stability of the steady state in a three-variable system with a pure negative feedback loop. In this case,

$$g(\lambda) = \lambda^3 + (\alpha+\beta+\gamma)\lambda^2 + (\alpha\beta+\beta\gamma+\gamma\alpha)\lambda + \alpha\beta\gamma + c_1c_2\phi = 0$$

and the Routh-Hurwitz Theorem implies that the steady state is unstable if and only if

$$(\alpha+\beta+\gamma)(\alpha\beta+\beta\gamma+\gamma\alpha) < \alpha\beta\gamma + c_1c_2\phi$$

Furthermore, if equality holds, then $g(\lambda)$ has conjugate roots on the imaginary axis at $\pm i\sqrt{\alpha\beta+\beta\gamma+\gamma\alpha}$.

9.4.3 The Goodwin Oscillator

The quintessential example of a biochemical oscillator based on negative feedback alone was invented by Brian Goodwin (1963), see Fig. (**??**). The kinetic equations describing this mechanism are

$$\begin{aligned} \frac{d[X_1]}{dt} &= \frac{v_0}{1 + ([X_3]/K_m)^p} - k_1[X_1] \\ \frac{d[X_2]}{dt} &= v_1[X_1] - k_2[X_2] \\ \frac{d[X_3]}{dt} &= v_2[X_2] - k_3[X_3] \end{aligned}$$

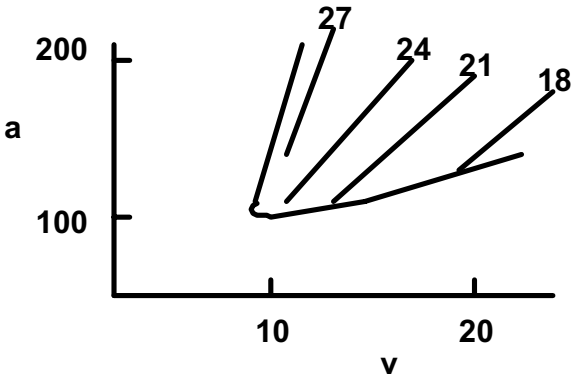

Figure 9.11 Locus of Hopf bifurcations in the Bliss-Painter-Marr equations (9.13), for b1 = b2 = 0.2 h-1. We also plot loci of constant period (18 - 27 h) within the region of limit cycle oscillations.

Here, $[X_1], [X_2]$ and $[X_3]$ are concentrations of mRNA, protein and endproduct, respectively; v_0, v_1 and v_2 determine the rates of transcription, translation and catalysis; k_1, k_2 and k_3 are rate constants degradation of each component; $1/K_m$ is the binding constant of endproduct to transcription factor; and p is a measure of the cooperativity of endproduct repression.

Next we introduce dimensionless variables:

$$x_1 = \frac{v_1 v_2 [X_1]}{k_2 k_3 K_m}, x_2 = \frac{v_2 [X_2]}{k_3 K_m}, x_3 = [X_3]/K_m$$
$$t' = \alpha t, \text{ where } \alpha = \frac{v_0 v_1 v_2}{K_m k_2 k_3}$$

In terms of these new variables, the dynamical system becomes

$$\frac{dx_1}{dt} = \frac{1}{1+x_3^p} - b_1 x_1, \frac{dx_2}{dt} = b_2(x_1 - x_2), \frac{dx_3}{dt} = b_3(x_2 - x_3) \tag{9.21}$$

where $b_1 = k_i/\alpha$

Furthermore, to make the example easier, we shall assume that $b_1 = b_2 = b_3$. In this case, the dynamical system has a steady state at $x_1 = x_2 = x_3 = \xi$, where ξ is the unique real positive root of $\frac{1}{1+\xi^p} = b\xi$. The Jacobian matrix at this steady state is $\mathbf{J}_-$, with $\alpha = \beta = \gamma = b, c_1 = c_2 = b$, and $\phi = \frac{p\xi^{p-1}}{(1+\xi^p)^2} = bp(1-b\xi)$. Hence, the characteristic equation is $(b+\lambda)^3 + b^2\phi = 0$, whose roots are

$$\lambda_1 = -b - b\sqrt[3]{p(1-b\xi)}$$
$$\lambda_{2,3} = -b + b\sqrt[3]{p(1-b\xi)}\{\cos(\pi/3) \pm i\sin(\pi/3)\}$$

Clearly, the steady state of Goodwin's model is unstable when $p(1-b\xi) > 8$, or, equivalently, $b\xi < \frac{p-8}{p}$. Hence, if p (the cooperativity of the negative feedback loop) is greater than 8, then we can choose k small enough to destabilize the steady state solution of Goodwin's equations. At the critical value of k, the steady state undergoes a Hopf bifurcation, spinning off small-amplitude periodic solutions with period close to $2\pi/\text{Im}(\lambda_{2,3}) = 2\pi/b\sqrt{3}$.

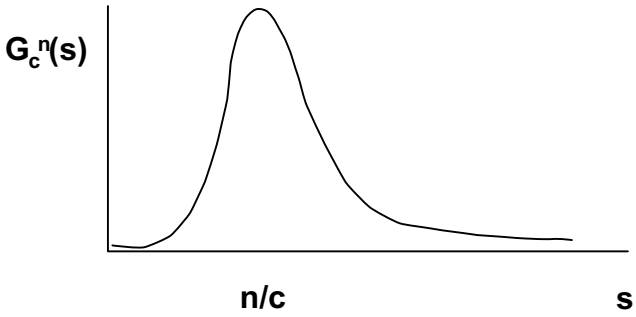

Figure 9.12 The kernel Gcn(s) for distributed time lag in Eqn. (**??**).

In Exercise (**??**), you are asked to generalize this derivation to negative feedback loops with an arbitrary number n of components. You will find that the steady state is unstable when $b\xi < \frac{p-p_{\min}}{p}$, where $p_{\min} = \sec^n(\pi/n)$. Notice that $p_{\min} \to 1^+$ as $n \to \infty$.

The analysis of Hopf bifurcations in Goodwin's model uncovers a number of problems with his negative feedback mechanism for biochemical oscillations (Griffith, 1968b). In a three-variable system (mRNA, Protein, Endproduct), the cooperativity of feedback must be very high, $p > 8$. Also, it is necessary, in this case, for the degradation rate constants of the three components to be nearly equal. If not, $p_{\min}$ increases dramatically; e.g., if one of the k_i's is ten-fold larger than the other two, then $p_{\min} = 24$. The value of $p_{\min}$ can be reduced by lengthening the loop ($p_{\min} \to 1^+$ as $n \to \infty$), but one must still ensure that the k_i's are nearly equal.

Bliss, Painter & Marr (1982) fixed these problems by a slight modification of Goodwin's equations:

$$\frac{dx_1}{dt} = \frac{a}{1+x_3} - b_1 x_1, \frac{dx_2}{dt} = b_1 x_1 - b_2 x_2, \frac{dx_3}{dt} = b_2 x_2 - \frac{c x_3}{K + x_3} \tag{9.22}$$

Notice that the feedback step is no longer cooperative ($p = 1$) and the uptake of endproduct is now a Michaelis-Menten function. The steady state of this system is $(x_1^*, x_2^*, x_3^*) = (a/b_1(1+\xi), a/b_2(1+\xi), \xi)$, where ξ is the unique real positive root of $\frac{a}{1+\xi} = \frac{c\xi}{K+\xi}$. The stability of this steady state is determined by the roots of the characteristic equation $(b_1 + \lambda)(b_2 + \lambda)(\beta + \lambda) + b_1 b_2 \phi = 0$ where $\beta = \frac{cK}{(K+\xi)^2}$ and $\phi = \frac{a}{(1+\xi)^2}$.

The characteristic equation is hard to solve in this completely general case. In order to get a start on it, we make some simplifying assumptions. First, suppose that $K = 1$, so $\xi = a/c$. Next, suppose $b_1 = b_2 < c$, and choose $a = c\left(\sqrt{c/b_1} - 1\right)$ so that $\beta = b_1$ as well. Furthermore, $\phi = b_1 a/c = b_1\left(\sqrt{c/b_1} - 1\right)$. In this case, the eigenvalues of the Jacobian matrix are $\lambda_1 = -b_1\left(1 + \sqrt[3]{a/c}\right), \lambda_{2,3} = -b_1 + b_1\sqrt[3]{a/c}\{\cos(\pi/3) \pm i\sin(\pi/3)$. The dynamical system has a Hopf bifurcation at $c = 81b_1$, provided $a = 8c = 648b_1$. If we set $b_1 = 0.1$, then the Hopf bifurcation occurs at $c = 8.1, a = 64.8$. Starting at this point, we can use *XppAut* to trace out the locus of Hopf bifurcations as a, c and b_1 change; e.g. Fig. (**??**).

9.5 Time-Delayed Negative Feedback

In Goodwin's equations and Bliss-Painter-Marr's modified version, we assumed implicitly that there are no time delays in the processes of transcription, translation, or endproduct repression. However, there are surely some delays in transcription and translation associated with mRNA and protein processing in the nucleus and cytoplasm, respectively. And there are also bound to be delays in the feedback term, because the endproduct must move into the nucleus, bind with transcription factors, and interact with the "upstream" regulatory sites of the gene to affect its rate of transcription. If we lump all these delays together, we can write a delayed-differential equation for negative feedback:

$$\frac{d[X]}{dt} = \frac{a}{1+(Z/K_m)^p} - b[X] \tag{9.23}$$

where $z(t)$ is a functional of the past history of $x(t)$. For a discrete time lag,

$$Z(t) = [X](t-\tau), \text{ with } \tau = \text{ constant.} \tag{9.24}$$

For a distributed time lag,

$$Z(t) = \int_{-\infty}^{t} [X](s) G_c^n(t-s) ds, \text{ with } G_c^n(s) = \frac{c^{n+1}}{n!} s^n e^{-cs}. \tag{9.25}$$

The kernel, $G_c^n(s)$, is plotted in Fig. 9.x. It is easy to show that G has a maximum at $s = n/c$. As n and c increase, with n/c fixed, the kernel approaches a delta function, and the distributed time lag approaches the discrete time lag with $\tau = n/c$.

9.5.1 Distributed time lag and the linear chain trick

If we define

$$Z_j(t) = \int_{-\infty}^{t} [X](s) G_c^j(t-s) ds, j = 0, 1, \ldots, n$$

then the system Eqn. (9.23) and Eqn. (9.25) can be written as the set of ODEs:

$$\begin{aligned}
\frac{d[X]}{dt} &= \frac{a}{1+(Z/K_m)^p} - b[X] \\
\frac{dZ_0}{dt} &= c([X] - Z_0) \\
\frac{dZ_j}{dt} &= c(Z_{j-1} - Z_j), j = 1, 2, \ldots, n
\end{aligned}$$

That is, the distributed time-delay model, with kernel $G_c^n(s)$, is identical to a classical Goodwin negative feedback loop of length $n+2$. If $c = b$, then the loop has a Hopf

bifurcation at $\xi = \frac{a}{bK_m} \cdot \frac{p-p_{\min}}{p}$, where $p_{\min} = \left[\sec\left(\frac{\pi}{n+2}\right)\right]^{n+2}$ and the dimensionless number ξ is the unique real positive root of $\xi^{p+1} + \xi - \frac{a}{bK_m} = 0$.

As an example, suppose $n = 6$ and $p = 4$. In this case, $p_{min} = 1.88$ and the Hopf bifurcation occurs at $0.78 = \frac{bk_m}{a}\xi = \frac{1}{1+\xi^4}$, or $\xi = 0.73$. Hence, the critical value of b is $b_{crit} = 1.07a/K_m$, and oscillations occur for $b < b_{crit}$. Small values of b mean long time delays, $\tau = n/c = 6/b$. The minimal time delay for oscillations is, hence, $\tau_{\min} = 5.6K_m/a$.

9.5.2 Discrete Time lag

For the case of a discrete time lag, we must solve the delay-differential equation

$$\frac{dx}{dt} = \frac{1}{1 + x(t-\tau)^p} - bx \tag{9.26}$$

where x and t have been scaled to eliminate the parameters a and K_m from Eqn. (9.23). Eqn. (9.26) has a steady state solution, x^*, satisfying $x^{p+1} + x - b^{-1} = 0$. To investigate the stability of the steady state, we rewrite Eqn. (9.26) in terms of $y(t) = x(t) - x^*$,

$$\frac{dy}{dt} = -\phi y(t-\tau) - by(t) + \text{higher order terms, and}$$
$$\phi = \frac{p(x^*)^{p-1}}{\left(1 + (x^*)^p\right)^2} = pb(1 - bx^*) = \frac{pb}{1 + (x^*)^{-p}}.$$

Looking for solutions of the form $y(t) = y_0 e^{\lambda t}$, we find that λ must satisfy the characteristic equation $\lambda + b = -\phi e^{-\lambda\tau}$. At a Hopf bifurcation, the eigenvalue λ must be purely imaginary; $\lambda = \pi\omega$. Thus, for Eqn. (9.26) to exhibit periodic solutions (with period $= 2\pi/\omega$) at a Hopf bifurcation, we must insist that

$$b = -\phi\cos(\omega\tau), \quad \omega = \phi\sin(\omega\tau) \tag{9.27}$$

From these equations, we can determine the oscillatory frequency (ω) and critical time delay (τ) at the onset of limit cycle oscillations:

$$\omega = \sqrt{\phi^2 - b^2} = b\sqrt{\{p/[1 + (x^*)^{-p}]\}^2 - 1}$$
$$\tau = \frac{\cos^{-1}\left(-[1 + (x^*)^{-p}]/p\right)}{b\sqrt{\{p/[1 + (x^*)^{-p}]\}^2 - 1}}$$

Hence, a necessary condition for Hopf bifurcation is $1 + (x^*)^{-p} < p$. For example, if $p = 4$, then x^* must be $> (1/3)^{1/4} \approx 0.760$, which implies that b must be $< 3^{5/4}/4 \approx 0.987$. If $b = 1/2$, then $x^* = 1$ and $\omega = \sqrt{3}/2, \tau = 2\pi\sqrt{3}/9$. Hence, for $b = 1/2$ and $p = 4$, small amplitude oscillations, with period≈ 7.255, bifurcate from the steady state as the time delay increases beyond 1.209.

9.6 Circadian Rhythms

Everyone is familiar with his or her own 24-hour sleep-wake cycle. Many other aspects of human physiology also exhibit daily rhythms, including body temperature, urine production, hormone secretion, and skin cell division. Such rhythms are observed in all kinds of plants, animals and fungi, as well as unicellular organisms, and even bacteria. Because these rhythms persist in the absence of external cues (light intensity, temperature, etc.), they reflect an endogenous oscillator within cells that runs at a period close to 24 h ("circa-dian" means "nearly daily").

Biologists have long been puzzled by the molecular basis of circadian rhythms. Although a fundamental breakthrough was made by Konopka and Benzer in 1971, with their discovery of the per gene in Drosophila (mutations of which alter the endogenous circadian rhythm of affected flies), it was 25 years before the molecular details of the circadian oscillator began to come clear. We know now that PER protein inhibits transcription of the per gene, through a complicated process involving phosphorylation by DBT kinase, binding to TIM subunits, transport into the nucleus, and interaction with the transcription factors (CLK and CYC).

It is clear to all that the control system is dominated by a time-delayed, negative feedback loop, quite close in principle to Goodwin's original negative feedback oscillator. Numerous theoreticians have exploited the interesting nonlinear dynamics of delayed negative feedback in order to model certain characteristics of circadian rhythms. Ruoff and Bensing (1996) have explored the capabilities of Goodwin's equations Eqn. (9.21), with $p = 9$, to account for temperature compensation, entrainment, and phase resetting. Goldbeter (1995) proposed a more complicated model, based loosely on Goodwin's idea (with $n = 5$ and $p = 4$), supplemented with reversible phosphorylation steps and nuclear transport (see Exercise 9.7.15). Like Bliss, Painter and Marr, Goldbeter used Michaelis-Menten kinetics for many steps in his mechanism and found that oscillations were very robust (persisting even for $p = 1$). In subsequent papers, Leloup and Goldbeter (1997, 1998) have studied temperature compensation and phase resetting in this model. Perhaps the simplest model of circadian rhythms is negative feedback with discrete time delay, Eqn. (9.23) and Eqn. (9.24). In a recent paper, Lema, Golombek and Echave (2000) have explored the capabilities of these equations to account for phase-response curves and entrainment.

Tyson et al. (1999) have taken a different approach, noting that phosphorylation of PER by DBT induces rapid degradation of PER, but multimers of PER and TIM are not readily phosphorylated by DBT. They show that a mechanism of this sort can be described by a two-component model with autocatalysis (PER inhibits its own degradation). Their "substrate-depletion" model is pursued in Exercise (**??**).

9.7 Combination Oscillators

We have been discussing simple models of biochemical oscillators that can be described either by two-component mechanisms with autocatalysis (positive feedback) or by time-delayed negative feedback. Realistic models of some biochemical control systems call for both positive and negative feedback loops. The behavior of such models combines the properties of the oscillators we have been discussing. Two important examples are cell cycle controls in frog eggs (Novak and Tyson, 1973; Borisuk and Tyson, 1998) and bursting oscillations in pancreatic b cells (Bertram, 1995; Sherman, 1997).

Exercises

1. Activator-inhibitor system. Consider the mechanism which can be described by the (scaled) differential equations

$$\frac{dx}{dt} = \frac{a + bx^2}{1 + x^2 + ry} - x, \frac{dy}{dt} = \epsilon(cx + y_0 - y)$$

   Basal parameter values: $a = 1, b = 5, c = 4, r = 1, y_0 = 0, \epsilon = 0.1$

   (a) Why is this called an "activator-inhibitor" system?
   (b) Draw phase plane portrait (nullclines and typical trajectories) for the basal parameter values.
   (c) Vary c and find the Hopf bifurcation points.
   (d) As you vary both c and y_0, how many qualitatively different phase plane portraits can you find? Sketch them.

2. Substrate-depletion system. Consider the mechanism which can be described by the (scaled) differential equations

$$\frac{dx}{dt} = a - xy^2, \frac{dy}{dt} = \epsilon + xy^2 - by$$

   Basal parameter values: $a = 0.5, b = 1, \epsilon = 0.05$

   (a) Why is this called a "substrate-depletion" system?

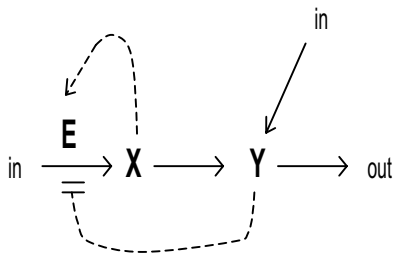

Figure 9.13 Exercise (1)

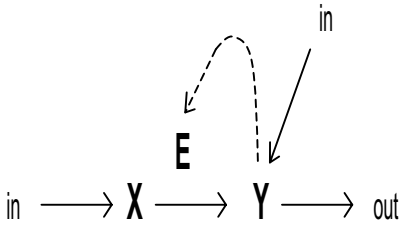

Figure 9.14 Exercise (2)

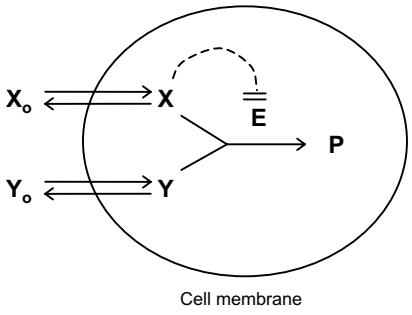

Figure 9.15 Exercise (3)

(b) Rewrite the ODEs in terms of y and $z = x + y$.
(c) Draw phase plane portrait (nullclines and typical trajectories) for the basal parameter values.
(d) Classify the stability of the steady state as a varies.

3. Substrate-inhibition oscillator. Perhaps the simplest example of a biochemical oscillator was proposed by Murray (*J. Theor. Biol.* **88**, 161-199, 1981):
The rate equations for this mechanism are

$$\frac{dX}{dt} = a(X_0 - X) - \frac{vXY}{K_{m1} + X + (X^2/K_{m2})}$$
$$\frac{dY}{dt} = a(Y_0 - Y) - \frac{vXY}{K_{m1} + X + (X^2/K_{m2})}$$

where a, b are membrane permeabilities, v is a rate constant, and the K_m's are dissociation constants of the enzyme-substrate complexes. Basal parameter values: $a = 1, b = 0.15, X_0 = 1, Y_0 = 6, v = 30, K_{m1} = 1, K_{m2} = .005$.

(a) Plot nullclines and some characteristic trajectories.
(b) Find points of Hopf bifurcation as Y_0 varies.
(c) For $b = 1, X_0 = 1.5, Y_0 = 4$, plot nullclines and trajectories
(d) Find the region of bistability in the (X_0, Y_0) plane.

4. Bifurcation theory. To learn the basic types of bifurcations possible in biochemical reaction systems, a simple model to practice on is

$$\frac{dx}{dt} = x(1-x)(1+x) - y, \frac{dy}{dt} = (x-a)(b-y) - c$$

Notice, first of all, that these ODEs do not describe a chemical reaction system (where x and y are chemical concentrations). Why? Because we are not dealing with chemistry *per se* here, we can let the parameters take on both + and - values. Although this model is not chemically realistic, all the bifurcations observed herein are also seen in *bona fide* biochemical kinetics.

   (a) Start with the parameter set: $a = -0.5, b = 0.5, c = 0.1$. Plot nullclines. Find steady states and their stability. Is there an oscillatory solution?
   (b) Set $b = 0$ and $a = -0.8$. Plot nullclines. Find steady states and their stability. Draw the "invariant sets" of the saddle point. Repeat for $a = -0.78, -0.77, -0.76, -0.7, -0.65$. For $a = -0.765$, show that there exists an unstable limit cycle around the steady state at $x = -0.498, y = -0.374$.
   (c) Use AUTO or LocBif to characterize the codimension-one bifurcations in this model. Plot x as a function of a, and look for Hopf points and saddle-node points. Then "grab" these bifurcation points and follow them in two parameters (a and b). The saddle-node points will trace out loci in the (a, b) plane that come together at a cusp point (a codimension-two bifurcation point). The Hopf points will trace out a locus that merges with a curve of saddle-nodes at a codim-2 bifurcation point called a Takens-Bogdanov bifurcation. For more information on these typical bifurcation sets, see the papers by Guckenheimer and Borisuk-Tyson in the reference list.
   (d) Set $a = -0.7, c = 0.53$. Vary b between 0.80 and 0.84. What happens to the limit cycle, the saddle point and the node? This bifurcation is called a SNIC (saddle-node on an invariant circle), or SNIPER (saddle-node infinite-period), or SNL1 (saddle-node-loop, codimension-one).

5. Gene expression (from Jeff Hasty, Boston Univ.). Consider a bacterial operon expressing two genes, *genX* and *genY*.

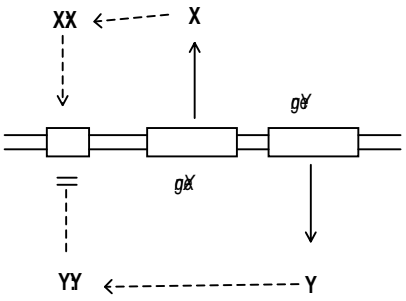

Figure 9.16 Exercise (5)

The proteins, X and Y, form homodimers, X_2 and Y_2, which then bind to the upstream regulatory sequence and affect the expression of *genX* and *genY*. X_2-binding stimulates gene expression, but Y_2-binding inhibits it. Assume that the homodimers are very stable and that they bind to the regulatory sequence with equal affinity.

(a) Show that the mechanism can be described by a pair of (scaled) ODEs

$$\frac{dx}{dt} = 1 + \frac{\alpha x^2}{1 + x^2 + y^2} - \beta x, \frac{dy}{dt} = \epsilon \left(1 + \frac{\alpha x^2}{1 + x^2 + y^2} \right) - \gamma x$$

where ϵ is the rate of expression of Y relative to that of X.

(b) Construct a phase plane portrait for this system, when $\alpha = 50, \beta = 10, \gamma = 1, \epsilon = 0.2$.

(c) Would you describe this oscillator as "activator-inhibitor" or "substrate-depletion."

(d) Find the locus of Hopf bifurcations in the (β, γ) parameter plane.

6. Glycolysis. In Sec 9.2.1 we studied a simple model of the glycolytic oscillator, Eqn. (9.12), and found that oscillations exist within a limited range of substrate injection rates, $k_{1,\text{lower}} < k_1 < k_{1,\text{upper}}$, where $k_{1,\text{lower}} = \epsilon k_3 K_l$, and $k_{1,\text{upper}} = \frac{k_3 K_l}{\sqrt{1+\nu}}$, where $v = v_2/k_3$ (see Eq. 9.10b).

(a) Show that the period of oscillation close to the two Hopf bifurcation points is given by

$$T_{\text{lower}} = \frac{2\pi}{k_3 \epsilon \sqrt{2v}}, T_{\text{upper}} = \frac{2\pi}{k_3} \sqrt{\frac{2+v}{v}}$$

(b) Hess & Boiteux (in Chance et al., 1973, p. 237) reported that $k_{1,\text{lower}} = 0.33$ mM/min, $T_{\text{lower}} = 8.6$ min, and $k_{1,\text{upper}} = 2.5$ mM/min, $T_{\text{upper}} = 3.5$ min. Supposing that $v \ll 1$, show that $\epsilon \cong k_{1,\text{lower}}/k_{1,\text{upper}} = 0.13$ and $T_{\text{upper}}/T_{\text{lower}} \cong 2\epsilon \cong 0.25$, which is not too far from the observed ratio, 0.4.

(c) For the parameter values, $\epsilon^2 = 0.017, K_l = 0.25mM, v_2 = 1$ min^{-1} and $k_3 = 10$ min^{-1}, use PhasePlane to compute $k_{1,\text{lower}}, T_{\text{lower}}, k_{1,\text{upper}}$, and T_{upper}, and compare your results to the observations of Hess & Boiteux.

7. For the model of cell cycle control in budding yeast, Eq. (9.11), with the parameter values given in Fig. 9.10, find the region of limit cycle oscillations in the (c, τ) plane. For extra credit, explore the bifurcations of this model in the (c, ϵ) plane.

8. Cyclic AMP dynamics. Martiel & Goldbeter (*Biophys. J.* **52**, 807-828, 1987) have presented a model of cyclic AMP oscillations in *Dictyostelium discoideum* that can be reduced to a set of three ODEs:

$$\frac{d\beta}{dt} = q\phi(\rho, \gamma) - k_{it}\beta$$
$$\frac{d\gamma}{dt} = k_{ht}\beta - k_e\gamma$$

$$\frac{d\rho}{dt} = f_2(\gamma)(1-\rho) - f_1(\gamma)\rho$$

where β = (scaled) concentration of intracellular cAMP, γ = (scaled) concentration of extracellular cAMP, ρ = fraction of cAMP membrane receptor in active form,

$$\phi(\rho,\gamma) = \frac{\epsilon + \alpha Y^2}{1+(1+\alpha)Y^2}, Y = \frac{\rho\gamma}{1+\gamma},$$
$$f_1(\gamma) = \frac{k_1 + k_2\gamma}{1+\gamma}, f_2(\gamma) = \frac{k_1' + k_2' c\gamma}{1+c\gamma}$$

Martiel & Goldbeter estimate the parameter values to be
Rate constants (units = min^{-1}): $q = 2400$, $k_{it} = 2.6, k_{ht} = .18, k_e = 5.4, k_1 = 0.36, k_2 = 0.0033, k_1' = 0.036, k_2' = 0.67$
Dimensionless parameters: $\epsilon = 0.0003, \alpha = 3, c = 10$.

(a) Martiel & Goldbeter say that, to a good approximation, $\beta = \frac{q}{k_{it}}\phi(\rho,\gamma)$. Why is this true? (Hint: singular perturbation argument.) Use this approximation to reduce the Martiel-Goldbeter model to two ODEs and study these equations with Phase Plane. Plot nullclines and time-courses. Study the bifurcations in these equations as the rate constants are varied.

(b) To model the response of cells to fixed levels of extracellular cAMP, let γ = constant, and solve

$$\frac{d\beta}{dt} = q\phi(\rho,\gamma) - k_{it}\beta, \frac{d\rho}{dt} = f_2(\gamma)(1-\rho) - f_1(\gamma)\rho$$

Plot $\beta(t)$ and $\rho(t)$ for stepwise increases of γ from 0 to 0.1, 1, or 10. The behavior you will observe is called "adaptation."

9. Positive feedback on gene transcription (*Griffith, J. Theor. Biol.* **20**, 209-216, 1968). Consider the simple case of a protein that activates transcription of its own gene: This mechanism is described by a pair of ODEs:

$$\frac{d[M]}{dt} = v_1\frac{\epsilon^2 + ([P]/K_l)^2}{1+([P]/K_l)^2} - k_2[M], \frac{d[P]}{dt} = k_3[M] - k_4[P]$$

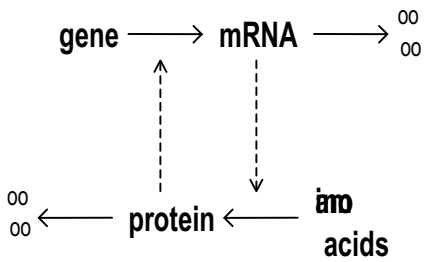

Figure 9.17 Exercise (9)

(a) How must the variables be scaled to write the ODEsin dimensionless form:

$$\frac{dm}{dt} = \frac{\epsilon^2 + p^2}{1 + p^2} - m, \frac{dp}{dt} = \kappa(\sigma m - p)?$$

(b) Assume that $\epsilon = 0.2, \kappa = 1$, and draw phase plane portraits for several values of σ.
(c) Find the bifurcation values of σ.
(d) Plot the steady state concentration of P as a function of σ.

10. Generalize the positive feedback system in the previous problem to a loop of arbitrary length.

(a) Show that, when properly scaled, the steady state solution of the dynamical equations is given by the roots of

$$\phi z = \frac{\epsilon^p + z^p}{1 + z^p}(*)$$

where ϕ = constant.
(b) Show that the system has saddle-node bifurcation points when (*) is satisfied simultaneously with

$$\phi = \frac{p z^{p-1}(1 - \epsilon^p)}{(1 + z^p)^2}(**)$$

(c) For $\epsilon \ll 1$, show that (*) and (**) are satisfied simultaneously for

$$z \approx \sqrt[p]{p-1}, \phi \approx \frac{1}{p}\sqrt[p]{(p-1)^{p-1}} \text{ and}$$
$$z \approx \epsilon\sqrt[p]{2/(p-1)}, \phi \approx \epsilon^{p-1}\sqrt[p]{(2/(p-1))^{p-1}}$$

(d) Compute the saddle-node bifurcation points for $p = 2$, 3, 4, and compare to numerical results from PhasePlane (pick some small value of ϵ).

11. Goodwin's equations. Generalize the analysis in Section 9.3.3 to a negative feedback loop with n components,

$$\frac{dx_1}{dt'} = \frac{1}{1 + x_n^p} - b_1 x_1, \frac{dx_j}{dt'} = b_j(x_{j-1} - x_j), j = 2, 3, \ldots, n.$$

Assume that $b_1 = b_2 = \ldots = b_n = b$, and show that the steady state ($x_1 = x_2 = \ldots = x_n = \xi$) is unstable when $b\xi < \frac{p - p_{\min}}{p}$, where $p_{\min} = \sec^n(\pi/n)$. Compute $p_{\min}$ for $n = 4, 8, 16$.

12. Modify the Bliss-Painter-Marr equations (9.13), by writing $\frac{a}{1+x_3^p}$ in the first differential equation. Let $a = 1, b_1 = b_2 = 0.1, K = 1$. Plot the locus of Hopf bifurcation points in the (p, c) parameter plane.

13. . Calcium-induced calcium release. Goldbeter, Dupont & Berridge (*Proc. Natl. Acad. Sci.* **87**, 1461-1465, 1990) have presented a two-variable model for Ca^{2+}

oscillations in cells:

$$\frac{dX}{dt} = v_0 + v_1\beta - V_2 + V_3 - k_4X + k_5Y, \frac{dY}{dt} = V_2 - V_3 - k_5Y$$

where

$$V_2 = v_2\frac{X^2}{K_2^2 + X^2}, V_3 = v_3\frac{Y^2}{K_R^2 + Y^2} \cdot \frac{X^4}{K_A^4 + X^4}.$$

In these equations, $X = [\mathrm{Ca}^{2+}]_{\text{cytosolic}}, Y = [\mathrm{Ca}^{2+}]_{\text{vesicular}}$,

v_0 = slow leak of Ca^{2+} into the cytosol from extracellular fluid
$v_1\beta$ = IP_3-induced release of Ca^{2+} into the cytosol from intracellular stores
V_2 = ATP-dependent Ca^{2+} pump
V_3 = Ca^{2+}-induced Ca^{2+}-release from storage vesicles
k_4 = Ca^{2+} elimination through the plasma membrane
k_5 = Ca^{2+} leak from storage vesicles

Goldbeter et al. estimated the parameters to be

$$v_0 = 1\mu M/s, v_1 = 7.3\mu\mathrm{M/s}, \beta = 0, v_2 = 65\mu M/s, K_2 = 1\mu M,$$
$$v_3 = 500\mu M/s, K_R = 2\mu M, K_A = 0.9\mu M, k_4 = 10s^{-1}, k_5 = 1s^{-1}$$

(a) Draw phase plane portraits for the basal parameter values.
(b) Increase β (the IP_3 signal) from 0 to 1 (its maximum value), and find values that correspond to Hopf bifurcations.
(c) To simulate a pulse of IP_3, let $\beta(t) = \beta_0 e^{-\alpha t}$, with $\alpha = 0.25\ \mathrm{s}^{-1}$. Try $\beta_0 = 0.85$ and 0.95. Plot $X(t)$. Compare to experimental results in *Xenopus* eggs (Fig. 9.12 in Goldbeter's book).

14. For the distributed time lag defined in Eq. (9.15b), show that

$$(a)\int_0^\infty G_c^n(s)ds = 1$$
$$(b)\frac{d}{ds}G_c^n(s) = c\left(G_c^{n-1}(s) - G_c^n(s)\right)$$
$$(c)G_c^n(s) \text{ has a maximum at } s = n/c.$$

15. Goldbeter (*Proc. R. Soc. Lond. B* **261**, 319-324, 1995) has presented a model for circadian rhythms of PER protein based on delayed negative feedback. His mechanism is
The corresponding kinetic equations are

$$\frac{dM}{dt} = \frac{v_s}{1 + (P_n + k_1)^n} - \frac{v_m M}{K_{m1} + M}$$
$$\frac{dP_0}{dt} = k_s M - \frac{V_1 P_0}{K_1 + P_0} + \frac{V_2 P_1}{K_2 + P_1}$$

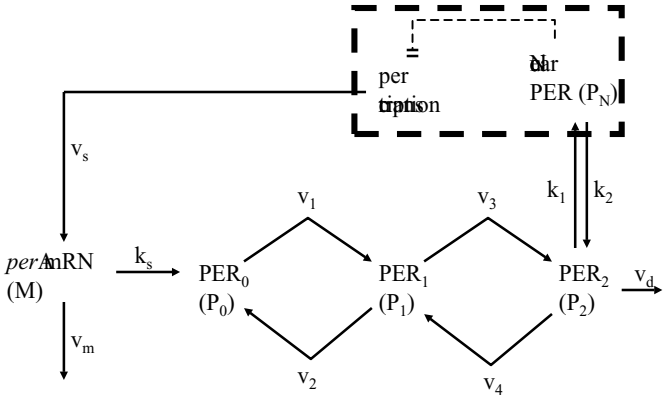

Figure 9.18 Exercise (15)

$$\frac{dP_1}{dt} = \frac{V_1 P_0}{K_1 + P_0} - \frac{V_2 P_1}{K_2 + P_1} - \frac{V_3 P_1}{K_3 + P_1} + \frac{V_4 P_2}{K_4 + P_2}$$
$$\frac{dP_2}{dt} = \frac{V_3 P_1}{K_3 + P_1} - \frac{V_4 P_2}{K_4 + P_2} - k_1 P_2 + k_2 P_N - \frac{v_d P_2}{K_d + P_2}$$
$$\frac{dP_N}{dt} = k_1 P_2 + k_2 P_N$$

with basal parameter values: $n = 4$,

$$v_s = 0.76\mu M/h, v_m = 0.65\mu M/h, v_d = 0.95\mu M/h,$$
$$k_s = 0.38h^{-1}, k_1 = 1.9h^{-1}, k_2 = 1.3h^{-1},$$
$$V_1 = 3.2\mu M/h, V_2 = 1.58\mu M/h, V_3 = 5\mu M/h, V_4 = 2.5\mu M/h,$$
$$K_1 = K_2 = K_3 = K_4 = 2\mu M, K_I = 1\mu M, K_{m1} = 0.5\mu M, K_d = 0.2\mu M.$$

(a) Solve these equations numerically, plotting M, P_N and P_T = [total PER protein] as functions of time (hours). Plot a projection of this orbit in the (M, P_T) plane.

(b) Plot the period of oscillation as a function of PER degradation rate, $0.5 < v_d < 2.5$. How might you use these results to explain the phenotypes of per^S and per^L mutant alleles, which cause short- and long-period autonomous rhythms (19 h and 28 h, respectively)?

(c) Construct a one-parameter bifurcation diagram for this model, showing the amplitude (P_{Tmin} and P_{Tmax}) and period of oscillations as functions of v_s (*per* gene dosage), for $0 < v_s < 4$.

(d) Construct a two-parameter bifurcation diagram, showing the locus of Hopf bifurcations in the (v_s, v_d) plane.

16. Tyson et al. (*Biophys. J.* **77**, 2411-2417, 1999) have presented a model for circadian rhythms of PER protein based on positive feedback. Their mechanism is

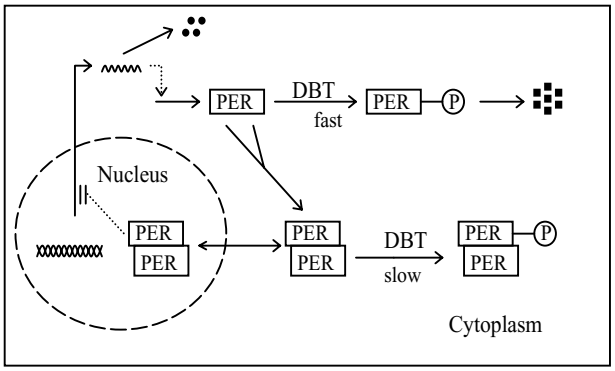

Figure 9.19 Exercise (16)

(a) Show that this mechanism can be described by three ODEs

$$\frac{dM}{dt} = \frac{v_m}{1+(P_2/A)^2} - K_m M$$
$$\frac{dP_1}{dt} = v_p M - \frac{k_1 P_1}{J + P_1 + 2P_2} - k_3 P_1 - 2k_a P_1^2 + 2k_d P_2 + \frac{2k_2 P_2}{J + P_1 + 2P_2} + 2k_3 P_2$$
$$\frac{dP_2}{dt} = k_a P_1^2 - k_d P_2 - \frac{2k_2 P_2}{J + P_1 + 2P_2} - 2k_3 P_2$$

where M = [mRNA], P_1 = [Protein], P_2 = [Dimer],

v_m, v_p = rate constants for synthesis of mRNA and protein
k_m, k_3 = rate constants for non-specific degradation of mRNA and protein
k_1, k_2 = rate constants for phosphorylation of protein and dimer
k_a, k_d = rate constants for association and dissociation of dimer
J, A = Michaelis constants for binding protein (and/or dimmer) to phosphatase and transcriptional regulation factors.

List all assumptions made in deriving these equations.

(b) Suppose the dimerization reaction is in rapid equilibrium. Show that

$$q = \frac{2}{1+\sqrt{1+8KP_T}}, P_1 = qP_T, P_2 = \frac{1-q}{2}P_T (\#)$$

where $P_T = P_1 + 2P_2$ = [total protein] and $K = k_a/k_d$ = equilibrium binding constant.

(c) Show that the system can now be described by a pair of ODEs

$$\frac{dM}{dt} = \frac{v_m}{1+(P_2/A)^2 - k_m M},$$
$$\frac{dP_T}{dt} = v_p M - \frac{k_1 P_2 + 2k_2 P_2}{J + P_T} - k_3 P_T$$

with P_1 and P_2 given as functions of P_T by (#) above.

Table 9.1 Biochemical and Cellular Rhythms Source: Goldbeter (1996), Rapp (1979).

Rhythm	Period
Membrane potential oscillations	10 ms - 10 s
Cardiac rhythms	1 s
Smooth muscle contraction	seconds - hours
Calcium oscillations	seconds - minutes
Protoplasmic streaming	1 min
Glycolytic oscillations	1 min - 1 h
cAMP oscillations	10 min
Insulin secretion (pancreas)	minutes
Gonadotropic hormone secretion	hours
Cell cycle	30 min - 24 h
Circadian rhythms	24 h
Ovarian cycle	weeks - months

(d) Given basal parameter values: $v_m = 1, v_p = 0.5, k_m = k_3 = 0.1, k_1 = 10, k_2 = 0.03, J = 0.05, K = 200, A = 0.1$, explore the dynamics of this regulatory system, using PhasePlane to plot phase portraits as various parameters are twiddled.

(e) Find the locus of Hopf bifurcations in the (k_1, K) plane.

9.8 Table

CHAPTER 10

Cell Cycle Controls

John Tyson and Bela Novak

07-28

In recent years, molecular biologists have uncovered a wealth of information about the proteins controlling cell growth and division in eukaryotes. The regulatory system is so complex that it defies understanding by verbal arguments alone. To probe into the details of cell cycle control requires mathematical modeling of the type practiced in this book. As in previous chapters, we will disassemble the complex control mechanism into manageable pieces, develop mathematical representations of the component parts, and then reassemble realistic models of the growth and division of yeast cells, embryonic cells, and somatic cells of multicellular organisms. But, first, what are the basic features of cell reproduction that we want to understand?

10.1 Physiology of the Cell Cycle in Eukaryotes

The cell cycle is the sequence of events by which a growing cell duplicates all its components and divides into two daughter cells, each with sufficient machinery and information to repeat the process (Fig. 1.2). The most important components are the cell's chromosomes, which contain linear DNA molecules in association with proteins. First, each DNA molecule must be accurately replicated, and then the two copies must be carefully segregated to daughter cells at division. In eukaryotic cells, these two processes occur in temporally distinct stages (Fig. 10.1). During S phase, a new copy of each

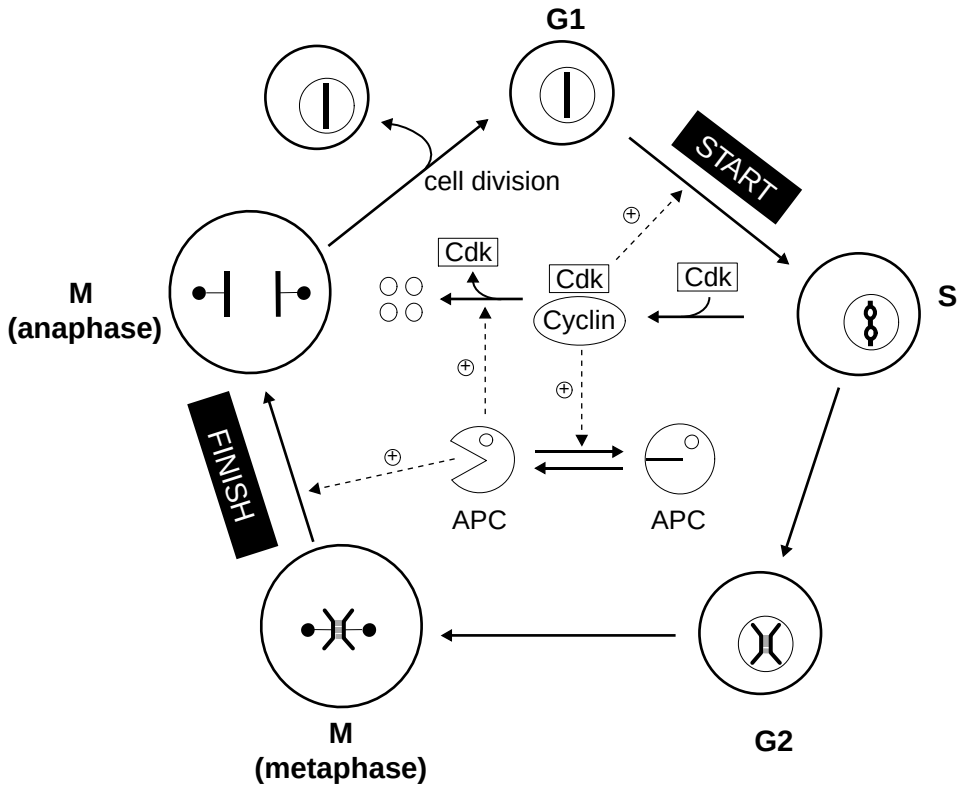

Figure 10.1 The cell cycle. Outer ring illustrates the chromosome cycle. The nucleus of a newborn cell contains unreplicated chromosomes (represented by a single bar). At Start, the cell enters S phase and replicates its DNA (signified by replication bubbles on the chromosome). At the end of S phase, each chromosome consists of a pair of sister chromatids (X) held together by tethering proteins. After a gap (G2 phase), the cell enters mitosis (M phase), when the replicated chromosomes are aligned on the metaphase spindle, with sister chromatids attached by microtubules to opposite poles of the spindle. At Finish, the tether proteins are removed so that the sister chromatids can be segregated to opposite sides of the cell (anaphase). Shortly thereafter the cell divides to produce two daughter cells in G1 phase. The inner icons represent the fundamental molecular machinery governing these transitions. Start is triggered by a protein kinase, Cdk, whose activity depends on association with a cyclin subunit. Cdk activity drives the cell through S phase, G2 phase, and up to metaphase. Finish is accomplished by proteolytic machinery, APC, which destroys the tethers and cyclin molecules. In G1 phase, APC is active and Cdk inactive, because it lacks a cyclin partner. At Start, the APC must be turned off so that cyclins may accumulate. Cdk and APC are antagonistic proteins: APC destroys Cdk activity by degrading cyclin, and cyclin/Cdk dimers inactivate APC by phosphorylating one of its subunits.

chromosome is synthesized. (The two identical DNA molecules are called sister chromatids.) Some time later, during M phase (mitosis), the sister chromatids are separated so that each daughter cell receives a copy of each chromosome.

DNA synthesis and sister chromatid separation (alternating S and M phases) make up the chromosome cycle of the cell. In parallel to it runs the growth cycle, whereby the cell's "hardware" (proteins, RNA, phospholipid bilayers, carbohydrates) is also duplicated and partitioned, more-or-less evenly, between daughters. During normal cell proliferation, these two cycles turn at the same rate, so that each round of DNA synthesis and mitosis is balanced by doubling of all other macromolecules in the cell. In this way, the DNA/protein ratio of the cell is maintained within advantageous limits. Of course, there are exceptions to this rule, such as oocytes, which grow very large without dividing, and fertilized eggs (embryos), which divide rapidly in the absence of growth. Nonetheless, the long-term viability of a cell line depends on balanced growth and division.

The chromosome cycle is usually subdivided into four phases (G1, S, G2, M), but it is better to think of it as two alternative "states" (G1 and S-G2-M) separated by two transitions (Start and Finish), as in Fig. 10.1 (Nasmyth, 1996). In G1, chromosomes are unreplicated and the cell is uncommitted to the replication-division process. At Start (the transition from G1 to S phase), a cell confirms that internal and external conditions are favorable for a new round of DNA synthesis and division, and commits itself to the process. The decision is irreversible; once DNA synthesis commences, it goes to completion.

During the process of DNA replication, sister chromatids are tethered together by specific proteins, called cohesins. As the mitotic spindle forms in M phase, microtubules from the spindle poles attach to chromosomes and pull them into alignment at the center of the spindle (metaphase). When DNA replication is complete and all chromosomes are aligned, the second irreversible transition of the cycle (Finish) is triggered. The cohesins are destroyed, allowing sister chromatids to be pulled to opposite poles of the spindle (anaphase). Shortly thereafter, daughter nuclei form around the segregated chromatids (telophase), and the incipient daughter cells separate.

These major events of the cell cycle must be tightly regulated. For instance, balanced growth and division is achieved in most cells by a size requirement for the Start transition. That is, cells must grow to a critical size before they can commit to chromosome replication and division. If this requirement is compromised by mutation, cells may become morbidly large or small. A second crucial regulatory constraint is to hold off the Finish transition if there have been any problems with DNA replication or chromosome alignment. Were anaphase to commence under such conditions, then daughter nuclei would not receive a full complement of chromosomes, which is usually a fatal mistake.

10.2 Molecular Mechanisms of Cell Cycle Control

Cell cycle events are controlled by a network of molecular signals, whose central components are cyclin-dependent protein kinases (Cdks). Cdks, when paired with suitable cyclin partners, phosphorylate many target proteins involved in cell cycle events. For

instance, by phosphorylating proteins bound to chromosomes at "origins of replication" (specific nucleotide sequences, where DNA replication can start), Cdks trigger the onset of DNA synthesis. By phosphorylating histones (proteins involved in DNA packaging), Cdks initiate chromosome condensation at the G2-M transition. Clearly, to understand the timing of these basic cell cycle events, one must understand the patterns of activation and inactivation of Cdks.

Cdk activities can be regulated throughout the cell cycle in many ways. In principle, cells could regulate the availability of Cdk subunits, but this is uncommon; most Cdks are present in constant abundance throughout the cell cycle. Their activity is regulated, instead, by the availability of cyclin partners. Cyclin abundance is determined by the rates of cyclin synthesis and degradation, both of which can be regulated during the cell cycle, as we shall see. Secondly, Cdk/cyclin dimers can be put out of commission by binding a third partner, a stoichiometric inhibitor, generally referred to as a CKI (cyclin-dependent kinase inhibitor). CKIs come and go, because their synthesis and degradation rates are also cell-cycle regulated. Finally, Cdk/cyclin activity depends on phosphorylation of the Cdk subunit. To be active, Cdk must be phosphorylated on a threonine residue on the "T-loop;" this phosphorylation is carried out by an enzyme called CAK, which is active throughout the cell cycle (i.e., T-loop phosphorylation is not involved in cell cycle regulation). Cdk may be inhibited by phosphorylation on a tyrosine residue (residue #15 in fission yeast Cdk), and the phosphorylation state of tyrosine-15 varies during the cell cycle as the activities of the tyrosine kinase (Wee1) and tyrosine phosphatase (Cdc25) fluctuate.

Because cells of higher eukaryotes contain many different Cdks and cyclins, "combinatorics" might play a major role in cell cycle progression, as the Cdk and cyclin subunits change partners. However, lower eukaryotes accomplish all the same basic tasks with many fewer components (one Cdk and 2-4 crucial cyclins), indicating that one Cdk is sufficient and that Cdk/cyclin holoenzymes can substitute for one another, to a large extent. Thus, progress through the cell cycle is not just a "square dance," with Cdks and cyclins swapping partners to a steady rhythm, as some textbook diagrams might suggest, but rather a complex, nonlinear, dynamical system of interactions between Cdk/cyclin dimers and their regulatory agents: transcription factors, degradation machinery, CKIs, and tyrosine-modifying enzymes. Our task will be to understand the basic principles of this dynamical system, but first we need some more mechanistic details.

Nasmyth's two cell-cycle states, G1 and S-G2-M, are correlated with low and high Cdk activity, respectively (see Fig. 1). Cdk activity is low in G1 because its obligate cyclin partners are missing. Cyclin levels are low in G1 because cyclin mRNA synthesis is inhibited and cyclin protein is rapidly degraded. At Start, cyclin synthesis is induced and cyclin degradation inhibited, causing a dramatic rise in Cdk activity, which persists throughout S, G2 and M. The initial rise in Cdk activity is sufficient to initiate DNA replication, but further increase is required to drive cells into mitosis (Stern and Nurse, 1996).

At Finish, a group of proteins, making up the anaphase-promoting complex (APC), is activated. The APC attaches a "destruction label" to specific target proteins, which are subsequently degraded by the cell's proteolytic machinery. The APC consists of a core complex of about a dozen polypeptides plus two auxiliary proteins, Cdc20 and Cdh1, whose apparent roles (when active) are to recognize specific target proteins and present them to the core complex for labeling. Activation of Cdc20 at Finish is necessary for degradation of cohesins at anaphase, and for activation of Cdh1. Together, Cdc20 and Cdh1 label cyclins for degradation at telophase, allowing the control system to return to G1. We must distinguish between these two different auxiliary proteins, because Cdc20 and Cdh1 are controlled differently by cyclin/Cdk, which activates Cdc20 and inhibits Cdh1.

10.3 Division Controls in Yeast Cells

A major challenge for theoretical molecular biologists is to explain the physiology of cell proliferation in a variety of unicellular and multicellular organisms in terms of their underlying molecular control systems. Of necessity, such connections will be made by ambitious computational models that reflect some of the inescapable complexity of real cell cycle controls. In order to design such models and understand how they work, we first need a solid grasp of the basic control principles of the cell cycle.

To this end, we draw attention to a simple theme that runs through the morass of molecular details. The irreversible transitions of the cell cycle (Start and Finish) are consequences of a hysteresis loop that derives from a fundamental antagonistic relationship between the central components of the machinery: the APC extinguishes Cdk activity by destroying its cyclin partners, whereas cyclin/Cdk dimers inhibit APC activity by phosphorylating Cdh1 (Fig. 10.1). This antagonism creates two, alternative, stable steady states of the control system: a G1 state, with high Cdh1/APC activity and low cyclin/Cdk activity, and an S-G2-M state, with high cyclin/Cdk activity and low Cdh1/APC activity.

10.3.1 Hysteresis in the interaction of cyclin B/Cdk and Cdh1/APC

The biochemical reactions in the center of Fig. 10.1 can be described by a pair of nonlinear ordinary differential equations (ODEs):

$$\frac{d[CycB]}{dt} = k_1 - (k_2' + k_2''[Cdh1])[CycB] \tag{10.1}$$

$$\frac{d[Cdh1]}{dt} = \frac{(k_3' + k_3''A)(1 - [Cdh1])}{J_3 + 1 - [Cdh1]} - \frac{k_4 \cdot m \cdot [CycB] \cdot [Cdh1]}{J_4 + [Cdh1]} \tag{10.2}$$

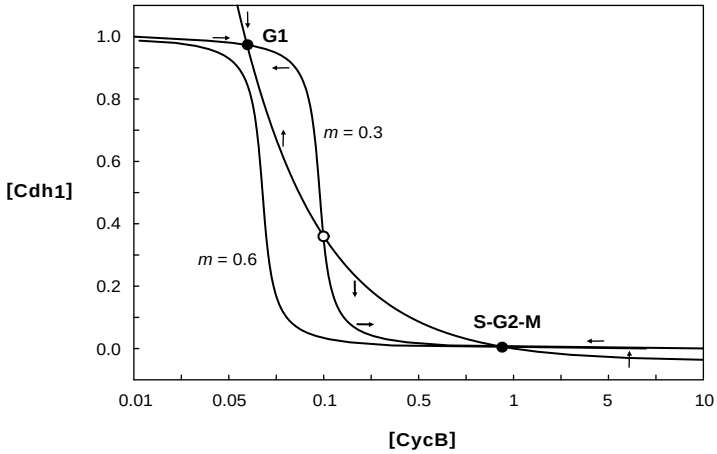

Figure 10.2 Phase plane portrait for the pair of nonlinear ODEs (10.1) and (10.2). Parameter values are given in Table 1. Curves are nullclines (see text) for $A = 0$, $m = 0.3$ and 0.6. Arrows indicate direction field for $m = 0.3$ only. For $m = 0.3$, the control system has three steady states: a stable node (G1) at ([CycB], [Cdh1]) $\approx$ (0.039,0.97), a saddle point near (0.10, 0.36), and another stable node (S-G2-M) near (0.90, 0.0045). Suppose a newborn cell resides at G1 (Cdh1 active and CycB missing). As the cell grows (m increases), the G1 steady state is lost by a saddle-node bifurcation (at $m \approx 0.53$), and the control system is forced to the S-G2-M steady state. This figure was created using Phase Plane file 10_3_1.ode.

In these equations, [CycB] and [Cdh1] are the average concentrations of cyclin B/Cdk dimers and active Cdh1/APC complexes, respectively. We assume that cyclin B molecules combine rapidly with an excess of Cdk subunits and accumulate in the nucleus, where their effective concentration increases as the cell grows; hence, $m\ cdot[CycB]$ is the intranuclear concentration of CycB/Cdk dimers, where m represents cell "mass" (not to be confused with M for "mitosis"). We also assume that APC cores are in excess, and that the total Cdh1 concentration is constant and scaled to 1. The k's are rate constants, the J's are Michaelis constants, and A is a parameter used to activate Cdh1 at Finish. (In the next section, we will show how A relates to Cdc20.)

The phase plane portrait for system (10.1)-(10.2) is illustrated in Fig. 10.2. The nullclines are described by simple algebraic equations:

$$[CycB] = \frac{\beta}{J_2 + [Cdh1]}$$
$$[CycB] = p\frac{(1 - [Cdh1])(J_4 + [Cdh1])}{[Cdh1](J_3 + 1 - [Cdh1])}$$

where $\beta = \frac{k_1}{k_2''}, J_2 = \frac{k_2'}{k_2''}$ and $p = \frac{k_3' + k_3'' A}{k_4 \cdot m}$. The CycB nullcline is a simple hyperbola. For $J_3 = J_4 \ll 1$, the Cdh1 nullcline is a sigmoidal curve passing through $[CycB] = p$ at $[Cdh1] = 1/2$.

The Cdh1 nullcline can be rewritten for $[Cdh1]$ as a function of $[CycB]$, $[Cdh1] = G(p, [CycB], J_3, J_4)$, where G is the Goldbeter-Koshland function (see Exercise 10.8.1):

$$G(V_a, V_i, J_a, J_i) = \frac{2c}{b + \sqrt{b^2 - 4ac}}$$
$$a = V_i - V_a, b = V_i - V_a + V_a J_i + V_i J_a, c = V_a J_i.$$

This function will come in handy later.

The control system has steady state solutions wherever the nullclines intersect. The number of intersections depends on the value of p (Fig. 10.3). For $p_1 < p < p_2$, the ODEs (10.1)-(10.2) have three steady states: two stable nodes separated by a saddle point. The stable nodes we refer to as **G1** (Cdh1 active, CycB low) and **S-G2-M** (Cdh1 inactive, CycB high); in bold face to distinguish the theoretician's stable steady state from the experimentalist's cell cycle phase. In Exercise 10.8.2 you are asked to show that, when $J_2 = J_3 = J_4 = \epsilon \ll 1$, the saddle-node bifurcations occur at:

$$\begin{aligned} p_1 &\approx \beta\{1 + 2\sqrt{\epsilon} + O(\epsilon^{3/2})\}, [Cdh1] \approx 1 - \sqrt{\epsilon} + \epsilon, [CycB] \\ &\approx \beta(1 + \sqrt{\epsilon} - \epsilon) \\ p_2 &\approx \beta/(4\epsilon), [Cdh1] \approx \epsilon, [CycB] \approx \beta/(2\epsilon). \end{aligned}$$

Progress through the cell cycle can be thought of as a tour around the hysteresis loop in Fig. 10.3. For a small, newborn cell in G1 phase (with $A \approx 0$ and $p \approx k_3'/k_4 m > p_1$), the CycB-Cdh1 control system is attracted to the stable **G1** steady state. As the cell grows, m increases and p decreases. Eventually, p drops below p_1, and the **G1** steady state disappears, forcing the control system to jump irreversibly to the **S-G2-M** steady state. High CycB/Cdk activity initiates the processes of DNA synthesis and later mitosis, as the cell continues to grow. We assume that, when DNA replication is complete and the chromosomes are properly aligned on the mitotic spindle, the parameter A increases abruptly, forcing p to increase above p2. Consequently, the **S-G2-M** steady state is lost by a saddle-node bifurcation, and the control system jumps irreversibly back to the **G1** state. The cell divides ($m \to m/2$), A decreases back to 0, and the control system returns to its starting condition.

In this simple model, the irreversible transitions of the cell cycle (Start and Finish) are the abrupt jumps of the hysteresis loop, at the saddle-node bifurcation points. The **G1** $\to$ **S-G2-M** transition is driven by cell growth, and the reverse transition is driven by chromosome alignment on the mitotic spindle.

10.3.2 Activation of the APC at Anaphase

To fill out the picture in the previous section, we must identify the activator of Cdh1/APC and describe why A increases abruptly at the metaphase $\to$ anaphase transition and decreases in G1 phase. The activator is a phosphatase (Cdc14) that removes from Cdh1 the inhibitory phosphate groups placed there by CycB/Cdk. At

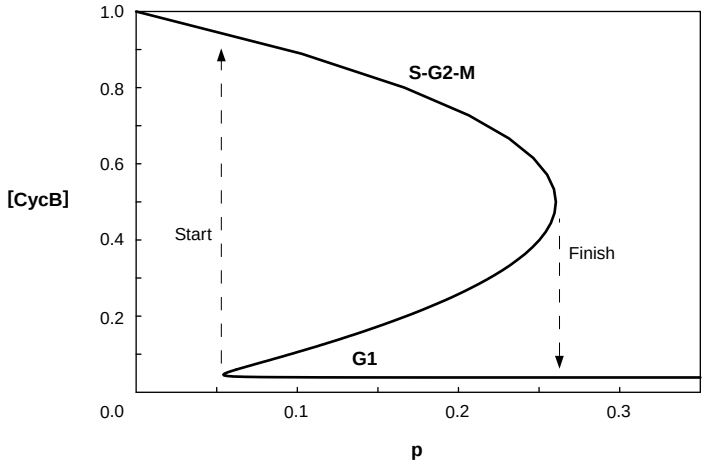

Figure 10.3 Bifurcation diagram for Eqs. (10.1)-(10.2). The steady state concentration of CycB is plotted as a function of the bifurcation parameter, $p = \frac{k_3' + k_3'' A}{k_4 \cdot m}$. Other parameters: $\beta = \epsilon = 0.04$. Saddle-node bifurcations occur at $p_1 \approx 0.05418$ and $p_2 \approx 0.2604$.

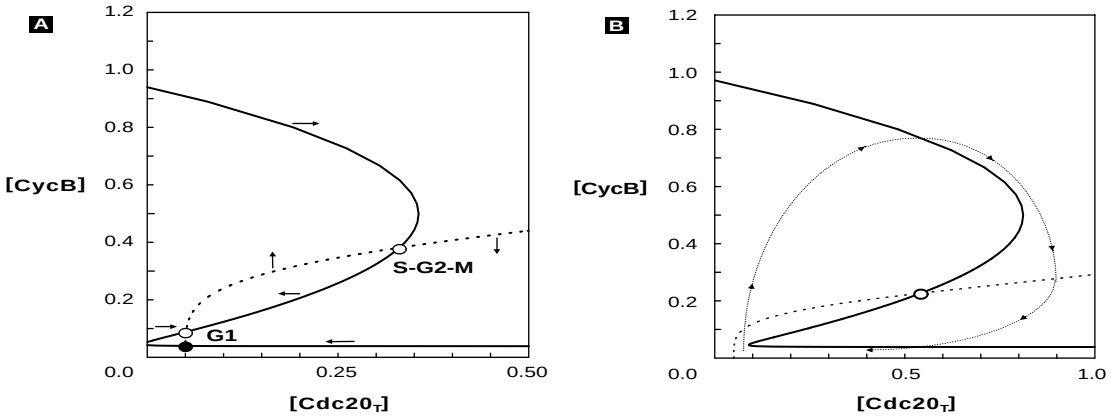

Figure 10.4 Phase plane portrait for Eqs. (10.1) and (10.3). [Cdh1] is computed from [CycB] by solving for the steady-state of Eq. (10.2). Parameter values given in Table 10.1. (A) $m = 0.5$; (B) $m = 1$. Solid curve: CycB nullcline. Dashed curve: Cdc20 nullcline. Dotted curve: trajectory. The control system undergoes a saddle-node-loop bifurcation at $m \approx 0.8$. (Phase plane file: 10_3_2A.ode)

the metaphase $\rightarrow$ anaphase transition, Cdc14 is activated indirectly by Cdc20/APC, which disengages a complex pathway of Cdc14-inhibition. To keep our model as simple as possible, we assume that $A \propto [Cdc14] \propto [Cdc20]$ and write a differential equation for the production of Cdc20:

$$\frac{d[Cdc20_T]}{dt} = k_5' + k_5'' \frac{([CycB] \cdot m)^n}{j_5^n + ([CycB] \cdot m)^n} - k_6[Cdc20_T] \tag{10.3}$$

Because Cdc20 is synthesized only in S-G2-M phase of the budding yeast cell cycle, we have assumed that its transcription factor is turned on by CycB/Cdk according to a Hill function with parameters n and J5. (The significance of the subscript T will become clear shortly.) Notice that CycB, Cdc20 and Cdh1 are involved in a long, negative feedback loop: CycB activates Cdc20, which indirectly activates Cdh1, which destroys CycB.

By supposing that Cdh1 activity responds rapidly to changes in [CycB] and [Cdc20T], we can solve Eq. (10.2) for $[Cdh1] = G(k_3' + k_3''[Cdc20_T], k_4 m[CycB], J_3, J_4)$, where G is the Goldbeter-Koshland function defined earlier. With this assumption, our control system is still representable by a pair of ODEs, (10.1) and (10.3), and by phase plane portraits (Fig. 10.4). Consider a newborn cell in G1 phase (Fig. 10.4A). As the cell grows, the CycB nullcline moves to the right and the control system undergoes a saddle- node-loop bifurcation at a critical value of m ($m_{crit} \approx 0.8$). When the **G1** steady state is destroyed by coalescence with the saddle point, [CycB] starts to increase (see the dotted trajectory in Fig. 10.4B). CycB-dependent kinase activity drives the cell into S phase and mitosis, and it turns on synthesis of Cdc20. Cdc20 can drive the cell out of mitosis because, unlike Cdh1, it is not inhibited by Cdk-induced phosphorylation. After Cdc20 has done its job at Finish, it must be destroyed during the subsequent G1 phase, to prepare the control system for the next Start transition.

Notice that the **S-G2-M** steady state in Fig. 10.4B is unstable: as Cdc20 accumulates, the control system loops around the unstable steady state. Cdh1/APC is activated by Cdc20, CycB is destroyed, and the cell exits mitosis. At cell division, m is reduced two-fold, and the nullclines readopt the configuration in Fig. 4A. The control system is captured by the stable **G1** steady state, until cell size, $m(t)$, once more increases to m_{crit}.

In this picture, cells exit from mitosis "automatically" a certain time after Start (the time required to make enough Cdc20 to activate APC); there is no connection between alignment of replicated chromosomes on the metaphase plate and the transition to anaphase. In budding yeast, the connection is established through further controls on Cdc20 (see bottom part of Fig. 10.6). Newly synthesized Cdc20 is inactive. A Cdc20-activating signal derives indirectly from CycB/Cdk; some intermediate steps between CycB synthesis and Cdc20 activation assure a minimum time lag for DNA synthesis and chromosome alignment to be completed before anaphase commences. If they are not completed on time, a Cdc20-inactivating signal is imposed by the MAD-family of spindle checkpoint genes. To take these additional feature into account, we write

$$\begin{aligned}\frac{d[Cdc20_A]}{dt} = & \frac{k_7[IEP]([Cdc20_T] - [Cdc20_A])}{J_7 + [Cdc20_T] - [Cdc20_A]} - \frac{k_8[Mad] \cdot [Cdc20_A]}{J_8 + [Cdc20_A]} \\ & - k_6[Cdc20_A]\end{aligned} \tag{10.4}$$

$$\frac{d[IEP]}{dt} = k_9 m[CycB](1 - [IEP]) - k_1 0([IEP]) \tag{10.5}$$

Here, $[Cdc20_A]$ is the concentration of "active" Cdc20, and [Cdc20T] is the total concentration of both active and inactive forms. From now on, we set $A = [Cdc20_A]$ in Eq. (10.2). [IEP] is the concentration of the active form of an intermediary enzyme, whose total concentration is scaled to 1. We treat [Mad] as a parameter; [Mad] = 1, if chromosome alignment is completed on schedule, and = some large number, if not.

To complete this primitive model of cell cycle controls, we provide a differential equation for cell growth:

$$\frac{dm}{dt} = \mu m \left(1 - \frac{m}{m_*}\right) \tag{10.6}$$

where $m*$ is the maximum size to which a cell may grow if it does not divide, and m is the specific growth rate when $m \ll m*$. Our model consists of Eqs. (10.1)-(10.6), with the proviso that $m \to m/2$, whenever the cell divides (i.e., when [CycB] drops below some threshold level, taken to be 0.1). A typical simulation is presented in Fig. 10.5. This simple model fulfills all the requirements of a functional, eukaryotic cell cycle, with two irreversible transitions, Start (dependent on cell growth) and Finish (dependent on chromosome alignment). However, all organisms that have been studied in detail have additional layers of control on Cdk activity.

10.3.3 Stoichiometric Inhibitors

Yeast cells have a stoichiometric inhibitor (CKI) that keeps Cdk activity low in G1 phase. The CKI binds to CycB/Cdk to form inactive trimers (Fig. 10.6). The existence of trimers changes slightly the interpretation of Eq. (10.1):

$$\frac{d[CycB_T]}{dt} = k_1 - (k_2' + k_2''[Cdh1] + k_2''[Cdc20_A])[CycB_T]$$

where $[CycBT] = [CycB] + [Trimer]$. We also need a kinetic equation for total CKI:

$$\frac{d[CKI_T]}{dt} = k_{11} - (k_{12}' + k_{12}''[SK] + k_{12}' m[CycB])[CKI_T] \tag{10.7}$$

In Eq. (10.7), the rate of CKI degradation depends on CycB/Cdk activity, because CycB- dependent phosphorylation of CKI renders it unstable. Thus, CKI and CycB/Cdk are mutual antagonists. The model (Fig. 10.6) postulates a "starter" kinase (SK) that phosphorylates CKI in the absence of CycB/Cdk activity.

Notice also, in Eq. (10.1'), that we have given Cdc20 some ability to degrade cyclin B. This well-known interaction enforces the negative feedback loop at exit from mitosis: CycB activates IE, which activates Cdc20, which degrades CycB directly, as well as activating Cdh1.

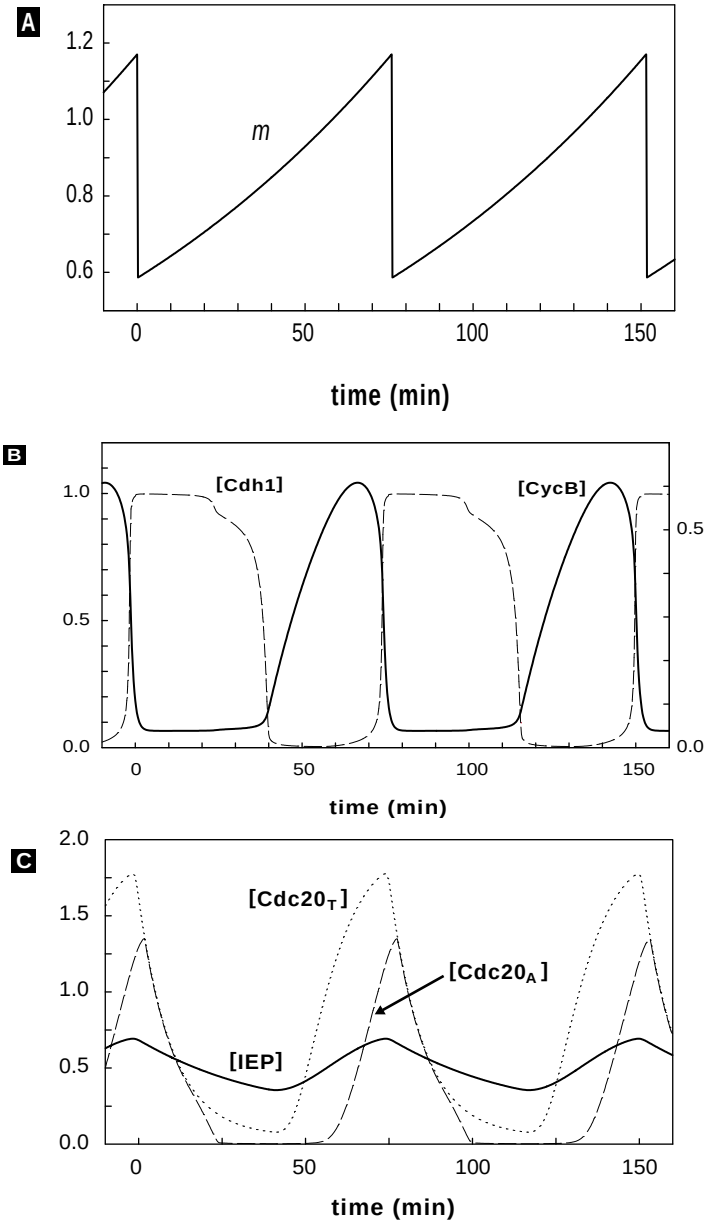

Figure 10.5 Simulation of Eqs. (10.1)-(10.6), with parameter values in Table 10.1. Middle panel: CycB (solid curve) scale to the right. Cell division occurs when [CycB] crosses 0.1 from above. (Phase plane file: 10_3_2B.ode)

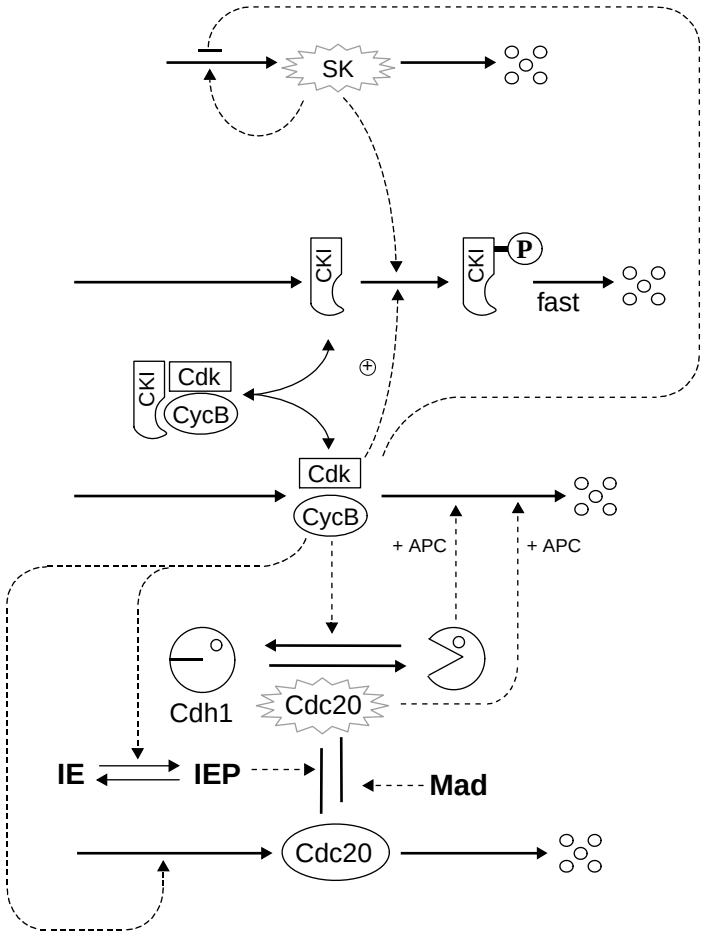

Figure 10.6 The basic cell cycle engine in eukaryotic cells. The generic components in this mechanism correspond to specific gene products in well-studied organisms (see Table 10.2). Dynamical properties of this mechanism are determined by a set of kinetic equations (10.1'), (10.2) - (10.9), with $A = [Cdc20_A]$. A basal set of parameter values, suitable for yeast cells, is given in Table 10.1.

We assume that CKI/CycB/Cdk trimers are always in equilibrium with CKI monomers and CycB/Cdk dimers: $[Trimer] = K_eq[CycB][CKI] = K_eq \cdot ([CycBT] - [Trimer]) \cdot ([CKIT] - [Trimer])$, or

$$[Trimer] = (2 \cdot [CycB_T] \cdot [CKI_T]) \cdot \{[CycB_T] + [CKI_T] + K_{eq}^{-1} + \sqrt{([CycB_T] + [CKI_T] + K_{eq}^{-1})^2 - 4 \cdot [CycB_T] \cdot [CKI_T]}\}^{-1} \quad (10.8)$$

To understand how the CKI part of the control system works, let us consider the [CycBT], [CKIT] phase plane (Fig. 10.7) defined by Eqs. (10.1') and (10.7). In

Table 10.1 Parameter Values

Component	Rate constants (min^{-1})	Dimensionless constants
CycB	$k_1 = 0.04, k_2' = 0.04, k_2'' = 1, k_2''' = 1$	$[CycB]_{threshold} = 0.1$
Cdh1	$k_3' = 1, k_3'' = 10, k_4' = 2, k_4 = 35$	$J_3 = 0.04, J_4 = 0.04$
$Cdc20_T$	$k_5' = 0.005, k_5'' = 0.2, k_6 = 0.1$	$J_5 = 0.3$
$Cdc20_A$	$k_7 = 1, k_8 = 0.5$	$J_7 = 10^{-3}, J_8 = 10^{-3}, [Mad] = 1$
IE	$k_9 = 0.1, k_{10} = 0.02$	
CKI	$k_{11} = 1, k_{12}' = 0.2, k_{12}'' = 50, k_{12}''' = 100$	$K_{eq} = 103$
SK	$k_{13}' = 0, k_{13}'' = 1, k_{14} = 1,$ $k_{15}' = 1.5, k_{15}'' = 0.05, k_{16}' = 1, k_{16}'' = 3$	$J_{15} = 0.01, J_{16} = 0.01$
Wee1	$k_{wee}' = 0.01, k_{wee}'' = 1,$ $V_{awee} = 0.25, V_{iwee}' = 0, V_{iwee}'' = 1$	$J_{awee} = 0.01, J_{iwee} = 0.01$
Cdc25	$k_{25}' = 0.05, k_{25}'' = 5,$ $V_{a25}' = 0, V_{a25}'' = 1, V_{i25} = 0.25$	$J_{a25} = 0.01, J_{i25} = 0.01$
m	$\mu = 0.01$	$m_* = 10$

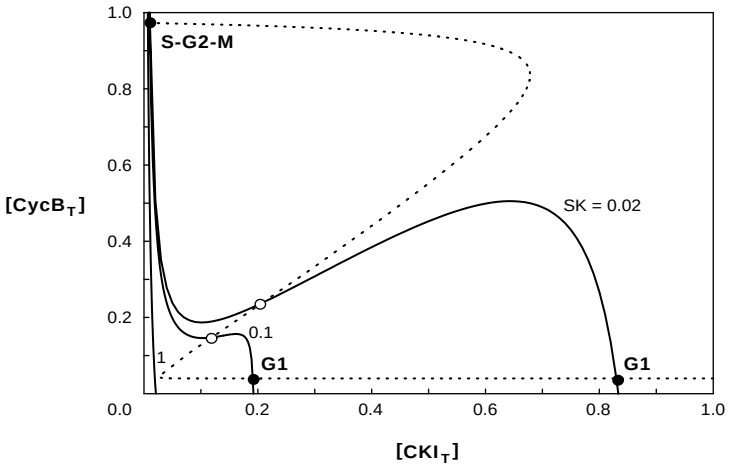

Figure 10.7 Phase plane portrait for Eqs. (10.1') and (10.7). [Cdh1] is computed from [CycB] by solving for the steady state of Eq. (10.2). Parameter values in Table 10.1, plus $[Cdc20_A] = 0, m = 1$, [SK] adjustable. Dashed curve: CycB nullcline. Solid curves: CKI nullclines, for [SK] = 0.02, 0.1 and 1. = stable steady state, o = unstable steady state. The control system has a saddle-node bifurcation at [SK] $\approx$ 0.9. (Phase plane file: 10_3_3A.ode)

these equations, $[Cdh1] = G(k_3' + k_3''[Cdc20_A], k_4 m[CycB], J3, J4), [CycB] = [CycB_T] - [Trimer]$, with $[Trimer]$ given by the equation directly above, and [SK], $[Cdc20_A]$ and m are treated as parameters. The CKIT-nullcline is N-shaped because of the antagonism between CycB and CKI, and the CycBT-nullcline is N-shaped because of the antagonism between CycB/Cdk and Cdh1/APC.

For proper choice of parameters (Table 10.1), the control system exhibits bistability, with a stable **G1** state (CycB low, Cdh1 active, CKI abundant) and a stable **S- G2-M** state (CycB high, Cdh1 inactive, CKI missing). Exit from mitosis (**S-G2-M** $\rightarrow$ **G1**) is carried out by Cdc20, as described in the previous section. To start the chromosome cycle (**G1** $\rightarrow$ **S-G2-M**), we assume that synthesis of the "starter kinase" is turned on when the cell reaches a characteristic size. As [SK] increases, the local maximum of the CKIT-nullcline is depressed (Fig. 10.7), destroying the **G1** steady state by a saddle-node bifurcation.

Like CycB/Cdk, the starter kinase must phosphorylate CKI, but unlike CycB/Cdk, it must be immune to inhibition by CKI and degradation by Cdh1/APC. These properties allow SK to flip the switch from G1 to S. After SK has done its job, CycB/Cdk can maintain the cell in **S-G2-M**. In order to prepare the control system for the next Finish transition, SK then disappears. To write a dynamical equation for the time course of [SK], we take our hint again from budding yeast, where two cyclins, Cln1 and Cln2, in combination with Cdc28 (the catalytic subunit), phosphorylate CKI at Start, permitting B-type cyclins (Clb1-6) to accumulate and drive the cell through S and M phases. Synthesis of Cln1-2 is controlled by a transcription factor that is activated by Cln/Cdc28 and inhibited by Clb/Cdc28, so we write

$$\begin{aligned} \frac{d[SK]}{dt} &= k'_{13} + k''_{13}[TF] - k_{14}[SK] \\ [TF] &= G(k'_{15}m + k''_{15}[SK], k'_{16} + k''_{16}m[CycB], J_{15}, J16) \end{aligned} \tag{10.9}$$

where $G(...)$ is a Goldbeter-Koshland function describing the activity of the transcription factor (TF) that regulates production of the starter kinase. Size control at Start enters this model through the term $k'_{15}m$ in the first argument of G; when the cell gets sufficiently large, $k'_{15}m \approx k'_{16}$, it begins to synthesize SK. Increasing [SK] activates its own transcription, Eq. (10.9), and destroys CKI, Eq. (10.7). We also assume that SK phosphorylates Cdh1, although not as efficiently as CycB/Cdc28; that is, in Eq. (10.2) we replace $k_4m[CycB][Cdh1]$ by $(k'_4[SK] + k_4m[CycB])[Cdh1]$, with $k'_4 \ll k_4$.

With these changes, the system of equations (10.1'), (10.2)-(10.9) accounts for many characteristic features of wild type and mutant budding yeast cells. Wild type cells have a long G1 (unbudded period) and short S-G2-M (budded period); see Fig. 10.8A. Throughout G1, SK (Cln) level steadily rises, causing CKI (Sic1) level to fall. In late G1, several events occur in close succession. First, TF is activated and [SK] rises sharply, causing rapid destruction of the remaining CKI. When [CKI] drops below [CycBT], active CycB/Cdc28 dimers make their appearance, helping SK to inactivate Cdh1. As Cdh1 activity drops off rapidly, CycB level rises further. Newly produced CycB/Cdc28 initiates DNA synthesis at about the same time that Cln/Cdc28 initiates a new bud. Meanwhile, CycB/Cdc28 turns off SK production and SK level drops. CKI and Cdh1 do not make a comeback because CycB/Cdc28 keeps these proteins phosphorylated. Persistent CycB/Cdc28 activity drives the cell into M phase. After a delay of about 45 min (during which IE is activated–not shown in Fig. 10.8A), Cdc20 is activated and

destroys enough CycB to allow Cdh1 to reactivate and CKI to reaccumulate. When CycB drops low enough, the cell divides. (In Fig. 10.8A, we assume symmetric division for simplicity, although budding yeast cells typically divide asymmetrically.)

Mutant cells lacking SK ($k'_{13} = k''_{13} = 0$) block in G1 with abundant CKI and active Cdh1 (Fig. 10.8B), which is the phenotype of cells in which all Cln-cyclins are deleted ($cln1\Delta\ cln2\Delta\ cln3\Delta$). (Although Cln3 plays a different role than Cln1-2, it can serve as their backup; so it too must be deleted to see the expected phenotype.) Because the only essential job of the Cln-cyclins is to remove Sic1 (CKI), the quadruple-deletion mutant $cln1\Delta\ cln2\Delta\ cln3\Delta\ sic1\Delta$ is viable; see Fig. 10.8C. For a more thorough analysis of the budding yeast cell cycle, consult Chen et al. (2000).

10.3.4 Enzymatic Inhibitors

Properly interpreted (Table 10.2), Eqs. (10.1'), (10.2)-(10.9) also provide a reasonable description of cell cycle controls in fission yeast cells lacking Wee1 ($wee1\Delta$ mutants); but, to describe wild type fission yeast, we must add a new level of control, involving tyrosine phosphorylation and dephosphorylation of Cdk subunits.

As described in Section 10.2, Wee1 inhibits CycB/Cdk activity by phosphorylating the Cdk subunit on tyrosine-15. Cdc25 reverses the inhibitory phosphorylation. Wee1 and Cdc25 are, in turn, targets of CycB/Cdk phosphorylation: Wee1P is less active and Cdc25P more active than the unphosphorylated forms. Thus, Wee1 and CycB/Cdk are antagonistic proteins, whereas Cdc25 and CycB/Cdk are involved in a mutually enhancing feedback loop.

We can incorporate these regulatory signals into the model in the previous section by noticing that $[CycB_T]$ is now the sum of four forms, $[CycB/Cdk] + [CycB/CdkP] + [CKI/CycB/Cdk] + [CKI/CycB/CdkP]$. Letting $[Trimer] = [CKI/CycB/Cdk] + [CKI/CycB/CdkP]$ and $[PF] = [CycB/CdkP] + [CKI/CycB/CdkP]$, we can write a differential equation for the phosphorylated forms (PF) that accounts for the actions of Wee1 and Cdc25:

Table 10.2 Cell Cycle Regulatory Proteins in Yeasts and Vertebrates

Component	Budding Yeast	Fission Yeast	Frog Egg	Mammalian Cell
Cdk	Cdc28	Cdc2	Cdc2	Cdk1
CycB	Clb1-6	Cdc13	Cyclin B	Cyclin B
Cdh1	Cdh1	Ste9	Fizzy-related	Cdh1
Cdc20	Cdc20	Slp1	Fizzy	p55cdc
IE	Cdc5?	Plo1?	Plx1?	Plk1?
CKI	Sic1	Rum1	Xic1	$p27^{Kip1}$
SK	Cln1-2	Cig2	Cyclin E?	Cyclin D, E

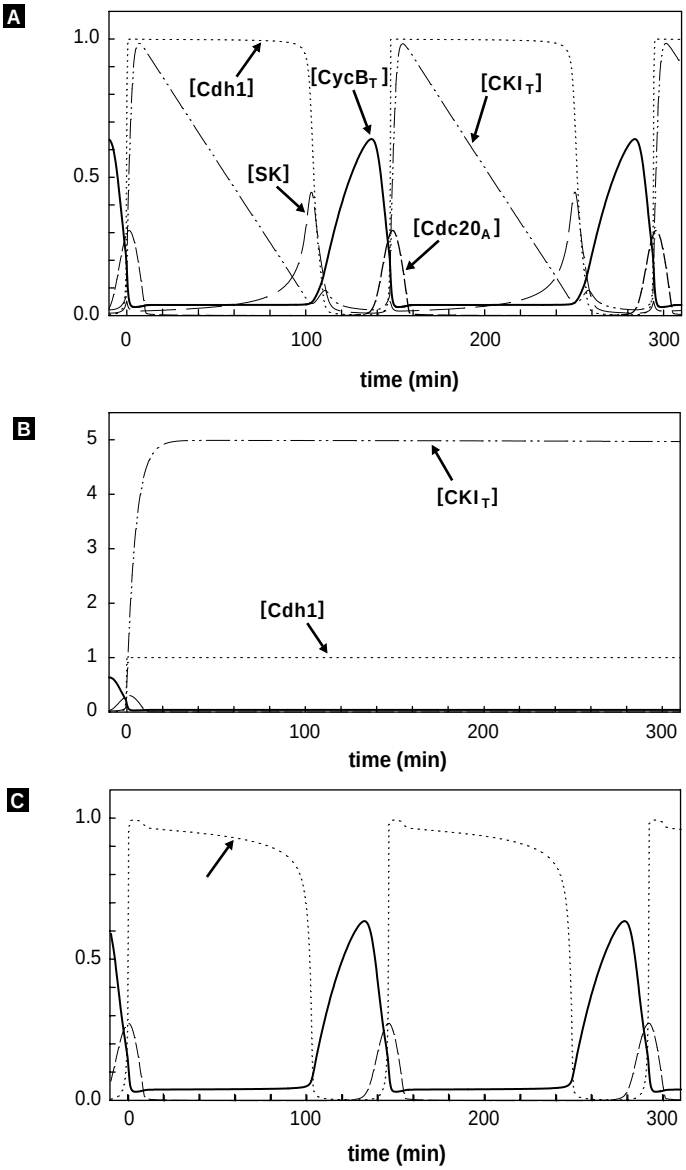

Figure 10.8 The budding yeast cell cycle. In each panel, the topmost trace is cell size, $m(t)$, whose scale is to the right. (A) Wild type cells: simulation of Eqs. (10.1'), (10.2)- (10.9), with parameter values in Table 10.1, except m = 0.005 min-1. (B) Mutant cells lacking SK ($k_{13} = 0$) block in G1 with copious CKI and active APC. Compare to $cln1\Delta$ $cln2\Delta$ $cln3\Delta$ cells. (C) Mutant cells lacking SK and CKI ($k_{11} = k_{13} = 0$) are viable; compare to $cln1\Delta$ $cln2\Delta$ $cln3\Delta$ $sic1\Delta$ cells. (Phase plane file: 10_3_3B.ode)

$$\begin{aligned}\frac{d[PF]}{dt} &= k_{wee}([CycB_T] - [PF]) - k_{25}[PF] \\ &\quad - (k_2' + k_2''[Cdh1])[PF] \\ k_{wee} &= k_{wee}' + k_{wee}'' G(V_{awee}, V_{iwee}' + V_{iwee}''[MPF], J_{awee}, J_{iwee}) \\ k_{25} &= k_{25}' + k_{25}'' G(V_{a25}' + V_{a25}''[MPF], V_{i25}, J_{a25}, J_{i25})\end{aligned} \tag{10.10}$$

We have assumed that Wee1 and Cdc25 function as Goldbeter-Koshland ultrasensitive switches. The kinase that phosphorylates Wee1 and Cdc25 is CycB/Cdk (called here MPF, "M-phase promoting factor"). V_{awee} and V_{i25} refer to phosphatase activities that oppose MPF. To compute [MPF] from [CycBT], [Trimer] and [PF], we use the approximate expression (see Exercise 10.8.7):

$$[MPF] \approx ([CycB_T] - [Trimer])\{1 - ([PF]/[CycB_T])\} \tag{10.11}$$

Figure 10.9 shows a simulation of this model of the fission yeast cell cycle. Parameter values for the Wee1-Cdc25 interactions have been chosen so that size control in wild type fission yeast occurs at the G2-M transition, rather than at G1-S. This is evident from the large size of cells at birth and the short duration of G1 phase. A $wee1\Delta$ mutant ($k_{wee}'' = 0$) behaves much like Fig. 10.8: cells divide at about half the size of wild type and have a long G1 phase, exactly as observed. (The wee1 mutant, discovered by Paul Nurse in 1975, played a central role in unraveling the molecular machinery of the cell cycle.) It should be clear that $cdc25^-$ is a lethal mutation, but the double mutant, $cdc25^-$ $wee1^-$, is viable and small (see Exercise 10.8.6).

10.3.5 Checkpoints and surveillance mechanisms

A basic job of the cell cycle engine (Fig. 10.6) is to coordinate DNA synthesis and mitosis with overall cell growth. We have seen how cell size (m) might feed into the engine to ensure balanced growth and division. If cells are too small, the engine stops at a stable steady state (**G1** in Fig. 10.7). Only when m exceeds some critical value is this stable steady state lost by coalescence with an unstable steady state (saddle-node bifurcation). When the **G1** attractor is lost, the cell can proceed into S phase. In this way, Start can be controlled by cell size. In fission yeast, size control operates at the G2-M transition by the same principle: a stable G2 steady state (lots of inactive CycB/CdkP dimers) is lost when cells grow beyond a critical size, preMPF is converted into active MPF, and the cell enters mitosis.

Figure 10.9 The fission yeast cell cycle. Simulation of Eqs. (10.1'), (10.2)-(10.11), with parameter values in Table 10.1, except $\mu = 0.005 min^{-1}$. This simulation represents wild- type cells, whereas Fig. 10.8A represents wee1- mutant cells. Notice that, as observed, $wee1^-$ mutants are about half the size of wild-type cells and have a considerably longer G1 phase. (Phase plane file: 10_3_4.ode)

We believe that this is a general principle of cell cycle control. A checkpoint corresponds to a stable steady state of the cell cycle engine (no further progress). The checkpoint is lifted by changes in crucial parameters, carrying the control system across a bifurcation. The crucial parameters are controlled by surveillance mechanisms that monitor the internal and external milieus of the cell. For instance, if DNA synthesis stalls for any reason, an inhibitory signal suppresses mitosis until the genome is fully replicated. If DNA is damaged in G1 or G2 phases, other surveillance mechanisms suppress entry into S phase or M phase, respectively. If chromosome alignment on the metaphase plate is delayed for any reason, a signal inactivates Cdc20 and blocks progression from metaphase to anaphase.

10.4 Division Controls in Egg Cells

The physiology of animal eggs is quite different from yeast cells. In the ovary, oocytes grow very large without dividing: the cytoplasm is packed with supplies, and the nucleus is arrested in G2 phase (DNA replicated, lots of CycB/CdkP, low MPF activity). In response to hormone signals, a clutch of these "immature" oocytes leaves the G2-arrested state and proceeds through meiosis I and II. Frog eggs stop at metaphase of meiosis II (haploid complement of replicated chromosomes aligned on the spindle, high MPF activity). In this state, the "mature" oocyte awaits fertilization. Sperm entry triggers the egg to exit meiosis II, the sperm and egg nuclei replicate their DNA and fuse to form a diploid G2 nucleus. In the frog, the first mitotic cycle takes about 1 h and is followed by eleven rapid (30 min), synchronous, mitotic cycles without checkpoints. These cell cycles are not size-regulated (the cells get smaller at each division), they are not stopped by drugs that block either DNA synthesis or spindle formation, and there is little or no tyrosine phosphorylation of Cdk subunits during these cycles. In the fertilized egg, the checkpoints (stable steady states) are missing, and the cell cycle engine exhibits its capacity for free-running oscillation.

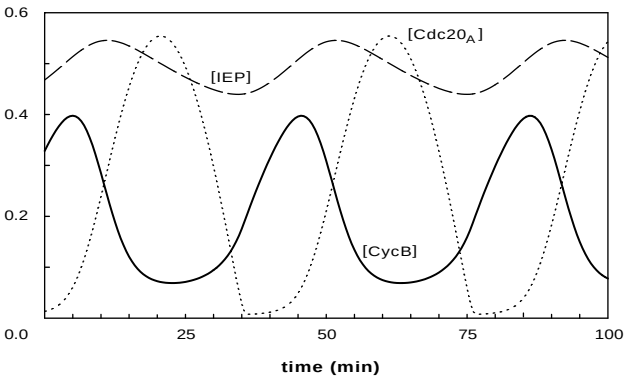

Figure 10.10 Spontaneous oscillations of CycB/Cdk activity in early embryonic cells. Simulation of Eqs. (10.10)-(10.12), with parameter values in Table 10.1. Period = 41 min. (Phase plane file: 10_4_1.ode)

10.4.1 Spontaneous Oscillations in Fertilized Eggs

The cyclin/Cdk network controlling cell divisions in early embryos is a stripped-down version of Fig. 10.6, lacking CKI and Cdh1. With CKI missing, SK has no role to play in the model. Also, Wee1 is inactivated, so we can neglect tyrosine phosphorylation reactions. All the antagonistic interactions are gone, leaving only the delayed negative feedback loop:

$$\frac{d[CycB]}{dt} = k_1 - (k_2' + k_2''[Cdc20_A])[CycB] \tag{10.12}$$

$$\frac{d[IEP]}{dt} = k_9[CycB](1 - [IEP]) - k_{10}[IEP] \tag{10.13}$$

$$\frac{d[Cdc20_A]}{dt} = \frac{k_7[IEP]([Cdc20_T] - [Cdc20_A])}{J_7 + [Cdc20_T] - [Cdc20_A]} - \frac{k_8[Mad] \cdot [Cdc20_A]}{J_8 + [Cdc20_A]} \tag{10.14}$$

For simplicity, we assume that Cdc20 is a stable protein in the early embryo and set $[Cdc20_T] = 1$ in Eq. (10.14). Furthermore, $[Mad] = 1$, because the spindle assembly checkpoint is inoperative. Cell size (m) does not appear in these equations, because the embryo is not growing.

The system of equations (10.12)-(10.14) is a classical negative-feedback oscillator; see Chapter 9 and Exercise 10.8.9. As shown in Fig. 10.10, it has limit cycle solutions, corresponding to spontaneous oscillations in activity of CycB/Cdk (usually called MPF in the frog-egg literature). After 12 rapid, synchronous divisions, the frog egg undergoes an abrupt reorganization of the cell cycle (called the midblastula transition). Expression of zygotic genes provides the missing components of the cell cycle checkpoints. Consequently the pace of cell division slows, as the controls described in Section 10.5 are put into place.

10.4.2 Immature and Mature Oocytes

To describe the characteristic arrested states of frog oocytes, we must add tyrosine phosphorylation of Cdk subunits to the negative-feedback oscillator above. So, to Eqs. (10.12)-(10.14), we add

$$\frac{d[MPF]}{dt} = k_1 - k_{wee}[MPF] + k_{25}([CycB] - [MPF]) - (k_2' + k_2''[Cdc20_A])[MPF] \tag{10.15}$$

where k_{wee} and k_{25} are defined below Eq. (10.10), and [CycB]-[MPF] is just the concentration of tyrosine-phosphorylated dimers. In Eq. (10.13), we must replace [CycB] by [MPF], the active form of CycB/Cdk dimers.

Figure 10.11 Phase plane portraits for a model of frog oocytes: Eq. (10.12) and (10.15), with $[Cdc20_A]$ given by (10.16). Parameter values as in Table 10.1, except $k_1 = 0.06$, and k_8 varied. (A) Immature oocyte: $k_8 = 0.4$. Stable steady state with copious cyclin B, and MPF dimers in the inactive, tyrosine-phosphorylated form. (B) Mature oocyte: $k_8 = 0.8$. Stable steady state with copious cyclin B and high MPF activity. (C) Oscillating extract: $k_8 = 0.55$. Periodic oscillation of cyclin B level and MPF activity; period = 28 min. (Phase plane file: 10_4_2.ode)

System (10.12)-(10.15) can be reduced to two variables and analyzed by phase-plane methods, if we make pseudo-steady state approximations to [IEP] and $[Cdc20_A]$. In this case, we are left with Eqs. (10.12) and (10.15), with

$$[Cdc20_A] = G\left(\frac{k_7[MPF]}{(k_{10}/k_9) + [MPF]}, k_8, J_7, J_8\right) \tag{10.16}$$

Phase plane portraits for this model are illustrated in Fig. 10.11. With proper choice of parameter values, one can observe stable G2 arrest (immature oocyte), stable metaphase arrest (mature oocyte), and stable limit cycle oscillations (reminiscent of MPF oscillations in frog egg extracts, which exhibit periodic tyrosine phosphorylation).

The full model, Eqs. (10.12)-(10.15), with both positive and negative feedback loops, can be studied by bifurcation theory; see Borisuk and Tyson (1998), Fig. 10(c).

10.5 Growth and Division Controls in Metazoans

In multicellular organisms, cell growth and division are under additional "social" constraints, because most somatic cells, though they find themselves bathed in a richly nutritious medium, are restrained from proliferating. Only if they receive specific "permission" from the body as a whole may these cells grow and divide. The permission slips include growth factors (small polypeptides secreted into the blood stream or interstitial fluids), and signals that reflect cell-cell contacts and adhesion to the extracellular matrix. Surveillance mechanisms monitor these signals and hold the cell in a resting state (alive but not proliferating) until conditions permit cell growth and division. If these surveillance mechanisms become mutated so that a cell loses crucial social constraints, it becomes transformed, in stages, to an invasive cancer, whose uncontrolled proliferation eventually interferes with some vital function and kills the organism.

10.5.1 The Cell Cycle Engine

Kohn (1999) has recently summarized our knowledge of the molecular signals controlling the cell cycle in mammals. The "wiring" diagram extends in fine print over four journal pages, and most people would agree that we are only beginning to unravel the details. How are we to make sense of a control system of such complexity? In this chapter we have seen that the molecular regulation of cell division can be understood in terms of some basic building blocks. Antagonistic interactions between CycB and Cdh1 and

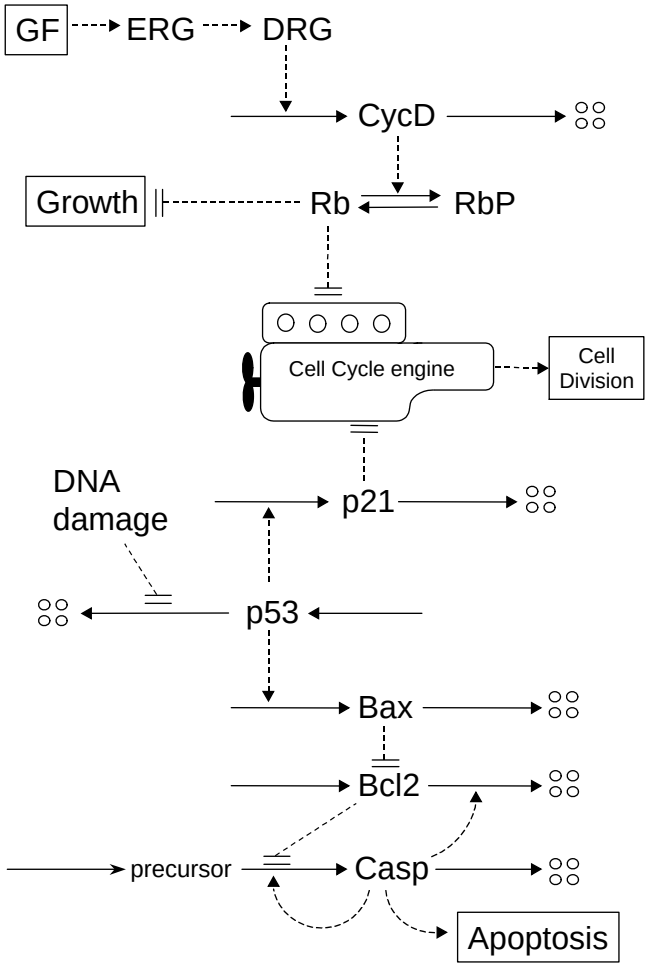

Figure 10.12 Cell cycle controls in mammals. The central icon represents the basic cell cycle engine (as in Fig. 10.6). The Retinoblastoma protein (Rb) inhibits progress through the cell cycle and overall growth of the cell. This inhibition is relieved, in response to growth factors (GF), by cyclin D-dependent kinase activity, which phosphorylates and inactivates Rb. ERG = early response genes, DRG = delayed response genes. DNA damage inhibits the cell cycle engine through a CKI (p21), which is synthesized in response to rising levels of p53. If the damage cannot be repaired, p53 stimulates synthesis of Bax1, which initiates apoptosis by binding to and inhibiting Bcl2. Casp = active form of caspase.

between CycB and CKI create the fundamental distinction between G1 and S-G2-M, starter kinases trigger the G1-S transition (Start), tyrosine phosphorylation of Cdk enforces a G2 checkpoint, and Cdc20 activation induces exit from mitosis (Finish). Within the complex wiring diagram of mammalian cell cycle controls, we can easily find all these basic building blocks. In other words, the generalized cell cycle control system in Section 10.3 applies equally well to mammalian cells as to yeast. Although

the full mammalian control system has lots of extra bells and whistles, at its core lies a yeast-like cell cycle engine. What makes metazoans different from single-celled yeasts are the "social controls" on the brakes and accelerators of the engine. To illustrate this idea, we propose (Fig. 10.12) a simple model of the pathways that respond to growth factor and DNA damage.

10.5.2 Accelerators and Brakes

In mammalian cells, the Retinoblastoma protein (Rb) represses progress through the cell cycle (by inactivating transcription of essential cyclins) and overall growth of the cell (by inactivating transcription of ribosomal and transfer RNAs). The "default" state of Rb is its active form. Active Rb keeps a somatic cell in the resting state (often called G0). For this cell to proliferate, Rb must be inactivated. Cyclin D, in combination with Cdk4 and Cdk6, is principally responsible for inactivating Rb (by phosphorylation) and bringing a resting cell out of G0 and into G1-S-G2-M.

Cyclin D is a growth factor sensor in mammalian cells. If growth factor is absent, so is CycD and the cell rests. When growth factor is provided to a resting cell, it binds to a membrane receptor and initiates a cascade of events: transcription of early response genes, which in turn stimulate transcription of delayed response genes, including CycD. As CycD-dependent kinase activity rises, Rb is phosphorylated and the brakes on growth and division are released.

DNA damage is relayed to the cell cycle engine through p53 and p21. The transcription factor, p53, is normally very unstable and consequently rare. However, in response to DNA damage, p53 is stabilized and its concentration increases. p53 induces synthesis of p21, which binds to and inhibits cyclin/Cdk complexes essential to progress through the cell cycle. The cell pauses in the cycle, as it tries to repair the damage. If the damage can be repaired in a timely fashion, p53 and p21 disappear and the cycle resumes. If the damage is too extensive to be repaired, p53 induces synthesis of Bax, which binds to and inhibits Bcl2. The role of Bcl2 in a normal, undamaged cell is to block the self-activation of caspases, a family of proteolytic enzymes that carry out a cell-suicide program known as apoptosis. When Bax inhibits Bcl2, the caspases turn on and destroy the damaged cell before it can pass on its genetic defects to future generations.

As explored in Exercise 10.8.10, the caspase control system has the potential for hysteretic switching. The default state of the system is Casp OFF ("do not self-destruct"). The p53-Bax-Bcl2 pathway may flip the switch to the Casp ON state, and the cell commits suicide. The hysteretic nature of the switch makes the self-destruct decision irreversible, just like Start and Finish.

10.6 Evolution of Cell Cycle Controls

We have taken a modular approach to the cell cycle control network, breaking it down into fundamental dynamical components (small sets of interacting proteins) and then

reassembling these components into ever more complicated and realistic models of present-day organisms. Of course, we can play the game backwards, speculating on the simplest, functional control system the primitive eukaryotic cell and on the selective pressures that drove the evolution of modern, multifunctional control systems.

In our view, the cell cycle is organized by a hysteresis loop (Fig. 10.3). Proliferating cells alternate between two stable attractors, **G1** and **S-G2-M**, driven by irreversible transitions, Start and Finish, at saddle-node bifurcations. Such a loop can be created by an antagonistic interaction between cyclin/Cdk and one of its negative regulators, either APC or CKI. (Wee1 is also an opponent of Cdk activity, but it is involved in stabilizing G2 phase, so it is not likely to have been the original "enemy" of Cdk.) Thus, we can imagine two scenarios for the evolution of modern cell cycle control.

10.6.1 Scenario 1: Cdh1/APC First

In this scenario, the cell cycle of the primordial eukaryote was organized around the antagonism between CycB/Cdk and Cdh1/APC; see Eqs. (10.1) and (10.2), and Fig. 10.3. As we have seen, such a control system would have had two checkpoints, in G1 phase and metaphase, governed by growth and chromosome readiness, respectively. S and M phases overlapped, which was acceptable as long as chromosomes were small (as in present-day budding yeast). As chromosomes lengthened and needed to be condensed before the mitotic spindle could handle them, mitosis became incompatible with ongoing DNA synthesis. In order to separate the onset of M from the end of S, tyrosine phosphorylation of Cdk by Wee1 might have been introduced. If the tyrosine- phosphorylated form were compatible with ongoing DNA synthesis but not active enough to support mitosis, a G2 checkpoint would have been created. Size control in vegetative cells could easily have migrated from the G1 checkpoint to the G2 checkpoint (as in present-day fission yeast). In this scenario, the third step involved introduction of CKIs to stabilize the G1 state, in order to permit sexual reproduction. (Yeast mutants that cannot halt in G1 because crucial CKIs are missing are sterile.) Much later, with the evolution of multicellularity, social controls over cell division would have been added, exploiting CKIs and transcriptional regulators as brakes on cell proliferation.

10.6.2 Scenario 2: CKI First

Equally well, the primordial control system could have centered on the antagonism between CycB/Cdk and CKI (see Exercise 10.8.13), with Cdc20/APC a "downstream" component involved only in cohesin degradation. As in scenario 1, Wee1 and Cdc25 evolved next to create a G2 checkpoint. Then, presumably by gene duplication, a Cdc20 homolog (Cdh1) evolved the capacity to degrade mitotic cyclins, giving cells the advantage of more robust arrest in G1. Social controls evolved with multicellularity.

10.7 Spontaneous Limit Cycle or Hysteresis Loop?

Almost by definition, the cell cycle is a periodic process, and for years this observation has tempted theoreticians to think of cell-cycle progression as a limit cycle solution of the underlying dynamical control system. By contrast, in this chapter we have been emphasizing a quite different picture: the cell cycle as an alternation between two self- maintaining states, **G1** (unreplicated DNA) and **S-G2-M** (DNA replication and mitosis). From a dynamical point of view, these two self-maintaining states are stable steady states of the kinetic equations describing the production of cyclin/Cdk activity and its destruction by cyclin proteolysis and CKI accumulation.

The control system is bistable because of the fundamental antagonism between Cdk and its "enemies. As expected for a dynamical system of this sort, bistability is observed only within a restricted region of parameter space; the boundaries of this region are parameter values where saddle-node bifurcations occur (e.g., Fig. 10.3). The control system can be driven from one state to the other by parameter changes that carry the system across saddle-node bifurcation points. Because the stable state initially occupied by the cell (**G1**) is lost at the saddle-node bifurcation, the cell is forced to make an irreversible transition (Start) to the other stable state (**S-G2-M**). In general, the opposite transition (Finish) can only be induced by parameter changes that carry the system across a different boundary, where the **S-G2-M** state is lost and the system jumps irreversibly to **G1**. When traced out in a diagram like Fig. 10.3, these parameter changes and state transitions create a "hysteresis loop."

The parameter changes that drive cells through Start and Finish are carried out by additional components of the control system, called "helper" molecules. The role of starter kinases is to destroy CKI so that the cell can leave G1, and the role of Cdc20 is to activate Cdh1 and stabilize CKI so that the cell can reenter G1. The helpers do not participate in the antagonistic interactions: starter kinases are not inhibited by CKI and not degraded by Cdh1/APC, and Cdc20 is not inhibited by cyclin/Cdk. Helper activity is only transient: it rises to induce a transition, but then falls back down in preparation for the reverse transition. Were the helper activity to stay high, it would impede the reverse transition. Mutations that interfere with the rise and fall of helper proteins are usually inviable or severely compromised in progress through the cell cycle.

If production and destruction of the helpers are included in the ODEs, converting former parameters into dynamical variables, don't we retrieve the notion of a limit cycle solution to the expanded equations? For instance, isn't Fig. 5 a limit cycle solution to Eqs. (10.1)-(10.6)? Indeed, it is a stable periodic solution, but it lacks many of the properties that we usually associate with limit cycles. Our intuition about limit cycles has been honed on continuous, autonomous ODEs, but system (10.1)-(10.5) is discontinuous and non-autonomous, with $m = m(t)$ given by solution of Eq. (10.6) and the prescription that $m \to m/2$ whenever the cell exits mitosis. Hence, over a broad range of parameter values, the period of the cell cycle rhythm is identical to the mass-doubling time, $T_d \approx ln2/\mu$, and independent of all other kinetic parameters

of the dynamical system. In our opinion, it is more profitable to think of m not as a dynamical variable, but as an external parameter that drives the control network, Eqs. (10.1)-(10.5), back and forth between regions of stable steady states (Fig. 10.4A, when m is small) and stable limit cycles (Fig. 10.4B, when m is large).

The principle of balanced growth and division necessitates size control operating somewhere in the cell cycle. If all size controls are removed by mutation (e.g., in fission yeast, $wee1^{ts}$ removes size control at the G2 checkpoint and rum1D removes it at the G1 checkpoint), then the underlying limit cycle oscillation of the cyclin/Cdk control network is revealed. But it is fatal! The double mutation, $wee1^{ts}$ $rum1\Delta$, is lethal: because its division cycle runs faster than its growth cycle, this cell divides at ever-smaller size until it dies.

Fertilized eggs behave something like autonomous limit cycle oscillators, because all checkpoint requirements have been bypassed. But this is a temporary affair. At the midblastula transition, the rapid, synchronous, autonomous cycles of the early embryo disappear as checkpoints are reinserted in the control system. The egg replaces limit cycle oscillations by checkpoint-controlled progression (from one stable steady state to another), and it is high time theoreticians did the same!

Exercises

1. In a trail-blazing paper, Goldbeter and Koshland (1981) showed that covalent modification of proteins (like the phosphorylation of Cdh1, described in Section 10.3.1) can generate abrupt, switch-like changes in activity of the modified protein. Let X be the active form of the protein, XP its inactive form, and assume that the total amount of protein is constant ($X + XP = 1$). Then

$$\frac{dX}{dt} = \frac{V_a(1-X)}{J_a + 1 - X} - \frac{V_i + X}{J_i + X}$$

   If inactivation occurs by phosphorylation, then V_a and J_a would be the activity and Michaelis constant of the phosphatase, and similarly V_i and J_i for the kinase. Clearly, the steady state activity of the protein is given by a quadratic equation, $AX^2 - BX + C = 0$, where $A = V_i - V_a, B = V_i - V_a + V_aJ_i + V_iJ_a, C = V_aJ_i$.

   (a) Show that $X = G(V_a, V_i, J_a, J_i) - \frac{2C}{B+\sqrt{B^2-4AC}}$.

   (b) Why is it not a good idea (from a computational point of view) to write? $G = (B \pm \sqrt{B^2 - 4AC})/2A$

2. The equations for the CycB and Cdh1 nullclines in Section 10.3.1, assuming $J_2 = J_3 = J_4 = \epsilon$, can be written

$$Y = \frac{\beta}{\epsilon + x}, y = p\frac{(1-x)(\epsilon + x)}{x(\epsilon + 1 - x)}$$

Saddle-node (SN) bifurcations occur when these two curves "touch" each other tangentially; i.e.,

$$\frac{\beta/p}{\epsilon+x} = \frac{(1-x)(\epsilon+x)}{x(\epsilon+1-x)}$$
$$\frac{-\beta/p}{(\epsilon+x)^2} = \frac{x(\epsilon+1-x)(1-\epsilon-2x)-(1-x)(\epsilon+x)(\epsilon+1-2x)}{x^2(\epsilon+1-x)^2}$$

Show that, if $\epsilon \ll 1$, these equations have two solutions: $x \approx \epsilon$, $\beta/p \approx 4\epsilon$, and

$$x = 1-\sqrt{\epsilon}+\epsilon+O(\epsilon^{3/2}), p/\beta = 1+2\sqrt{\epsilon}+O(\epsilon^{3/2})$$

3. Rewrite Eqs. (10.1)-(10.2) as

$$\frac{d[CycB]}{d\tau} = \beta-(J_2+[Cdh1])[CycB]$$
$$\alpha\frac{d[Cdh1]}{dt} = p\frac{(1-[Cdh1])}{J_3+1-[Cdh1]}-[CycB]\frac{[Cdh1]}{J_4+[Cdh1]}$$

Basal parameter values are $\beta = J_2 = J_3 = J_4 = 0.04, \alpha = k_2''/k_4 m = 0.05, p = 0.1$.

   (a) Use *XppAut*or *Winpp*to reproduce Fig. 10.3.
   (b) Let $J_2 = J_3 = J_4 = \epsilon$, and follow the saddle-node bifurcation points in two parameters, p and ϵ. (Answer: cusp at $p = 0.0522$ and $\epsilon = 0.265$.)
   (c) For $\beta = J_2 = 0.04$ and $p = 0.1$, find the region of bistability in the J_3, J_4 parameter plane. (Answer: cusp at $J_3 = 0.946$ and $J_4 = 0.530$.)

4. Figure 10.4 was constructed from Eqs. (10.1) and (10.3) with $[Cdh1] = G(k_3' + k_3''[Cdc20_T], k_4 m[CycB], J_3, J_4)$, and the parameter values in Table 10.1.

   (a) Create a one-parameter bifurcation diagram to show how steady-state and limit-cycle solutions depend on cell size, m. (Answer: saddle-nodes at $m = 0.510$ and 0.797, and Hopf at $m = 1.731$.)
   (b) Using k_2'' as the second parameter, follow the saddle-node and Hopf bifurcation points in part (a) to create a two-parameter bifurcation diagram. (Hint: cusp at $m = 0.457, k_2'' = 0.491$; the full bifurcation diagram is quite a challenge!)

5. Figure 10.8 was constructed from Eqs. (10.1'), (10.2)-(10.9) and the parameter values in Table 10.1. You should verify the results in Fig. 10.8A, for wild-type budding yeast cells, before continuing.

   (a) Supposing DNA synthesis starts when CycB activity rises above 0.1 and cell division occurs when CycB activity falls below 0.1, determine the durations of G1 phase (time from birth to beginning of S phase) and S-G2-M phase (from onset of DNA synthesis to cell division), and determine cell size at birth, at onset of DNA synthesis, and at division. Check your results against Table 10.3.

Table 10.3 Budding Yeast Mutants

Genotype	Parameter Changes	Duration of G1	Duration S-G2-M	Size at Birth	Size at DNA Syn.	Size at Division	Phenotype
Wild type	none	108	39	0.40	0.66	0.80	wild type
$sk\Delta$	$k_{13} = 0$	-	-	-	-	-	block in G1
$sk\Delta cki\Delta$	$k_{11} = k_{13} = 0$	105	42				viable
$cki\Delta$	$k_{11} = 0$						viable
$cdh\Delta$	$k_2'' = 0$						viable
$cki\Delta cdh\Delta$	$k_{13} = k_2'' = 0$	-	-	-	-	-	block in M
$cdc20^{ts}$	$k_3'' = k_2''' = 0$	-	-	-	-	-	block in M
$CDC20^{OP}$	$k_5' = 0.2$						viable
SK^{OP}	$k_{13}' = 0.3$					0.75	viable
SK^{OP}	$k_{13}' = 0.4$	-	-	-	-	-	inviable
$SIC1$ non-	$k_{12}'' =$						
degradable	$k_{12}''' = 0$						
$CDC20$	$k_6 = 0.01$						
non-degr							

Notes: The duration of S-G2-M in the model is too short, compared to experimental observations ($\sim$60 min).

(b) By simulation, confirm that $sk\delta$ mutant cells are inviable, but $sk\Delta$ $cki\Delta$ double mutant cells are viable (Fig. 10.8B,C). Fill in row 3 of Table 10.3.

(c) By simulation, show that $cki\Delta$ mutant cells are viable, and so are $cdh1\Delta$ mutants, but $cki\Delta cdh1\Delta$ double mutants are inviable. Fill in rows 4-6 of Table 10.3.

(d) Finish the rest of Table 10.3.

6. In the same way that you investigated budding yeast mutants in the previous problem, fill in the missing elements in Table 10.4 for fission yeast mutants.
7. Show that Eq. (10.11) is exact if

$$\frac{[CycB/CdkP]}{[CycB/Cdk]} = \frac{[CKI/CycB/CdkP]}{[CKI/CycB/Cdk]}$$

Why should this condition be true?

8. Consider the negative feedback oscillator, Eq. (10.12)-(10.14) with $[Cdc20_T] = [Mad] = 1$.

(a) Use *XppAut*to find the unstable steady state and then follow it as parameter k_9 varies between 0 and 1. You should find two Hopf bifurcation points, at $k_9 = 0.042$ and 0.23.

(b) Follow the Hopf bifurcation points in two parameters, k_9 and k_2''.

9. Consider again the negative feedback oscillator in the previous problem.

Table 10.4 Fission Yeast Mutants

Genotype	Parameter Changes	Duration of G1	Duration S-G2-M	Size at Birth	Size at DNA Syn.	Size at Division	Phenotype
Wild type	none	16	136	0.70	0.76	1.40	wild type
$wee1^-$	$k''_{wee} = 0.01$			0.40		0.80	small
$wee1^- cki\Delta$	$k_{11} = 0$, $k''_{wee} = 0.01$						
$cki\Delta$	$k_{11} = 0$						wild type
$cdh\Delta$	$k'_2 = 0$						vialble
$cki\Delta cdh\Delta$	$k_{13} = k'_2 = 0$						
$cdc25^-$	$k''_{25} = 0.05$						
$wee1^-$ $cdc25^-$	$k''_{wee} = 0.01$, $k''_{25} = 0.05$						viable

Notes: There are two major discrepancies between the model and observations. (1) The simulated double mutant, $wee1^-$ $cki\Delta$, is small but viable; whereas, in reality, these mutant cells become very small and die. (2) The simulated $cdc25-$ mutant grows very large but eventually divides; whereas, in reality, these mutant cells block in G2.

(a) Show that, to find the steady state, one must solve a cubic equation in $z = [Cdc20_A]$:

$$\frac{k_1 k_9}{k''_2 k_{10}} = \frac{k_8 z(J_7 + 1 - z)(z + \epsilon)}{k_7(1 - 7(J_8 + z) - k_8 z(J_7 + 1 - z)}$$

where $\epsilon = k'_2/k''_2$.

(b) Show that, if $k_7 > k_8$ and both J_7 and J_8 are $\ll 1$, the steady state is given approximately by

$$[Cdc20_A] = \left(\frac{k_1 k_9}{k''_2 k_{10}}\right)\left(\frac{k_7 - k_8}{k_8}\right) - \frac{k'_2}{k''_2}$$
$$[IEP] = \frac{k_8}{k_7}, [CycB] = \frac{k_{10}}{k_9}\left(\frac{k_8}{k_7 - k_8}\right)$$

(c) Show that the characteristic equation, which determines the stability of this steady state, is

$$\lambda\left[\lambda + \frac{k_1 k_9(k_7 - k_8)}{k_8 k_{10}})\right]\left[\lambda + \frac{k_7 k_{10}}{k_7 - k_8}\right] + k''_2 k_8 k_{10} = 0$$

(d) At a Hopf bifurcation, λ must be purely imaginary, $\lambda = \pm i\omega$. Show that the conditions for a Hopf bifurcation are

$$\omega^2 = \frac{k_1 k_7 k_9}{k_8} = \frac{k''_2 k_8^2 k_{10}^2 (k_7 - k_8)}{k_1 k_9 (k_7 - k_8)^2 + k_7 k_8 k_{10}^2}$$

(e) With all the parameters fixed at their values in Table 10.1, except k_9, show that the conditions for a Hopf bifurcation are satisfied when $k_9 \approx 0.23$ and $\omega \approx 0.135$. What is the period of the limit cycle oscillation close to this Hopf bifurcation?

10. Programmed cell death, also known as "apoptosis," is initiated by a set of proteolytic enzymes called caspases. Like most proteases, caspases are encoded as "proenzymes," *i.e.*, the primary gene product is an inactive polypeptide chain. The proenzyme must be cleaved in two places; of the resulting polypeptide chains, one is discarded and the other two associate to form the active protease. Active caspase itself can cleave the proenzyme, so the process of activation is autocatalytic:

In the diagram, we have distinguished between effector caspases, which carry out the cell suicide program, and initiator caspases, which get the process started. We can describe this simple diagram mathematically by a single ODE for C = activity of effector caspase:

$$\frac{dC}{dt} = k_1' + k_1'' \frac{C^n}{J^n + c^n} - k_2 C$$

where we have assumed that the autocatalytic step is a cooperative process, described by a Hill function.

(a) Recast this equation in dimensionless form

$$\frac{dx}{d\tau} = \epsilon + \frac{x^n}{1 + x^n} - \kappa x$$

Which parameter depends on initiator caspase activity?

(b) * For $n = 2$, find the region in (e,k) parameter space where the ODE has multiple steady states. Repeat for $n = 3, 4, 5$. Notice that the region of bistability increases with n. Prove that bistability is impossible for $n = 1$.

(c) From these results, it should be clear that programmed cell death can be controlled by initiator caspase activity. In normal cells, Bcl2 inhibits activation of initiator caspases. To turn on apoptosis, Bcl2 can be inhibited by a family of proteins (Bax, Bad,), which respond to different cellular insults. For example, DNA damage stabilizes p53, which induces synthesis of Bax (Fig. 10.12). Design a mathematical model for this signal transduction pathway, with effector caspase as the final component.

(d) Hysteresis in the modeled developed so far depends on our assumption of nonlinear (cooperative) auto-activation of effector caspases. There is another way to generate hysteresis in the model. Because caspases degrade Bcl2 and Bcl2 inhibits caspase activation, these two components are antagonistic proteins. Develop a model of these antagonistic interactions, along the lines of CycB/Cdk

and Cdh1/APC. Find conditions on the kinetic parameters that will permit apoptosis to be activated by the p53 - Bax - Bcl2 pathway.

11. Show that the ODE in 10.8.9(a) has saddle-node bifurcations whenever

$$\kappa \frac{nx^{n-1}}{(1+x^n)^2} and \epsilon = \frac{x^n(n-1-x^n)}{(1+x^n)^2}$$

Since we are looking for solutions with ϵ and $x > 0$, it is clearly necessary that $n > 1$. In addition, show that, for bistability, we must have $\epsilon < \epsilon_{crit} = (n-1)^2/4n$, and plot ϵ_{crit} as a function of n.

12. In the absence of growth factors (GF), both early response genes (ERG) and delayed response genes (DRG) are not transcribed. When GF is provided, first ERG proteins appear, then later DRG proteins, then ERG proteins disappear, but DRG proteins remain abundant. ERG proteins come and go over the course of about 6 h. Design a circuit (interactions among GF, ERG, DRG) that will account for these facts. Simulate your mechanism using Phase Plane. Design the circuit so that the output (DRG present or absent) shows hysteresis in response to provision and withdrawal of GF.
13. Because growth factors are soluble peptides secreted into the interstitial fluid and circulatory system, they allow multicellular organisms to regulate the proliferation of target cells far from the secretory cell. In addition to such long-range signaling, cell proliferation in metazoans is also controlled by local signals from extracellular matrix attachements and nearest neighbor contacts. The rules are given roughly by the Boolean function

Design a biochemical signaling mechanisms to implement this logic.

14. Suppose the primitive eukaryotic control system relied only on the antagonism between CycB/Cdk and CKI, without any help from Cdh1/APC. Then

$$\frac{d[CycB_T]}{dt} = k_1 - k_2'[CycB] - k_2''[Trimer]$$
$$\frac{d[CKI_T]}{dt} = k_{11} - (k_{12}' + k_{12}''m[CycB])[CKI_T]$$

Input		Output
ECM Attachment	Cell-Cell Contact	Cell Cycle Engine
No	No	Stop
Yes	No	Go
No	Yes	Stop
Yes	Yes	Stop

where $[CycB] = [CycBT] - [Trimer]$, and $[Trimer]$ is given by Eq. (10.8). We have assumed that CKI binding renders CycB unstable ($k_2'' \gg k_2'$).

(a) Draw phase portraits for this system. Show that cell growth can drive a Start transition.

(b) To execute Finish, we must assume that Cdc20 degrades CycB at anaphase. Modify the ODEs to incorporate this signal, and show how Cdc20 activation returns the control system to G1.

CHAPTER 11

Stochasticity and Discreteness

Gregory D. Smith and Joel Keizer

06-27

The underlying molecular nature of cellular processes is sometimes easy to see. For example, the recent discovery of Ca^{2+} puffs and sparks is intriguing because these spatially localized Ca^{2+} elevations are due to Ca^{2+} release from a small number of intracellular Ca^{2+} channels (see Section (**??**)). Just as the patch clamp technique allows single channel electrical recording of plasma membrane ion channels, confocal microfluorimetry provides optical measurements of the macroscopic consequences of a molecular event: the gating of an intracellular Ca^{2+} channel.

It is intriguing that in these electrical and optical recordings a random or *stochastic* phenomenon is uncovered by *discreteness* in an experimental measurement. For example, in the case of Ca^{2+} puffs and sparks, the optical resolution of the confocal microscope (on the order of 1 μm^3), is sufficient to distinguish between Ca^{2+} release from neighboring clusters of intracellular channels. In the case of a voltage clamp recording using an inside-out patch one or a few ion channels are physically and electrically isolated (see Fig. (**??**)). These exquisite measurements are discrete in the sense that the observables, though changing in time, only take on particular values.

When modeling a macroscopic current, a gating variable often represents the time-varying fraction of open channels. When ordinary differential equations are written describing the dynamics of these gating variables, the fraction f_i of channels in a given state i can take on any value between 0 and 1. However, for a cellular membrane containing N ion channels, each either open or closed, a careful accounting gives exactly $N+1$

possible fractions of open channels: $f \in \{0, 1/N, 2/N, \cdots, (N-2)/N, (N-1)/N, 1\}$. Indeed, the fraction of open channels can only take on arbitrary values between 0 and 1 when the number of ion channels is effectively infinite. In the case of a single two-state channel, the open 'fraction' is always 1 or 0, all or none. The ODE models discussed in previous chapters implicitly assume N is large enough that continuous (as opposed to discrete) gating variables are a good approximation.

In this Chapter we will show how the ODEs used in deterministic modeling arise from microscopic descriptions of stochastic ion channel kinetics. In addition, we will discuss Brownian motion, ionic current and membrane potential fluctuations due to the stochastic gating of collections of ion channels, and dynamic phenomena, such as stochastic excitability, induced by channel noise in cells and cellular models. In the process we will introduce several important modeling techniques that are applicable when stochasticity and discreteness are important aspects of a cellular phenomena of interest.

11.1 Brownian motion

When molecular events are observed experimentally, many other events are not observed. These hidden variables make the measurement of molecular processes inherently statistical. For example, Ca^{2+} puffs in immature *Xenopus* oocytes have an average duration of 250 ms, whilst Ca^{2+} sparks, observed in cardiac myocytes, are much faster events. However, the statement that Ca^{2+} sparks in cardiac myocytes have a duration of approximately 40 ms is, of course, a statistical characterization. Single Ca^{2+} release sites observed over extended periods show tremendous variability in spark brightness, duration, and size. This observation cannot be explained by heterogeneity among release sites, but rather suggests that molecular processes underlying Ca^{2+} sparks are inherently stochastic.

Similarly, the erratic movement of a Brownian particle is random precisely because we are unable to describe comprehensively what is essentially a deterministic system: a large particle buffeted by many water molecules. The problem with a deterministic theory of Brownian motion is that an extremely large number of water molecules influence the particle's motion. Though in principle it is only a technical difficulty to simultaneously integrate Newton's equations of motion for all water molecules of interest, it will always be impossible to accurately choose initial conditions to such a problem. For this reason, theoretical descriptions of Brownian motion are statistical in nature.

An important model for Brownian motion is a one-dimensional *random walk*. Imagine the motion of a particle restricted to movement along the real number line, and let $X(t)$ be a random variable that indicates it's position at time t. Let's further assume the particle is 'released' at the origin ($X(0) = 0$) and upon increments of time of duration Δt the particle moves with probability p ($0 \leq p \leq 1$) a particular distance Δx to the right, and with probability $1 - p$ the same distance to the left. Because

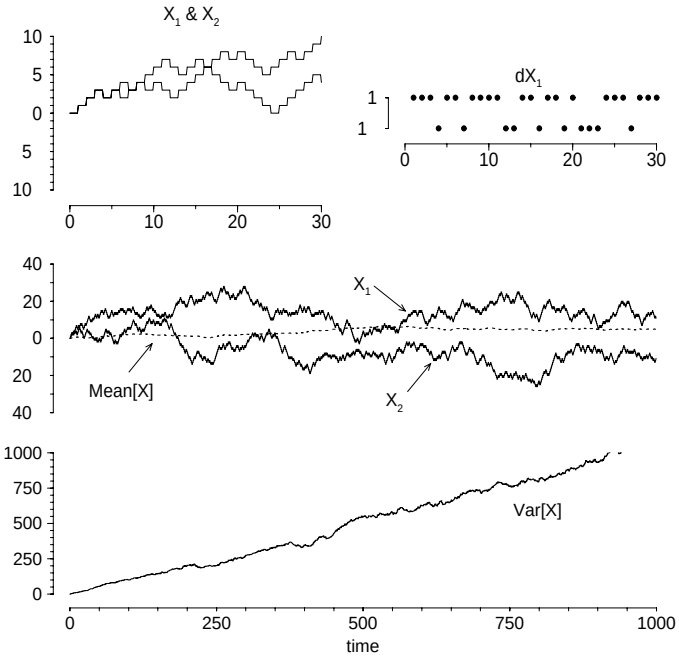

Figure 11.1 Two instantiations, X_1 and X_2, of an unbiased random walk are plotted, as well as the increments (ΔX_1) for the upper trajectory. The simulation is continued for 1000 time steps. The mean of 100 trials is near zero while he variance of 100 trials increases linearly with time. Note that the increments (ΔX_1) are distributed according to $\text{Prob}\{\Delta X = 1\} = \text{Prob}\{\Delta X = -1\} = 1/2$.

$\text{Prob}\{\Delta X = 1\} = \text{Prob}\{\Delta X = -1\} = 1/2$ the average increment in the position is zero

$$\langle \Delta X \rangle = 0$$

and after one such time step the particle will either be at position Δx or $-\Delta x$ with probabilities

$$\begin{aligned} \text{Prob}\{X(\Delta t) = \Delta x\} &= p \\ \text{Prob}\{X(\Delta t) = -\Delta x\} &= 1 - p \end{aligned}$$

Following the same rule of movement for the particle, let us repeat the process a total of i times, for a total elapsed time of $T = i\Delta t$. Accounting for the particles current position, $X(t)$, the movement rule can be written as

$$\begin{aligned} \text{Prob}\{X(t + \Delta t) = x + \Delta x | X(t) = x\} &= p \\ \text{Prob}\{X(t + \Delta t) = x - \Delta x | X(t) = x\} &= 1 - p \end{aligned}$$

where the vertical bar indicates a conditional probability, $\text{Prob}\{A|B\}$ is the probability of A given B, that is, $\text{Prob}\{A \cap B\}/\text{Prob}\{B\}$. For example, at the end of the second

step, $i = 2$ and

$$\begin{aligned}
\text{Prob}\{X(2\Delta t) = -2\Delta x\} &= p^2 \\
\text{Prob}\{X(2\Delta t) = 0\} &= 2p\,(1-p) \\
\text{Prob}\{X(2\Delta t) = 2\Delta x\} &= (1-p)^2
\end{aligned}$$

The reader can confirm *conservation of probability*, that is, because the particle must be somewhere, the sum of the probabilities of these three possible outcomes is 1.

With further reflection, we can derive the probability distribution for $X(t)$ for any number of steps i. We do this by noting that with each step the probability of moving to the right is p, and thus after i iterations the number of rightward steps taken (K) is a binomially distributed random variable with parameters i and p,

$$\text{Prob}\{K = k\} = \left(\begin{array}{c} i \\ k \end{array} \right) p^k (1-p)^{i-k} \tag{11.1}$$

where the first term is the "i choose k" formula

$$\left(\begin{array}{c} i \\ k \end{array} \right) = \frac{i!}{i!\,(i-k)!}$$

Our knowledge of the probability distribution for K will allow us to find the probability distribution for X. This is because K and X are simply related to each other. If the Brownian particle has moved K steps to the right, then there were $i - K$ steps in which it moved to the left, giving a final position of

$$X = [K - (i-K)]\,\Delta x = (2K - i)\,\Delta x$$

Averaging both sides of this equation we find the expected position of the Brownian particle after i steps,

$$\langle X \rangle = (2\langle K \rangle - i)\,\Delta x \tag{11.2}$$

Because K is binomially distributed, it has mean

$$\langle K \rangle = ip$$

that can be substituting into Eqn. (11.2) to give

$$\langle X \rangle = i\,(2p-1)\,\Delta x$$

Thus, if the particle always moves to the right ($p = 1$), the expected value of its position is $i\Delta x$; if the particle always moves to the left ($p = 0$), the expected value of its position is $-i\Delta x$. Interestingly, if the random walk is *unbiased*, that is, the probability of moving to the left and right are equal ($p = 1 - p = 1/2$), the expected value of the position of the particle is $\langle X \rangle = 0$. There has been no net movement!

This is not the end of the story, however. Another important statistical parameter for our particle is the mean square displacement, $\langle X^2 \rangle$. This number will be nonnegative

and related to $\langle K^2 \rangle$ and $\langle K \rangle$ by

$$\langle X^2 \rangle = \langle [(2K - i)\,\Delta x]^2 \rangle = [4\langle K^2 \rangle - 4\langle K \rangle i + i^2]\,(\Delta x)^2$$

Now the mean square value of the binomially distributed K is

$$\langle K^2 \rangle = (ip)^2 + ip\,(1-p)$$

giving a variance of

$$\langle (K - \langle K \rangle)^2 \rangle = \langle K^2 \rangle - \langle K \rangle^2 = ip\,(1-p)$$

These facts allow us to calculate the mean square displacement of the Brownian particle,

$$\langle X^2 \rangle = i\,(\Delta x)^2$$

Interestingly, although the mean displacement of the particle is zero, the mean square displacement increases by the fixed amount $(\Delta x)^2$ with each iteration. Remembering that i was related to time by $T = i\Delta t$, and defining the parameter D to be $D = (\Delta x)^2 / 2\Delta t$, we can write

$$\langle X^2 \rangle = 2DT$$

Here we see explicitly that the mean square displacement of the particle is linearly proportional to time. Fig. (11.1) confirms this by showing two example random walk trajectories, $X_1(t)$ and $X_2(t)$, as well as the mean square displacement (calculated from 100 trials) plotted as a function of time. In this simulation, $\Delta x = 1$ and Δt=1, so the proportionality constant, $2D$, is 1.

11.2 Stochastic Processes on Molecular States

In previous chapters we have seen several diagrams represent various molecular states and transitions between them due to conformational changes and binding or unbinding of ligands. If we assume a large number of molecules, we have seen in previous chapters how to write rate equations consistent with these diagrams. However, in order to mathematically interpret a transition-state diagram representing a single molecule, or a small number of molecules? The short answer to this question is that transition rates can be interpreted as transition probabilities per unit time.

For example, consider a single GLUT molecule and the four states (S_1, S_2, S_3, S_4) and transitions shown in Fig. (**??**). Define s to be a random variable taking values $s \in \{1, 2, 3, 4\}$ corresponding to these four states, and write Prob$\{s = i, t\}$ (or for short, $P_i(t)$) to represent the probability that $s(t) = i$, that is, the molecule is in state i at time t. Because the molecule must be in one of the four states, total probability must be conserved and we have

$$\sum_{i=1}^{4} P_i(t) = 1$$

Now consider the possibility that the GLUT transporter is in state 1 at time t. If this is the case, then the rate or flux $j_{12} = k_{12}[G]_{out}$ (e.g., with units of s^{-1}) is related to the probability that in a short interval of time Δt the GLUT transporter will associate with glucose, thereby transitioning out of state 1 and into state 2. That is,

$$j_{12}\Delta t = \text{Prob}\{s = 2, t + \Delta t | s = 1, t\} \tag{11.3}$$

where $j_{12}\Delta t$ is dimensionless (a pure number) and $\text{Prob}\{s = 2, t + \Delta t | s = 1, t\}$ is the probability, given the channel is in state 1, of a $1 \to 2$ transition occuring in the interval $[t, t+\Delta t]$. Multiplying by $P_1(t)$, the probability that the GLUT transporter is indeed in state 1, we find that $j_{12}P_1(t)\Delta t$ is the probability that transition $1 \to 2$ actually occurs.

Fig. (**??**) and Table (**??**) indicate four possible ways for the GLUT transporter to enter or leave state 1. Accounting for all of these, we have

$$P_1(t + \Delta t) = P_1(t) - k_{12}[G]_{out}P_1(t)\Delta t - k_{14}P_1(t)\Delta t + k_{21}P_2(t)\Delta t + k_{41}P_4(t)\Delta t$$

Writing three additional equations relating $P_i(t + \Delta t)$ and $P_i(t)$ for $i = \{2,3,4\}$ and taking the limit $\Delta t \to 0$ gives,

$$\frac{dP_1}{dt} = -k_{12}[G]_{out}P_1 + k_{21}P_2 + k_{41}P_4 - k_{14}P_1 \tag{11.4}$$

$$\frac{dP_2}{dt} = +k_{12}[G]_{out}P_1 - k_{21}P_2 - k_{23}P_2 + k_{32}P_3 \tag{11.5}$$

$$\frac{dP_3}{dt} = +k_{23}P_2 - k_{32}P_3 - k_{34}P_3 + k_{43}[G]_{in}P_4 \tag{11.6}$$

$$\frac{dP_4}{dt} = +k_{34}P_3 - k_{43}[G]_{in}P_4 - k_{41}P_4 + k_{14}P_1 \tag{11.7}$$

Note the similarity of these equations to Eqn. (**??**), the kinetic equation for average fraction of N GLUTS in state 1. This is not accident. The equation governing changes in probabilities for a single molecule always has same form as the rate equation for a large number of molecules. Furthermore, we can always eliminate one of equation using the conservation of probability. For example, $P_4(t)$ is always given by $P_4(t) = 1 - P_1(t) - P_2(t) - P_3(t)$.

11.3 An ensemble of two-state ion channels

In the previous section we argued that the equation governing changes in probabilities for a single molecule has the same form as the rate equation for a large number of molecules. Though true, this connection can be made more rigorous by specifying the number of molecules we are considering in advance. To simplify calculations we will consider a simple transition-state diagrams encountered first in Chapter (**??**), the

kinetic scheme for ion channel with two states, one closed (C) and the other open (O),

$$C\,(\text{closed}) \underset{k_-}{\overset{k_+}{\rightleftharpoons}} O\,(\text{open}) \tag{11.8}$$

11.3.1 Probability of finding N channels in a the open state

Let us write N as the number of molecules, and let $P_O(n,t)$ and $P_C(n,t)$ be the probability of having n molecules in state O or C, respectively. Because we will ultimately be interested in the statistics of current fluctuations, we will focus our attention on $P_O(n,t)$. In any case, the presence of n open channels implies $N-n$ closed channels, i.e.,

$$P_C(n,t) = P_O(N-n,t) \qquad (0 \le n \le N)$$

Assume all N molecules are independent and consider a time interval $[t, t+\Delta t]$ short enough that only one molecule has appreciably probability of making a $C \to O$ or $O \to C$ transition. During this short time interval, there are four events that can influence $P_O(n,t)$, the probability that there n open channels. For example, it is possible that there are currently n open channels, and during the time interval $[t, t+\Delta t]$ one of these channels closes. This probability is given by

$$\text{loss}_- = k_- n P_O(n,t)\Delta t$$

where the parameter k_- is the transition probability for $O \to C$, $P_0(n,t)$ is the probability that there were n open channels to begin with, and the n scales this probability to account for the fact that any one of the n independent open channels can close with equivalent result. Similar reasoning leads to the expression,

$$P_O(n,t+\Delta t) = P_O(n,t) + \text{gain}_+ - \text{loss}_+ + \text{gain}_- - \text{loss}_- \tag{11.9}$$

where

$$\begin{aligned}
\text{gain}_- &= k_-(n+1)P_O(n+1,t)\Delta t \\
\text{loss}_+ &= k_+(N-n)P_O(n,t)\Delta t \\
\text{gain}_+ &= k_+(N-n+1)P_O(n-1,t)\Delta t
\end{aligned}$$

To give one more example, the gain_+ term in this equation represents a probability flux due to the possibility that there are $n-1$ open channels and one of the closed channels opens. This transition probability is given by is given by $k_+(N-n+1)P_O(n-1,t)\Delta t$, because any one of the $N-(n-1) = N-n+1$ closed channels can open with equivalent result.

Taking limit $\Delta t \to 0$ of Eqn. (11.9) gives the following ordinary differential equation

$$\begin{aligned}
\frac{d}{dt}P_O(n,t) &= k_+(N-n+1)P_O(n-1,t) - k_+(N-n)P_O(n,t) \\
&\quad + k_-(n+1)P_O(n+1,t) - k_- n P_O(n,t)
\end{aligned} \tag{11.10}$$

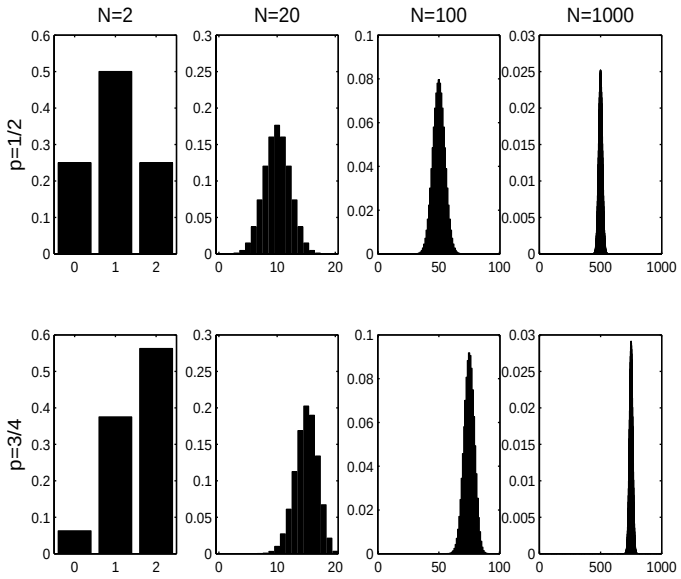

Figure 11.2 For an equilibrium ensemble of N two-state channels with open probability p, the likelihood of observing n open channels is given by the binomial probability distribution with parameters N and p (see Eqn. (11.11)). The binomial probability distribution has mean Np, variance $Np(1-p)$, and coefficient of variation $[(1-p)/Np]^{1/2}$. Note that as the equilibrium open probability, p, increases the mean number of open channels increases (rightward shift). The $N^{-1/2}$ factor in the coefficient of variation is reflected in the narrowing of the distributions (from left to right).

This rather complicated expression is called a *master equation*. It actually represents $N+1$ coupled ordinary differential equations, one for each $P_O(n,t)$ for $0 \leq n \leq N$ (all possible values for the number of open channels).

The equilibrium solution to the master equation is $N+1$ time-independent probabilities, $P_O^\infty(n)$, given by the binomial distribution,

$$P_O^\infty(n) = \left(\begin{array}{c} N \\ n \end{array} \right) p^n (1-p)^{N-n} \tag{11.11}$$

where $p = k_+/(k_+ + k_-)$ and

$$\left(\begin{array}{c} N \\ n \end{array} \right) = \frac{N!}{N!(N-n)!}$$

Fig. (11.2) shows several binomial probability distributions with parameters N and p varied. Given an ensemble of N two-state channels, these distributions represent the equilibrium probability of finding n channels in the open state. In the top row, the equilibrium open probability, of $p = 0.5$ results in a centered distribution: the likelihood of observing n open channels is equal to the likelihood of observing $N-n$

open channels. In the bottom row $p = 0.75$ and the enhanced likelihood that channels are open is evident in the rightward shift of the distributions.

11.3.2 The average number of open channels

The equilibrium solution to the master equation for the two-state channel given by Eqn. (11.11) is the binomial distribution, and thus the average number of open channels at equilibrium is $\langle N_O \rangle_\infty = Np$. But what about the time dependence of the average number of open channels? Because the average number of open channels is given by

$$\langle N_O \rangle = \sum_{n=0}^{N} n P_O(n,t) \tag{11.12}$$

we can find an equation for $d\langle N_O \rangle / dt$ by multiplying Eqn. (11.10) by n and summing. This gives

$$\begin{aligned} \frac{d\langle N_O \rangle}{dt} &= k_+ \sum_{n=0}^{N} n(N-n+1) P_O(n-1,t) - k_+ \sum_{n=0}^{N} n(N-n) P_O(n,t) \\ &\quad + k_- \sum_{n=0}^{N} n(n+1) P_O(n+1,t) - k_+ \sum_{n=0}^{N} n(N-n) P_O(n,t) \end{aligned} \tag{11.13}$$

In Exercise (2) the reader can show that this equation can be reduced to

$$\frac{d\langle N_O \rangle}{dt} = k_+ \left(N - \langle N_O \rangle \right) - k_- \langle N_O \rangle \tag{11.14}$$

where

$$N - \langle N_O \rangle = \langle N_C \rangle \tag{11.15}$$

Note that Eqn. (11.14) is identical to the rate equation for a population of two-state channels derived by other means in Chapter (**??**). For the duration of this chapter, we will refer to such an equation as an *average* rate equation. Also note that the equilibrium average number of open ($\langle N_O \rangle_\infty$) and closed ($\langle N_C \rangle_\infty$) channels can be found by setting the left hand side of Eqn. (11.14) to zero, that is,

$$\langle N_O \rangle_\infty = N \frac{k_+}{k_+ + k_-} = Np \tag{11.16}$$

$$\langle N_C \rangle_\infty = N \frac{k_-}{k_+ + k_-} = N(1-p) \tag{11.17}$$

in agreement our knowledge of the mean of a binomial distribution.

If we divide Eqn. (11.14) by the total number of channels, N, we find the average rate equation for the fraction of open channels,

$$\frac{d\langle f_O \rangle}{dt} = k_+ \left(1 - \langle f_O \rangle \right) - k_- \langle f_O \rangle \tag{11.18}$$

where $\langle f_O \rangle = \langle N_O \rangle / N$, $\langle f_C \rangle = \langle N_C \rangle / N$, and Eqn. (11.15) implies $\langle f_O \rangle + \langle f_C \rangle = 1$. The equilibrium fraction of open and closed channels are $\langle f_O \rangle_\infty = k_+ / (k_+ + k_-) = p$ and $\langle f_C \rangle_\infty = k_- / (k_+ + k_-) = 1 - p$. We thus see explicitly for a two-state channel that the master equation implies an average rate equation of the sort introduced in Chapter (**??**). This is true in general. In Exercise (3) the reader is encouraged to derive the master equation for the GLUT transporter, corresponding the average rate equations given by Eqn. (11.4) thru Eqn. (11.7).

11.3.3 The variance of the average number of open channels

One advantage of beginning with a master equation is that in addition to the average rate equation, an evolution equation for the variance in the number of open channels can be derived. The variance in the number of open channels is defined as

$$\sigma^2_{N_O} = \langle (N_O - \langle N_O \rangle)^2 \rangle = \sum_{n=0}^{N} (n - \langle N_O \rangle)^2 P_O(n,t) \tag{11.19}$$

Similarly, the variance in the number of closed channels is

$$\sigma^2_{N_C} = \langle (N_C - \langle N_C \rangle)^2 \rangle = \sum_{n=0}^{N} (n - \langle N_C \rangle)^2 P_C(n,t) \tag{11.20}$$

Again, we are ultimately interested in the statistics of current fluctuations, so we focus on $\sigma^2_{N_O}$. However, for the two-state channel under consideration, it is shown in Exercise (4) that these quantities are equal.

Beginning with Eqn. (11.19) and the master equation, Eqn. (11.10), it can be shown that the variance, $\sigma^2_{N_O}$, satisfies the following ODE

$$\frac{d\sigma^2_{N_O}}{dt} = -2(k_+ + k_-)\sigma^2_{N_O} + k_+(N - \langle N_O \rangle) + k_- \langle N_O \rangle \tag{11.21}$$

The equilibrium variance, $\left(\sigma^2_{N_O}\right)_\infty$, is thus given by steady-states of this equation. Using the methods of Chapter (**??**), we find

$$\left(\sigma^2_{N_O}\right)_\infty = N \frac{k_+ k_-}{(k_+ + k_-)^2} = Np(1-p) \tag{11.22}$$

From this equation it is clear that the equilibrium variance is proportional to N, the total number of channels. However, a relative measure of the variance known as the coefficient of variation is more meaningful. The coefficient of variation of the number of open channels, CV_{N_O}, is given by the ratio of the standard deviation, σ_{N_O} (the square root of the variance) and the mean, $\langle N_O \rangle$. At equilibrium, we have

$$(CV_{N_O})_\infty = \frac{(\sigma_{N_O})_\infty}{\langle N_O \rangle_\infty} = \frac{1}{\sqrt{N}} \sqrt{\frac{k_-}{k_+}} = \sqrt{\frac{1-p}{Np}}$$

where the last equality is in agreement with the mean and variance of a binomially distributed random variable being Np and $Np(1-p)$, respectively. From this expression

it is clear that the equilibrium coefficient of variation for the number of open channels is inversely proportional to the square root of the number of channels, N. Thus, in order to decrease this relative measure of channel noise by a factor of two, the number of channels must be increased by a factor of 4.

11.4 Simulation of single channel gating

11.4.1 The transition probability matrix

Following our analysis of the GLUT transporter and Eqn. (11.3), we know that for a channel closed at time t, $k_+\Delta t$ is the probability that it undergoes a transition and opens in the time interval $[t, t+\Delta t]$ provided Δt is small. By conservation, we also know that the probability that the channel remains closed during the same interval is $1-k_+\Delta t$. Because a similar arguments applies when the channel is open at time t, we can write the following *transition probability matrix*,

$$Q = \begin{bmatrix} \text{Prob}\{\text{C}, t+\Delta t|\text{C}, t\} & \text{Prob}\{\text{C}, t+\Delta t|\text{O}, t\} \\ \text{Prob}\{\text{O}, t+\Delta t|\text{C}, t\} & \text{Prob}\{\text{O}, t+\Delta t|\text{O}, t\} \end{bmatrix} = \begin{bmatrix} 1-k_+\Delta t & k_-\Delta t \\ k_+\Delta t & 1-k_-\Delta t \end{bmatrix} \tag{11.23}$$

where the elements of Q_{ij} (row i, column j) correspond to the transition probability from state j to state i, and conservation of probability ensures that all the columns sum to one, that is, for each column j,

$$\sum_i Q_{ij} = 1 \tag{11.24}$$

The transition probability matrix is especially useful when we write the current state of the channel as the vector,

$$\vec{P}(t) = \begin{bmatrix} \text{Prob}\{\text{C}, t\} \\ \text{Prob}\{\text{O}, t\} \end{bmatrix} \tag{11.25}$$

Using this notation, state of the channel at $t+\Delta t$ is given by the matrix multiplication

$$\vec{P}(t+\Delta t) = Q\vec{P}(t) \tag{11.26}$$

For example, if the channel is known to be closed at time t, then

$$\vec{P}(t) = \begin{bmatrix} 1 \\ 0 \end{bmatrix}$$

and the distribution of probability after one time step is

$$\vec{P}(t+\Delta t) = \begin{bmatrix} 1-k_+\Delta t & k_-\Delta t \\ k_+\Delta t & 1-k_-\Delta t \end{bmatrix} \begin{bmatrix} 1 \\ 0 \end{bmatrix} = \begin{bmatrix} 1-k_+\Delta t \\ k_+\Delta t \end{bmatrix}$$

Applying Eqn. (11.26) iteratively, we see that if the channel is closed at time t, the probability that is closed or open at time $t + 2\Delta t$ is given by,

$$\vec{P}(t + 2\Delta t) = Q\left[Q\vec{P}(t)\right] = Q^2\vec{P}(t)$$

or more generally,

$$\vec{P}(t + n\Delta t) = Q^n\vec{P}(t) \tag{11.27}$$

This iterative procedure can be used to calculate the evolution of the probability that the two-state channel is in an open or closed state. It amounts to using Euler's method to solve the master equation given by Eqn. (11.13) for a single channel ($N = 1$).

11.4.2 Dwell times for the two-state channel

Using the transition probability matrix, it is possible to derive an expression for the average amount of time that channel remains in the open or closed state, i.e., the open and closed *dwell times*. We have already seen that if a channel is closed at time t, the probability that it remains open at time $t + \Delta t$ is $1 - k_+\Delta t$. The probability that the channel remains closed for the following time step as well is thus $(1 - k_+\Delta t)^2$. In general, we can write

$$\text{Prob}\{C, [t, t + n\Delta t]|C, t\} = (1 - k_+\Delta t)^n \tag{11.28}$$

This expression is actually much simpler than Eqn. (11.27) because here we are insisting that the channel remain closed for the entire interval $[t, t + n\Delta t]$. Eqn. (11.27), on the other hand, accounts for the possibility that the channel changes states multiple times. If we define $\tau = n\Delta t$, we can rewrite Eqn. (11.28) as

$$\text{Prob}\{C, [t, t + \tau]|C, t\} = \left(1 - \frac{k_+\tau}{n}\right)^n$$

which is an approximate expression that becomes more accurate (for fixed τ) as $\Delta t \to 0$ and $n \to \infty$. Taking this limit and using

$$\lim_{n\to\infty}\left(1 - \frac{\alpha}{n}\right)^n = e^{-\alpha}$$

we find

$$\text{Prob}\{C, [t, t + \tau]|C, t\} = e^{-k_+\tau}$$

Thus, the probability that a channel closed at time t remains closed until $t + \tau$ is an exponentially decreasing function of τ.

In order to complete our calculate of the closed dwell time for the two-state channel, we must consider the probability that a channel closed at time t stays closed during the interval $[t, t + \tau]$ and then opens for the first time in the interval $[t + \tau, t + \tau + \Delta t]$. This probability is given by

$$\text{Prob}\{C, [t, t + \tau]|C, t\}\text{Prob}\{O, t + \tau + \Delta t|C, t + \tau\} = e^{-k_+\tau}k_+\Delta t$$

Thus, the average closed time will be given by

$$\langle \tau_c \rangle = \int_0^\infty \tau e^{-k_+ \tau} k_+ d\tau = \frac{1}{k_+}$$

where we have used

$$\int_0^\infty t e^{-t} dt = 1$$

Similar calculations show that for a channel is open at time t, the probability that it remains continuously open until time $t + \tau$ is

$$\text{Prob}\{O, [t, t+\tau] | O, t\} = e^{-k_- \tau}$$

and thus the average open time is given by

$$\langle \tau_o \rangle = \int_0^\infty \tau e^{-k_- \tau} k_- d\tau = \frac{1}{k_-}$$

11.4.3 Monte-Carlo simulation of the two-state channel

The elements Q_{ij} of the transition probability matrix represent the probability of making a transition from state j to state i in a time step of duration Δt. A simple method for simulating the transitions of a two-state channel is based on Eqn. (11.24). Because conservation of probability ensures that each column of Q will sum to unity, we can divide the interval [0,1] into regions, each corresponding to a possible change of state (or lack of change of state). Next, we choose a random number, Y, uniformly distributed on the interval [0,1] and make a transition (or not) based upon the subinterval in which Y falls. For example, let's return to the transition probability matrix for the two-state channel given by Eqn. (11.23). If the current state is open, then a transition to the closed state occurs if $0 \leq Y \leq k_- \Delta t$ and the channel remains open if $k_- \Delta t < Y \leq 1$, an interval of length $1 - k_- \Delta t$. Similarly, if the channel is closed, it remains closed if $0 \leq Y \leq 1 - k_+ \Delta t$ and a transition to the open state occurs if $1 - k_+ \Delta t < Y \leq 1$.

A Monte-Carlo simulation of the two-state channel can be easily performed using XPP by declaring a Markov variable:

```
# Example two state channel simulation
params kp=0.1, km=0.1, tauavg=1000
po(0)=0.5
markov n 2
{}{kp}
{km}{}
po'=-(po-n)/tauavg
aux n=n
done
```

In this XPP file, the line `markov n 2` declares a two state Markov variable, `n`, that

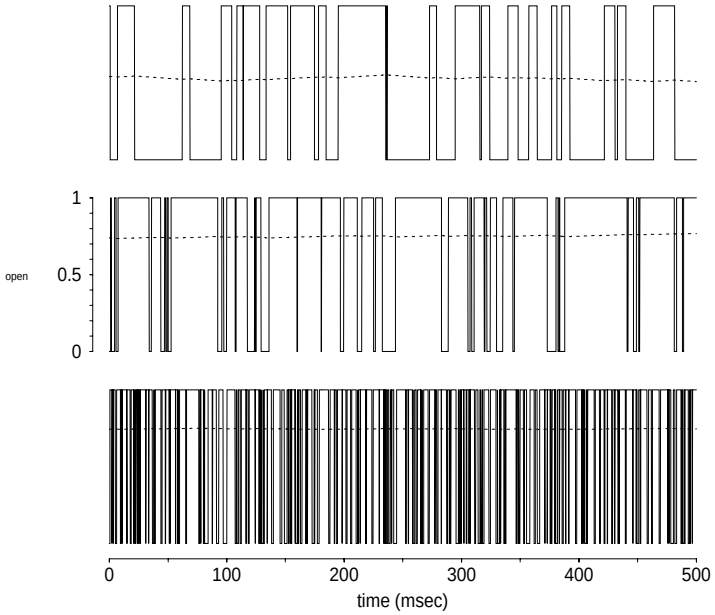

Figure 11.3 A Monte-Carlo simulation of the two-state ion channel simulated using XPP. Top: $k_+ = 0.1$ ms^{-1}, $k_- = 0.1$ ms^{-1}, giving an equilibrium open probability (dotted lines) of 0.5. Middle: k_+ changed to 0.3 ms^{-1}, and now the equilibrium open probability is 0.75. Bottom: transition probabilities increased by factor of 5 ($k_+ = 1.5$ ms^{-1}, $k_- = 0.5$ ms^{-1}). Note that average open time and average close time are shorter in this case, as evidenced by many more transitions between states.

will by convention take values of 0 and 1. The 2 x 2 matrix that follows is related to the transition probability matrix of Eqn. (11.23). To be consistent with XPP syntax, we have reversed the rows and columns of the transition probability matrix, so that the element in row i and column j now corresponds to a transition from state i to state j (that is, Q^{XPP} is the transpose of the matrix Q). Furthermore, the diagonal elements of the transition probability matrix are not included in the XPP file because XPP automatically calculates the diagonal elements using conservation of probability. (According to the row/column convention in XPP, each *row* must sum to unity). The auxiliary variable `n` is included so the Markov variable can be plotted. In addition, the differential equation `po'=-(po-n)/tauavg` performs a running average of `n` over the last `tauavg` milliseconds. Since `n=1` corresponds to an open channel, and `n=0` corresponds to a closed channel, this running average approximates the open probability of the channel.

Fig. (11.3) gives several example simulations of stochastic gating of a two-state channel using the Monte-Carlo method. By comparing open probabilities and dwell times in the three simulations shown, one can see how the transition probabilities, k_+ and k_-, lead to distinct channel kinetics. The reader is invited to reproduce this Fig. (11.3) using the XPP file presented above. In Exercise (6) the Monte-Carlo method

is shown to extend naturally to more complicated models, for example, the four state GLUT transporter model discussed in Section (11.2).

11.4.4 Simulating large numbers of independent channels

The gating of multiple independent channels can be simulated in one of several ways. Though it is possible to simulate a collection of N two-state channels in XPP by implementing N Markov variables with identical transition probability matrices, this method is cumbersome when N is large.

Under the assumption of identical and independent channels, an alternative method is to define a single Markov variable for the number of open channels. As discussed above, there are $N+1$ possibilities for the number of open channels, and the changes in this number occur via gain and loss terms in the master equation. If we are considering a time step small enough so that the likelihood of more than one channel changing state is negligible, then we can use Eqn. (11.10) as a guide to write a tridiagonal transition probability matrix,

$$Q^{XPP} = \begin{bmatrix} D_0 & Nk_+\Delta t & & & \\ k_-\Delta t & D_1 & (N-1)k_+\Delta t & & \\ & & \ddots & & \\ & & (N-1)k_-\Delta t & D_{N-1} & k_+\Delta t \\ & & & Nk_-\Delta t & D_N \end{bmatrix} \tag{11.29}$$

where we use XPP's convention that element Q_{ij}^{XPP} corresponds to the transition probability from state i to state j. Thus, the entry Q_{ij}^{XPP} represent the probability, given there are currently $n = i$ open channels, that an open or closed channel changes state to give $n = j$ open channels. With this row/column convention, the diagonal terms are such that each row sums to 1, that is,

$$\begin{aligned} D_0 &= 1 - Nk_+\Delta t \\ D_1 &= 1 - k_-\Delta t - (N-1)k_+\Delta t \\ D_{N-1} &= 1 - (N-1)k_-\Delta t - k_+\Delta t \\ D_N &= 1 - Nk_-\Delta t \end{aligned}$$

For example, to simulate 4 two-state ion channels using XPP, part of the `.ode` file would contain,

```
markov n 5
  {}    {4*kp}    {0}      {0}      {0}
 {km}     {}     {3*kp}    {0}      {0}
  {0}   {2*km}     {}     {2*kp}    {0}
  {0}     {0}    {3*km}     {}     {1*vp}
  {0}     {0}     {0}    {4*km}     {}
```

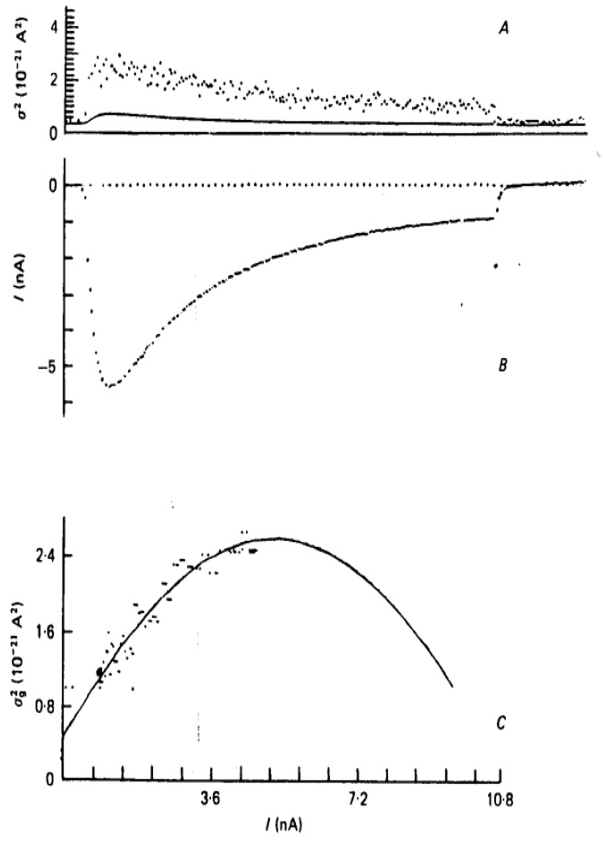

Figure 11.4 Variance and mean sodium current measured from voltage-clamped single myelinated nerve fibers from *Rana pipiens* depolarized to −15 mV after 50 ms prepulses to −105 mV. After carefully accounting for contributions to the variance due to thermal noise (A, solid line), variance arising from the stochastic gating of sodium channels remains (A, dots). This variance evolves as a function of time, as does the mean current (B). The parabolic relationship between variance and mean shown in (C) implies a single channel conductance is drawn with N=20,400 and i_{unit} = −0.55 pA. Reproduced with permission from Sigworth FJ. The variance of sodium current fluctuations at the node of Ranvier. *J. Physiol. (Lond).* 307:97-129, 1980.

The reader is encouraged to implement a simulation for $N = 4$ (or more) identical and independent two-state channels and confirm the analytical results from Section (11.3).

11.5 Fluctuations in macroscopic currents

When the voltage clamp technique is applied to isolated membrane patches, openings and closings of single ion channels can be observed. Recall the single-channel recordings of T-type Ca^{2+} currents shown in the top panels of Fig. (**??**)). Importantly, the bottom panel of Fig. (**??**) shows that when several hundred single-channel recordings are summed, the kinetics of rapid activation and slower inactivation of the T-type Ca^{2+} current are evident. In this summed trace, the relative size of the fluctuations in the macroscopic current is much smaller than those observed in the single-channel recordings; however, the fluctuations in ionic current are still noticeable.

During voltage clamp recordings of large numbers of ion channels, stochastic gating leads to current fluctuations. For example, panel B of Fig. (11.4) shows the time-

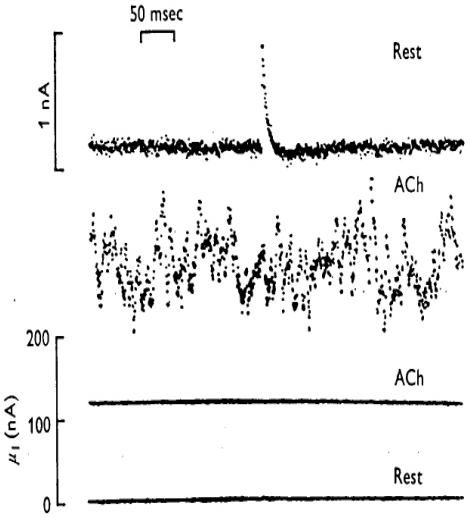

Figure 11.5 Acetylcholine produced current noise due to fluctuations in ionic conductance of voltage clamped end-plates of *Rana pipiens* nerve-muscle preparation. Iontophoretic application of ACh resulted in an increase in mean current as well as variance. The second trace labeled "Rest" also shows a spontaneous miniature end-plate current. Reproduced with permission from Anderson CR, Stevens CF. Voltage clamp analysis of acetylcholine produced end-plate current fluctuations at frog neuromuscular junction. *J. Physiol. (Lond).* 235(3):655-91, 1973.

evolution of the mean sodium current measured from voltage-clamped single myelinated nerve fibers of *Rana pipiens* (frog) that were depolarized to -15 mV after 50 ms prepulses to -105 mV. After carefully accounting for contributions to the variance of the sodium current due to thermal noise (panel A, solid line), the variance arising from the stochastic gating of sodium channels remains (panel A, dots). Fig. (11.5) shows macroscopic current fluctuations induced by the iontophoretic application of acetylcholine (ACh) to voltage clamped end-plates of a *Rana pipiens* nerve-muscle preparation. Interestingly, iontophoretic application of ACh increased the variance of the end-plate current as well as the mean. While the second trace in Fig. (11.5) shows a spontaneous miniature end-plate current, the phenomenon of interest is the 10-fold increase in variance observed throughout the duration of the second trace compared to the first.

In order to understand the relationship between fluctuations in macroscopic currents and the underlying single-channel kinetics, consider the statistics of ionic current implied by the two-state channel model presented in the previous section. In the simplest case, the unitary current of each two-state channel will be a random variable taking the value zero when the channel is closed or a fixed value, i_{unit}, when the channel is open. That is, the unitary current will be a random variable, I_{unit}, given by

$$I_{unit} = \begin{cases} i_{unit} = g_{unit}\,(V_{rev} - V) & \text{when open} \\ 0 & \text{when closed} \end{cases} \tag{11.30}$$

where V is a fixed command voltage, V_{rev} is the reversal potential for the single channel conductance, g_{unit}, and the unitary current, I_{unit}, is directly proportional to the conductance of the open channel. With these assumptions, it is straightforward to apply the results of Section (11.3) and derive the statistics of a fluctuating current that will

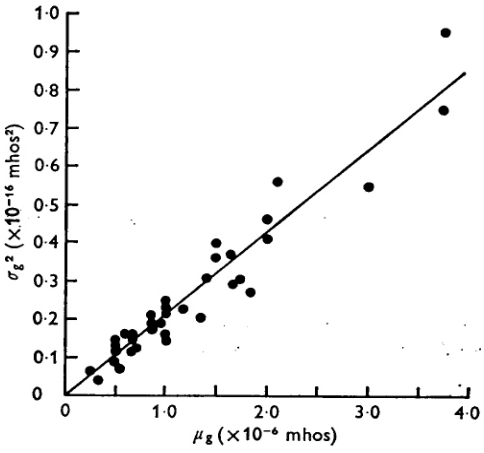

Figure 11.6 Variance of conductance fluctuations as a function of mean end-plate conductance of *Rana pipiens* nerve-muscle preparation. Because the unitary conductance of end-plate channels is small, the relationship is linear and the slope of 0.19×10^{-10}mho $= 19$ pS gives the single channel conductance. Reproduced with permission from Anderson CR, Stevens CF. Voltage clamp analysis of acetylcholine produced end-plate current fluctuations at frog neuromuscular junction. *J. Physiol. (Lond).* 235(3):655-91, 1973.

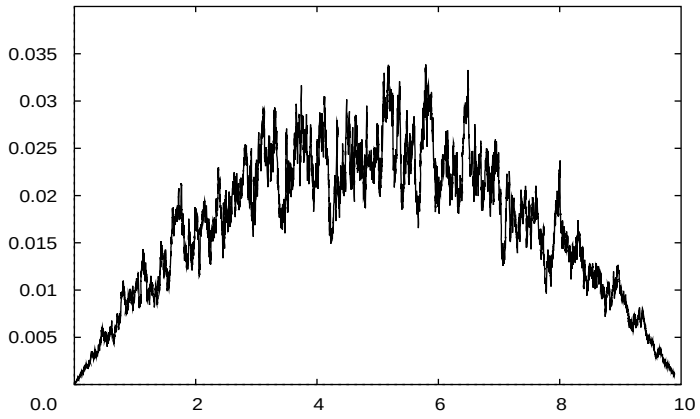

Figure 11.7 The parabolic relationship between the variance and mean of ionic current through 10,000 two-state channels. Mean and variance are from 100 simulations performed simultaneously using XPP, each involving a Langevin equation as described in text.

result from N two-state channels, each with unitary current given by Eqn. (11.30). The fluctuating macroscopic current will be a random variable defined by

$$I_{macro} = n\, i_{unit} \qquad (0 \leq n \leq N)$$

where n is once again the number of open channels. Because the macroscopic current is directly proportional to n, we can use Eqn. (11.12) to find the equilibrium average macroscopic current,

$$\langle I_{macro} \rangle_\infty = i_{unit} \langle N_O \rangle_\infty$$

Similarly, the equilibrium variance in the number of open channels, $(\sigma^2_{N_O})_\infty$, given by Eqn. (11.22), determines the equilibrium variance of the macroscopic current,

$$(\sigma^2_{I_{macro}})_\infty = i^2_{unit}(\sigma^2_{N_O})_\infty$$

Recall that if we write $p = k_+/(k_+ + k_-)$ the equilibrium mean and variance for the number of open channels are given by $\langle N_O \rangle_\infty = Np$ and $(\sigma^2_{N_O})_\infty = Np(1-p)$. Thus, the equilibrium mean and variance for the macroscopic current are given by $\langle I_{macro} \rangle_\infty = i_{unit} Np$ and $(\sigma^2_{I_{macro}})_\infty = i^2_{unit} Np(1-p)$. Combining these expressions and eliminatinating p gives

$$(\sigma^2_{I_{macro}})_\infty = i_{unit}\langle I_{macro} \rangle_\infty - \langle I_{macro} \rangle^2_\infty / N \tag{11.31}$$

where both $\langle I_{macro} \rangle_\infty$ and $(\sigma^2_{I_{macro}})_\infty$ are parameterized by p.

Eqn. (11.31) is the basis of a standard technique of membrane noise analysis whereby current fluctuations can be used to estimate the number of ion channels in a membrane patch. By repeatedly manipulating the fraction of open channels channels, p, an estimate of $(\sigma^2_{I_{macro}})_\infty$ as a function of $\langle I_{macro} \rangle_\infty$ is obtained. According to Eqn. (11.31), the relationship will be will be parabolic with zero variance at $\langle I_{macro} \rangle_\infty = 0$ and $i_{unit}N$ and a maximum variance of $(\sigma^2_{I_{macro}})_\infty = Ni^2_{unit}/4$ at $\langle I_{macro} \rangle_\infty = i_{unit}N/2$. In panel C of Fig. (11.4) this technique was applied to voltaged-clamped single myelinated nerve fibers from *Rana pipiens*. The parabolic relationship between mean and variance of implied N=20,400 sodium channels at this node of Ranvier and a unitary current of $i_{unit} = 0.55$ pA.

In Fig. (11.6) this technique was applied to end-plate conductance fluctuations of *Rana pipiens* nerve-muscle preparation. Here, the equilibrium variance of the macroscopic conductance, $\left(\sigma^2_{g_{macro}}\right)_\infty$ is plotted against the mean conductance, $\langle g_{macro} \rangle_\infty$, where the macroscopic conductance is related to the unitary conductance through $g_{macro} = Ng_{unit}$. Using Eqn. (11.31) and the relations

$$\langle g_{macro} \rangle_\infty = \frac{\langle I_{macro} \rangle_\infty}{V_{rev} - V} \qquad (\sigma^2_{g_{macro}})_\infty = \frac{(\sigma^2_{I_{macro}})_\infty}{(V_{rev} - V)^2} \qquad i_{unit} = g_{unit}\,(V_{rev} - V)$$

the reader can confirm that this relationship is also expected to be parabolic, that is,

$$(\sigma^2_{g_{macro}})_\infty = g_{unit}\langle g_{macro} \rangle_\infty - \langle g_{macro} \rangle^2_\infty / N$$

However, because the unitary end-plate channel conductance of *Rana pipiens* nerve-muscle preparation is very small ($\langle g_{macro} \rangle^2_\infty / N \approx 0$) the relationship is effectively linear,

$$(\sigma^2_{g_{macro}})_\infty = g_{unit}\langle g_{macro} \rangle_\infty$$

Indeed, the slope of the line in Fig. (11.6) gives a single channel conductance of 19 pS for the open end-plate channel.

11.6 Modeling fluctuations in macroscopic currents with stochastic ODEs

Fig. (11.7) shows an XPP simulation reproducing the parabolic relationship between the variance and mean of current fluctuations due to the stochastic gating of ion channels. This simulation includes 10,000 identical two-state channels with unitary conductance of 0.01 pA. A hundred trials were simultaneously performed and averaged to calculate the mean and variance as the open probability, p, was ranged from 0 to 1. Because the methods discussed in Section 11.4.3 would require the declaration of a Markov variable with 10,001 possible states, the reader may be wondering how this simulation was performed in XPP.

Indeed, when using XPP to simulate the stochastic gating of large numbers of ion channels, the Monte-Carlo method becomes impractical. However, when N is large, fluctuations in macroscopic currents can instead be described using a stochastic ordinary differential equation, called a Langevin equation, that takes the following form,

$$\frac{df}{dt} = g(f) + \xi$$

In this equation, the familiar deterministic dynamics given by $g(f)$ are supplemented with a rapidly varying random forcing term, $\xi(t)$. Because ξ is a random function of time, solving Eqn. (11.6) often means finding a solution $f(t)$ that satisfies the equation for a particular instantiation of ξ. Alternatively, if the statistics of ξ are given, we may be interested in deriving the statistics of the new random variable $f(t)$ that is formally defined by Eqn. (11.6).

The most common fluctuating force to consider are the increments of a Wiener process. Similar to the unbiased random walk discussed in Section (11.1), a Wiener process, B, is a random function of time that has zero mean,

$$\langle B(t) \rangle = 0 \tag{11.32}$$

and variance directly proportional to time

$$\langle B(t)^2 \rangle = t \tag{11.33}$$

Indeed, the instantiations of a Wiener process, B_1 and B_2, shown in Fig. (11.8) are remarkably similar to the random walks presented in Fig. (11.1). Just as the increments of the random walk were $\pm\Delta x$ with equal probability, resulting in an increment with mean zero $\langle \Delta X \rangle = 0$, the increments of the numerical approximation to a Wiener process shown in Fig. (11.8) are normally distributed with mean zero

$$\langle \Delta B \rangle = 0$$

In order to understand variance of the increments of this simulated Wiener process, we must remember that unlike the random walk shown in Fig. (11.1), a Wiener process is a continuous function of time, $B(t)$. A relevant statistic for the increments of a Wiener

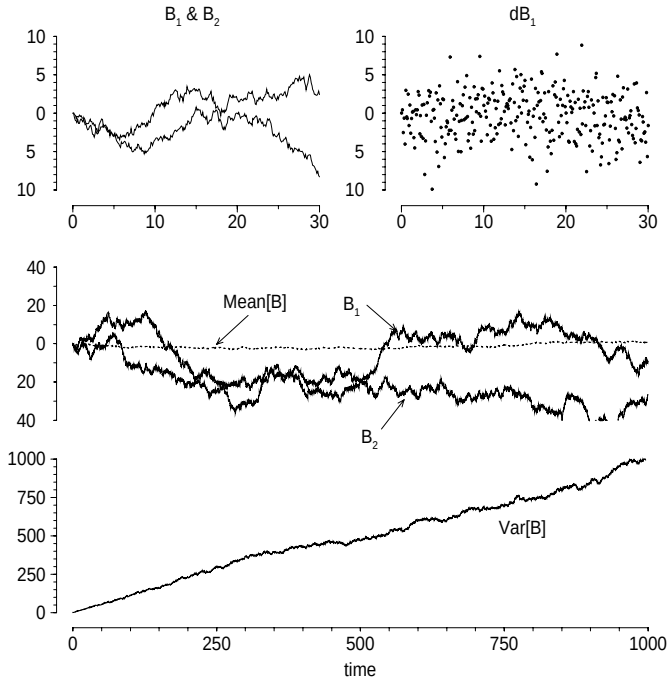

Figure 11.8 Two instantiations of a Wiener process, B_1 and B_2, have trajectories very similar to the random walks shown in Fig. (11.1). The mean of 100 trials is near zero, while the variance of 100 trials increases linearly with time. In these simulations, the increments (ΔB) are normally distributed with mean zero and variance $1/\Delta t$, where Δt is the integration time step.

process is the two-time covariance or *autocorrelation function*

$$\langle \Delta B(t) \Delta B(t') \rangle = \delta (t - t') \tag{11.34}$$

which implies that the Wiener process increments at any two different times are independent and uncorrelated. Eqn. (11.34) may appear unusual, especially if the reader is unfamiliar with the delta function, defined by $\delta(t) = 0$ for $t \neq 0$ and

$$\int_{-\infty}^{\infty} \delta(t) dt = 1$$

Eqn. (11.34) is perhaps best clarified through a discussion of how the `wiener` declaration is implemented in XPP.

The following XPP file demonstrates the statistics of a Wiener variable by implementing a simple Langevin equation.

```
# Demonstration of Wiener variable
wiener db
b'=db
aux db=db
```

```
done
```

Integrating `b` as a function of time results in Wiener trajectories similar to panels A and C of Fig. (11.1), while plotting the Wiener increment `db` reveals an erratic function of time (compare to panel B). The reader can confirm that decreasing the size of the integration time step in XPP increases the variance of `db`, i.e., the Wiener increments are have higher variance. In spite of this, the trajectories of `b` will appear to be macroscopically very similar. In fact, the increased variance in of `db` for small time steps is consistent with Eqn. (11.34). In XPP, the Wiener increment `db` is a normally distributed random variable with zero mean that is held fixed the time interval $[t, t+\Delta t]$ and updated after the integration time step is complete. If we rewrite Eqn. (11.34) to account for XPP's piecewise constant approximation to the Wiener process $W(t)$, we find

$$\langle \Delta B(t) \Delta B(t') \rangle = \begin{cases} 1/\Delta t & t' \in [t, t+\Delta t] \\ 0 & \text{otherwise} \end{cases}$$

XPP is thus correct to automatically adjust the variance of `db` depending on the integration time step, resulting in a numerical approximation to a Wiener process consistent with Eqn. (11.32) and Eqn. (11.33).

11.6.1 Langevin equation for an ensemble of two-state channels

In order to use a Langevin equation of the form of Eqn. (11.6) to simulate a large number of ion channels, we must make an appropriate choice for both the deterministic function ($g(f)$) as well as the statistics of the random variable, ξ. Recalling the average rate equation for the dynamics of the open fraction of channels, Eqn. (11.18), we write

$$\frac{df_O}{dt} = k_+ (1 - f_O) - k_- f_O + \xi \tag{11.35}$$

$$= -\frac{\langle f_O \rangle_\infty - f_O}{\tau_f} + \xi \tag{11.36}$$

where $f_O = N_O/N$ is a random variable, the fluctuating fraction of open channels, $\langle f_O \rangle_\infty = k_+/(k_+ + k_-)$, and $\tau_f = 1/(k_+ + k_-)$. For Eqn. (11.36) to be meaningful, we must specify the statistics of ξ. Although derivation of this fact is a result from statistical physics beyond the scope of this chapter, an appropriate choice for ξ is a fluctuating function of time that has zero mean,

$$\langle \xi(t) \rangle = 0$$

and an autocorrelation function given by

$$\langle \xi(t) \xi(t') \rangle = \gamma \delta (t - t')$$

where γ is inversely proportional to N and proportional to the sum of the rates of both the $O \to C$ and $C \to O$ transitions, that is,

$$\gamma = \frac{k_+ (1 - f_O) + k_- f_O}{N} \tag{11.37}$$

An appropriate choice for ξ is thus $\xi = \sqrt{\gamma}\Delta B$ where the ΔB are the increments of a Wiener process.

Although we haven't fully justified this choice for ξ, we can check that this random variable and Eqn. (11.36) define the random variable, f_O, in a manner consistent with the work in previous sections. To do this we use the fluctuation-dissipation theorem [1, 2] from statistical physics that relates γ, which occurs in the correlation function of ξ, to the equilibrium variance of f_O. The relationship depends on the relaxation time constant τ_f and is given by

$$\gamma = \frac{2\left(\sigma^2_{f_O}\right)_\infty}{\tau_f} \tag{11.38}$$

Using Eqn. (11.22), and remembering that $\left(\sigma^2_{f_O}\right)_\infty = \left(\sigma^2_{N_O}\right)_\infty / N^2$, the reader can confirm that the last equality holds at equilibrium.

Fig. (11.9) shows XPP simulations of the open fraction, f_O, of 1000 two-state ion channels calculated by integrating Eqn. (11.36). The transition rates used were $k_+ = k_- = 0.05$ ms^{-1} in A and $k_+ = k_- = 0.005$ ms^{-1} in B, giving a time constant τ_f of 10 and 100 ms, respectively. This difference in relaxation time constants is evident in the (normalized) autocorrelation functions compared in C. It can be shown that for an infinitely long simulation the autocorrelation functions for f_O is

$$\langle f_O(t) f_O(t') \rangle = \left(\sigma^2_{f_O}\right)_\infty e^{|t-t'|/\tau_f}$$

The narrower autocorrelation function in panel C thus corresponds to case with small time constant, τ_f. Note that although the time constant for relaxation to $\langle f_O \rangle_\infty = 0.5$ is faster in A than in B, the equilibrium variance, $\left(\sigma^2_{f_O}\right)_\infty$, shown in panel D is approximately equal in the two cases, as expected according to Eqn. (11.22).

11.6.2 Fokker-Planck equation for an ensemble of two-state channels

Rather than calculating trajectories for the fraction of open channels, f_O, using a Langevin equation, an alternative is to calculate the evolution of the probability distribution function (PDF) for f_O. While the binomial distribution encountered in Section (11.3) is an example of a discrete probability distribution (N_O takes on N+1 discrete values), the Langevin equation for f_O, Eqn. (11.36), implies that f_O can take on any value on the interval [0,1]. Thus, the PDF for f_O is continuous and defined as

$$P(f,t)\, df = \text{Prob}\{f_O \in (f, f + df)\}$$

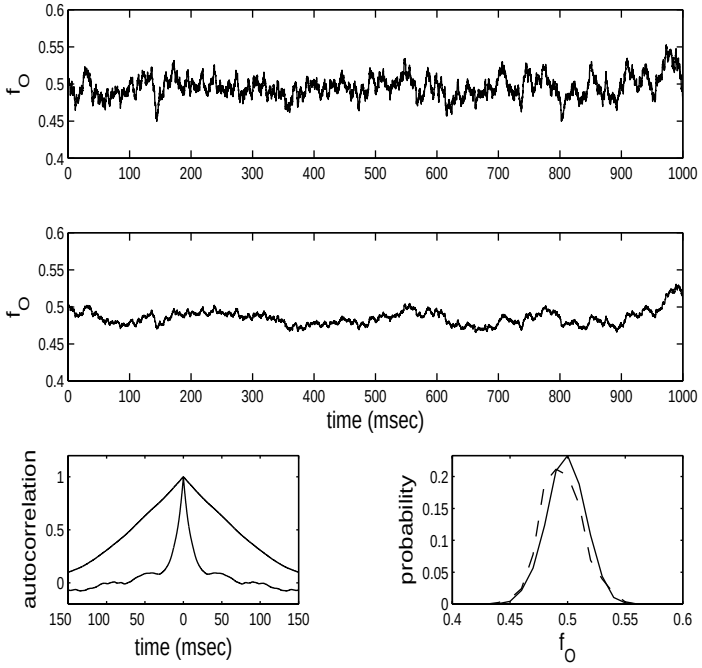

Figure 11.9 A,B) The open fraction, f_O, of 1000 two-state ion channels simulated using a Langevin equation in XPP. Transition rates are ten times faster in A than B so that the time constant τ_f is 10 and 100 ms, respectively. C) Numerically calculated autocorrelation function of f_O. D) The equilibrium variance of f_O is approximately equal in the two cases.

where conservation of probability gives

$$\int_0^1 P(f,t)\,df = 1 \tag{11.39}$$

We can write an evolution equation for $P(f,t)$, known as a Fokker-Planck equation, that corresponds to the Langevin description given by Eqn. (11.36),

$$\frac{\partial P(f,t)}{\partial t} = -\frac{\partial}{\partial f}\left[J_{adv}\left(f,t\right) + J_{dif}\left(f,t\right)\right] \tag{11.40}$$

In this equation, $J_{adv}(f,t)$ is a probability flux due to the deterministic dynamics given by

$$J_{adv}(f,t) = -\frac{f - \langle f_O \rangle_\infty}{\tau_f} P(f,t) \tag{11.41}$$

and $J_{dif}(f,t)$ is a diffusional flux that accounts for the spread of probability induced by the random variable, ξ. This diffusional probability flux is given by

$$J_{dif}(f,t) = -\frac{\gamma(f)}{2}\frac{\partial P(f,t)}{\partial f} \tag{11.42}$$

where γ is the function of f given by Eqn. (11.37). Rewrite Eqn. (11.41) in terms of the total probability flux, $J_{tot} = J_{adv} + J_{dif}$, we have

$$\frac{\partial P(f,t)}{\partial t} = -\frac{\partial J_{tot}(f,t)}{\partial f} \tag{11.43}$$

with associated boundary conditions

$$J_{tot}(0,t) = J_{tot}(1,t) = 0$$

that imply no flux of probability out of the physical range for f_O. An appropriate choice of initial conditions would be $P(f,0) = \delta(f - \langle f_O \rangle_\infty)$, implying that the system is known to be in equilibrium at $t = 0$.

Setting the left hand side of Eqn. (11.40) equal to zero, we see that the equilibrium probability distribution, $P_\infty(f)$, solves $J_{tot}^\infty = 0$, that is,

$$-\frac{f - \langle f_O \rangle_\infty}{\tau_f} P_\infty(f) - \frac{\gamma(f)}{2}\frac{dP_\infty(f)}{df} = 0 \tag{11.44}$$

This is an ordinary differential equation that can be solved numerically. However, we obtain more insight by approximating $\gamma(f)$, by

$$\gamma_\infty = \frac{k_+ (1 - \langle f_O \rangle_\infty) + k_- \langle f_O \rangle_\infty}{N}$$

a procedure that is valid when fluctuations of f_O away from equilibrium, $\langle f_O \rangle_\infty$, are small (that is, when N is large). It is left as an exercise for the reader to show that if we make this approximation the probability distribution

$$P_\infty(f) = A \exp\left[\frac{f\left(2\langle f_O \rangle_\infty - f\right)}{\gamma_\infty \tau_f}\right] \tag{11.45}$$

satisfies Eqn. (11.44), where the normalization constant, A, is chosen to satisfy conservation of probability, Eqn. (11.39). While this expression may not look familiar, when γ_∞ is sufficiently small (N is sufficiently large), P_∞ is well approximated by the Gaussian,

$$P_\infty(f) = \frac{1}{\sqrt{2\pi\left(\sigma_{f_O}^2\right)_\infty}} \exp\left[-\frac{\left(f - \langle f_O \rangle_\infty\right)^2}{2\left(\sigma_{f_O}^2\right)_\infty}\right]$$

that is, at equilibrium f_O will be a normally distributed random variable with mean $\langle f_O \rangle_\infty$ and variance $\left(\sigma_{f_O}^2\right)_\infty = \gamma_\infty \tau_f / 2$, in agreement with Eqn. (11.38). Fig. (11.9) panel D shows that $P_\infty(f)$ is approximately Gaussian for $N = 1000$.

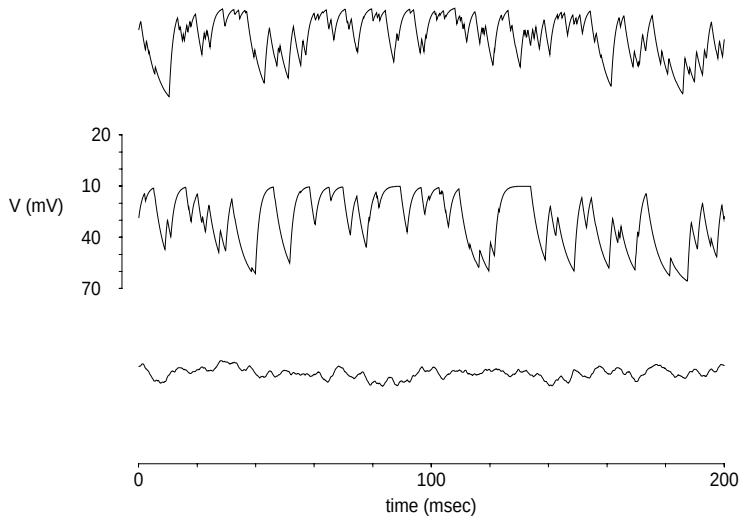

Figure 11.10 Membrane voltage fluctuations due to the stochastic gating of one or more sodium channels. In the top two panels a single channel is simualted. Transition probabilities are a factor of two slower in the second panel, leading to longer dwell times and fewer transitions as evidenced by 'kinks' in graph. In the bottom panel twenty channels are simulated. As the number of sodium channels the variance in membrane voltage decrease.

11.7 Membrane voltage fluctuations

In Section (11.5) we discussed macroscopic current fluctuations experimentally observed in voltage clamp recordings and a membrane noise analysis technique that can be used to measure the number N and unitary current i_{unit} of two-state ion channels. In this section we will simulate electrical recordings in which the membrane potential is not clamped, but rather fluctuates under the influence of two-state ion channels. Although a misnomer, such measurements are sometimes referred to as *current clamp* recordings. This is a considerably more complicated situation that is best modeled using a Fokker-Planck equation. To illustrate the method, let's assume that membrane voltage obeys the current balance equation,

$$C\frac{dV}{dt} = -g_L\,(V - V_L) - g_{Na}\,(V - V_{Na}) \tag{11.46}$$

where g_L is leakage conductance with reversal potential $V_L = -70$ mV, and g_{Na} a sodium conductance with reversal potential $V_{Na} = 60$ mV.

If membrane voltage fluctuations are due to a single two-state sodium channel, there are two relevant PDFs, each conditioned on the state of the channel,

$$P_C(v,t)dv = \text{Prob}\{V \in (v, v+dv)|C,t\}$$
$$P_O(v,t)dv = \text{Prob}\{V \in (v, v+dv)|O,t\}$$

where conservation of probability implies

$$\int_{-\infty}^{\infty} P_C(v,t)dv + \int_{-\infty}^{\infty} P_O(v,t)dv = 1$$

The equations for the evolution of these conditional PDFs are

$$\frac{\partial}{\partial t}P_C(v,t) = -\frac{\partial}{\partial v}J_C(v,t) - k_+P_C(v,t) + k_-P_O(v,t) \tag{11.47}$$

$$\frac{\partial}{\partial t}P_O(v,t) = -\frac{\partial}{\partial v}J_O(v,t) + k_+P_C(v,t) - k_-P_O(v,t) \tag{11.48}$$

where, in analogy with J_{adv} in the previous section, $J_C(v,t)$ and $J_O(v,t)$ are probability fluxes due to membrane voltage obeying Eqn. (11.46). These fluxes are given by

$$J_C(v,t) = -\frac{1}{C}\left[g_L\left(v - V_L\right)\right]P_C(v,t)$$

$$J_O(v,t) = -\frac{1}{C}\left[g_L\left(v - V_L\right) + g_{Na}\left(v - V_{Na}\right)\right]P_O(v,t)$$

where the sodium current term occurs only in $J_O(v,t)$ because the dynamics of membrane potential depends on whether the sodium channel is open or closed. The reaction terms that appear in Eqn. (11.47) and Eqn. (11.48) account for the stochastic gating of the sodium channel. For example, the conditional probability $P_C(v,t)$ can decrease due to channel opening at a rate of $k_+P_C(v,t)$ and increase due to closing of open channels at a rate of $k_-P_O(v,t)$. The reaction terms occur with opposite sign because any increase or decrease in the conditional probability, $P_C(v,t)$, due to a channel gating implies an commensurate change in $P_O(v,t)$ (and vice-versa).

The top panel of Fig. (11.11) shows the equilibrium conditional probability distribution functions for the membrane voltage, $P_C^\infty(v)$ and $P_O^\infty(v)$, calculated numerically

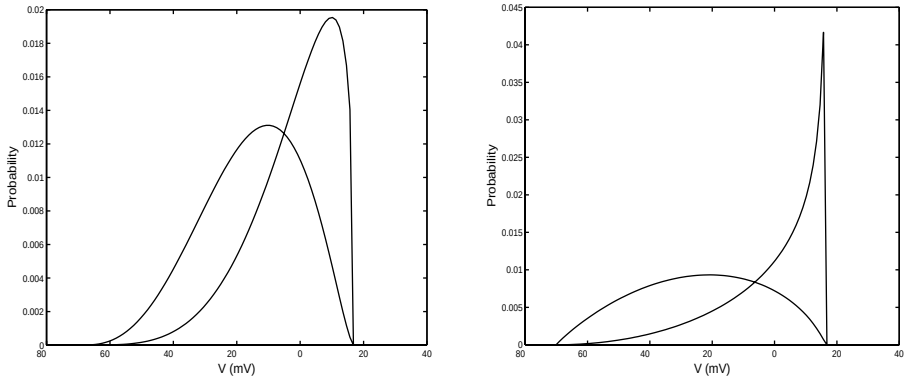

Figure 11.11 Probability distribution functions (PDFs), $P_C^\infty(v)$ and $P_O^\infty(v)$ for the membrane voltage conditioned on the state of a single two-state sodium channel. In the top panel transition probabilities are $k_+ = 1$ ms^{-1} and $k_- = 1$ ms^{-1}, while for bottom panel the transition probabilities are a factor of two slower. The difference in dwell times results in distinct equilibrium PDFs.

from Eqn. (11.48) and Eqn. (11.48). The simulation was run for 1 sec, corresponding to 1000 changes in channel state. As expected, $P_O^\infty(v)$ is shifted toward the right (depolarized V) relative to $P_C^\infty(v)$. The astute reader will note that the PDFs are not symmetric. This is because probability advects toward V_{Na} when the channel is open faster than it advects toward V_L when the channel is closed, i.e., an open sodium channel leads to a smaller membrane time constant. The bottom panel of Fig. (11.2) presents a simulation similar to that of the top panel, except that the rate constants k_+ and k_- are a factor of ten slower. In this case, more probability accumulating near both V_L and V_{Na}.

11.7.1 Membrane voltage fluctuations with an ensemble of two-state channels

The Fokker-Planck formulation described above can be extended to the case where membrane voltage fluctuations are due to an ensemble N two-state channels. If we write $P_O(n, v, t)$ for the conditional probability density for membrane voltage given n open sodium channels, we have

$$\begin{aligned}\frac{\partial}{\partial t}P_O(n,v,t) = &-\frac{\partial}{\partial v}J_O(n,v,t) \\ &+ k_+(N-n+1)P_O(n-1,v,t) - k_+(N-n)P_O(n,v,t) \\ &+ k_-(n+1)P_O(n+1,v,t) - k_-nP_O(n,v,t)\end{aligned} \tag{11.49}$$

where the reaction terms are based on the master equation formulation presented in Section (11.3.1), $J_O(n, v, t)$ is given by

$$J_O(n,v,t) = -\frac{1}{C}\left[g_L\left(v - V_L\right) + g_{Na}\frac{n}{N}\left(v - V_{Na}\right)\right]P_O(n,v,t)$$

and g_{Na} is the macroscopic sodium conductance. Note that Eqn. (11.49) represents $N + 1$ coupled partial differential equations, one for each $P_O(n, v, t)$ where $0 \leq n \leq N$.

Fig. (11.12) shows equilibrium conditional PDFs, $P_O^\infty(n, v)$, for membrane voltage fluctuations induced by 20 two-state sodium channels. As before, these PDFs are calculated by numerically solving a Fokker-Planck equation, Eqn. (11.49), until a steady-state is achieved. Careful inspection of the figure shows that in the case of high n (more open channels), the equilibrium distribution of membrane voltage is shifted toward V_{Na}. Note that these PDFs appear to be consistent with a binomial distribution for the total equilibrium probability for a given value of n, that is,

$$P_O^\infty(n) = \int_{-\infty}^{\infty} P_O^\infty(n,v)dv$$

is in agreement with Eqn. (11.16).

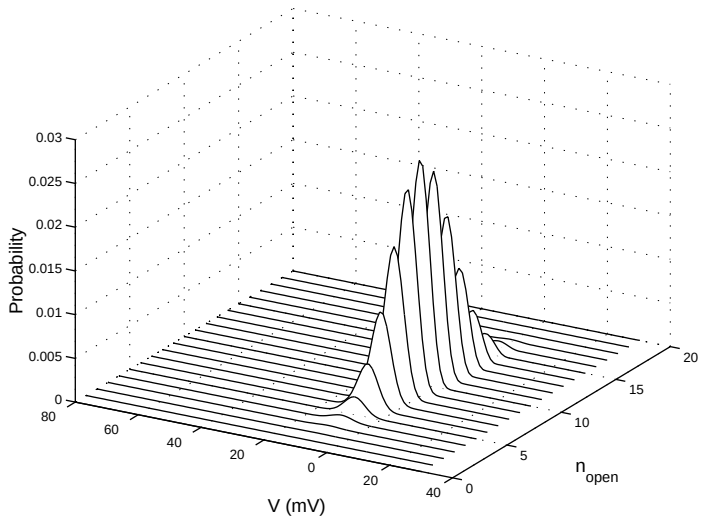

Figure 11.12 Conditional probability distribution functions for membrane voltage fluctuations due to stochastic gating of 20 two-state sodium channels. Parameters as in the top panel of Fig. (11.11).

11.8 Stochasticity and discreteness in an excitable membrane model

Using the results of previous sections, we are prepared to explore the consequences of stochasticity and discreteness in an excitable membrane model. The deterministic Morris-Lecar model for the excitability of barnacle muscle fiber is

$$C\frac{dV}{dt} = I_{app} - g_L\left(V - V_L\right) - g_k w\left(V - V_K\right) - g_{Ca} m_\infty(V)\left(V - V_{Ca}\right) \tag{11.50}$$

$$\frac{dw}{dt} = \frac{w_\infty(V) - w}{\tau_w(V)} \tag{11.51}$$

where the activation function for the Ca^{2+} current, $m_\infty(V)$, the activation function for the K^+ current, $w_\infty(V)$, and voltage-dependent time scale for activation of K^+ current, $\tau_w(V)$, are given in the Appendix.

In Eqn. (11.51), w is usually thought to represent the fraction of open K^+ channels. However, we now understand that this differential equation is actually an average rate equation similar to Eqn. (11.18). To be clear, let us write this deterministic average rate equation as

$$\frac{d\langle w\rangle}{dt} = \frac{w_\infty(V) - \langle w\rangle}{\tau_w(V)}$$

where w (a random variable) represent the fraction of open K^+ channels. The reader can easily verify that this average rate equation corresponds to the two-state kinetic

scheme

$$C\,(\text{closed}) \underset{\beta(V)}{\overset{\alpha(V)}{\rightleftharpoons}} O\,(\text{open})$$

where C and O indicate closed and open states of the K^+ channel, and the voltage-dependent transition rates, $\alpha(V)$ and $\beta(V)$ are given by

$$\alpha(V) = \frac{w_\infty(V)}{\tau_w(V)}$$
$$\beta(V) = \frac{1 - w_\infty(V)}{\tau_w(V)}$$

This, in turn, implies that the equilibrium fraction of open K^+ channels is

$$\langle w \rangle_\infty = w_\infty(V) = \frac{\alpha(V)}{\alpha(V) + \beta(V)}$$

and the time constant, $\tau_w(V)$ is

$$\tau_w(V) = \frac{1}{\alpha(V) + \beta(V)}$$

With these preliminaries, we can see that a Morris-Lecar simulation that includes channel noise due to a small number of K^+ channels could easily be performed in XPP by declaring several Markov variables using the voltage-dependent transition probability matrix,

$$Q^{XPP} = \begin{bmatrix} 1 - \alpha(V)\Delta t & \alpha(V)\Delta t \\ \beta(V)\Delta t & 1 - \beta(V)\Delta t \end{bmatrix}$$

for each channel. Alternatively, a larger collection of N channels can be simulated by tracking only a single Markov variable, the number of open K^+ channels. In this case, the following tridiagonal transition probability matrix would be implemented in XPP,

$$Q^{XPP} = \begin{bmatrix} D_0 & N\alpha & & & \\ \beta & D_1 & (N-1)\alpha & & \\ & \ddots & \ddots & \ddots & \\ & & (N-1)\beta & D_{N-1} & \alpha \\ & & & N\beta & D_N \end{bmatrix} \tag{11.52}$$

where it is implicit that both α and β are functions of V, and the diagonal terms are such that each row sums to 1, that is,

$$D_0 = 1 - N\alpha$$
$$D_1 = 1 - \beta - (N-1)\alpha$$

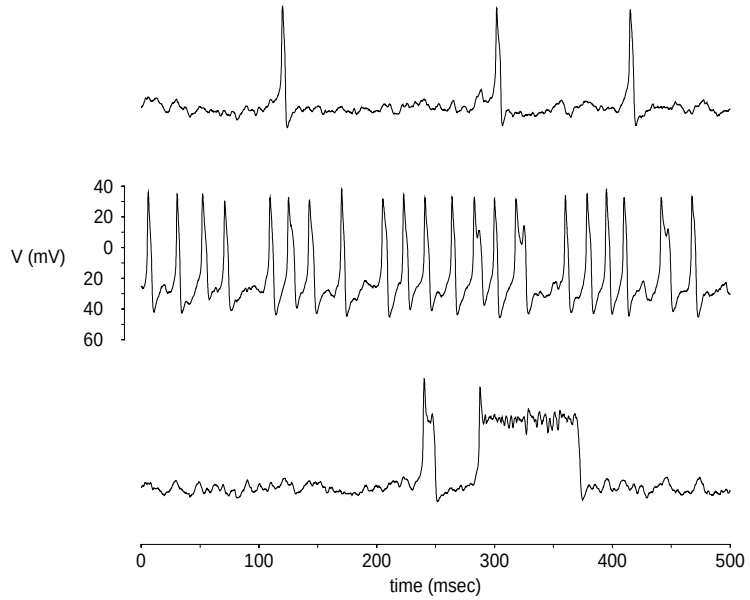

Figure 11.13 Morris-Lecar simulations including stochastic gating of 100 K^+ channels. Top: spontaneous excitability driven by channel noise is observed when $I_{app} = 10$ and the deterministic model is excitable. Middle: Stochastic oscillations are observed when $I_{app} = 12$ and the deterministic model is oscillatory. Bottom: Stochastic bistability is observed when the deterministic model is bistable ($I_{app} = 12$ and $v_3 =$ 15 mV (rather than standard value of 10 mV).

$$D_{N-1} = 1 - (N-1)\beta - \alpha$$
$$D_N = 1 - N\beta$$

11.8.1 Phenomenon induced by stochasticity and discreteness

Fig. (11.13) and Fig. (11.14) show stochastic Morris-Lecar simulations performed in XPP using a hybrid of the two methods discussed above. As detailed in the Appendix, these simulations include the stochastic voltage-dependent gating of 100 K^+ channels. In the top panel of Fig. (11.13) spontaneous action potentials are induced by this realistically simulated channel noise. We will refer to this phenomenon as "stochastic excitability," because it is understood a sampling of the "excitable" phase space of the deterministic model made possible by membrane potential fluctuations due to the stochastic gating of K^+ channels. Fig. (11.14) shows the trajectories from Fig. (11.13) in the (V, w) phase plane. The stochasticity and discreteness of the K^+ gating variable, w, allows trajectories to fluctuate around the fixed point of the deterministic model (lower left of top panel). Occasionally, K^+ channels spontaneously inactivate (w fluctuates toward 0) and a regenerative Ca^{2+} current leads to an action potential. This type of stochastic excitability has been observed in stochastic versions of the Hodgkin-Huxley

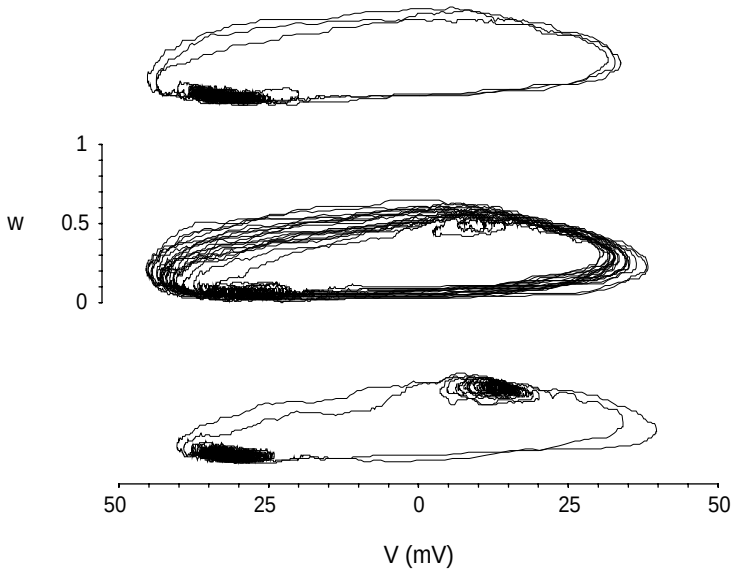

Figure 11.14 Morris-Lecar simulations with stochastic gating of 100 K^+ channels shown in the (V, w) phase plane. Top, middle, and bottom panels correspond to stochastic excitability, oscillations, and bistability shown in Fig. (11.13).

equations [3, 4] and is though to influence subthreshold membrane potential oscillations and excitability of stellate neurons of the medial entorhinal cortex of the hippocampal region [5, 6].

In the middle panel of Fig. (11.13) parameters are such that the deterministic model (as $N \to \infty$) is oscillatory. However, when $N = 100$ channel noise results in irregular oscillations. In the bottom panel of Fig. (11.13) stochastic bistability is observed. When parameters are chosen so that the deterministic model is bistable, channel noise allows the alternate sampling of two stable fixed points in the (V, w) phase plane, a phenomenon known as basin hoping.

11.8.2 Fokker-Planck equations for the stochastic Morris-Lecar model

The Fokker-Planck formulations described in Section (11.6.2) can be applied to the stochastic Morris-Lecar model described above. The evolution equations for the conditional PDFs take the following form

$$\begin{aligned}\frac{\partial}{\partial t}P_O(n,v,t) = &-\frac{\partial}{\partial v}J_O(n,v,t)\\ &+\alpha(v)(N-n+1)P_O(n-1,v,t)\\ &-\alpha(v)(N-n)P_O(n,v,t)\end{aligned} \tag{11.53}$$

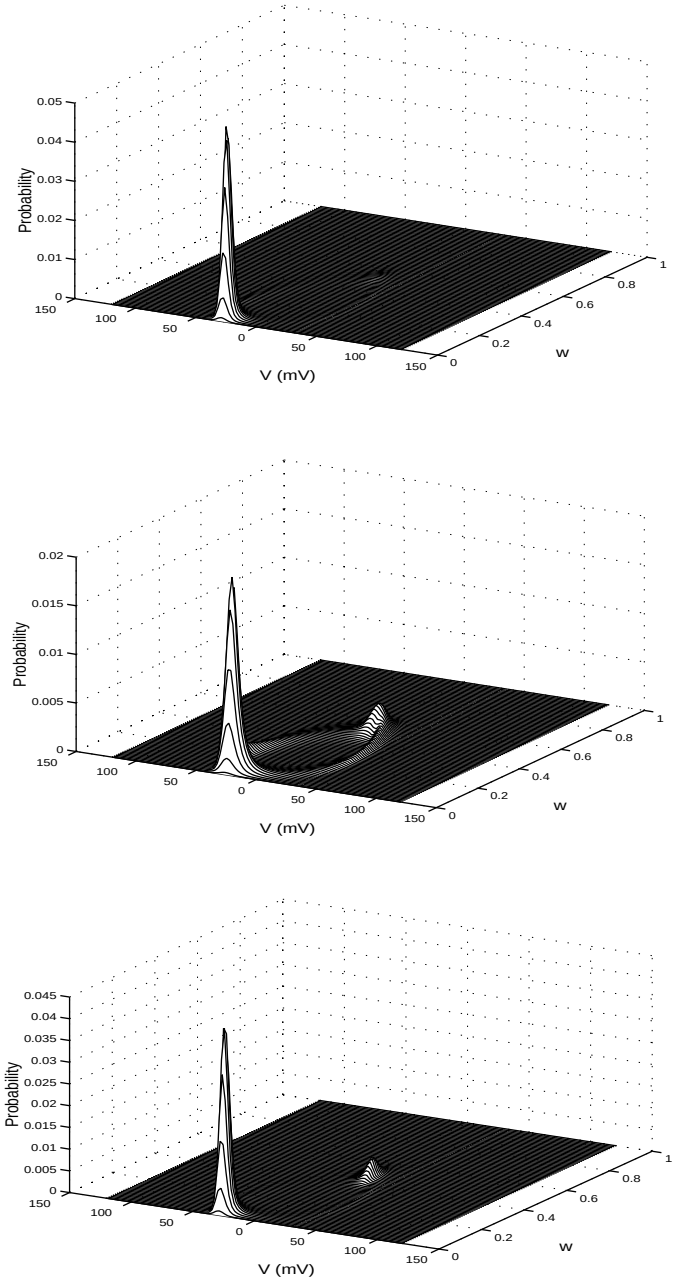

Figure 11.15 Probability distribution functions for the membrane voltage of the stochastic Morris-Lecar model conditioned on the number of open K^+ channels. The equilibrium PDFs show evidence of stochastic excitability, oscillations, and bistability, corresponding to the trajectories shown in Fig. (11.14).

$$+ \beta(v)(n+1)P_O(n+1,v,t) - \beta(v)nP_O(n,v,t)$$

similar to Eqn. (11.49) except that the transition probabilities are now voltage-dependent, and the probability fluxes, $J_O(n,v,t)$, are given by the Morris-Lecar current balance equation, Eqn. (11.50), that is

$$\begin{aligned} J_O(n,v,t) = -\frac{1}{C}\Big[& I_{app} - g_L\,(v - V_L) - g_k \frac{n}{N}\,(v - V_K) \\ & - g_{Ca} m_\infty(v)\,(v - V_{Ca})\Big]\,P_O(n,v,t) \end{aligned}$$

Fig. (11.15) shows equilibrium PDFs for the membrane voltage of the stochastic Morris-Lecar model conditioned on the number of open K^+ channels. These equilibrium PDFs are steady-state solutions to Eqn. (11.53) and correspond to the three types of trajectories shown in Fig. (11.14). The amount of time that trajectories spend in different regions of the (V,w) phase plane is reflected in these distributions. The top panel, for example, reveals that the Morris-Lecar model exhibiting stochastic excitability spends a large proportion of time near the threshold for excitation.

11.8.3 Langevin formulation for the stochastic Morris-Lecar model

To consider the behavior of the Morris-Lecar model under the influence of channel noise from a large number of K^+ channels, it is most convenient to use the Langevin formulation presented in Section (11.6.1). We do this by supplementing the rate equation for the average fraction of open K^+ channels, Eqn. (11.51), with a rapidly varying forcing term

$$\frac{dw}{dt} = \frac{w_\infty(V) - w}{\tau_w(V)} + \xi$$

where w is a random variable, $\langle \xi \rangle = 0$, and the autocorrelation function of ξ is given by

$$\langle \xi(t)\xi(t') \rangle = \gamma(w)\delta\,(t - t')$$

Following Eqn. (11.37), $\gamma(w)$ is chosen to be

$$\begin{aligned} \gamma(w) &= \frac{\alpha(V)\,(1-w) + \beta(V)w}{N} \\ &= \frac{1}{N}\frac{(1 - 2w_\infty(V))\,w + w_\infty(V)}{\tau_w(V)} \end{aligned}$$

Thus, ξ is a random variable defined by $\xi = \sqrt{\gamma(w)}\Delta B$ where ΔB is the increments of a Wiener process.

Fig. (11.16) presents stochastic Morris-Lecar model simulations implemented in XPP using the Langevin formulation described above. Interestingly, the existence of stochastic excitability depend on the the number of K^+ channels included. When N is

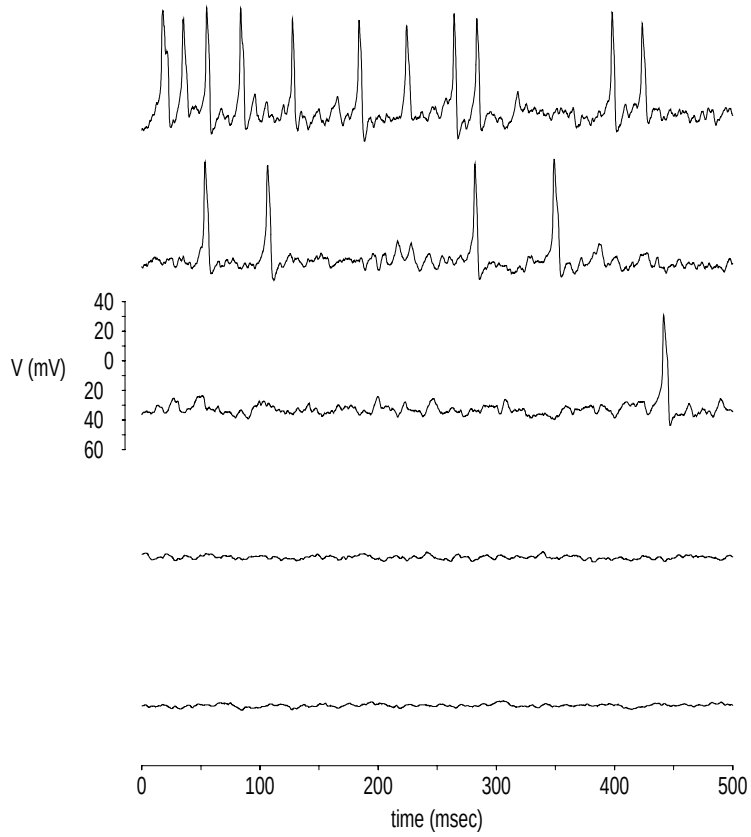

Figure 11.16 The stochastic Morris-Lecar model simulated using a Langevin equation for w, the fraction of open K^+ channels. As the number of K^+ channels is increased (N = 25, 50, 100, 500, or 1000) spontaneous action potentials induced by stochastic gating are eliminated. For large N, the model is excitable, but essentially deterministic, i.e., fluctuations in w are small and spontaneous action potentials are no longer observed without applied current.

relatively small ($N = 25$, 50, 100) membrane potential fluctuations are large and spontaneous action potentials are frequent. However, when more K^+ channels are included ($N = 500$, 1000), the model becomes essentially deterministic. Although the model is still excitable, as $N \to \infty$ fluctuations in w become smaller and spontaneous action potentials are no longer observed.

11.9 Appendix: Stochastic Morris-Lecar model

The following XPP file is the deterministic Morris-Lecar model (modified slightly from [7]) used as the starting point for the stochastic simulations presented in Fig. (11.13), Fig. (11.14), and Fig. (11.16).

```
# The deterministic Morris-Lecar model
# Based on Ermentrout and Rinzel's chapter in Koch & Segev
params v1=-1, v2=15, v3=10, v4=14.5, gca=1.33, phi=.333
params vk=-70, vl=-50, iapp=10, gk=2.0, gl=.5, c=1
minf(v)=.5*(1+tanh((v-v1)/v2))
winf(v)=.5*(1+tanh((v-v3)/v4))+0.05
tauw(v)= 1/(phi*cosh((v-v3)/(2*v4)))
v'= (iapp-gl*(v-vl)-gk*w*(v-vk)-gca*minf(v)*(v-100))/c
w'= (winf(v)-w))/tauw(v)
```

A stochastic Morris-Lecar simulation can be implemented in XPP by defining a Markov variable corresponding to the number of open K^+ channels. In the case of 4 channels, there are 5 possible values for the number of open channels, and the markov variable `n` is defined as

```
markov n 5
  {}   {4*vp}    {0}      {0}      {0}
 {vm}    {}    {3*vp}    {0}      {0}
  {0}  {2*vm}    {}     {2*vp}    {0}
  {0}    {0}   {3*vm}     {}     {1*vp}
  {0}    {0}     {0}    {4*vm}     {}
```

where the quantities `vp` and `vm` are defined in the XPP file by

```
vp=winf(v)/tauw(v)
vm=(1-winf(v))/tauw(v)
```

and the K^+ conductance term in the voltage equation is modified to give

```
v'= (iapp-gl*(v-vl)-gk*n/4*(v-vk)-gca*minf(v)*(v-100))/c
```

In the simulations presented in Fig. (11.13) this method was extended to 5 collections of 20 channels. The markov variables were `n1`, `n2`, `n3`, `n4`, `n5`, and total conductance was given by `gk*(n1+n2+n3+n4+n5)/100`.

The Langevin formulation of the stochastic Morris-Lecar model can be implemented very simply: declare the `wiener` parameter `db` and modify the ODE for `w` in the following way

```
wiener db
w'= (winf(v)-w))/tauw(v)+sqrt(((1-2*winf(v))*w+winf(v))/(n*tauw(v)))*db
```

Using this method the reader can reproduce the simulations shown in Fig. (11.16).

Exercises

1. Using Eqn. (11.12)) as a guide, write an expression for the average number of closed channels, $\overline{N}_C$, in terms of $P_C(n,t)$. Then show that $N - \overline{N}_O = \overline{N}_C$, as stated in Eqn. (11.15). Hint: You will need to use $P_C(n,t) = P_O(N-n,t)$ and $\sum_{n=0}^{N} nP_O(N-n,t) = \sum_{n=0}^{N}(N-n)P_O(n,t)$.
2. Using the result of Exercise (1), confirm that Eqn. (11.14) is equivalent to Eqn. (11.15). In order to do so, you will need to show that

$$-\overline{N}_O = \sum_{n=0}^{N} n\,(n+1)\,P_O(n+1,t) - \sum_{n=0}^{N} n^2 P_O(n,t)$$

and

$$\overline{N}_C = \sum_{n=0}^{N} n\,(N-n+1)\,P_O(n-1,t) - \sum_{n=0}^{N} n\,(N-n)\,P_O(n,t)$$

3. Eqn. (11.13) is the master equation for the two-state channel with kinetic scheme given by Eqn. (11.8). The mathematically inclined reader may wish to derive the the master equation for the GLUT transporter discussed in Section (11.2). The easiest way to do this is to write three equations of the form of Eqn. (11.13), corresponding to $3\,(N+1)$ coupled ODEs, where N is the number of GLUT transporters.
4. Show that in the case of the two-state channel, the variances defined with respect to fluctuations in open channel number, $\sigma^2_{N_O}$, and closed channel number, $\sigma^2_{N_C}$, are equal. You will need some of the relations from Exercise (1) as well as Eqn. (11.19) and Eqn. (11.20).
5. Confirm Eqn. (11.21), the equation for the time-dependence of the variance of the two-state channel. Hint: differentiate Eqn. (11.19), to obtain

$$\frac{d\sigma^2_{N_O}}{dt} = \sum_{n=0}^{N}\left\{-2\left(n-\overline{N}_O\right)\frac{d\overline{N}_O}{dt}P_O(n,t) + \left(n-\overline{N}_O\right)^2\frac{dP_O(n,t)}{dt}\right\} \tag{11.54}$$

Now check to see if the right hand sides of Eqn. (11.21) and Eqn. (11.54) are equal. Use Eqn. (11.14) and Eqn. (11.10) as well as

$$\sum_{n=0}^{N}\left(n-\overline{N}_O\right)^2(N-n+1)\,P_O(n-1,t) = \sum_{n=0}^{N-1}\left(n+1-\overline{N}_O\right)^2(N-n)\,P_O(n,t)$$

$$\sum_{n=0}^{N}\left(n-\overline{N}_O\right)^2(n+1)\,P_O(n+1,t) = \sum_{n=1}^{N}\left(n-1-\overline{N}_O\right)^2 nP_O(n,t)$$

6. Beginning with Eqn. (11.4) through Eqn. (11.7), write an XPP file to simulate the four state GLUT transporter model discussed in Section (11.2) and Chapter **??**. It will be necessary to implement a Markov variable defined by the transition

probability matrix,

$$Q^{XPP} = \begin{bmatrix} D_1 & k_{12}[G]_{out}\Delta t & 0 & k_{14}\Delta t \\ k_{21}\Delta t & D_2 & k_{23}\Delta t & 0 \\ 0 & k_{23}\Delta t & D_3 & k_{34}\Delta t \\ k_{41}\Delta t & 0 & k_{43}[G]_{in}\Delta t & D_4 \end{bmatrix}$$

where the diagonal entries are such that each row sums to 1, that is,

$$\begin{aligned} D_1 &= 1 - k_{12}[G]_{out}\Delta t - k_{14}\Delta t \\ D_2 &= 1 - k_{21}\Delta t - k_{23}\Delta t \\ D_3 &= 1 - k_{23}\Delta t - k_{34}\Delta t \\ D_4 &= 1 - k_{41}\Delta t - k_{43}[G]_{in}\Delta t \end{aligned}$$

Remember that XPP implements the diagonal entries automatically, so that it will suffice to include a matrix of the form

```
markov n 4
   {}    {J12}  {J13}  {J14}
 {J21}    {}    {J23}  {J24}
 {J31}  {J32}    {}    {J34}
 {J41}  {J42}  {J43}    {}
```

7. Confirm the form of the conditional PDFs shown in Fig. (11.11) using XPP. This can be done using the following XPP file,

```
# Example two state channel simulation
params kp=0.5, km=0.5
params c=2, gl=0.5, gch=1.0, vl=-70, vch=20
v(0)=0
markov n 2
{}{kp}
{km}{}
v'=(-gl*(v-vl)-gch*n*(v-vch))/c
aux n=n
@ total=5500,trans=500,DT=.001
@ maxstore=1000000,bounds=10000
done
```

After a run is complete, view v as a function of time. Then select nUmerics/stocHastic/Histogram and set the lower bound to -70, upper bound to 20 mV, number of bins to 90, and condition to n==0 (or n==1). The resulting histogram will appear in the Data Table and can be viewed by selecting Window/View. You should observe a PDF qualitatively similar to those in Fig. (11.11). Now change

`km` and `kp` to 0.5, recalculate the voltage trajectory, compute the histograms, and observe PDFs as in Fig. (11.12).

References

[1] Keizer, J., *Statistical thermodynamics of nonequilibrium processes*, Springer-Verlag, New York, 1987.

[2] *** Gardiner, G.W., *Handbook of stochastic methods for physics, chemistry, and the natural sciences*, 2nd edition, Springer-Verlag, New York, 1990.

[3] *** Chow, C.C., and J.A. White, *Spontaneous action potentials due to channel fluctuations*, Biophys J., 71:3013–21, 1996.

[4] *** Fox, R.F., *Stochastic versions of the Hodgkin-Huxley equations*, Biophys J., 72:2068–2074, 1997.

[5] White, J., T. Budde, and A. Kay, *A bifurcation analysis of neuronal subthreshold oscillations*, Biophys J., 69(4):1203–17, 1995.

[6] *** White, J.A., J.T. Rubinstein, and A.R. Kay, *Channel noise in neurons*, TINS, 23(3):131–137, 2000.

[7] Rinzel, J., and B. Ermentrout, *Analysis of neural excitability and oscillations*, In: Methods in neuronal modeling : from ions to networks, Editors: Koch, C. and I. Segev, The MIT Press, Cambridge, 1998.

If there is a further reading section please include references preceeded by ***.

CHAPTER 12

Molecular Motors

Alex Mogilner, George Oster and Joel Keizer

07-28

Evolution has created a class of proteins that have the ability to convert chemical energy into mechanical force. Some of these use the free energy of nucleotide hydrolysis as fuel, while others employ ion gradients. Some are 'walking motors', others rotating engines. Some are reversible, others are unidirectional. Could there be any common principles amongst such diversity?

The mechanics of proteins are counterintuitive because their motions are dominated by Brownian motion. The most obvious effect of Brownian movement is to 'smear out' deterministic trajectories. However, it introduces other effects as well. For example, it serves as a very effective 'lubricant' allowing molecules to pass over high energy barriers that would arrest a deterministic system. More subtly, it make possible 'uphill' motions against an opposing force by 'capturing' occasional large thermal fluctuations.

After discussion of the motion on the molecular scale and derivation of a mathematical formalism quantifying such motion, we will focus our attention to a subset of motor proteins that function by using chemical energy to rectify Brownian motion - so called 'Brownian ratchets'. These do not exhaust the varieties of molecular motors, but they have certain unique features that make them interesting both biologically and theoretically. We will derive and treat a 'toy' models of a protein whose structure and biochemistry is known with some degree of certainty, for this will force us to forsake abstract formulations and confront the realities of macromolecular geometry, chemical kinetics and thermodynamics. This protein will be ATP synthase - main agent of energy

transduction in a living cell. The chapter will conclude with a review of different motor proteins including a molecular machine for mitochondrial protein import, kinesin and polymerization ratchet.

The conversion of chemical energy into mechanical work is one of the main themes of modern biology. Biochemists characterize energy transduction schemes by a free energy diagram. But thermodynamics tells only what cannot happen. Recent advances in laser trap and optical technology, along with advances in molecular structure determination can augment traditional biochemical kinetic and thermodynamic analyses to make possible a more mechanistic view of how protein motors function. The result of these advances has been data that yield load-velocity curves and motion statistics for single molecular motors. This sort of data enables a more detailed, mechanistic level of modeling. Here we will consider several situations where mathematical modeling yields new insights into the mechanism of energy transduction, and provides expressions for the load-velocity curve of a molecular motor that can be compared to experiment.

12.1 Modeling Molecular Motions

The botanist Robert Brown first observed Brownian movement in 1827. While studying a droplet of water under a microscope, he noticed tiny specks of plant pollen dancing around. Brown first guessed, and later proved, that these were not living, although at the time he had no clue as to the mechanism of their motion. It was not until Einstein contemplated the phenomenon 75 years later that a quantitative explanation emerged. In order to develop an intuition about molecular dynamics we begin with some simple remarks on Brownian motion of proteins in aqueous solutions.

12.1.1 The Langevin model

A water molecule is about 0.1 nm in diameter, while diameter of proteins, d, is two orders of magnitude larger, in the range 2-10 nm. This size difference suggest that we can view the fluid as a continuum. A protein moving through the fluid is acted on by frequent and uncorrelated momentum impulses arising from the thermal motions of the fluid. We model these fluctuations as a random 'Brownian force', $f_B(t)$, where t whose statistical properties can be mimicked by the random number generator in a computer in a fashion described below. At the same time, the fluid continuum exerts a frictional drag force, $f_d = -\zeta v$ proportional to the protein's velocity, $v = dx/dt$. Here x is the 1-dimensional coordinate, and ζ is the frictional drag coefficient (see Box 1). Assuming that the frictional and stochastic forces add we can write Newton's law (Feynman) for the motion of a protein moving in a one-dimensional domain of length L:

$$m\frac{d^2x}{dt^2} = -\zeta v + f_B(t), \quad 0 \le x(t) \le L. \tag{12.1}$$

The mass, m, of a typical protein is $\sim 10^{-21}$kg (Alberts).

Box 1: *The drag coefficient.*
Natural units of distance and force on molecular scale are nanometers (1nm $= 10^{-9}$m) and piconewtons (1pN $= 10^{-12}$N), respectively. In this units, the viscosity of water at room temperature is $\eta \simeq 10^{-9}$pN·sec/nm^2. Then, a typical value for the hydrodynamic drag coefficient of a sphere of radius R is $\zeta = 6\pi\eta R \simeq 10^{-7}$pN·sec/nm (for a typical protein, we use $R \sim 10$nm). Drag coefficients for other shapes, factored by a dimensionless geometric coefficient of order one, are given in (Berg), a good source of intuition on Brownian motion. A dimensionless number that measures the ratio of inertial to viscous forces is the Reynolds Number: $Re \equiv \rho v R/\eta$, where ρ is the density of water (10^3kg/m^3 $= 10^{-21}$pN·sec^2/nm^4) (Happel, Purcell). Typical velocities of molecular motors are $v < 10^3$nm/sec, so on the molecular scale, Reynolds number is very small indeed: $Re \sim 10^{-8}$. This confirms our calculation below that we can safely ignore the inertial term in equation (12.1).

If we multiply equation (12.1) by $x(t)$ and use the chain rule, we get:

$$\frac{m}{2}\frac{d^2(x^2)}{dt^2} - mv^2 = -\frac{\zeta}{2}\frac{d(x^2)}{dt} + x f_B(t). \tag{12.2}$$

In order to see the consequences of equation (12.2) for molecular motions we first must average (12.2) over a large number of proteins so that the peculiarities of any particular trajectory are averaged out. We use the notation $< . >$ to denote this *ensemble* average:

$$\frac{m}{2}\frac{d^2 < x^2 >}{dt^2} - < mv^2 >= -\frac{\zeta}{2}\frac{d < x^2 >}{dt} + < x f_B(t) > . \tag{12.3}$$

Next we take advantage of a central result from statistical mechanics called the *Equipartition Theorem* which states that which states that each degree of freedom of a Brownian particle carries average energy:

$$< E >= k_B T/2, \quad [Equipartition\ Theorem] \tag{12.4}$$

where k_B is Boltzmann's constant and T the absolute temperature (Landau, see Box 2). Therefore, the second term in equation (12.3) is just twice the average kinetic energy of the protein: $< mv^2 >= k_B T$. Because the random impulses from the water molecules are uncorrelated with position, $< x f_B(t) >= 0$. Introducing these two facts into equation (12.3) and integrating twice between 0 and t with $x(0) = 0$, we obtain:

$$\frac{d < x^2 >}{dt} = \frac{k_B T}{\zeta}(1 - e^{-\zeta t/m}), \quad < x^2 >= \frac{k_B T}{\zeta}[t - \frac{1}{\tau}(1 - e^{-t/\tau})], \tag{12.5}$$

where we have introduced the time constant $\tau = m/\zeta$.

Box 2: *The Equipartition Theorem.*
Let us consider a collision of a two particles of masses m_1 and m_2 with velocities v_1 and v_2 before the collision, and with velocities v_1' and v_2' after the collision, respectively. Conservation of energy and momentum guarantee conservation of the velocity of the center-of-mass after the collision, as well as of the absolute value of the relative velocity (Feynman). One of the central assumptions of statistical mechanics is that the velocities of the scattered particles are uncorrelated. From this one can show that $< m_1 v_1'^2 > =< m_2 v_2'^2 >$. Thus the mean kinetic energy of a point particle moving in 1-D is constant equal to $< mv^2/2 >= k_B T/2$. At room temperature, the quantity $k_B T \simeq 4.1$pN·nm is the 'unit' of thermal energy, natural unit of energy on molecular scale.

• **Exercise 1:** For a 10nm sphere moving in water, compute the relaxation time τ.

•

• **Exercise 2:** Use conservation of energy and momentum to demonstrate that the velocity of the center-of-mass, $V_{cm} = (m_1 v_1 + m_2 v_2)/(m_1 + m_2)$, and the absolute value of the relative velocity, $|v_1 - v_2|$, are conserved after the collision. Then, assuming that the velocities of the scattered particles are uncorrelated: $< v_1' \cdot v_2' >= 0$ and $< V_{cm} \cdot v_{1,2}' >= 0$, prove that $< m_1 v_1'^2 > =< m_2 v_2'^2 >$. •

For very short times, $t \ll \tau$, we can expand the exponential in (12.5) to the second order to obtain:

$$< x^2 >= \frac{k_B T}{m} t^2, \quad t \ll \tau. \tag{12.6}$$

That is, at very short times the protein behaves as a ballistic particle moving with a velocity $v = \sqrt{k_B T/m}$. For a protein with $m = 10^{-21}$kg $= 10^{-18}$pN·sec^2/nm, $v \simeq 2$m/s. However, in a fluid the protein moves at this velocity only for a time $\tau \simeq 10^{-13}$sec, much faster than any motion of interest in a molecular motor. During this short time the protein travels a distance $v \cdot \tau \simeq 0.02$nm before it collides with another molecule. This is only a fraction of a diameter, so the ballistic regime is very short lived indeed! Very quickly, the kinetic energy of the protein comes into thermal equilibrium with the fluid environment (gets 'thermalized'). Thus when $t \gg \tau$, the exponential term disappears and (12.5) becomes

$$< x^2 >= 2\frac{k_B T}{\zeta} t, \quad t \gg \tau. \tag{12.7}$$

Comparing (12.7) with a familiar relationship between the mean square displacement of a particle and its *diffusion coefficient*, D:

$$< x^2 >= 2Dt. \tag{12.8}$$

Einstein recognized that the same force that create the frictional drag on a moving body was caused by random collisions with the fluid molecules, which is the same effect as the Brownian force that gives rise to the diffusive motion of the body. Therefore, there must be a connection between the drag coefficient and diffusive motion. This is

captured in the famous Einstein relation:

$$D = k_B T/\zeta, \tag{12.9}$$

where the diffusion coefficient of the protein is typically $D \sim 10^7 \text{nm}^2$ /sec.

Thus, at a time scale of interest, inertial effect can be neglected, and protein movements can be modeled by the equation $\zeta dx/dt = f_B(t)$. Finally, if an external force, F, acts on the protein, this can be added to this equation, so that it becomes: $\zeta dx/dt = F(x,t) + f_B(t)$. In general, forces acting on proteins can be characterized by a potential, $F(x,t) = -\partial\phi(x,t)/\partial x \equiv -\phi'(x,t)$, so the equation of motion for a protein moving through a fluid becomes:

$$\zeta \frac{dx}{dt} = F(x,t) + f_B(t) = -\frac{\partial \phi(x,t)}{\partial x} + f_B(t). \tag{12.10}$$

Equation (12.10) is frequently referred to as a Langevin equation, although this term more properly applies to the corresponding equation (12.1) that includes inertia.

Equation (12.8) suggests a method for modeling the Brownian force term, $f_B(t)$, on a computer: in a time interval Δt, $f_B(t)$ should produce a root mean square displacement of $\sqrt{2D\Delta t}$. Since the force is random, the displacement consists of a large number of uncorrelated spatial steps. According to the Central Limit Theorem of statistics (Ross), these steps should be symmetrically distributed about the mean value, so we can model the random force as

$$\frac{1}{\zeta}\int_0^{\Delta t} f_B(t) = \sqrt{2D\Delta t}\cdot N(0,1), \qquad [Brownian force]$$

where $N(0,1)$ is the unit normal distribution, i.e. with mean 0 and variance 1. The random number generator, $N(0,1)$ is generally a standard function in most programming languages. Using this model Brownian force, equation (12.10) is very easy to simulate numerically using the Euler method with time step Δt:

$$x(t+\Delta t) = x(t) - \frac{D}{k_B T}F(x(t),t)\Delta t + \sqrt{2D\Delta t}\cdot N(0,1). \tag{12.11}$$

We can nondimensionalize (12.11) by defining time and space scales. If the domain $0 \le x \le L$, the spatial variable can be normalized as x/L. A time scale can be defined by $\tau = L^2/D$, characteristic time to diffuse across the domain. Introducing the space and time scales, (12.11) can be written in dimensionless form as:

$$x(t+\Delta t) = x(t) + w\Delta t + \sqrt{2\Delta t}\cdot N(0,1), \quad w = \frac{FL}{k_B T}, \tag{12.12}$$

where t and x are now dimensionless.

• **Exercise 3:** Simulate equation (12.11) with the double well potential $\phi(x) = k_B T[(x/L)^4 - (x/L)^2]$ and $x(0) = -L$. Remember that you have to choose small steps: $\tilde{h} \ll 1$ (think why). Run simulations until (i) $t_{end} = L^2/D$, (ii) $t_{end} = 10L^2/D$, (iii) $t_{end} = 100L^2/D$. Discuss results. •

Although simulating equation (12.12) on a computer is easy, it is also easy to generate erroneous results, e.g. numerical instabilities which look very like random

displacements due to Brownian motion, or currents that do not vanish at equilibrium. A better numerical method of simulating random motions that does not have these problems will be given in Chapter .

12.1.2 The Smoluchowski model

Consider the motion of a protein moving under the influence of a constant external force, for example, an electric field. Because of Brownian motion no two stochastic trajectories will look the same. Moreover, even a detailed examination of the path cannot distinguish whether a particular displacement 'step' was caused by a Brownian fluctuation or the effect of the field. Only by tracking the particle for a long time and computing the average position vs. time can one detect that the diffusion of the particle exhibits a 'drift velocity' in the direction of the force. Therefore, a better way to think about stochastic motion is to imagine a large collection of independent particles moving together. Then we can define the *concentration* of particles at position x and time t as $c(x,t)$ [#/nm], and track the evolution of this *ensemble*.

As the cloud of particles diffuses and drifts we can write an expression for the *flux* of particles, J_x [#/sec]. The diffusive motion of the particles is modeled well by Fick's law (Chapter 6): $J_x = -D\partial c/\partial x$. The external field exerts a force on each particle, $F = -\phi'$ which, in the absence of any diffusive motion, would impart a drift velocity proportional to the field: $v = F/\zeta$. Thus the motion of the body is the sum of the Brownian diffusion and the field-driven drift: $J_x = -D\partial c/\partial x + vc$, which can be written in several ways:

$$J_x = -D\frac{\partial c}{\partial x} - \frac{D}{k_B T}\cdot\frac{\partial \phi}{\partial x}\cdot c = -D(\frac{\partial c}{\partial x} + \frac{\partial(\phi/k_B T)}{\partial x}\cdot c) = -\frac{1}{\zeta}(k_B T\frac{\partial c}{\partial x} + c\cdot\frac{\partial \phi}{\partial x}). \quad (12.13)$$

At equilibrium the flux vanishes: $(k_B T/c_{eq})(\partial c_{eq}/\partial x) + \partial\phi/\partial x = 0$. Integrating this over all x, shows that the concentration of particles at equilibrium in an external field is given by the *Boltzmann distribution*:

$$c_{eq} = c_0 e^{-\phi/k_B T}. \quad [Boltzmann\ distribution] \quad (12.14)$$

• **Exercise 4:** Plot the Boltzmann distribution in the case of the double well potential (Exercise 3). Discuss results. •

Box 3: *Some connections with thermodynamics.*
Note that the flux (12.13) can also be written as $J_x = -\frac{c}{\zeta}\frac{\partial}{\partial x}(k_B T \ln c + \phi)$. There can be many *steady states* characterized by a constant flux: $J_x = \text{const}$; one of these is the special case of *equilibrium*: $J_x = 0$. At equilibrium, one can define the quantity $\mu = (k_B T \ln c_{eq} + \phi)$ called the *chemical potential*. The equilibrium distribution of $c_{eq}(x)$ can be computed by setting the gradient in chemical potential to zero, so that μ =const; this is exactly equivalent to enforcing a Boltzmann distribution, (12.14).
The chemical potential is also the free energy *per mole*, $G = \mu N$, where N is the mole number (mole is $\simeq N_a$ molecules of a substance; $N_a \simeq 6 \cdot 10^{23}$ is Avogadro's number). At *equilibrium* we can define the *entropy*, $S \equiv -k_B N \ln c_{eq}$ and the *enthalpy* as $H = \phi N$. Then we arrive at the definition of the free energy: $G = H - TS$. These definitions will prove useful when we discuss chemical reactions. Here we note simply that diffusion smoothes out the concentration leading to an increase in entropy. Thus entropic increase accompanying the motion of the ensemble is handled by the Fickian diffusion term in the flux (12.13).
When the particles are charged (e.g. protons), then the chemical potential difference between two states, or across a membrane, is written as: $\Delta\mu = \mu_2 - \mu_1 = (\phi_2 + k_B T \ln c_2) - (\phi_1 + k_B T \ln c_1) = (\phi_2 - \phi_1) + k_B T(\ln c_2 - \ln c_1) = \Delta\phi - 2.3\ k_B T\ \Delta\text{pH}$. Here $\text{pH} = -\log_{10} c_{H^+}$. The protonmotive force is defined as p.m.f. $= \Delta\mu/e = \Delta\psi - 2.3\ (k_B T/e)\ \Delta\text{pH}$, where e is the electronic charge, and $\Delta\psi = \Delta\phi/e$, [mV], is the transmembrane electric potential.

Since the number of particles in the swarm remains constant, $c(x,t)$ must obey the conservation law (see Chapter 6):

$$\frac{\partial c}{\partial t} = -\frac{\partial J_x}{\partial x}, \quad [\textit{conservation of particles}] \tag{12.15}$$

Rather than focussing our attention on the swarm of particles, we can rephrase our discussion in terms of the *probability* of finding a *single* particle at (x,t). To do this we normalize the concentration in equation (12.13) by dividing by the total population, $p(x,t) = c(x,t)/(\int_0^L c(x,t)dx)$. Inserting equation (12.13) expressed in terms of $p(x,t)$ into the conservation law (12.15) yields the Smoluchowski equation:

$$\frac{\partial p}{\partial t} = D[\frac{\partial}{\partial x}(p\frac{\partial(\phi/k_B T)}{\partial x}) + \frac{\partial^2 p}{\partial x^2}]. \tag{12.16}$$

Comparing this with the Langevin equation (12.10) shows that the Brownian force is replaced by the diffusion term and the effect of the deterministic forcing is captured by the drift term.

We can nondimensionalize (12.16) scaling time and space similarly to (12.12). In terms of the dimensionless t and x, (12.16) can be written in the form:

$$\frac{\partial p}{\partial t} = \frac{\partial}{\partial x}(p\frac{\partial \phi}{\partial x}) + \frac{\partial^2 p}{\partial x^2}, \tag{12.17}$$

where the potential, ϕ, is measured in units of the thermal energy, k_BT. Equation (12.17) must be augmented by appropriate boundary conditions that will depend on the system being modeled.

An important generalization is necessary to model molecular motors. We have spoken of the potential, $\phi(x,t)$, that provides the deterministic forcing as an *external* force. However, for a molecular motor $\phi(x,t)$ generally includes forces generated *internally* by the motor itself which drive the motor forward. Thus the potential term in equation (12.17) must be broken into two parts: $\phi(x,t) = \phi_i(x,t) + \phi_l(x,t)$, where $\phi_i(x,t)$ is internally generated force, and $\phi_l(x,t)$ is the external load force. A common situation is a constant load force, F_l, in which case $\phi_l(x,t) = F_l x$, so that $-\partial\phi/\partial x = -F_l$; i.e. the load force acts to oppose the motor's forward progress. The internally generated force potential will generally depend on the chemical state of the system. That is, the mechanical evolution of the system's geometrical coordinates governed by equation (12.17) is coupled to the chemistry. Each *chemical state* is characterized by its own probability distribution, $p_k(x,t)$, where k ranges over all the chemical states, and each chemical state is typically characterized by a separate driving potential, $\phi_k(x,t)$. Thus there will be a Smoluchowski equation (12.17) for each chemical state, and these equations must be solved simultaneously to obtain the motor's motion. To see how to couple these equations together to make a complete mechanochemical model for a molecular motor, we next discuss how one can model chemical reactions.

Box 4: *A motor driven by a 'flashing potential'.*
A protein is driven by alternating its exposure to two potentials, ϕ_1 (solid line) and ϕ_2 (dashed line), as shown in the figure below. While in either potential, the motion of the particle is given simply by $\zeta dx/dt = -d\phi_i/dx, i = 1,2$. If switching between the potentials is governed by a chemical reaction (vertical arrows) which is timed to occur only at the bottom of each potential, then the protein moves steadily forward. The arrows show the forward progress of the motor, although all steps are reversible. ΔG_{sw} is the free energy difference associated with switching between potentials $1 \to 2$. The motion down the potential $2 \to 3$, generates an amount of heat Q. The free energy consumption in the reaction cycle $1 \to 2 \to 3$ is ΔG. Note that in this situation, the heat generated by frictional dissipation due to motion is actually larger than the free energy drop in the reaction cycle $Q > \Delta G$. (Where does the 'extra' energy come from?)

12.1.3 Modeling chemical reactions

The energy to drive a molecular motors is supplied by chemical reactions. Two of the most common energy sources are nucleotide hydrolysis and transmembrane protonmotive force. The former uses the energy stored in the covalent bond that attaches the terminal phosphate (γ-phosphate) to the rest of the nucleotide. The latter uses the electrical and entropic energy arising from a difference in ion concentrations across a lipid

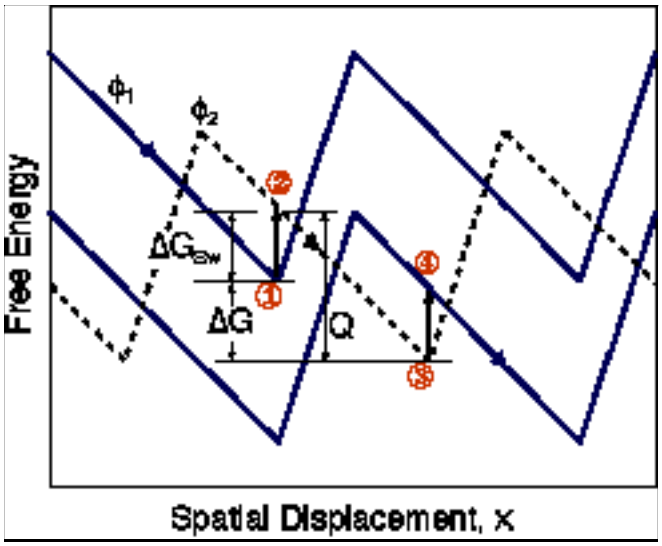

Figure 12.1

bilayer. Hydrolysis is a complicated process, still incompletely understood. Therefore, we will introduce the reaction model using the simple example of a positively charged ion (e.g. H^+) binding to a negatively charged amino acid: $H^+ + A^- \longleftrightarrow H \cdot A$. If we focus our attention on the amino acid, we see it exists in two states: charged (A^-) and neutral ($H \cdot A \equiv A^0$), so that the neutralization reaction from the viewpoint of the amino acid is simply

$$A^- \underset{k_{-1}}{\overset{k_1 \cdot [H^+]}{\rightleftarrows}} A^0. \tag{12.18}$$

Here we use the chemists' convention of denoting concentrations in brackets: $k_1 \cdot [H^+]$ and k_{-1} are the forward and reverse rate constants; the forward rate constant depends on the ion concentration, $[H^+]$, which we will treat as a constant parameter (i.e. we shorten our notation to $k_1 \cdot [H^+] \equiv k_1$, where k_1 is called a *pseudo*-first order rate constant).

The rate constants in reaction (12.18) conceal a great deal of physics, for the process of even a simple reaction as this is, at the atomic level, quite complex. To model this reaction at a more microscopic level involves introducing additional coordinates to describe the process by which an ionic chemical bond is made and broken. These coordinates have a spatial scale much smaller than the motion of the motor itself (e.g. angstroms vs. nanometers), and a time scale much faster than any motion of the motor (picoseconds vs. microseconds). This is because all reactions involve a redistribution

of electrons, and electrons, being very small, move very rapidly. Moreover, in all but the simplest cases, their movements are governed by quantum mechanics rather than classical mechanics. Nevertheless, it is instructive to use the Smoluchowski model to derive a more detailed expression for the rate constants. A more detailed discussion can be found in (Billing, Warshel, Naray-Szabo).

The fundamental concept underlying the modeling of reactions is the notion of a 'reaction coordinate', which we denote by ξ. In molecular dynamics simulations, this is actually a 1-D path through a very high dimensional state space along which the system moves from reactants to products (Billing, Warshel, Naray-Szabo). For the reaction (12.18), $\xi(t)$ is the distance between the ion (H^+) and the amino acid charge, (A^-). The spatial scale of this coordinate is much smaller (i.e. angstroms) than the spatial scale of the motor's motion, but we can imagine a 'super-microscopic' view of the process as shown in Figure 12.2a, where we have plotted the free energy change, ΔG, during a reaction as a function of the reaction coordinate, ξ. The reason for using free energy is because there are many 'hidden' degrees of freedom that must be handled statistically, as will become clear presently. Here the chemical states of the amino acid, A^- and A^0, are pictured as energy wells separated by a barrier of heights ΔG_1^+ and ΔG_2^+, and whose difference in depth is ΔG. The 'transition state' (TS) is located at the top of the pass between the two wells.

For a fixed H^+ concentration, the forward chemical reaction $A^- \rightarrow A^0$ proceeds with a rate $k_1 \cdot [A^-]$ [#/sec]. However, this rate is a statistical average over many 'hidden' events. For a particular reaction to take place, the proton must diffuse to within a few angstroms of the amino acid charge so that the electrostatic attraction between them is felt. Moreover, if the amino acid is located within a protein, there will be steric diffusion barriers that must be circumvented before the two ions 'see' each other electrostatically. As the concentration of H^+ increases, there will be more 'tries' at neutralization (i.e. hops from the right well to the left well).

Similarly, the reverse reaction, $A^0 \rightarrow A^-$ takes place when a thermal fluctuation confers enough kinetic energy on the proton to overcome the electrostatic attraction. Even then, the 'free' proton will more often than not diffuse back and rebind to the amino acid, especially if the route between the solution and the amino acid is tortuous. Only when the proton manages a successful escape into solution (the left well) does it count in computing k_{-1}.

The *net* flux over the barrier is

$$J_\xi = k_1 \cdot [A^-] - k_{-1} \cdot [A^0]. \tag{12.19}$$

After a long time the net flux between the two wells will vanish: $J_\xi = 0$, so that the population of neutral and charged sites will distribute themselves between the wells in a fixed ratio, which we denote by K_{eq} (the equilibrium constant): $K_{eq} \equiv [A^0_{eq}]/[A^-_{eq}] = k_1/k_{-1}$. If the transition state is high ($\Delta G_1^+ > k_B T$), then we can assume that population apportions between the two wells according to the generalized Boltzmann distribution: $K_{eq} = \exp(\Delta G/k_B T)$ (compare this formula with (12.14)). We know that $\Delta G = \Delta H - T\Delta S$ (Box 3). The enthalpy term, ΔH, is due to the electrostatic attrac-

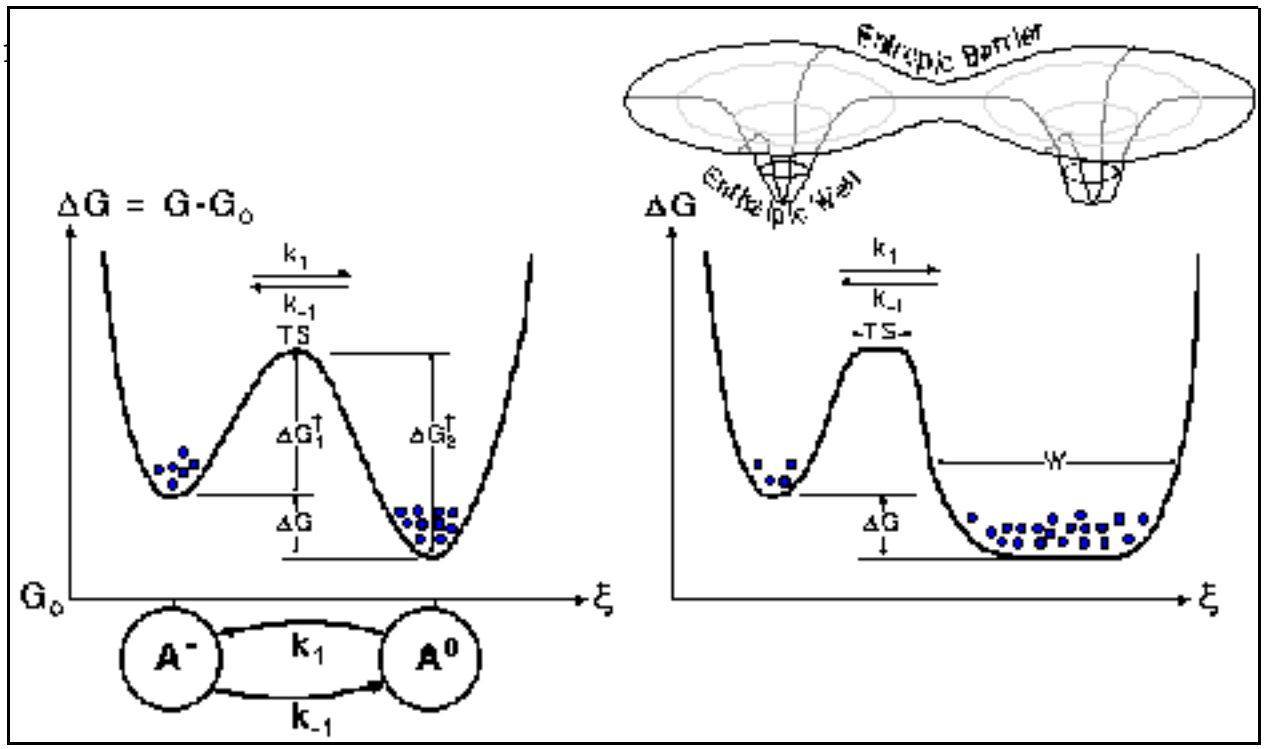

Figure 12.2 (a) Free energy diagram illustrating the chemical reaction $A \longleftrightarrow B$ and the corresponding Markov model. The transition state, TS, is ΔG_1^+ above the left well and ΔG_2^+ above the right well. ΔG is the free energy difference between the well bottoms. The equilibrium distribution between the wells depends only on ΔG. (b) The effect of entropic factors on the reaction $A \longleftrightarrow B$. The equilibrium populations in each well remain the same, but the transition rates between the wells are different due to the entropic effects of widening the transition state, TS, and the width, W, of the right well.

tion between the proton and the charged site. The entropic term, $T\Delta S$, incorporates all the effects that influence the diffusion of the proton to the site and its escape from it, the 'hidden coordinates'. Note that the value of ΔG determines *how far the reaction goes*, independently of the absolute height of the TS.

There is one effect that is very significant in biochemical reactions, and which illustrates the importance of entropic effects: hydration. Before the proton can bind to the amino acid, it must divest itself of several 'waters of hydration'. This is because water, being a dipole, will tend to cluster about ions in solution, hindering them from binding to a charged site which is also insulated by its own hydration shell. Suppose for the sake of illustration that the energies binding the waters to the two reactants are just equal to the electrostatic energy of binding between the reactants. Binding seems unfavorable since the proton will loose its translational and rotational degrees of freedom ($\sim 3k_BT$ according to the equipartition theorem, Box 2). The binding reaction can still proceed strongly because the liberation of the hydration waters is accompanied by a large entropy increase since each water gains $\sim 3k_BT$ of rotational and translational energy, and so the term $-T\Delta S$ is strongly negative.

Box 5: *Jumping beans and entropy.*
An analogy may make the role of entropic factors more clear. Imagine that the left well is filled with Mexican jumping beans whose hops are random in height and angle. We can vary the equilibrium populations of beans in each well without altering the height of the barrier by simply increasing the width of the transition state or of one of the wells. This is shown in Figure 12.2b. Now a bean in the right well may execute many more futile jumps before hurdling the barrier: if it jumps from the right side of the well it will fall back into the well even if its jump is high enough, or if it reaches the transition state it must diffuse (hop) along the plateau randomly with a high probability of hopping back into the right hand well. Both of these effects make it more difficult to escape from the right well, and so the equilibrium population there will increase, as will K_{eq}, the equilibrium population ratio.
The rate at which beans can pass the barrier from right to left will have the form

$$k_{-1} = \nu \cdot \exp(\Delta G_2^+ / k_B T) = \nu \cdot \exp(\Delta S / k_B) \cdot \exp(-\Delta H / k_B T),$$

where ν is a frequency factor (number of jumps/unit time). For reactions that involve an atomic vibration, this is approximately $k_B T/\hbar$, where $\hbar$ is Planck's constant. For diffusion controlled reactions this can estimated from more detailed models (Hanggi, Risken). The entropic term, $e^{\Delta S/k_B}$, accounts for geometric and 'hidden variables' effects. The enthalpic term, $e^{\Delta H/k_B T}$, accounts for the electrostatic and/or hydrophobic interactions. Note that the height of the barrier, ΔG_2^+ determines *how fast the reaction goes*. The exponent $\exp(\Delta G_2^+/k_B T)$ is called the *Arrhenius factor*. Because of this factor the reaction rate depends dramatically on the height of the energy barrier.

All this means that the rate constants summarize the statistical behavior of a large number of 'hidden' coordinates that are very difficult to compute explicitly, but may be easy to measure phenomenologically (see, for example (Hanggi)). For our purposes, we shall adopt this phenomenological view of chemical reactions, and assume that the rate constants can be specified, so that the only entropic effect we need deal with explicitly is the concentrations of the reactants, such as $[H^+]$ in equation (12.18). Therefore, we can treat reactions using Markov chain theory, as indicated by the 2-state model shown at the bottom of Figure 12.2a, whose equations of motion are:

$$\frac{d}{dt}[A^0] = -\frac{d}{dt}[A^-] = \text{net flow over the energy barrier} = J_\xi = k_1[A^-] - k_{-1}[A^0],$$

or in the vector form:

$$\frac{d}{dt}\mathbf{A} = \mathbf{J}_\xi = \mathbf{K} \cdot \mathbf{A}, \quad \mathbf{A} = \begin{pmatrix} [A^-] \\ [A^0] \end{pmatrix}, \quad \mathbf{K} = \begin{pmatrix} k_1 & -k_{-1} \\ -k_1 & k_{-1} \end{pmatrix}. \tag{12.20}$$

In general, the net chemical flux will have the form $\mathbf{J}_\xi = \mathbf{K}(\mathbf{A}) \cdot \mathbf{A}$, where the matrix $\mathbf{K}(\mathbf{A})$ is the matrix of transition rates, i.e. pseudo-first order rate constants which may

contain reactant concentrations that are held parametrically constant. Implicit in this formulation are the assumptions that (i) the actual reaction takes place instantaneously (electronic rearrangements are very fast), so that a substance remains in a chemical state for an exponentially distributed mean time before jumping (reacting) to another state; (ii) the transition out of a state depends only on the state itself, and not an any previous history.

12.1.4 A mechanochemical model

We can now assemble a complete formalism for modeling mechanochemical systems. We use the Smoluchowski model (12.16) to model the spatial degrees of freedom of the motor, and a Markov chain (12.20) to model the chemical reactions. Thus the total change in probability, $p(x, \xi, t)$ is given by

$$\frac{\partial}{\partial t}\begin{pmatrix} p_1 \\ p_2 \end{pmatrix} = -\begin{pmatrix} (\partial/\partial x_1)J_{x_1} \\ (\partial/\partial x_2)J_{x_2} \end{pmatrix} + \begin{pmatrix} J_{\xi_1} \\ J_{\xi_2} \end{pmatrix} =$$
$$-D\begin{pmatrix} -(\partial/\partial x_1)[p_1(\phi_1/k_BT) + (\partial p_1/\partial x_1)] \\ -(\partial/\partial x_2)[p_2(\phi_2/k_BT) + (\partial p_2/\partial x_2)] \end{pmatrix} + \begin{pmatrix} k_{-1}p_2 - k_1 p_1 \\ k_1 p_1 - k_{-1}p_2 \end{pmatrix}, \qquad (12.21)$$

where the probability densities $\phi_i(x_i, t), i = 1, 2$ now keep track of the motion along the spatial and reaction coordinates. We can visualize the mechanochemical coupling by plotting the spatial and reaction coordinates as shown in Figure 12.3.

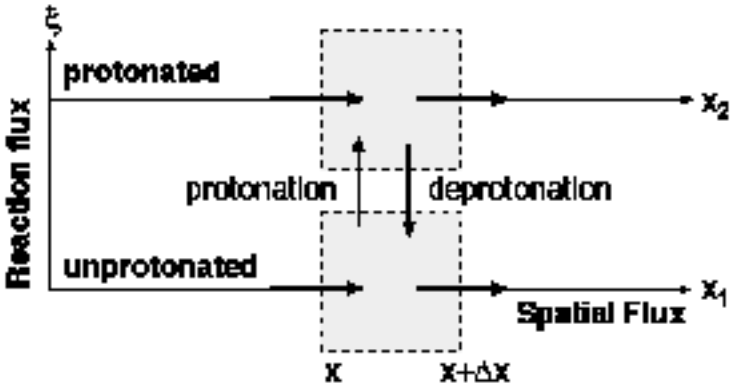

Figure 12.3 The mechanochemical phase plane. A point is defined by its spatial and reaction coordinates $(x(t), \xi(t))$. The flow of probability in the spatial direction is given by the Smoluchowski model (12.16), and the flow in the reaction direction is given by the Markov model (12.20).

12.2 Model of a Simple Molecular Motor

To illustrate the formalism, we shall examine in detail a simplified model of the ion-driven Fo motor of ATP synthase (Elston, Dimroth). This will illustrate many of the principles of mechanochemical energy conversion by proteins, but is sufficiently simple to analyze analytically. The motor is sketched schematically in Figure 12.4. It consists of two reservoirs separated by an ion impermeable membrane. The reservoir on the left is acidic (high proton concentration), and the reservoir on the right is basic (low concentration). The motor itself consist of two 'parts': (i) a 'rotor' carrying negatively charged sites spaced a distance L apart that can be protonated and deprotonated; (ii) a 'stator' consisting of a hydrophobic barrier that is penetrated by a polar strip that can allow a protonated site to pass through the membrane, but will block the passage of an unprotonated site.

Qualitatively, the motor works like this. Rotor sites on the acidic side of the membrane are nearly always protonated. In this state (a nearly neutral dipole) the rotor can diffuse to the right allowing the protonated site to pass through the membrane-stator interface to the basic reservoir. Once exposed to the low proton concentration in the basic reservoir, the proton quickly dissociates from the rotor site. In its charged state, the rotor site cannot diffuse backwards across the interface: its diffusion is 'ratcheted'. A transmembrane potential, $\Delta\psi$, will add an additional electrostatic driving force to the right.

We will assume that the rotor can exist in two possible states, shown in Fig. (**??**A). The state with two empty binding sites is *static*. In another state, all but *one* site are protonated. This nearly neutral site can diffuse through the membrane-stator interface. This diffusion is limited from both sides by the neighboring unprotonated sites that cannot pass through the membrane. We call this state is *rotating*. For the sake of simplicity, we forbid the state, in which more than one site is protonated. The transitions between these states depend on the position of the rotor. In the rotating state, the constant 'internal' (electrostatic) force, $F_i = e\Delta\psi/L$, and the external load force, $-F_l$, are applied to the rotor.

The most important characteristics of a molecular motor is its *force-velocity relation* showing functional dependence between the rate of movement and the load. Because of the microscopic scale and omnipresence of the brownian movement, protein machines have another important quantitative characteristics accounting for the stochastisity of motor's movement, which is *rate of growth of displacement variance*.

12.2.1 Force-velocity relation: fast diffusion, slow reaction kinetics

The model can be described in terms of the probability that the sites at the sides of the membrane are de-protonated, $p_d(t)$ [n/d], and the probability that one site is protonated and is at the distance x from the membrane midline, $p_p(x,t)$ [1/nm],$-L/2 \le x \le L/2$.

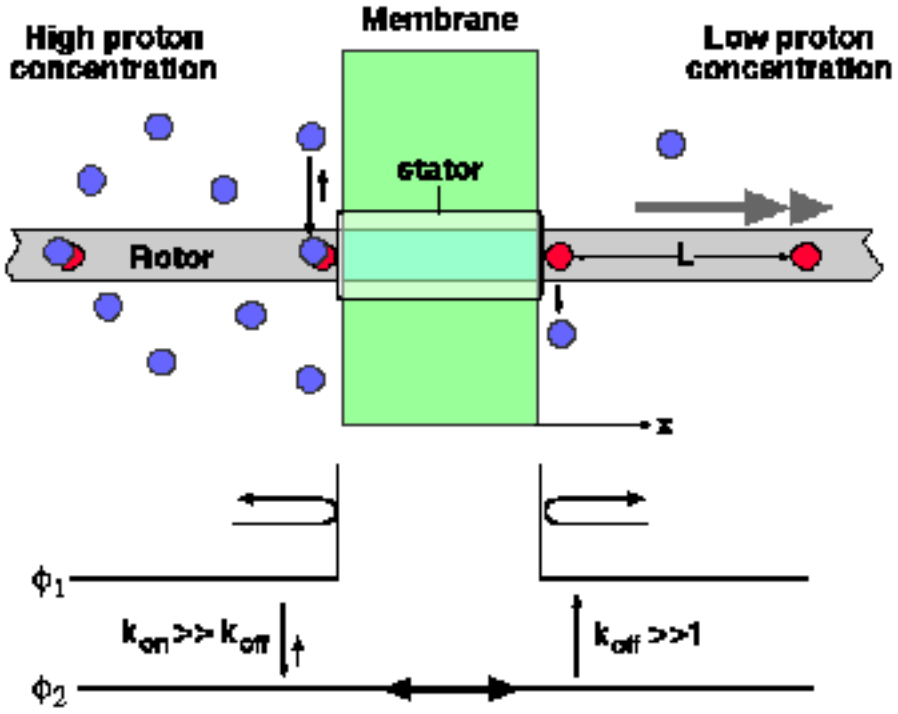

Figure 12.4 Simplified model illustrating the principle of the F_o motor.

The equations governing the probabilities have the form:

$$\frac{dp_d}{dt} = -k_p p_d + k_d p_p(\frac{L}{2}) + k_d p_p(-\frac{L}{2}), \tag{12.22}$$

$$\frac{\partial p_p}{\partial t} = k_p p_d - k_d p_p(\frac{L}{2}) - k_d p_p(-\frac{L}{2}) + D\frac{\partial}{\partial x}(\frac{\partial p_p}{\partial x} - \frac{F_i - F_l}{k_B T} p_p). \tag{12.23}$$

The first terms in (12.22-12.23) describe the protonation from the acidic reservoir and basic reservoirs with the rate k_p [1/sec], respectively. The second and third terms in these equations account for dissociation of a proton to the basic and acidic reservoirs. The corresponding rates are proportional to the probabilities of the protonated site reaching the basic and acidic reservoirs, $p_p(L/2)$ and $p_p(L/2)$, respectively. The proportionality coefficient, k_d has dimension [nm/sec]. The last two terms in (12.23) describe the rotor's diffusion and drift. No flux boundary conditions at $x = \pm L/2$ complete equation (12.23).

Choosing L as the length scale, the time scale of the de-protonation reaction, L/k_d, as the time scale, we rescale the model variables: $x' = x/L, t' = k_d t/L$. The non-

dimensionalized equations have the form (where we omitted primes):

$$\frac{dp_d}{dt} = -\kappa p_d + p_p(\frac{1}{2}) + p_p(-\frac{1}{2}), \tag{12.24}$$

$$\frac{\partial p_p}{\partial t} = -\kappa p_d + p_p(\frac{1}{2}) + p_p(-\frac{1}{2}) + \Lambda \frac{\partial}{\partial x}(\frac{\partial p_p}{\partial x} - w p_p), \tag{12.25}$$

$$\Lambda = D/k_d L, \quad w = (F_i - F_l)L/k_B T, \quad \kappa = k_p L/k_d. \tag{12.26}$$

The model's behavior depends on three dimensionless parameters. Parameter Λ is the ratio of the reaction and diffusion time scales. Parameters κ is the ratio of the protonation and de-protonation rates. Parameter w is the work done by the total force on the spatial scale measured in the units of thermal energy.

Here we will discuss the situation when the diffusion is much faster, than the reaction: $\Lambda \gg 1$, which is true for F_o motor. In this case, powerful apparatus of perturbation theory (Lin and Segel) can be applied. We perform the corresponding analysis heuristically. One can see from the right hand sides of equations (12.24-12.25) that the diffusion and drift terms in equation (12.25) are large, and thus describe the movement of the rotor on the 'fast' diffusion time scale. All the other terms of order one account for the reactions taking place on a 'slow' time scale. The conjecture is that on the the slow, reaction, time scale, the mechanical fluctuations relax to the thermal equilibrium described by Boltzmann distribution. In the zeroth approximation, $p_p(x,t) = p_p(t)\phi(x)$, where $p_p(t)$ is the probability of the rotating state, and $\phi(x)$ is the equilibrium probability density for the rotor's position relative to the stator. Effectively, the fast brownian dynamics is separated from the slow, reaction dynamics. The function $\phi(x)$ can be found from the requirement that, on the slow time scale, the last terms in (12.25) have to be of order one. Because of the greatness of parameter Λ, in the zeroth approximation, the expression in the last brackets in (12.25) has to be equal to zero. Therefore, function $\phi(x)$ has to obey the stationary Smoluchowski equation with no flux boundary conditions:

$$\frac{d\phi}{dx} - w\phi = 0, \quad \phi(x) = \frac{w\ e^{wx}}{2sinh(w/2)}, \quad -\frac{1}{2} \le x \le \frac{1}{2}. \tag{12.27}$$

Boltzmann distribution $\phi(x)$ is normalized on 1. Thus, $p_p(\pm\frac{1}{2},t) = p_p(t)\phi(\pm\frac{1}{2})$. Substituting this expression into equation (12.24) and using the conservation of the total probability, $p_d(t) + p_p(t) = 1$, we obtain:

$$\frac{dp_d}{dt} = -\frac{dp_p}{dt} = -\kappa p_d + \phi_+ p_p + \phi_- p_p, \quad \phi_\pm = \frac{we^{\pm w/2}}{2sinh(w/2)}. \tag{12.28}$$

Effectively, we reduced the complex motor's mechanochemistry to the simple effective reaction kinetics.

¿From (12.28), the stationary probabilities to find the motor in the protonated and de-protonated states are:

$$p_p = \frac{\phi_+ + \phi_-}{\kappa + \phi_+ + \phi_-}, \quad p_d = \frac{\kappa}{\kappa + \phi_+ + \phi_-}. \tag{12.29}$$

respectively.

There is a simple way to find the *average* rate of the rotor's motion. When empty rotor site is protonated from the acidic reservoir with the rate k_p^a, the rotor effectively makes an average step of the size $L/2$ to the right (because the site localized at $-L/2$ starts to diffuse between $-L/2$ and $L/2$). Similarly, when empty rotor site is protonated from the basic reservoir with the rate k_p^b (note that $k_p \equiv k_p^b + k_p^a$), the rotor effectively makes a step $L/2$ to the left. Thus, the average rate of displacement factored by the probability to be in the de-protonated state is $(L/2)p_p(k_p^a - k_p^b)$. By analogy, release of the proton to the basic or acidic reservoir corresponds to the step to the right or to the left respectively. Corresponding average rate displacement factored by the probability to be in the protonated state is $(L/2)p_d(k_d\phi_+ - k_d\phi_-)$. Adding these rates of displacement, we obtain the dimensional expression for the average velocity of the motor:

$$V = \frac{L}{2}[p_p(k_p^a - k_p^b) + p_d(k_d\phi_+ - k_d\phi_-)]. \tag{12.30}$$

We assume that the rates of protonation are proportional to the corresponding proton's concentrations: $k_p^a = \tilde{k}_p c_a, k_p^b = \tilde{k}_p c_b$. Then, the dimensional expression for the *force-velocity relation* has the form:

$$V(f) = \frac{L}{2}\frac{w\tilde{k}_p k_d\ (c_a e^{w/2} - c_b e^{-w/2})}{\tilde{k}_p L(c_a + c_b)\ \sinh(w/2) + k_d w\ \cosh(w/2)}, \quad w = \frac{(F_i - F_l)L}{k_B T}. \tag{12.31}$$

Let us examine the numerator of equation (12.31). Clearly, if there is a symmetry in the system, $F_i = F_l = 0, c_a = c_b$, then $V(0) = 0$, but if either $c_a > c_b$, or $F_i > 0$, or both, then $V(0) > 0$.

In Fig. 12.5, we plotted the average motor's velocity as a function of the load force for the pure brownian ratchet case ($c_a > c_b, F_i = 0$). The shape of the force-velocity curve may vary depending on the values of the model parameters. Fitting the result of the mathematical model to an experimental data provides valuable information on the motor's mechanochemical cycle.

At certain force, the average velocity becomes equal to zero - the motor is *stalled*. The corresponding *stall force*, F_s, can be easily found equalizing the numerator in (12.31) to zero:

$$F_s = F_i + \frac{k_B T}{L} ln[\frac{c_a}{c_b}]. \tag{12.32}$$

In the pure power stroke limiting case ($c_a = c_b, F_i > 0$), $F_s = F_i$: when the load force exactly balances the membrane potential, the motor is stalled. In the pure brownian ratchet limiting case, $F_s = (k_B T/L) ln[c_a/c_b]$. In most important cases, the logarithmic factor is of the order of unity (in the case of the proton driven motor, this factor is equal to $(-\Delta pH)$). Thus, the order of magnitude of the force generated by the brownian ratchet mechanism is equal to *thermal energy divided by the motor's step size*. The stall force (12.32) for our simple motor is the direct sum of the force generated by the power stroke and brownian ratchet mechanisms. Note, that the expression in the right hand

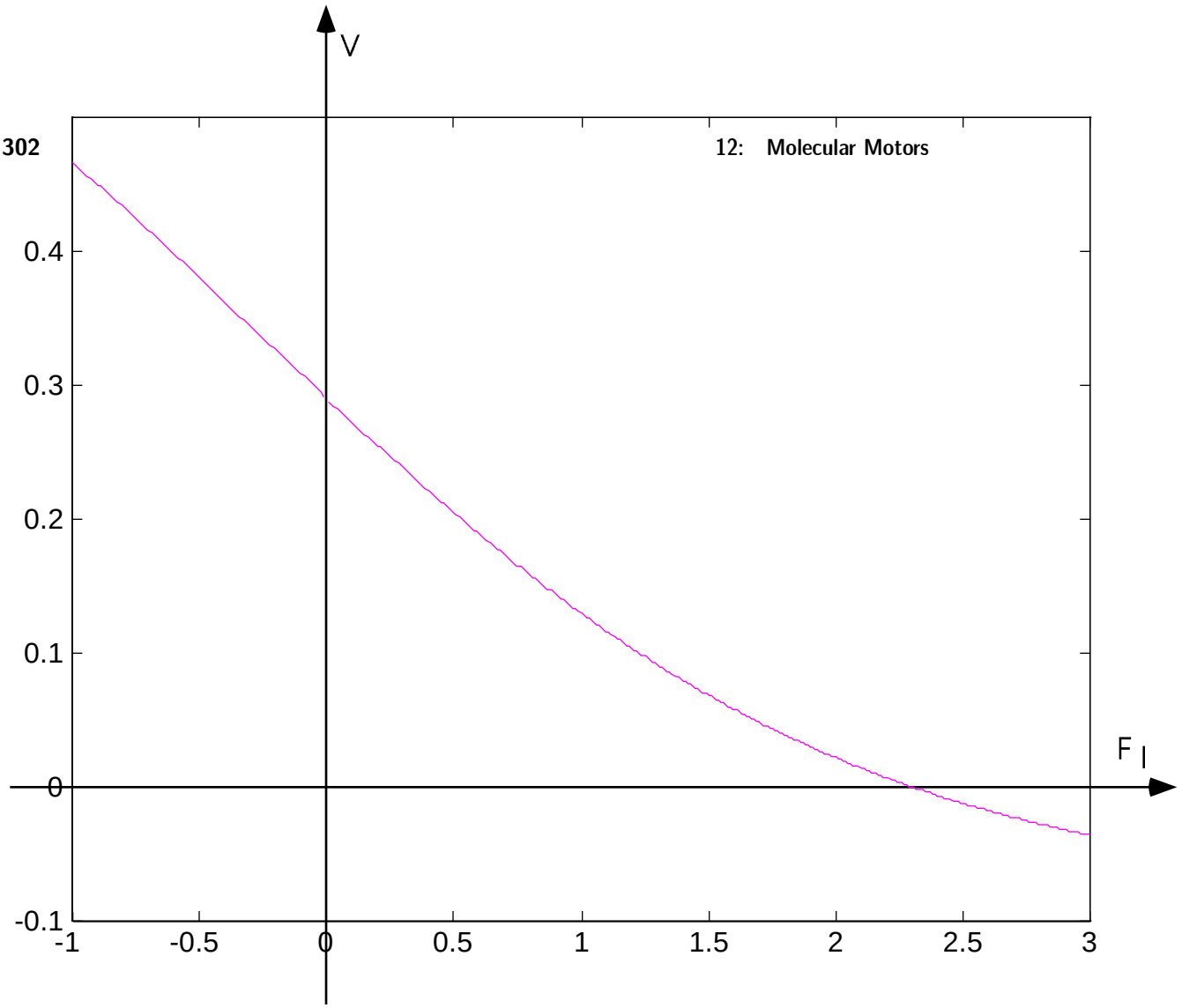

Figure 12.5 Force-velocity curve

side of formula (12.32) multiplied by L becomes the expression for the protonmotive force per one proton: $p.m.f. = FL + k_B T ln[c_a/c_b] = e\Delta\psi - 2.3 k_B T \Delta\text{pH}$. Near the stall, when the motor moves slowly close to a thermodynamic equilibrium, the work done by the motor, $F_s L$, is equal to the protonmotive force, so the motor's efficiency approaches 100%.

Note also that, hypothetically, if the temperature is lowered to the absolute zero (of course, life would stp, so this is a mental experment), the power stroke mechanism would still work. Meanwhile the brownian ratchet depending on thermal fluctuations to operate would stop. The brownian movement is a 'lubricant' that can 'freeze'.

12.2.2 Statistical behavior of the motor

Because of the omnipresence of brownian motion on the molecular scale, motor's advancement is not deterministic. A useful measure of the corresponding fluctuations is the variance of the motor's displacement: $var =< x^2 > - < x >^2$. Here, we look at the variance in the limiting situation, when both the membrane potential is very strong, $F \gg k_B T/L$, and the pH gradient is very high, $c_a \gg c_b$. In this case, the processes of the protonation from the basic reservoir and dissociation into the acidic reservoir can be neglected, and the mechanochemical cycle simplifies considerably Fig. (**??**C).

Effectively, the cycle consists of two 'half-steps' of size $L/2$ each made with the rates k_1 and k_2, respectively. Both half-steps are stochastic Poisson processes. Using simple tools of the probability theory (Ross), it is easy to compute the mean duration of the full step, $< \tau_s >= k_1^{-1} + k_2^{-1}$, and its variance, $\sigma^2 = (k_1^2 + k_2^2)/k_1^2 k_2^2$. According to the theory of stochastic processes (Ross), the expected number of full steps of size L over the time interval Δt is $n = \Delta t/ < \tau_s >$, while the variance of this number is $\sigma^2 \Delta t/ < \tau_s >^3$. Respectively, the average velocity, $V = L/ < \tau_c >$, is just the step size divided by the average duration of the cycle. The rate of growth of the displacement variance, $d(var)/dt = (\sigma^2/\tau_s^2)LV$. This expression shows that the variance of dispalcement grows at the constant rate proportional to the product of the step size and average velocity. The dimensionless proportionality coefficient, $r = \sigma^2/\tau_s^2 = (k_1^2 + k_2^2)/(k_1 + k_2)^2$, is called *randomness parameter* due to the following reasons.

With the help of elementary calculus, one can confirm easily that $0.5 \leq r \leq 1$. The randomness parameter reaches the maximal value of 1 as the ratio of the rates of the half-steps, k_1/k_2, approaches either zero, or infinity, and the minimal value of 0.5 as this ratio is equal to 1. There is a notion of a *Poisson stepper* - hypothetic walker that makes steps of fixed size and direction. The steps are made at time moments distributed according to Poisson distribution, with certain constant average rate. Our motor becomes the Poisson stepper, when the ratio k_1/k_2 approaches either zero, or infinity, and duration of one of the half-steps can be neglected relative to the other. So, for the Poisson stepper, the randomness parameter is equal to 1: in certain sense, this is the 'most stochastic' mode of propulsion. If the rates of the half-steps are comparable, the motor becomes *less stochastic*, $r < 1$. The motor is the most deterministic when the durations of both half-steps are equal, and the displacement variance grows with the rate half that of the corresponding Poisson stepper. Of course, the motor gets even more deterministic if each cycle involves more chemical steps.

Note, that we could define the *effective diffusion constant*, $D_{eff} = (var)/2t$ for long times. Its value accounts for both variance due to Brownian movement and the randomness along the reaction coordinate. The randomness parameter and the effective diffusion constant are related by $r = 2D_{eff}/LV$, or $r = D_{eff} LVr/2$. Both parameters bear the same information. However, in some situations it is more appropriate to use one of them rather than the other. For example, if the reaction process is reversible, but the spatial step is not (motor only steps forward), the $(1/r)$ gives a lower bound on the number of reaction processes per step. Then, knowing the step size and measuring

the variance and displacement, one can find an information about the chemical cycle. Alternatively, if the number of reaction processes per step is known, the step size can be estimated. Meanwhile, spatial diffusion does not affect the effective dispersion. This situation is better treated using the randomness parameter. In the general case, neither r, nor D_{eff} gives information about the number of reaction processes per step.

12.3 Other Motor Proteins

12.3.1 'Walking motor': kinesin

The cytoplasm of eucaryotic cells is filled with cytoskeleton, dynamic meshwork of linear protein filaments providing mechanical support and mobility for the cell and serving as tracks for transport between different cell regions. Microtubules (MTs) are one of three major types of linear cytoskeletal polymers. They are polar structures that have distinct plus and minus ends. Structurally, MTs are long, straight hollow cylinders with an outer diameter of 25 nm. Their walls consist of 13 protofilaments, each of which is a linear polar assembly of 8 nm longtubulin subunits. Tubulin is a dimeric protein assembled of α- and β-subunits.

A host of motor proteins uses MTs as lines of transport. One of this motors (or, rather, one of the motor *families*), kinesin is a dimeric motor protein that converts the energy of ATP hydrolysis into mechanical work, transporting organelles toward the plus ends of MTs (Bray, 1992). Kinesin 'walks' along a single MT's protofilament in a stepwise manner using tubulin dimers as 'steps of the ladder' (Ray et al., 1993, last Vale). The length of a step is $8nm$ (Svoboda et al., 1993), the same as protofilament period. Kinesin mainly interacts with β-tubulin. This walk, at speeds of few hundreds nanometers per second, is resisted by viscous drag of the cytoplasm. At such speeds the viscous drag is negligeable, but at higher loads the rate of motion slows down, and the motor gets stalled by forces of 5-6 pN (Svoboda & Block, 1994). The motor can therefore produce an energy of $\simeq$ 40 pN·nm per step, which is about 50% of the energy available from one ATP molecule (Bray, 1992). Conventional dimeric kinesin is a highly processive motor able to move along more than 100 tubulin units before detaching (Block et al., 1990; Vale et al., 1996).

Essential features of the kinesin's mechanical behavior are captured by a 'head-over-head' model (Peskin & Oster, 1995) based on the following remarkable structure of the motor molecule. Kinesin contains two 7 nm globular domains - heads - connected to a 75 nm tail by the neck linker (Vale & Fletterick, 1997). Each head has a 'catalytic core' that binds ATP and MTs. Affinity of the heads to MTs is coupled to ATP hydrolysis cycle. Details of the mechanochemical cycle are still not completely known, but based on the available data, the following cycle can explain the motor's processive motion (there are alternative models, see ()).

When ATP is bound to one of the heads, this head is strongly bound to MT. Its neck linker is docked to the catalytic core of the head in the forward pointing state. This keeps

the other, ADP-head, bound to the β-tubulin site 8 nm ahead of the ATP-head. Next, *coordinated* events of hydrolysis and phosphate release from the rear head and ADP release from the front head lead to the state, in which the front head remains bound to MT. Meanwhile, the rear head looses its affinity to MT in new chemical state. The neck linker of the bound nucleotide-free head is flexible, so ADP-head diffuses over the bound head 'in search' of an MT binding site. Finally, binding of ATP molecule to the nucleotide-free head docks its neck linker in the forward pointing position completing the cycle. As a result, one ATP molecule is hydrolyzed, and kinesin advances 8 nm toward MT plus end.

In this model, asymmetry in hydrolysis rate between front and rear heads and the geometry of the head's binding and associated *elastic power stroke* drive the motor forward. This power stroke is assisted by thermal diffusion. The reason we introduce the model of kinesin walk here, besides this motor's importance and despite the fact that the details of the hydrolysis cycle are much more complicated than the process of utilizing the protonmotive force, is that, mathematically, the kinesin walking model is equivalent to the model of the previous section!

Indeed, the state when the rotor is static with two sites nearest to the membrane unprotonated is equivalent to the state with two kinesin's heads bound to two adjacent β-tubulin sites. The state with one head bound to MT and the other fluctuating between the adjacent MT's binding sites is equivalent to the state with one protonated rotor's site diffusing between the membrane's faces (see figure). The finite length of the tether between kinesin's heads limit this diffusion to the interval ± 8 nm similar to how the hydrophobic barrier limits the rotor's fluctuations to $\pm L$. The transmembrane potential is equivalent to a protein elastic force created as a result of a conformation change induced by the ATP binding. Protonation from the acidic or basic reservoir that make rotor mobile is analogous to dissociation of the rear or front head of kinesin respectively. Smaller rate of the dissociation of the rear head is due to coupling of the hydrolysis cycle to head's strain, which depends on the head's relative locations. Proton's release in the stator-rotor model is analogous to binding of ATP to the diffusing head and consequent association of this head with MT. Binding of the diffusing head to the β-tubulin site 8 nm ahead of the stationary head corresponds to the proton's release into the basic reservoir. Higher rate of this event compared to binding 8 nm behind the stationary head is due to the bias by the elastic force that keeps the diffusing head mostly in the forward pointing position. Finally, in both systems diffusion is much faster, than reactions (refs).

Because of this complete quantitative analogy between the models, we can rely on the analysis of the previous section to immediately write down the expression for the force-velocity relation of kinesin:

$$V(f) = L\frac{wk_a\ (k_d^r e^w - k_d^f e^{-w})}{(k_d^r + k_d^f)\ \sinh(w) + k_a w\ \cosh(w)}, \quad w = \frac{(F_e - F_l)L}{k_B T}. \tag{12.33}$$

Here $L = 8$nm is the distance between two adjacent β-tubulin sites - kinesin's step. F_e and F_l are elastic and load forces, respectively. Parameters k_a, k_d^r, k_d^f are the rates of

ATP binding (and immediate head's association) and rear and front head's dissociation, respectively.

The stall force in this model is given by the equation:

$$F_s = F_e + \frac{k_B T}{L} \ln[\frac{k_d^r}{k_d^f}]. \tag{12.34}$$

Force-velocity relation for single kinesin motors were measured independently by few groups (Block, Vale). Comparing the measurements with theoretical results, Oster and Peskin and Mogilner et al. () estimate the effective degree of coordination between the rear and front heads (quantitatively, the ratio k_d^r/k_d^f) as $k_d^r/k_d^f \simeq 20$. This means that brownian ratchet mechanism can generate $(k_B T/L)\ \ln(k_d^r/k_d^f) \simeq (4\text{pN} \cdot \text{nm}/8\text{nm})$ $\times 3 \simeq 1.5\text{pN}$. At the same time, the measured stall force is $\simeq 5-6\text{pN}$. Thus, $65-80\%$ of the force is generated by protein elasticity. This conclusion is supported by independent facts.

12.3.2 'One shot' assembly motor: polymerization ratchet

The simplest mechanism for converting chemical energy into mechanical force is via polymerization of a filament. The elongation velocity of a freely polymerizing filament is given simply by the net rate of the polymerization times the 'polymerization step':

$$V_p = L(k_{on} M - k_{off}). \tag{12.35}$$

Here the polymerization step L [nm] is the size of a monomer, M [μM] is the local monomer concentration, and k_{on} [1/(sec $\cdot\mu$M)] and k_{off} [1/sec] are the polymerization and depolymerization rate constants, respectively.

Now, imagine an object with diffusion coefficient D placed in front of a growing polymer, which is assumed to be perfectly rigid (figure). In order to add a monomer onto the end of the polymer the object must diffuse at least a distance L away from the tip to allow a monomer of size δ to intercalate between the filament tip and the object. Suppose for the moment that the object diffuses freely, and that $k_{off} = 0$, so that the polymerization can be considered irreversible. The natural length scale of the system is the monomer's size, L. Two characteristic temporal scales are the scale of the polymerization, $1/(k_{on}M)$, and the scale of diffusion, L^2/D. Here we will consider the limiting case of fast polymerization and slow diffusion, $k_{on}M \gg D/\delta^2$, opposite to that treated in the previous section. In this limit, the polymerization can be considered instantaneous. This is a perfect brownian ratchet: each time the object diffuses a distance L to the right, a monomer is instantly inserted that prevents it from diffusing back to the left. How fast does the object move to the right? This can be viewed as a first passage time problem (Van Kampen). The mean first passage time for the object to diffuse the distance L is simply $\tau_{fp} = L^2/2D$. Over many such intervals, the mean velocity is $V = L/\tau_{fp}$. Thus the velocity of a perfect brownian ratchet is $V = 2D/L$, the result remarkable in its simplicity.

Note that it seems that if the monomer's size could be reduced, then we would be able to get a faster motor. However, the dependence $V \sim 1/L$ is only true as far as $k_{on}M \gg D/L^2$, or $L \gg \sqrt{D/k_{on}M}$. At smaller values of the monomer's size, the rate of polymerization becomes the limiting factor, and the velocity $V \simeq Lk_{on}M$ becomes a decreasing function of the monomer's size. The greatest velocity that can be achieved by the perfect brownian ratchet $V \sim \sqrt{Dk_{on}M}$. It is an increasing function of parameters D, k_{on}, M, and is achieved at certain monomer's size $L \sim \sqrt{D/k_{on}M}$.

When the load force, $f > 0$, resists the object's motion to the right, energy must be supplied to push the load. This energy is provided by the free energy associated with monomer addition to the tip of the filament. The purely entropic free energy of polymerization is given by $\Delta G_p = k_B T \ln(k_{on}M/k_{off})$. The process of polymerization against a load can be represented as shown in figure,where the object is diffusing on a staircase energy surface, $V(x)$, with a step height of ΔG_p. The stall force, F_s, of the polymerization ratchet can be found from the argument that close to thermodynamic equilibrium, the work against the load over one polymerization step is equal to the free energy of polymerization: $F_s L = k_B T \ln(k_{on}M/k_{off})$. Thus:

$$F_s = \frac{k_B T}{L} \ln[\frac{k_{on}M}{k_{off}}]. \tag{12.36}$$

12.3.3 Protein translocation

If the polymerization rate is very large compared to the load's diffusion, while the depolymerization rate is very small, the approximate force-velocity relation can be obtained with the help of the following calculations.

Average position of the diffusing particle can be computed by solving a Smoluchowski equation of the form:

$$\frac{\partial p}{\partial t} = D[\frac{d^2 p}{dx^2} + \frac{1}{l}\frac{dp}{dx}], \tag{12.37}$$

where $p(x,t)$ is the probability of finding the particle at position x at time t, and the parameter $l = k_B T/F_l$ [nm]. The problem has to be solved on the interval $[0, L]$ with the following boundary conditions. We put an absorbing boundary at $x = L$, because as soon as the distance between the filament's tip and the object is L, the process of monomer's assembly onto the tip occurs. Mathematically, $p(L,t) = 0$. Therefore, we have to allow certain influx through the left boundary of the domain. Let us find the *stationary solution* of the corresponding Smoluchowski equation, $(d^2p/dx^2) + (1/l)(dp/dx) = 0$.

Integrating once, we find: $dp/dx + (p/l) = -J/D$, where J is an unknown constant flux. Integrating the second time, we obtain the stationary solution: $p = -(Jl/D) + A\exp(-x/l)$, where A is the integration constant. The flux can be expressed in terms of the normalization constant A with the help of the absorbing boundary condition: $p(L) = 0,\ J = (AD/l)\ \exp(-L/l),\ p(x) = A[\exp(-x/l) - \exp(-L/l)]$. The constant of integration can be found from the condition that exactly one object is at the interval

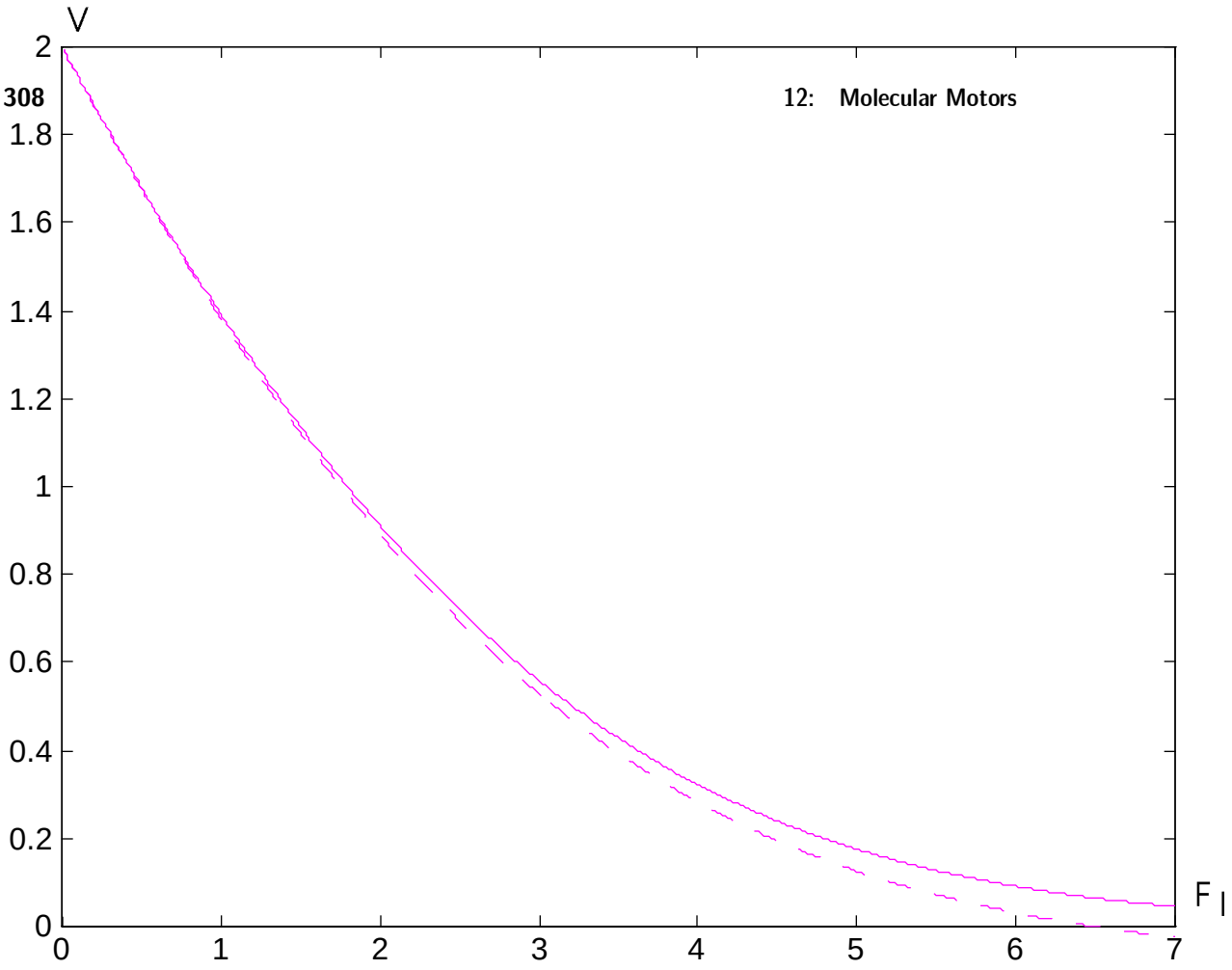

Figure 12.6 Force-velocity curve

$[0, L]$: $\int_0^L p(x)dx = Al[1 - \exp(-w)(1 + w)] = 1, w = (F_l L/k_B T)$. Then:

$$J = \frac{D}{L^2} \cdot \frac{w^2}{\exp(w) - 1 - w}.$$

The flux has the dimension $[\sec^{-1}]$ and can be interpreted as the rate of making a step L forward. Effective rate of polymerization is then:

$$V = LJ = \frac{D}{L} \cdot \frac{w^2}{\exp(w) - 1 - w}, \qquad w = \frac{F_l L}{k_B T}. \tag{12.38}$$

The corresponding force-velocity curve is plotted in Figure 12.6.

This situation is applicable to some cellular processes driven by polymerization: protein synthesis on cytoplasmic ribosomes. Subsequently, proteins must be imported into membrane compartments where they assume their biochemical duties. The process by which proteins are targetted to and imported into intracellular organelles has been studied extensively and many of the proteins involved have been identified. The me-

chanical process by which an unfolded peptide chain is transported across a lipid bilayer begins when the unfolded chain binds to a transmembrane pore called the translocation channel

12.3.4 Protrusion of the cell's leading edge and motion of cellular pathogens

When the polymerization rate is finite, then the picture becomes somewhat more complicated. Now the particle is diffusing along a sequence of potentials, $V(x + nL)$, offset by the monomer size, L, with transition rates between them, as shown in figure. Equations () are now replaced by a differential-difference equation. The resulting expression for the load-velocity relationship is more complicated (Peskin).

In these cases polymerization and depolymerization rates are much slower than the ideal ratchet velocity (i.e. $Lk_{on}M$ and $Lk_{off} \ll 2D/L$). Then, the load-velocity relationship takes the simple, intuitive form:

$$V = L(k_{on}MP_L(f) - k_{off}),$$

where $P_L(f)$ is the probability of a gap of size L between the filament tip and the object. When the polymer is perfectly rigid, $P_L(f) = exp(-w)$, where $w = fL/k_BT$ is the work done against the load force in moving one ratchet distance, L, in units of thermal energy. More complicated formulas for $P_L(f)$ govern the cases when the polymer is flexible and when it impinges on the barrier an angle, but the basic principle remains the same: the work of pushing a load is performed by brownian motion, with the energy to rectify the fluctuations being supplied by the binding free energy of the polymerization reaction (Mogilner).

Exercises

Exercise 1
Use equations (1) and (4) to prove that the relative velocity of two particles does not change after the collision.
Hint: rather than going through a tedious process of solving quadratic equations, consider the molecules in the coordinate system moving with the center-of-mass velocity. Demonstrate that in this coordinate system the molecules either move with unchange velocities after the collision, or they *exchange* their respective velocities.

Exercise 2
1) Write a subroutine for Matlab code 1 to get a hystogram showing how many times the working domain visited each of 20 small intervals
$[-1, -0.9], [-0.9, -0.8], ..., [0.9, 1]$. Analyze such hystograms at increasing values of the computation time, t_{end}.
1) again to estimate characteristic time scales for crossing the potential barrier.

2) Write a subroutine for Matlab code 1 to compute intervals of time between moments when the protein passes the point $x = 0$. Using this subroutine and running the code at increasing values of t_{end}, estimate the average rates of transition from the left to the right and back.
3) Repeat parts 1 and 2 in the case of weak force..

Exercise 3
Use Matlab or any other software to plot numerically Boltzmann distribution in the limit of weak force. Find the ratio of probability densities at $x = 0, -1, 1$.

Exercise 4
1) Modify Matlab code 2 to solve Fokker-Planck equation in the same limit of weak force, as in the stochastic simulations. Note, that it would be wiser to use the faster diffusion scale in this limit. Therefore, re-do scaling and non-dimensionalization. Discuss the biological meaning of the results.
2) Change initial condition to estimate numerically the rate of transition *from the right to the left*.
3) In both limits, compare the ratio $p(1)/p(0)$ numerically obtained at the end of a long (say, 100 time units) simulations with the same ratio computed analytically from Boltzmann distribution. Explain the discrepancy (is this numerical error, model error, something else?). *Hint*: compare analytical solutions of continuous stationary Fokker-Planck equation with constant force on a finite interval and discretized equation, and remember that $e^x \simeq 1 + x$ at small values of x, but $e^x \neq 1 + x$.

Exercise 5
Prove the formulae of section 6.4.

Exercise 6

APPENDIX A

Qualitative Analysis of Differential Equations

Bard Ermentrout and Joel Keizer

07-28

As noted in Chapter (1), nonlinear ordinary differential equations are notoriously difficult or impossible to solve analytically. On the other hand, the solution to linear equations–like those encountered in the kinetic model of the GLUT transporter Section (**??**)–can be expressed in terms of simple functions, and their behavior analyzed using standard results from linear algebra. In Section (**??**) of this chapter we summarize the main results for linear equations with two dependent variables. Although one often encounters models like the GLUT transporter that involve more than two variables, the basic ideas for two-variable ODEs carry over more or less unchanged for larger sets of linear equations. Thus the intuition gained from understanding simple two variable ODEs is enormously useful in understanding more complicated models. To help develop this intuition, we introduce the notion of the *phase plane* in Section Section (**??**) and use phase plane analysis to help understand the solution of two-variable linear equations in Section (**??**). Another reason for focusing on linear equations is that the stability of nonlinear ODEs can be understood by examining the behavior of small deviations around steady or oscillatory states. In Section (**??**) we show how the properties of linearized equations can be used to understand stability of steady states for a membrane with a gated ion channel.

A.1 Linear ODEs

The simplest time-dependent differential equations to solve are linear in the dependent variables and first order in the time. *First order* implies that only the first time derivative appears on the left hand side of the equations and linear implies that the right hand side is a linear function of the dependent variables. The most general equations of this type in n variables have the form

$$\begin{aligned} dx_1/dt &= a_{11}x_1 + a_{12}x_2 + \cdots + a_{1n}x_n + y_1 \\ dx_2/dt &= a_{21}x_1 + a_{22}x_2 + \cdots + a_{2n}x_n + y_2 \\ &\vdots \\ dx_n/dt &= a_{n1}x_1 + a_{n2}x_2 + \cdots + a_{nn}x_n + y_n. \end{aligned} \tag{A.1}$$

Here we consider only the case where the a_{ij} and y_i are parameters that are independent of time. For simplicity, we focus in this chapter on the special case of two variables, which shares the main features of the more general case. Using the column vector and matrix notation introduced in Section (**??**), we can write these equations concisely as:

$$d\mathbf{x}/dt = \hat{A}\mathbf{x} + \mathbf{y} \tag{A.2}$$

with

$$\mathbf{x} = \begin{pmatrix} x_1 \\ x_2 \end{pmatrix}, \mathbf{y} = \begin{pmatrix} y_1 \\ y_2 \end{pmatrix}, \hat{A} = \begin{pmatrix} a_{11} & a_{12} \\ a_{21} & a_{22} \end{pmatrix}. \tag{A.3}$$

The basic properties of matrices that we will need are summarized in the appendix to this chapter. Using the rules for differentiation of vectors, matrix multiplication, and vector addition it is easy to verify that the vector equation (Eqn. (A.2)), when written in terms of component vectors, is the special case of Eqn. (A.1) for two variables, *i.e.*

$$dx_1/dt = a_{11}x_1 + a_{12}x_2 + y_1 \tag{A.4}$$

$$dx_2/dt = a_{21}x_1 + a_{22}x_2 + y_2 \tag{A.5}$$

In this book we will be interested in equations for which there is a unique *steady state* solution, $\mathbf{x}^{ss}$. This is a solution that is independent of time, so that setting the left hand side of Eqn. (A.2) equal to zero and rearranging gives $\mathbf{y} = -\hat{A}\mathbf{x}^{ss}$. Using this expression we can eliminate $\mathbf{y}$ from Eqn. (A.2) by defining $\mathbf{x}' = \mathbf{x} - \mathbf{x}^{ss}$, to get

$$d\mathbf{x}'/dt = \hat{A}\mathbf{x}'. \tag{A.6}$$

This has the same form as Eqn. (A.2) with $\mathbf{y} = \mathbf{0}$. In the next section we will show how to solve equations of this type using simple algebra.

A.1.1 Solution of $d\mathbf{x}/dt = \hat{A}\mathbf{x}$

The simplest way to solve an equation like (Eqn. (A.2)) is to use the component form of the equation to obtain a new equation that is second order in time. For simplicity

we focus on the special case that $\mathbf{y} = \mathbf{0}$ and introduce the notation $\dot{x}_1$ for the first time derivative and $\ddot{x}_1$ for the second, so that

$$\dot{x}_1 = a_{11}x_1 + a_{12}x_2 \tag{A.7}$$
$$\dot{x}_2 = a_{21}x_1 + a_{22}x_2. \tag{A.8}$$

Thus differentiating both sides of Eqn. (A.7) with respect to time gives:

$$\begin{aligned}\ddot{x}_1 &= a_{11}\dot{x}_1 + a_{12}\dot{x}_2 \\ &= a_{11}\dot{x}_1 + a_{12}(a_{21}x_1 + a_{22}x_2) \\ &= a_{11}\dot{x}_1 + a_{12}a_{21}x_1 + a_{22}(a_{12}x_2) \\ &= a_{11}\dot{x}_1 + a_{12}a_{21}x_1 + a_{22}(\dot{x}_1 - a_{11}x_1) \\ &= a_{11}\dot{x}_1 + a_{22}\dot{x}_1 - a_{11}a_{22}x_1 + a_{12}a_{21}x_1\end{aligned} \tag{A.9}$$

where in rewriting the right hand side we have first used Eqn. (A.8) to replace $\dot{x_2}$ and the used Eqn. (A.7) to eliminate the term $a_{12}x_2$. Using the last equality in (Eqn. (A.9)) and the definitions of the trace and determinant of $\hat{A}$ in the Appendix, gives a second order equation for x_1:

$$\ddot{x}_1 - (tr\hat{A})\dot{x}_1 + (det\hat{A})x_1 = 0. \tag{A.10}$$

Using similar manipulations, an identical second order equation can be derived for x_2 (see Exercise 2.1):

$$\ddot{x}_2 - (tr\hat{A})\dot{x}_2 + (det\hat{A})x_2 = 0. \tag{A.11}$$

To solve Eqn. (A.10), we try the exponential function $x_1(t) = c\exp(\lambda t)$ ($c \neq 0$). Substituting this into the left hand side of (Eqn. (A.10)) gives

$$c\lambda^2 \exp(\lambda t) - c\lambda \exp(\lambda t) tr\hat{A} + c\exp(\lambda t) det\hat{A}. \tag{A.12}$$

Therefore, $c\exp(\lambda t)$ is a solution to (Eqn. (A.10)) if

$$\lambda^2 - (tr\hat{A})\lambda + det\hat{A} = 0. \tag{A.13}$$

This is called the *characteristic equation* of the matrix $\hat{A}$. It is a quadratic equation in λ with the well-known solution:

$$\lambda_{\pm} = \frac{tr\hat{A} \pm \left((tr\hat{A})^2 - 4det\hat{A}\right)^{1/2}}{2}. \tag{A.14}$$

For example if $\hat{A} = \begin{pmatrix} 1 & -1 \\ 3 & 6 \end{pmatrix}$, then $tr\hat{A} = 7$, $\det \hat{A} = 9$, and $\lambda_{\pm} = (7 \pm \sqrt{13})/2$. As long as $\lambda_+ \neq \lambda_-$, then the solution to the characteristic equation gives two independent solutions to Eqn. (A.10). In this case because Eqn. (A.10) is linear, it is easy to verify that the sum of these two solutions, $c_+ \exp(\lambda_+ t) + c_- \exp(\lambda_- t)$, is also a solution.

The argument of the square root in Eqn. (A.14) is the *discriminant* of the matrix $\hat{A}$ defined in the Appendix. As long as $disc\hat{A} \neq 0$, then it is clear from Eqn. (A.14)

that there are two independent solutions for $x_1(t)$. Using the result in Eqn. (A.10), it follows that the solution for $x_2(t)$ also has the same form. We write this concisely as

$$x_i(t) = b_{i1}\exp(\lambda_+ t) \; + b_{i2}\exp(\lambda_- t) \tag{A.15}$$

with $i = 1, 2$. The values of the constants b_{1i} and b_{2i} need to be chosen to satisfy the initial conditions. This is easily worked out, for example, for x_1. Recall that there are two initial conditions, $x_1(0)$ and $x_2(0)$, since there are two equations. Using Eqs. (Eqn. (A.7)) and (Eqn. (A.15)) it follows that:

$$x_1(0) = b_{11} + b_{12} \tag{A.16}$$

$$\dot{x}_1(0) = a_{11}x_1(0) + a_{12}x_2(0) = b_{11}\lambda_+ + b_{12}\lambda_-. \tag{A.17}$$

Since $x_1(0)$, $x_2(0)$, λ_+, and $\lambda_-$are known, Eqn. (A.16) and the second equality in Eqn. (A.17) provide two independent equations for the two unknowns, b_{11} and b_{12}. Solving these using elementary algebra gives:

$$b_{11} = \frac{\dot{x}_1(0) - \lambda_- x_1(0)}{\lambda_+ - \lambda_-} \tag{A.18}$$

$$b_{12} = \frac{-\dot{x}_1(0) + \lambda_+ x_1(0)}{\lambda_+ - \lambda_-} \tag{A.19}$$

Since $\lambda_+ \neq \lambda_-$, the denominators of these equations are different from zero.

The time dependence of $x_1(t)$ is strongly dependent on the nature of the characteristic values. There are three possibilities that are determined by the sign of the discriminant and the trace. If $disc\hat{A} > 0$, then according to Eqn. (A.14) the two characteristic values will be distinct real numbers since for a matrix with real components, $tr\hat{A}$ is a real number. However, if $disc\hat{A} < 0$, then the roots will be either conjugate complex numbers (if $tr\hat{A} \neq 0$) or conjugate pure imaginary numbers (if $tr\hat{A} = 0$).

When the characteristic values are complex or pure imaginary, Eq. (Eqn. (A.15)) can be reexpressed in terms of sines, cosines, and exponentials. This follows from the representation of the exponential of a complex number, $r + i\omega$ (with $i = \sqrt{-1}$) as

$$\exp(r + i\omega) = \exp(r)\exp(i\omega) = \exp(r)\left(\cos(\omega) + i\sin(\omega)\right). \tag{A.20}$$

If we express the characteristic values in this fashion as $\lambda_\pm = r \pm i\omega$, then it is not difficult to show using Eqs. (Eqn. (A.15))-(Eqn. (A.19)) that

$$x_1(t) = \exp(rt)\left(x_1(0)\cos(\omega t) - \frac{(\dot{x_1}(0) - r x_1(0))}{\omega}\sin(\omega t)\right). \tag{A.21}$$

Straightforward differentiation of this expression verifies that it satisfies the initial conditions and that it is identical to the expression in Eqn. (A.15).

The solution to Eqn. (A.10) is slightly different when $disc\hat{A} = 0$. In this case, according to Eqn. (A.14) $\lambda_+ = \lambda_-$, and there is only a single characteristic value $\lambda = tr\hat{A}/2$. In this case in addition to $c\exp(\lambda t)$ there is a second solution to Eqn. (A.10), which is $c't\exp(\lambda t)$. This can be verified using the facts that $tr\hat{A} = 2\lambda$ and

(since $disc\hat{A} = (tr\hat{A})^2 - 4det\hat{A} = 0$) that $det\hat{A} = \lambda^2$. Substituting these expressions for the $tr\hat{A}$ and $det\hat{A}$ into Eqn. (A.10) gives:

$$\ddot{x}_1 - 2\lambda\dot{x}_1 + \lambda^2 x_1 = 0. \tag{A.22}$$

It is easy to show then by substitution (see Exercise 2.3) that $c't\exp(\lambda t)$ solves Eqn. (A.22). Thus when $disc\hat{A} = 0$, the general solution to Eqn. (A.10) is:

$$x_1(t) = b_{11}\exp(\lambda t) + b_{12}t\exp(\lambda t). \tag{A.23}$$

Using the initial conditions

$$x_1(0) = b_{11} \tag{A.24}$$

$$\dot{x}_1(0) = a_{11}x_1(0) + a_{12}x_2(0) = \lambda b_{11} + b_{12}, \tag{A.25}$$

it is easy to show that in this case

$$b_{11} = x_1(0) \tag{A.26}$$

$$b_{12} = \frac{a_{11} - a_{22}}{2}x_1(0) + a_{12}x_2(0). \tag{A.27}$$

Although matrices with a vanishing discriminant are not typical, it is easy to construct specific examples, *e.g.*, $\hat{A} = \begin{pmatrix} -3 & 5 \\ 0 & -3 \end{pmatrix}$. For this matrix $tr\hat{A} = -6$, $det\hat{A} = 9$, $disc\hat{A} = 0$, and $\lambda = -3$, and the solution for x_1 is easily found from Eqs. (Eqn. (A.23))-(Eqn. (A.27)) to be

$$x_1(t) = (x_1(0) + 5tx_2(0))\exp(-3t). \tag{A.28}$$

A.1.2 Numerical Solutions with *XppAut*

Although we have characterized the solutions to Eqs. (Eqn. (A.7))-(Eqn. (A.8)) analytically, it is just as easy to solve them numerically. For example, a simple *XppAut* file that does this for the matrix $\hat{A} = \begin{pmatrix} 1 & -1 \\ 3 & 6 \end{pmatrix}$ is

```
#linear2.ode
init x1=1,x2=1
param a11=1,a12=-1,a21=3,a22=6
dx1/dt=a11*x1+a12*x2
dx2/dt=a21*x1+a22*x2
done
```

The characteristic values of this matrix are $\lambda_\pm = (7 \pm \sqrt{13})/2 = 5.31$ and 1.70. Since these values are distinct, we know from Section 2.2.1 that the solution is a sum of two exponentials with positive exponents. Thus as long as $x_1(0) \neq 0$ *and* $x_2(0) \neq 0$, the magnitude of x_1 and x_2 will increase exponentially with time. This is shown in Fig.

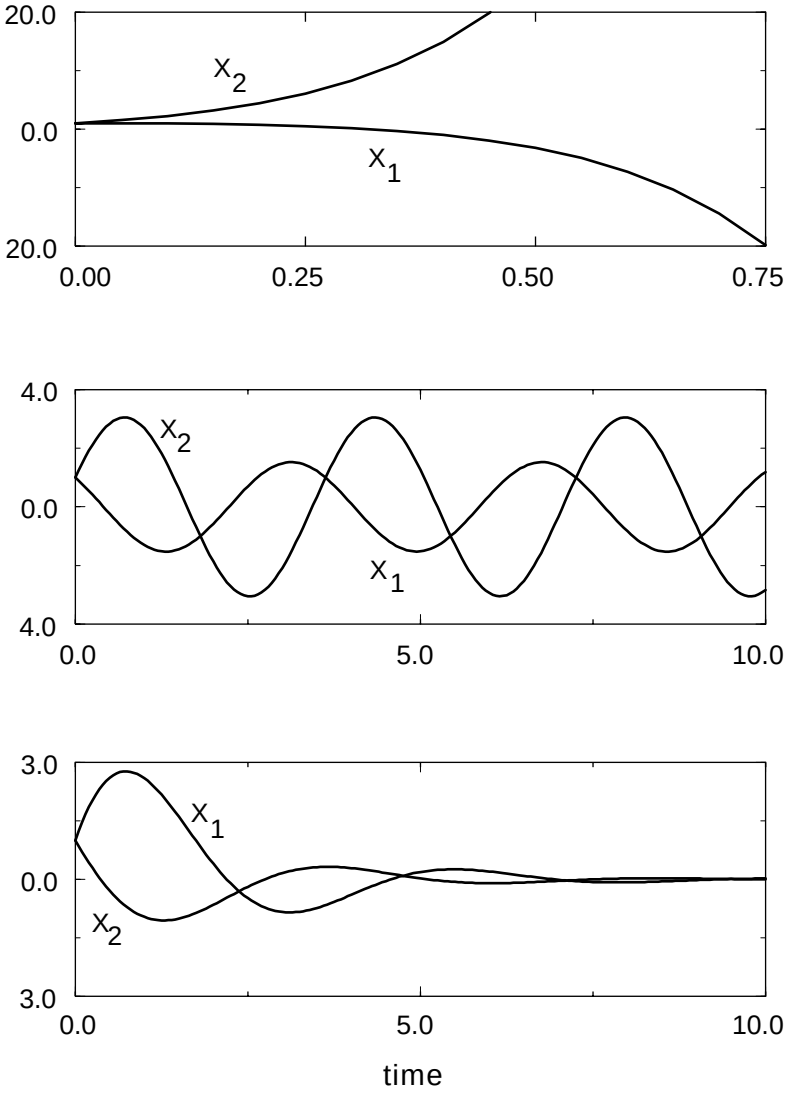

Figure A.1 Solution of the 2×2 linear equations using the file *linear2.ode* in *XppAut*. Panels A-C give the time course of the solutions for the three matrices descibed in the text.

2.1A, where the solution generated using *XppAut.* is plotted. Notice that x_1 rapidly declines whereas x_2 increases even more rapidly. The difference is due to the coefficients of the two exponentials, which can be calculated explicitly from the formulae in Eqs. (Eqn. (A.18)) and (Eqn. (A.19)).

Figure 2.1B shows another solution for the matrix $\hat{A} = \begin{pmatrix} -1 & -1 \\ 4 & 1 \end{pmatrix}$ for which $disc\hat{A} = -16$ and, therefore, $\lambda_{\pm} = \pm 4i$. Since the characteristic values are imaginary, Eqn. (A.21) shows that the solution is a sum of sines and cosines, as shown in the figure. The matrix $\hat{A} = \begin{pmatrix} -2 & -1 \\ 4 & 1 \end{pmatrix}$, on the other hand, has complex solutions with a real part equal to -1. Thus the solution for this matrix will be a sum of sines and cosines multiplied by $\exp(-t)$. Using *XppAut* to solve the equations leads to the damped oscillations shown in Fig. 2.1C.

A.1.3 Eigenvalues and Eigenvectors

The characteristic values of $\hat{A}$ are also the *eigenvalues* corresponding to the *eigenvectors* of the matrix. An eigenvector, e_λ, of $\hat{A}$ has the property that

$$\hat{A}e_\lambda = \lambda e_\lambda, \tag{A.29}$$

where λ is a number called the eigenvalue. In other words, the matrix $\hat{A}$ transforms an eigenvector into a constant multiple of the eigenvector. This equation can be rewritten in component form as:

$$\begin{aligned} (a_{11} - \lambda)e_{1\lambda} + a_{12}e_{2\lambda} &= 0 \\ a_{21}e_{1\lambda} + (a_{22} - \lambda)e_{2\lambda} &= 0. \end{aligned} \tag{A.30}$$

The only way to have a non-zero solution to this equation for $\mathbf{e}_\lambda$ is that the determinant of the coefficients on the left hand side of Eqn. (A.30) vanishes, *i.e.*:

$$det\hat{A} = \begin{pmatrix} a_{11} - \lambda & a_{12} \\ a_{21} & a_{22} - \lambda \end{pmatrix} = 0. \tag{A.31}$$

Expanding the determinant, one obtains the characteristic equation (Eqn. (A.13)), which shows that the eigenvalues are the same as the characteristic values of the matrix.

The eigenvectors of a matrix are defined only upto a multiplicative constant since if $\mathbf{e}_\lambda$ satisfies Eqn. (A.29), then so does $c\mathbf{e}_\lambda$. As long as $\lambda_+ \neq \lambda_-$, then it is not difficult to a verify that the eigenvectors are given by the simple formula:

$$\mathbf{e}_\lambda = \begin{pmatrix} 1 \\ (\lambda - a_{11})/a_{12} \end{pmatrix}. \tag{A.32}$$

For example, for the matrix $\hat{A} = \begin{pmatrix} 1 & 1 \\ 2 & 1 \end{pmatrix}$ $tr\hat{A} = 2$, $det\hat{A} = -1$, and $\lambda_{\pm} = 1 \pm \sqrt{2}$. Applying Eqn. (A.32) the eigenvectors are:

$$\mathbf{e}_+ = \begin{pmatrix} 1 \\ \sqrt{2} \end{pmatrix} \text{ and } \mathbf{e}_- = \begin{pmatrix} 1 \\ -\sqrt{2} \end{pmatrix}. \tag{A.33}$$

A useful property of eigenvectors of $\hat{A}$ is that if $\mathbf{e}_\lambda$ is the initial condition for Eqs. (Eqn. (A.7)) and (Eqn. (A.8)), then the solution is

$$\mathbf{x}(t) = \exp(\lambda t)\mathbf{e}_\lambda. \tag{A.34}$$

This result can be verified by differentiating the right hand side of Eqn. (A.34) to get $\dot{\mathbf{x}}(t) = \lambda \exp(\lambda t)\mathbf{e}_\lambda$ and then noticing that Eqn. (A.29) implies that

$$\hat{A}\mathbf{x}(t) = \hat{A}\exp(\lambda t)\mathbf{e}_\lambda = \exp(\lambda t)\hat{A}\mathbf{e}_\lambda = \lambda \exp(\lambda t)\mathbf{e}_\lambda, \tag{A.35}$$

which shows that $\mathbf{x}(t)$ solves the equations. We apply this result in the following sections.

A.2 Phase Plane Analysis

Obtaining a "solution" to first order ODEs means that you have expressed all of the dependent variables as functions of the time. In the case of the 2×2 linear equations in Sections 2.1.1, this means that we have the time series for x_1 and x_2. A great deal can be learned about these solutions by plotting the dependent variables as a function of time as done in Fig. 2.1. However, there are other ways of plotting solutions that give additional insight. For example, one can plot $\dot{x}_1$ versus time, or some function of x_1 and x_2 versus time. Perhaps the most useful plot is a *phase plane* plot in which x_2 is plotted versus x_1 with time serving only as a parameter. It is easy to make this type of plot using *XppAut*, since the *Data Viewer* window tabulates the value of x_1 and x_2 for each time point (see Exercise 2.8). Saving the table from the *Data Viewer* we have made phase plane plots in Figs. 2.2A-C of the numerical solutions given in Figs. 2.1A-C. This type of plot represents the *trajectory* of the solution just as the arc of a baseball thrown in the air is a trajectory in three dimensional space.

Technically, the phase plane (or phase space for more than two variables) is a Cartesian plane with coordinates (x_1,x_2). Since the initial condition for the ODEs is arbitrary, any one of these points could be the initial point of a trajectory like those in Figs. 2.2A-C. Continuing the analogy of phase space trajectories to the trajectory of a baseball, it makes sense to associate a *velocity* with the trajectory that goes through a point in phase space. This can be done directly using the differential equations, since the right hand side of the equations are explicit expressions for $\dot{x}_1$ and $\dot{x}_2$ as a function of x_1 and x_2. Thus for the matrix $\hat{A} = \begin{pmatrix} -2 & -1 \\ 4 & 1 \end{pmatrix}$ that gives rise to the trajectory in Fig. 2.2C, the x_1 component of the velocity at the point (x_1, x_2) is $-2x_1 - x_2$, whereas the x_2 component of the velocity is $4x_1 + x_2$. For the initial point (0.5,0.5) of the trajectory in Fig. 2.2C the velocity the vector at that point has components (-1.5,2.5). In the figure, the head of the arrow on the velocity vector indicates its direction and the length is proportional to its magnitude. Just as the velocity of a baseball is parallel to its trajectory, so is the velocity vector in phase space parallel to its trajectory (see Exercise 2.10).

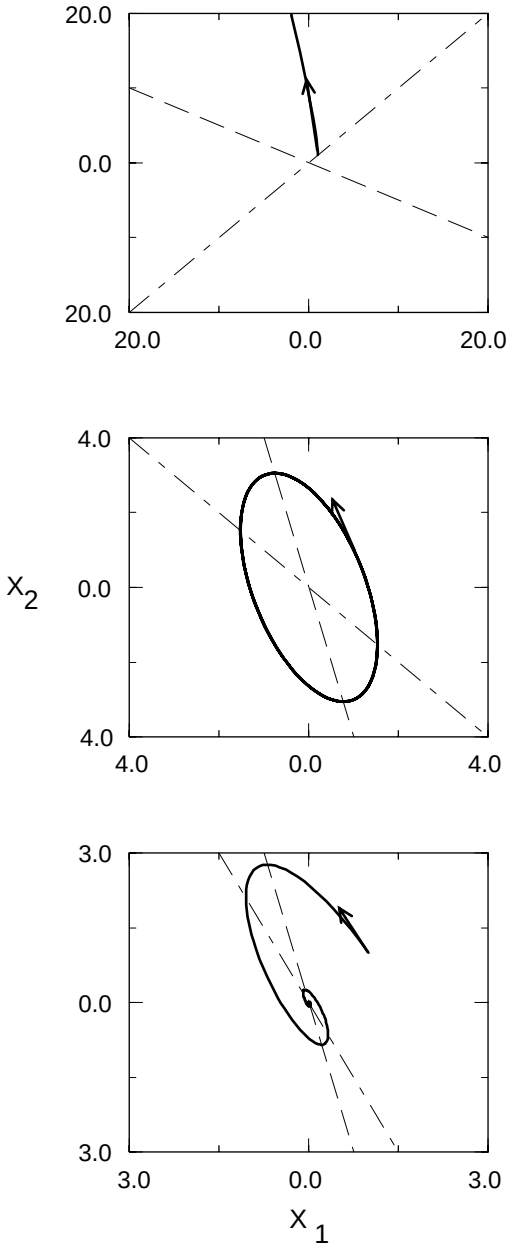

Figure A.2 The three solutions in Fig. 2.1A-C represented in phase plane plots in corresponding Panels A-C. The arrow represents the direction of the initial point on the trajectory, which is given by the full line. The dashed line is the x_2 nullcline, the broken dashed line is the x_1 nullcline, and their intersection is the steady state, which is unstable in Panel A, marginally stable in Panel B, and stable in Panel C.

There are a number of important curves and points in the phase plane that are defined by the differential equations. *Isoclines* are lines in the phase plane where the time rate of change of a variable are constant. For example, for the matrix in the previous paragraph, the isoclines for x_1 are defined by $c = -2x_1 - x_2$, *i.e.*, $x_2 = -2x_1 + c$, and the isoclines for x_1 are given by $x_2 = -4x_1 + c$, where c is a constant. A particularly useful

isocline is the *nullcline* for which the time rate of change is zero, *i.e.*, $c = 0$. So for this special case the nullclines are given by the straight lines through the origin, $x_2 = -2x_1$ and $x_2 = -4x_1$, shown in Fig. 2.2C. It is straightforward to show that the nullclines for the general 2×2 linear equations (Eqn. (A.4)) and (Eqn. (A.5)) are also straight lines (see Exercise 2.11). Since $\dot{x}_1 = 0$ on the x_1 nullcline, x_1 cannot decrease if the trajectory crosses the nullcline from the right and cannot increase if the trajectory crosses it from the left. This means, as can be verified by looking at Fig. 2.2, that the trajectory must cross the x_1 nullcline perpendicular to the x_1 axis. Similary, the trajectory crosses the x_2 nullcline perpendicular to the x_2 axis.

Steady states are defined as points in the phase space at which both $\dot{x}_1 = 0$ and $\dot{x}_2 = 0$. These points, which are also known as *singular points*, *equilibrium points*, or *stationary points*, have the property that neither variable changes as a function of time. They are determined graphically by the intersection of the nullclines. However, just because the variables do not change in time at a steady state does not mean that trajectories starting from nearby points will end up at the steady state. Three different situations are illustrated in Fig. 2.2. In panel A the steady state is at the origin, (0,0). However, the trajectory starting at (0.5,0.5) grows without bound. In panels B and C the steady states are also at the origin, but the trajectory in B circles the origin periodically whereas in C it spirals into the steady state.

XppAut provides excellent tools for analyzing solutions of 2-variable ODEs in the phase plane. Indeed, the "pp" in *XppAut* stands for phase plane. *XppAut* will calculate the nullclines when the plotting windows is set-up for the two independent variables. It will also plot a *direction field*, which is a set of lines parallel to trajectories at a uniform grid of points. Other options can be used to generate trajectories for a fixed time interval starting at a uniform grid of points in the plotting window. *XppAut* also has options for calculating singular points. This phase plane functionality is not restricted to linear equations. In Chapter 3 we analyze nonlinear equations using *XppAut* and its phase plane options.

A.3 Stability of Steady States

As we saw in the preceding section, a steady state may or may not be an *attractor* for nearby trajectories, *i.e.*, just because an initial condition is close to the steady state, it does not mean that after a time the trajectory will approach the steady state. However, when this is the case, the steady state is said to be *stable and attractive* or *asymptotically stable*. Three qualitatively different behaviors near steady state are illustrated by the solutions of the linear ODEs in Figs. 2.2A-C. The matrix for the ODEs in panel A has positive eigenvalues and the trajectory is repelled, not attracted by the steady state. So the steady state in panel A is asymptotically unstable. In panel B the trajectory is circular and periodically returns to the initial condition, (0.5,0.5). In this case the steady state is neither attractive nor repulsive and is said to be *marginally stable*. Finally, in panel C the trajectory spirals into the steady state, which is stable and attractive.

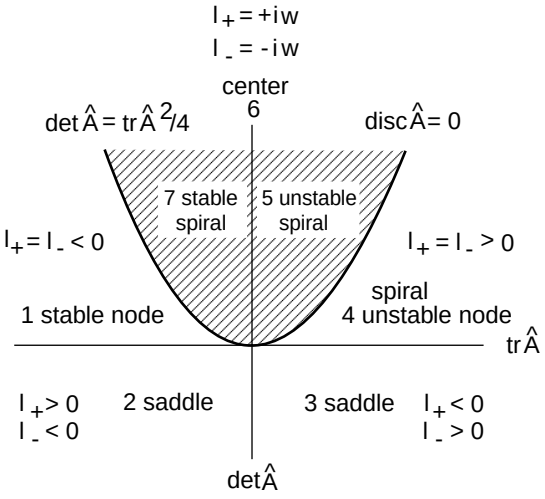

Figure A.3 Graphical representation of the stability properties of 2×2 matrices. The trace is plotted on the x-axis and the determinant on the y-axis. The eigenvalues in the cross hatched region are complex and real elsewhere. These two regions are separated by the parabola $det\hat{A} = tr\hat{A}^2/4$ on which $disc\hat{A} = 0$. Seven egions with various stability are indicated by the sign of the eigenvalues.

The attentive reader may have noticed a correlation between the eigenvalues of the three matrices represented in Fig. 2.2A-C and the stability of the steady states. Indeed, unstable states of linear equations are characterized by at least one eigenvalue with a positive real part. If, in addition, both eigenvalues are positive, as in Fig. 2.2A, then the state is called a *unstable node*. An asymptotically stable state like that in Fig. 2.2C, on the other hand, has negative real parts for all of its eigenvalues. Marginal (or neutral) stability occurs when the real part of a pair of eigenvalues vanish, as is the case in Fig. 2.2B. A 2-variable linear equation has only two eigenvalues and a marginally stable steady state implies sinusoidal solutions, as we have seen in Section 2.1.1. Another name for a marginal state for a two variable system is a *center*.

Because we have at our disposal the analytical form of the solutions for 2×2 linear equations, it is possible to give a complete description of the stability of their steady states. Fig. 2.3 gives a graphical representation of the stability behavior of a matrix $\hat{A}$ as a function of the trace (plotted on the x-axis) and the determinant (plotted on the y-axis). The $tr\hat{A}$,$det\hat{A}$-plane in Fig. 2.3 is divided into seven distinct regions separated by the two axes and the parabola $det\hat{A} = tr\hat{A}^2/4$, which is the curve on which $disc\hat{A} = 0$. According to the expression for the characteristic values in Eqn. (A.14), $\lambda_+ = \lambda_-$ on the parabola, and in the quadrant with $tr\hat{A} > 0$ the eigenvalues are both positive, whereas for $tr\hat{A} < 0$, both eigenvalues are negative. Marginal stability occurs when the real part of both eigenvalues is zero, *i.e.*, when $tr\hat{A} = 0$ and $det\hat{A} > 0$, which occurs on the positive y-axis. Using Eqn. (A.14) it is easy to verify that complex eigenvalues occur only in the cross-hatched region above the parabola (since $disc\hat{A} < 0$ there). In that region to the right of the y-axis, $tr\hat{A} > 0$, the eigenvalues have positive real parts, and the steady states are unstable spirals (region 5), whereas in region 7 the spirals are stable. When $tr\hat{A}$ and $det\hat{A}$ have values in regions 1 and 4, the steady state is a stable or unstable node node, respectively. Below the x-axis (where $det\hat{A} < 0$) the

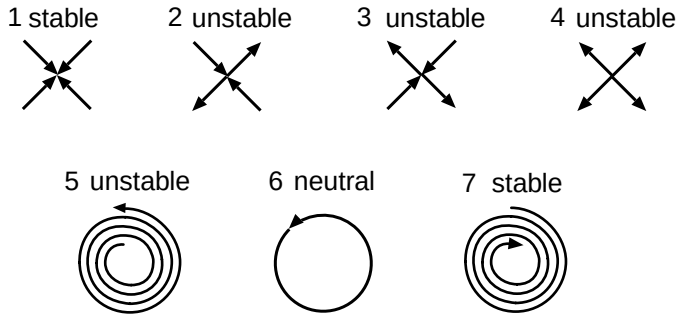

Figure A.4 Schematic representation of phase space trajectories near the steady states in the seven regions shown in Fig. 2.3. Unstable states have trajectories that diverge from the steady state, whereas stable steady states have converging trajectories, and neutrally stable states are surrounded by closed trajectories. The states shown in 2 and 3 are saddle points, with both converging and diverging trajectories in the directions of the eigenvectors of the matrix.

steady states are unstable with the property that they have two real eigenvalues, one positive and one negative. Unstables states like this are called *saddle* points, because trajectories that start in the direction of the positive eigenvector recede from the steady state exponentially. Trajectories along the direction of the negative eigenvector move toward the steady state, also exponentially (see Exercise 2.12).

Using Fig. 2.3 we can classify the qualitative behavior of phase plane trajectories for 2×2 linear ODEs based on the value of their trace and determinant. Representative trajectories are illustrated in Fig. 2.4 for each of the seven regions in Fig. 2.3. Region 1 is a stable node and the two trajectories correspond to the directions of the two stable eigenvectors, which have velocity vectors directed at the steady state. Regions 2 and 3 are saddle points, with eigenvectors that move towards or away from the steady state, whereas the unstable node in Region 4 has both eigenvectors moving away. Regions 5 and 7 have trajectories that spiral away from or towards the steady state. In region 6 the trajectories are circles, corresponding to sinusoidal oscillations.

A.4 Stability of a Nonlinear Steady State

What we've learned about stability of steady states for linear systems can be transfered partially to nonlinear ODEs. To be specific, let's consider a biological membrane with a gated ion channel. To do this we combine the model of ion gating in Section 1.3.4 with Eqn. (A.38) that governs the membrane potential. If n represents the gating variable and V the voltage, then the two are coupled by the differential equations

$$CdV/dt = -gn(V - V_{rev}) + I_{app} \tag{A.36}$$

$$dn/dt = -(n - n_\infty(V))/\tau, \tag{A.37}$$

where V_{rev} is the reversal potential. For definiteness, we assume that n_∞ has the the following voltage dependence

$$n_\infty(V) = \frac{1}{1+\exp(-(V+V_{0.5})/S)} \tag{A.38}$$

with $V_{0.5}$ and S positive constants, which is typical of an activation gate (see Chapter 3). Equations (Eqn. (A.36)) and (Eqn. (A.37)) are both nonlinear due to the factor $n(V-V_{rev})$ in Eqn. (A.36) and the voltage dependence of n_∞ in Eqn. (A.37).

To analyze the stability of the steady states of these equations we first must find the steady states by setting the right hand sides of the equations equal to zero. This gives:

$$gn^{ss}(V^{ss}-V_{rev}) = I_{app} \tag{A.39}$$

$$n^{ss} = n_\infty(V^{ss}), \tag{A.40}$$

which can be written as a single nonlinear equation to solve for V^{ss}:

$$\frac{I_{app}}{g} = \frac{V^{ss}-V_{rev}}{1+\exp(-(V^{ss}+V_{0.5})/S)}. \tag{A.41}$$

This equation cannot be solved in closed form, and a much simpler way to locate the steady state is graphically in the (V,n) phase plane using the nullclines. Setting the left hand sides of Eqs. (Eqn. (A.36)) and (Eqn. (A.37)) separately equal to zero and solving for n as a function of V gives:

$$n(V) = \frac{I_{app}}{g(V-V_{rev})} \quad \text{V-nullcline} \tag{A.42}$$

$$n(V) = n_\infty(V) = \frac{1}{1+\exp(-(V+V_{0.5})/S)} \quad \text{n-nullcline.} \tag{A.43}$$

The V- and n-nullclines are plotted in Fig. 2.5A, along with representative trajectories obtained using *XppAut* (see Exercise 2.13). Due to the nonlinearities in Eqs. (Eqn. (A.36)) and (Eqn. (A.37)) the nullclines are curved rather than straight lines. This curvature influences the shape of the trajectories, which must cross the nullcline perpendicular to the axis of the variable. Close to the steady state, however, both nullclines become approximately straight lines, as is seen in Fig. 2.5B, which is the same phase plane as in Fig. 2.5A, but zoomed-in around the steady state.

If we restrict the initial conditions for trajectories to be close to the steady state, then the nonlinear equations are well-approximately by a 2×2 linear system. This can be seen in detail if we define as new variables $x_1 = V - V^{ss}$ and $x_2 = n - n^{ss}$, the deviations of the voltage and gating variable from their steady state values. Since the steady state values are constants, it follows that $dx_1/dt = dV/dt$ and $dx_2/dt = dn/dt$ so that we can use Eqs. (Eqn. (A.36)) and (Eqn. (A.37)) to obtain differential equations for x_1 and x_2. In particular, if the initial conditions are close to the steady state, then we can substitute $V = V^{ss}+x_1$ and $n = n^{ss}+x_2$ into the right hand sides of (Eqn. (A.36)) and (Eqn. (A.37)) and then use a Taylor series expansion in the small deviations x_1

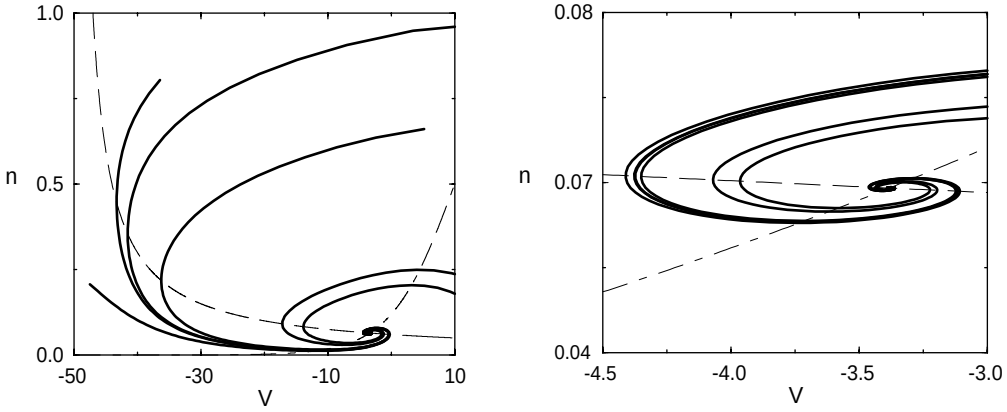

Figure A.5 Phase plane plots for Eqs. (()) showing typical trajectories (full lines), the V-nullcline (dashed line), and the n-nullcline (broken dashed line). Panel B is zoomed-in around the steady state, illustrating that the nullclines are approximately straight lines near the steady state.

and x_2. Explicitly:

$$\begin{aligned} dx_1/dt &= \left(g(n^{ss}+x_2)(V^{ss}+x_1-V_{rev})+I_{app}\right)/C \\ &= [gn^{ss}(V^{ss}-V_{rev})+I_{app}]/C + (gn^{ss}x_1+g(V^{ss}-V_{rev})x_2)/C \\ &\quad + gx_1x_2/C \end{aligned} \tag{A.44}$$

$$\begin{aligned} dx_2/dt &= -\left(n^{ss}+x_2-n_\infty(V^{ss}+x_1)\right)/\tau \\ &= -[n^{ss}-n_\infty(V^{ss})]/\tau + (dn_\infty/dV)^{ss}x_1/\tau - x_2/\tau \\ &\quad + \text{higher order terms in } x_1 \end{aligned} \tag{A.45}$$

In the second equality in both Eqs. (Eqn. (A.44)) and (Eqn. (A.45)) the terms in square brackets vanish because of the steady state conditions in Eqs. (Eqn. (A.39)) and (Eqn. (A.39)); the second terms are linear in x_1 and x_2; and the third terms are quadratic or higher order in x_1 and x_2. Thus keeping the lowest order terms gives the linear equations:

$$dx_1/dt = (gn^{ss}/C)x_1 + (g(V^{ss}-V_{rev})/C)x_2 \tag{A.46}$$

$$dx_2/dt = (dn_\infty/dV)^{ss}x_1/\tau - x_2/\tau. \tag{A.47}$$

Once the elements of the matrix of this 2×2 linear equation have been evaluated, the behavior of the solution in a neighborhood of the steady state can be evaluated. This type of linear analysis, which gives information only about trajectories nearby the steady state, is called *linear stability analysis*.

The trajectories in Fig. 2.5B make it clear that the steady state is asymptotically stable, and according to the catalogue of possibilities in Fig. 2.4, the steady state is a stable spiral. However, *XppAut* provides an alternative way of assessing stability that circumvents the need to linearize the ODEs. *XppAut* contains an option, called

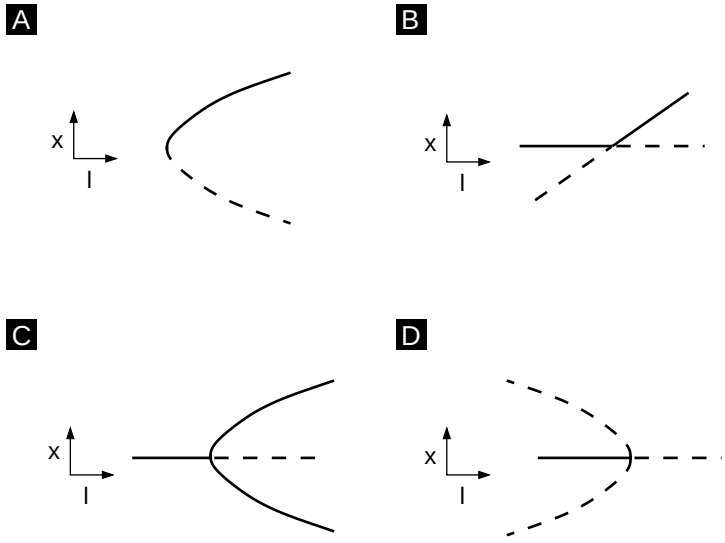

Figure A.6 Bifurcations of new fixed points: (A) saddle-node bifurcation, (B) transcritcial bifurcation, (C) supercritical pitchfork bifurcation, (D) subcritical pitchfork bifurcation. Stable fixed points are solid and unstable are dashed.

Sing pts, that finds the steady states numerically and, in addition, determines the stability of the steady state by numerical evaluation of the eigenvalues (see Exercise 2.13). Combining the analytical tools developed in this chapter with the numerical tools available in *XppAut*, we are ready to explore the dynamics of a variety of cellular and neural dynamical system in the remaining chapters.

A.5 Bifurcation theory

In many systems of differential equations, there are parameters that we would like to vary. As these parameters vary, we want to know if the solutions to the equations remain similar in nature. For example, as current is injected into a cell, we want to know if the cell will remain at rest or whether some other phenomena that are qualitatively different will take place. The changes in the qualitative nature of solutions to differential equations as a parameter varies is called bifurcation theory. In this section, we will review simple bifurcations from equilibrium of ordinary differential equations. Bifurcation from equilibrium solutions is intimately related to the stability of equilibria, a subject described earlier in this chapter. Suppose that we have found an equilibrium solution to a system of differential equations and study it's stability as some relevant parameter varies. The stability is determined from the eigenvalues of the linearized system. There are two simple ways that stability can change as a parameter varies: (i) a real negative eigenvalue can cross through zero and becomes positive; (ii) A pair of complex

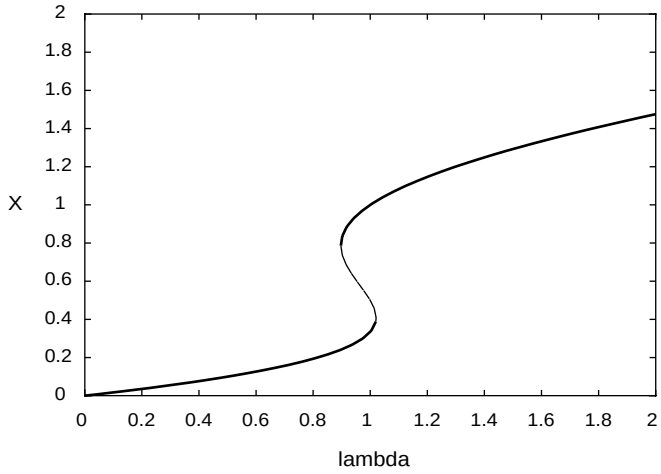

Figure A.7 Numerically computed bifurcation diagram for the autocatalytic chemical model. Stable fixed points are solid and unstable are dashed.

conjugate eigenvalues with negative real parts crosses through the imaginary axi and becomes a pair of complex eigenvalues with positive real parts. In a fully nonlinear system these changes in stability will often lead to the appearance of new solutions to the differential equations. Because these are new baranches of solutions that were not there, the system has undergone a qualitative change in behavior.

A.5.1 Bifurcation at a zero eigenvalue.

Consider the differential equation

$$\frac{dx}{dt} = \lambda - x^2 \tag{A.48}$$

where λ is a parameter. For $\lambda < 0$ there are no real equilibria. However if $\lambda > 0$ then there are two equililibrium solutions, $x = \pm\sqrt{\lambda}$. Consider the case $\lambda > 0$. The linearization about the positive fixed point is $-2\sqrt{\lambda}$. Thus, it is a stable fixed point. Note that as λ tends to zero the eigenvalue of this 1×1 matrix goes to zero. Any time an eigenvalue of the linearization around an equilibrium point crosses zero, we can expect to see more than one fixed point in the neighborhood of the parameter. The graph of the equilibrium solution agains the parameter along with the stability inforamtion is called a *bifurcation diagram.* Fig. (A.6A) shows the bifurcation diagram for Eqn. (A.48). This type of bifurcation is called a saddle-node. The auto-catalytic chemical model:

$$\frac{dx}{dt} = \lambda - 6x + \frac{10x^2}{1 + x^2}$$

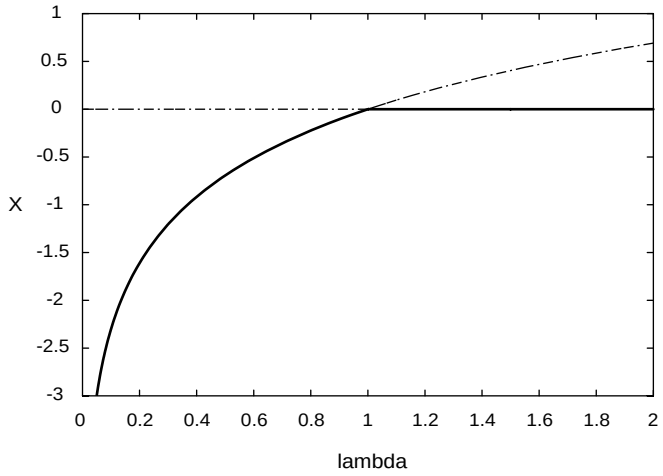

Figure A.8 Numerically computed bifurcation diagram for the example transcritical bifurcation. Stable fixed points are solid and unstable are dashed.

has a two saddle-node bifurcations as the input λ increases from 0. For $0 < \lambda < 0.9$ there is a single equilibrium point. At $\lambda \approx 0.9$ a new pair of equilibria appear at $x \approx 0.8$. As λ continues to increase these new equilibria drift apart and at $\lambda \approx 1.02$ the leftmost equilibrium merges with the middle one and disappears at $x \approx 0.4$. We can use XPP to draw a complete bifurcation diagram of this. Fig. (A.7) illustrates the complete bifurcation diagram. Note the two saddle-node bifurcations; for λ between these two values, there are three equilibria (two stable and one unstable) while for λ outside the two values, there is a unique stable equilibrium point. technoiques from nonlinear analysis can be used to show that every saddle-node bifurcation (no matter what the dimension of the system) is equivalent and can be transformed into Eqn. (A.48).

Consider next the differential equation:

$$\frac{dx}{dt} = \lambda x - x^2. \tag{A.49}$$

In some model systems there is always a "trivial" equilibrium point, no matter what the parameter is. (In this case, 0, is always a solution.) For $\lambda < 0$ $x = 0$ is a stable equilibrium and for $\lambda > 0$ it is unstable. The equilbrium point $x = \lambda$ is unstable (stable) for $\lambda < 0$ ($\lambda > 0$). Thus as λ crosses zero the two fixed points "exchange stability." This is called a *transcritical* or *exchange of stability* bifurcation. Fig. (A.6B) illustrates this bifurcation. For example, consider the system:

$$\frac{dx}{dt} = x(1 - \lambda y) \quad \frac{dy}{dt} = e^{-x} - y.$$

Clearly, one fixed point is $(0, 1)$ and the Jacobian matrix for the linearization about this point is

$$J = \begin{pmatrix} 1-\lambda & 0 \\ -1 & -1 \end{pmatrix}.$$

The eigenvalues are -1 and $-1+\lambda$. Thus at $\lambda = 1$ we expect that there could be a bifurcation. It is not a saddle-node since there always exists the trivial equilibrium, $(0, 1)$. Since there are no additional symmetries in the problem (see below), it is likely a transcritical bifurcation. The diagram is shown in Fig. (A.8). As with the saddle-node bifurcation, all transcritical bifurcations can be transformed into Eqn. (A.49) near the bifurcation.

Many biological and chemical systems are characterized by symmetries. In this case, the behavior as parameters vary is analogous to:

$$\frac{dx}{dt} = x(\lambda \pm x^2). \tag{A.50}$$

As with the transcritical bifurcation, $x = 0$ is always a solution to this problem. For $\lambda < 0$, the fixed point 0 is stable and for $\lambda > 0$ this trivial fixed point loses stability. At $\lambda = 0$ the linearized system has a zero eigenvalue. There can be *two* additional solutions depending on λ. Unlike the two bifurcations we previously described, the sign of the nonlinearity is important in this one. If we take the negative sign in Eqn. (A.50), then the diagram in figure Fig. (A.6C) is obtained. The new solutions are $x = \pm\sqrt{\lambda}$, they are both stable, and they occur for $\lambda > 0$. The branches open in the same direction as the trivial fixed point loses stability. This bifurcation is called a *supercritical pitchfork bifurcation.* If we take instead the positive sign for the nonlinearity in Eqn. (A.50), then there are two solutions $x = \pm\sqrt{-\lambda}$ and they occur for $\lambda < 0$. As can easily be shown, they are both unstable. This is called a *subcritical pitchfork bifurcation* since the branches open in the direction opposite from the change of stability of the trivial equilibrium point.

For example consider the simple coupled system:

$$\frac{dx}{dt} = -x + \lambda\frac{y}{1+y^2} \quad \frac{dy}{dt} = -y + \lambda\frac{x}{1+x^2}.$$

It is easy to see that $x = y = 0$ is always a fixed point and that it is stable as long as $\lambda < 1$. At $\lambda = 1$ the Jacobian matrix has a zero eigenvalue, so we expect a bifurcation to occur. Fig. (A.9) shows that it is a supercritical pitchfork bifurcation. Every system that has a pitchfork bifurcation can be transformed into Eqn. (A.50) near the bifurcation point. Unlike the saddle-node and the transcritical bifurcation, the details of the nonlinearity are crucial for determing the stability of the new branches of solutions.

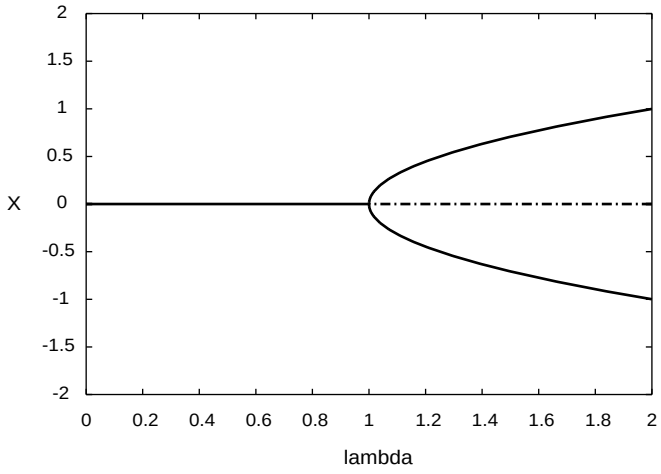

Figure A.9 Numerically computed bifurcation diagram for the coupled system showing a pitchfork bifurcation. Stable fixed points are solid and unstable are dashed.

A.5.2 Bifurcation at a pair of imaginary eigenvalues.

Limit cycles and periodic solutions are extremely important in physiology. Thus, one is often interested in whether or not they occur in a given system. Unlike fixed points which can be found exactly or graphically, it is much more difficult to determine whether or not there are limit cycles in a system. There is one method that is arguably the best and perhaps only systematic method of finding parameters where there may be periodic solutions in any system of differential equations. The existence of periodic solutiuons emanating from a fixed point is established from the Hopf bifurcation theorem which we now state.

Hopf bifurcation theorem. *Suppose that* $X' = F(X, \lambda)$ *has an isolated fixed point,* $X_0(\lambda)$. *Let* $A(\lambda)$ *be the linearized matrix about this fixed point. Suppose that the matrix* A *has a pair of complex conjugate eigenvalues,* $\alpha(\lambda) \pm i\omega(\lambda)$. *Suppose the following conditions hold for some* λ_0.

1. $\alpha(\lambda_0) = 0$;
2. $\omega(\lambda_0) = \omega_0 > 0$;
3. $\nu \equiv d\alpha(\lambda)/d\lambda|_{\lambda=\lambda_0} \neq 0$;
4. $A(\lambda_0)$ *has no other eigenvalues with zero real part.*

Then, the system contains an isolated limit cycle for $|\lambda - \lambda_0|$ *small for either* $\lambda > \lambda_0$ *or for* $\lambda < \lambda_0$. *The magnitude of the limit-cycle is proportional to* $\sqrt{|\lambda - \lambda_0|}$ *and the frequency is close to* ω_0. *If* $\nu > 0$ *and the limit cycle exists for* $\lambda > \lambda_0$ *or if* $\nu < 0$ *and the limit cycle exists for* $\lambda < \lambda_0$ *then it is stable. Otherwise it is unstable.*

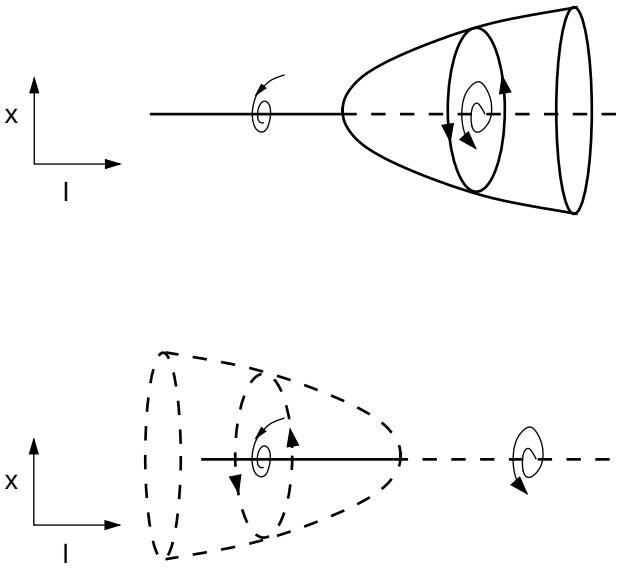

Figure A.10 Illustration of the Hopf bifurcation of limit cycles. As the parameter changes, a branch of periodic solutions emerges from the fixed point. Top figure shows super-critical emergence of stable limit cycles and bottom show sub-critical emergence of unstable periodic orbits.

Thus, the best way to try to find periodic solutions in a system of differential equations is to look for parameter values where the stability of an equilibrium is lost as a complex conjugate pair of eigenvalues crosses the imaginary axis. For a two-dimensional system, this situation occurs when the seterminant of A is positive and the trace of A changes from negative to positive. The following system illustrates the theorem:

$$\begin{aligned} \frac{dx}{dt} &= \lambda x - y \pm x(x^2+y^2) \\ \frac{dy}{dt} &= \lambda y + x \pm y(x^2+y^2) \end{aligned} \tag{A.51}$$

Clearly, $(0,0)$ is always a fixed point. The eigenvalues of the linearization are $\lambda \pm i$ so that as λ goes from negative to positive, there is a pair of eigenvalues with imaginary real part at $\lambda = 0$. If we convert Eqn. (A.52) to polar coordinates, $x = r\cos\theta$, $y = r\sin\theta$ then we obtain:

$$\frac{dr}{dt} = r(\lambda \pm r^2) \quad \frac{d\theta}{dt} = 1.$$

The equation for r is just like Eqn. (A.50) and thus the direction of bifurcation depends on the sign of the nonlinearity. We see that $r = \sqrt{\mp\lambda}$. Clearly the solution to the θ equation is $\theta = t + C$ where C is an arbitrary constant. We conclude that if the nonlinearity has a positive sign, then there is an unstable periodic solution for $\lambda < 0$ given by $(x(t), y(t)) = \sqrt{-\lambda}(\cos(t+C), \sin(t+C))$. If the nonlinearity has a negative sign, then the limit cycle exists for $\lambda > 0$ and it is stable. Fig. (A.10) illustrates the behavior for both cases. We remark that every system that undergoes a Hopf bifurcation can be transformed to Eqn. (A.52).

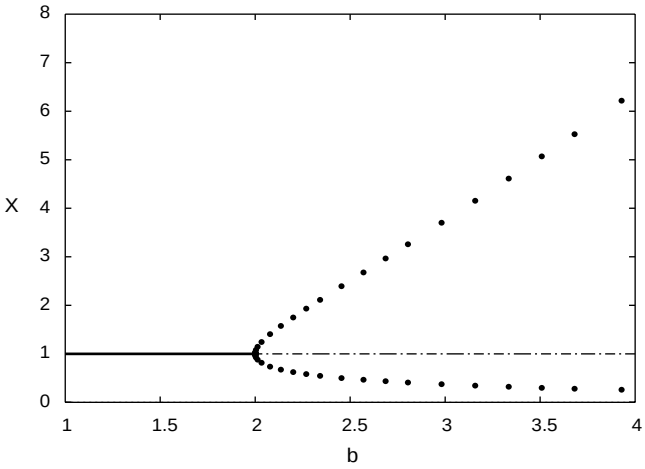

Figure A.11 Numerically computed bifurcation diagram for the Brusselator as the parameter b varies. Stable fixed points are solid and unstable are dashed. Stable periodic orbits are filled circles.

As an example, we consider the Brusselator, a classic model for chemical oscillations:

$$\frac{dx}{dt} = a - (b+1)x + x^2 y, \quad \frac{dy}{dt} = bx - x^2 y.$$

The fixed points for this are $(x, y) = (a, b/a)$ and the linearization about the fixed point is

$$A = \begin{pmatrix} b-1 & a^2 \\ -b & -a^2 \end{pmatrix}.$$

The determinant of A is $a^2 > 0$. The trace is $b - 1 - a^2$. Thus, if b is the parameter, then as b increases past $1 + a^2$ there will be a Hopf bifurcation. The full bifurcation diagram is shown in Fig. (A.11).

A.6 Perturbation theory

As we have noted, nonlinear differential equations are not readily solved. In fact, even linear equations cannot be solved in closed form if the coefficients are nonconstant in time. For this reason, one of the most powerful tools in applied math is perturbation theory. In perturbation theory, some parameter in the equation is assumed to be small. Then it is set to zero and this results in a simpler system of equations which can be solved. The idea is to assume that when the parameter is not zero, then we can use the simple case as a starting solution and expand the full solution in a power series in the small parameter. Typically, we only need to expand the series to one otr two terms to see the effects on the solution.

A.6.1 Regular perturbation.

Let us first consider the general solution and then work some examples. Consider

$$\frac{dx}{dt} = f(x, \epsilon) \tag{A.52}$$

where ϵ is a small parameter. Suppose that we can solve the equation with $\epsilon = 0$, that is, we can find a solution, $x_0(t)$ to

$$\frac{dx}{dt} = f(x, 0).$$

Formally, lets look for a solution of the form:

$$x(t, \epsilon) = x_0(t) + \epsilon x_1(t) + \epsilon^2 x_2(t) + \dots \tag{A.53}$$

and substitute this into Eqn. (A.52). This leads to a sequence of equations:

$$\begin{aligned}
\frac{dx_0}{dt} &= f(x_0, 0) \\
\frac{dx_1}{dt} &= D_x f(x_0, 0)x_1 + D_\epsilon f(x_0, 0) \\
\frac{dx_2}{dt} &= D_x f(x_0, 0)x_2 + D_{x\epsilon} f(x_0, 0)x_1 + \frac{1}{2}(D_{xx} f(x_0, 0)x_1^2 + D_{\epsilon\epsilon} f(x_0, 0)
\end{aligned}$$

where D_a is the derivative of f with respect to a evaluated at $x = x_0, \epsilon = 0$. Note that all but the first equation are linear. If the linear equation

$$\frac{dx}{dt} - D_x f(x_0, 0)x = g$$

is invertible, then we can continue this series method forever. As we will see later, when the equation is not invertible, then we run into problems and other techniques are required. Another situation that can arise is when the small parameter multiplies dx_k/dt for one of the variables x_k. We will also consider this type of perturbation below.

Let's look at a simple example. Consider the differential equation for population growth subject to periodic forcing:

$$\frac{dx}{dt} = x(1 + \epsilon \sin(\omega t) - x).$$

We are interested in the steady state behavior; thus we want to find solutions which are periodic or constant. Obviously, $x = 0$ is a solution for any ϵ but this solution is of no interest as it is unstable. When $\epsilon = 0$, another solution is $x = 1$. We will perturb from this solution:

$$x(t, \epsilon) = 1 + \epsilon x_1 + \epsilon^2 x_2 + \dots.$$

Substituting this into the equation, we get

$$\frac{dx_1}{dt} = -x_1 + \sin(\omega t)$$

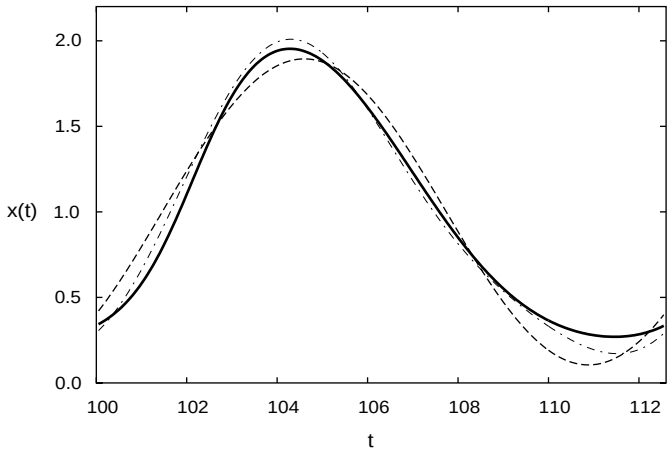

Figure A.12 The true solution (solid lines) and the first two terms in the perturbation series for the linear time-dependent logistic equation.

$$\frac{dx_2}{dt} = -x_2 + -x_1^2 + x_1 \sin(\omega t)$$

and so on. The x_1 equation has a periodic solution:

$$x_1(t) = \frac{\sin(\omega t) - \omega \cos(\omega t)}{1 + \omega^2}.$$

Thus, to order ϵ

$$x(t) = 1 + \epsilon \frac{\sin(\omega t) - \omega \cos(\omega t)}{1 + \omega^2}$$

To do even better, we can go to the next order. A simple bit of calculus shows that

$$x_2(t) = \frac{2\omega^4 \cos(2\omega t) - 5\omega^3 \sin(2\omega t) - 4\omega^2 \cos(2\omega t) + \omega \sin(2\omega t)}{/} 2 + 12\omega^2 + 18\omega^4 + 8\omega^6$$

Fig. (A.12) shows the numerical solution to the sample problem as well as the approximations, $y_1(t) = 1 + \epsilon x_1(t)$ and $y_2(t) = y_1(t) + \epsilon^2 x_2(t)$ for $\epsilon = 1$ and $\omega = 0.5$. (For smaller values of ϵ and larger values of ω the approximation is much better.)

A.6.2 Resonances.

In many applied problems, the general perturbation scheme describes above breaks down. Typically, this arises when there is a family of solutions to the lowest order perturbation and the linear equations that arise from higher order perturbations are not invertible.

A typical example of this would be perturbation of eigenvalues of a matrix. For example, suppose that the matrix A_0 is simple and we can find the eigenvalues easily.

We now ask what the eigenvalues of the matrix $B = A_0 + \epsilon A_1$ are. Suppose that λ_0 is an eigenvalue and v_0 is the corresponding eigenvector. That is

$$A_0 v_0 = \lambda_0 v_0.$$

To find the eigenvalue of B near λ_0 we suppose that both the eigenvalue and the eigenvector depend on ϵ :

$$v(\epsilon) = v_0 + \epsilon v_1 + \dots$$
$$\lambda(\epsilon) = \lambda_0 + \epsilon \lambda_1 + \dots$$

Making the substitutions we get

$$(A_0 - \lambda_0 I)v_1 = \lambda_1 v_0 - A_1 v_0 \equiv w. \tag{A.54}$$

There are two unknowns, v_1 and λ_1. However, the matrix $C = A_0 - \lambda_0 I$ is not invertible, so we cannot expect to solve this unless λ_1 is chosen so that w is in the range of the matrix C. This condition uniquely determines the parameter λ_1. Then we can solve for v_1.

How do we know when a vector w is in the range of a matrix M? The following theorem tells us precisely the conditions:

Fredholm Alternative Theorem. *The matrix equation*

$$My = w$$

has a solution y if and only if $w \cdot q = 0$ for every solution q to the equation $M^* q = 0$. The matrix M^* is the transpose complex conjugate of the matrix M.

An analogous theorem holds for many other linear operators. Returning to Eqn. (A.54), let q_0 be the solution to

$$C^T q_0 = 0 \qquad q_0 \cdot v_0 = 1.$$

Then the Fredholm Alternative Theorem implies that we must have

$$q_0 \cdot (\lambda_1 v_0 - A_1 v_0) = 0$$

or

$$\lambda_1 = q_0 \cdot A_1 v_0.$$

Another classic example is to find a periodic solution to a weakly nonlinear differential equation. The van der Pol oscillator is the standard example:

$$\ddot{x} + x = \epsilon \dot{x}(1 - x^2). \tag{A.55}$$

We seek periodic solutions to this problem. Expanding $x(t)$ in epsilon:

$$x(t) = x_0(t) + \epsilon x_1(t) + \dots$$

and substituting into Eqn. (A.55) we get

$$\ddot{x_0} + x_0 = 0$$
$$\ddot{x_1} + x_1 = \dot{x_0}(1 - x_0^2).$$

The solution to the first equation is

$$x_0(t) = A\cos t + B\sin t.$$

Note that we can rewrite this as $x_0(t) = C\cos(t+\phi)$ where ϕ is a phase shift. Since the equation is autononmous, there is always an arbitrary phase shift, so we can set this to zero. In other words, we can assume $x_0(t) = A\cos t$ where A is an arbitrary amplitude as yet unknown. The second equation is:

$$\ddot{x_1} + x_1 = -A\sin t(1 - A^2\cos t).$$

This does not generally have a periodic solution. In fact, it is easy to solve explicitly (using a symbolic algebra program, like Maple). The key point is that the solution will be of the form:

$$x_1(t) = P(t) + tQ(t)$$

where $P(t), Q(t)$ are periodic. Unless $Q(t) = 0$, the perturbed solutions $x_1(t)$ will not be periodic so, we must make $Q(t) = 0$. A simple calculation reveals that

$$Q(t) = A\frac{4 - A^2}{8}\cos t$$

thus, we choose $A = 2$ and to lowest order

$$x(t) = 2\cos t.$$

Exercises

1. Find the periodic solution to the perturbed differential equation:

$$\ddot{x} + x = \epsilon\dot{x}(a + bx^2 - x^4)$$

A.6.3 Singular Perturbation Theory

In many physiological systems there are vast differences in the time scales involved in the phenomena. For example in a bursting neuron, there is the period between bursts compared with the interspike interval of the action potential within a burst. Some variables may act much more slowly than other variables while others act much more rapidly. Consider for example the simple linear differential equation:

$$\epsilon\frac{dx}{dt} = y - x \quad \frac{dy}{dt} = -x,$$

along with initial conditions $y = 1, x = 0$. We can easily solve this exactly using the methods of the previous section for any value of ϵ. However, typically, in a real problem, the solutions are not so readily obtained. Let's suppose that we can set $\epsilon = 0$. Then we must have $0 = y - x$ or $x = y$. Thus our problem is now:

$$\frac{dy}{dt} = -y \quad y(0) = 1$$

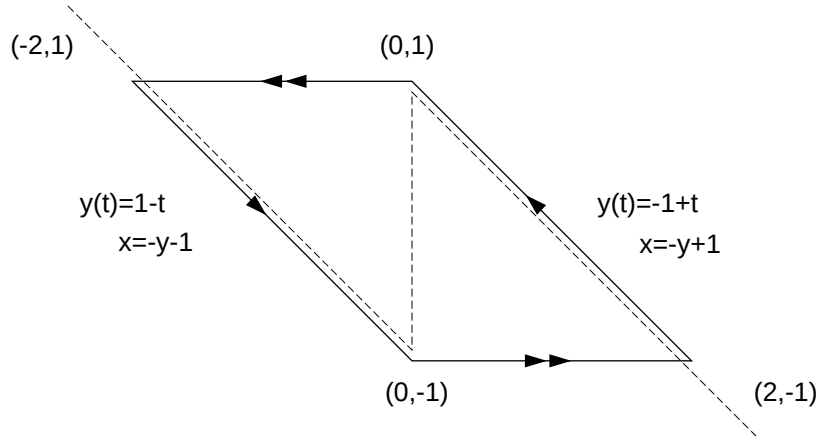

Figure A.13 x-nullclines for the relaxation oscillator example.

which has a solution $y(t) = \exp(-t)$. Furthermore, since $x = y$, we also have $x(t) = \exp(-t)$. Unfortunately, our "solution" does not satisfy the initial conditions $x(0) = 0$. Because we have reduced the order of the differential equation from 2 to 1, we cant expect to generally find a solution for all initial conditions. This is why the problem is said to be *singular.*

The way that we can fix this is to use a technique called matching. A complete description of matching goes well beyond this book, so we will just sketch this and another example. There are more examples throughout the text. The idea is to rescale time. Since the problems we are having occur at $t = t_0 = 0$, we introduce a new variable $\tau = (t - t_0)/\epsilon$. Under this change of variables our equation is

$$\frac{dX}{d\tau} = Y - X \quad \frac{dY}{d\tau} = -\epsilon X.$$

(I have used capitalized letters to differentiate these solutions from the $t-$dependent solutions.) Now, we see that Y is "slow" in the new time scale. Set $\epsilon = 0$. This means that $dY/d\tau = 0$ so that Y is constant. The obvious constant to use it the initial value of Y, so we substitute $Y = 1$ into the X equation:

$$\frac{dX}{d\tau} = 1 - X \quad X(0) = 0.$$

The solution to this is $X(\tau) = 1 - \exp(-\tau)$. Thus we have two sets of solutions, $(x(t), y(t))$ and $(X(\tau), Y(\tau))$. The (X, Y) solutions are valid for times near zero and the (x, y) are valid for larger times. Thus, to obtain the full solution, we add these two together and subtract the "common" part. To see what the common part is, we replace τ by t/ϵ in the (X, Y) system and t by $\epsilon\tau$ in the (x, y) system. We take the limit as $\epsilon \to 0$ and obtain $(1, 1)$ for both sets of limits. This is the common part. Thus, our approximate solution is $(X(\tau) + x(t) - 1, Y(\tau) + y(t) - 1)$. Putting everything in terms

of the original time, t, we obtain

$$x_c(t) = e^{-t} - e^{-t/\epsilon} \quad y_c(t) = e^{-t}$$

I close this section with another example that produces a singular nonlinear oscillator. The equations are

$$\epsilon \frac{dx}{dt} = -x + \text{sgn}(x) - y \quad \frac{dy}{dt} = y + x.$$

sgn(x) is the signum function, it is +1 for $x > 0$ and -1 for $x < 0$. The nullclines are depicted in Fig. (A.13). For ϵ small, we expect that the solution will hug the $x-$nullcline since we must have $-x+\text{sgn}(x)-y$ nearly zero; the equation for the x-nullcline. Setting $\epsilon = 0$ we must solve

$$-x + \text{sgn}(x) - y$$

for x in terms of y. Unfortunately, for y between -1 and 1 there are two roots $x = -y \pm 1$. For the moment, lets pick $x = -y + 1$. We must have $-y + 1 > 0$ since our choice of $+1$ for sgn(x) assumes that $x > 0$. Substituting this into the y equation yields

$$\frac{dy}{dt} = 1$$

so that $y(t) = y(0) + t$. Notice that as long as $y(t) < 1$ then this is a valid solution since $x > 0$. However, eventually $y(t)$ will exceed 1 and our root $x = -y + 1$ is no longer valid. So, what happens? Let t_0 be the time at which $y(t) = 1$. To see what happens, we must once again, introduce a scaled time, $\tau = (t - t_0)/\epsilon$. Then our equations are

$$\frac{dX}{d\tau} = -X + \text{sgn}(X) - Y \quad \frac{dY}{d\tau} = \epsilon(Y + X).$$

Setting $\epsilon = 0$, this means that Y must be constant. Since $y(t_0) = 1$ we will take $Y = 1$ as the constant. We must solve

$$\frac{dX}{d\tau} = -X + \text{sgn}(X) - Y \quad X(0) = 0.$$

Note that for any $\tau > 0$, $X(\tau)$ is negative, so that sgn$(X) = -1$ and

$$X(\tau) = -2(1 - \exp(-\tau)).$$

This says that in the expanded time scale, $X(\tau)$ will drop from 0 down to -2. All the while, Y is essentially constant at 1. Once X has made the jump from 0 to -2, we can set $y = 1, x = -2$ and solve the $y(t)$ equation again. In this case, $x + y = -1$ since sgn$(x) = -1$ and we must solve

$$\frac{dy}{dt} = -1 \quad y(0) = 1.$$

The solution to this is $y(t) = 1 - t$. As above this is only valid as long as $x = -y + \text{sgn}(x) = -y - 1$ is negative. That is, as long as $y(t) > -1$. Once $y(t)$ crosses -1, then x will be positive and we will have to jump back across to $x = +2$ keeping $y = -1$

constant again using the rescaled time. In retrospect, we see now that in the calculation on the right hand branch (when $x > 0$), the correct initial condition for y is $y(0) = -1$.

This completes the calculation of the singular trajectory. Fig. (A.13) illustrates this. We have the following:

$$\begin{aligned} y(t) = -1 + t \quad x(t) = 2 - t \text{ for } 0 < t < 2 \\ y(t) = 1 - (t-2) \quad x(t) = -2 + (t-2) \text{ for } 2 < t < 4 \end{aligned}$$

in the normal time coordinates. In the scaled time coordinates, $x(t)$ jumps from 0 to -2 while $y = 1$ satisfying:

$$x(t) = -2(1 - \exp((t-2)/\epsilon))$$

and from 0 to 2 while $y = -1$

$$x(t) = 2(1 - \exp(-(t-4)/\epsilon)).$$

The period of the oscillation is 4 to lowest order. $y(t)$ is continuous along the trajectory. The complete solution for $x(t)$ over one period is

$$\begin{aligned} x(t) = 2 - t - 2\exp(-t/\epsilon) \text{ for } 0 \le t < 2 \\ x(t) = t - 4 + 2\exp((2-t))/\epsilon)] \text{ for } 2 \le t < 4. \end{aligned}$$

A.7 Appendix

A.7.1 Matrix and Vector Manipulation

Matrices can be multiplied, added, multiplied by scalar numbers, and differentiated according to the rules of linear algebra. Here we summarize these results for the 2×2 matrices and two-component column vectors that appear in Section (**??**). The matrix $\hat{A}$ multiplying the vector $\mathbf{x}$ acts a linear operator that produces a new vector, $\mathbf{z}$, according to the formula:

$$\mathbf{z} = \hat{A}\mathbf{x} = \begin{pmatrix} a_{11} & a_{12} \\ a_{21} & a_{22} \end{pmatrix} \begin{pmatrix} x_1 \\ x_2 \end{pmatrix} = \begin{pmatrix} a_{11}x_1 + a_{12}x_2 \\ a_{21}x_1 + a_{22}x_2 \end{pmatrix} \tag{A.56}$$

It can be verified using Eqn. (A.56) that the identity matrix, $\hat{I} = \begin{pmatrix} 1 & 0 \\ 0 & 1 \end{pmatrix}$, leaves vectors unchanged, *i.e.*, $\mathbf{z} = \hat{I}\mathbf{x} = \mathbf{x}$. Matrices can be added together, as can vectors, using the rules:

$$\hat{A} + \hat{B} = \begin{pmatrix} a_{11} + b_{11} & a_{12} + b_{12} \\ a_{21} + b_{21} & a_{22} + b_{22} \end{pmatrix} \text{ and } \mathbf{x} + \mathbf{y} = \begin{pmatrix} x_1 + y_1 \\ x_2 + y_2 \end{pmatrix}. \tag{A.57}$$

To multiply either a matrix or a vector by a number, c, each component is multiplied by c, *e.g.*

$$c\hat{A} = c\begin{pmatrix} a_{11} & a_{12} \\ a_{21} & a_{22} \end{pmatrix} = \begin{pmatrix} ca_{11} & ca_{12} \\ ca_{21} & ca_{22} \end{pmatrix} \tag{A.58}$$

Differentiation of matrices and vectors is also carried out on each component separately. Thus

$$d\mathbf{x}/dt = \begin{pmatrix} dx_1/dt \\ dx_2/dt \end{pmatrix} \tag{A.59}$$

The *trace*, *determinant*, and *descriminant* are important scalars that characterize matrices and that appear in the solution to Eqn. (A.2). We use the short hand notation $tr\hat{A}$ for the trace of $\hat{A}$, $det\hat{A}$ for its determinant, and $disc\hat{A}$ for the descriminant. In terms of matrix elements they are defined as:

$$tr\hat{A} = a_{11} + a_{22} \tag{A.60}$$

$$det\hat{A} = a_{11}a_{22} - a_{21}a_{12} \tag{A.61}$$

$$disc\hat{A} = (tr\hat{A})^2 - 4det\hat{A} \tag{A.62}$$

For example, for the matrix

$$\hat{A} = \begin{pmatrix} 1 & -1 \\ 3 & 6 \end{pmatrix}, \tag{A.63}$$

$tr\hat{A} = 7$, $\det\hat{A} = 9$, and $disc\hat{A} = 13$.

The inverse of a matrix is the generalization of division by a number. The inverse of $\hat{A}$ is written as $\hat{A}^{-1}$ and is a matrix with the property that

$$\hat{A}^{-1}\hat{A} = \hat{I} \tag{A.64}$$

with $\hat{I}$ the identity matrix. The inverse of a matrix is useful in solving linear algebraic equations. For example, the solution of the linear equation

$$\hat{A}\mathbf{x} = \mathbf{y}, \tag{A.65}$$

has the solution

$$\mathbf{x} = \hat{A}^{-1}\mathbf{y}, \tag{A.66}$$

which can be verified by multiplying both sides of Eqn. (A.65) by $\hat{A}^{-1}$ and using Eqn. (A.64). For a 2×2 matrix it is easy to verify by carrying out the matrix multiplication in Eqn. (A.64) that if $\hat{A}$ is not *singular*, *i.e.*, as long as $det\hat{A} \neq 0$, then

$$\hat{A}^{-1} = \frac{1}{det\hat{A}}\begin{pmatrix} a_{22} & -a_{12} \\ -a_{21} & a_{11} \end{pmatrix}. \tag{A.67}$$

A.7.2 A brief review of power series.

One of the most useful tehniques in all of applied mathematics is the method of power series expansion. The basic idea is that many functions can be expressed a series in one or more variables. For example, the familiar exponential function can be written as

$$e^t = 1 + \frac{t}{1!} + \frac{t^2}{2!} + \ldots + \frac{t^n}{n!} + \ldots$$

or more compactly as

$$e^t = \sum_{n=0}^{\infty} \frac{t^n}{n!}$$

where we define $0! = 1$. The series converges for all t both real and complex. Given a function $f(t)$ and a point $t = t_0$, suppose that all the derivatives of f at the point t_0 are defined. Then we can formally develop a power series approximation of the function f around the point t_0. The formal power series is

$$f(t) = \sum_{n=0}^{\infty} f^{(n)}(t_0) \frac{(t - t_0)^n}{n!}. \tag{A.68}$$

Here $f^{(k)}(t_0)$ is the kth derivative of the function f evaluated at the point t_0. That is, given the derivatives of a function at a point, we can approximate the function over some interval containing that point by using a series approximation. This series is called a *Taylor series of f about the point t_0*. When the point, $t_0 = 0$, the series is often called a Maclauren series.

If all of the derivatives of the given function exist at the point t_0, then the finite approximation to the taylor series:

$$S_N(t) = \sum_{n=0}^{N} f^(n)(t_0) \frac{(t - t_0)^n}{n!}$$

is also defined for all t since it is just a finite sum of polynomials. We say that the series *converges* for t in some interval, I, containing t_0 if the limit of $S_N(t)$ exists as $N \to \infty$ for all t in I. The interval, I for which convergence is obtained is called the *interval of convergence* for the series. For the exponential series given above, the interval of convergence is the whole real line. Infinite series do not always converge on the whole line. For example the geometric series

$$S(t) = 1 + t + t^2 + t^3 + \ldots + t^n + \ldots$$

converges for $|t| < 1$. A useful test for the convergence of a series of the form

$$S = \sum_{n=0}^{\infty} a_n$$

is the ratio test. Let $R_n = |a_{n+1}/a_n|$. If

$$\lim_{n \to \infty} R_n < 1$$

then the series converges. Let's apply this to the exponentia series above. $a_n = t^n/n!$ so $|a_{n+1}/a_n = t/(n+1)|$ and the limit of this as n goes to infinity is zero for any finite t so that the series converges for all t.

Here are some examples. Let's find a series approximation for $f(0) = \sin(t)$ about $t = 0$. Note that $f(0) = 0, f'(0) = 1, f''(0) = 0, f'''(0) = -1$ and the higher derivatives just cycle arount these numbers. That is derivatives of order 1,5,9, etc are equal to 1, those of order 3,7,11, etc are equal to -1, and all others are zero. Thus

$$\sin(t) = t - \frac{t^3}{3!} + \frac{t^5}{5!} + \ldots + (-1)^m \frac{t^{2m+1}}{(2m+1)!} + \ldots.$$

The ratio $|a_{m+1}/a_m| = t^2/(2m+2)(2m+3)$ which tends to 0 as m goes to infinity so the sine series converges for all t.

You can similarly verify the

$$\cos(t) = \sum_{m=0}^{\infty} (-1)^m \frac{t^{2m}}{(2m)!}.$$

As a final example, consider the series for the square root function evaluated at $t = 1$. We have the following first few derivatives:

$$f(1) = 1 \quad f'(1) = \frac{1}{2} \quad f''(1) = \frac{-1}{2}\frac{1}{2} \quad f'''(1) = \frac{-3}{2}\frac{-1}{2}\frac{1}{2}$$

Thus the n^{th} derivative $(n > 1)$ is

$$c_n = (-1)^{n+1} \frac{(2n-3)(2n-5)\ldots 1}{2^n}.$$

Thus,

$$\sqrt{(t)} = 1 + \frac{1}{2}(t-1) + \sum_{n=2}^{\infty} (-1)^{n+1} \frac{c_n (t-1)^n}{n!}.$$

We can apply the ratio test to this, noting that $|c_{n+1}/c_n| = n - \frac{1}{2}$ so that

$$R_n = |t-1|(n - \frac{1}{2})/(n+1).$$

As $n \to \infty$ this ratio goes to $|t-1|$. The interval of convergence satisfies $|t-1| < 1$ or $0 < t < 2$.

Exercises

1. Using manipulations comparable to those used to obtain Eqn. (A.10) show that x_2 in Eqn. (A.5) also satisfies the second order equation (Eqn. (A.10)).
2. Show by substitution that if $\mathbf{x}'$ and $\mathbf{x}$ are two different solutions to Eqn. (A.6), then $c'\mathbf{x}' + c\mathbf{x}$ is also a solution.

3. Show by substition into Eqn. (A.22) that $c't\exp(\lambda t)$ is a second solution to Eqn. (A.10) when $disc\hat{A} = 0$. [Hint: Recall that $(t\exp(\lambda t)) = (1+\lambda t)\exp(\lambda t)$; use this to show that $(t\exp(\lambda t)) = \lambda(2+t)\exp(\lambda t)$.]
4. Show that any 2×2 matrix of the following form $\hat{A} = \begin{pmatrix} a & b \\ 0 & a \end{pmatrix}$ with a and b arbitrary real numbers has $disc\hat{A} = 0$ and $\lambda = a$.
5. Use the solution to the characteristic equation for $\hat{A}$, Eqn. (A.14), to show that $tr\hat{A} = \lambda_+ + \lambda_-$ and that $det\hat{A} = \lambda_+\lambda_-$.
6. Verify that the expression for the eigenvector of $\hat{A}$ given in Eqn. (A.32) is correct by multiplying that expression by $\hat{A}$. [Hint: You will need to use the fact that $det\hat{A} = \lambda^2 - (a_{11} + a_{22})\lambda$ as follows from (Eqn. (A.14)).]
7. The following *XppAut* file can be used to solve the general two-variable linear equations (Eqn. (A.4))-(Eqn. (A.5)):

```
x1(0)=1
x2(0)=1
param a11=1,a12=0,a21=0,a22=1
param y1=0,y2=0
dx1/dt=a11*x1+a12*x2+y1
dx2/dt=a21*x1+a22*x2+y2
done
```

   Use this file to find $x_1(t)$ and $x_2(t)$ for the following matrices: $\hat{A} = \begin{pmatrix} 0 & -1 \\ 1 & 0 \end{pmatrix}$, $\hat{A} = \begin{pmatrix} 1 & -1 \\ 1 & 1 \end{pmatrix}$, and $\hat{A} = \begin{pmatrix} -2 & 1 \\ -3 & 1 \end{pmatrix}$ and $y_1 = y_2 = 0$. Determine the characteristic values of all three matrices and compare your solutions using *XppAut* to the solutions that you would expect based on the characteristic values. Explore how the solutions change when you change the values of y_1 and y_2.
8. Use *XppAut* (*cf.* previous problem) to solve Eqs. (Eqn. (A.4))-(Eqn. (A.5)) for the matrix $\hat{A} = \begin{pmatrix} 1 & -1 \\ 3 & 6 \end{pmatrix}$ and $y_1 = 1$ and $y_2 = 2$. Compare your result to that it Eqn. (A.28).
9. Use *XppAut* to make a phase plane plot of the solutions to the linear ODEs plotted as time series in Figs. 2.1A-C. [Hint: Use the *ViewAxes* option and choose a 2D plot with x_1 for the X-axis and x_2 for the Y-axis.] Use the Addco option in the *Data Viewer* window to add a new column representing $\dot{x}_1$ and experiment with various possible combinations of variables to plot.
10. Show that the velocity vector for a point in phase space is parallel to the trajectory at the point. [Hint: Calculate the slope of the trajectory, dx_2/dx_1, using the ODEs.]
11. Show that the nullclines for the general 2×2 linear equations (Eqn. (A.4)) and (Eqn. (A.5)) are linear.

12. Using the result in Eqn. (A.34) verify the statement in Section 2.3 that for a saddle point trajectories that start in the direction of the positive eigenvector grow away from the steady state exponentially, while those in the direction of the negative eigenvector approach the steady state exponentially.
13. Write an *XppAut* file to solve the ODEs for the voltage gated membrane in Eqs. (Eqn. (A.36)) and (Eqn. (A.37)) using the parameters in the legend of Fig. 2.5. Use the *Nullcline* option to draw the nullclines and the *Sing pt* option to find the steady states and eigenvalues. [Note: The eigenvalues will appear in the window that you used to start *XppAut*, whereas the values of V and n at the steady state will appear in window titled *equilibria*. The *equilibria* window also gives information about the number of complex eigenvalues with negative real parts, etc.] Use the *Initial-conds/(M)ouse* option to check how the trajectories depend on initial conditions. Check that the trajectories cross the nullclines properly. Alter the values of $V_{0.5}$, V_{rev}, and I_{app} to see how the nullclines change. How do these parameter changes influence the stability of the steady state?
14. Construct the solution to the initial value problem that arises in enzyme kinetics

$$x' = 1 - xy \quad \epsilon y' = -xy + 1 - y$$

with the initial conditions $x(0) = 0, y(0) = 0$.
15. Find the periodic solution to

$$\epsilon x' = f(x) - y \quad y' = x$$

where

$$f(x) = \begin{cases} -x - 2 & \text{for} \quad x < -1 \\ x & \text{for} \quad -1 \leq x \leq 1 \\ -x + 2 & \text{for} \quad x > 1 \end{cases}$$

16. Develop Taylor series for the following functions

- $\cos(t)$ around $t = 0$
- $\ln(t)$ around $t = 1$.
- $\exp(t^2)$ around $t = 0$. (Hint, use the exponential series we have already determined.)